Coal Pyrolysis Models for Use in Massively Parallel Oxyfuel-Fired Boiler Simulations

Andrew Richards

A dissertation/thesis submitted to the faculty of
Brigham Young University
in partial fulfillment of the requirements for the degree of

Doctor of Philosophy

Thomas H. Fletcher, Chair
David O. Lignell
Matthew J. Memmott
Andrew R. Fry

Department of Chemical Engineering

Brigham Young University

ABSTRACT

Coal Pyrolysis Models for Use in Massively-parallel
Oxy-fuel-fired Boiler Simulations

Andrew Richards
Department of Chemical Engineering, BYU
Doctor of Philosophy

Accurately modeling key aspects of coal combustion allows for the virtual testing and application of new technologies and processes without the need for investments in lab- and pilot-scale facilities, since such facilities may only be used for a few small tests. However, modeling of subprocesses must not only be accurate but computationally efficient. Modeling of coal devolatilization reactions and processes are one of the important parts of large-scale simulations of coal combustion systems. The work presented here details efforts to improve the modeling of coal devolatilization processes in massively-parallel simulations of coal combustors, including: (1) devolatilization rate/yield models, (2) modeling various chemical, physical, and thermodynamic properties of coal, char, and tar (including structural NMR parameters like carbon aromaticity, the elemental composition of coal char and tar, and the heating value of coal-based and other fuels), and (3) the application of various simplifying assumptions to equilibrium calculations of coal devolatilization products using multiple levels of fuel mixture fractions. Using several different advanced statistical methods, the models discussed here were developed and improved by careful comparison with large sets of experimental data. The advanced statistical methods and procedures show large improvements in these models over previous work.

Keywords: coal, pyrolysis, devolatilization, yield, rate, modeling, statistical analysis

ACKNOWLEDGEMENTS

This dissertation may hold my name as the single author, but there are many people who have worked tirelessly behind the scenes to support me in my research and other aspects of my life. There have been too many to name personally here, however, there are a few that have been the most instrumental for me throughout my graduate student career. First, I would like to thank my advisor, Dr. Thomas H. Fletcher, for all his support and guidance, not just on the technical aspects of my project, but to help me become a better researcher, student, and person. He has helped me to think about and approach problems in ways I couldn't have done before I met him. I would also like to thank my current committee members, Dr. Lignell, Dr. Memmott, and Dr. Fry for their support and guidance. In addition to my current committee, I was also fortunate to have other past committee members, Dr. Pitt from Brigham Young University and Dr. Smith from the University of Utah, who have helped me tremendously.

I also would like to express my gratitude for those I met and worked with during my brief time at Sandia National Laboratories. These researchers helped me to discover a passion for computer modeling and statistical analysis that I never thought I would have. In particular, Dr. Christopher Shaddix and Dr. Habib Najm were instrumental in helping me to learn how to use advanced statistical tools in my research.

I have been able to supervise a number of undergraduate students in my research, many of whom helped to perform experiments with the hope of using the information to validate the modeling I worked on. These undergraduates went above and beyond to improve the work I asked them to complete: Spencer Jensen, Brighton Rust, Garrett Horton, Samantha Schacterle, Derek Holmstead, Sam Valdez, Colson Johnson, Gustavo Preciado, Tim Shutt, Denver Haycock,

and Jacob Frandsen. These students along with other graduate students and colleagues from both BYU and the UofU helped me to think about my research in different ways.

I would also like to thank my parents for supporting me not only in my graduate work, but in all aspects of my life. My brothers also helped in a lot of ways, including their prodding and gentle teasing about becoming a “doctor,” but not a medical doctor. I have also had many other extended family members offer encouragement and support throughout this process, as well as many dear friends I have been fortunate to meet along the way.

Finally, the bulk of this work would not have been possible without funding. This material is based on work supported in part by the Department of Energy, National Nuclear Security Administration, under Award Number DE-NA0002375.

Funding for this work was also provided by the Department of Energy through the Carbon Capture Simulation Initiative. This report was prepared as an account of work sponsored by an agency of the United States Government. Neither the United States Government nor any agency thereof, nor any of their employees, makes any warranty, express or implied, or assumes any legal liability or responsibility for the accuracy, completeness, or usefulness of any information, apparatus, product, or process disclosed, or represents that its use would not infringe privately owned rights. Reference herein to any specific commercial product, process, or service by trade name, trademark, manufacturer, or otherwise does not necessarily constitute or imply its endorsement, recommendation, or favoring by the United States Government or any agency thereof. The views and opinions of authors expressed herein do not necessarily state or reflect those of the United States Government or any agency thereof.

TABLE OF CONTENTS

LIST OF TABLES

LIST OF FIGURES

NOMENCLATURE

Parameter	Description
A	Arrhenius pre-exponential factor, used in pyrolysis yield/rate models, see Section 2.3.1 and Chapter 4
a, b, c, etc.	1. Fitting coefficients, see Section 2.3.2 and Chapter 6 2. Fitting coefficients in Utah model ultimate yield curve, see Section 2.3.1 and Chapter 4 3. average molar compositions of a generic fuel used for complete combustion calculations, see Section 2.3
$a_{i,j}$	The number of atoms of element j in component i (for example, a sample fuel of benzene, C_6H_6 would have an a_{ij} of 6 for both carbon and hydrogen)
α	Stoichiometric amount of oxygen needed for complete combustion
C	1. Unreacted or raw coal (see Section 2.3.1 and Chapter 4) 2. Carbon mass/mole fraction (see Sections 2.3.2, 2.3.3, 2.5, 5, 6, and 7) 3. Graphite mass/mole fraction, C(s) (see Chapter 8)
c_0	NMR structural parameter used in the CPD model and other correlation applications, corresponds to the number of stable bridges in the parent coal
c_i	Fitting coefficients, see Section 2.3 and Chapters 4 and 7
DI	Coal-specific index used in Biagini and Tognotti model, see Section 2.3.1 and Chapter 4
E or E_a	Arrhenius activation energy, used in pyrolysis yield/rate models, see Section 2.3.1 and Chapter 4
E_0	Mean activation energy in distributed activation energy models, see Section 2.3.1 and Chapter 4
E_{eff}	Effective activation energy, includes mean activation energy and the distribution in the distributed activation energy models
F	Modification factor of the Arrhenius pre-exponential factor, used in a few pyrolysis rate/yield models, see Section 2.3.1 and Chapter 4
f_a	Total or apparent aromatic carbon contribution, includes carbonyl contribution
f_a'	Corrected or true fraction of aromatic carbon, without the carbonyl contribution
f_i	Component mixture fraction of component i, e.g., mixture fraction of methane
H	Hydrogen mass/mole fraction
ΔH	Enthalpy of, used with heating values (ΔH_c), heat of vaporization (ΔH_{vap}), or heat of reaction (ΔH_r), units of MJ/kg used here
Infinity norm	Maximum absolute error over a domain, see Equation 2-16
K	The number of fitted coefficients pus one in a model of interest, used in AIC calculations, see Section 2.4.3
L_1 norm	A statistical measure of error, is the average absolute error over a domain, see Equation 2-14
L_2 norm	A statistical measure of error, is the Euclidian norm, shows the root-mean-squared error (RMSE), see Equation 2-15

M_{cl}	NMR structural parameter used in the CPD model and other correlation applications, corresponds to the average molecular weight of clusters in a coal molecule
M_{δ}	NMR structural parameter used in the CPD model and other correlation applications, corresponds to the average molecular weight of the side-chains or attachments to clusters
M_i	Mass of component i in a mixture
M_{ox}	Mass of oxidizer (e.g., air)
N	1. Nitrogen mass/mole fraction 2. Total number of data points in a data set (statistics) 3. Total number of components in a mixture
n	1. Used to tell a generic index value (statistics) 2. number of moles, e.g., moles of water, moles of component i, moles of oxidizer, etc.
N_{coeff}	Number of fitted coefficients in a model of interest
N_{var}	Number of independent variables in a model of interest
ν_i	Stoichiometric coefficient of compound i
O	Oxygen mass/mole fraction
p_0	NMR structural parameter used in the CPD model and other correlation applications, corresponds to the number of intact bridges in the parent coal
ϕ_i	Equivalence ratio of component i, see Equation 2-5
R	Ideal gas constant
R^2	Sometimes called coefficient of determination, used to measure goodness of fit of a model, see Equation 2-7
R^2/N_{coeff}	An "adjusted" R^2 value, used to determine model "utility," or how well a model fits compared to the number of fitted coefficients
S	Sulfur mass/mole fraction
σ_E	Standard deviation of the activation energy in distributed activation energy models, Section 2.3.1 and Chapter 4
$\sigma + 1$	NMR structural parameter used in the CPD model and other correlation applications, corresponds to lattice coordination number or total number of attachments per cluster
T or $T_{gas,max}$	Temperature, used in several different chapters. Particle temperature (Chapter 4), maximum gas temperature (Chapter 6), equilibrium gas temperature (Chapter 8)
T_{ignite}	Ignition temperature, used in the Utah model ultimate yield curve, see Section 2.3.1 and Chapter 4
T_{st}	Reference temperature constant, used in the Biagini and Tognotti model, see Section 2.3.1 and Chapter 4
t or t_{res}	Residence time
V	Volatiles yield, used in pyrolysis rate/yield models, see Section 2.3.1 and Chapter 4
V_{ASTM}	ASTM volatiles yield, found by a standard ASTM test
V_{max}	Maximum volatiles yield in a set of pyrolysis reaction measurements
V_{norm}	Normalized volatiles yield, ratio of V/V_{max}, can range from 0 to 1

V_∞	"Prescribed" ultimate volatiles yield, see Section 2.3.1 and Chapter 4
W_i or W_j	Molecular weight of component i or element j
X	Dry, ash-free mass fraction of any element (CHONS), see Appendix C
X_{coal}	A type of extent of reaction (pyrolysis), see Section 2.3.1 and Chapter 4
Y_i	1. Yield factor for kinetic step i, see Section 2.3.1 and Chapter 4 2. Mass fraction of component i
y	Observed or experimental value
$\hat{y}$	Predicted value
Y_{vol}	Percent volatiles of the total fuel mixture in mixture fraction analysis, (0 to 100%), a Y_{vol} of 0% means the fuel is completely char
Z	Generic distribution variable used in distributed activation energy models, see Section 2.3.1 and Chapter 4
Z_j	Elemental mixture fraction of element j (used here as CHONS elemental mixture fractions)
Abbreviations	
AIC	Akaike information criterion, see Section 2.4.3
AM	Aromaticity model, see Table 2-2
an	Coal rank, anthracite
Aus.	Country, Australia
Avg	Average
bit	Coal rank, bituminous
BT	Short for Biagini and Tognotti model, see Section 2.3.1 and Chapter 4
CFD	Computational fluid dynamics
Col	Country, Columbia
CPD	Chemical percolation devolatilization Model, see Section 2.3.1 and Chapter 4
DAEM	Distributed activation energy model, see Section 2.3.1 and Chapter 4
DAF	Dry, ash-free, a basis used in determining mass and mole fractions of elements and other measured quantities
DM	Devolatilization model, see Table 2-1
DMMF	Dry, mineral-matter free, a basis used in determining mass and mole fractions of elements and other measured quantities
$erfinv$	Inverse error function used in distributed activation energy models, MATLAB has built-in version, see Section 2.3.1 and Chapter 4
Germ	Country, Germany
HHV	Higher heating value, also known as gross calorific value, the heat of combustion with liquid water as a product of complete combustion
HM	Heating value model, see Table 2-3
Indo	Country, Indonesia
LHV	Lower heating value, also known as net calorific value, the heat of combustion with gaseous water as a product of complete combustion
Liq Gas	Liquids and gaseous fuels
Man	Country, Manchuria
Meta-an	Coal rank, meta-anthracite
MSE	Mean square error, see Equation 2-12

NASA-CEA	NASA's Chemical Equilibrium with Applications program (occasionally abbreviated as "NASA" in figure legends)
NMR	Nuclear magnetic resonance, used to determine several structural parameters of coal and other compounds
PAH	Polycyclic aromatic hydrocarbon, typically used in coal research as a generic name for tar precursors
Prop	Propellants and explosives
RE	Relative error, see Equation 2-13
RF	Short for Richards-Fletcher, or the modified two-step model with corrective factor, see Section 4.3.7
RFE	Short for Richards-Fletcher Energy, or the modified two-step model with distributed activation energy, see Section 4.3.8
RMSE	Root-mean-squared error, see L_2 norm
Semi-an	Coal rank, semi-anthracite
SK	Singh and Kakati models, see Table 2-2
SSE	Sum of squared error, see Equation 2-11
Tomasz	Author, Tomaszewicz
VUQ	Field of verification, validation, and uncertainty quantification, uses applied statistical methods to compare mathematical model predictions to real-world data
Subscripts	
0	Mixture fraction analysis, denotes a property of the oxidizer stream
1, 2, 3	Mixture fraction analysis, denotes a property of a fuel stream
char	A parameter of the char
coal	A parameter of the parent or raw coal
Genetti	Indicates an NMR parameter calculated using one of Genetti's correlations
H_2O	Indicates a property of water
i	Indicates an index value, used in mixture fraction analysis to specify a fuel component
$i0$	Corresponds to a parent coal composition, used in conjunction with X in Appendix C
j	Mixture fraction analysis, an index value corresponding to element j, (e.g., CHONS)
ox	A value corresponding to the oxidizer component, mixture fraction analysis
refit	Corresponds to NMR structural parameters using a re-fit of Genetti's original correlations
$stoich$	A property at stoichiometric conditions
tar	A parameter of the tar
vap	A parameter of vaporization (e.g., ΔH_{vap} is enthalpy of vaporization)
Superscripts	
1, 2, 3	Mixture fraction comparison, denotes elemental mixture fractions of a one-, two-, or three-mixture fraction method

1 INTRODUCTION

Many cultures have myths as to the origin of fire. Perhaps one of the best known in modern times is the Greek myth of Prometheus, who stole fire from the gods to bring to humans (Weinberg, 1975). No matter how man's pursuit of fire started, it has fascinated us for many thousands of years. Coal combustion research, by comparison, is a much more modern endeavor, with coal being used as a fuel in Europe in the 4th century BC and some reports in China as early as 1000 BC (Miller, 2017b). The U.S. Energy Information Agency puts out an Annual Energy Review (updated every month) with an overview of how much energy is produced in the U.S. from each source. In the first seven months of the year 2020, approximately 79 percent of the total energy in the U.S. came from fossil fuels, with almost 25 percent of the total energy from coal alone (EIA, 2020). While the percentage of energy production by coal has decreased in recent years, coal is still an important part of energy resources both in the U.S. and worldwide.

Coal reactions were modeled early in the 1960s, however, comprehensive models of coal combustion systems were not developed until the late 1970s to early 1980s (Smoot and Smith, 1985). While these early models represented a large step in coal research, modeling efforts have improved greatly to produce modern simulations of coal combustion applications that include multiple physics-based models to accurately reflect the chemical and physical processes of coal. Of particular interest is the process of coal devolatilization, which is the first major reaction that occurs in coal combustion (after any moisture loss due to particle heating). Many researchers

over the years have worked on efforts to improve modeling of coal devolatilization processes, detailed in the Literature Review chapter of this dissertation.

The work detailed in this dissertation details efforts to further improve various aspects of coal devolatilization modeling in massively-parallel simulations of coal combustors, including improvement in the following aspects of the devolatilization reaction: (1) devolatilization rate/yield models, (2) modeling various chemical, physical, and thermodynamic properties of coal, char, and tar (including structural NMR parameters like carbon aromaticity, the elemental composition of coal char and tar, and the heating value of coal-based and other fuels), and (3) the application of various simplifying assumptions to equilibrium calculations of coal devolatilization products using multiple levels of fuel mixture fractions. This research benefitted from several different statistical methods used to compare model predictions to real-world values.

2 LITERATURE REVIEW

The following literature review explores prior work done on coal pyrolysis modeling efforts, starting with pyrolysis rate/yield models, followed by the elemental and structural composition of coal and other coal-based fuels like char and tar, and finally some thermochemical properties and equilibrium states of coal-based and other fuels. This review also summarizes some of the key statistical methods used here. This review also summarizes the extensive searches of the literature for experimental data sets for the various modeling efforts discussed and presented here.

2.1 Coal Reactions

The chemical and physical structure of coal and its products has been the subject of a large history of research (Smoot and Smith, 1985; Smith et al., 1994). Coal is made up of organic matter that has been fossilized through a process called coalification. The organic material that eventually turns into coal is widely varied, and this variability remains in the coal as it forms. This variability comes in the form of a complex mix of aromatic structures, aliphatic bridges, and side chain groups. Because of this variability, no one coal molecule can be used to describe coal, either physically or in a combustion reaction mechanism. Several researchers have proposed potential “model” compounds of a coal molecule, which can be used to describe an “average” coal molecule. Figure 2-1 shows one of these proposed coal molecules, reprinted with permission from (Serio et al., 1987). Copyright (1987) American Chemical Society.

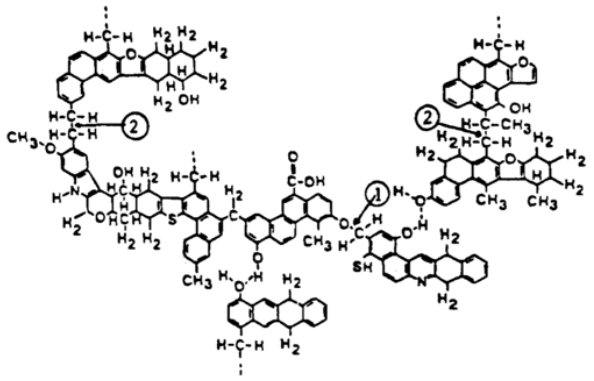

Figure 2-1. A proposed depiction of a coal molecule.

In large-scale simulations and modeling of coal science, average compositions, structures, and physical properties tend to be used in the place of complex reaction mechanisms and bulky molecular models (Smoot, 1981; Smoot et al., 1984; Williams et al., 2002). These average values can be found using a wide variety of standard tests, performed the same way every time. Details of the chemical composition can be found in a set of tests called a proximate (more general information, such as moisture and volatile content, etc.) and ultimate (elemental compositions of both organic and inorganic parts of a coal sample) analyses.

With the extra complexity in physical and chemical structure comes a more complex reaction scheme. Coal combustion is typically divided into several main reaction steps: primary pyrolysis, secondary pyrolysis, and char conversion. Figure 2-2 shows a simplified depiction of a coal combustion process. In reality, these reaction steps are generally much more complex than depicted here. These reactions are discussed at greater length below.

In coal research, several terms are used that may mean slightly different things in other fields of research. Parent coal refers to the raw, unreacted coal. The parent coal can be either pulverized to a fine powder (typical for industrial applications) or kept in larger chunks (for applications such as steel-making and smaller, less efficient power generation purposes). As heat

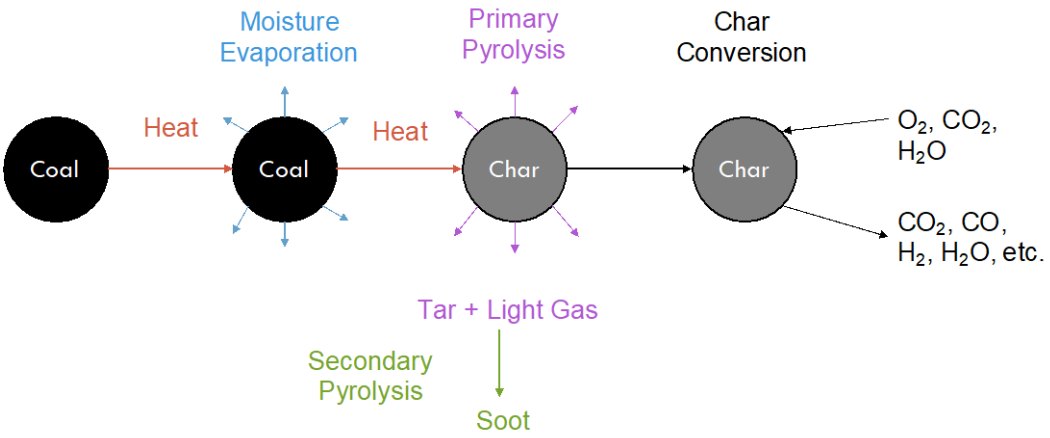

Figure 2-2. Simplified representation of coal particle reactions

is applied, inherent moisture evaporates at fairly low temperatures. At higher temperatures, the coal goes through what is called primary pyrolysis, which is a thermal decomposition reaction, meaning heat breaks apart weaker chemical bonds in the coal causing small molecules to vaporize into what are called the total volatiles. These total volatiles are broken into two main categories: tar (molecules that condense into a sticky liquid at room temperature) and light gases (molecules that remain as gas at room temperature). After primary pyrolysis (frequently called devolatilization), the solid that remains behind that is called char. These three compounds (char, tar, and light gases) make up the primary products of primary pyrolysis, which can then further react in various ways. These products can further completely oxidize with O_2 to form combustion products, or they can gasify with CO_2 and water vapor to form CO and H_2. Some of the tar can combine to form soot (Smoot and Smith, 1985; Smith et al., 1994).

2.1.1 Primary Pyrolysis

Pyrolysis generally occurs and is studied in an inert atmosphere, with little to no oxidizer present (Smith et al., 1994). With the coal introduced into a heated atmosphere, weaker bonds

start to break and release light gas molecules (from some of the smaller side-chains). As the particle temperature rises, some of the more stable bonds (aliphatic bridges between aromatic clusters) start to break and form a thick, viscous liquid called metaplast inside the coal structure. This liquid can further decompose as the coal temperature continues to rise, releasing more volatile compounds from the coal. As the temperature continues to rise and the pyrolysis reaction nears a quasi-steady state, the remaining liquid metaplast starts to reform some bonds in a process called cross-linking. When enough bonds have been reformed between the liquid metaplast and solid coal, the solid remaining is called the char.

2.1.2 Char Reactions

Two main sets of reactions occur during the char combustion phase: oxidation and gasification. These heterogeneous reactions typically occur with or just after primary pyrolysis, depending mainly on reaction temperatures (Saito et al., 1991). Oxidation and gasification may occur simultaneously, but the rates will depend on gas compositions near the coal. Oxidation reactions occur when O_2 diffuses to the surface of the coal and reacts primarily with carbon to form CO and CO_2 which can then diffuse back to the bulk gas. Gasification reactions tend to be a bit more complex, and occur when other gases (mainly CO_2, H_2O, and H_2) diffuse to the surface to also react with carbon in the coal, forming CO, H_2, and CH radicals that may further react and form other small molecules or oxidize to form CO_2 and H_2O (Smith et al., 1994). Primary pyrolysis conditions (particle temperature history, gas compositions, etc.) can also affect char structure and chemical reactivity (Gale et al., 1993; Gale et al., 1995a; Gale et al., 1995b; Gale et al., 1996).

2.1.3 Secondary Pyrolysis

Secondary pyrolysis tends to be a catch-all for any reaction occurring with primary pyrolysis products at higher temperatures and residence times in the coal combustion reaction. These reactions depend on the products of primary pyrolysis (Solomon et al., 1993). One of the main reasons secondary pyrolysis is a hot topic in coal research is soot chemistry. Soot is made up of small particles (from 25 nm and larger) that are formed in fuel-rich portions of the reaction environment. Soot highly contributes to radiative heat transfer in a coal boiler, especially near the burner region. Small particles of soot are formed from soot pre-cursors, more generally known as polycyclic aromatic hydrocarbons (PAHs). Coal tar is considered to be the largest contributor to coal-based soot in coal systems since the tar consists of a large number of different PAH compounds. Like the other "solids" in a coal reaction, soot particles can gasify or oxidize (Ma, 1996) along with other complex chemical and physical changes (Josephson et al., 2017).

2.2 Oxy-fuel Combustion

Environmental concerns about coal pollution (especially CO_2 emissions) have led to improvements in carbon capture and storage. Throughout history, most combustion applications have used air to burn various fuels, which leads to a large amount of N_2 in exhaust streams. It can be expensive and difficult to separate CO_2 from an exhaust gas that consists primarily of N_2. One idea to mitigate this cost is to use an air separator to burn fuels with pure O_2 (Buhre et al., 2005). This type of combustion without background N_2 is called oxy-fuel combustion. When oxy-fuel combustion is used in coal systems, the exhaust gas includes mainly carbon dioxide and steam, with a small amount of particulate matter, fuel NO_x, and SO_x. These compounds can be removed before the carbon dioxide is captured. Some industrial applications of oxy-fuel

combustion use pure O_2 in the boiler and others recycle part of the exhaust gas stream to dilute the O_2 atmosphere to reduce operating temperatures. Many researchers have conducted experiments using different compositions of O_2 and exhaust gas (Buhre et al., 2005; Toftegaard et al., 2010; Chen et al., 2012b; Chen et al., 2014; Lei et al., 2014; Liu et al., 2014a, b; Warzecha and Boguslawski, 2014; Yi et al., 2014; Bhuiyan and Naser, 2015; Liu et al., 2015; Muto et al., 2015; Rebola and Azevedo, 2015; Liu et al., 2017).

Oxy-fuel combustion was first proposed by two main groups of researchers in the early 1980s. Frederick Horn and Meyer Steinberg (in 1982) proposed an oxy-fuel fired power plant to assist in oil well production and recovery, developing the idea to help with environmental concerns, particularly with greenhouse gas mitigation (Steinberg, 1992). In their study, Horn and Steinberg concluded that removing CO_2 in this way expends less energy and is less expensive than other processes. The second group, Abraham et al. (also in 1982), independently proposed an oxy-fuel combustion process for oil recovery (Abraham et al., 1982).

Oxy-fuel combustion environments have three main benefits: (1) the ability to capture and remove CO_2 emissions, (2) reduced NO_x emissions (Chen et al., 2014), and (3) higher reactor efficiency from higher oxygen concentrations and higher combustion temperatures as a result (Toftegaard et al., 2010). However, higher reaction temperatures may also cause materials problems (more exotic metals to handle higher temperatures) unless recycled exhaust is utilized.

2.3 Modeling Pyrolysis Behavior

Large-scale simulations of coal boilers, gasifiers, and other combustion processes require adequate submodels to represent the different aspects of the simulation (Alvarez et al., 2013). These simulations must accurately describe the pyrolysis behavior of coal particles in a

numerically efficient manner. Modeling of pyrolysis behavior typically falls in one of three main coal pyrolysis modeling groups: (1) pyrolysis yield/rate models, (2) elemental composition of pyrolysis products, and (3) physical and chemical properties during gas-phase equilibrium reactions. Some comprehensive models even attempt to combine more than one of these main groups.

2.3.1 Yield/Rate Models

Most devolatilization yield and rate models are categorized as either a global kinetic model or a network (or mechanistic) model. There are three main network models in coal science: the chemical percolation devolatilization (CPD) model (Grant et al., 1989; Fletcher et al., 1992b), the FLASHCHAIN model (Niksa, 1988), and the FG-DVC model (Solomon et al., 1988). The CPD model is preferred because of its availability, ease of use, computational speed, and high versatility. There is one major trade-off between the two model types: computational speed versus predictive capabilities. Network models sacrifice computational speed for greater predictive capabilities whereas the global models are the opposite. Extra computational complexity (Smith et al., 1994) of these network models directly impacts the amount of time required to run complex simulations (Brewster et al., 1995), and because of this extra time, global models are generally preferred for large-scale simulations. One of the main disadvantages of global models is that they typically do not apply to as broad a range of coal types and temperature histories as network models do, and therefore need to be optimized (or fit) to trusted data or predictions.

The CPD model is based on the chemical structure of the parent coal (Grant et al., 1989; Fletcher et al., 1992b). Coal structure is approximated by aromatic clusters connected by

aliphatic bridges with attachments to these aromatic clusters including some side chains. Quantitative measurements of coal chemical structure were performed using solid-state ^{13}C NMR (Fletcher et al., 1990) and are used directly in the CPD model. Not all coals (or other fuels) have available NMR data, so Genetti et al. (1999) developed correlations for these NMR parameters based on ultimate and proximate analyses. Also included in the CPD model are rates for bridge breaking and side chain release, percolation lattice statistics to relate the number of broken bridges to the distribution of clusters that detach from the lattice, vapor-liquid equilibrium to determine the sizes of detached clusters that vaporize to form tar, and crosslinking of non-vaporized detached fragments that become part of the char. The CPD model has been widely tested and has been shown to agree with pyrolysis data for a wide range of coals, heating rates, temperatures, and pressures (Fletcher et al., 1992a; Fletcher et al., 1992b; Genetti and Fletcher, 1999; Genetti et al., 1999; Genetti, 1999; Sheng and Azevedo, 2000; Tian et al., 2001; Veras et al., 2002; Jupudi et al., 2009; Fletcher et al., 2012; Jovanovic et al., 2012; Lewis and Fletcher, 2013; Li et al., 2013; Goshayeshi and Sutherland, 2014; Herce et al., 2014; Yan et al., 2014b; Yang et al., 2014a; Yang et al., 2014b; Fletcher et al., 2015; Li et al., 2015; Rebola and Azevedo, 2015; Wang et al., 2015; Yang et al., 2015; Fletcher, 2019).

Global models fall broadly into three main categories: one-step kinetic models, two-step kinetic models, and distributed activation energy models. The number of steps in each model type refers to the number of kinetic pathways that the reaction can take; for example, a two-step model has two competing reaction pathways that the reaction can take to completion. While these models are generally fit to experimental data, several researchers have attempted to fit several simple global models to more complex network models. Ko et al., (1988) developed a correlation for the activation energy and pre-exponential factor of a one-step model to fit results

from a distributed activation energy model. Zhao et al. (1997) suggested using the FG-DVC model to generate coefficients for a one-step devolatilization model at a nominal condition in a CFD model, followed by iteratively generating coefficients if the nominal condition does not match the conditions in the simulation. Niksa (Niksa et al., 2003; Liu and Niksa, 2004) developed a method for a given heating rate to determine coefficients for a one-step devolatilization model from PC Coal Lab using his FLASHCHAIN network model and other similar char chemistry models. Li et al. (2013) also developed a package to interface with computational fluid dynamics software to develop coefficients for a one-step devolatilization model based on several different network models for coal combustion, called Carbonaceous Chemistry for Computational Modeling, nicknamed C3M. Hashimoto and Shirai (2014) used an iterative technique to generate coal devolatilization rate parameters for a CFD model, taking the particle temperature history from each previous CFD particle trajectory to determine rate parameters for the next iteration.

Several global kinetic models were considered for this work. The model forms are shown in Table 2-1. Each global devolatilization model is labeled with a model number DM-# to distinguish them from non-devolatilization models presented later.

The single first-order model (DM-1 in Table 2-1) is one of the simplest devolatilization rate and yield models and is based on simple Arrhenius kinetics. Many researchers have used this simple model over the years (Badzioch and Hawksley, 1970; Anthony et al., 1975; Kobayashi et al., 1977; Solomon and Colket, 1979), and it continues to be a go-to model even now, mainly due to its simplicity and ability to fit experimental data well.

Yamamoto et al. (2011) modified the single first-order model to expand the predictive capabilities of the first-order model without adding too much computational complexity.

Table 2-1. Global kinetic coal devolatilization models

Model Number	**Name**	**Source**	**Model Form**
DM-1	Single First-Order	(Badzioch and Hawksley, 1970; Anthony et al., 1975; Kobayashi et al., 1977; Solomon and Colket, 1979)	$\frac{d(V)}{dt} = A \cdot e^{-\frac{E}{RT}} \cdot (V_\infty - V)$
DM-2	Yamamoto	(Yamamoto et al., 2011; Pedel, 2012; Pedel et al., 2012)	$\frac{d(C)}{dt} = -F \cdot A \cdot e^{-\frac{E}{RT}} \cdot C$ $F = e^{\sum_{i=0}^{5} c_i (X_{coal})^i}$ $X_{coal} = 1 - C$ $V = V_\infty \cdot X_{coal}$
DM-3	Biagini and Tognotti (BT)	(Biagini and Tognotti, 2014)	$\frac{d(V)}{dt} = A \cdot e^{-\frac{E}{RT}} \cdot (V_\infty - V)$ $V_\infty = 1 - e^{-DI \cdot \frac{T}{T_{st}}}$
DM-4	Distributed Activation Energy (DAEM)	(Anthony and Howard, 1976; Lakshmanan and White, 1994; Cai et al., 2014; Soria-Verdugo et al., 2014)	$\frac{d(V)}{dt} = A \cdot e^{\frac{-E_a - \sigma_E \cdot Z}{RT}} \cdot (V_\infty - V)$ $Z = erfinv\left(1 - 2 \cdot (V_\infty - V)\right)$
DM-5	Modified Biagini and Tognotti (also called Utah model)	(Schroeder, 2015)	$\frac{d(V)}{dt} = A \cdot e^{\frac{-E_0 - \sigma_a \cdot Z}{T}} \cdot (V_\infty - V)$ $V_\infty = \frac{a}{2} \cdot \left(1 - \tanh\left((b + c \cdot a) \cdot \frac{T_{ignite} - T}{T} + (d + e \cdot a)\right)\right)$ $Z = \sqrt{2} \cdot erfinv\left(1 - 2 \cdot \frac{V_\infty - V}{a}\right)$
DM-6	Simple Two-Step	(Kobayashi et al., 1977; Ubhayakar et al., 1977)	$\frac{d(C)}{dt} = -\left(A_1 \cdot e^{-\frac{E_1}{RT}} + A_2 \cdot e^{-\frac{E_2}{RT}}\right) \cdot C$ $\frac{d(V)}{dt} = \left(Y_1 \cdot A_1 \cdot e^{-\frac{E_1}{RT}} + Y_2 \cdot A_2 \cdot e^{-\frac{E_2}{RT}}\right) \cdot C$

Yamamoto's modified first-order model (DM-2) uses a modification factor to the pre-exponential factor in the rate law. In addition, the Yamamoto model uses a type of conversion factor, X_{coal} to determine how far the pyrolysis reaction has progressed. This model also

introduces the idea of "unreacted" coal, which is not a measured value, but is instead used in conjunction with the conversion factor to show extent of reaction (Pedel, 2012; Pedel et al., 2012).

Biagini and Tognotti (2014) also modified the single first-order model like Yamamoto, but instead of going after the Arrhenius kinetics, they modified the yield factor, V_∞ (DM-3 in Table 2-1). They correlated some extra parameters in this yield factor in an effort to make the single first-order model more predictive of a wider range of coals. One of the main drawbacks of most first-order models is the fact that they use a "prescribed" yield factor, or V_∞, which must be fit to each condition and changes with both coal type and combustion conditions. By correlating this yield factor, Biagini and Tognotti tried to improve overall utility of the single first-order model without significantly increasing the model complexity.

The distributed activation energy model (DAEM) has been very popular in coal pyrolysis (Anthony and Howard, 1976) as well as biomass and other types of solid fuels (Lakshmanan and White, 1994; Hillier and Fletcher, 2011; Cai et al., 2014). This type of model is set apart from other one-step models in the idea of a distributed activation energy, or the idea that aliphatic bridge bonds in coal broken during pyrolysis have a range of bond-breaking energies. The classical DAEM model (Anthony and Howard, 1976) was developed with parallel activation energies so that all reaction pathways are possible over the whole reaction. This isn't quite true to reality since the lowest activation energies generally react first. The CPD model (Fletcher et al., 1992a) also uses a distributed activation energy to describe a variability in activation energies, however, a sequential distributed activation energy is used. This sequential method uses an inverse error function to calculate an effective activation energy, E_{eff}, from a Gaussian (or normal) distribution function based on the extent of reaction. In testing, the sequential

method seems to work as well as the parallel method and is much easier to implement and much faster computationally. There are a number of different forms of the distributed activation energy model, with Anthony and Howard using a Gaussian distribution (1976), while others use different forms or distributions (Lakshmanan and White, 1994; Cai et al., 2014; Soria-Verdugo et al., 2014). The distributed activation energy model more closely conforms to the physical reality of coal pyrolysis reactions by using a variable activation energy over the course of the reaction, and very closely models experimental results. The simple DAEM here uses the sequential method proposed by the CPD model rather than the parallel method in the classical DAEM.

The modified Biagini and Tognotti model (DM-5 in Table 2-1), also called the Utah model, is largely a combination of the original Biagini and Tognotti model and the distributed activation energy model. Schroeder (2015) proposed this modification to include the sequential distributed activation energy to further exhibit the correct ultimate volatiles yield at different temperatures and heating rates. The Utah model not only modifies the activation energy, but further modifies the yield factor V_∞ to include extra parameters that are fit to long residence time predictions from network models or experimental data. This modification is included to ensure model functionality with widely variable time steps, especially when small time steps are not possible in a simulation, eliminating numerical instabilities. One of the key disadvantages of the Utah model is the need for long residence time data to fit the coefficients on the yield curve, which are not always available before a simulation.

The original two-step model (Kobayashi et al., 1977) was proposed to allow the final volatiles yield to vary with heating rate and temperature history. This model uses two competing kinetic steps with widely varying activation energies. This allows one step to prevail at lower temperatures and the other step at higher temperatures. Both the original Kobayashi parameters

as well as those taken from Ubhayakar et al. (1977) are often used in large-scale simulations, however, greater accuracy can be achieved by re-fitting the coefficients to experimental data. Like the Yamamoto model, the two-step models use the concept of "raw coal" that reacts to form volatiles and char. The raw coal starts as one and goes to zero upon completion of the pyrolysis reaction. The simple two-step model uses Arrhenius kinetics along with two yield factors.

2.3.1.1 Factors Affecting Pyrolysis Yields

There are a number of factors affecting the overall pyrolysis yields of coal, both condition- and coal-specific factors. Coal-specific factors include primarily coal rank, structure, and chemical composition, and condition-specific factors include pyrolysis gas composition (N_2, CO_2, argon, H_2, etc.) and temperature history (encapsulated mostly by particle heating rate and residence time). Experiments suggest that as particle heating rate increases, the temperature at which devolatilization happens also increases (Anthony et al., 1975; Saxena, 1990; Yan et al., 2014a). In addition, as heating rate increases, the ultimate volatiles yield, or final volatiles fraction after devolatilization, also increases (Jamaluddin et al., 1986; Gibbins-Matham and Kandiyoti, 1988). These trends are shown in Figure 2-3, with curves generated using the CPD model with Sufco coal chemical compositions and NMR parameters.

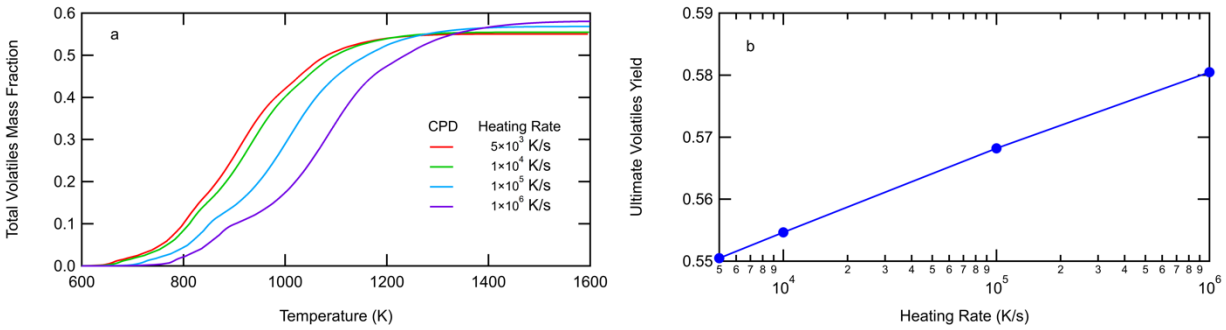

Figure 2-3. Trends with increasing heating rate: a) pyrolysis temperature increases and b) ultimate volatiles yield increases log-linearly.

While these figures show the yield curves for the total volatiles (which include tar and light gases), coal tar follows similar curves, although to a lower final yield. Ultimately, it is very important to accurately model pyrolysis rates and yields in large-scale coal combustion simulations since the rates influence several aspects of coal combustion such as particle swelling and char reactivity (Solomon et al., 1992).

2.3.2 Elemental and Chemical Composition of Coal Pyrolysis Products

While current areas of coal research have advanced the understanding of processes involved in coal pyrolysis, not enough is known about the elemental and chemical compositions of the products of coal pyrolysis, especially the tar species. Few experimentalists collect tar during coal pyrolysis reactions, and even fewer analyze the collected tar for species or elemental composition and properties. Accurately knowing or predicting these compositions can greatly influence the overall accuracy and utility of large-scale simulations, however, the detailed species composition of coal volatiles is often too complex to use in large-scale simulations. For this reason, many simulations often use a simpler average elemental composition combined with equilibrium analysis to generate the necessary chemical and turbulence interactions in a coal combustion system.

Volatiles contain a greater fraction of hydrogen and oxygen than the char, meaning the volatiles become enriched in hydrogen and oxygen while the char becomes enriched in carbon (Fletcher and Hardesty, 1992; Smith et al., 1994; Watt, 1996). The distribution of elements into combustion products is highly influenced by both combustion conditions and parent fuel properties. The distribution of nitrogen and sulfur in the combustion products are of particular interest (even if they are small fractions in the parent fuel), since they can influence the NO_x and SO_x compositions of the flue gas (Cai et al., 1993).

Accurately predicting tar species yields is very difficult in coal pyrolysis since coal tar is made up of a large number of different species (Pielsticker et al., 2017a). The key network models (CPD, FLASHCHAIN, and FG-DVC) predict the key light gas components, usually the lightest hydrocarbons, and then lump the remainder into an "other hydrocarbons" category. Some models even lump the tar and light gases together and use a global volatiles combustion rate (Backreedy et al., 2006). Other approaches use approximations or simple surrogates (like methane) in place of pyrolysis products (see Section 2.3.4 for more detail on these simplified approaches). All these assumptions lead to modeling that is inconsistent with the measured elemental compositions of char and tar (Pugmire et al., 1991; Perry et al., 2000).

Many of the same factors that affect pyrolysis yields also affect the chemical compositions of the char and tar. Different coals have different parent coal compositions and structures, which significantly influence primary pyrolysis product yields and compositions (Xu and Tomita, 1987a). Coal type also influences the general structural makeup of the coal and tar molecules that are sometimes measured by NMR solid-state spectroscopy (Solum et al., 1989; Fletcher and Hardesty, 1992; Watt, 1996; Watt et al., 1996; Hambly, 1998; Hambly et al., 1998; Genetti et al., 1999; Perry, 1999; Perry et al., 2000). The thermal environment (i.e. gas temperature, residence time, particle heating rate, etc.) that the coal particle experiences also impacts the yields and compositions of char, tar, and light gases (Xu and Tomita, 1987b).

2.3.2.1 Coal Aromaticity

Coal aromaticity has been measured using NMR spectroscopy and has frequently been used in correlations of other coal properties. Several correlations have been developed to predict coal aromaticity based on proximate and ultimate analyses. These correlations are found in Table 2-2.

Table 2-2. Correlations of Coal Aromaticity

Model Number	**Name**	**Source**	**Model Form**
AM-1	Gerstein	(Gerstein et al., 1982)	$f_a' = 0.0159C_{coal} - 0.564$
AM-2	Ko	(Ko et al., 1989)	$f_a = 0.830526 - 2.008147\left(\frac{C^*_{coal}}{100}\right) + 2.241218\left(\frac{C^*_{coal}}{100}\right)^2$
AM-3	Maroto-Valer	(Maroto-Valer et al., 1998)	$f_a = 1.22 - 0.58\left(\frac{H_{coal}}{C_{coal}}\right)$
AM-4	SK1	(Singh and Kakati, 2003)	$f_{a1} = 1.202913 - 0.0126V^*_{ASTM}$
AM-5	SK2	(Singh and Kakati, 2003)	$f_{a2} = 1.36396 - 0.53715\left(\frac{O^\alpha_{coal}}{C^\alpha_{coal}}\right) - 0.7846\left(\frac{H^\alpha_{coal}}{C^\alpha_{coal}}\right)$
AM-6	SK3	(Singh and Kakati, 2003)	$f_{a3} = 1.365615 - 0.51187\left(\frac{O^\alpha_{coal}}{C^\alpha_{coal}}\right) - 0.02108\left(\frac{O^\alpha_{coal}}{H^\alpha_{coal}}\right) - 0.78645\left(\frac{H^\alpha_{coal}}{C^\alpha_{coal}}\right)$
AM-7	SK4	(Singh and Kakati, 2003)	$f_{a4} = 174.4405 + 621.6823\left(\frac{O^\alpha_{coal}}{C^\alpha_{coal}}\right) - 856.495\left(\frac{O^\alpha_{coal}}{H^\alpha_{coal}}\right) - 629.617\left(\frac{H^\alpha_{coal}}{C^\alpha_{coal}}\right) - 9.133897V^*_{ASTM}$

* variables are on a wt.% dry, mineral-matter-free basis
α elemental ratios are on an atomic basis

These model forms were chosen to use here because they are based on proximate and ultimate analyses of the coal. Other researchers developed correlations based on other fuel properties such as vitrinite reflectance (Carr and Williamson, 1990). Some of these models were developed to predict the true or corrected aromatic carbon content (f_a'), while others were developed to correlate the total aromatic carbon contribution (f_a), which is sometimes called the

apparent aromaticity. The main difference between the two aromaticities is that the apparent or total aromaticity includes contributions from carbonyl groups. This artificially inflates the aromaticity value which is why the true aromaticity is preferred in structural modeling.

2.3.3 Enthalpy of Combustion of Coal and Other Fuels

Another key physical property of coal and other fuels is the enthalpy, or heat, of combustion (also called a heating value), which is a measure of the reaction enthalpy of the combustion reaction. While the heating value can be measured using calorimetry, this can be expensive and time-intensive to measure for each fuel of interest. In addition, most complex fuels change composition over the course of the entire combustion reaction (Fletcher and Hardesty, 1992). Accurately knowing the heating value of coal-based fuels and other traditional and non-traditional fuels can improve the computation of local gas temperatures in large-scale simulations.

A number of correlations of the heating value of coal have been developed for a limited number of coals based on characteristics of coal such as elemental organic composition (CHONS) and volatile matter, as reviewed by van Krevelen (1993) and Channiwala and Parikh (2002). Some of these correlations and others have been reviewed for other fuels and a limited number of coal chars (Sciazko, 2013; Mathews et al., 2014). Some of the most widely used heating value correlations based on the organic elemental composition of the parent fuel are found in Table 2-3.

Original coefficients for each of these models are found in the cited literature for each model. All models are tuned to predict the higher heating value with units of kJ/kg on a DAF basis. All elemental compositions used in these models must also be on a wt.% DAF basis. Some

Table 2-3. Heating Value Correlations

Number	Model Name	Units	Model Form
HM-1	Dulong (Van Krevelen, 1993; Sciazko, 2013)	kJ/kg	$\Delta H_c = aC + b\left(H - \frac{O}{8}\right) + cS$
HM-2	Strache-Lant, D'Huart, Boie (Strache and Lant, 1924; D'Huart, 1930; Boie, 1953; Van Krevelen, 1993; Channiwala and Parikh, 2002; Sciazko, 2013)	kJ/kg	$\Delta H_c = aC + bH + cO + dS$
HM-3	Steuer (Steuer, 1926; Channiwala and Parikh, 2002)	kJ/kg	$\Delta H_c = a\left(C - \frac{3}{8}O\right) + b\left(\frac{3}{8}O\right) + c\left(H - \frac{1}{16}O\right) + dS$
HM-4	Seylor (Seylor, 1938; Van Krevelen, 1993; Channiwala and Parikh, 2002)	kJ/kg	$\Delta H_c = aC + bH + cO^2 + d$
HM-5	Gumz, Channiwala-Parikh (Gumz, 1938; Channiwala and Parikh, 2002; Sciazko, 2013)	kJ/kg	$\Delta H_c = aC + bH + cN + dS + eO$
HM-6	Dulong-Berthelot (Grabosky and Bain, 1981; Channiwala and Parikh, 2002)	kJ/kg	$\Delta H_c = aC + bH - \frac{c(N + O - 1)}{8} + dS$
HM-7	IGT (IGT, 1978; Channiwala and Parikh, 2002)	kJ/kg	$\Delta H_c = aC + bH + c + d(O + N)$
HM-8	VDI (Ocheduszko, 1967; Sciazko, 2013)	kJ/kg	$\Delta H_c = aC + b\left(H - \frac{O}{8}\right) + cS + dH$
HM-9	Mott-Spooner (Van Krevelen, 1993; Channiwala and Parikh, 2002)	kJ/kg	$\Delta H_c = \begin{cases} aC + bH + cO + dS, & O < 15\% \\ aC + bH + eO + fO^2 + gS, & O > 15\% \end{cases}$
HM-10	Given et al. (Given et al., 1986; Van Krevelen, 1993)	kJ/kg	$\Delta H_c = aC + bH + cO + dS + e$

of the models have been combined (HM-2 and HM-5) since they have the same mathematical form, however, their original coefficients are different in each cited article.

Several other correlations (Demirbaş, 1997, 1998, 2001; Mathews et al., 2014; Go and Conag, 2018) have been developed using other coal- or fuel-specific properties (including fixed carbon, volatile matter, ash content, etc.), but these models are not as desirable because of a lack of complete proximate analyses in the literature. Some other models use bond energies and functional groups to determine a heating value (Kaiho et al., 2019). Bond energy models are not explored here because they require a functional group breakdown, typically involving advanced spectroscopy (NMR, FTIR, MS, etc.), which are too expensive to perform for many new fuels, especially fuels as complex as coal. Other approaches use the heats of formation of the parent fuel and products of combustion or pyrolysis to calculate the heat of reaction (Merrick, 1983), but heats of formation are not generally available for complex fuels.

Fuel heating values are particularly useful in calculating the enthalpies of formation of the fuel. These are not usually known, but can be calculated by assuming complete combustion, which is shown in Equation 2-1.

$$C_aH_bO_cN_dS_e + \alpha O_2 \rightarrow aCO_2 + \frac{b}{2}H_2O + \frac{d}{2}N_2 + eSO_2 \quad (2\text{-}1)$$

where a, b, c, d, and e are stoichiometric coefficients based on the elemental composition of the fuel and α is the stoichiometric amount of oxygen needed for complete combustion, as calculated in Equation 2-2. This stoichiometric amount of oxygen can then be added to the correct percentage of nitrogen to determine the total amount of air necessary for complete combustion in air.

$$\alpha = a + \frac{b}{4} - \frac{c}{2} + e \quad (2\text{-}2)$$

Fuel heating values can be reported in one of two formats: a higher heating value (HHV) where the heating value is calculated by assuming the water formed from combustion is a liquid, and a lower heating value (LHV) where the heating value is calculated by assuming water is a vapor. An LHV can be converted to an HHV using the enthalpy of vaporization of water, as shown in Equation 2-3.

$$HHV = LHV + n_{H_2O,comb}\Delta H_{vap} \quad (2\text{-}3)$$

where ΔH_{vap} is the heat of vaporization of water (40.65 kJ/g-mole) and $n_{H_2O,comb}$ is the moles of water produced by complete combustion of one kilogram of fuel.

2.3.4 Mixture Fractions and Equilibrium Modeling

Gas-phase reactions are an integral part of coal combustion simulations, and influence the bulk gas composition, local gas temperature, and can have implications on fluid flow, heat transfer, and mass transfer (Smoot and Smith, 1985). Simplifying assumptions are often used in large-scale simulations to decrease computational complexity, especially if computational resources are limited.

Many of the simplifying assumptions used in gas-phase equilibrium of coal systems deal with simplifying coal-based fuel compositions, particularly the compositions of pyrolysis products (char, tar, and other volatile gases). Frequently coal char is modeled as pure carbon with the thermochemical properties of either graphite (Barnhart and Laurendeau, 1982; Barnhart et al., 1982; Borghi et al., 1985; Bhuiyan and Naser, 2015; Vascellari et al., 2015; Rieth et al., 2017b; Bhunia et al., 2018; Wen et al., 2018) or of the parent coal (Backreedy et al., 1999; Bradley et al., 2006; Van Essendelft et al., 2014; Tufano et al., 2019). This is perhaps useful in heterogenous char reactions since oxidation and gasification reactions primarily target the carbon

in the char. However, this approach falls short in calculating other combustion products (i.e., H_2O and other hydrogen-based products), since the char retains some hydrogen and other atoms such as oxygen, nitrogen, and sulfur (Fletcher and Hardesty, 1992; Pielsticker et al., 2017a).

Other simulations have simplified the compositions and energies of the volatile species, often using one or more of several simple hydrocarbons in the place of the more complex tars and other volatile gases. Some simulations use methane in the place of the total volatiles (Bradley et al., 2006; Jovanovic et al., 2012; Al-Abbas et al., 2013; Costa et al., 2014; Cui et al., 2014; Hashimoto and Shirai, 2014; Bhuiyan and Naser, 2015; Guo et al., 2015; Rabaçal et al., 2015; Watanabe and Yamamoto, 2015; Lisandy et al., 2016; Wen et al., 2016; Watanabe et al., 2017; Wen et al., 2018) or other simple C_2 hydrocarbons (Vascellari et al., 2017). Other approaches use a mix of common pyrolysis gases (CH_4, C_6H_6, CO, CO_2, H_2, N_2, H_2S, etc.) in variable quantities to ensure elemental balance between the original coal and gaseous species (Veras et al., 1999; Costa et al., 2014; Hashimoto and Shirai, 2014; Messig et al., 2017). Some even use constant generic hydrocarbon estimates ($C_xH_yO_z$) to better approximate volatile species (Backreedy et al., 1999; Backreedy et al., 2006; Jovanovic et al., 2012; Franchetti et al., 2013; Rabaçal et al., 2015; Rebola and Azevedo, 2015; Vascellari et al., 2015; Tufano et al., 2019), often approximated using the composition of the original coal. While these simplified approaches may be appropriate for smaller-scale or simplified calculations, they may be inadequate for accurate large-scale simulations, especially since inaccuracies in CO_2 and H_2O gas compositions greatly affect other parts of the coal combustion system like radiative heat transfer (Chen and Ghoniem, 2012). Volatile gases released during coal pyrolysis do contain many of these simple hydrocarbons, but the total volatiles tend to be much more complex, particularly the tar species (Theron and le Roux, 2015; Pielsticker et al., 2017a).

Equilibrium modeling can take a variety of forms, usually including variables to help with mixing and reacting streams. Large scale simulations can use flamelet modeling and progress variables (Xu et al., 2013; Goshayeshi and Sutherland, 2014; Knappstein et al., 2017; Rieth et al., 2017b; Rieth et al., 2019), mixture fractions (Brewster et al., 1988; Flores and Fletcher, 2000; Pedel et al., 2013; Stollinger et al., 2013a, b; Rieth et al., 2016; Wen et al., 2017b), full equilibrium (Smoot, 1981), approximations to equilibrium such as the water-gas shift reactions (Radulovic et al., 1995), detailed kinetic mechanisms of simpler hydrocarbon fuels such as GRI3.0 (Cui et al., 2014; Goshayeshi and Sutherland, 2014; Guo et al., 2015; Tufano et al., 2016; Knappstein et al., 2017; Wen et al., 2019), or even a combination of several of these different approaches (Watanabe and Yamamoto, 2015; Rieth et al., 2016; Rieth et al., 2017b; Watanabe et al., 2017; Rieth et al., 2019).

2.3.4.1 Mixture Fractions

A common assumption in simulations of large combustors is that the gas-phase reactions are limited by mixing of fuel and oxidizer species. The temperatures in these combustors are often very high (1800-2200 K), so gas-phase chemical reactions are very fast, approaching equilibrium quickly. Most large-scale combustor simulations do not have the computational resources (i.e., computational time and storage) to use detailed or even global reaction schemes, hence the popularity of mixture fraction approaches (Smoot and Smith, 1985) or the use of the eddy breakup scheme (Magnussen and Hjertager, 1977) which takes the minimum of the mixing rate and a single simplified global reaction rate.

At its most simple definition, a mixture fraction analysis involves defining a reacting system (e.g., combustion of a hydrocarbon fuel with air) into two types of streams—one that includes all fuels and another that includes the oxidizing gases. In most gas-phase combustion

reactions of simple hydrocarbon fuels, mixture fractions can be considered "conserved scalars," which means that the mixture fraction does not change with reacting conditions (assuming no loss or gain of thermal energy). Conserved scalars simplify reacting flow calculations and can be anything from elemental mass fractions to enthalpies of the different reacting streams, as long as it is a stream property that remains the same throughout the reacting system (Turns, 2012). This approach is a simple way to track material when it mixes and reacts to equilibrium.

Mixture fractions in coal-based systems are not usually considered conserved scalars because the mixture fractions typically include a separate source term to describe the addition of material into the gas phase from a solid coal particle (Smoot and Smith, 1985; Flores and Fletcher, 2000). This source term is necessary because coal combustion is not a homogeneous reaction that occurs only in the gas phase, but instead involves a complex reaction between a solid coal particle and other background gases (Smith et al., 1994). While using a source term is helpful in describing the physical processes of a coal combustion reaction, it can complicate transport and reaction equations, making a mixture fraction description of coal combustion difficult to incorporate into large-scale simulations.

The mixture fractions used in this dissertation are slightly different from those used traditionally in simple hydrocarbon reactions and from previous work on coal-gas mixture fractions. For this reason, an overview of the mixture fractions and other equations is shown here. Chapter 8 details the derivation of the complete mixture fraction analysis using these generalized equations. While there are multiple ways of defining a mixture fraction, including the widely used Bilger's mixture fraction (Bilger et al., 1990; Bilger, 1993; Peters, 2000), this dissertation explores two main types of mixture fractions. The first is a more traditional form of mixture fraction (named here as a "component" or "fuel" mixture fraction and labeled as f_i to

avoid confusion with other mixture fractions) which is the mass fraction of material originating in each stream. This component mixture fraction, f_i, is calculated by dividing the mass of one fuel stream (e.g., gas generated by a coal molecule) by the total mass of the mixture (Turns, 2012), shown in general form in Equation 2-4. Turns (2012) mainly details the mixture fraction of a one-mixture fraction system, however, a combustion system can be comprised of more than one fuel stream, so the component mixture fraction can be extended to two or more in a system (Fox, 2003). The extension of the component mixture fraction to one-, two-, and three-mixture fraction coal combustion systems is discussed in greater detail in Chapter 8.

$$f_i = \frac{M_i}{M_0 + \sum_{i=1}^{N} M_i} \tag{2-4}$$

where f_i is the component mixture fraction of component i (coal, char, tar, oxidizer, etc.), M_i is the total mass of species i, M_0 is the total mass of the oxidizer component (e.g., air), and N indicates the total number of fuel components. The sum of all component mixture fractions (including the oxidizer mixture fraction) adds to one, and the total number of fuel mixture fractions to completely describe a reacting system is N.

This type of component mixture fraction is commonly used in combustion modeling applications to describe a system of one fuel stream and one oxidizer stream—otherwise known as a one-mixture fraction system. While one-mixture fraction systems are common in many types of gas-phase combustion applications (e.g., methane, ethylene, and other simpler fuels with air), this type of component mixture fraction can be extended to two, three, or even more (Fox, 2003).

The second type of mixture fraction explored in this dissertation is called the “elemental” mixture fraction and labeled as Z_j to distinguish from the component mixture fraction. This type of mixture fraction describes the total mass fraction of each element in the reacting system

(Peters, 2000; Poinsot and Veynante, 2005). The elemental mixture fraction is shown in Equation 2-5.

$$Z_j = W_j \sum_{i=1}^{N} \frac{a_{ij} Y_i}{W_i} \tag{2-5}$$

where Z_j is the elemental mixture fraction of element j (i.e., carbon, hydrogen, etc.), W_j is the molecular weight of element j, W_i is the molecular weight of component i (including oxidizer and all fuels), Y_i is the mass fraction of component i (the component mixture fraction), and a_{ij} is the number of atoms of element j in component i (for example, a sample fuel of benzene, C_6H_6 would have an a_{ij} of 6 for both carbon and hydrogen). In most simple hydrocarbon combustion systems, the total number of primary elements is four (CHON), however, in coal combustion applications, sulfur is present, leading to five total elemental mixture fractions to describe the primary organic elements (CHONS) present in the fuel and oxidizer streams. Like the component mixture fraction, the elemental mixture fractions sum to one. The elemental mixture fractions are defined here to not include a source term that adds material to the gas phase from a heterogeneous reaction (like coal and char combustion). If a source term were to be incorporated directly with the elemental mixture fractions, they would have to be re-normalized to again sum to one.

Another useful parameter in combustion modeling is the equivalence ratio (Turns, 2012), which is shown in Equation 2-6. The equivalence ratio relates the fuel-to-oxidizer ratio of a mixture to its stoichiometric fuel-to-oxidizer ratio.

$$\phi_i = \frac{\frac{n_i}{n_{ox}}}{\left(\frac{n_i}{n_{ox}}\right)_{stoich}} \tag{2-6}$$

where ϕ_i is the equivalence ratio of fuel i, n_i is the number of moles of fuel i, n_{ox} is the moles of oxidizer (i.e., air), and the subscript $stoich$ is the oxidizer-to-fuel ratio at stoichiometric proportions. The equivalence ratio or component mixture fraction can be used to determine the total moles of oxidizer in the system if the moles of fuel are fixed to a constant value.

2.3.4.2 Equilibrium Codes

Two widely-used chemical equilibrium programs for combustion systems are used here: the stand-alone version of the NASA-CEA program (Gordon and McBride, 1994; McBride and Gordon, 1996) and the Python interface of Cantera (Goodwin et al., 2018). Both programs calculate equilibrium states based on an input of initial conditions, including chemical and thermodynamic properties of reactants, relying primarily on Gibbs free energy minimization. Both programs also use similar thermodynamic property models with polynomial representations of heat capacity, enthalpy, and entropy states of chemical species. Additionally, both programs calculate an adiabatic equilibrium temperature, which can be used as a comparison between fuels, however, real combustion systems are never truly adiabatic. Large-scale simulations would take this into account by including a heat loss term. The NASA-CEA code is not set up to directly deal with any heat loss in a real system (to include any heat loss, the enthalpies of formation of each component would need to be adjusted before calculating equilibrium states of different fuels, potentially involving an iterative process to correctly address heat loss), however, Cantera is flexible enough that it could be used in conjunction with stand-alone research codes that adequately address heat loss concerns. Modifications were made to Cantera to adequately address the complexity of coal-based fuels. These modifications are discussed at greater length in Chapter 8.

2.3.5 Turbulent Mixing

Gas-phase chemical reactions can exhibit a wide range of different behaviors. In most industrial applications, coal combustion typically behaves as turbulent, non-premixed combustion (Turns, 2012). In non-premixed (or diffusion) flames, combustion occurs at the boundary between fuel and oxidizer (Poinsot and Veynante, 2005), like the well-known Burke-Schumann Flames (Burke and Schumann, 1928). Turbulence (quantified by sufficiently high Reynolds numbers) causes shear forces in the fluid, which in turn produces vorticity that is stochastic in nature, changing in both time and location (Smoot and Smith, 1985). These vortexes are typically called eddies in combustion modeling. Eddies are important in accurately modeling the combustion behavior of gaseous fuels, and in most cases of turbulent, non-premixed flames, the observed reaction rate is limited by mixing (meaning the actual chemical reaction rate is much faster than the rate of mixing), which occurs in eddies locally (Poinsot and Veynante, 2005).

Due to the stochastic nature of eddy mixing, the local composition (species and elemental) of the eddies changes based on a number of different variables, including time, position in the flow, flow characteristics (momentum, velocity, temperature, etc.), and other variables (Bird et al., 2007). Solid fuels like coal make this even more difficult by including a source of mass from both pyrolysis and char combustion/gasification reactions (Smoot and Smith, 1985). For practical coal combustion modeling, this means that the elemental and species compositions are very different depending on local conditions.

2.4 Statistics/VUQ

The topic of verification, validation, and uncertainty quantification (VUQ) is becoming more prevalent in a lot of research areas and particularly combustion modeling. Verification and

validation might mean different things to different people. This dissertation uses the definition from Oberkampf and Barone (2006), in that verification refers to the process of ensuring mathematical and model implementation accuracy and validation refers to the process of comparing model predictions to real-world values. The uncertainty quantification comes from using what are called "validation metrics" or statistical values that compare model predictions to the real-world values. In addition to specific validation metrics, sometimes more generally called statistical measures of fit, there are a number of processes researchers use that can find and/or eliminate any model fitting bias (caused either by overfitting or underfitting model coefficients). These methods fall into a general category called cross-validation.

2.4.1 Statistical Measures of Fit

Classical statistical analyses rely on several well-known validation metrics, starting with the R^2 value, which is often called the coefficient of determination. The coefficient of determination ranges from 0 to 1, with 0 generally representing the poorest fit possible while a value of 1 means the model perfectly fits the experimental data. There are several ways to calculate the R^2 value, but perhaps the most widely used (Walpole and Myers, 1978) is shown in Equations 2-7 to 2-10.

$$R^2 = \left(\frac{S_{xy}}{\sqrt{S_{xx}S_{yy}}}\right)^2 \tag{2-7}$$

$$S_{xy} = \sum_{n=1}^{N}(\hat{y}_n y_n) - \frac{1}{N}\left(\sum_{n=1}^{N}\hat{y}_n\right)\left(\sum_{n=1}^{N} y_n\right) \tag{2-8}$$

$$S_{xx} = \sum_{n=1}^{N}(\hat{y}_n)^2 - \frac{1}{N}\left(\sum_{n=1}^{N}\hat{y}_n\right)^2 \tag{2-9}$$

$$S_{yy} = \sum_{n=1}^{N}(y_n)^2 - \frac{1}{N}\left(\sum_{n=1}^{N} y_n\right)^2 \tag{2-10}$$

where $\hat{y}_n$ is the predicted value given by a proposed model, y_n is the experimentally observed (or measured value, and N is the total number of points in the comparison data set.

The R^2 value is widely used and can be a good indication of model fit, however, it can sometimes give a false sense of security, especially when model slopes are high. In addition, R^2 is highly dependent on the number of points used in a comparison, so a high R^2 value does not automatically indicate a good model fit and a low R^2 value does not automatically indicate a bad model fit. This is a good reason to use any statistical parameter in conjunction with other statistical tests to ensure a "good" fit is really a good fit.

Another classical statistical parameter that is especially important in regression and model fitting is the sum of squared errors (SSE). The SSE is shown in Equation 2-11. Related to the sum of squared errors is the mean of the sum of squared errors (MSE). This value normalizes the sum of squared errors by the total number of data points in the data set used to fit model parameters. Smaller data sets generally have smaller SSE values, so the MSE is particularly helpful when comparing models over a wide range of data set sizes. The MSE is found in Equation 2-12.

$$SSE = \sum_{n=1}^{N} (\hat{y}_n - y_n)^2 \tag{2-11}$$

$$MSE = \frac{SSE}{N} = \frac{1}{N} \left(\sum_{n=1}^{N} (\hat{y}_n - y_n)^2 \right) \tag{2-12}$$

Another useful statistical measure of fit is the relative error. This type of error measurement normalizes the absolute error by the experimentally observed value. This makes an error value that is a percentage, typically below 100% if the predicted and observed values are similar. The relative error is given in Equation 2-13. Several useful things can be done with the

relative error, including taking the minimum, average, and maximum relative errors in a data set comparison. Maximum relative error can give an indication of the maximum "spread" of the model when compared to real-world data, and the average relative error can show on average how close the "spread" is. The minimum relative error is perhaps the least useful of these three, usually being very close to zero if any of the individual data points are well-matched with real-world data points.

$$RE = \left|\frac{y_n - \hat{y}_n}{y_n}\right| \tag{2-13}$$

Some researchers have started using various vector norms to compare model predictions to experimental data (Oberkampf and Barone, 2006; Oberkampf and Roy, 2010): (1) the L_1 norm gives an average absolute error, shown in Equation 2-14, (2) the L_2 or Euclidian norm gives the root mean squared error (RMSE), shown in Equation 2-15, and (3) the infinity norm gives the maximum absolute error, shown in Equation 2-16.

$$L_1 = \|\hat{y} - y\|_1 = \frac{1}{N}\sum_{n=1}^{N}|\hat{y}_n - y_n| \tag{2-14}$$

$$L_2 = \|\hat{y} - y\|_2 = \left(\frac{1}{N}\sum_{n=1}^{N}(\hat{y}_n - y_n)^2\right)^{\frac{1}{2}} \tag{2-15}$$

$$infinity = \|\hat{y} - y\|_\infty = \max|\hat{y}_n - y_n| \tag{2-16}$$

While all of these validation metrics are valid and widely used in the literature, they each show a slightly different picture of the error between model predictions and real-world values. There are many more ways of expressing this error, but these nine validation metrics (R^2, SSE, MSE, minimum, average, and maximum relative error, and the L_1, L_2, and infinity norms) tend

to show a good picture of the overall model error, especially using a combination of several of the validation metrics in one comparison.

2.4.2 Cross-Validation

Cross-validation has been used to decrease the overall bias of mathematical models (Esbensen and Geladi, 2010), and can take a number of different forms, with most following similar algorithms. The basic cross-validation process (Schaffer, 1993), which is commonly known as *k*-fold cross-validation, is commonly thought to have four main steps:

1. The data set is split into randomly assigned groups (can be any number of groups, but most commonly used are 10 sets of roughly equal size, but fewer groups can be used for smaller data sets)
2. One of the groups is left out as a test set. The remaining groups are used to train each model (i.e., to curve-fit the data for all but the test set). The resulting correlation is then evaluated using the one test set excluded from the curve fit. This process is repeated for each group, so each group eventually acts alone as a test set.
3. The validation metrics of all these curve fits are averaged, and the best model is chosen. A better value for a chosen validation metric indicates that the model has a better ability to predict data using new conditions on which it was not trained.
4. Finally, the chosen model or models are trained on the complete data set to produce a prediction model.

A model can be trained using a variety of techniques, but perhaps the easiest and most common way is using a simple least squares analysis which is done by minimizing the sum of

squared error between the model and experimental values. The remaining validation metrics can then be calculated based on the trained (or fit) model.

Another procedure commonly applied to VUQ along with cross-validation is some sort of model refinement. Typically, this takes the form of what are called "nested functions," which means one fitted coefficient at a time is removed from a chosen model to determine if any of the coefficients are extraneous.

2.4.3 Information Theory

Another branch of applied statistics and VUQ is called information theory (Burnham and Anderson, 2002). Information theory basically seeks to infer data from complex information. One thing information theory can do well is compare various model forms, especially if the models are not "nested." Many model comparison approaches only apply to nested models, where a full or parent model is being reduced to form a smaller nested model that is really just a subset of the parent. Information theory differs from some other model comparison approaches in the fact that it does not assume there is one "true" model describing the data, but rather some models are more likely to be correct than others, relying on what is called "information entropy," or how likely (or unlikely) a specific outcome will occur (Stone, 2015). Bayesian statistics are an example of information theory.

Many information theory criteria include two parts: a measure of the likelihood of a model to be correct, and something to correct for potential overfitting bias (especially with large numbers of fitted coefficients and small data sets). There are two commonly used and related approaches: the Bayesian Information Criterion (BIC) and the Akaike Information Criterion (AIC) (Burnham and Anderson, 2002). The AIC method is used here because of some useful

simplifications to the calculations that can be performed when a least-squares analysis is used to fit the model(s) of interest. The key AIC formula is shown in Equation 2-17.

$$AIC = N \cdot \ln\left(\frac{SSE}{N}\right) + 2K = N \cdot \ln(MSE) + 2K \tag{2-17}$$

where N is the number of points in a data set and K is the number of fitted model coefficients plus 1. A corrected AIC score (AIC_c), in Equation 2-18, can be calculated for a high number of fitted coefficients and small data sets.

$$AIC_c = AIC + \frac{2K(K+1)}{N-K-1} \tag{2-18}$$

When the data set size is high and the number of fitted coefficients low, the AIC and AIC_c scores will be almost equivalent. The forms of AIC and AIC_c shown here are the simplified versions used when a sum of squared errors analysis is used to fit the models. If this type of fitting analysis is not used, the AIC value is much more complicated, using the log of the likelihood function. By itself, the AIC or AIC_c score can be either positive or negative and is only meaningful when comparing two models. This is done by subtracting the AIC_c score of one model from another, as shown in Equation 2-19.

$$\Delta AIC_c = AIC_{c,1} - AIC_{c,2} = N \cdot \ln\left(\frac{MSE_1}{MSE_2}\right) + 2(K_1 - K_2) + \frac{2K_1(K_1+1)}{N-K_1-1} - \frac{2K_2(K_2+1)}{N-K_2-1} \tag{2-19}$$

When comparing models using the AIC_c scores, the model with the lowest value is the most likely to be correct, however, this does not mean a lot by itself. The AIC method can go further and show how much more likely the best model is to be correct. Two values can be

calculated to show how much more likely the best model is to be correct: (1) the Akaike probability (also called Akaike weights), shown in Equation 2-20, and (2) the evidence ratio, which is the ratio of Akaike probabilities, shown in Equation 2-21 (Burnham and Anderson, 2002).

$$probability = \frac{e^{-0.5\Delta AIC_c}}{1+e^{-0.5\Delta AIC_c}} \quad (2\text{-}20)$$

$$evidence\ ratio = \frac{1}{e^{-0.5\Delta AIC_c}} \quad (2\text{-}21)$$

The AIC method is fairly straightforward to implement in model comparisons. For example, if a hypothetical Model A has an AIC_c of 400 and Model B has an AIC_c of 405, the Akaike probability of Model A is 0.92 and the evidence ratio is 0.082. This means that Model A is 92 percent more likely to be correct than Model B, and Model B is more than 12 times (inverse of the evidence ratio) less likely to be correct compared to Model A. An Akaike probability of 50 percent indicates that both models are equally likely to be correct, while a probability greater than 50 percent means that model 1 (Model A in the example) is more likely to be correct and less than 50 percent means that model 2 (Model B in the example) is more likely to be correct. Using these probabilities and evidence ratios, the model comparison can determine if any models other than the "best" can be considered close enough to be statistically similar.

2.5 Selection of Experimental Data

Statistical analyses in general require large amounts of data to adequately determine statistical viability. Cross-validation in particular benefits from large data sets. Experimental data selected from the published literature were included in three main data sets: (1) elemental composition of primary pyrolysis products (char and tar), (2) coal aromaticity, and (3) heating

values of coal and other fuels. There is some overlap in all of these data sets, and all data sets were selected based on several criteria. These data sets are detailed in full in Appendix B.

The elemental composition data set was gathered based on the following criteria: (1) tar must be primary tar (tar formed at temperatures below 1100 K, to limit secondary tar reactions), (2) low residence times (no hold times), (3) particle heating rates of at least 1000 K/s, and (4) compositions must be reported on a dry, ash-free (DAF) basis, or have enough information to convert to a DAF basis. Data from fluidized bed systems were not used unless accurate particle residence times were available. Frequently fluidized bed systems are reported with either an average estimated particle residence time or a fluid residence time. This can be different than a particle residence time. Table 2-4 lists the sources of experimental data along with key experimental conditions for each set of data.

The aromaticity data set was chosen to include elemental composition (proximate and ultimate analysis results), measured and calculated chemical structure parameters from NMR analysis, and the aromaticity must be a corrected or true aromaticity (f_a'). Many of these data were also used by Genetti et al. (1999) to fit chemical structure parameters for the CPD model. The data come from the following sources: Genetti et al. (1999), Solum et al. (1989), Hambly (1998), Perry et al. (Perry, 1999; Perry et al., 2000), Fletcher and Hardesty (1992), Watt (1996), Gerschel and Schmidt (2016), Cui et al. (2019), Ahmed et al. (2003), Lin et al. (2016), Suggate and Dickinson (2004), and Zhang et al. (1995).

The following criteria were used for the heating value data set: (1) proximate and ultimate analyses must be presented on a DAF basis, or enough information must be available to calculate the data on a DAF basis, (2) the data must include a heating value, preferably the higher heating value, and (3) char and tar analyses must be on pure products, i.e., with no

Table 2-4. Elemental Composition of Pyrolysis Products—Experimental Data

Author(s)	Institution	Apparatus	Gas Temp (K)	Char/Tar	Coal Types
Freihaut, et al (1989a; 1989b).	United Technologies Research Center	Entrained flow reactor	780-1069	Char and Tar	hvAb, bit, subC, lvb
Hambly (1998)	Brigham Young University	Drop tube reactor	820 and 1080	Char and tar	ligA, subA, hvCb, hvAb, lvb
Perry (Perry, 1999; Perry et al., 2000)	Brigham Young University	Drop tube reactor	895-1085	Char and tar	Sub, hvb, mvb, lvb
Fletcher and Hardesty (1992)	Sandia National Laboratories	Entrained flow reactor	1050	Char	Lig, sub, hvBb, hvAb, lvb
Watt (1996)	Brigham Young University	Drop tube reactor	850-1050	Char and tar	ligA, subC, hvCb, hvAb, lvb
Parkash (1985)	Devon Coal Research Centre	Laminar, entrained flow, atmospheric pressure reactor	820-980	Char	subB
Tyler (1980)	CSIRO	Heated fluidized bed reactor	873	Tar	bit, sub

solvent-based transformations. This data set not only includes coal-based fuels, but a variety of other fuel types. The sources of data are listed in Table 2-5.

Some of the coal (char and tar) and biomass data points did not include a reported sulfur content, with many reporting a combined oxygen and sulfur content (O+S). This is not as important for the biomass samples since sulfur is typically very low in most biomass fuels. For the coals, particularly the char and tar samples, an estimate was used to infer the split between oxygen and sulfur contents. For char and tar samples that did not include a reported oxygen or sulfur content (Edwards et al., 1983; Vorres, 1990; Glick and Davis, 1991; Proscia et al., 1994;

Riaza et al., 2017a; Riaza et al., 2017b), the oxygen-to-sulfur ratio was set equal to that of the parent coal. All three data sets are detailed in Appendix B.

Table 2-5. Heating Value of Different Fuels—Experimental Data

Author/Institution	**Number of Samples**
Argonne National Labs (Vorres, 1990)	8 Coal[a]
Pennsylvania State University Coal Database (Glick and Davis, 1991)	15 Coal
Foster Wheeler (Bryers, 1988)	7 Coal
Ahmed et al. (2010)	1 Coal, 1 Char[c]
Proscia et al. (1994)	2 Coal, 8 Char[b], 4 Tar[b,d]
Shamsi et al. (2004)	4 Char
Lazaro et al. (1998)	2 Coal
Ferrara et al. (2014)	2 Coal, 1 Biomass[b,e]
Tomaszewicz and Mianowski (2017)	11 Coal
Tourunen et al. (2009)	1 Coal
Ding et al. (2016)	2 Coal, 2 Petroleum Coke
Kajitani et al. (2002)	2 Coal
Roberts et al. (2003)	3 Coal
Wang, et al (2014)	2 Coal
Franchetti, et al (2013)	1 Coal
Suggate and Dickinson (2004)	35 Coal, 8 Peat
Ra et al. (2014)	1 Coal
Reichel et al. (2015)	1 Coal
Riaza et al. (2014; 2017a)	4 Coal, 3 Biomass
Riaza et al. (2017b)	1 Coal[b]
Seo et al. (2011)	1 Coal
Shadle et al. (2001)	3 Coal
Shaw et al. (1991)	14 Coal
Tufano et al. (2016)	1 Coal
Vascellari et al. (2015)	4 Coal, 1 Coal+Limestone
Weiland et al. (2012)	1 Coal, 1 Biomass
Wen, et al (2016)	1 Coal
Wu and Harrison (1986)	2 Coal
Sahu et al. (1988)	3 Coal
Parkash and Chakrabartty (1986)	11 Coal
The Babcock and Wilcox Company (1990)	2 Coal
Miller (2017a)	49 Coal
Al-Abbas et al. (2013)	1 Coal
Alvarez et al. (2013)	2 Coal
Benito et al. (1994)	4 Coal

Table 2-5. Heating Value of Different Fuels—Experimental Data, CONTINUED

Author/Institution	**Number of Samples**
Bharadwaj et al. (2004)	2 Biomass
Brewster, et al (1995)	3 Coal
Chakravarty et al. (1990)	19 Tar, 2 Oil Shale Tar, 1 Resinite Tar, 1 Tar Sand Tar
Channiwala and Parikh (2002)	36 Biomass, 7 Biomass Char, 15 Liquid and Gaseous Fuels, 10 Coal, 1 Coke, 1 Peat, 23 Other Fuels[f], 1 Char
Chern and Hayhurst (2005)	4 Coal
Cope et al. (1989)	3 Coal
Costa et al. (1990)	2 Coal
Daood et al. (2012)	1 Coal
Eatough and Smoot (1996)	2 Coal
Hees et al. (2016)	1 Coal
Huéscar Medina et al. (2014)	4 Biomass, 1 Coal
Ibarra et al. (1991)	9 Coal
Idris et al. (2012)	1 Coal, 3 Biomass
Arenillas et al. (2003)	6 Coal
Jayaraman et al. (2015)	1 Coal
Jin et al. (2013)	1 Coal, 5 Other Fuels[f]
Khan (1987)	2 Coal
Khatami et al. (2012)	4 Coal
Lemaire et al. (2015)	1 Coal
Lloyd et al. (1989)	6 Coal
Lu et al. (2013)	1 Biomass[b], 2 Biomass Char[b], 1 Coal
Man and Gibbins (2011)	7 Coal
Matali et al. (2015)	1 Coal, 1 Other Fuel[f]
Nugroho et al. (2000)	4 Coal[b]
Park and Song (2017)	4 Coal
Pielsticker et al. (2017b)	1 Coal
Saito et al. (1991)	1 Coal
CSIRO (Edwards et al., 1983)	7 Coal, 30 Char[b], 21 Tar[b]
Stournas et al. (1987)	2 Coal, 1 Peat
Niessen (2002)	24 Coal, 20 Biomass, 15 Liquid and Gaseous Fuel, 34 Other Fuel[f]
Biagini and Tognotti (2014)	20 Coal
Chen et al. (2012a)	1 Coal, 1 Biomass
Gövert et al. (2017)	1 Coal
Guo et al. (2015)	1 Coal
Hashimoto and Shirai (2014)	3 Coal
Rabaçal et al. (2015)	1 Coal
Rieth et al. (2016; 2017a; 2017b)	2 Coals
Sadhukhan et al. (2011)	3 Coal

Table 2-5. Heating Value of Different Fuels—Experimental Data, CONTINUED

Author/Institution	Number of Samples
Sorensen, et al (1996)	1 Coke
Toftegaard et al. (2010)	1 Coal
Tolvanen et al. (2013)	2 Coal, 1 Biomass, 1 Peat
Wen et al. (2017a; 2017c)	1 Coal
Yang et al. (2018)	2 Coal
Zhang et al. (2016)	1 Coal, 6 Char
Zhang et al. (2015)	1 Coal
Ringen et al. (1979)	28 Oil Shale
Annamalai et al. (1987)	6 Other Fuel[f]
Sun et al. (2015)	6 Propellant and Explosive
Lee et al. (1989)	7 Liquid and Gaseous Fuels, 15 Propellant and Explosive

[a] Coal refers to raw (or parent) coal
[b] Elemental analysis for these samples included C, H, N, and (O+S)
[c] Char refers only to coal char
[d] Tar refers to only coal tar
[e] Many of the biomass samples only have C, H, O reported reliably, with N reported for most, and S reported for some
[f] Other fuels is a general descriptor for any non-traditional fuels, including municipal solid waste, animal waste, food waste, rubber, leather, etc.
[g] Propellants and explosives include a reported heat of combustion

2.6 Summary and Conclusions

Much of the previous work in coal pyrolysis modeling has focused on improving simple models using simplified assumptions of real-world systems. This has been beneficial with limited computational resources, however, as computer technologies advance, larger and more complex problems can be simulated. This means that more complex submodels are needed to decrease overall error and uncertainty. This perhaps would help to bridge the gap between existing simple models (like the global pyrolysis models discussed in Section 2.3.1) and more complex models (e.g., network devolatilization models like CPD). New experiments and greater understanding of the processes that occur during coal pyrolysis make older models potentially less accurate and certainly less flexible in their application to new and challenging problems.

This problem might be easily solved by adjusting existing models, by improving some of the simplifying assumptions made in previous work, or may even require the development of newer, more complex models to adequately model coal pyrolysis reactions in modern coal systems.

3 OBJECTIVE AND TASKS

The objective of this research is to develop, evaluate, and implement improved, simple coal pyrolysis models for use in large-scale simulations of oxy-fuel fired coal boilers. This research focuses on all aspects of primary pyrolysis reactions, as detailed in the literature review chapter. The overarching goal is to add improved coal pyrolysis models to large-scale simulations designed to evaluate existing coal boiler technologies and to design and validate potential new technologies in the future.

3.1 Tasks

The following tasks were implemented to advance the objective:

1. Evaluate simple coal pyrolysis yield and rate models from the literature by comparison to the CPD model and develop improved simple models based on the best of the literature models.
2. Evaluate correlations describing coal aromaticity found in the literature and develop and test improved models based on comparison to a data set of coal aromaticity values from experiments in the literature. Aromaticity can then be used as a fitting parameter for other important coal properties.
3. Correlate reported elemental compositions (CHONS) of the products of primary pyrolysis (char and tar, with the light gases calculated by difference) based on experimental data from

established literature. These correlations calculate the elemental composition using several coal- and condition-specific variables. This analysis also uses a cross-validation technique to better quantify uncertainty and bias in each model when compared to experimental data.

4. Evaluate several correlations to calculate heats of combustion (heating values) using a large set of experimental data from established literature. This task primarily evaluates these models using coal, char, and tar data; however, the large data set includes data for several other types of fuels, including biomass, other fossil fuels, propellants and explosives, and others.
5. Use the correlations from task 4 to evaluate various mixture fraction approaches for modeling equilibrium reactions of coal pyrolysis products over a range of oxidizer concentrations.

All of the above tasks support improvements in the combined use of equilibrium chemistry and mixture fraction approaches in large coal combustor simulations. Equilibrium calculations require the combined gas-phase elemental composition, the pressure, and the energy content (i.e., the enthalpy). The combined elemental composition at any location in the combustor is related to the rates and yields of pyrolysis. This dissertation is therefore organized as follows. Coal pyrolysis rate models are evaluated in Chapter 4, along with newly proposed models. As part of the research on the correlation of the elemental composition of pyrolysis products, a new correlation for parent coal aromaticity was developed, and is presented in Chapter 5. Chapter 6 then describes correlations of the elemental compositions of coal tar and char based on parent coal composition and pyrolysis conditions, building on the aromaticity correlations from Chapter 5. Correlations of heating values of tar and char (and several other

non-coal fuels) are presented in Chapter 7. Finally, the use of improved elemental compositions and heating values are discussed in mixture fraction calculations combined with equilibrium modeling of coal combustion applications (Chapter 8). Chapter 9 presents a summary and conclusions from this work, along with recommendations for future work. Also included in this dissertation are several appendix chapters that discuss mathematical and computational tools in more detail as well as presenting additional analysis information that was not included in the main chapters of the dissertation.

4 COAL PYROLYSIS YIELDS AND RATES

This chapter details the work done on modeling coal pyrolysis yields and rates, particularly those of the total volatiles that include both tar and light gas fractions evolved during the coal pyrolysis reaction. This chapter is modified from the work published in Richards and Fletcher (2016). In this chapter, several pyrolysis rate models from the literature are tested and two improved rate models were developed based on the best aspects of the literature models.

4.1 Introduction

Simulations of coal boilers, gasifiers, and other combustion processes require adequate submodels to represent each aspect of the simulation (Alvarez et al., 2013). For coal combustion simulations, one of these important submodels describes the devolatilization behavior of coal particles. There are two main forms of devolatilization models in the literature: global models and network models. Network models include the chemical percolation devolatilization (CPD) model (Grant et al., 1989; Fletcher et al., 1992b), FLASHCHAIN model (Niksa, 1988), and the FG-DVC model (Solomon et al., 1988). These network models have been shown to be very accurate in their predictions of devolatilization behavior, however, they are computationally complex (Smith et al., 1994), which directly impacts the amount of time needed to run complex simulations (Brewster et al., 1995). Because of this, most large-scale coal combustion simulations use global devolatilization models instead of the more complex network models.

Global models are less computationally complex, but typically do not apply to as broad a range of coal types, heating rates, and temperatures as network models, and therefore need to be tuned, or optimized, using trusted experimental data or predictions. Several of the most widely used coal devolatilization models are found in Table 2-1 and are discussed at length in Section 2.3.1.

The global models fall into two main categories: one kinetic step and two kinetic steps. While it is possible to get a one-step model to fit predictions for one heating rate, it is desirable to develop a simple model that can give reasonable predictions of rate and yield over a range of heating rates simultaneously.

4.2 Approach

Particle heating rates in coal combustion simulations and experiments have been reported to be as high as 10^6 K/s (Anthony et al., 1975; Kobayashi et al., 1977; Ubhayakar et al., 1977; Maloney et al., 1991; Therssen et al., 1995; Backreedy et al., 2006; Chen et al., 2012b; Alvarez et al., 2013; Authier et al., 2014; Lemaire et al., 2015). The CPD model was used to predict the devolatilization behavior of a Utah bituminous Sufco coal (see Table 4-1 for proximate and ultimate analysis) using four heating rates (5×10^3 K/s, 1×10^4 K/s, 1×10^5 K/s, and 1×10^6 K/s) with a temperature range of 300 to 1600 K with no hold time at 1600 K. Models tuned to this set of predictions will only hold true for this particular range and coal type, however, this procedure can be re-applied for other heating rates, temperatures, or coal types. These four heating rates were used to capture the range of heating rates expected in a pulverized coal boiler.

Each model form was coded in MATLAB using an explicit Euler method to numerically integrate the rate to find the yield. The model coefficients were "tuned" to the CPD predictions using MATLAB's built-in *fmincon* optimizer, which was used to minimize the sum of squared

Table 4-1. Sufco coal proximate and ultimate analyses.

Proximate Analysis (as rec'd)		Ultimate Analysis (dry)	
Moisture	6.11	C	67.87
Ash	8.36	H	5.45
Volatile Matter	38.49	O (by difference)	16.87
Fixed Carbon	47.04	N	1.09
HHV (BTU/lb)	11899	S	0.36

errors (see Equation 2-11) between the global model predictions and the CPD model predictions. Non-linear constraints were used for the two-step kinetic models to ensure one kinetic pathway dominates at lower temperature and the other dominates at high temperatures. Literature coefficients were used as an initial guess for the optimizer. Upper and lower bounds on model coefficients were chosen based on known literature values and expected behavior. Although this analysis focused on the total volatiles, the same procedure can be used to fit model coefficients for tar yields, as long as tar yield data or trusted predictions are used. More details on MATLAB optimizers are found in Appendix A.

Each model was evaluated for goodness of fit based on three key trends in devolatilization behavior (see Figure 2-3): (1) total volatiles yield as a function of temperature and heating rate, (2) ultimate volatiles yield at each heating rate, and (3) rate of volatiles formation during devolatilization.

4.3 Results and Discussion

The results of each of the six literature models in Table 2-1 are shown and discussed in the following section. In addition, two new pyrolysis models were developed and are discussed here. Finally, the results are summarized, and several models are suggested based on their accuracy and utility in large-scale simulations.

4.3.1 Single First-Order Model Comparisons

The single first-order model was optimized for all four heating rates simultaneously. Table 4-2 shows the optimized coefficients for the Sufco coal, and Figure 4-1 shows the comparison of the optimized results with the CPD model calculations, with Figure 4-1a showing the yield trends versus temperature and Figure 4-1b showing the ultimate yield (total yield at the final time and temperature) versus heating rate.

Table 4-2. Optimized Single First-Order Model Coefficients

Coefficient	Value
V_∞	0.560
A	2.95×10^{13} s^{-1}
E/R	2.38×10^{4} K

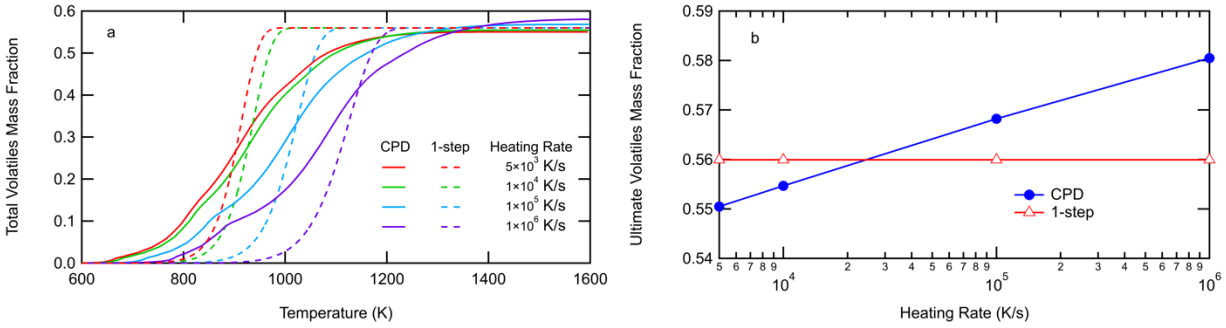

Figure 4-1. Single first-order model predictions for Sufco coal, (a) total volatiles fraction vs. particle temperature (K) and (b) ultimate volatiles yield vs. heating rate.

The optimized first-order model shows rates that are too steep with temperature when compared to the CPD model predictions of the same coal, however, the average devolatilization temperature for each heating rate is generally in the correct spot, but devolatilization occurs much faster according to the first-order model. In addition, the first-order model does not show the expected increase of ultimate volatiles yield with increasing heating rate. This is because of

limitations with the single first-order model, which has a set yield coefficient. While the single first-order model does not follow all three devolatilization trends, it is one of the simplest models discussed here, with only three fitted coefficients.

4.3.2 Yamamoto Model Comparisons

The Yamamoto model (DM-2 in Table 2-1) was also optimized for all four heating rates simultaneously. Table 4-3 shows the optimized Yamamoto model coefficients for the Sufco coal, and Figure 4-2 shows a comparison of the Yamamoto model predictions with the CPD model predictions.

Table 4-3. Optimized Yamamoto Model Coefficients

Coefficient	Value
V_∞	0.560
A	1.04×10^{12} s^{-1}
E/R	3.52×10^{4} K
c_0	25.5
c_1	-56.4
c_2	131
c_3	-176
c_4	122
c_5	-38.6

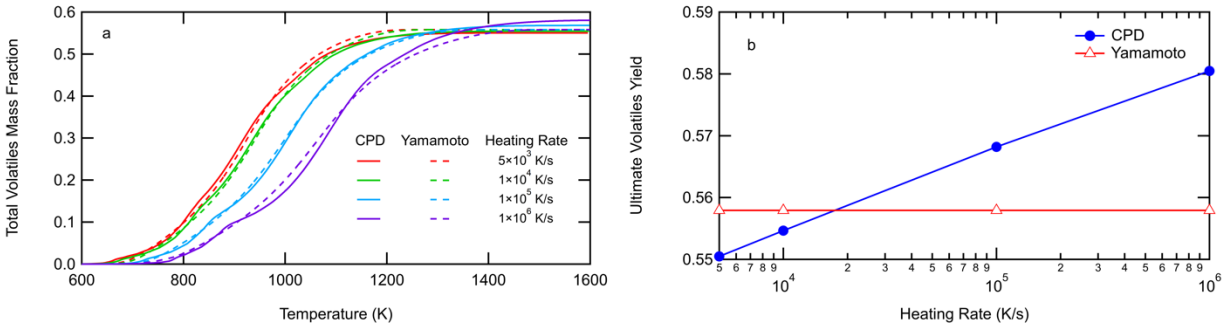

Figure 4-2. Yamamoto model predictions for Sufco coal, (a) total volatiles fraction vs. particle temperature (K) and (b) ultimate volatiles yield vs. heating rate.

The Yamamoto model is a modified version of the single first-order model, so it is expected to follow the three devolatilization trends better than the single first-order model. The devolatilization rates and temperatures (Figure 4-2a) match up very well between the Yamamoto and CPD model predictions, however, the ultimate yield (Figure 4-2b) is still uniform for all heating rates. Like the single first-order model, the prescribed yield factor for the Yamamoto model does not change with temperature or heating rate information.

4.3.3 Biagini and Tognotti Model Comparisons

The Biagini and Tognotti (BT) model (DM-3 in Table 2-1) is also a modified version of the single first-order model. Biagini and Tognotti (2014) not only developed this model to improve the single first-order model predictions, but they also correlated the major model coefficients (A, E/R, and DI) with some coal-specific parameters in an effort to increase the model utility with different coal types. Table 4-4 shows the BT model coefficients both for the coefficients suggested in the literature (based on Sufco coal parameters) and re-optimized coefficients based on the comparison with the CPD model predictions. Figure 4-3 shows a comparison of the BT model with CPD model predictions.

Table 4-4. Biagini and Tognotti Model Coefficients

Coefficient	Literature	Optimized
A	895 s^{-1}	2.95×10^{13} s^{-1}
E/R	3.87×10^{3} K	2.38×10^{4} K
DI	0.690	0.690

The suggested (literature) coefficients do not match the CPD model predictions very well at all, either in the yield versus temperature or the ultimate volatiles yield. It appears that the correlations in Biagini and Tognotti (2014) were optimized for a heating rate of 1×10^{4} K/s, but

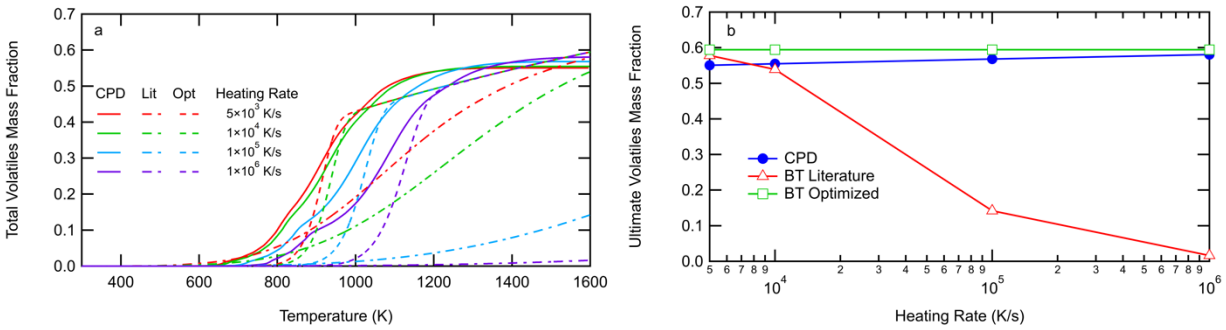

Figure 4-3. Biagini and Tognotti model predictions for Sufco coal, (a) total volatiles fraction vs. particle temperature (K) and (b) ultimate volatiles yield vs. heating rate.

predictions using these literature values do not agree with the CPD model, perhaps due to a time-step inconsistency. The re-optimized coefficients performed better than the literature coefficients when compared to the CPD model predictions, however, the BT model predictions still do not match the CPD model predictions. While the BT model does allow for the prescribed yield factor to change based on temperature, it does not change with heating rate, which again leads to a constant ultimate yield with increasing heating rate.

4.3.4 Utah Model Comparisons

The Utah model (DM-5 in Table 2-1, also called the modified BT model) is a modified version of the BT model, and was modified to include a yield curve that allows the BT model to accurately predict yields at long-time values. Table 4-5 shows the optimized coefficients for the Utah model. Like the original BT model, Table 4-5 shows both the literature (Schroeder, 2015) and re-optimized values for the model coefficients. Figure 4-4 shows the comparison of the predictions of the Utah and CPD models.

Table 4-5. Utah Model Coefficients

Coefficient	Literature	Optimized
a	0.550	0.587
b	14.3	0.438
c	-10.6	22.0
d	3.19	-13.4
e	-1.23	37.9
T_{ignite}	590 K	304 K
E_0/R	1.11×10^4 K	7.88×10^3 K
σ_a/R	826 K	2.62×10^3 K
A	1.97×10^7 s^{-1}	5.0×10^7 s^{-1}

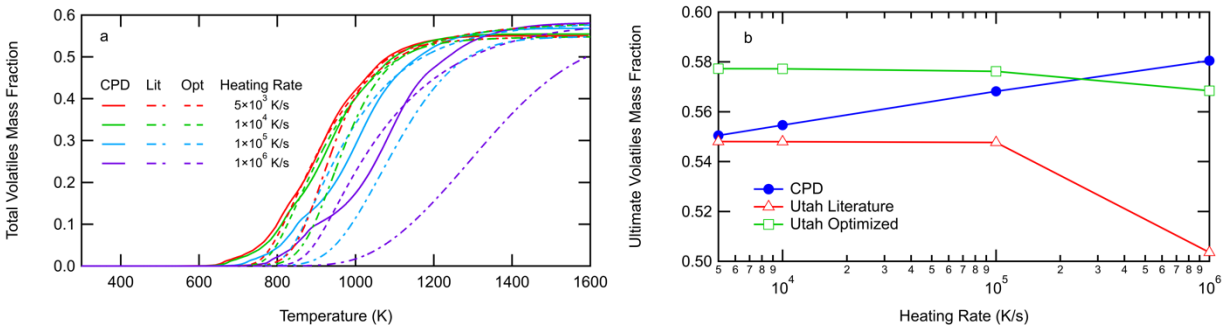

Figure 4-4. Utah model predictions for Sufco coal, (a) total volatiles fraction vs. particle temperature (K) and (b) ultimate volatiles yield vs. heating rate.

The Utah model matches the CPD model yield vs temperature predictions (Figure 4-4a) much better than the other simple models, however, the ultimate yield values actually decrease as heating rate increases (see Figure 4-4b). The devolatilization temperature is fairly accurate over all four heating rates, but the rate does not match as well, being too fast at lower temperatures and too slow at higher temperatures, especially at higher heating rates. The Utah model shows some improvement over the original BT model, but may not be enough to justify the additional fitted coefficients. A disadvantage of the BT model form is that the volatiles yield approaches 1.0 (complete conversion to volatile gases) at higher temperatures, which is not predicted by the CPD model or observed in the literature. The ultimate yield of the Utah model also continues to

increase with temperature above the yields predicted by the CPD model. This is only an advantage at significantly long hold times, where the particle is expected to be at steady state.

4.3.5 Distributed Activation Energy Model Comparisons

The distributed activation energy model (DAEM, DM-4 in Table 2-1) was a modification of the simple first-order model that includes a distribution of activation energies. This makes the model more physically accurate to coal pyrolysis processes than any of the other first-order models, since the molecular bonds in coal that break during pyrolysis have a wide range of bond energies. Table 4-6 shows the optimized model coefficients for the sequential DAEM. Figure 4-5 shows the comparison of the fitted DAEM to CPD model predictions.

Table 4-6. Optimized DAEM Coefficients

Coefficient	Value
A	8.78×10^{17} s^{-1}
E_0/R	3.04×10^{4} K
σ_E/R	9.60×10^{3} K
V_∞	0.566

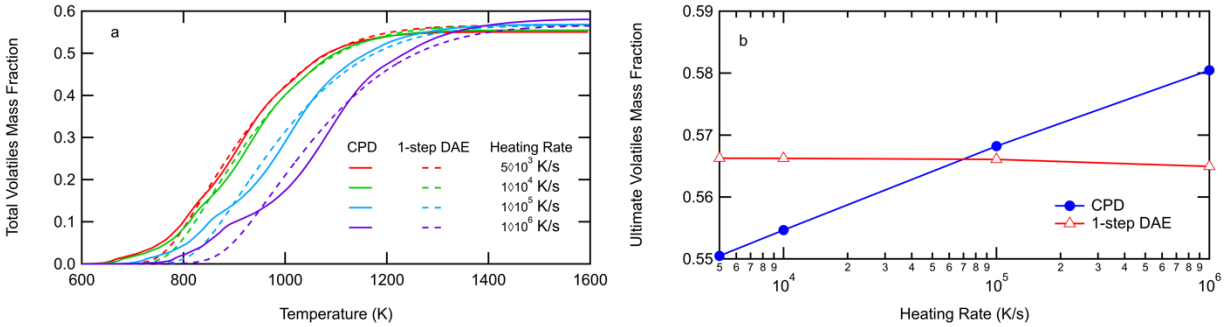

Figure 4-5. DAEM predictions for Sufco coal, (a) total volatiles fraction vs. particle temperature (K) and (b) ultimate volatiles yield vs. heating rate.

The one-step DAEM accurately predicts the devolatilization rates and effective temperature of devolatilization as shown in Figure 4-5a, but it again predicts a constant ultimate yield with increasing heating rate, like the other one-step models. The only one-step model that does better at matching CPD predictions for total volatiles yield as a function of particle temperature is the Yamamoto model, but compared to the nine fitted coefficients of the Yamamoto model, the DAEM only has four, which means the DAEM is almost as accurate as the Yamamoto model while having less than half the coefficients.

4.3.6 Simple Two-Step Model Comparisons

The simple two-step model (DM-6 in Table 2-1) is an improvement on the one-step models because it allows two kinetic "steps" to occur over the extent of the pyrolysis reaction, with one step dominating at lower temperatures and the other dominating at higher temperatures. Table 4-7 shows the optimized coefficients for each "step" in the simple two-step model. The comparison of the simple two-step model predictions with the CPD model predictions is found in Figure 4-6.

Table 4-7. Optimized Simple Two-Step Model Coefficients

Coefficient	**Step 1**	**Step 2**
Y_i	0.5	0.576
E_i/R	8.37×10^3 K	2.78×10^4 K
A_i	3.0×10^5 s^{-1}	1.24×10^{15} s^{-1}

The effective temperature of devolatilization as predicted by the simple two-step model matches the CPD predictions, and the two-step model also comes very close to matching the CPD ultimate yield predictions, especially at heating rates between 1×10^4 and 1×10^5 K/s. The

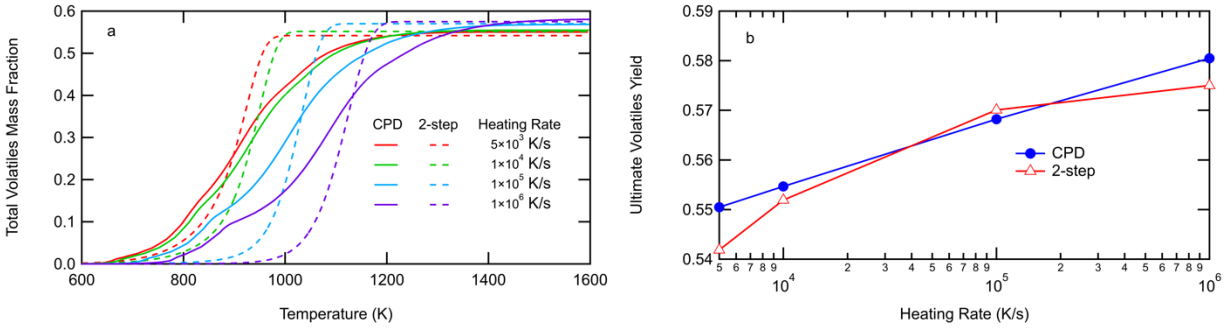

Figure 4-6. Simple two-step model predictions for Sufco coal, (a) total volatiles fraction vs. particle temperature (K) and (b) ultimate volatiles yield vs. heating rate.

simple two-step model is the first of the simple models to actually show an increase in ultimate volatiles yield with an increase in heating rate. However, the devolatilization rates as predicted by the two-step model are much too steep compared to CPD model predictions when fit to four heating rates simultaneously, in a similar fashion to the single first-order model.

4.3.7 Modified Two-Step Model with Correction Factor

The modified two-step model with correction factor (or RF model) was developed as part of this dissertation to combine the attributes of the simple two-step and Yamamoto models. The simple two-step model was the best with respect to ultimate yield while the Yamamoto model was the best at predicting the devolatilization rates. The model form for the RF model is shown in Equations 4-1 to 4-3.

$$\frac{d(C)}{dt} = -\left(F_1 A_1 e^{-\frac{E_1}{RT}} + F_2 A_2 e^{-\frac{E_2}{RT}}\right) C \tag{4-1}$$

$$\frac{d(V)}{dt} = \left(F_1 Y_1 A_1 e^{-\frac{E_1}{RT}} + F_2 Y_2 A_2 e^{-\frac{E_2}{RT}}\right) C \tag{4-2}$$

$$F_n = e^{\sum_{i=0}^{5} c_{i,n} [X_{coal}]^i} \tag{4-3}$$

where F_n is the corrective factor of kinetic step n, C is the "raw" coal value (which ranges from 1 to 0 over the pyrolysis reaction), and X_{coal} acts as an extent of reaction, like the original Yamamoto model. The optimized coefficients for the RF model are found in Table 4-8. Figure 4-7 shows the comparison between RF and CPD model predictions.

Table 4-8. Optimized RF Model Coefficients

Coefficient	**Step 1**	**Step 2**
Y_i	0.195	0.592
E_i/R	1.50×10^4 K	3.18×10^4 K
A_i	4.11×10^5 s^{-1}	1.0×10^8 s^{-1}
c_0	-56.8	29.8
c_1	75.9	-48.3
c_2	538	88.8
c_3	-798	-67.2
c_4	-129	6.03
c_5	30.6	3.81

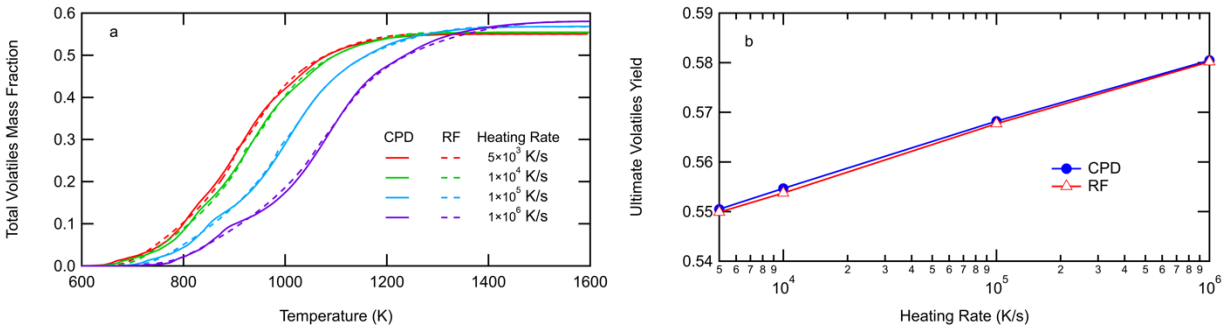

Figure 4-7. RF model predictions for Sufco coal, (a) total volatiles fraction vs. particle temperature (K) and (b) ultimate volatiles yield vs. heating rate.

The RF model very accurately reflects the trends predicted by the CPD model, in terms of the devolatilization rate, effective devolatilization temperature, and ultimate volatiles yield trends. Of all the simple models tested, the RF model is the most accurate when compared to

CPD predictions, however, with 18 fitted model coefficients, the RF model could prove too computationally complex for some simulations.

4.3.8 Modified Two-Step Model with Distributed Activation Energies

In an effort to reduce the number of model coefficients while maintaining accuracy, the modified two-step model with distributed activation energies (RFE model) was developed here to combine the simple two-step model with the sequential DAEM. The one-step DAEM was the second-most accurate one-step model behind the Yamamoto model. The RFE model form is shown in Equations 4-4 to 4-6.

$$\frac{d(C)}{dt} = -\left(A_1 e^{-\frac{E_1+\sigma_{E1}Z}{RT}} + A_2 e^{-\frac{E_2+\sigma_{E2}Z}{RT}}\right) C \tag{4-4}$$

$$\frac{d(V)}{dt} = \left(Y_1 A_1 e^{-\frac{E_1+\sigma_{E1}Z}{RT}} + Y_2 A_2 e^{-\frac{E_2+\sigma_{E2}Z}{RT}}\right) C \tag{4-5}$$

$$Z = \sqrt{2} \cdot erfinv\big(1 - 2(1 - C)\big) \tag{4-6}$$

where $erfinv$ is the inverse error function and the values for Y, A, E, and σ_E are different for each kinetic step. Table 4-9 shows the optimized coefficients for the RFE model. Figure 4-8 shows the RFE model predictions compared to the CPD model predictions.

Table 4-9. Optimized RFE Model Coefficients

Coefficient	**Step 1**	**Step 2**
Y_i	0.208	0.578
E_i/R	1.50×10^4 K	3.01×10^4 K
A_i	2.0×10^7 s^{-1}	9.6×10^{15} s^{-1}
σ_{Ei}/R	3.12×10^3 K	4.88×10^3 K

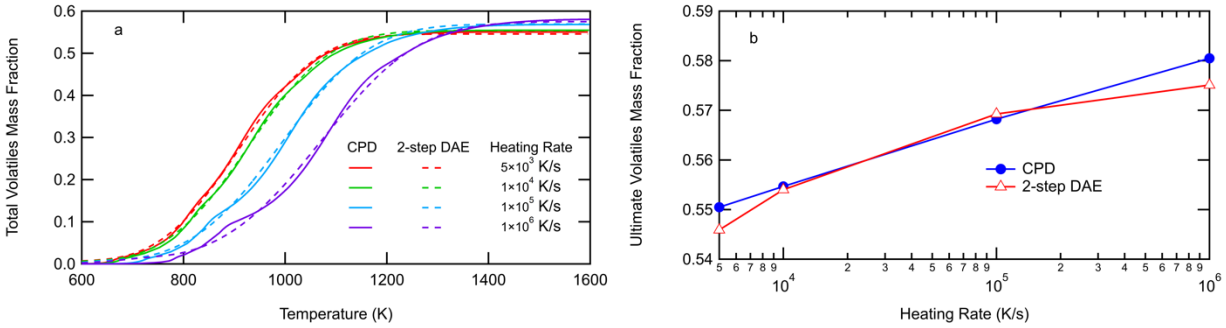

Figure 4-8. RFE model predictions for Sufco coal, (a) total volatiles fraction vs. particle temperature (K) and (b) ultimate volatiles yield vs. heating rate.

The RFE model does almost as well as the RF model in matching the CPD model predictions but is slightly less accurate both in terms of the devolatilization rates as well as the ultimate volatiles yields, especially at the lowest and highest heating rates, however, the RFE model is the second most accurate of the simple devolatilization models tested here. In addition, the RFE model has only 8 model coefficients compared to the RF model's 18, which means the RFE model is potentially better in terms of computational complexity in large-scale simulations.

4.4 Extension to Additional Coals

The analysis of the simple coal pyrolysis rate/yield models presented in this chapter was completed using only the Sufco coal properties, however, the curve fitting and analysis presented here can easily be extended to other coals. The models were fit to CPD model predictions using coal-specific chemical and structural properties and several different temperature histories by minimizing the sum of squared error between the simple model predictions and the CPD model calculations. The re-fitting process of the simple model coefficients is as follows:

1. Obtain the proximate and ultimate analyses of the coal of interest.

2. Generate particle temperature history (or histories)—from a constant heating value or based on histories observed in an experimental apparatus (e.g., drop tube, flat flame burner, etc.).
3. Calculate NMR structural parameters for CPD model calculations (Genetti et al., 1999).
4. Use temperature history, coal-specific properties, and other CPD inputs to generate CPD model predictions for every condition of interest.
5. Choose simple model(s) for pyrolysis rate/yield (RF, RFE, DAEM, etc.).
6. Optimize simple model coefficients using a sum of squared errors analysis between CPD and simple model predictions.
7. Incorporate simple model with optimized coefficients into large-scale simulation or other analysis.

4.5 Summary, Conclusions, and Recommendations

Based on accurate CPD model predictions, simple devolatilization models must follow three main trends when modeling devolatilization behavior: (1) the predicted rates of devolatilization cannot be too steep or too shallow, (2) the effective temperature at which devolatilization occurs increases with increasing heating rate, and (3) the ultimate volatiles yield must also increase with increasing heating rate. Each of the simple models tested here might be very accurate in predicting these trends while using only one particle heating rate, however, some of the models do not perform as expected when optimized to multiple heating rates simultaneously. These observations are summarized in Table 4-10.

The two-step models generally outperformed the one-step models for all three devolatilization behavior trends for all heating rates, however, the two-step models also tend to be more computationally complex than the one-step models. The results described here indicate

Table 4-10. Devolatilization Model Performance Summary

Model	No. of Coefficients	Heating Rate Effect on Ultimate Yield	Heating Rate Effect on Effective Devolatilization Temperature
1-Step	3	None	Poor
Yamamoto	9	None	Good
BT	4	None	Poor
Utah	8	Marginal	Poor
DAEM	4	None	Good
2-Step	6	Poor	Marginal
RF	18	Good	Good
RFE	8	Good	Good

that the form of the devolatilization model used in a large-scale simulation is important, especially when the simulation has enough resolution to include adequate time-steps for the integration of devolatilization rates. Worthy to note is that these models can be re-fit for any coal type, both for total volatiles and tar yields, using trusted data or model predictions.

The modified two-step models both perform well when fit over a wide range of heating rates. The RF model in particular is suggested for its incredible accuracy if the number of model coefficients is not a concern, however, if fewer coefficients are necessary, the RFE model predicts coal devolatilization behavior almost as well as the RF model with almost a third of the model coefficients. The BT and Utah models include modifications that may improve ultimate yields in very long-time calculations, including in simulations where numerical accuracy is harder to maintain with large time steps.

While the results presented in this chapter are mainly based on a curve-fit comparison between two different types of pyrolysis models, this work has improved several aspects of the modeling of coal pyrolysis reactions. Much of the previous work in simple coal pyrolysis modeling has focused on only one combustion condition (one coal type and one temperature history) at a time. This work extends some of the more common simple models and two new models to several conditions (one coal type and four temperature histories) at a time, which in

turn allows the model to be used to greater utility in large-scale simulations. Finally, this analysis has showed that the two new models match a greater number of pyrolysis trends over a wider range of simultaneous combustion conditions than any of the other common simple coal pyrolysis rate/yield models, which means that most large-scale simulations that implement either of the two new models will be more accurate (assuming the simulation time steps are small enough to maintain stability during numerical integration).

5 AROMATICITY OF COAL

This chapter details work done in testing models to predict coal aromaticity. This chapter is modified from work presented in Richards et al. (2019). Several literature models as well as a new proposed model are discussed here. The motivation for this work was to test correlations of coal aromaticity for possible use in modeling other coal characteristics, such as the elemental composition of coal char and tar after pyrolysis (see Chapter 6) or heating values of coal, char, or tar (Chapter 7).

5.1 Introduction

Coal aromaticity is a structural parameter unique to each coal that is calculated as part of the complete solid-state ^{13}C NMR analysis of the coal (Solum et al., 1989; Fletcher and Hardesty, 1992; Watt, 1996; Watt et al., 1996; Hambly, 1998; Hambly et al., 1998; Genetti et al., 1999; Perry, 1999; Perry et al., 2000). As part of the NMR analysis, there are two aromaticity measurements: (1) the total aromatic carbon contribution (f_a), which is also called the apparent aromaticity and includes the carbonyl contribution, and (2) the true or corrected aromatic carbon content (f_a'), which removes the carbonyl contribution. Seven models found in the literature were tested against a set of coal aromaticity data. The literature model forms are found in Table 2-2 and the data set is found in Table B-3 in Appendix B.

5.2 Approach

The seven literature aromaticity models plus 44 additional model forms (see Table C-1 in Appendix C) were evaluated using the aromaticity data set that includes elemental composition (both proximate and ultimate analysis results) and measured and calculated chemical structure parameters from NMR analysis. Testing of these different models was performed in two ways. First, the literature models with their suggested coefficients were compared against the aromaticity data set. Second, the coefficients for each model form were refit using this current aromaticity data set. This second step was included to ensure that the seven literature correlations were treated equally with the additional model forms. In Table C-1, the last seven models (37-44) are the refit versions of the literature models, with the remaining models based on prior knowledge of variables that can affect coal aromaticity. Also included in the aromaticity correlations are other structural and chemical parameters that can be measured by various standard tests or predicted by simple correlations in the literature, such as Genetti's (1999) NMR structural parameter correlations.

The models were refit using MATLAB's built-in optimizers with a simple least-squares analysis. Each model fit (with both literature and refit coefficients) was tested using five key validation metrics: R^2 (Equation 2-7), SSE (Equation 2-11), the L_1 norm (Equation 2-14), the L_2 norm (Equation 2-15), and the infinity norm (Equation 2-16).

5.3 Results and Discussion

Only the results of the seven literature model forms (using both original and refit coefficients) plus the best overall model (proposed) are presented in this chapter. The complete results of the other tested models are found in Appendix C. The statistical results of the model comparisons are found in Table 5-1. This table is divided in two main sections, with the first

Table 5-1. Statistical Results of Coal Aromaticity Model Comparison

	Original Coefficients					Refit Coefficients				
Model	**L_1 Norm**	**L_2 Norm**	**Infinity Norm**	**SSE**	**R^2**	**L_1 Norm**	**L_2 Norm**	**Infinity Norm**	**SSE**	**R^2**
Proposed						0.033	0.044	0.166	0.118	0.797
Ko	0.058	0.076	0.215	0.458	0.595	0.053	0.070	0.228	0.395	0.641
Gerstein	0.075	0.088	0.195	0.626	0.549	0.063	0.079	0.198	0.497	0.549
MV[a]	0.091	0.112	0.367	1.012	0.626	0.056	0.040	0.274	0.411	0.626
SK[b] 1	0.055	0.082	0.349	0.406	0.649	0.040	0.058	0.232	0.204	0.649
SK 2	0.052	0.070	0.231	0.394	0.716	0.047	0.062	0.201	0.304	0.724
SK 3	0.052	0.070	0.231	0.394	0.716	0.046	0.061	0.212	0.298	0.729
SK 4	27.5	45.6	2.74×10^2	1.27×10^5	0.057	0.034	0.046	0.176	0.129	0.777

[a] MV is short for Maroto-Valer

[b] SK is short for Singh and Kakati

showing the statistical results of the literature models using the original coefficients, and the second showing the statistical results of all models using the refit coefficients.

As Table 5-1 shows, the SK2 and SK3 models (Singh and Kakati, 2003) (see Table 2-2) performed the best out of all the literature correlations while using the original coefficients. Upon refitting of the literature correlation coefficients, all performed better than the original correlations. This was expected, since the literature correlations were not originally fit to the same data set used here. Some of the literature correlations rely on elemental compositions on a dry, mineral-matter free (DMMF) basis, however, the experimental data set in Table B-3 has elemental compositions on a dry, ash-free (DAF) basis, which may account for part of the poorer fit of a number of the literature models with original coefficients. Surprisingly, the worst original literature correlation (SK 4) became the best literature correlation upon refitting. The proposed model form, however, outperformed all the literature correlations by all five measures of fit, but it has nine coefficients and four independent variables, which is more than the other literature correlations. The proposed model form follows the same form as Genetti's correlations, as shown in Equation 5-1. The model coefficients fit to the aromaticity data set are shown in Table 5-2.

$$f_a' = c_1 + c_2 C_{coal} + c_3 C_{coal}^2 + c_4 H_{coal} + c_5 H_{coal}^2 + c_6 O_{coal} + c_7 O_{coal}^2 + c_8 V_{ASTM} + c_9 V_{ASTM}^2 \quad (5\text{-}1)$$

Table 5-2. Proposed Aromaticity Correlation Coefficients

c_1	c_2	c_3	c_4	c_5	c_6	c_7	c_8	c_9
4.384	-8.679E-2	5.352E-4	2.601E-2	-6.879E-3	3.525E-3	-5.710E-4	-2.666E-3	5.659E-6

Figure 5-1 shows parity plots for the coal aromaticity model form tests, showing the predictions using both the original coefficients and the refit coefficients. Note that the plot

showing the SK4 model (purple diamonds), the markers showing the model with the original coefficients are not visible. This is not a mistake—the fit for the original coefficients is so poor that the markers appear well outside the bounds of the re-fit coefficients. This would distort the plot enough to skew the information of the re-fit model.

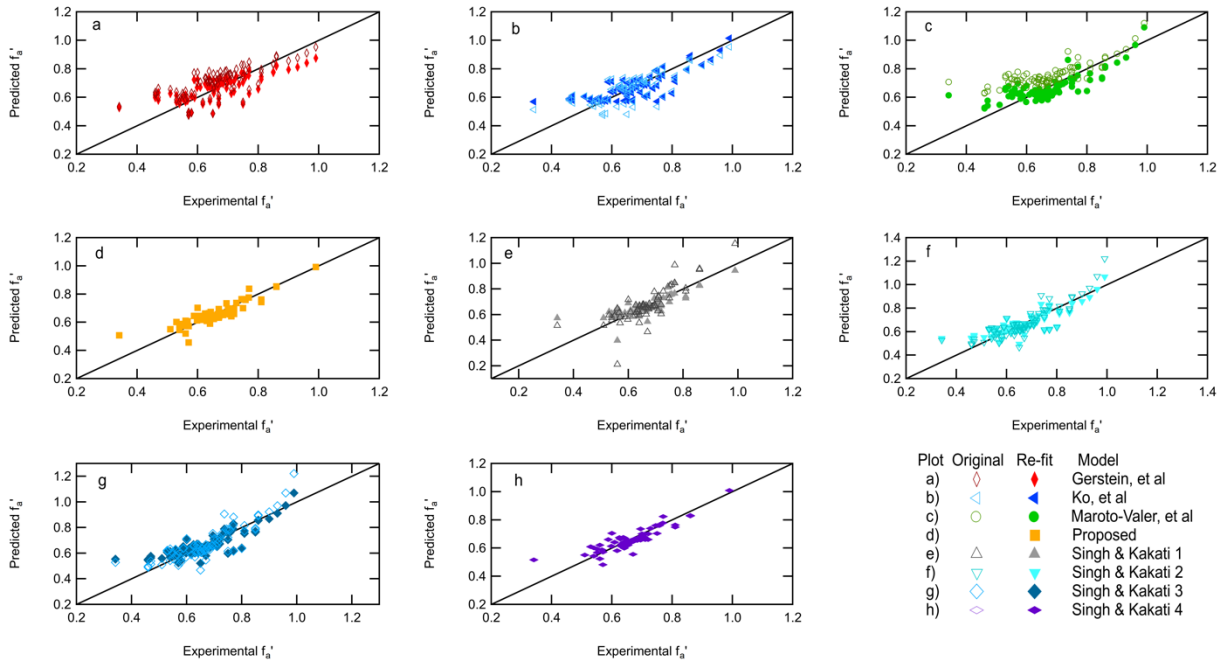

Figure 5-1. Parity relationship of the proposed aromaticity correlation and seven aromaticity correlations from the literature using both original and re-fit coefficients.

These plots are shown as visual confirmation that the SK2 and SK3 correlations perform the best out of all the literature correlations while using the original coefficients. The SK4 correlation performed the best of the literature models using the re-fit coefficients, which is all the more surprising considering the poor performance of the original coefficients. However, even with the vast improvement of the SK4 correlation, the proposed correlation fits the aromaticity data the best.

5.4 Summary and Conclusions

A large data set of measured carbon aromaticity in coal was gathered from the literature. This data set was curated to include sources that reported the corrected or true carbon aromaticity which removes the NMR contribution of carbonyl groups. This can make a large difference in modeling since certain coals contain a larger contribution of carbonyl coals than other coals.

Several models found in the literature were developed to calculate coal aromaticity based on several coal-specific parameters, with many using one or more of the elements (CHONS) of the raw coal along with the ASTM volatile matter that is typically determined in a proximate analysis. For many of these literature correlations, it is unclear whether they were developed using the true aromaticity or the aromaticity that includes carbonyl contributions. To adequately test each literature correlation, the suggested model coefficients were tested along with coefficients re-fit to the aromaticity data set. All literature models improved when the coefficients were re-fit, especially the SK4 correlation (Singh and Kakati, 2003). Using the original literature coefficients, the SK4 correlation predicted coal aromaticities several orders of magnitude larger than are even possible.

In addition to testing several correlations found in the literature, more than 40 different model forms were tested using the aromaticity data set to determine if any improvement was possible over the literature models. Several of these additional models performed better than the literature models, including the proposed model discussed here. The proposed model performed better than the literature models in all statistical measures, with an R^2 of almost 0.8, which means the proposed model will calculate the carbon aromaticity of the coal more accurately than any of the commonly used literature models. The next best literature model had an R^2 of 0.77.

6 ELEMENTAL COMPOSITION OF PYROLYSIS PRODUCTS

This chapter details efforts to correlate the primary organic elemental composition (CHONS) of the products of primary pyrolysis, primarily char and tar. If the compositions of coal, char, and tar are known, the average composition of the light gas can be calculated by difference. This chapter is modified from work presented in Richards et al. (2019). Additional analysis is found in Appendix C.

6.1 Introduction

Simulations of large-scale combustors include submodels to describe many of the physical and chemical processes in combustion, including fluid and particle flow, heat transfer, mass transfer, gas and solid reactions, etc. Simplified empirical models tuned using experimental data are used to decrease the computational complexity and time requirements. Many times there are not enough experimental data or even model dexterity to provide an accurate prediction of physical behavior, so simplifying assumptions are used. These assumptions can lead to great inaccuracies in the simulation, so these simple submodels are constantly updated to include better (or more complete) data, conditions, and mathematics to increase their accuracy and predictive capabilities.

The advanced devolatilization network models, such as the CPD model (Grant et al., 1989; Fletcher et al., 1992b), FLASHCHAIN (Niksa, 1988), and FG-DVC (Solomon et al.,

1988), accurately predict devolatilization and also output some form of light gas compositional information, however, they are typically too complex to run in large-scale simulations (Smith et al., 1994), leading to greater computational expenses (Brewster et al., 1995). Turbulence-chemistry interactions in the gas phase add challenges that often results in the need for very simple treatments of coal pyrolysis products. Light gas composition information can be calculated using a light gas submodel, such as the FG model. Simple kinetic mechanisms have been used to predict the light gas composition, sine the kinetic parameters can be easily derived from pyrolysis experiments (Suuberg et al., 1978). The large number of tar species evolved are very difficult to treat in a detailed manner in large simulations. Several different approaches have been used in boiler simulations to treat coal chemistry. These different approaches are discussed in greater detail in Chapter 8, with most using some form of simplifying assumptions. While these simplifying assumptions can be beneficial to reduce the computational time of large simulations, these assumptions are not consistent with measured elemental compositions of tar and char (Pugmire et al., 1991; Perry et al., 2000).

Many variables influence the composition of pyrolysis products, including, but not limited to: parent coal composition (proximate and ultimate analysis), chemical structural parameters (such as aromaticity or other NMR or FTIR parameters), heating rate, peak pyrolysis temperature, and residence time.

6.2 Approach

The elemental composition data set was comprised of experimental data found in the literature, as detailed in Section 2.5. The full set of data is found in Table B-1 and Table B-2 in Appendix B. While this analysis was completed for only the char and tar, the light gas elemental composition can be calculated by difference from the parent coal. The first step in this analysis

was to determine potential model forms based on known variables that affect pyrolysis product composition. After the models and data were developed, a cross-validation procedure was used to determine not only which model matched the data the best but could also how well each model could handle "new" conditions (new coals and/or new heating conditions) for which the model was not fit. Once the "best" models were selected, they underwent a novel model refinement procedure to determine if any of the fitted coefficients could be excluded as unnecessary. These procedures are detailed in the following sections.

6.2.1 Model Form Development

The first step was to develop several simple model forms to test against the experimental data. This involved a graphical analysis where the normalized compositions of the char and tar (e.g. C_{char}/C_{coal}) were plotted against several dependent variables, which included: the corrected aromaticity (f_a'), the maximum gas temperature (in K), the particle residence time (in milliseconds), the normalized volatiles yield (V_i/V_{max} where this ratio is equal to 1 at the maximum volatile yield for a given pyrolysis reaction), the mass fraction of each element in the parent coal (including H/C and O/C ratios), the ASTM volatile matter on a dry, ash-free (DAF) basis, and key NMR structural parameters (c_0, M_{cl}, M_δ, p_0, and $\sigma + 1$) as predicted by Genetti's correlations (1999). Figure 6-1 shows examples of the char compositions and Figure 6-2 shows examples of the tar compositions, all plotted against the parent coal carbon content, which is often used as an indicator for coal rank.

The complete list of model forms developed for each element in the char and tar are found in Table C-4 in Appendix C. Some model forms are similar across all elements, but many are unique to individual elements in either the char or the tar.

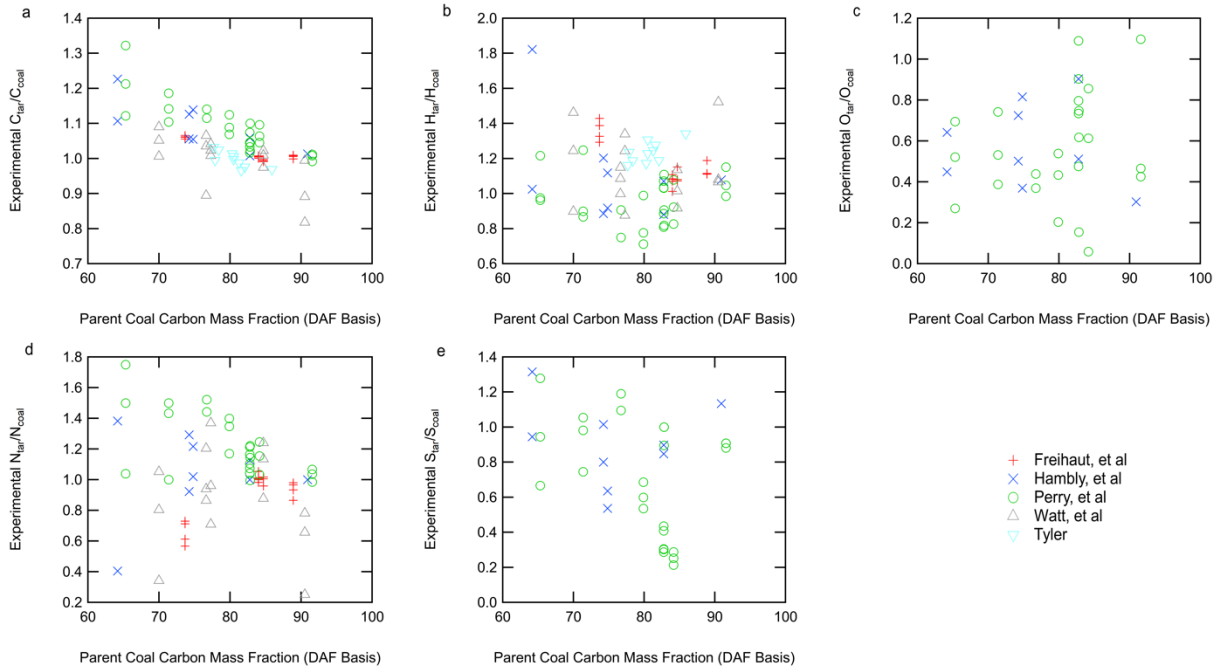

Figure 6-1. Example plots for the normalized mass fraction of C, H, O, N, and S in the char vs. parent coal carbon content (C_{coal}).

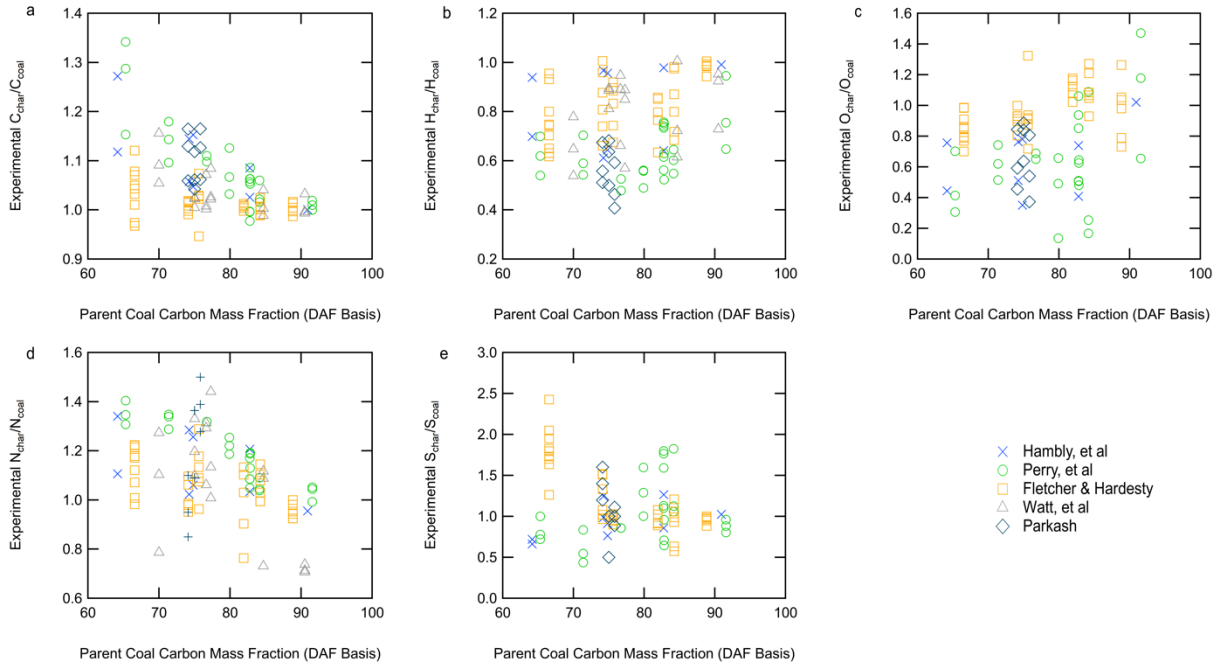

Figure 6-2. Example plots for the normalized mass fraction of C, H, O, N, and S in the tar vs. parent coal carbon content (C_{coal}).

Figure 6-3 is a Van Krevelen plot, which shows the oxygen-to-carbon ratio against the hydrogen-to-carbon ratio for coals, chars, and tars. Data were plotted here on a mass basis, rather than an atomic basis, as van Krevelen demonstrated (1950).This figure indicates that, on average, the tar seems to have a similar composition to the parent coal and the char becomes enriched in carbon but decreases in both hydrogen and oxygen content. The progression of char and tar composition is shown for three of the coals in the data set (two lignites and a subbituminous coal). The final tar and char composition from these three coals were somewhat similar to each other and had decreased amounts of both H and O, but neither char was close to 100% C.

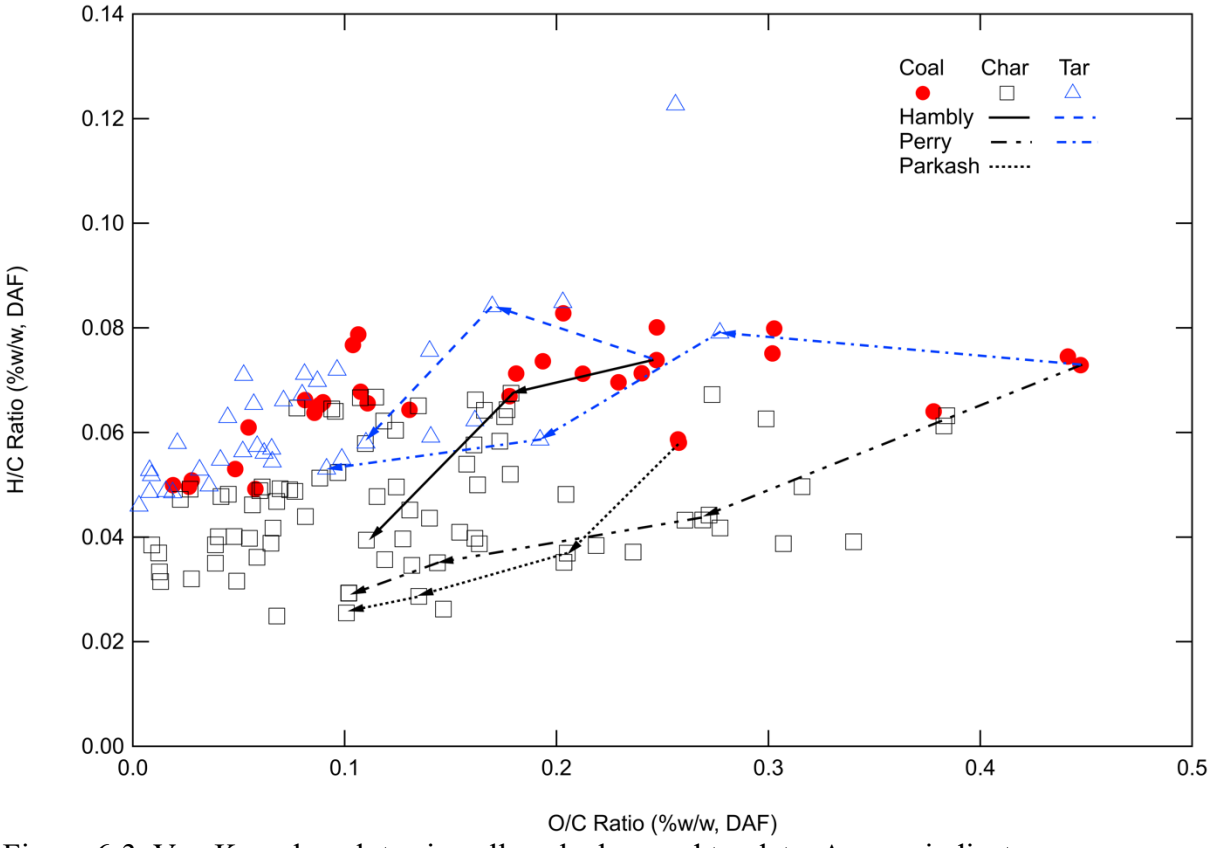

Figure 6-3. Van Krevelen plot using all coal, char, and tar data. Arrows indicate the progression of char and tar compositions with increasing residence time for three of the coals in the data set.

6.2.2 Cross-Validation and VUQ

The cross-validation procedure is defined in more detail in Section 2.4.2. This procedure was used with the elemental composition data set to determine which models fit the data the best as well as which models had the best potential to calculate "new" conditions. The cross-validation approach used five validation metrics to determine goodness of fit: the L_1 norm (Equation 2-14), the L_2 norm (Equation 2-15), the infinity norm (Equation 2-16), the total sum of squared errors (SSE, Equation 2-11), and the R^2 value (Equation 2-7). While all these metrics were used in this analysis to provide deeper insight into different aspects of model error, more weight was given to the R^2 value.

The cross-validation process was applied here for each element in both the char and tar compositions. The data set used here allowed for five groups for the tar oxygen and tar sulfur compositions and 10 groups for the remaining elemental compositions. The reason for the lower number of groups for the tar oxygen and sulfur compositions is that fewer oxygen and sulfur compositions are reported in the literature. Oxygen is harder to measure and is typically reported as a difference, sometimes even being a negative value. Some researchers even report a combined oxygen and sulfur composition. These combined values were not used here, since they could not be separated using the provided information. Each model form was tested using the cross-validation procedure, then the best of these model forms were fit using the full data set (also called final training) and the validation metrics were again calculated for the overall model fit. The validation metrics mean slightly different things in cross-validation and final training. For example, a higher R^2 value in cross-validation means that the model is expected to give better and more accurate predictions using conditions or coals for which the model was not

originally fit. Comparatively, a higher R^2 value in final training means that the model fits the entire suite of experimental data better.

Model training was performed in MATLAB, using five different built-in optimizers (discussed in greater detail in Appendix A) based on a simple least-squares analysis. Multiple optimizers were used to increase the chances of finding a true optimal solution and obtaining the best possible fit.

Only correlations with the best predictive capabilities were chosen to move forward to the model refinement process. To ensure the best fit with the fewest fitted coefficients, a modified R^2 value was calculated by dividing it by the number of fitted coefficients (R^2/N_{coeff}). This modified value provides an insight into each model's "utility." Typically, this modified value is higher for models with fewer coefficients, however, consideration was taken to make sure the R^2 value with fewer coefficients was within a reasonable range of the highest R^2 achieved with large numbers of coefficients. Two model forms for each element moved forward to the model refinement process, the model with the best R^2 value and the model with the best R^2/N_{coeff} value. These two model forms were the same for a few of the elements but were different for most. This scheme for choosing models was to find the best overall fit and the best fit with the fewest coefficients.

6.2.3 Model Refinement

In addition to the cross-validation procedure used to minimize model bias, a model refinement procedure was used in an effort to minimize the risk of overfitting the data. This was done by eliminating one coefficient at a time until no improvement was observed over previous models. While some statistics programs include a similar approach, this model refinement

technique differs from standard approaches. The entire cross-validation and model refinement procedures are shown in detail in Figure 6-4.

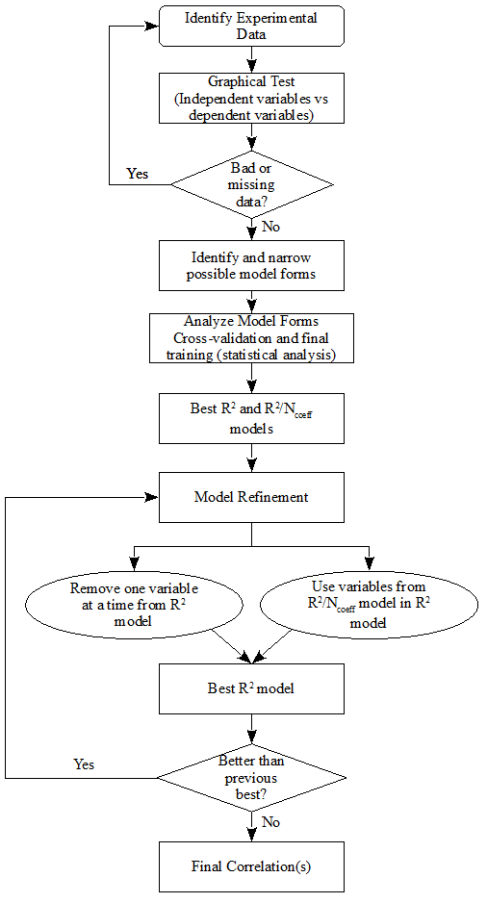

Figure 6-4. Process used to develop elemental composition correlations.

Two "toy" models are described here in an effort to illustrate this non-standard approach: Model A with seven fitted coefficients and an R^2 value of 0.9 and an R^2/N_{coeff} of 0.129 (Equation 6-1) and Model B with three coefficients and an R^2 of 0.75 and an R^2/N_{coeff} of 0.25 (Equation 6-2). The more complex Model A might provide more accurate predictions, but the simpler model will provide almost as good of a prediction with fewer coefficients.

$$y_A = c_1 + c_2 x_1 + c_3 x_1^2 + c_4 x_1^3 + c_5 x_2 + c_6 x_2^2 + c_7 x_2^3 \quad (6\text{-}1)$$

$$y_B = c_1 + c_2 \ln(x_1) + c_3 \ln(x_2) \quad (6\text{-}2)$$

In this example, the cross-validation procedure from the previous section resulted in Model A with the highest R^2 and Model B with the highest utility, or R^2/N_{coeff}. The model refinement procedure includes two key steps: reducing one coefficient at a time from Model A (the best R^2) and hybridizing the best features of Model A and Model B. This leads to an increase in model forms to test, shown in Equations 6-3 to 6-9 for the first step.

$$y_{A.1} = c_2x_1 + c_3x_1^2 + c_4x_1^3 + c_5x_2 + c_6x_2^2 + c_7x_2^3 \quad (6\text{-}3)$$

$$y_{A.2} = c_1 + c_3x_1^2 + c_4x_1^3 + c_5x_2 + c_6x_2^2 + c_7x_2^3 \quad (6\text{-}4)$$

$$y_{A.3} = c_1 + c_2x_1 + c_4x_1^3 + c_5x_2 + c_6x_2^2 + c_7x_2^3 \quad (6\text{-}5)$$

$$y_{A.4} = c_1 + c_2x_1 + c_3x_1^2 + c_5x_2 + c_6x_2^2 + c_7x_2^3 \quad (6\text{-}6)$$

$$y_{A.5} = c_1 + c_2x_1 + c_3x_1^2 + c_4x_1^3 + c_6x_2^2 + c_7x_2^3 \quad (6\text{-}7)$$

$$y_{A.6} = c_1 + c_2x_1 + c_3x_1^2 + c_4x_1^3 + c_5x_2 + c_7x_2^3 \quad (6\text{-}8)$$

$$y_{A.7} = c_1 + c_2x_1 + c_3x_1^2 + c_4x_1^3 + c_5x_2 + c_6x_2^2 \quad (6\text{-}9)$$

The first step is accomplished by removing one coefficient at a time from the best R^2 model (Model A). The second step, or hybridization switches the terms for each variable (x_1 and x_2) between Model A and Model B, as shown in Equations 6-10 and 6-11.

$$y_{B.1} = c_1 + c_2\ln(x_1) + c_3x_2 + c_4x_2^2 + c_5x_2^3 \quad (6\text{-}10)$$

$$y_{B.2} = c_1 + c_2x_1 + c_3x_1^2 + c_4x_1^3 + c_5\ln(x_2) \quad (6\text{-}11)$$

Both steps endeavor to reduce the number of fitted coefficients of the final correlation. In this example, all nine of the "new" model forms (Equations 6-3 to 6-11) are again fit over the entire data set and the model with the highest R^2 value is again chosen, replacing Model A in Equation 6-1 with the "new" model. This process is followed until either the R^2 value fell well

below the original best fit value or the number of fitted coefficients decreased to the level of the original highest R^2/N_{coeff} model. This iterative process was used for all 10 elemental correlations (CHONS for char and tar). The best of these refined models are presented here, but the results of the complete cross-validation and model refinement process are presented in Appendix C. The best models were subject to a separate cross-validation and final training.

6.3 Results and Discussion

There are a couple of steps involved in the development of the final elemental composition correlations. First, results are presented and discussed on the cross-validation procedure, which was used to narrow the number of potential best-fit model forms. Finally, the results of the model refinement and final correlations are presented and discussed. All model numbers here correspond to the matching model forms in Table C-4 of Appendix C, which also details the complete results for the entire analysis summarized here.

6.3.1 Correlation of Elemental Compositions Using Cross-Validation

Using the cross-validation procedure previously described in Sections 2.4.2 and 6.2.2, 10 randomized groups of the entire data set were used to test each of the proposed model forms for carbon, hydrogen, oxygen, nitrogen, and sulfur in the char and for carbon, hydrogen, and nitrogen in the tar. Five groups were used for each of the proposed model forms for oxygen and sulfur in the tar. The best of the model forms were allowed to move on to the final training step where the model form is fit to the full data set.

As an example of the cross-validation results, Table 6-1 shows the results of cross-validation for carbon in the tar. A total of 22 different model forms were tested for carbon in the tar. The model numbers in Table 6-1 line up with the model numbers in Table C-4 of Appendix

C. The data were divided into 10 groups for the cross-validation procedure, and Table 6-1 shows the average of the 10 tests performed using the 10 groups.

Table 6-1. Averaged Tar Carbon Cross-Validation Results for 22 Model Forms.

Model	N_{coeff}	R^2	R^2/N_{coeff}	L_1 Norm	L_2 Norm	Infinity Norm	SSE
22	13	0.573	0.044	0.028	0.035	0.067	0.010
4	5	0.914	0.183	0.034	0.046	0.106	0.017
5	5	0.914	0.183	0.034	0.046	0.106	0.017
6	9	0.922	0.102	0.032	0.044	0.105	0.016
7	5	0.887	0.177	0.044	0.060	0.135	0.028
8	17	0.886	0.052	0.032	0.043	0.102	0.016
23	14	0.791	0.057	0.024	0.028	0.051	0.006
34	16	0.794	0.050	0.023	0.027	0.053	0.006
25	14	0.843	0.060	0.022	0.027	0.050	0.006
26	14	0.785	0.056	0.025	0.030	0.057	0.007
28	14	0.823	0.059	0.022	0.027	0.051	0.006
29	15	0.814	0.054	0.023	0.027	0.051	0.006
35	15	0.819	0.055	0.023	0.028	0.052	0.006
36	14	0.804	0.057	0.022	0.028	0.053	0.006
30	14	0.826	0.059	0.031	0.039	0.076	0.013
31	15	0.847	0.056	0.029	0.038	0.079	0.012
37	15	0.836	0.056	0.031	0.040	0.079	0.013
38	19	0.791	0.042	0.024	0.030	0.054	0.007
21	17	0.869	0.051	0.045	0.059	0.131	0.031
2	9	0.908	0.101	0.034	0.046	0.104	0.017
3	17	0.586	0.034	0.027	0.034	0.062	0.010
33	15	0.854	0.057	0.021	0.029	0.056	0.006

The full results of the cross-validation process are found in Appendix C. The best models from the cross-validation process moved to final training, which used the complete data set to fit the best correlations. The "best" models from the cross-validation process are the best at predicting "new" data, which gives the user more confidence that the final correlations can predict elemental composition for coals or conditions for which the correlations were not fit. In addition, cross-validation can provide a small check against overfitting, which can cause a model to fit all the data very well but not accurately predict new data.

6.3.2 Model Training and Model Refinement Using the Complete Data Set

The final step in cross-validation is to train the chosen model form(s) using the complete data set. In many cases, this final training is the final step to produce the final model form, however, in this analysis, final training is an intermediary step to provide a maximum of two models to the model refinement analysis. The results for the final training are briefly summarized in the next section on model refinement. While the full results are only included in Appendix C, a summary of the cross-validation and final training results for carbon in the tar are shown in Table 6-2 for an example of what final training looks like, repeated for each element in both the char and tar. The information gathered from the initial cycle of cross-validation and final training were then used to inform the model refinement procedure, described in detail in Section 6.2.3.

Table 6-2. Summary of Tar Carbon Model Training Using the Complete Data Set

Step	**Model**	N_{coeff}	R^2	R^2/N_{coeff}	**L_1 Norm**	**L_2 Norm**	**Infinity Norm**	**SSE**
Cross-validation, best R^2	21	17	0.869	0.051	0.045	0.059	0.131	0.031
Final training, best R^2	21	17	0.824	0.048	0.021	0.031	0.108	0.070
Cross-validation, best R^2/N_{coeff}	5	5	0.914	0.183	0.034	0.046	0.106	0.017
Final training, best R^2/N_{coeff}	5	5	0.743	0.149	0.027	0.037	0.117	0.103

Most of the model forms from the initial cross-validation and final training cycle had a large number of fitted coefficients. There are two risks when a model has too many coefficients:

(1) the model might be at risk of overfitting, which means it fits the data well, but gives wildly inaccurate predictions outside of the data set, and (2) too many coefficients might make the model too computationally complex to use in large-scale simulations. The model refinement process attempts to remove some of the fitted coefficients in order to get the model prediction as accurate as possible while having as few coefficients as possible. The best models found in the model refinement procedure are presented in the following sections, with the complete results found in Appendix C. The results are presented in the following order: carbon, hydrogen, oxygen, nitrogen, and sulfur in the tar, followed by carbon, hydrogen, oxygen, nitrogen, and sulfur in the char.

6.3.3 Tar Carbon

The cross-validation and final training procedure identified Models 21 (highest R^2 value) and 5 (highest R^2/N_{coeff} value) to move forward to the model refinement process. In total, the tar carbon correlation was refined eight times, leaving Model 154, shown in Equation 6-12.

$$\frac{C_{tar}}{C_{coal}} = c_1 + c_2 T_{gas,max} + \frac{1}{c_3 T_{gas,max}^3 + c_4 T_{gas,max}^4} + c_5 t_{res} + \frac{1}{c_6 t_{res}^2 + c_7 t_{res}^4} + \frac{1}{1 + c_8 V_{norm}^3} + c_9 C_{coal} + \frac{1}{c_{10} C_{coal}^2 + c_{11} C_{coal}^4} \quad (6\text{-}12)$$

where C_{tar} is the dry, ash-free mass fraction of carbon in the tar, C_{coal} is the dry, ash-free mass fraction of carbon in the parent coal, $T_{gas,max}$ is the maximum gas temperature of the reactor (in K), t_{res} is the particle residence time in milliseconds, and V_{norm} is the normalized volatile yield (V_i/V_{max}, which is equal to 1 if a single experiment under the same conditions is performed or between 0 and 1 for multiple experiments performed at the same temperature but different residence times). The results for this model for both cross-validation and final training are found

in Table 6-3. Values for the fitted coefficients in Equation 6-12 are found in Table 6-4, which includes fitted coefficients for all tar composition correlations presented here.

Table 6-3. Tar Carbon Model Refinement

Step	**Model**	N_{coeff}	R^2	R^2/N_{coeff}	**L_1**	**L_2**	**Infinity**	**SSE**
Cross-validation	154	11	0.884	0.080	0.041	0.050	0.110	0.020
Final training	154	11	0.825	0.075	0.022	0.031	0.115	0.070

The parity relationship between Equation 6-12 and the experimental data is shown in Figure 6-5, which also includes parity plots for the other four tar elemental correlations. As shown in Figure 6-5, most of the tar compositions showed an increase in carbon content over the original parent coal composition (shown with dashed lines at 1.0 on the x-axis) as well as a decrease in both the hydrogen and oxygen compositions. On average, the nitrogen and sulfur compositions were close to the parent composition, however, the char nitrogen skewed slightly above the parent nitrogen and the char sulfur slightly below the parent sulfur.

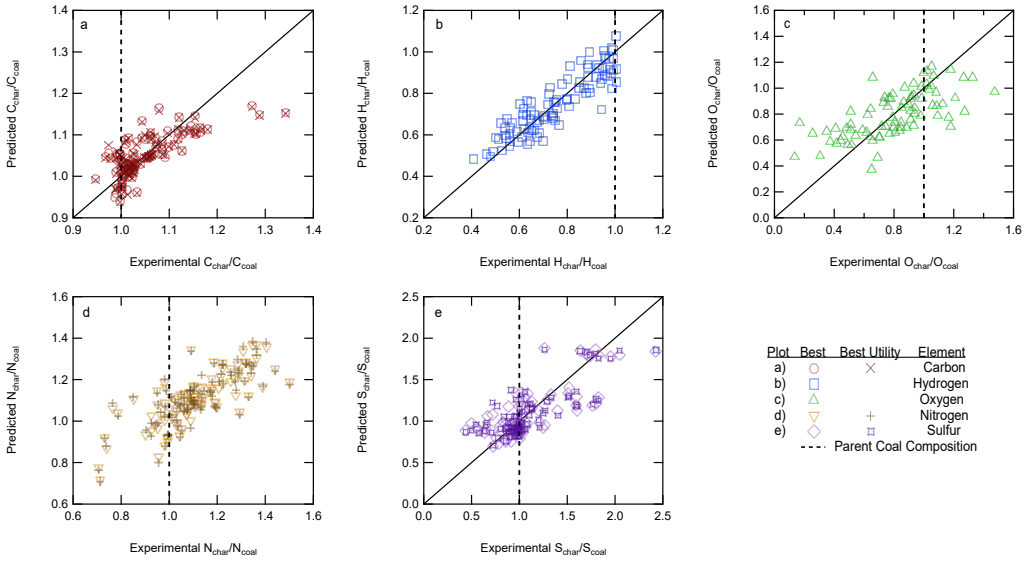

Figure 6-5. Parity plots for the finalized correlations in the tar.

Table 6-4. Tar Correlation Coefficients

Coeff.	**C**[a]	**H**	**O, best R^2**	**O, best utility**	**N, best R^2**	**N, best utility**	**S, best R^2**	**S, best utility**
Model[b]	154	157	159	161	166	168	9	7
N_{var}^{c}	4	4	5	5	8	7	4	4
c_1	-1.059	2.356×10^{3}	-1.700×10^{-3}	-5.845×10^{2}	0.323	0.400	9.966×10^{2}	-1.994×10^{3}
c_2	0.161	-1.034	3.344	0.176	4.560×10^{-4}	3.923×10^{-4}	-1.105×10^{11}	4.094×10^{2}
c_3	-1.052	-2.843	-2.493×10^{-3}	-8.812×10^{-4}	-0.451	-0.163	-2.998×10^{3}	3.865×10^{9}
c_4	0.614	9.306×10^{-3}	12.243	15.762	-3.370×10^{3}	-4.349×10^{3}	3.356×10^{10}	-3.171×10^{3}
c_5	-0.147	-8.391×10^{-6}	-1.795×10^{-2}	-2.485×10^{-2}	6.133×10^{3}	8.781×10^{3}	-3.586×10^{3}	3.337×10^{2}
c_6	8.371×10^{-2}	3.537×10^{3}	-2.165×10^{2}	-1.543×10^{3}	-3.042×10^{3}	-4.860×10^{3}	3.453×10^{2}	7.242×10^{3}
c_7	-2.379×10^{-5}	-6.336×10^{3}	-1.017×10^{3}	9.242×10^{2}	3.078×10^{2}	1.623×10^{2}	7.137×10^{3}	-1.570×10^{2}
c_8	-12.444	3.234×10^{3}	6.063×10^{2}	-63.059	-3.140×10^{2}	22.101	-2.129×10^{2}	
c_9	-3.115	-37.700	-2.907	67.100	35.669	-0.489	8.338×10^{2}	
c_{10}	0.980	0.597	63.601	-14.443	0.741	44.154		
c_{11}	-3.288×10^{-5}		-13.794		-52.266	11.627		
c_{12}					5.350			
c_{13}					15.977			

[a] Elements listed here (CHONS) refer to the corresponding correlations, which predict the normalized compositions, e.g., C_{tar}/C_{coal}

[b] Model number, corresponds to the model number in Table C-4

[c] N_{var} refers to the number of variables in the correlation, e.g., $T_{gas,max}$, t_{res}, etc.

6.3.4 Tar Hydrogen

The cross-validation process identified Models 7 and 62 as the best to move on to model refinement for the hydrogen in the tar. These models were refined a total of four times, identifying Model 157 as having the best R^2 and fewest fitted coefficients. The statistical values from the final cycle of cross-validation and final training for Model 157 are shown in Table 6-5.

Table 6-5. Tar Hydrogen Model Refinement

Step	**Model**	N_{coeff}	R^2	R^2/N_{coeff}	**L_1**	**L_2**	**Infinity**	**SSE**
Cross-validation	157	10	0.465	0.047	0.118	0.147	0.281	0.147
Final Training	157	10	0.800	0.080	0.067	0.087	0.305	0.490

Model 157 had the best R^2 value of 0.80 in final training, which was far higher than that of Model 62, with an R^2 value of 0.697 in the initial cross-validation and final training cycle (see Appendix C). With a final training R^2 value of 0.80, Model 157 fits the entire data set very well. With a cross-validation R^2 value of 0.465, this model may not be the best predictor of new data; however, the other validation metrics are a little more promising with lower values (which are an indication of a better fit). In addition, Model 157 has fewer fitted coefficients than Model 62. The model form of Model 157 is shown in Equation 6-13, and the parity relationship between Model 157 and the experimental data is found in Figure 6-5b. Values of coefficients for Model 157 are found in Table 6-4.

$$\frac{H_{tar}}{H_{coal}} = c_1 + c_2 T_{gas,max} + c_3 t_{res} + c_4 t_{res}^2 + c_5 t_{res}^3 + c_6 V_{norm} + c_7 V_{norm}^2 + c_8 V_{norm}^3 + c_9 M_{\delta,Genetti} + c_{10} M_{\delta,Genetti}^2 \quad (6\text{-}13)$$

where H_{tar} is the dry, ash-free mass fraction of hydrogen in the tar, H_{coal} is the dry, ash-free mass fraction of hydrogen in the parent coal, and $M_{\delta,Genetti}$ is the NMR structural parameter indicating the average side-chain molecular weight, as predicted by Genetti's correlation (1999), shown in Equation 6-14.

$$M_\delta = 4.220 \times 10^2 - 8.647C_{coal} + 4.639 \times 10^{-2}C_{coal}^2 - 8.473H_{coal} + 1.182H_{coal}^2 + 1.154O_{coal} - 4.340 \times 10^{-2}O_{coal}^2 + 0.557V_{ASTM} - 6.546 \times 10^{-3}V_{ASTM} \quad (6\text{-}14)$$

where O_{coal} is the dry, ash-free mass fraction of oxygen in the parent coal and V_{ASTM} is the dry, ash-free ASTM volatile matter of the parent coal (typically from a proximate analysis).

6.3.5 Tar Oxygen

Most of the models tested for oxygen in the tar performed very well. Model refinement identified two models that performed almost equally well: Model 159 did the best overall and Model 161 had the best utility (highest R^2 value with the fewest fitted coefficients). Table 6-6 shows the statistical results for both these models.

Model 159 had the highest R^2 value of 0.843, which was slightly better than Model 97 with an R^2 value of 0.842 in the initial cross-validation cycle (see Appendix C). Not only are the final training R^2 values for Models 159 and 161 high, but the cross-validation R^2 values are also very high. This indicates that both tar oxygen correlations presented here predicted new data very well, both with a relatively small number of coefficients. Model 159 is shown in Equation 6-15.

$$\frac{O_{tar}}{O_{coal}} = c_1 + c_2T_{gas,max} + c_3T_{gas,max}^2 + c_4t_{res} + c_5t_{res}^2 + c_6V_{norm} + c_7V_{norm}^2 + c_8V_{norm}^3 + c_9O_{coal} + c_{10}S_{coal}^2 + c_{11}S_{coal}^3 \quad (6\text{-}15)$$

Table 6-6. Tar Oxygen Model Refinement

Step	**Model**	N_{coeff}	R^2	R^2/N_{coeff}	**L1**	**L2**	**Infinity**	**SSE**
Cross-validation, best R^2	159	11	0.839	0.076	0.096	0.113	0.201	0.090
Final Training, best R^2	159	11	0.843	0.077	0.082	0.097	0.229	0.322
Cross-validation, best R^2/N_{coeff}	161	10	0.832	0.083	0.100	0.113	0.191	0.090
Final Training, best R^2/N_{coeff}	161	10	0.842	0.084	0.082	0.097	0.235	0.323

where O_{tar} is the dry, ash-free mass fraction of oxygen in the tar and S_{coal} is the dry, ash-free mass fraction of sulfur in the parent coal. Model 161 also had a high R^2 value of 0.842 with fewer fitted coefficients than Model 159. Model 161 is found in Equation 6-16.

$$\frac{O_{tar}}{O_{coal}} = c_1 + c_2 T_{gas,max} + c_3 T_{gas,max}^2 + c_4 t_{res} + c_5 t_{res}^2 + c_6 V_{norm}^2 + c_7 V_{norm}^3 + c_8 \log_{10} O_{coal} + c_9 S_{coal}^2 + c_{10} S_{coal}^3 \quad (6\text{-}16)$$

Model 159 is the best overall fit for tar oxygen, but 161 is almost as good a fit with fewer coefficients. This means that Model 159 in Equation 6-15 will likely give the most accurate results, but Model 161 will give almost as accurate of results with fewer coefficients, leading to greater computational efficiency. Coefficients for Equations 6-15 and 6-16 are found in Table 6-4 and the parity relationship between both models and the experimental data is shown in Figure 6-5c.

6.3.6 Tar Nitrogen

The initial cross-validation cycle identified Models 7 and 119 to move on to model refinement, which took place a total of seven times. Like the tar oxygen correlation, two models were identified as part of the model refinement process: Model 166 with the highest R^2 value and Model 168 with the best utility. Statistical results for the final cycle of cross-validation and final training for Models 166 and 168 are shown in Table 6-7.

Table 6-7. Tar Nitrogen Model Refinement

Step	**Model**	N_{coeff}	R^2	R^2/N_{coeff}	L_1	L_2	**Infinity**	**SSE**
Cross-validation, best R^2	166	13	0.760	0.058	0.094	0.113	0.197	0.085
Final Training, best R^2	166	13	0.747	0.057	0.105	0.139	0.388	1.250
Cross-validation, best R^2/N_{coeff}	168	11	0.812	0.074	0.084	0.104	0.186	0.070
Final Training, best R^2/N_{coeff}	168	11	0.747	0.068	0.105	0.139	0.436	1.252

Model 166 had the highest R^2 value of 0.747, which was higher than that of Model 119 with a value of 0.717 in the initial cross-validation cycle (see Appendix C). Model 119 is shown in Equation 6-17.

$$\frac{N_{tar}}{N_{coal}} = c_1 T_{gas,max} + c_2 T_{gas,max}^2 + c_3 t_{res} + c_4 V_{norm} + c_5 V_{norm}^2 + c_6 V_{norm}^3 + \frac{c_7}{N_{coal}} + \frac{c_8}{1+c_0} + c_9 M_{\delta,Genetti} + c_{10} M_{\delta,Genetti}^2 + c_{11} S_{coal} + c_{12} S_{coal}^2 + c_{13} V_{ASTM} \quad (6\text{-}17)$$

where N_{tar} is the dry, ash-free mass fraction of nitrogen in the tar, N_{coal} is the dry, ash-free mass fraction of nitrogen in the parent coal, c_0 is the number of stable bridges in the parent coal, as used in the CPD model and as detailed by Genetti et al. (1999) and found in Equation 6-18, and $M_{\delta,Genetti}$ is the average side-chain molecular weight (in Equation 6-14).

$$c_0 = \min[0.36, max\{(0.118C_{coal} - 10.1), 0.0\}] + \min[0.15, max\{(0.014O_{coal} - 0.175), 0.0\}] \quad (6\text{-}18)$$

Model 168 had the best utility with a high R^2 value of 0.747 (only equal to that of model 166 due to rounding), which was also better than that of Model 119 in the initial cross-validation cycle. Model 168 is found in Equation 6-19.

$$\frac{N_{tar}}{N_{coal}} = c_1 T_{gas,max} + c_2 T_{gas,max}^2 + c_3 t_{res} + c_4 V_{norm} + c_5 V_{norm}^2 + c_6 V_{norm}^3 + \frac{c_7}{N_{coal}} + c_8 M_{\delta,Genetti} + c_9 M_{\delta,Genetti}^2 + \frac{c_{10}}{S_{coal}} + c_{11} V_{ASTM} \quad (6\text{-}19)$$

Fitted coefficients for both models are found in Table 6-4 and the parity relationship for both models with experimental data is found in Figure 6-5d. While Model 166 had the highest R^2 value and will most likely yield the most accurate results, Model 168 will give very similar results with fewer coefficients and higher computational efficiency. Both correlations show great values for all validation metrics for both final training and cross-validation. This means that both correlations fit all the data well and predicted new data well.

6.3.7 Tar Sulfur

The initial cross-validation cycle identified Models 2 and 4 for model refinement, which took place a total of two times. Model refinement again identified two models as the best

models: Model 2 was the best overall with the highest R^2 value and Model 172 had the highest utility. Model 2 was not only identified as a part of the initial cross-validation cycle but was also identified as the best from the model refinement procedure. The statistical results for both models are shown in Table 6-8.

Table 6-8. Tar Sulfur Model Refinement

Step	**Model**	N_{coeff}	R^2	R^2/N_{coeff}	L_1	L_2	**Infinity**	**SSE**
Cross-validation, best R^2	2	9	0.880	0.098	0.083	0.105	0.201	0.086
Final Training, best R^2	2	9	0.765	0.085	0.121	0.151	0.358	0.779
Cross-validation, best R^2/N_{coeff}	172	7	0.955	0.136	0.062	0.076	0.147	0.042
Final Training, best R^2/N_{coeff}	172	7	0.763	0.109	0.122	0.152	0.337	0.785

Model 2 performed the best overall with a high R^2 value of 0.765 in the final training step. This is the same value as was achieved during the initial cross-validation cycle (see Appendix C). Model 2 is shown in Equation 6-20.

$$\frac{S_{tar}}{S_{coal}} = c_1 + c_2 T_{gas,max}^{c_3} + c_4 t_{res}^{c_5} + c_6 V_{norm}^{c_7} + c_8 S_{coal}^{c_9} \quad (6\text{-}20)$$

where S_{tar} is the dry, ash-free mass fraction of sulfur in the tar. Model 172 performed almost as well as Model 2 with a high R^2 value of 0.763. This means that Model 172 will yield results

almost as accurate as Model 2 with fewer fitted coefficients. Model 172 is shown in Equation 6-21.

$$\frac{S_{tar}}{S_{coal}} = c_1 + c_2 \ln\left(T_{gas,max}\right) + c_3 t_{res}^{c_4} + c_5 V_{norm}^{c_6} + c_7 S_{coal} \tag{6-21}$$

Both tar sulfur models have great validation metrics, especially in the cross-validation cycle. Model 172 performed particularly well, with an R^2 value of 0.955, which is the best of all models presented here. This indicates that Model 172 is very well suited to predict new data with good accuracy. Model coefficients for both Models 2 and 172 are found in Table 6-4 and the predictive capabilities of both models are shown in Figure 6-5.

6.3.8 Char Carbon

The initial cross-validation cycle identified Models 6 and 8 to move on to the model refining procedure, which was performed a total of six times. Model refinement identified Model 121 with the highest R^2 value and Model 126 with the best utility. The statistical results for both models are found in Table 6-9.

Model 121 had the highest R^2 value at 0.551, which was higher than that of model 8 from the initial cross-validation cycle (see Appendix C). Model 121 is shown in Equation 6-22.

$$\begin{aligned}\frac{C_{char}}{C_{coal}} = {} & c_1 + c_2 T_{gas,max} + c_3 T_{gas,max}^{\frac{1}{2}} + c_4 T_{gas,max}^{\frac{1}{3}} + c_5 T_{gas,max}^{\frac{1}{4}} + c_6 t_{res} \\ & + c_6 t_{res}^{\frac{1}{2}} + c_8 t_{res}^{\frac{1}{3}} + c_9 t_{res}^{\frac{1}{4}} + c_{10} V_{norm} + c_{11} V_{norm}^{\frac{1}{2}} + c_{12} V_{norm}^{\frac{1}{3}} \\ & + c_{13} V_{norm}^{\frac{1}{4}} + c_{14} C_{coal} + c_{15} C_{coal}^{\frac{1}{2}} + c_{16} C_{coal}^{\frac{1}{4}}\end{aligned} \tag{6-22}$$

where C_{char} is the dry, ash-free mass fraction of carbon in the char.

Table 6-9. Char Carbon Model Refinement

Step	**Model**	N_{coeff}	R^2	R^2/N_{coeff}	**L1**	**L2**	**Infinity**	**SSE**
Cross-validation, best R^2	121	16	0.663	0.041	0.037	0.049	0.108	0.025
Final Training, best R^2	121	16	0.551	0.034	0.033	0.045	0.188	0.204
Cross-validation, best R^2/N_{coeff}	126	11	0.671	0.061	0.036	0.049	0.107	0.025
Final Training, best R^2/N_{coeff}	126	11	0.548	0.050	0.033	0.046	0.190	0.205

Model 126 had a high R^2 value of 0.548, which is also higher than that of model 8 from the initial cross-validation cycle, indicating that Model 126 will yield predictions almost as accurate as those of Model 121 with fewer coefficients and greater computational efficiency. The model form for Model 126 is found in Equation 6-23.

$$\frac{C_{char}}{C_{coal}} = c_1 + c_2 T_{gas,max} + c_3 T_{gas,max}^{\frac{1}{2}} + c_4 T_{gas,max}^{\frac{1}{4}} + c_5 t_{res} + c_6 t_{res}^{\frac{1}{2}} + c_7 t_{res}^{\frac{1}{3}} + c_8 t_{res}^{\frac{1}{4}} + c_9 \exp(V_{norm}) + c_{10} C_{coal} + c_{11} C_{coal}^{\frac{1}{2}} \quad (6\text{-}23)$$

Model 126 was formed by taking out excess coefficients and combining the variables from Models 6 and 8, by replacing all V_{norm} polynomial-type variables with $\exp(V_{norm})$. Coefficient values for Equations 6-22 and 6-23 are found in Table 6-10. Predictions from both models are shown in Figure 6-6a, which also shows parity plots for the other elements in the char.

Table 6-10. Char Correlation Coefficients

Coeff.	**C[a], best R^2**	**C, best utility**	**H**	**O**	**N, best R^2**	**N, best utility**	**S, best R^2**	**S, best utility**
Model No.[b]	121	126	127	134	62	142	143	148
N_{var}^{c}	4	4	5	5	5	5	4	4
c_1	9.174×10^{3}	1.025×10^{3}	-2.609×10^{4}	7.662	17.520	0.330	-0.186	-1.090
c_2	2.647	1.292	3.335×10^{4}	-4.265×10^{-3}	1.001×10^{-5}	2.056	-7.586×10^{2}	-9.211×10^{2}
c_3	-4.109×10^{2}	-1.689×10^{2}	-5.592×10^{2}	-4.651	2.313×10^{3}	-2.083×10^{-3}	-4.173×10^{2}	3.572×10^{-2}
c_4	8.319×10^{2}	1.117×10^{3}	2.696×10^{4}	1.160×10^{-2}	3.621	-4.066×10^{2}	-5.797×10^{2}	2.089×10^{2}
c_5	9.245×10^{2}	-2.055	-5.503	-9.854×10^{-6}	-8.835×10^{-3}	9.430×10^{2}	0.492	2.483×10^{2}
c_6	-3.955	2.362×10^{2}	-1.381×10^{2}	1.151×10^{2}	7.171×10^{-6}	-6.225×10^{2}	3.403×10^{2}	1.942×10^{3}
c_7	4.000×10^{2}	-8.559×10^{3}	1.964×10^{3}	-1.352×10^{2}	-7.362×10^{2}	-2.110×10^{2}	-5.961×10^{2}	50.417
c_8	-6.016×10^{2}	5.622×10^{2}	1.486×10^{4}	1.494×10^{4}	1.640×10^{3}	58.039	9.768×10^{2}	62.874
c_9	-7.694×10^{2}	-33.779	-3.229×10^{3}	-2.231×10^{3}	-9.938×10^{2}	42.666	8.907×10^{2}	-2.029×10^{5}
c_{10}	-2.475×10^{2}	18.491	-7.507×10^{-6}	-2.012×10^{2}	4.729×10^{2}	-0.555	1.305×10^{4}	2.671×10^{4}
c_{11}	3.999×10^{2}	-4.095×10^{2}	4.219×10^{3}	6.199	-6.054×10^{2}		-3.538×10^{4}	1.507×10^{4}
c_{12}	-2.843×10^{2}			-6.033×10^{-2}	1.599×10^{2}		3.100×10^{4}	
c_{13}	90.505				41.613		76.299	
c_{14}	23.009				-0.543		-1.769×10^{5}	
c_{15}	-6.063×10^{2}						9.786×10^{4}	
c_{16}	6.987×10^{2}						-1.266×10^{4}	

[a] Elements listed here (CHONS) refer to the corresponding correlations, which predict the normalized compositions, e.g., C_{tar}/C_{coal}

[b] Model number, corresponds to the model number in Table C-4

[c] N_{var} refers to the number of variables in the correlation, e.g., $T_{gas,max}$, t_{res}, etc.

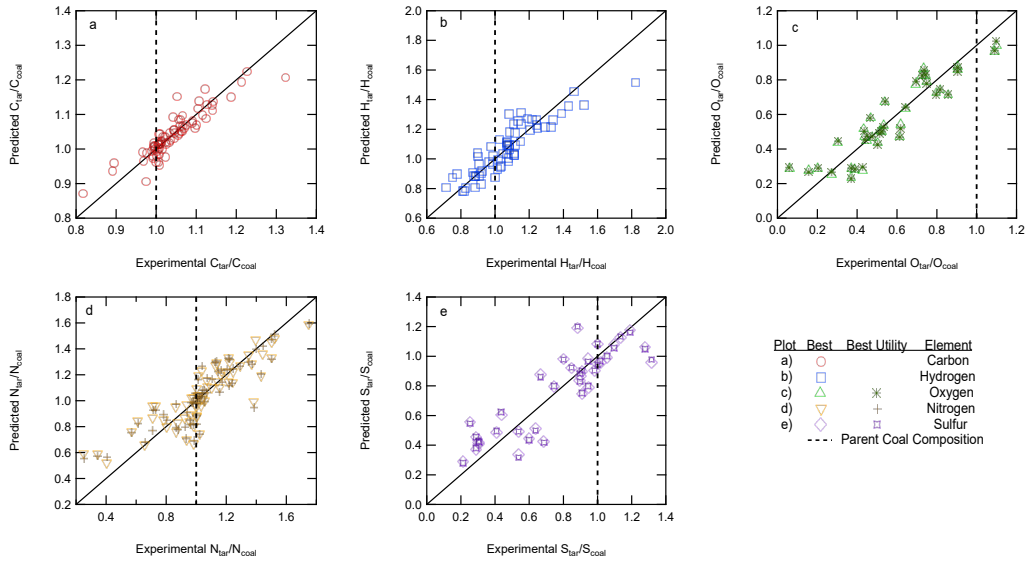

Figure 6-6. Parity plots for the finalized correlations in the char

While both models 121 and 126 were the best performers and predict the carbon composition of char slightly better than the models tested in the initial cross-validation cycle, neither performed well. Looking at Figure 6-6a, both models appear to underpredict the compositions on both the lower end and the higher end and overpredict the compositions in the middle. This indicates the possibility of different dependencies to predict the carbon in the char or of inaccuracies or biases in the data.

As Figure 6-6 shows, the carbon and nitrogen in the char tend to increase from the parent coal composition, with the carbon increasing by as much as 40% and the nitrogen by as much as 100%. The hydrogen and oxygen tend to decrease, by up to almost 100%, and the sulfur tends to on average stay around the parent composition.

6.3.9 Char Hydrogen

The initial cross-validation cycle identified Models 2 and 31 to move forward to model refinement, which was iterated a total of three times. The model refinement procedure identified

only one model as the best for predicting hydrogen in the char—Model 127. The statistical results for this model are found in Table 6-11. No other models were found to have better utility (the highest R^2 value with the fewest fitted coefficients).

Table 6-11. Char Hydrogen Model Refinement

Step	**Model**	N_{coeff}	R^2	R^2/N_{coeff}	L_1	L_2	**Infinity**	**SSE**
Cross-validation	127	11	0.831	0.076	0.055	0.067	0.134	0.046
Final training	127	11	0.800	0.073	0.058	0.072	0.221	0.509

Model 127 performed the best of all models, with a high R^2 value of 0.80, which was higher than that of Model 31 at 0.753 in the initial cross-validation cycle (see Appendix C). Model 127 is shown in Equation 6-24.

$$\frac{H_{char}}{H_{coal}} = c_1 + c_2 T_{gas,max}^{c_3} + c_4 t_{res}^{c_5} + c_6 V_{norm}^{c_7} + c_8 H_{coal}^{c_9} + c_{10} V_{ASTM}^{c_{11}} \quad (6\text{-}24)$$

where H_{char} is the dry, ash-free mass fraction of hydrogen in the char. Good validation metrics (very high R^2 values and low values for the other metrics) for Model 127 indicate that this char hydrogen correlation fits all the data well and was a good predictor for new data. This means that Model 127 in Equation 6-24 can be reliably used to predict the composition of hydrogen in the char from a wide variety of different coals. Coefficient values for Equation 6-24 can be found in Table 6-10, and the predictive capabilities of this model are shown in Figure 6-6b.

6.3.10 Char Oxygen

Initial cross-validation identified Models 5 and 21 for model refinement, which were refined a total of four times. This led to Model 134 with the best overall R^2 value. No other models from the model refinement procedure had better utility than Model 134. Statistical results for this model are shown in Table 6-12.

Table 6-12. Char Oxygen Model Refinement

Step	Model	N_{coeff}	R^2	R^2/N_{coeff}	L_1	L_2	Infinity	SSE
Cross-validation	134	12	0.628	0.052	0.138	0.174	0.325	0.251
Final training	134	12	0.447	0.037	0.160	0.203	0.565	3.327

Model 134 had the highest R^2 value of 0.447, which was higher than that of Model 21 with a value of 0.438 in the initial cross-validation cycle (see Appendix C). The model form for Model 134 is shown in Equation 6-25.

$$\frac{O_{char}}{O_{coal}} = c_1 T_{gas,max} + c_2 T_{gas,max}^2 + c_3 t_{res} + c_4 t_{res}^2 + c_5 t_{res}^3 + c_6 V_{norm} + c_7 V_{norm}^2 + c_8 \exp(c_9 O_{coal}) + c_{10} V_{ASTM} + c_{11} V_{ASTM}^2 + c_{12} V_{ASTM}^3 \quad (6\text{-}25)$$

where O_{char} is the dry, ash-free mass fraction of oxygen in the char. Model 134 was created by removing unnecessary coefficients and replacing the variables of O_{coal} in Model 21 with $\exp(O_{coal})$ from Model 5. Like the carbon in the char, Equation 6-25 may give the best predictions for oxygen in the char, but there is still room for improvement. The fitted coefficients are found in Table 6-10 and the predictive capabilities are found in Figure 6-6c. The parity relationship shows that this model tends to overpredict the lowest values and underpredict the

highest values of oxygen in the char. Char oxygen is usually determined by difference and, hence, has more scatter than the other elements. For this reason, the best R^2 value from a curve fit is less than 0.5.

6.3.11 Char Nitrogen

The cross-validation cycle for nitrogen in the char was unique, only identifying one model (Model 62) to move on to model refinement. The model refinement procedure was repeated a total of four times. Model 62 remained the best overall fit with the highest R^2 value, with Model 142 having a higher utility than Model 62. The statistical results for both models are shown in Table 6-13.

Table 6-13. Char Nitrogen Model Refinement

Step	**Model**	N_{coeff}	R^2	R^2/N_{coeff}	**L_1**	**L_2**	**Infinity**	**SSE**
Cross-validation, best R^2	62	14	0.600	0.043	0.077	0.097	0.185	0.097
Final Training, best R^2	62	14	0.597	0.043	0.077	0.105	0.312	1.084
Cross-validation, best R^2/N_{coeff}	142	10	0.682	0.068	0.076	0.090	0.156	0.079
Final Training, best R^2/N_{coeff}	142	10	0.585	0.059	0.077	0.106	0.324	1.117

Model 62 was still the best overall fit with a moderate R^2 value for final training of 0.597 and a cross-validation R^2 of 0.6. This indicates that this model is moderately accurate across all the data and will predict new data moderately well. Model 62 is shown in Equation 6-26.

$$\frac{N_{char}}{N_{coal}} = c_1 + c_2 T_{gas,max}^{c_3} + c_4 t_{res} + c_5 t_{res}^2 + c_6 t_{res}^3 + c_7 V_{norm} + c_8 V_{norm}^2 + c_9 V_{norm}^3 + c_{10} N_{coal} + c_{11} N_{coal}^2 + c_{12} N_{coal}^3 + c_{13} M_{\delta,Genetti} + c_{14} M_{\delta,Genetti}^2 \quad (6\text{-}26)$$

where N_{char} is the dry, ash-free mass fraction of nitrogen in the char and $M_{\delta,Genetti}$ is the average side-chain molecular weight, as predicted by Genetti's correlation (1999) in Equation 6-14. Model 142 had a moderately high R^2 value of 0.585, which is less than that of Model 62; however, Model 142 had a higher R^2/N_{coeff}, giving it greater utility. This means the predictions will be slightly less accurate, but it has fewer fitted coefficients and greater computational efficiency. Model 142 is shown in Equation 6-27.

$$\frac{N_{char}}{N_{coal}} = c_1 T_{gas,max} + c_2 t_{res} + c_3 t_{res}^2 + c_4 V_{norm} + c_5 V_{norm}^2 + c_6 V_{norm}^3 + c_7 N_{coal}^2 + c_8 N_{coal}^3 + c_9 M_{\delta,Genetti} + c_{10} M_{\delta,Genetti}^2 \quad (6\text{-}27)$$

The fitted coefficient values for Equations 6-26 and 6-27 are found in Table 6-10. Predictions for both models are shown in the parity plot in Figure 6-6d.

6.3.12 Char Sulfur

The initial cross-validation cycle identified Models 6 and 21 as the best to move on to model refinement, which were refined a total of five times. Model refinement identified Model 143 as the best overall fit and Model 148 having the best utility. The statistical results for Models 143 and 148 are shown in Table 6-14.

Model 143 had the highest R^2 value of 0.605, which was higher than that of Model 21 at 0.565 in the initial cross-validation cycle (see Appendix C). This model form is shown in Equation 6-28.

$$\frac{S_{char}}{S_{coal}} = c_1 T_{gas,max} + \frac{1}{c_2 T_{gas,max}^2 + c_3 T_{gas,max}^3 + c_4 T_{gas,max}^4} + c_5 t_{res} + \frac{1}{c_6 t_{res}^2 + c_7 t_{res}^3 + c_8 t_{res}^4}$$
$$+ c_9 V_{norm} + \frac{1}{1 + c_{10} V_{norm}^2 + c_{11} V_{norm}^3 + c_{12} V_{norm}^4} + c_{13} S_{coal} + \frac{1}{c_{14} S_{coal}^2 + c_{15} S_{coal}^3 + c_{16} S_{coal}^4} \quad (6\text{-}28)$$

Table 6-14. Char Sulfur Model Refinement

Step	**Model**	N_{coeff}	R^2	R^2/N_{coeff}	**L₁**	**L₂**	**Infinity**	**SSE**
Cross-validation, best R^2	143	16	0.428	0.027	0.214	0.272	0.512	0.597
Final Training, best R^2	143	16	0.605	0.038	0.180	0.241	0.620	4.703
Cross-validation, best R^2/N_{coeff}	148	11	0.417	0.038	0.261	0.322	0.581	0.903
Final Training, best R^2/N_{coeff}	148	11	0.605	0.055	0.182	0.241	0.601	4.702

where S_{char} is the dry, ash-free mass fraction of sulfur in the char. Model 148 had an R^2 value close to that of Model 143 (0.605 with rounding), meaning that the predictions from Model 148 are almost as accurate with fewer coefficients and greater computational efficiency. Model 148 is shown in Equation 6-29.

$$\frac{S_{char}}{S_{coal}} = c_1 T_{gas,max} + \frac{1}{c_2 T_{gas,max}^3} + c_3 t_{res} + \frac{1}{c_4 t_{res}^2 + c_5 t_{res}^4}$$
$$+ c_6 \exp(c_7 V_{norm}) + c_8 S_{coal} + \frac{1}{c_9 S_{coal}^2 + c_{10} S_{coal}^3 + c_{11} S_{coal}^4} \quad (6\text{-}29)$$

Fitted coefficients for Equations 6-28 and 6-29 are found in Table 6-10. Predictions for both models are shown in a parity plot in Figure 6-6e. As with oxygen, sulfur values are not always measured separately and are often either lumped in with the oxygen compositions or the sulfur types (pyritic, organic, etc.) are not distinguished. This can lead to inaccuracies in experimental data that are then passed along to the fitted model.

6.4 Summary and Conclusions

Several sets of elemental composition data for tars and chars were obtained from the literature. Most of the tar and char carbon values increased over the parent coal composition, meaning that the tar and char become enriched in carbon (increasing up to almost 40% more than the parent coal composition in both the char and tar). This indicates that, in general, the light gas has a lower carbon content than both the char and the tar. The hydrogen in the char tended to increase over the parent coal composition (with most increasing by up to 85% more than the parent coal composition), whereas the hydrogen in the tar decreased by as much as 80% from the parent coal hydrogen content. The light gas hydrogen content likely increases from the parent coal composition. Both the tar and char oxygen content decreases compared to the parent coal composition (with some samples decreasing to almost nothing), indicating that the light gas species are generally enriched in oxygen. Nitrogen in the char on average stayed around the parent composition (somewhat evenly spread between 30 and 170% of the parent coal nitrogen values). The nitrogen in the tar generally increased from the parent coal values by up to 60%, however, there were a few outliers that decreased by up to 30%. The trends in nitrogen content in the char and tar mean that the light gas species likely increase in nitrogen composition. The sulfur in the char tended to decrease by as much as 80% from the parent coal sulfur content with a few outliers that increased by as much as 40%. The sulfur in the tar is fairly evenly split on

both sides of the parent coal composition, however the sulfur content of the tar has the largest spread of all the elements, ranging between 40 and 250% of the parent coal composition. The large range of sulfur values in the tar is due to either the fact that most coals do not contain much sulfur or that sulfur is one of the more difficult elements to measure of the CHONS elements.

A cross-validation procedure coupled with a model refinement procedure was used to develop a set of correlations describing the elemental compositions of primary coal tar and the corresponding char. Consideration was given to the model form that gave the best overall fit as well as model forms with the best utility, meaning the highest possible R^2 value with the fewest fitted coefficients.

The trends in elemental composition changes in char and tar compared to the parent coals observed experimentally are reproduced by the correlations. All the correlations use inputs such as the reaction conditions (maximum gas temperature, particle residence time, and a normalized volatile yield) and parent coal structural and compositional information (element mass fractions, ASTM volatiles yield, and NMR structural parameters, such as the number of stable bridges and the average molecular weight of the side chains). Through careful statistical calculation, these correlations may reasonably be used to estimate the dry, ash-free mass fractions of each element in the char and the tar and may be applied to simulations of coal combustion to more accurately predict chemical interactions of various combustion products.

While the tar correlations show good agreement with the experimental data with R^2 values of at least 0.75, most of the char correlations fall below that, with the carbon and oxygen correlations having R^2 values of approximately 0.55 and 0.45, respectively. The char correlations might be improved in the future by fitting them to new and better experimental data. In addition, a careful analysis of the consistency of the experimental data may show possible outliers or bad

data, which upon the removal of these bad data could improve the fit and prediction capabilities of the correlations.

While the bulk of the work presented in this chapter took the form of curve-fitting, the correlations developed as part of this work have much broader implications for coal combustion modeling. Very few models have been developed to predict the composition of both char and tar compounds from different parent coals and at different reaction conditions; most large-scale simulations focus on light gas compositions. Many simulations use char and tar compositions that are the same as the parent coal, or even simplify char and tar to simpler compounds (e.g., char as pure carbon, tar as benzene, etc.). Implementing the elemental composition correlations presented here into a large-scale simulation allows for real-time tracking of char and tar compositions (and light gas compositions by difference from parent coal composition). The char and tar compositions are based on both coal- and reaction-specific parameters. Accurately tracking char and tar compositions in a large-scale simulation has greater improves other aspects of the coal combustion reaction (such as gas-phase chemistry, soot chemistry, pollutant generation, and others).

7 HEATING VALUE OF COAL CHAR, TAR, AND OTHER FUELS

This chapter details efforts to test several correlations found in the literature that predict the enthalpy of combustion (heating value) of primarily coal-based fuels, and to apply the correlations that were originally developed for coal-based fuels to other organic fuels. This chapter is modified from work presented in Richards et al. (2021). The motivation for this work was to find correlations that accurately predict the heating value of coal-based fuels in order to calculate the heat of formation to use in equilibrium modeling of different fuel mixtures (see Chapter 8 for more details on the equilibrium modeling work). In gathering a large data set of experimental data from the literature, this work grew from just coal-based fuels to include other fuels such as biomass, liquid and gaseous fuels, oil shale, propellants and explosives, and a number of other traditional and non-traditional fuels.

7.1 Introduction

Enthalpies of combustion (or heating values) are determined using calorimetry, which can be expensive and time-consuming. Many researchers have developed correlations to predict the heating value of coal based on several coal-specific parameters—mainly the elemental composition of the raw, or parent, coal. A few of the most widely used heating value correlations are found in Table 2-3. Some of these correlations have even been used to predict the heating values of other fuels such as biomass. Many of these correlations have only been applied to

coals, with limited applications to coal char and biomass fuels. None were found to have been applied to coal tar, which can be a bit more difficult to collect and test in most experimental apparatuses.

Accurately predicting the heating value of fuels (and by extension the heat of formation) can be very important in large-scale simulations that often use simplifying assumptions (see Chapter 8 for more details) to reduce the computational complexity and time. In addition, experimentalists can use these heating value correlations to determine if calorimetry tests have been accurately completed and new experimental coals are accurately characterized, especially if used in conjunction with Van Krevelen diagrams (1950, 1993). Coals of similar rank tend to have similar physical and chemical properties, with heating value and elemental composition being two of the closest properties (Smith et al., 1994). Comparing a research coal using accurate heating value correlations can show if a calorimetry measurement has been accurately completed.

In a more practical application, some industrial plants are working at characterizing the chemical compositions of the original fuels in real time by measuring the exhaust gases of the plant. These compositions may then be used along with these heating value correlations in process control to be able to model the heating processes of the plant, especially in rapidly solving material and energy balances to help with predictive control of the plant.

7.2 Approach

Testing and validating all the heating value models required a large amount of experimental data. The sources of these experimental data are found in Table 2-5 and the entirety of the data is in Table B-4 of Appendix B. This large data set includes the heating value and elemental composition of each fuel. In addition to the literature correlations discussed in Table

2-3, additional forms of correlations were also fit to the data set to see if any improvement could be made over the literature correlations. While this chapter only discusses the results of the testing of the literature correlations, the additional models are discussed in greater detail in Appendix D.

The complete data set includes a total of 11 major fuel groups, listed in Table 7-1, along with the number of points in each group. The greatest number of data points are coal-related (including coal char and tar).

Table 7-1. Major Heating Value Fuel Types

Fuel Type	**Number of Samples**
Coal (unreacted)	353
Coal char	50
Coal tar	44
Biomass	73
Biochar	9
Peat	11
Coke (including petcoke)	4
Oil shale, tar sands, etc.	32
Liquid and gaseous fuels	37
Propellants and explosives	21
Other (municipal solid waste, etc.)	69

The experimental data were further organized into smaller data sets based on fuel commonalities, as shown in Table 7-2, in order to permit prediction of heating values of different fuel groups. The propellants and explosives were included in the fossil fuels data set because many propellants and explosives share chemical and structural similarities to other fossil fuels. Many of the propellants used in this analysis are hydrocarbon backbones (ethane, propane, etc.) with different nitrogen attachments instead of hydrogen atoms.

Table 7-2. Heating Value Data Sets

Data Set	Fuel Groups Included
Coal	Coal
Char	Coal char
Tar	Coal tar
Coal-char	Coal and char
Combined coal	Coal, char, and tar
Fossil	Coal, char, tar, liquid and gaseous fuels, oil shale, tar sands, coke, peat, and propellants and explosives
Biomass	Biomass, biomass char (biochar), and peat
Other	Other fuels and propellants and explosives
Full	All fuel types listed in Table 7-1

7.2.1 Elemental Composition Dependence of Heating Value

Many of the literature model forms were developed for coal with respect to elemental composition, commonly using carbon, hydrogen, and oxygen in the correlations. A few correlations were developed using sulfur content, and even fewer included nitrogen content. Most coals typically have lower fractions of nitrogen and sulfur than the other elements, particularly on an atomic or molar basis (Van Krevelen, 1993; Smith et al., 1994). Other fuel types, especially propellants and explosives, tend to be enriched in nitrogen. Figure 7-1 shows the heating value dependence on organic elemental composition for all fuels.

In coal and fossil fuel science, a Van Krevelen plot (1950, 1993) is used to show related fuel compositions. This type of plot shows the relationship of O/C and H/C ratios, typically on an atomic or molar basis or occasionally a mass basis. Figure 7-2 shows the Van Krevelen relationship for all fuels used in this analysis.

Figure 7-2b shows what is commonly called the coal band, with the lower rank coals toward the right of the plot (with the highest O/C and H/C ratios). As coal rank increases, the coal decreases in oxygen content until the mid-rank coals (higher rank subbituminous to lower rank bituminous coals) at the “knee.” Increasing coal rank then starts to decrease the hydrogen

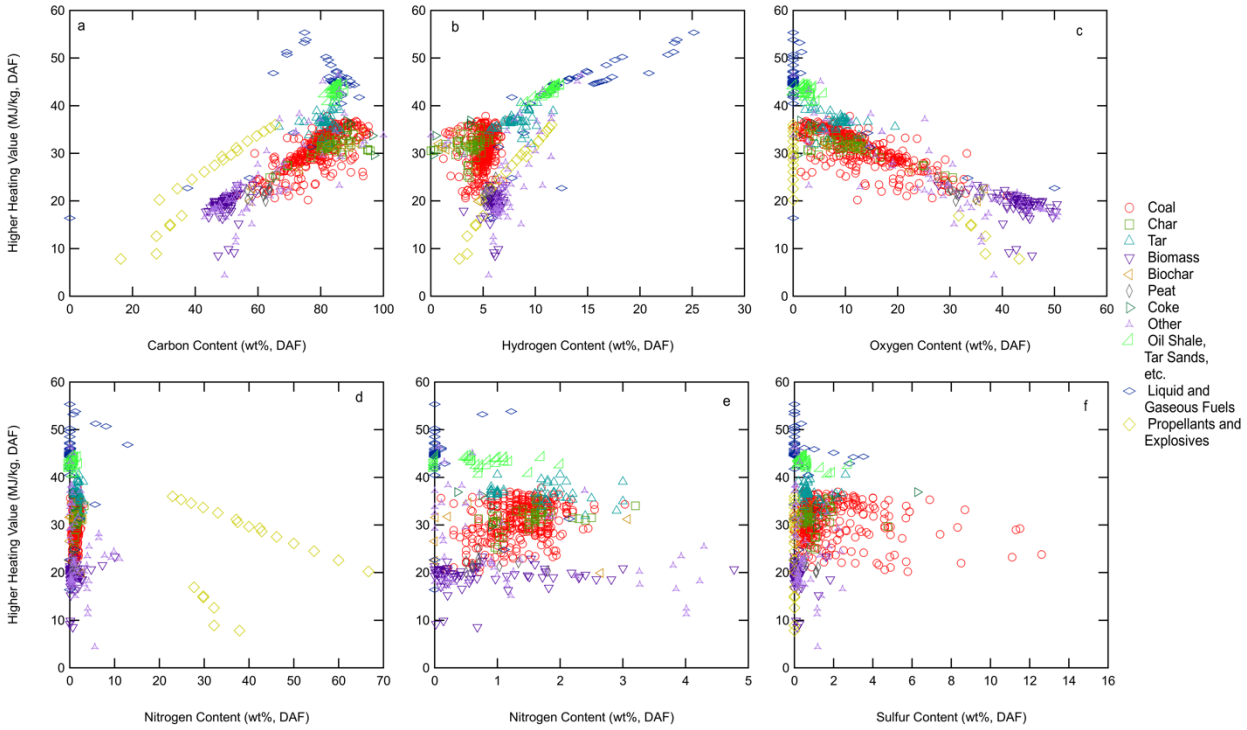

Figure 7-1. Heating value dependence on elemental composition (CHONS). Note that in plot f, H_2S at ~94 wt.% sulfur is excluded to make the plot easier to read.

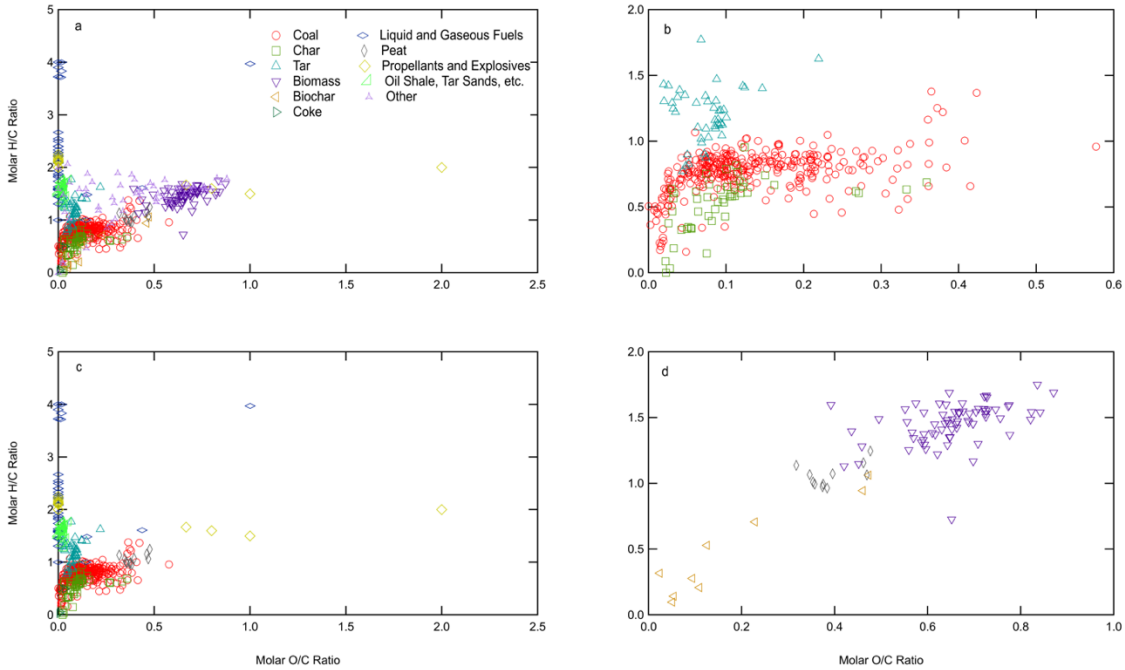

Figure 7-2. Van Krevelen diagram of all fuels used: a) full data set, b) coal, char, and tar only, c) fossil fuels, d) biomass, biochar, and peat.
Note the scale changes on the x- and y-axes.

content, becoming more aromatic in nature to anthracite coals. The chars tend to decrease in both oxygen and hydrogen content as the coals devolatilize, leading to the chars lying to the bottom or below the coal band. Conversely, tars (and other gases) tend to be more enriched in hydrogen and oxygen, which would put the tars above the coal band on the Van Krevelen diagram. Biomass samples tend to be even more enriched in oxygen and hydrogen compared to the coals, so these samples extend up and to the right of the coal band (see Figure 6-3). Chapter 6 discusses the elemental compositional differences of coal, char, and tar to a greater extent. Liquid and gaseous fuels are generally made up of simple hydrocarbons, many lacking oxygen, nitrogen, or sulfur atoms, which would place most of the liquid and gaseous fuels above and to the left of the coal band. The oil shale and tar sand samples bridge the gap between the liquid and gaseous fuels and the coal bands, having some similar properties to both coal and liquid fuels.

7.2.2 Optimization

The original literature model forms were first compared with the complete data set to determine goodness of fit. The literature model coefficients were then re-fit using the different data sets of interest using a simple sum-of-squared-error minimization. This optimization used two built-in optimizers in MATLAB (*fmincon* and *fminunc*, which are discussed at greater length in Appendix A) to re-fit the coefficients for each model. A separate optimization of each model form was performed for each of the nine data sets in Table 7-2. The parameter fits were then evaluated using three key measures of fit: SSE (Equation 2-11), MSE (Equation 2-12) and the AIC method (see Section 2.4.3 for equations and details on this method). The SSE value is useful for a minimization optimization but does not always give useful information for determining a best fit, especially with data sets as large as are used here, with SSE values generally smaller for smaller data sets. The mean square error (MSE) normalizes the SSE by the number of data points

in the data set, giving a more useful validation metric in comparing large data sets. The AIC method gives an indication on how likely a chosen model is to be correct.

In addition to the AIC test, models were compared using a ratio of the mean square error (MSE), with each model MSE divided by the best MSE value in each data set. A value of close to one for the MSE ratio means that the model of interest is very close in fit to the "best" model. While both the AIC_c score (Equation 2-18) and MSE are used in this analysis to find the "best" models, the AIC_c probabilities (Equation 2-20), evidence ratio (Equation 2-21), and the MSE ratio are used to determine if any of the remaining models are close enough to the "best" models to be considered statistically similar. A cutoff of two percent for the MSE ratio and of five percent for the AIC probability are used to determine if a model fit is close enough to be statistically similar to the "best" model for each data set.

Other measures of fit were considered, but not included in the results discussed here. The complete description of these extra statistics as well as the full statistical results for both the literature and "new" model forms are found in Appendix D.

7.3 Results and Discussion

The results of the evaluation of the literature model forms are presented in the following sections: (1) coal data sets (including all coal, char, and tar data sets), (2) fossil fuels data set, (3) biomass, (4) other fuels data set, and (5) the full data set. The key statistical results are included as well as parity plots showing how well the best model forms predict the higher heating value. While many model forms tested here may give good results, only the best results are included in this chapter. The complete results can be found in Appendix D.

7.3.1 Coal Data Sets

Coal (parent coal, char, and tar) heating values make up the bulk of the complete data set because this analysis began as a study of coal, char, and tar heating values. The coal heating values were divided into several key data sets: (a) parent coal only, (b) coal char only, (c) parent coal and coal char combined, (d) coal tar only, and (e) combined coal, char, and tar. The results of all five data sets are discussed in the following sections.

7.3.1.1 Parent Coal Only

The parent coal data set was the largest of the coal, char, or tar data sets. Predictions made using re-fit coefficients for all 10 literature model forms shown in Table 2-3 were compared against the predictions made using the original model coefficients. Table 7-3 shows the key statistical results (MSE, MSE ratio, AIC_c, AIC probability, and AIC evidence ratio) for the best models of the coal data set. This analysis compared the model fits using both the re-fit coefficients and the original coefficients for each model form. The best models according to mean square error (MSE) and AIC_c score are found in Table 7-3.

Table 7-3. Best Models Using the Coal-Only Data Set

Model	**MSE $(MJ/kg)^2$**	**MSE Ratio**	**AIC_c**	**Probability**	**Evidence Ratio**
Mott-Spooner	5.137	1.0*	594.1	0.223	3.487
Boie	5.192	1.011	591.6	0.5	1.0*

* These ratios are 1.0 since these models have the minimum MSE or AIC_c values

The re-fit Mott-Spooner model (HM-9 in Table 2-3) had the lowest MSE, hence the MSE ratio is 1.0. The re-fit Boie model (HM-2 in Table 2-3) had the lowest AIC_c score, hence the evidence ratio is 1.0. To determine if any other models were good enough, and MSE ratio was

taken by dividing the model MSE values by the minimum MSE value (5.137 by the re-fit Mott-Spooner model). A ratio between 1.0 and 1.02 would be considered good enough. Interestingly enough, all re-fit models fell within this two percent margin in MSE ratio except for the Dulong model (HM-1 in Table 2-3). The AIC_c score was also used to determine if any other models yielded statistically similar results. An Akaike probability of 0.5 means that a model is equally likely to be correct as the "best" model. A cut-off of 0.45 for the Akaike probability is considered to be statistically similar. No other models fell in this range. While the Mott-Spooner model had the lowest MSE value, which generally indicates a better fit, the AIC_c value penalizes the Mott-Spooner model for having too many fitted coefficients, which could potentially lead to overfitting. Figure 7-3 shows the parity relationship for the re-fit Mott-Spooner and Boie models from Table 7-3.

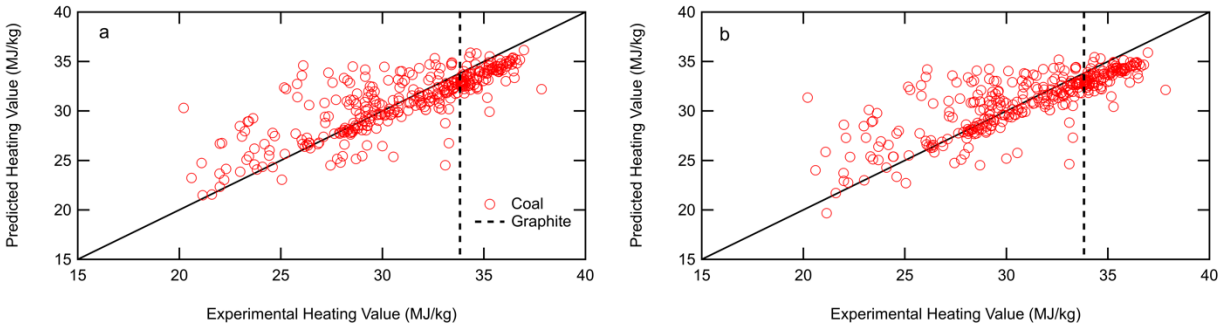

Figure 7-3. Parity plots of all best model forms for coal heating value: a) Mott-Spooner re-fit and b) Boie re-fit. Both plots include a vertical dashed line indicating the heating value of pure graphite.

Visually, the fit of both the Mott-Spooner and Boie re-fit models are very similar, especially at the upper ranges of the heating values. In both parity plots in Figure 7-3, a vertical dashed line indicates the experimental heating value of pure graphite.

Both the Mott-Spooner and Boie models performed well, so their model coefficients re-fit to the coal-only data set are shown in Table 7-4. The mean square error indicates that the

Mott-Spooner model is likely a slightly better fit than the Boie model, however, the AIC_c score suggests that the Mott-Spooner model may be overfit. According to the MSE ratio test, most of the other models with coefficients re-fit to the coal-only data set also perform well. See Appendix D for a full description of these other models.

Table 7-4. Coefficients of the Mott-Spooner and Boie Models Re-Fit to the Coal-Only Data Set

Coefficient	**a**	**b**	**c**	**d**	**e**	**f**	**g**
Mott-Spooner	318.6	1449	-139.0	16.47	-163.1	3.002	-30.47
Boie	316.5	1324	-73.58	203.1			

7.3.1.2 Coal Char Only

Coal char shares structural similarities with its parent coal, being more aromatic, and enriched in carbon compared to the parent coal (see Figure 7-2). As such, many of the coal heating value correlations may predict the heating value of char. The char data set was used to compare the literature model forms in Table 2-3, using both the original coefficients and a new set of coefficients re-fit to only the char data set. The best statistical results from this comparison are shown in Table 7-5.

Table 7-5. Best Models Using the Char-Only Data Set

Model	**MSE $(MJ/kg)^2$**	**MSE Ratio**	**AIC_c**	**Probability**	**Evidence Ratio**
Mott-Spooner	0.358	1.0*	-31.8	0.141	6.102
Boie	0.392	1.095	-35.4	0.5	1.0*

* These ratios are 1.0 since these models have the minimum MSE or AIC_c values

The Mott-Spooner model (HM-9 in Table 2-3) again performed well in the comparison using the char-only data set, again having the lowest MSE value of all the tested models. The re-fit Seylor model (HM-4 in Table 2-3) had the lowest AIC_c score. Like the coal-only comparison, the MSE ratio and Akaike probability cut-off values were used to determine if any other models could be considered good enough. No other models (re-fit or using original coefficients) fell within these cut-off values. The Mott-Spooner and Seylor re-fits are shown in parity plots in Figure 7-4.

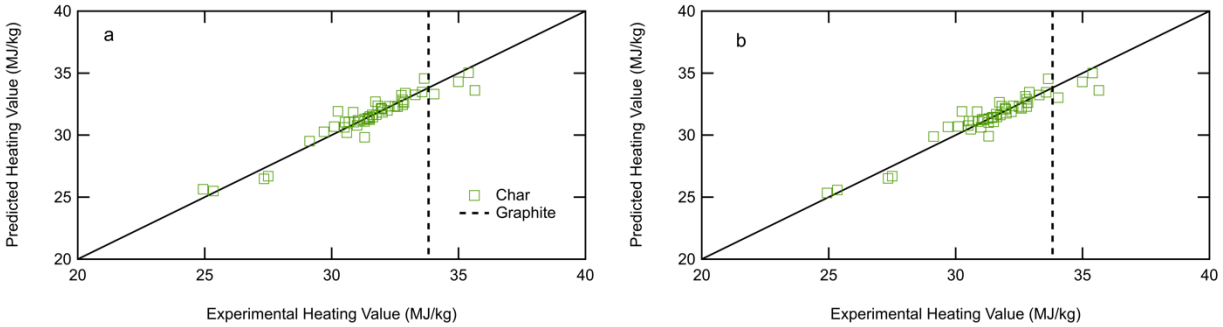

Figure 7-4. Parity plots of all best model forms for char heating value: a) Mott-Spooner re-fit and b) Seylor re-fit. Both plots include a vertical dashed line at the pure graphite heating value.

Both plots show a very good agreement between model calculations and experimental data, with the majority of the points lying on or very close to the parity line. Like the coal-only comparison, the vertical line in both plots in Figure 7-4 shows the heating value of pure graphite, which is often used as a coal char surrogate in large-scale simulations. Most of the char data lies below the graphite heating value. Visually it is very difficult to determine which model has a better fit. Statistically, the Mott-Spooner model has a slightly better fit, but like the coal-only comparison may suffer from overfitting. The re-fit Seylor model is suggested for almost as good of a fit with fewer coefficients than the Mott-Spooner model. Table 7-6 shows the coefficients for both the Mott-Spooner and Seylor models re-fit to the char-only data set.

Table 7-6. Coefficients of the Mott-Spooner and Seylor Models Re-Fit to the Char-Only Data Set

Coefficient	a	b	c	d	e	f	g
Mott-Spooner	328.2	1432	-99.96	-243.4	-297.4	7.824	1172
Seylor	471.5	1550	3.909	-14069			

7.3.1.3 Parent Coal and Coal Char Combined

Since raw coal and coal char are structurally similar, and since coal heating values are more frequently reported in the literature, the individual coal and char data sets were combined to determine if a better fit could be achieved for coals and chars. The best model fits were found using both original coefficients and the re-fit coefficients from the coal-char data set, and these best models are presented in Table 7-7.

Table 7-7. Best Models Using the Coal-Char Data Set

Model	MSE $(MJ/kg)^2$	MSE Ratio	AIC_c	Probability	Evidence Ratio
Mott-Spooner	4.321	1.0*	606.1	0.051	18.51
Boie	4.325	1.001	600.3	0.5	1.0*

* These ratios are 1.0 since these models have the minimum MSE or AIC_c values

Perhaps unsurprisingly the results of the combined coal-char data set are very similar to those of the coal-only comparison. This is due to the overwhelming amount of coal data compared to char data in this combined data set. Like the coal-only data set, the Mott-Spooner model (HM-9 in Table 2-3) had the lowest MSE value and the Boie model (HM-2 in Table 2-3) had the lowest AIC_c score. The comparisons of these two best models with the combined coal-char data set are shown in Figure 7-5.

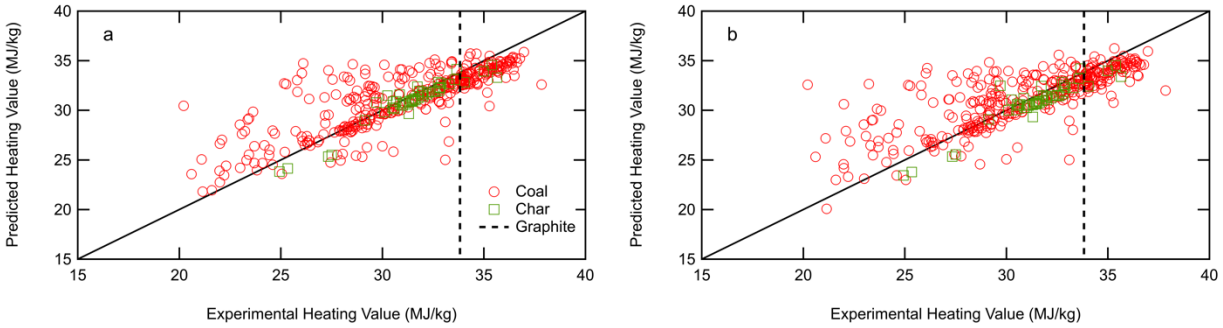

Figure 7-5. Parity plots of all best model forms for the coal (circles) and char (squares) heating values: a) Mott-Spooner re-fit and b) Boie re-fit. Both plots also include a vertical dashed line indicating the heating value of pure graphite.

This data set includes a total of 353 coal heating values and 50 char heating values, meaning this analysis was heavily influenced by the coal values. As such, it is no surprise that the parity relationships are almost identical to those shown in the coal-only analysis (see Figure 7-3 for comparison). However, since the char data seem to have a lower MSE, the MSE values for the combined coal-char data set are lower than for the coal-only data set.

Just like the coal-only analysis, the MSE ratio test shows that all re-fit models fall within two percent of the best value (4.321 from the Mott-Spooner model) except for the Dulong model (HM-1 in Table 2-3). Table 7-8 shows the coefficients for the Mott-Spooner and Boie models re-fit to the combined coal-char data set; the coefficients for the remaining models are found in Appendix C.

Table 7-8. Coefficients of the Mott-Spooner and Boie Models Re-Fit to the Combined Coal-Char Data Set

Coefficient	**a**	**b**	**c**	**d**	**e**	**f**	**g**
Mott-Spooner	325.0	1300	-78.83	-30.76	-137.9	2.766	-48.23
Boie	319.2	1215	-61.41	452.8			

7.3.1.4 Coal Tar Only

An extensive literature search discovered only 44 total tar heating values reported in the literature, with most from one report (Edwards et al., 1983). Coal tar is not only difficult to collect in some experimental applications but is frequently not collected in large enough quantities to test for elemental compositions and heating values. This part of the analysis compared the literature heating value correlations using the limited coal tar data set to determine if any of the models can be used to accurately predict the tar heating values. Table 7-9 details the best models to predict the tar heating values, using both original coefficients and coefficients re-fit to the tar-only data set.

Table 7-9. Best Models Using the Tar-Only Data Set

Model	MSE $(MJ/kg)^2$	MSE Ratio	AIC_c	Probability	Evidence Ratio
Gumz	1.942	1.0*	43.5	0.315	2.179
Boie	1.992	1.026	41.9	0.5	1.0*
Given	1.942	1.000	43.5	0.315	2.179

* These ratios are 1.0 since these models have the minimum MSE or AIC_c values

The Gumz model (HM-5 in Table 2-3) had the lowest MSE value and the Given model (HM-10 in Table 2-3) had an essentially equivalent fit (within the significant figures here). The Boie model again had the lowest AIC_c score of the models tested using the tar-only data set. These three models are shown in parity relationships in Figure 7-6.

The Gumz and Given models appear essentially identical (see Figure 7-6a and Figure 7-6c, respectively). There is a large spread of tar values, with a majority of the points being overpredicted by these models, especially the Boie model. The coefficients for the Gumz, Boie, and Given models re-fit to the tar-only data set are shown in Table 7-10.

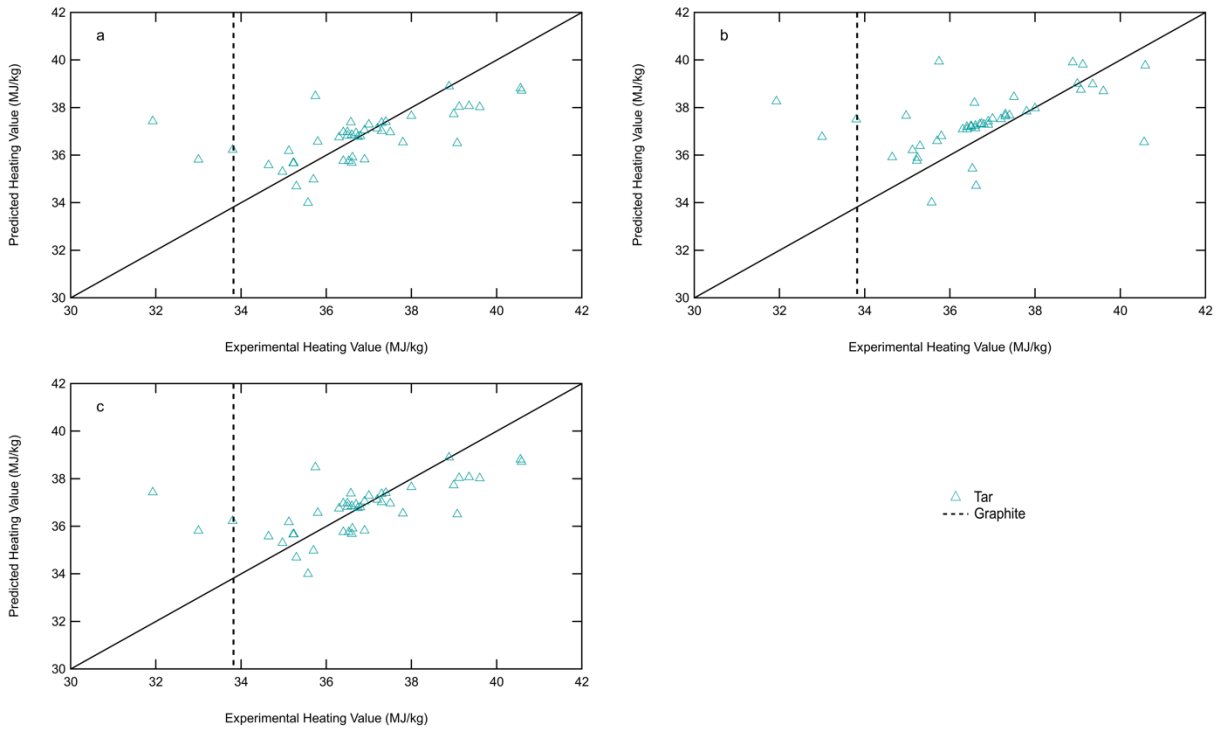

Figure 7-6. Parity plots of the best model forms for coal tar heating values: a) Gumz re-fit, b) Boie re-fit, and c) Given re-fit. All three plots include a vertical dashed line indicating the heating value of pure graphite.

Table 7-10. Coefficients of the Gumz, Boie, and Given Models Re-Fit to the Tar-Only Data Set

Coefficient	**a**	**b**	**c**	**d**	**e**
Gumz	353.5	970.6	-918.4	433.5	149.9
Boie	353.1	979.9	173.9	-841.1	
Given	1272	1889	1068	1351	-91802

While these are the best tar heating value models found using this tar data set, there is a lot of room for improvement. There are a number of reasons to be skeptical of the accuracy of these tar heating values or even the elemental compositions. Some coal devolatilization experiments do not collect the tar after devolatilization. Others collect the tar and soot together and must be separated if further testing is done on the tar. It is well known that primary tar may undergo secondary reactions and either crack to form lower molecular weight species or polymerize to form larger polycyclic aromatic hydrocarbons (PAH) and eventually form soot

(Fletcher et al., 1997; Josephson et al., 2017). Even in some experiments where the tar is collected, not enough is left to reliably test for elemental composition and heating value. Tar may not even be adequately captured during pyrolysis experiments, with the tar condensing either on the char or reactor surfaces (Fletcher and Hardesty, 1992). Heating value measurements require up to a gram of tar, whereas many coal pyrolysis experiments are performed with small amounts of coal. For these reasons, not many researchers have gathered or measured the heating values of coal tars. While these models show some promise in predicting the higher heating value of coal tar post-pyrolysis, a larger data set would benefit this analysis and allow for greater confidence in comparing the various model forms.

7.3.1.5 Combined Coal (Parent Coal, Char, and Tar)

Table 7-11 shows the best results for the combined coal data set, which includes all three individual data sets of coal, char, and tar. Like the combined coal-char comparison, this combined coal data set was used to determine if any of the models could be used to accurately predict any coal-based fuels.

Table 7-11. Best Models Using the Combined Coal-Char-Tar Data Set

Model	**MSE $(MJ/kg)^2$**	**MSE Ratio**	**AIC_c**	**Probability**	**Evidence Ratio**
Mott-Spooner	4.531	1.0*	691.7	0.161	5.212
Boie	4.56	1.006	688.4	0.5	1.0*
Steuer	4.56	1.006	688.4	0.5	1.0*
VDI	4.56	1.006	688.4	0.5	1.0*
Dulong-Berthelot	4.562	1.007	688.6	0.473	1.116
IGT	4.562	1.007	688.7	0.455	1.196

* These ratios are 1.0 since these models have the minimum MSE or AIC_c values

Like the coal-only and the combined coal-char comparisons, the combined coal-char-tar data set is largely coal data, which means the re-fit Mott-Spooner and Boie models (HM-9 and HM-2 in Table 2-3, respectively) again performed well. The Mott-Spooner model again had the lowest MSE value of 4.531, while the Boie model had the lowest AIC_c score of 688.4. Several other models also had almost identical AIC_c scores (identical in the number of significant figures), including the Steuer model (HM-3 in Table 2-3) and the VDI model (HM-8 in Table 2-3) with the Dulong-Berthelot (HM-6) and IGT (HM-7) models yielding slightly higher MSE or AIC_c values. All six models are shown in parity plots in Figure 7-7.

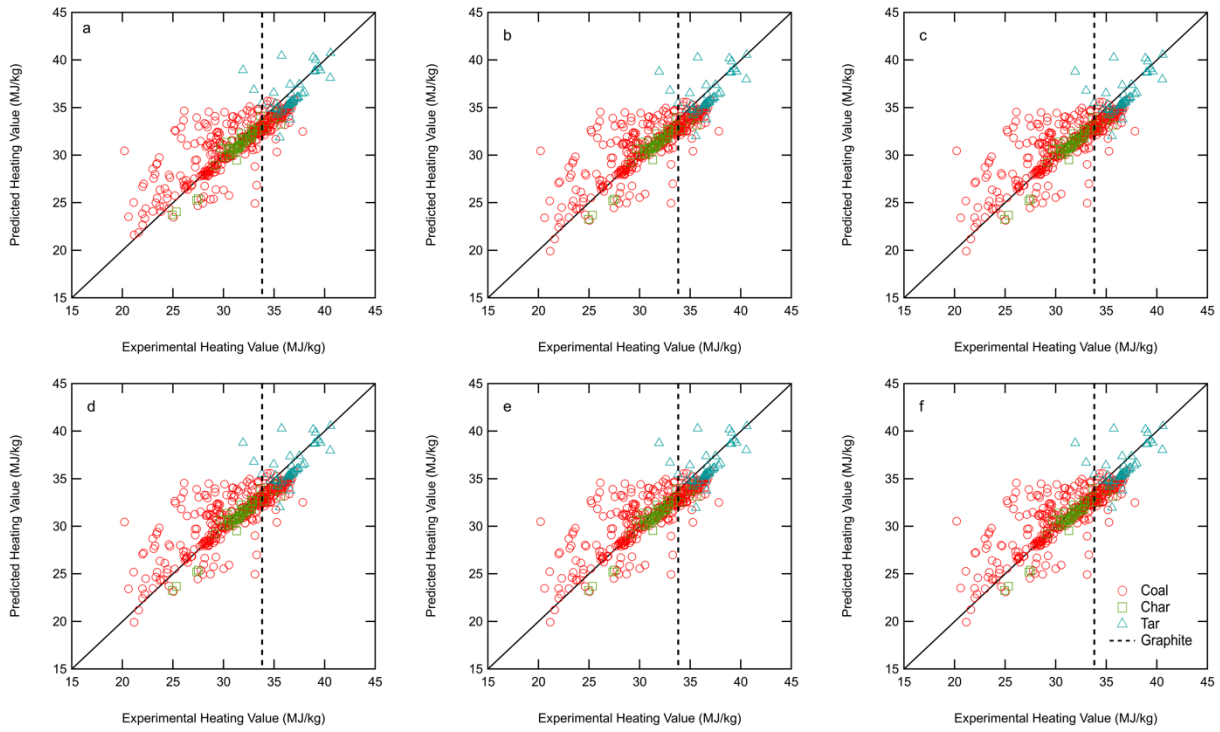

Figure 7-7. Parity plots of all best models for the combined heating value data set of coal, coal char, and coal tar: a) Mott-Spooner re-fit, b) Boie re-fit, c) Steuer re-fit, d) VDI re-fit, e) Dulong-Berthelot re-fit, and e) IGT re-fit.

All six models have a very similar fit to each other, with some subtle variations. The fits for char and tar might not be as accurate as their best models individually since the combined

coal-char-tar data set so heavily favors the coal values. However, any of these models could be used for coal-based heating values, if only one model is to be used in a simulation.

Like most of the other coal-based fuel comparisons, the Mott-Spooner model is the best fit according to MSE, however, this model might be overfit. The Boie, Steuer, or VDI models may have a slightly worse fit, but each have fewer fitted coefficients than the Mott-Spooner model. The re-fit coefficients for all four models are found in Table 7-12.

Table 7-12. Coefficients of the Mott-Spooner, Boie, Steuer, and VDI Models Re-Fit to the Combined Coal-Char-Tar Data Set

Coefficient	**a**	**b**	**c**	**d**	**e**	**f**	**g**
Mott-Spooner	323.4	1321	-86.59	-12.66	-136.4	2.621	-37.29
Boie	322.3	1308	-68.69	-26.28			
Steuer	322.3	357.2	1308	-26.28			
VDI	322.3	549.5	-26.28	758.6			

7.3.2 Fossil Fuels Data Set

In addition to coal fuels, other fossil fuels are of interest to combustion science. The fossil fuels data set includes coals, chars, tars, cokes (including petroleum cokes), liquid and gaseous fuels, oil shales and tar sands (and similar viscous fuels), peats (sometimes used for heating, cooking, and small-scale energy production), and explosives and propellants (which are frequently hydrocarbon-based fuels). Propellants and explosives are not fossil fuels but are included here because of structural and chemical similarities to other fossil fuels. The purpose of this data set analysis was to determine if any of the literature models accurately predict the heating value of any fossil-type fuel based on elemental composition. The best models are detailed in Table 7-13.

Table 7-13. Best Models Using the Fossil Fuels Data Set

Model	MSE $(MJ/kg)^2$	MSE Ratio	AIC_c	Probability	Evidence Ratio
Given	4.165	1.0*	799.7	0.5	1.0*
Gumz	4.170	1.001	800.4	0.411	1.430

* These ratios are 1.0 since these models have the minimum MSE or AIC_c values

The Given model (HM-10 in Table 2-3) was the best model according to both MSE and AIC_c values. The Gumz model (HM-5 in Table 2-3) came in a close second with the MSE ratio test, being only 0.1 percent away from the best MSE value of the Given model. Both models are shown in Figure 7-8.

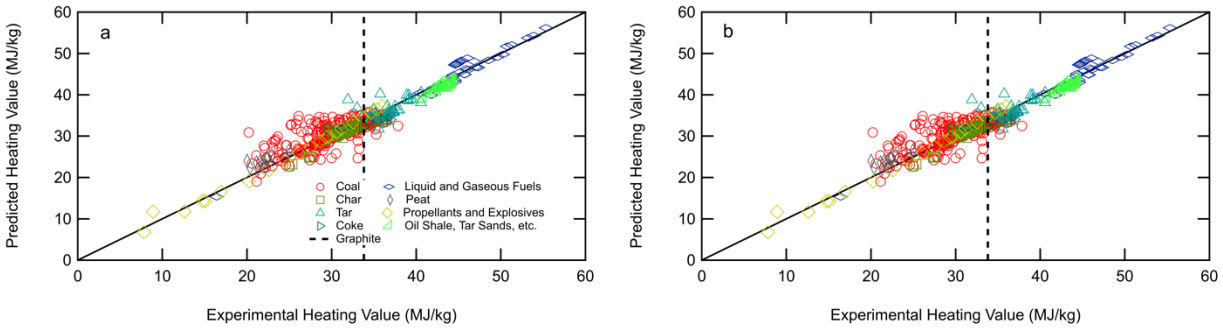

Figure 7-8. Parity plots of the best models for fossil fuels: a) Given re-fit and b) Gumz re-fit. A vertical line indicates the heating value of pure graphite.

Both models appear to give almost identical fits on a visual inspection of the parity relationship. The model coefficients of both models are included in Table 7-14, however, the Given model is suggested since it is a slightly better fit according to both the MSE and AIC_c values.

Table 7-14. Suggested Re-Fit Coefficients for the Fossil Fuels Data Set

Coefficient	a	b	c	d	e
Given	270.4	1208	-149.7	27.77	5571
Gumz	326.2	1263	55.08	83.23	-93.91

7.3.3 Biomass Data Set

Biomass is becoming a more widely used fuel for electricity production, especially in blends with coal or other solid fuels. For this reason, a biomass-only comparison was also performed. In this analysis, the biomass comparison included traditional biomass samples (typically different types of wood, wild plants, and grasses), biomass char (or biochar), and peat, which falls between typical biomass samples and coal samples on the Van Krevelen diagram (see Figure 7-2). Table 7-15 shows the best results for MSE and AIC_c values, along with the results of the MSE ratio test and Akaike probabilities. Note that the original model coefficients were from curve fits of coal, not biomass.

Table 7-15. Best Models Using the Biomass Data Set

Model	**MSE $(MJ/kg)^2$**	**MSE Ratio**	**AIC_c**	**Probability**	**Evidence Ratio**
Mott-Spooner	4.486	1.0*	157.3	0.103	8.749
Gumz	4.506	1.004	152.97	0.5	1.0*
Given	4.538	1.011	153.6	0.418	1.390

* These ratios are 1.0 since these models have the minimum MSE or AIC_c values

The Mott-Spooner (HM-9 in Table 2-3) and Gumz (HM-5) re-fit models again performed well, with the Mott-Spooner model having the lowest MSE value and the Gumz model having the lowest AIC_c score. In addition, the Given model also performed well, with an MSE value within two percent of the best value. These three best models are shown as parity plots in Figure 7-9.

The Mott-Spooner model appears to have the better fit on visual inspection, especially with the biochar heating value, however, the other two models appear to fit the experimental data almost as well for the biomass and peat heating values. Like the combined coal-char-tar

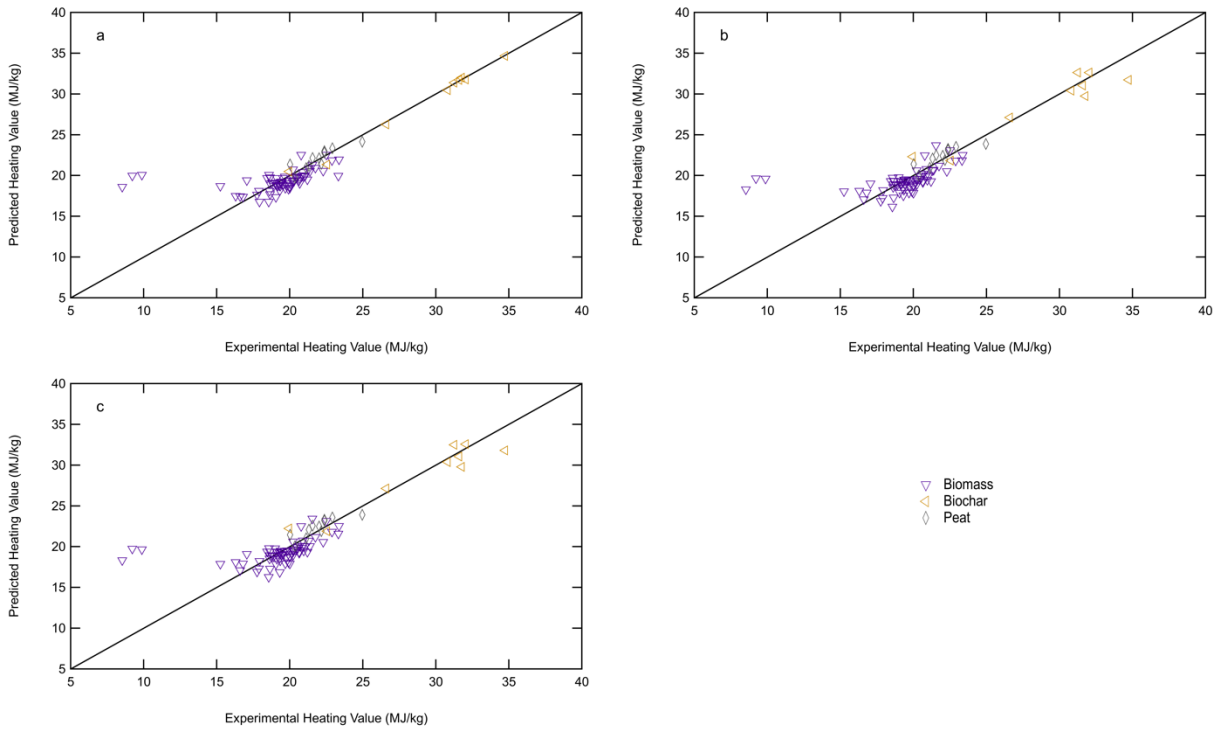

Figure 7-9. Parity plots of all best models of heating values for biomass, biochar, and peat: a) Mott-Spooner re-fit, b) Gumz re-fit, and c) Given re-fit.

comparison, this combined biomass data set is heavily weighted toward the biomass data, with fewer samples of peat and biochar. With a larger set of reliable data, a more accurate comparison for biomass samples (especially those of biochar) might be made.

There is a grouping of samples at the lower end of the measured heating values (7-10 MJ/kg) in which all heating values are significantly overpredicted. The three samples in this grouping are reported by Niessen (2002). The three fuels are listed as RDF (refuse-derived fuel), wood, and green logs, in ascending order of reported heating value. While the RDF is not a biomass by itself, Niessen compares it to the "wood" sample for structural and chemical similarities. For this reason, the RDF sample was included in the biomass data set, while alone it would have been instead added to the "other" fuels data set. It is unclear in Niessen's work what type of wood constitutes the "wood" sample compared to RDF, which makes it difficult to

determine if the heating value is simply an outlier or a mistake. Green logs contain a high amount of oxygen (~45 wt.%), which would lower the heating value considerably, however, this value might also be reported incorrectly since all tested heating value correlations calculate a much higher value than is reported.

Like the coal-base fuels, the Mott-Spooner model yielded the lowest MSE value, and also appeared to have a better fit on visual inspection of the parity relationship. However, with a large number of fitted coefficients, the Mott-Spooner model may suffer from overfitting. The Gumz and Given models have a better AIC_c score with slightly higher MSE values. For this reason, both the Mott-Spooner and Gumz models are suggested. The coefficients for these Mott-Spooner and Gumz models are found in Table 7-16.

Table 7-16. Coefficients of the Mott-Spooner and Gumz Models Re-Fit to the Biomass Data Set

Coefficient	**a**	**b**	**c**	**d**	**e**	**f**	**g**
Mott-Spooner	337.1	1074	19.67	622.9	-192.1	2.397	-1355
Gumz	348.4	518.1	370.1	-2034	-29.93		

7.3.4 Other Fuels Data Set

In an effort to reduce reliance on fossil fuels, many energy producers are researching blends of alternative fuels with fossil fuels. A similar comparison of the heating value correlations was completed for the "other" fuels data set, which includes some alternative fuel sources such as municipal solid waste, animal waste, food waste, etc. The best models for predicting the heating values of non-traditional fuels are found in Table 7-17.

The Gumz model (HM-5 in Table 2-3) showed the best agreement with the heating values of the "other" fuels data set, with the lowest MSE and AIC_c values of all models. The

Table 7-17. Best Models Using the "Other" Fuels Data Set

Model	MSE $(MJ/kg)^2$	MSE Ratio	AIC_c	Probability	Evidence Ratio
Gumz	12.3	1.0*	238.98	0.5	1.0*
Given	12.4	1.005	239.4	0.447	1.238

* These ratios are 1.0 since these models have the minimum MSE or AIC_c values

Given model (HM-10) also performed well, with an MSE value that is within 0.5 percent of the best value. There were no additional models that fell within the cut-off window of five percent for the AIC probability. These results are not surprising, since both of these model forms include a sulfur content, and the Gumz model form includes the nitrogen content. Many of these "other" fuels have much smaller carbon content and higher nitrogen and sulfur contents than most of the fossil fuels. These two best model fits for predicting the heating values from the "other" fuels data set are found in Figure 7-10.

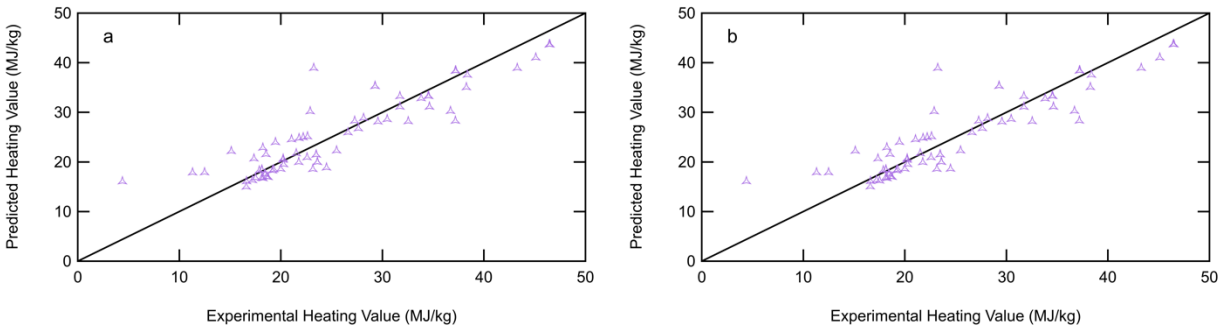

Figure 7-10. Parity plots of the best models for "other" fuel heating values:
a) Gumz re-fit and b) Given re-fit.

As shown in Figure 7-10, both the Gumz and Given models re-fit to the "other" fuels data set have very similar fits, visually. However, the Gumz model performs slightly better in both MSE and AIC_c tests. From this analysis, the re-fit of the Gumz model is suggested, until a more

comprehensive study on alternative fuels can improve on this fit. The re-fit coefficients for both the Gumz and Given models are found in Table 7-18.

Table 7-18. Coefficients of the Gumz and Given Models Re-Fit to the "Other" Fuels Data Set

Coefficient	a	b	c	d	e
Gumz	328.1	1091	81.83	-2513	-94.73
Given	247.3	1015	-174.9	-2582	8046

7.3.5 Full Data Set

The full data set includes all of the fuels listed in Table 7-1. Like the other data sets, a comparison of the heating value correlations was also performed for the full data set. A summary of the models with the best statistical results is found in Table 7-19.

Table 7-19. Best Models Using the Full Data Set

Model	MSE $(MJ/kg)^2$	MSE Ratio	AIC_c	Probability	Evidence Ratio
Given	6.285	1.0*	1304	0.5	1.0*
Boie	6.387	1.016	1314	0.009	105.1
Gumz	6.288	1.001	1305	0.453	1.207

* These ratios are 1.0 since these models have the minimum MSE or AIC_c values

Interestingly, the re-fit Given model (HM-10 in Table 2-3) is the best in both MSE and AIC_c values. In addition, the Gumz model (HM-5) performed well as did the Boie model (HM-2). It is not surprising that the Boie model performs well when calculating the heating values of a diverse collection of fuels, since this model was one of the few literature models that has been traditionally applied to a wider variety of fuels, including coals and biomass. The parity

relationships for these three models are found in Figure 7-11, with the major fuel groups differentiated using different marker symbols for each fuel type.

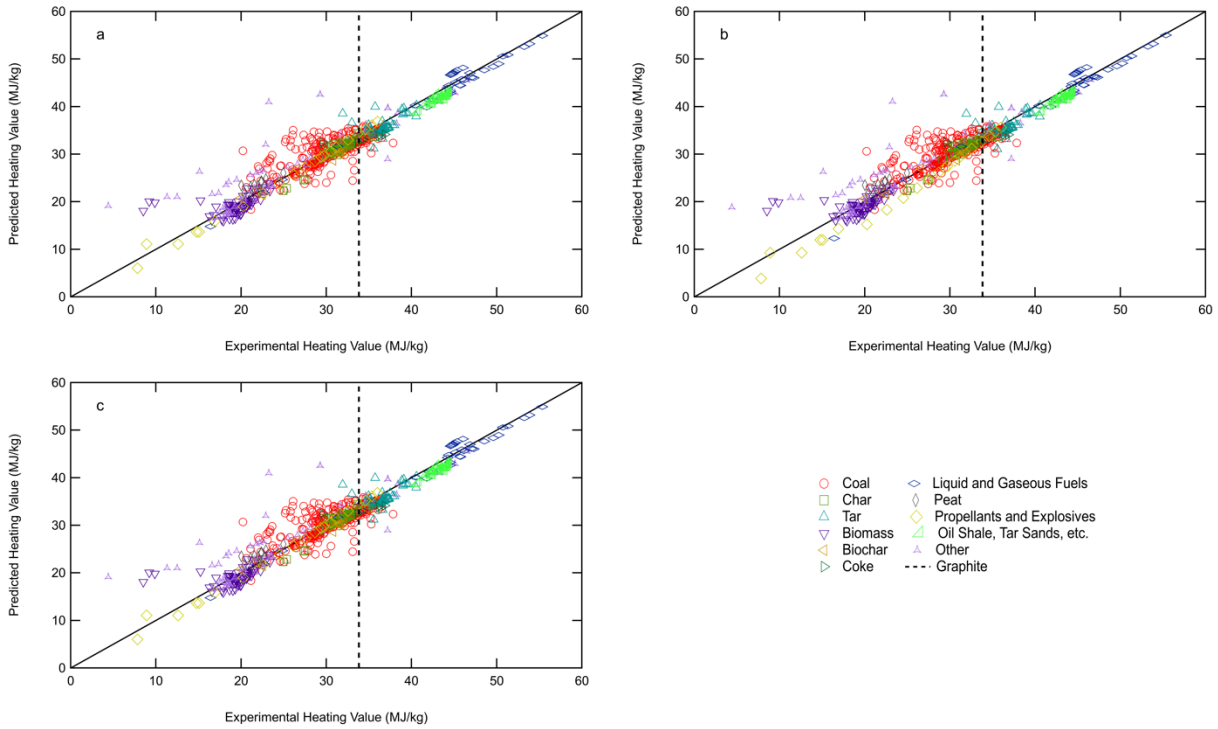

Figure 7-11. Parity plots of the best models for the full data set of heating values: a) Given re-fit, b) Boie re-fit, and c) Gumz re-fit. A vertical dashed line indicates the heating value of pure graphite.

Some similarities are observed between the fossil fuels and full data set comparisons. This is because the full data set is comprised primarily of the same data as the fossil fuels data set, adding 151 more heating values from the biomass, biochar, and "other" fuels. On a visual inspection, all three models appear to give a similar fit, except for the propellants and explosives category (yellow diamonds) for the Boie model (Figure 7-11b), which tends to underpredict the lowest of these heating values. However, the statistical measures of fit show that the Given model is slightly more accurate in terms of both MSE and AIC_c. Since the Given et al. model re-fit to the full data set more accurately predicts heating values, this model is suggested for

predicting heating values of any fuel type. In addition, the re-fit Gumz model satisfies both the two percent MSE ratio and five percent AIC probability criteria. This means that the Gumz model is only slightly less likely to be correct than the Given model. The Boie model also satisfies the two percent MSE ratio criterion, but fails to satisfy the five percent AIC probability, which means that the Boie model is still a potential good fit, but not as likely to be correct. The re-fit coefficients for the Given (preferred), Gumz (less preferred), and Boie (least preferred) models are found in Table 7-20.

Table 7-20. Coefficients of the Given, Gumz, and Boie Models Re-Fit to the Full Data Set

Coefficient	**a**	**b**	**c**	**d**	**e**
Given	274.1	1141	-167.3	24.79	5711
Gumz	331.2	1198	56.72	81.66	-110.4
Boie	332.5	1198	-110.7	55.59	

7.4 Discussion Summary

Different models were found to be optimal for each data set explored in this analysis. The ramifications of only using one model with one set of coefficients to describe each data set were explored. Since the re-fit Given model (HM-10 in Table 2-3) was found to yield the best fit of the overall data set, the re-fit coefficients from Table 7-20 were used to find the key statistical values for all nine data sets used in this analysis. These statistical results are found in Table 7-21. Note that the MSE ratio, AIC probability, and evidence ratios for each data set are in comparison with the best values found in each previous data set comparison, and not with the corresponding values from the full data set. The MSE ratios and AIC probabilities and evidence ratios are meaningless when compared to other data sets.

Table 7-21. Overall Statistical Results of the Given Model Re-Fit to the Full Data Set for all Data Sets

Data Set	**MSE (MJ/kg)^2**	**MSE Ratio**	**AIC_c**	**Probability**	**Evidence Ratio**
Coal	5.36	1.044	605.1	0.001	848.8
Char	1.10	3.068	18.64	1.84×10^{-12}	5.44×10^{11}
Tar	4.02	2.071	75.51	5.04×10^{-8}	1.99×10^{7}
Coal-char	4.56	1.056	623.9	7.44×10^{-6}	1.34×10^{5}
Combined coal	4.75	1.049	709.0	3.32×10^{-5}	3.01×10^{4}
Fossil fuels	4.26	1.023	812.1	0.002	500.8
Biomass	5.45	1.214	170.6	1.49×10^{-4}	6.70×10^{3}
Other fuels	17.95	1.459	272.9	4.33×10^{-8}	2.31×10^{7}
Full	6.29	1.0*	1304	0.5	1.0*

* This ratio is 1.0 since this model has the minimum MSE and AIC_c values for the full data set.

If only one model can be used, the re-fit of the Given model will give the most accurate results for all fuels, however, individual fuel groups are more accurately predicted by other correlations, as discussed in previous sections. As shown in Table 7-21, none of these data set comparisons using the Given model coefficients re-fit using the full data set came close to the best models suggested in each individual data set comparison. For this reason, the given model with coefficients re-fit to the full data set is only suggested for use with a data set that includes a wide range of fuel types and compositions, otherwise, the models suggested for each individual fuel type would give much more accurate heating values for those fuels.

The curve fits presented in this chapter are the best models for the respective data sets. Obviously, the number and quality of the data affect the accuracy of the curve fits. A few data points from each curve fit seem to lie well outside the range of most of the other data points, and hence should be examined more closely experimentally or repeated. Future improvements can be made by introducing a larger subset of non-traditional fuels, in particular propellants, explosives, and other fuels. A better characterization of these non-traditional fuels may even give rise to

more comprehensive heating value correlations when the chemical composition differences are better known for these unique fuel types.

7.5 Conclusions

Heating values are an important part of combustion experiments and modeling. In order to accurately predict heating values based solely on the primary organic (CHONS) elemental composition of the fuel of interest, a detailed comparison analysis was completed on 10 literature correlations (13 sets of unique, original coefficients) using a comprehensive data set that includes 11 major fuel types. Not only were the original literature models compared using this data set, but an optimization scheme was used to re-fit the literature model coefficients to a number of subsets of the full data set. Two key statistical parameters were used to assess the accuracy of each of these model forms in this analysis, both original and re-fit: mean square error (MSE) and the Akaike Information Criterion (AIC). The best statistical values were then found using subsets of the full data set: parent coal only, coal char only, coal tar only, combined coal-char, combined coal (parent coal, char, and tar), fossil fuels, biomass, "other" or non-traditional fuels, and the full data set.

For most of the coal data sets, the re-fit Mott-Spooner model had the lowest MSE value (for the coal-only, char-only, combined coal-char, and combined coal-char-tar comparisons). For the tar-only comparison, the re-fit Gumz model had the lowest MSE value. With seven fitted coefficients, however, the Mott-Spooner model may fall victim to overfitting. The AIC_c score shows that perhaps a better choice would be the re-fit Boie model (for all but the char-only comparison) and the re-fit Seylor model for the char-only comparison. In addition, the combined coal-char-tar comparison also showed that the re-fit Steuer, VDI, Dulong-Berthelot, and IGT models may give similar or good enough heating value calculations. Another interesting

observation was that while most of these literature models were originally developed for use with parent coal, the char heating values were predicted much more accurately than any of the other fuel types used in this analysis.

Fossil fuels were similarly analyzed, and two models give virtually identical results, both using re-fit coefficients: the Given model and the Gumz model, with the Given model being slightly better according to both MSE and AIC_c values. Both are similar in form and both have five fitted coefficients. The only difference in the model form is that the Given model does not include nitrogen content, whereas the Gumz and Channiwala-Parikh form does include nitrogen content. This might be significant when trying to predict the heating values for fuels with a wider range of nitrogen content.

Biomass was also analyzed in a similar way, and the Mott-Spooner model re-fit to the biomass data set performed the best according to MSE and the Gumz model having the best AIC_c value. The biomass data set includes three different major fuel: traditional biomass, biomass char, and peat. The biomass and peat heating values were more closely grouped than those of the biochar, which were typically the highest of the biomass fuel types. The Mott-Spooner model appears to have the best fit, especially with the biochar samples, however, with seven fitted coefficients, this might be an artifact of overfitting. The Gumz model is slightly less accurate according to MSE, but the fit is statistically close to the Mott-Spooner model but with fewer fitted coefficients.

Aside from the full data set, the “other” fuels data set varied the most in elemental composition. The best models to predict the heating value of these non-traditional fuels included nitrogen and sulfur content as variables, and a re-fit of the Gumz model showed the best promise according to both MSE and AIC_c values, with the Given model coming in at a close second. It is

not surprising that the Gumz re-fit model performed well for calculating “other” fuel heating values since the model form includes all five major elemental compositions (CHONS).

Using the full data set introduced a number of unique challenges, given the wide range of both heating values as well as chemical compositions. The more unique fuels (propellants and explosives, and “other” non-traditional fuel types) tended to have a higher nitrogen content and lower carbon content than many of the fossil-based fuels used in this analysis. A number of the literature models rely heavily on carbon, hydrogen, and oxygen contents and do not even consider nitrogen content. This analysis shows that the best overall heating value prediction comes from the re-fit Given model, followed closely by the re-fit Boie and Gumz models, especially for fossil-based fuels.

Future improvements can be made to these literature models by expanding the number of samples in the experimental data set, particularly for coal tars and more unique fuels such as propellants, explosives, municipal solid waste, etc. These latter fuel types are not as structurally and chemically similar to each other or as widely studied as parent coals or biomass samples. For example, 50% of this data set consisted of coals and 10% of biomass, with only 3% of the data set for propellants and 10% for other fuels including municipal solid waste. Potential improvement could also be made in the biomass analysis by including samples of biotar, which are lacking in the established literature.

8 MIXTURE FRACTION ANALYSIS

This chapter details the results of the mixture fraction analysis. The mixture fraction analysis was set up in an effort to quantify uncertainty in some common simplifying assumptions used in turbulence-chemistry interactions in large-scale coal combustion simulations. The work presented in this chapter is based on work in Richards et al. (2020). While the key results and discussion are presented here, additional work is detailed in Appendix E.

8.1 Introduction

The basic theory and equations for a mixture fraction analysis are presented in Section 2.3.4. However, in an effort to show how this analysis was performed, this chapter begins with additional motivation behind this analysis and a derivation of the complete set of equations used. Simplifying assumptions are often used to decrease computational complexity, especially when computational resources are limited. However, these simplifying assumptions can generate large errors and uncertainty in large-scale simulations.

This dissertation compares three different levels of mixture fraction analysis, including one, two, and three fuel mixture fractions for coal combustion scenarios. The one-mixture fraction approach assumes all mass originating in the coal has the same elemental composition and heating value as the parent coal and is the most common mixture fraction approach (Smith et al., 1981; Smoot, 1981; Smoot and Smith, 1985; Pedel et al., 2013).

Flores and Fletcher (2000) extended the approach developed Smith et al. (1981) to use two mixture fractions, however, Flores and Fletcher modified their approach from a more traditional two-mixture fraction method by using two mostly independent mixture fractions (meaning both fuel mixture fractions can fall between 0 and 1, independently). The two-mixture fraction approach treats volatiles and char compositions and heating values separately and was used in simulations of three laboratory-scale coal combustors. Results for the one- and two-mixture fraction approaches showed differences in calculated temperatures and species concentrations near the burner, especially with NO predictions.

The three-mixture fraction approach treats light gas, tar, and char separately. These three approaches are compared here using equilibrium calculations rather than performing simulations of pilot- or industrial-scale furnaces. This simplified approach allows focus on the chemical state spaces, which can be widely explored, and which would be encompassed in specific furnace simulations.

8.2 Approach

The mixture fraction approaches used here involved a few modifications to both the equations and equilibrium programs introduced in Section 2.3.4. This approach section first details the three levels of mixture fraction comparisons followed by a description of some new subroutines introduced into Cantera to deal with coal-based fuels. Finally, this section includes a brief discussion of the experimental data used in this analysis.

8.2.1 One-Mixture Fraction Comparison

A one-mixture fraction method divides a combustion mixture into two streams—one fuel stream and one oxidizer stream. This is a common method used in simple hydrocarbon

combustion applications and has also been applied to coal-gas mixtures (Smoot and Smith, 1985). The one-mixture fraction comparison is the simplest of the three detailed here. In coal systems, one mixture fraction is used to describe all gas from a raw coal mixing with the oxidizing gas. Coal gas is a mixture of a large number of different species with a wide variety of composition and energy properties. The fuel mixture fraction (as shown generally in Equation 2-4) of a one-mixture fraction system is shown in Equation 8-1:

$$f = \frac{M_1}{M_0 + M_1} \tag{8-1}$$

where f is the fuel mixture fraction (coal or any number of coal surrogate gases), M_0 is the mass of the oxidizer stream, and M_1 is the mass of the fuel stream. The index of 1 is dropped for the one-mixture fraction method (shown in Equation 8-1) out of convenience. The mass fraction of any element in the system can be found using the elemental mass fractions (shown generally in Equation 2-5), as shown in Equations 8-2 to 8-6 (in order of CHONS):

$$Z_C^I = W_C \left(\frac{a_{C,1} f}{W_1} + \frac{a_{C,0}(1-f)}{W_0} \right) \tag{8-2}$$

$$Z_H^I = W_H \left(\frac{a_{H,1} f}{W_1} + \frac{a_{H,0}(1-f)}{W_0} \right) \tag{8-3}$$

$$Z_O^I = W_O \left(\frac{a_{O,1} f}{W_1} + \frac{a_{O,0}(1-f)}{W_0} \right) \tag{8-4}$$

$$Z_N^I = W_N \left(\frac{a_{N,1} f}{W_1} + \frac{a_{N,0}(1-f)}{W_0} \right) \tag{8-5}$$

$$Z_S^I = W_S \left(\frac{a_{S,1} f}{W_1} + \frac{a_{S,0}(1-f)}{W_0} \right) \tag{8-6}$$

where Z_C^I is the elemental mixture fraction of carbon in a one-mixture fraction system (denoted by a superscript I), W_C is the molecular weight of carbon, $a_{C,1}$ is the number of atoms of carbon

in the fuel stream (estimated using the mole fraction of carbon in the case of coal-based fuels), f is the fuel mixture fraction (mass fraction of the fuel), and W_1 is the molecular weight of the fuel stream. Similar variables are used for each element, with a subscript of zero used to denote properties of the oxidizer stream added to the elemental mixture fractions (only meaningful if those elements exist in the oxidizer stream, e.g., oxygen and nitrogen for air). These are generalized equations, but for a typical coal combustion application, the elemental mixture fractions would be simpler than shown here. Air does not typically include any carbon, hydrogen, or sulfur, so the $a_{i,0}$ values (e.g., $a_{C,0}$) for each of those elements would be zero. These values would be different if different oxidizer gases were used (e.g., oxy-fuel combustion). Because there is only one fuel stream, only one equivalence ratio (shown generally in Equation 2-6) is needed to describe the system. The one-mixture fraction equivalence ratio is shown in Equation 8-7:

$$\phi = \frac{\frac{n_1}{n_0}}{\left(\frac{n_1}{n_0}\right)_{stoich}} \tag{8-7}$$

where subscripts of zero and one are again used to denote the moles of the oxidizer and fuel streams, respectively.

8.2.2 Two-Mixture Fraction Comparison

A two-mixture fraction system is a little more complex than a one-mixture fraction system. Instead of only using a single fuel stream, a two-mixture fraction system includes two fuel streams. While a two-mixture fraction method does not usually provide any benefit for simple hydrocarbon combustion reactions, these methods can benefit coal combustion reactions since pyrolysis and char combustion occur on different time scales. Coal reaction products can

therefore be treated as volatile gases (named the total volatiles) and the solid that remains after pyrolysis (named the char). These two general categories of pyrolysis products comprise the two fuel streams of a two-mixture fraction system. These two fuel mixture fractions are described in Equations 8-8 and 8-9:

$$f_1 = \frac{M_1}{M_0+M_1+M_2} \tag{8-8}$$

$$f_2 = \frac{M_2}{M_0+M_1+M_2} \tag{8-9}$$

where the oxidizer stream is again denoted with a zero subscript, and subscripts of 1 and 2 are used to denote the mass and mixture fractions of the char and volatiles streams, respectively. Like all mixture fractions here, f_1 and f_2 sum to one minus the oxidizer mixture fraction (f_0). The mass fractions of the major elements in the combustion system can again be calculated using the elemental mixture fractions in Equations 8-10 to 8-14:

$$Z_C^{II} = W_C\left(\frac{a_{C,1}f_1}{W_1} + \frac{a_{C,2}f_2}{W_2} + \frac{a_{C,0}(1-f_1-f_2)}{W_0}\right) \tag{8-10}$$

$$Z_H^{II} = W_H\left(\frac{a_{H,1}f_1}{W_1} + \frac{a_{H,2}f_2}{W_2} + \frac{a_{H,0}(1-f_1-f_2)}{W_0}\right) \tag{8-11}$$

$$Z_O^{II} = W_O\left(\frac{a_{O,1}f_1}{W_1} + \frac{a_{O,2}f_2}{W_2} + \frac{a_{O,0}(1-f_1-f_2)}{W_0}\right) \tag{8-12}$$

$$Z_N^{II} = W_N\left(\frac{a_{N,1}f_1}{W_1} + \frac{a_{N,2}f_2}{W_2} + \frac{a_{N,0}(1-f_1-f_2)}{W_0}\right) \tag{8-13}$$

$$Z_S^{II} = W_S\left(\frac{a_{S,1}f_1}{W_1} + \frac{a_{S,2}f_2}{W_2} + \frac{a_{S,0}(1-f_1-f_2)}{W_0}\right) \tag{8-14}$$

where Z_C^{II} is the elemental mixture fraction of carbon in a two-mixture fraction system (note, the superscript II is used here to differentiate from a squared value, to indicate that the elemental mixture fraction describes that of a two-mixture fraction system), and the other variables are

extensions of those previously described. Like the one-mixture fraction comparison, the five elemental mixture fractions sum to one and would simplify based on the oxidizer gases used. In addition to the two fuel mixture fractions, there are also two independent equivalence ratios that can be used to determine the amount of oxidizer in the system, shown in Equations 8-15 and 8-16:

$$\phi_1 = \frac{\frac{n_1}{n_0}}{\left(\frac{n_1}{n_0}\right)_{stoich}} \tag{8-15}$$

$$\phi_2 = \frac{\frac{n_2}{n_0}}{\left(\frac{n_2}{n_0}\right)_{stoich}} \tag{8-16}$$

with subscripts of 0, 1, and 2 describing the moles of oxidizer, char, and volatiles, respectively.

8.2.3 Three-Mixture Fraction Comparison

The three-mixture fraction comparison adds a third fuel mixture fraction. Like the two-mixture fraction comparison, three mixture fractions generally are not useful in most simple hydrocarbon combustion applications. Coal combustion systems, however, might benefit from three mixture fractions. The total volatiles can be further divided into two additional categories: tars and light gases. This leads to three total fuel streams—one for the char, one for the tar, and a third for the light gases. The three fuel streams are described by three fuel mixture fractions, shown in Equations 8-17 to 8-19:

$$f_1 = \frac{M_1}{M_0+M_1+M_2+M_3} \tag{8-17}$$

$$f_2 = \frac{M_2}{M_0+M_1+M_2+M_3} \tag{8-18}$$

$$f_3 = \frac{M_3}{M_0+M_1+M_2+M_3} \tag{8-19}$$

where a subscript of zero again describes the oxidizer stream values, a subscript of 1 corresponds to the char stream, a subscript of 2 details the tar stream, and a subscript of 3 indicates the light gas stream. All three fuel mixture fractions and the oxidizer mixture fraction (f_0) again sum to 1. The mass fractions of each element in the mixture can again be found by calculating the elemental mixture fractions, in Equations 8-20 to 8-24:

$$Z_C^{III} = W_C \left(\frac{a_{C,1} f_1}{W_1} + \frac{a_{C,2} f_2}{W_2} + \frac{a_{C,3} f_3}{W_3} + \frac{a_{C,0}(1-f_1-f_2-f_3)}{W_0} \right) \tag{8-20}$$

$$Z_H^{III} = W_H \left(\frac{a_{H,1} f_1}{W_1} + \frac{a_{H,2} f_2}{W_2} + \frac{a_{H,3} f_3}{W_3} + \frac{a_{H,0}(1-f_1-f_2-f_3)}{W_0} \right) \tag{8-21}$$

$$Z_O^{III} = W_O \left(\frac{a_{O,1} f_1}{W_1} + \frac{a_{O,2} f_2}{W_2} + \frac{a_{O,3} f_3}{W_3} + \frac{a_{O,0}(1-f_1-f_2-f_3)}{W_0} \right) \tag{8-22}$$

$$Z_N^{III} = W_N \left(\frac{a_{N,1} f_1}{W_1} + \frac{a_{N,2} f_2}{W_2} + \frac{a_{N,3} f_3}{W_3} + \frac{a_{N,0}(1-f_1-f_2-f_3)}{W_0} \right) \tag{8-23}$$

$$Z_S^{III} = W_S \left(\frac{a_{S,1} f_1}{W_1} + \frac{a_{S,2} f_2}{W_2} + \frac{a_{S,3} f_3}{W_3} + \frac{a_{S,0}(1-f_1-f_2-f_3)}{W_0} \right) \tag{8-24}$$

where Z_C^{III} describes the elemental mixture fraction of carbon in a three-mixture fraction system (note, the superscript III is used to differentiate from a cubed value, to indicate that the elemental mixture fraction describes that of a three-mixture fraction system), and the remaining variables are likewise extensions of those described in the one- and two-mixture fraction comparisons. Additionally, there are three independent equivalence ratios in a three-mixture fraction system:

$$\phi_1 = \frac{\frac{n_1}{n_0}}{\left(\frac{n_1}{n_0}\right)_{stoich}} \tag{8-25}$$

$$\phi_2 = \frac{\frac{n_2}{n_0}}{\left(\frac{n_2}{n_0}\right)_{stoich}} \tag{8-26}$$

$$\phi_3 = \frac{\frac{n_3}{n_0}}{\left(\frac{n_3}{n_0}\right)_{stoich}} \tag{8-27}$$

8.2.4 Equilibrium Programs

Section 2.3.4 gives a brief introduction to the two equilibrium programs used here (NASA-CEA and Cantera), however, this analysis required the introduction of a few novel subroutines to Cantera. While the NASA-CEA program has been used to calculate the equilibrium states of many types of fuels (including solid fuels), Cantera requires a solid-fuel mechanism. Cantera is not natively set up to deal with solid fuels, so the mechanism subroutine uses the elemental composition, enthalpy of formation, and the reference temperature at which the enthalpy of formation is calculated. These inputs are used to develop coefficients for the polynomial thermodynamic property models Finally, the thermodynamic coefficients and other relevant information are included in a solid-fuel mechanism file. This solid-fuel mechanism generator subroutine can be used to generate mechanism files for any coal-based fuels.

Some instabilities were observed in Cantera equilibrium calculations when just the coal mechanism files were used. To eliminate these instabilities, the Cantera mechanism for solid carbon (graphite) had to be introduced along with mechanism files for unreacted coal (or other solid fuel) and combustion/background gases. Additional mechanism files were created for coal surrogate and combustion gases.

A second subroutine was created around the Cantera solver to iterate over the range of equivalence ratios for each fuel stream. The mixture fractions were calculated at each equivalence ratio and for each equilibrium state. The additional subroutine made the Cantera calculations more convenient, especially for the two- and three-mixture fraction comparisons.

8.2.5 Experimental Data

Experimental data were gathered from several sources based on the following criteria: (a) reported elemental compositions must be reported on a dry, ash-free (DAF) basis or enough

information provided to calculate the elemental compositions on a DAF basis; (b) heating values (enthalpies of combustion) must be reported on a DAF basis, or enough information provided to calculate them on a DAF basis; (c) comparisons using two mixture fractions must have average elemental compositions and heating values for both char and either tar or total volatiles; and (d) data for the three-mixture fraction comparison must have enough information to calculate elemental compositions and heating values for coal char, tar, and light gas. A review of a large set of experimental heating values was reported by Richards et al. (2021), and all coal-based fuels were taken from that data set. Some common coal surrogate gases are also used here. All fuels used, along with their respective sources, are described in Table 8-1.

Table 8-1. Fuels Used in the Mixture Fraction Analysis

Fuel No.	**Fuel Name**	**Source**	**Coal Rank**
F-1	Graphite	Perry's Handbook (Green, 1984)	N/A
F-2	Benzene	Perry's Handbook (Green, 1984)	N/A
F-3	Methane	Perry's Handbook (Green, 1984)	N/A
F-4	Ethane	Perry's Handbook (Green, 1984)	N/A
F-5	Ethylene	Perry's Handbook (Green, 1984)	N/A
F-6	Pittsburgh #8 (Pitt 8) Coal	Proscia et al. (1994)	HVA
F-7	Lower Kittanning Coal	Proscia et al. (1994)	LVB
F-8	Millmerran Coal	Edwards et al. (1983)	Subbituminous
F-9	Liddell Coal	Edwards et al. (1983)	Bituminous
F-10	Mammoth Seam Coal	Miller (2017a)	Anthracite
F-11	Beulah Zap Coal	Miller (2017a)	Lignite
F-12	Buck Mountain Coal	Miller (2017a)	Anthracite
F-13	#8 Leader Seam Coal	Miller (2017a)	Anthracite
F-14	#8 Seam Coal	Miller (2017a)	Semi-anthracite
F-15	Gunnison Coal	Miller (2017a)	Semi-anthracite
F-16	L. Spadra Coal	Miller (2017a)	Semi-anthracite

All 16 fuels were used in the one-mixture fraction comparison, with fewer in the two-mixture fraction comparison, and only one (F-6, Pitt 8) used in the three-mixture fraction

comparison. The fuel cases for each mixture fraction comparison are described in the Results and Discussion section.

While the elemental compositions and heating values of most of the fuels listed in Table 8-1 can be found in Richards et al. (2021) and Appendix B, a brief summary of some of the compositional differences between fuels used here is warranted. Table 8-2 shows the DAF wt.% of carbon, hydrogen, oxygen, nitrogen, and sulfur for a few of the coal-based fuels. This table is to illustrate some of the compositional differences that occur between different coal-based fuels, including different coals, chars, and tars.

Table 8-2. Summary of Elemental Composition of Some Coal-Based Fuels

Fuel No.	**Fuel Name**	**C**	**H**	**O**	**N**	**S**
F-6	Pitt 8 Coal	82.36	5.51	8.56	1.65	1.92
F-6a	Pitt 8 Char	83.01	5.24	8.23	1.68	1.84
F-6b	Pitt 8 Tar	85.02	6.40	5.68	1.63	1.27
F-6c	Pitt 8 Volatiles	78.65	7.05	10.47	1.48	2.35
F-6d	Pitt 8 Light Gases	49.18	10.06	32.66	0.78	7.32
F-8	Millmerran Coal	78.40	6.70	13.10	1.20	0.60
F-11	Beulah Zap Coal	73.10	4.50	20.60	1.00	0.80
F-12	Buck Mountain Coal	90.80	2.60	5.20	0.80	0.60

Different coals and coal-based fuels have very different compositions, and this affects the compositions of combustion gases at equilibrium. The coal surrogate gases vary even more, with none having any oxygen, nitrogen, or sulfur as part of the fuel.

8.2.6 Equilibrium Calculation and Turbulent Mixing Procedure

The one-mixture fraction analysis used both the Cantera and NASA-CEA programs. The NASA-CEA code is trusted in the coal community for evaluating equilibrium states of coal-based fuels, so it is used to evaluate Cantera as a viable alternative for calculating equilibrium

states. Both equilibrium programs require similar inputs depending on if the fuel is included in the program data or is user-defined. Simple fuels are included in the NASA-CEA code and are directly available to Cantera via provided mechanism files; these include all five of the surrogate gases: graphite (carbon solid), benzene, methane, ethane, and ethylene. These simple fuels include all the composition and thermochemical properties required for the respective equilibrium programs. User-defined compounds need two main parameters for both programs: elemental composition (CHONS, on either a mass or mole basis) and an enthalpy (or heat) of formation. For most coal-based fuels, elemental compositions and heats of combustion (also called heating values) are reported for each fuel. Heats of formation can then be calculated for each fuel by converting from heating values by assuming complete combustion, as shown in Equations 2-1 and 2-2, with the overall heat of reaction shown in Equation 8-28.

$$\Delta H_r = \left(\sum_{i=1}^{n} \nu_i \Delta H_{i,f}\right)_{prod} - \left(\sum_{i=1}^{n} \nu_i \Delta H_{i,f}\right)_{react} \quad (8\text{-}28)$$

where ΔH_r is the enthalpy of reaction (also called heating value), ν_i is a generic stoichiometric coefficient of compound i, $\Delta H_{i,f}$ is the enthalpy of formation of compound i, subscripts $prod$ and $react$ refer to products (CO_2, H_2O, etc.) and reactants (fuel and O_2), respectively.

Equilibrium calculations require a pressure, an energy content, and a starting composition, which in this case can be an elemental composition of the mixture. The mixture fraction approach enables calculation of the combined energy content and elemental composition of a mixture. The mixture fractions for each fuel and oxidizer stream are calculated at each location in a simulation using the appropriate transport equations and the turbulent mixing model. These mixture fractions represent the fraction of mass that originated in each fuel or oxidizer stream in a local eddy (introduced in Section 2.3.5), permitting calculation of the of the

mixture elemental composition and energy content, which in turn permits an equilibrium temperature and composition for that mixture. The NASA-CEA code allows the input of a list of fuel mixture fractions (or even equivalence ratios), which makes calculating the equilibrium states using NASA-CEA very convenient. Cantera calculations require the total amount of oxidizer (on a mass or moles basis), which can be found either using the equivalence ratio or fuel mixture fraction.

Equilibrium calculations using the one-mixture fraction approach were performed for a range of equivalence ratios from 0.1 (fuel-lean) to 3 (fuel-rich), with a greater number of points around the stoichiometric point (equivalence ratio of 1). The one-mixture fraction comparison used this equivalence ratio range to calculate the total air necessary to calculate equilibrium states for each fuel and to approximate the differing local eddy compositions.

The procedure became more complicated with the two- and three-mixture fraction analyses. Because the analysis used a range of equivalence ratios rather than mixture fractions to determine the appropriate amounts of air for each fuel, a separate "mixing condition" was used to determine the ratio of the fuel streams and fully explore the range of possible local eddy compositions. If the fuel mixture fraction was used instead of the equivalence ratio, this fuel mixing condition would not be necessary. This fuel mixing condition is simply how much of each fuel stream is present prior to mixing with the oxidizer stream. The fuel mixing condition is allowed to vary between 0 and 1, with the sum of the fuel stream percentages not exceeding 1.0.

In a two-mixture fraction system, there are two extremes in local eddy compositions with respect to the fuel streams: (a) pure fuel 1 (mass of gas originating in the char) with no fuel 2 (volatiles); and (b) pure fuel 2 (volatiles) with no fuel 1 (mass from char). The first extreme would be defined as a fuel mixing condition of 0, which means that the fuel composition of the

local eddy only consists of fuel 1 (char). The other extreme would correspond to a fuel mixing condition of 1, or 100 percent volatiles in the local eddy. To span this fuel mixing space of local eddy compositions, five main fuel mixing cases were created with fuel ratios corresponding to 0, 25, 50, 75, or 100% volatiles (called Y_{vol}). This means that at 0% volatiles, the fuel is 100% mass from the char, and vice-versa. Additionally, the reported pyrolysis yield for each coal was used as a sixth fuel mixing ratio (between 10 and 60% depending on the fuel and pyrolysis conditions). Air was added to each fuel stream to vary the equivalence ratio independently between 0.1 and 3, with the total amount of oxidizer being a combination of the two equivalence ratios. This procedure was followed for all six fuel mixing ratios for the coal-based fuels with only five for the surrogate fuels. Following this procedure allows for better conformation to local eddy compositions without adding too much complexity.

The three-mixture fraction comparison was slightly more complex, but a similar procedure to the two-mixture fraction comparison was followed to span the three-mixture fraction fuel mixing space of local eddy compositions. The three fuel streams (char, tar, and light gas) were allowed to mix with the same six values as the two-mixture fraction comparison (i.e., 0, 25, 50, 75, and 100%, as well as the reported pyrolysis yield of char, tar, and light gas). There are, however, two constraints placed on these fractions: (a) the three fuel fractions sum to one (this constraint is the same for both two- and three-mixture fraction methods) and (b) all fuel fractions must be between 0 and 1 (no negative numbers). Air was added to each fuel stream to vary the equivalence ratio between 0.1 and 3 for each fuel stream independently. This allows for the calculation of the total amount of air at each mixing condition and equivalence ratio. Like the two-mixture fraction method, this procedure allows for the spanning of the entire local eddy composition range. This procedure generated six total fuel mixing conditions for each two-

mixture fraction comparison and 21 for each three-mixture fraction comparison. While these procedures allow for the complete eddy composition range, not all of the compositions in the entire range will be observed experimentally or in a realistic simulation.

Using the elemental compositions and enthalpies of formation for each fuel, and setting the pressure to one atmosphere, the equilibrium programs were used to calculate the compositions of a large number of combustion gases for each equilibrium state. This analysis used six key variables from each equilibrium state to compare between fuels and mixture fraction methods: temperature and the mole fractions of O_2, CO_2, CO, H_2O, and graphite (i.e., solid carbon). This equilibrium temperature is an adiabatic temperature and does not account for any heat loss that might be observed in any real-world combustion applications.

Several statistical parameters (Richards et al., 2019; Richards et al., 2021) were used to quantify error between the equilibrium states calculated by both NASA-CEA and Cantera, however, only one is presented here: the root-mean-square error (RMSE, otherwise known as the L_2 norm), found in Equation 2-15. The additional statistical parameters can be found in Appendix E.

The equation for RMSE is a statistical parameter where experimentally observed and model prediction values are generally used in place of the “true” and “questioned” values, respectively. Both NASA-CEA and Cantera give predicted values for equilibrium states, so in order to adequately compare NASA-CEA to Cantera, in this analysis the NASA-CEA values are considered to be the “true” values and the Cantera are the “questioned” values. This distinction is not as important with the RMSE; however, it does make a slight difference in other statistical parameters (see Appendix E).

8.3 Results and Discussion

The results are discussed based on the number of fuel mixture fractions considered, starting with the one-mixture fraction comparison, followed by the two-mixture fraction comparison, and finally the three-mixture fraction approach compared to the one- and two-mixture fraction approaches. Each section consists of a description of the fuels used for each case. After the results are presented and discussed, a final section summarizes the key findings and discusses application to physical processes. Additional details and discussion are found in Appendix E.

8.3.1 One Mixture Fraction

The one-mixture fraction approach breaks the components into one fuel stream (e.g., coal) and one oxidizer stream (air). These two streams are mixed in different proportions according to the equivalence ratio. The fuels used in the one-mixture fraction analysis are listed in Table 8-3.

Table 8-3. One-Mixture Fraction Fuel Cases

Case No.	Fuel No.	Fuel Name	Coal Rank
1-1	F-1	Graphite	N/A
1-2	F-2	Benzene	N/A
1-3	F-3	Methane	N/A
1-4	F-4	Ethane	N/A
1-5	F-5	Ethylene	N/A
1-6	F-6	Pitt 8 Coal	HVA
1-7	F-6a	Pitt 8 Char	HVA, char
1-8	F-6b	Pitt 8 Tar	HVA, tar
1-9	F-7	Lower Kittanning Coal	LVB
1-10	F-8	Millmerran Coal	Subbituminous
1-11	F-9	Liddell Coal	Bituminous
1-12	F-10	Mammoth Coal	Anthracite
1-13	F-11	Beulah Zap Coal	Lignite

Table 8-3. One-Mixture Fraction Fuel Cases, CONTINUED

Case No.	Fuel No.	Fuel Name	Coal Rank
1-14	F-12	Buck Mountain Coal	Anthracite
1-15	F-13	#8 Leader Seam Coal	Anthracite
1-16	F-14	#8 Seam Coal	Semi-anthracite
1-17	F-15	Gunnison Coal	Semi-anthracite
1-18	F-16	L. Spadra Seam Coal	Semi-anthracite

Two main questions were addressed in the one-mixture fraction comparison: (1) how closely do the results from the NASA-CEA and Cantera programs compare to each other; and (2) what is the difference between the various coal surrogates and several different coal types? The comparison between the NASA-CEA and Cantera programs is briefly discussed first followed by a comparison of the different cases from Table 8-3.

8.3.1.1 NASA-CEA vs. Cantera

The NASA-CEA equilibrium code has been widely used in the coal community over the years and is considered a standard in coal equilibrium calculations, but Cantera offers flexibility that makes its integration into existing codes beneficial for large-scale simulations. This study was therefore performed to determine how closely the Cantera results align with the NASA-CEA results.

Both Cantera and NASA-CEA were used to calculate equilibrium states for all fuel cases listed in Table 3, comparing temperature and the mole fractions of O_2, CO_2, CO, H_2O, and graphite (solid carbon). Figure 8-1 shows the root-mean-square error (RMSE) between the NASA-CEA and Cantera results (additional error analysis is given in Appendix E). Note that this is the RMSE over the entire range of equivalence ratio ranging from 0.1 to 3.0.

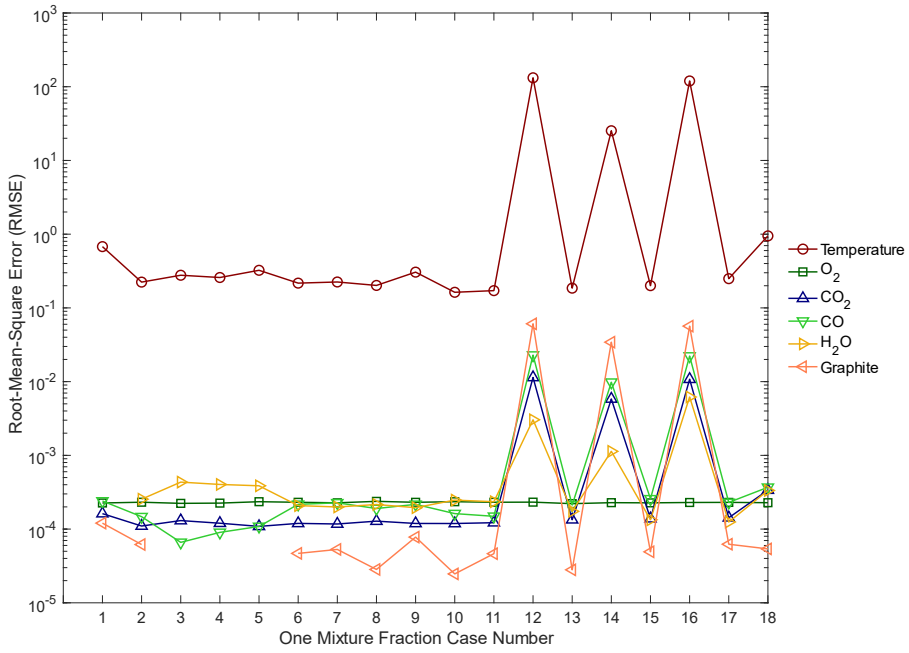

Figure 8-1. RMSE between NASA-CEA and Cantera Results

For the most part, there is good agreement between the NASA-CEA and Cantera results, however, a few of the highest rank coals (anthracites and semi-anthracites), the RMSE is quite high. From the statistical summary in Figure 8-1, it is unclear if those spikes in RMSE are a result of the deviation of a single point or multiple points in the equivalence ratio range. Results from NASA-CEA and Cantera were plotted against each other for each fuel over the range of equivalence ratios to determine where the deviations occur. Figure 8-2 shows an example of good agreement between NASA-CEA and Cantera (Pitt 8 coal, case number 1-6) and poor agreement (Mammoth seam coal, case number 1-12) for equilibrium temperature and the mole fractions of H_2O and graphite. These parameters help to illustrate the reason for the deviation between NASA-CEA and Cantera and in which conditions the deviations occur. The lines are

from NASA-CEA and the points are from Cantera. More detail on these equilibrium comparisons is found in Appendix E.

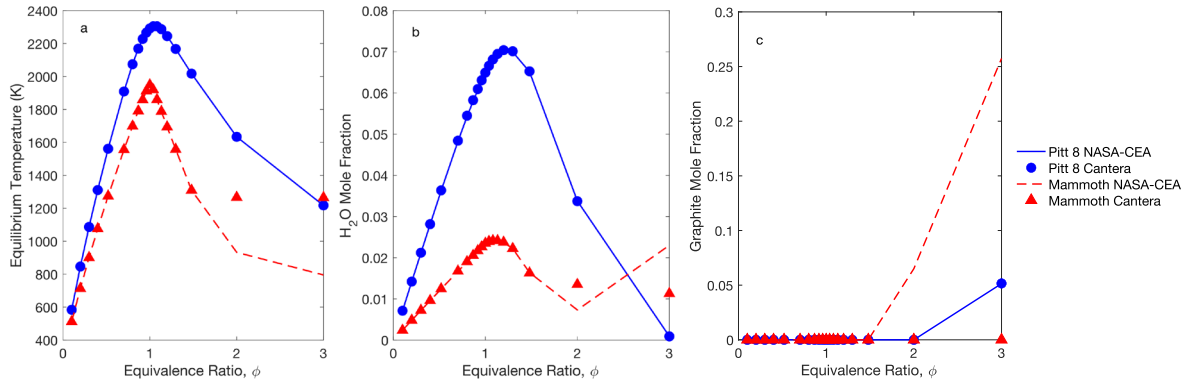

Figure 8-2. Comparison of NASA-CEA (lines) to Cantera (markers) results: (a) Temperature, (b) H_2O mole fraction, and (c) graphite mole fraction.

The statistical results shown in Figure 8-1 give an overall picture as to which fuels exhibit poor agreement. However, the poor agreement occurs only in fuel-rich conditions where $\phi > 1.5$, as illustrated in Figure 8-2. While the disagreement between the NASA-CEA and Cantera results could be from a numerical error (like a lack of convergence or similar errors), none of the fuels compared here exhibited any obvious numerical errors. NASA-CEA converts all unreacted fuel to graphite (indicated by the higher graphite mole fractions at higher equivalence ratios) whereas Cantera tends to leave some portion of the higher rank coals as unreacted fuel with the same composition and energy properties. This is likely because of the way the Cantera equilibrium solver was set up to reduce numerical instabilities, which included separate mechanisms for the combustion gases, graphite, and the solid fuel. Because Cantera leaves some of the material as unreacted coal instead of converting it to graphite, the amount of graphite present at the highest equivalence ratios as well as the amounts of the other equilibrium

products are decreased. The unreacted coal "species" contains higher amounts of hydrogen, oxygen, and other atoms than graphite. The disparity between NASA-CEA and Cantera only seems to occur with some higher rank coals. Most modern applications of coal combustion will fall outside of these extreme conditions when looking at the system as a whole, save for gasification or other specialized processes. However, there will likely be regions that are locally very fuel rich, especially in regions of coal pyrolysis where there are typically low concentrations of oxidizing gases close to the coal. Even with these few cases of deviation between NASA-CEA and Cantera, there is a low instance of disparity overall, which means Cantera can be used to adequately calculate the equilibrium states of multiple mixture fraction systems (with the exception of a few of the highest rank coals), which is more difficult to do with the stand-alone NASA-CEA code.

8.3.1.2 Full Fuel Comparison

The second question addressed by the one-mixture fraction comparison was to ascertain the difference between coal types and various coal surrogate gases. Coal surrogate gases such as gases with chemical and physical properties of graphite, benzene, methane, ethylene and others have been used in the place of coal and coal-based fuels (Fletcher, 2019). While these can be used in a combination to reach the correct atomic ratios, reaction and bond energies are harder to get correct, leading to inaccuracies in temperature and other important equilibrium factors. Surrogate gas enthalpies can be adequately matched to coal-specific values by changing the surrogate gas temperature to obtain the correct enthalpy, however, this can result in gas temperatures that are outside the bounds of the curve fits for the polynomial thermodynamic models, leading to inaccurate thermodynamic property predictions. The surrogates used in this

analysis do not have adjusted enthalpies but are instead used as a direct substitute for coal-based fuels.

To address these inaccuracies and to get an idea of how much error might be introduced into a large-scale simulation by using these simplifying assumptions, all fuel cases from Table 3 were directly compared against each other using equilibrium temperature and the mole fractions of O_2, CO_2, CO, H_2O, and graphite. Figure 8-3 shows the NASA-CEA results for equilibrium temperature, plotted using both the equivalence ratio and fuel mixture fraction. While this figure shows the results from the NASA-CEA code, the results from Cantera were virtually identical.

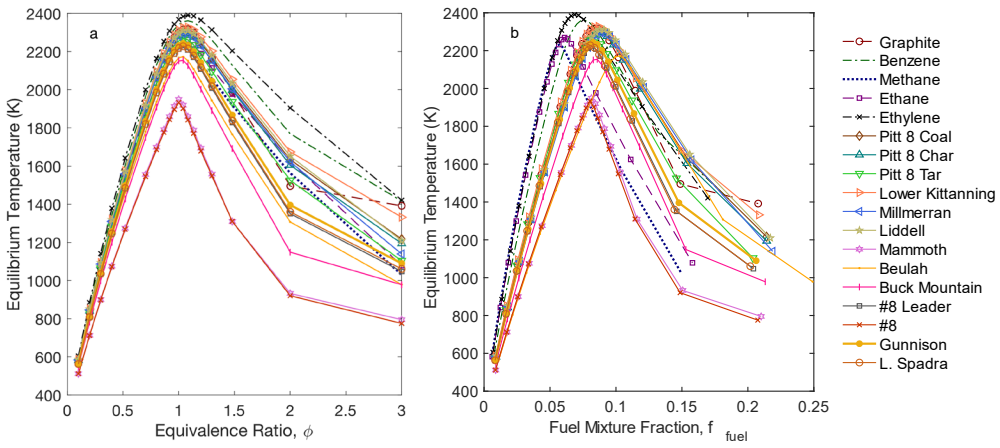

Figure 8-3. Equilibrium temperature calculations by the NASA-CEA code for all fuel cases: (a) vs. equivalence ratio and (b) vs. fuel mixture fraction.

Equilibrium temperature is strongly influenced by fuel type used, especially at or above stoichiometric mixtures. The peak temperature usually occurs at a mixture just fuel rich of the stoichiometric point and the difference is around 400 to 500 K between the highest temperature fuel (ethylene) and the lowest temperature fuel (Mammoth seam anthracite). The temperature difference is even greater in the fuel-rich conditions ($\phi > 1$). For most fuels, the difference is

minimal at very fuel lean conditions ($\phi \leq 0.5$), likely due to fuel being very dilute compared to the oxidizer. Using the fuel mixture fraction complicates the comparison slightly, shifting the peak temperatures to the left and right while keeping the peak temperature value the same (see Figure 8-3b). Equations 8-1 and 8-7 indicate a relationship between the component mixture fraction and equivalence ratio, however, they can't be substituted on a one-to-one basis. The mixture fraction depends on mass whereas the equivalence ratio depends on moles. Dividing the component mixture fraction at each equivalence ratio by the mixture fraction at stoichiometric conditions collapses the curves in a manner similar to that of using the equivalence ratio. The comparison vs. equivalence ratio therefore makes the comparison simpler and will be used in the remainder of this section. See Appendix E for the remainder of the comparison vs. fuel mixture fraction.

The O_2 mole fraction comparisons did not show a lot of variability between fuels and are not shown in this chapter (see Appendix E). This lack of variability in equilibrium O_2 between the fuels is because most of the oxygen comes from the air with little to none from the fuel. This is shown using Equation 2-1 and Table 8-2. Even in coals and other complex fuels (such as biomass), oxygen is not typically present in significant mole fractions (see also Chapter 6).

Figure 8-4 shows the CO_2 and CO mole fractions vs. equivalence ratio for the different fuels. There is wide variability in the equilibrium CO_2 mole fraction depending on which fuel is used, especially around stoichiometric conditions, which is where most industrial coal furnaces operate. Many of the coals fall in the middle range of the peak CO_2 mole fraction, with the coal surrogates lying toward both the top and bottom. The fraction of CO_2 would depend on the carbon content of the original fuel, with fuels enriched in carbon (high rank coals and graphite) generally having an increased CO_2 and CO content. The CO_2 content greatly influences the

overall heat transfer properties of a coal boiler since CO_2 blocks a lot of radiative heat transfer in the gaseous environment. Generally, the ratio between CO_2 and CO are dependent on local gas temperature and local oxygen content.

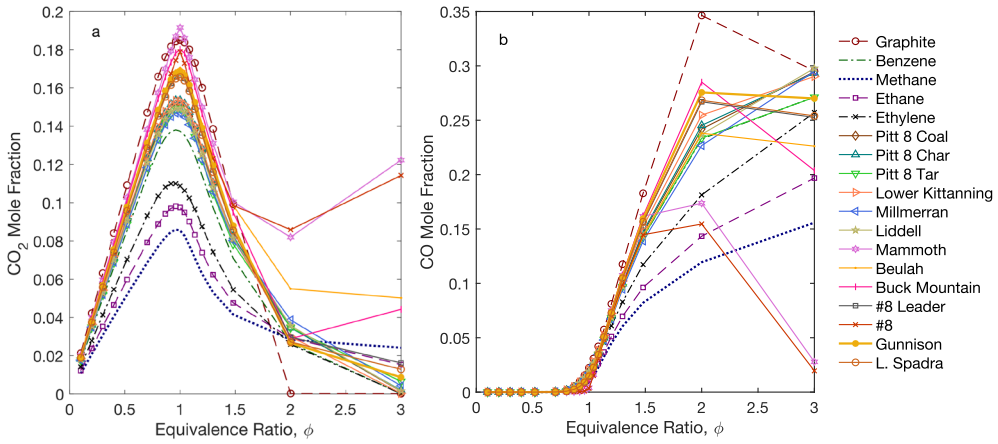

Figure 8-4. Equilibrium CO_2 and CO mole fraction calculations by the NASA-CEA code for all fuel cases: (a) CO_2 mole fraction vs. equivalence ratio and (b) CO mole fraction vs. equivalence ratio.

The CO mole fraction only becomes significant near stoichiometric conditions and moving into fuel rich conditions. This makes sense from a combustion perspective because there is less oxygen to completely oxidize the carbon in fuel rich conditions. The difference in calculated CO between fuels also increases at higher equivalence ratios. The decrease in CO (and increase in CO_2) at $\phi > 2$ is thought to be due to lower temperatures as well as the presence of graphite and unreacted fuel.

The H_2O and graphite mole fraction comparisons are shown in Figure 8-5. The H_2O mole fraction varies widely based on what fuel is used, from no H_2O with graphite to almost 20 mol% at the peak with methane. The amount will vary based solely on the amount of hydrogen in the

original fuel since there is no additional hydrogen in the air. Also like the CO_2 mole fraction, the amount of water in a gaseous environment greatly influences the radiative heat transfer of the system. The equilibrium H_2O compositions for most coals again fall in the middle range of all fuels, with several surrogate gases lying to the extreme highs and lows of H_2O compositions.

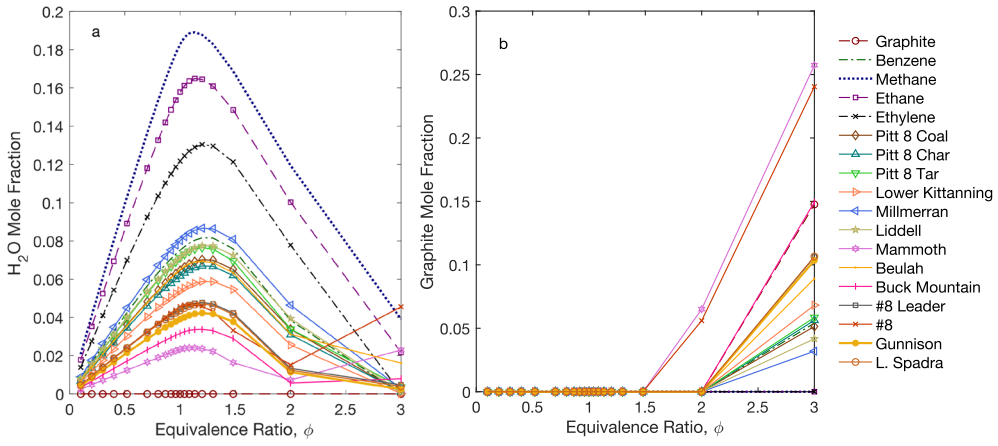

Figure 8-5. Equilibrium H_2O and graphite mole fraction calculations by the NASA-CEA code for all fuel cases: (a) H_2O mole fraction vs. equivalence ratio and (b) graphite mole fraction vs. equivalence ratio.

Graphite only shows up in the most fuel rich conditions, acting as a surrogate for "unreacted" fuel, char, and soot, with most fuel cases only showing graphite formation at equivalence ratios of 2 and higher. Unreacted fuel is almost always a problem if it is present at the end of combustion, especially when attempting to obtain the maximum amount of energy from a fuel.

Using simple hydrocarbons as surrogate gases for coal and coal-based fuels (char, tar, light gases, etc.) makes equilibrium calculations simpler and faster. However, using these surrogates as a direct replacement for coal-based fuels introduces a large amount of variability,

especially at higher equivalence ratios (extreme fuel-rich conditions). This is particularly the case for CO_2 and H_2O content, and to a lesser degree equilibrium temperature and CO content. The majority of the inconsistencies between real coal values and surrogate gases could perhaps be mitigated to a degree by dialing in the enthalpy of the surrogates by changing the reference temperature at which the enthalpy is calculated, however, this could potentially lead to improbable or even impossible temperatures. For these reasons, it is much better to use the actual physical and chemical properties of the coal (when available) instead of simplifying it with a surrogate gas.

8.3.2 Two Mixture Fractions

The two-mixture fraction comparison breaks the fuel stream into two separate streams, one for mass originating in the char and one for the volatiles. Like the one-mixture fraction comparison, there are two main questions addressed by the two-mixture fraction comparison: (1) how close are the results using the reported tar properties rather than full volatiles (by combining tar and light gas properties) and (2) can char and volatile surrogate gases be used in the place of real char and volatiles properties? The first question is raised because some pyrolysis experiments report only tar yields, compositions, and heating values but not light gas properties with which to calculate values for the total volatiles. Table 8-4 shows the fuel cases tested in the two-mixture fraction comparison. Note that Cantera was the only equilibrium program used in this comparison as a matter of convenience.

To get the whole range of fuel mixing conditions, equilibrium states for each case were calculated in the equivalence ratio range of 0.1 to 3 for each of 5 or 6 fuel mixing conditions ranging from no volatiles to all volatiles (Y_{vol} = 0, 25, 50, 75, and 100% of the fuel, and the reported volatiles yield for each of the coals, which is an intermediate percentage between 10 and

Table 8-4. Two-Mixture Fraction Fuel Cases

Case No.	Char	Volatiles	Reported Volatiles Yield
2-1	Graphite	Benzene	
2-2	Graphite	Methane	
2-3	Graphite	Ethane	
2-4	Graphite	Ethylene	
2-5	Pitt 8 Char (Low Temperature)	Pitt 8 TAR (Low Temperature)	0.1491
2-6	Pitt 8 Char (High Temperature)	Pitt 8 TAR (High Temperature)	0.4102
2-7	Pitt 8 Char (Low Temperature)	Pitt 8 VOLATILES (Low Temperature)	0.1491
2-8	Pitt 8 Char (High Temperature)	Pitt 8 VOLATILES (High Temperature)	0.4102
2-9	Millmerran Char (High Temperature)	Millmerran TAR (High Temperature)	0.545
2-10	Millmerran Char (High Temperature)	Millmerran VOLATILES (High Temperature	0.545
2-11	Millmerran Char (Low Temperature)	Millmerran TAR (Low Temperature)	0.313
2-12	Millmerran Char (Low Temperature)	Millmerran VOLATILES (Low Temperature)	0.313

60% of the DAF coal depending on pyrolysis conditions and coal type). The same variables of interest used in the one-mixture fraction comparison (temperature and the mole fractions of O_2, CO_2, CO, H_2O, and graphite) were compared for all cases listed in Table 8-4.

8.3.2.1 Temperature

To illustrate the temperature profiles for each fuel mixing condition, Figure 8-6 shows contour plots of the equilibrium temperature for two fuel cases (2-1, graphite and 2-8, Pitt 8 coal) for all fuel mixing conditions. The columns represent the percent of the fuel that was volatiles (vs. char) and the rows represent the given fuel considered.

Only two cases were used here to demonstrate the trends between cases and fuel mixing ratios. The plots for the other cases listed in Table 8-4 are found in Appendix E. A given column in Figure 8-6 shows a given fuel mixing condition for each type of fuel. The general shapes are

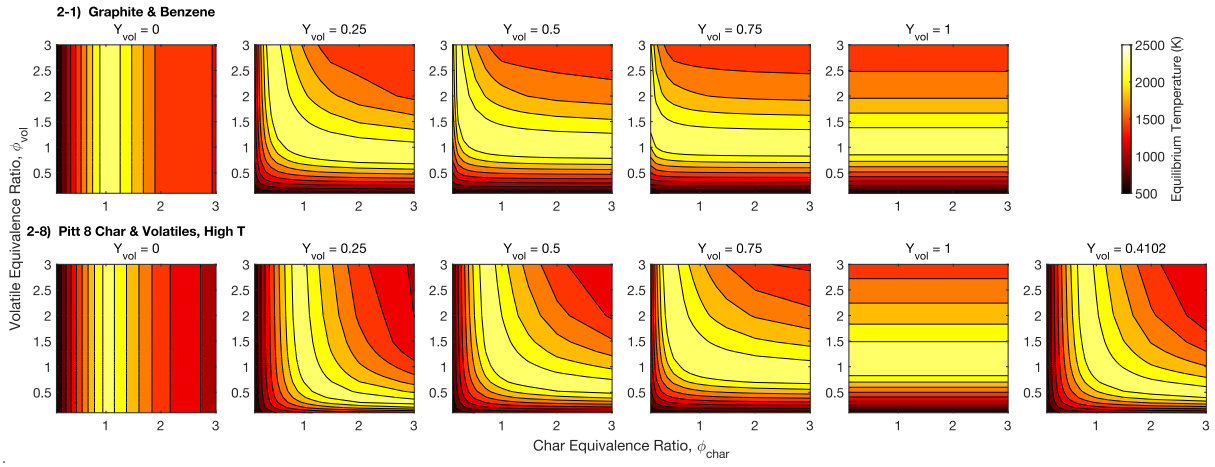

Figure 8-6. Equilibrium temperature calculations by Cantera.

similar, however, there are slight differences, especially with a higher volatiles mixture ($Y_{vol} \geq$ 75%). The difference in shape of the temperature curves is more pronounced between the coal-based fuels and the simpler surrogate gas fuels (not shown) but is less pronounced among the coal-based fuels, which is similar to the trends observed in the one-mixture fraction comparison. In addition, the simpler fuels tend to have higher temperatures than the coal-based fuels, particularly around stoichiometric conditions. Figure 8-7 shows the peak temperature ranges of all fuel cases listed in Table 8-4. The circles for each case represent the peak equilibrium temperature for each value of Y_{vol}. For example, the peak temperatures in each of the subplots in Figure 8-6 for Case 2-8 range from 2250 K for $Y_{vol} = 0$ to almost 2400 K for $Y_{vol} = 1$. These temperature differences, even small differences, can potentially impact the accuracy of large-scale simulations, especially in fuel-rich conditions where the difference is more pronounced.

The first part of this analysis was to determine if measured tar properties could reasonably be used as a surrogate for the total volatiles. There were four comparisons between tar and total volatiles: 1) cases 2-5 and 2-7, 2) cases 2-6 and 2-8, 3) cases 2-9 and 2-10, and 4) cases 2-11 and 2-12. Figure 8-7 shows that there is enough variability between the tar and

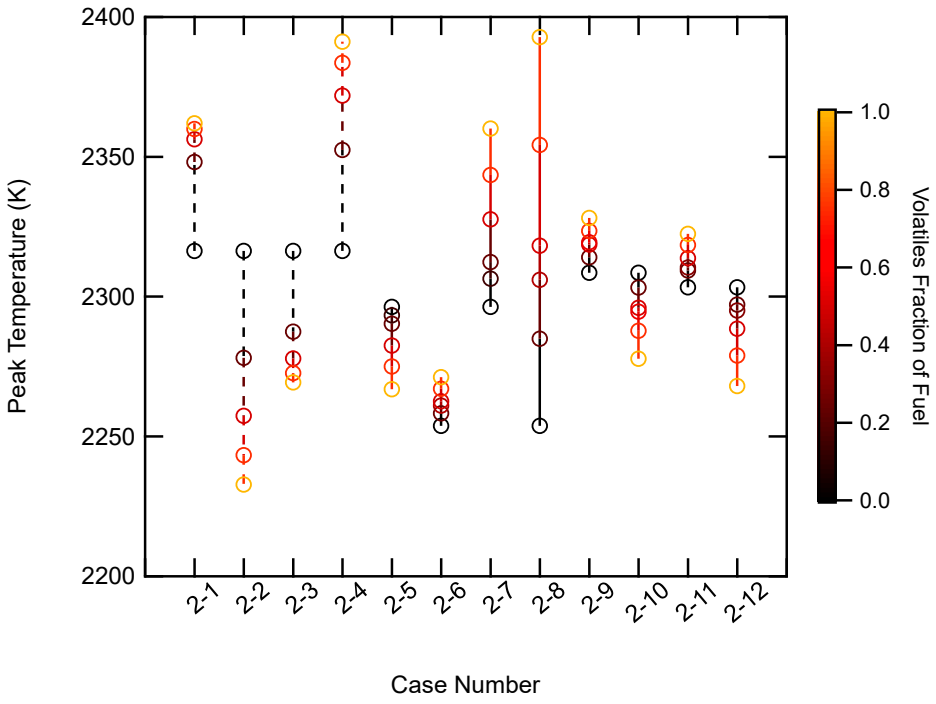

Figure 8-7. Peak temperature range for all fuel cases.

volatiles cases that it is not a good idea to use tar instead of total volatiles. For example, the temperature range for case 2-6 spans less than 50 K while that for case 2-8 spans almost 150 K. Most of the similarity in the calculated temperatures comes from the char-only fuel mixtures (black circles, where $Y_{vol} = 0$). The extremes of char-only (black circles) and volatiles-only (yellow circles, $Y_{vol} = 1$) fuel mixtures would fall directly in line with the one-mixture fraction results using char-only or volatiles-only fuels. The one-mixture fraction results using the original coal properties of fuel would likely be better compared to the two-mixture fraction results where the char and volatiles are more evenly split (close to a Y_{vol} of 0.5) or the pyrolysis yield results (e.g., Y_{vol} of 0.4102).

The peak temperature depends highly on the fuels used in the two-mixture fraction system. Some mixtures have larger ranges (2-8, which uses the measured properties of high

temperature Pitt 8 pyrolysis products), while many others have much smaller ranges. Some of the surrogate gas cases are encompassed by the measured coal-based fuel cases, but others have no overlap. There is a large variability in the range and limits of equilibrium temperature depending highly on the fuels used. While these are peak adiabatic temperatures, which occur near $\phi_{tot} = 1$, the discrepancies due to the fuel assumption would likely be very similar when used in real, non-adiabatic systems.

8.3.2.2 O_2 Mole Fraction

The mole fractions of the key combustion-related species at equilibrium were also compared in graphs like Figure 8-6 and Figure 8-7. Like the one-mixture fraction comparison, the O_2 mole fraction does not differ much between fuel cases, so the contour plots are not shown here, but can instead be found in Appendix E. Because of the similarity of the equilibrium O_2 mole fractions between fuels, the shapes and ranges are all very similar. This is understandable because the majority of the oxygen content comes from the air, even with coal-based fuels that have oxygen bound in the organic matrix. The peak O_2 mole fractions for each fuel case and fuel mixing condition are shown in Figure 8-8.

While Figure 8-8 seems to show a large variability in oxygen mole fraction, especially in the ranges between the simple coal gas surrogates (first four lines from the left) and the coal-based fuels, the axis range makes it seem larger. The peak O_2 mole fraction only ranges between 0.187 and 0.189. In addition, these peak O_2 mole fractions only occur at the lowest equivalence ratios, in extreme fuel-lean conditions. This shows that the equilibrium oxygen content is not highly dependent on the fuel used in equilibrium calculations, but more dependent on the fuel-to-oxidizer ratio used in the combustion process.

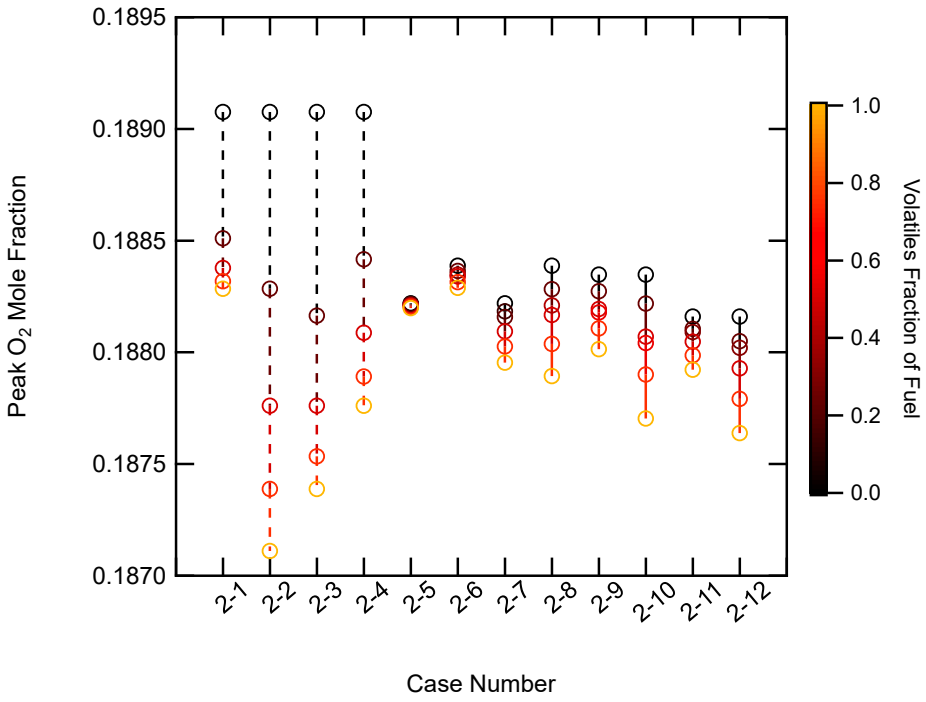

Figure 8-8. Peak O_2 mole fraction range for all fuel cases.

8.3.2.3 CO_2 Mole Fraction

In the one-mixture fraction comparison, the CO_2 mole fraction varied highly depending on the fuel type used. A representative CO_2 mole fraction comparison of contour plots for the two-mixture fraction calculations are shown in Figure 8-9 (a complete series of plots are given in Appendix E).

Like the one-mixture fraction comparison, CO_2 follows the same general trend as the temperature curves. However, like the temperature curves, the range of peak CO_2 mole fractions are very different for each fuel. There are major differences when comparing the coal-based mixtures to the coal surrogate gas mixtures. The four surrogate gas mixtures approximate the char as pure carbon (graphite) and the volatiles surrogate changes with each case. With more char (graphite), the CO_2 fraction is much greater than for the coal-based mixtures at the same

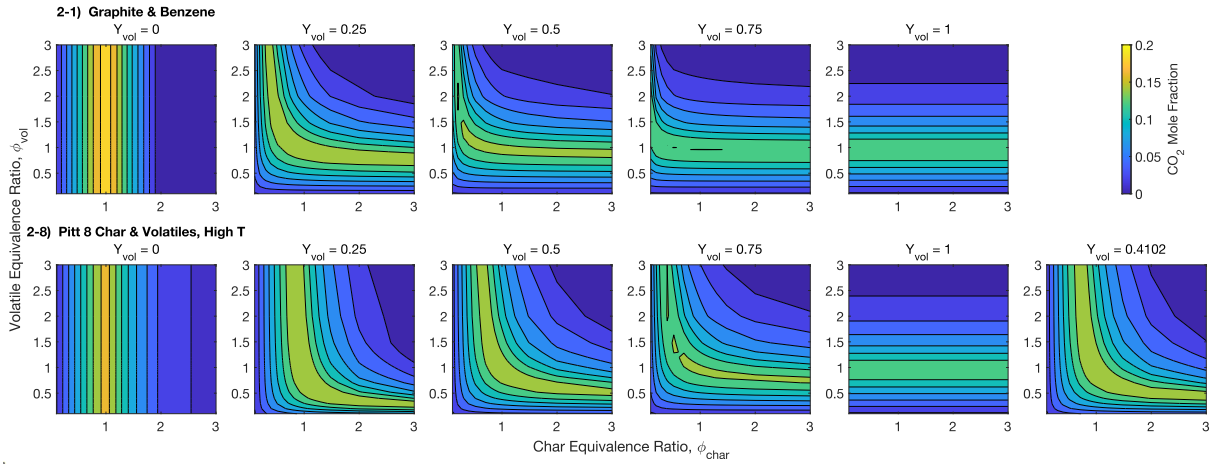

Figure 8-9. Equilibrium CO_2 mole fraction calculations by Cantera.

fuel mixing conditions, whereas when the volatiles are more favored in the mixture, the CO_2 mole fraction is a lot lower than the coal-based mixtures. This is because of the large discrepancy in the carbon content of the coals and coal surrogate gases. Graphite is pure carbon (much higher in carbon than any of the coal-based fuels) and the other simple hydrocarbon fuels have a lower carbon fraction than the coal-based fuels. The ranges of peak CO_2 mole fractions for each fuel case are shown in Figure 8-10.

The CO_2 mole fraction increases when more oxygen is present for complete combustion to occur. However, the peak CO_2 mole fraction differs from the O_2 mole fraction in the overall range of values. The peak CO_2 range is largest with the coal surrogate gases and smaller in the coal-based fuels, with a maximum range between 8 and 19%. Note that the coal-based fuels include some fuel-bound oxygen while the surrogates contain no additional oxygen.

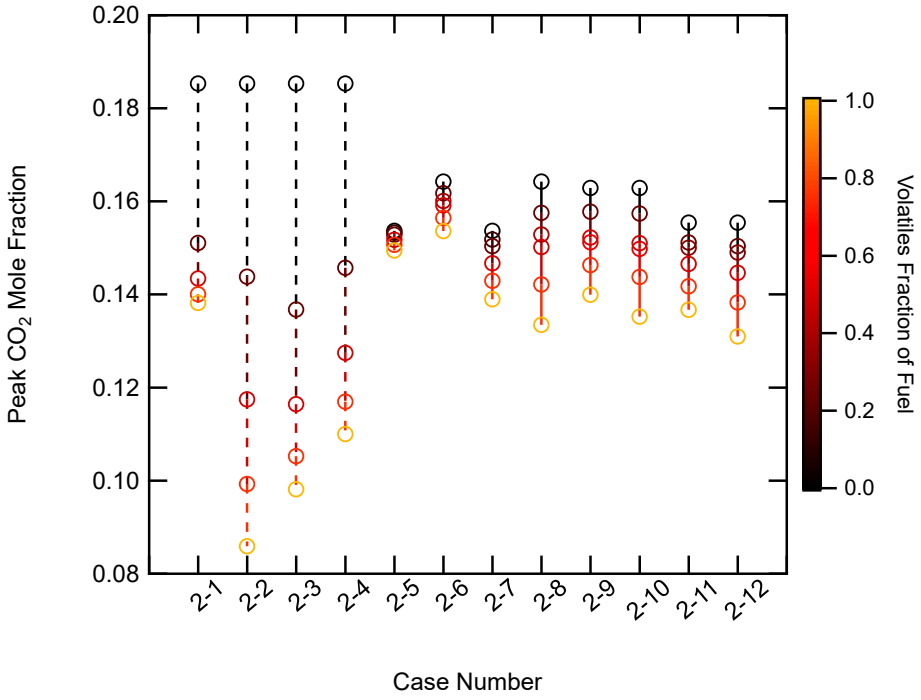

Figure 8-10. Peak CO_2 mole fraction range for all fuel cases.

8.3.2.4 CO Mole Fraction

The ratio between the CO_2 and CO mole fractions is dependent on both local temperature and O_2 content. Because of this, the CO/CO_2 ratio increases as ϕ increases until graphite starts to form. The CO mole fraction contours for cases 2-1 and 2-8 are shown in Figure 8-11.

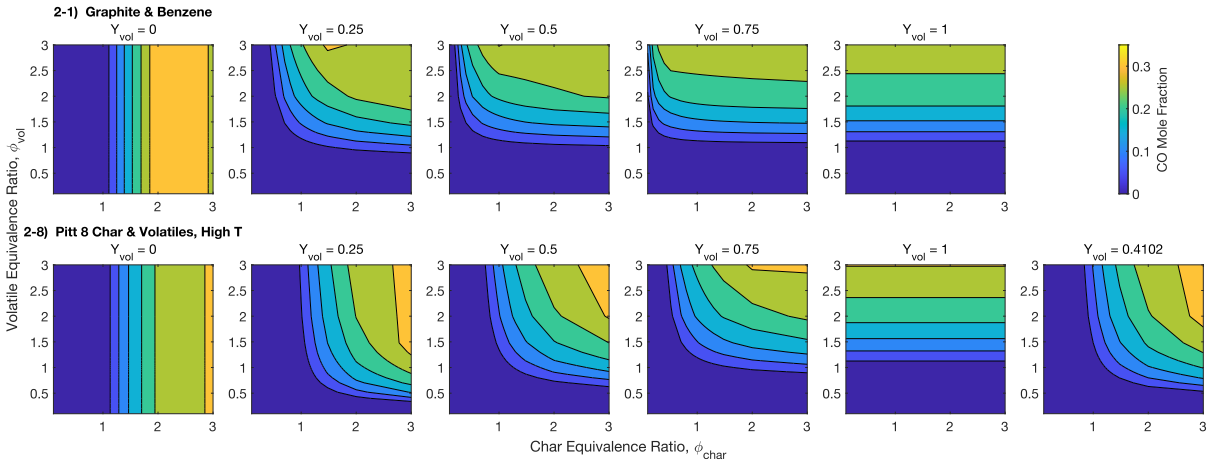

Figure 8-11. Equilibrium CO mole fraction calculations by Cantera.

Because of the lower oxygen content, CO becomes more prevalent in fuel rich conditions. There is very little difference in the shape of these contours between the CO mole fraction from tar properties compared to the CO mole fraction of total volatiles properties. Like the CO_2 mole fractions, the differences become slightly more pronounced with higher volatiles mixtures, particularly in the gradient, or how fast CO increases with increasing equivalence ratio.

There is a significant difference between the calculated CO of the coal-based fuels and the simplified surrogate gases, as seen for the CO_2 mole fractions. In mixtures that are almost all graphite, there is a larger range of very high CO mole fractions. However, with mostly volatile surrogates, the CO mole fraction is much smaller than with coal-based fuels. The peak CO mole fraction ranges for each fuel case are shown in Figure 8-12.

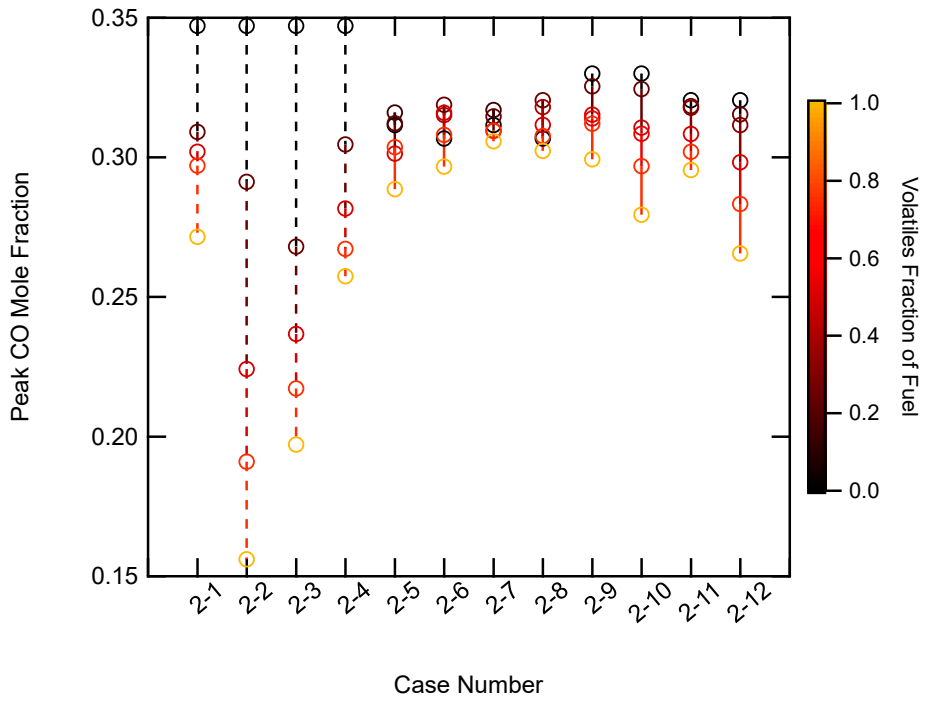

Figure 8-12. Peak CO mole fraction range for all fuel cases.

The peak CO mole fraction ranges follow a very similar trend as the CO_2 mole fractions, although with even greater ranges, from 15 to 35 mol%. The peak CO mole fractions, however, occur only in extreme fuel-rich conditions. This trade-off between the locations of greatest CO and CO_2 mole fractions is because the ratio of carbon dioxide and carbon monoxide are based on the available oxygen and temperature of the gas environment.

8.3.2.5 H_2O Mole Fraction

In the one-mixture fraction comparison, the H_2O mole fraction was very different depending on what fuel was used in the equilibrium calculations. The H_2O mole fraction contours for the two-mixture fraction comparison are given in Figure 8-13.

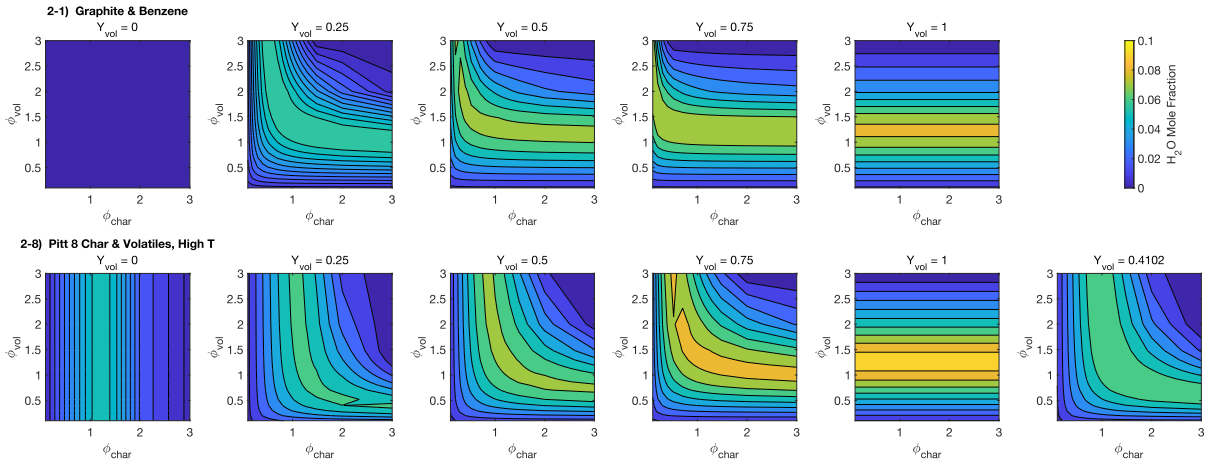

Figure 8-13. Equilibrium H_2O mole fractions as calculated by Cantera.

There is a significant difference in the H_2O mole fraction when using tar properties compared to total volatiles, and an even greater difference when using surrogate gases. It is worth noting in the "char only" (first column) mixtures of the surrogate fuels, the plots appear to be blank (solid blue). This is not a mistake, rather, the fuel mixture is entirely graphite in those equilibrium states, and therefore there is no fuel hydrogen to contribute to an equilibrium

moisture content. There is no additional hydrogen in the air, so the H_2O mole fraction at equilibrium is entirely dependent on the hydrogen content of the original fuel. In addition, the moisture content of the equilibrated mixture highly influences both gasification reactions and radiative heat transfer in the combustion system. The peak H_2O mole fraction ranges are shown in Figure 8-14.

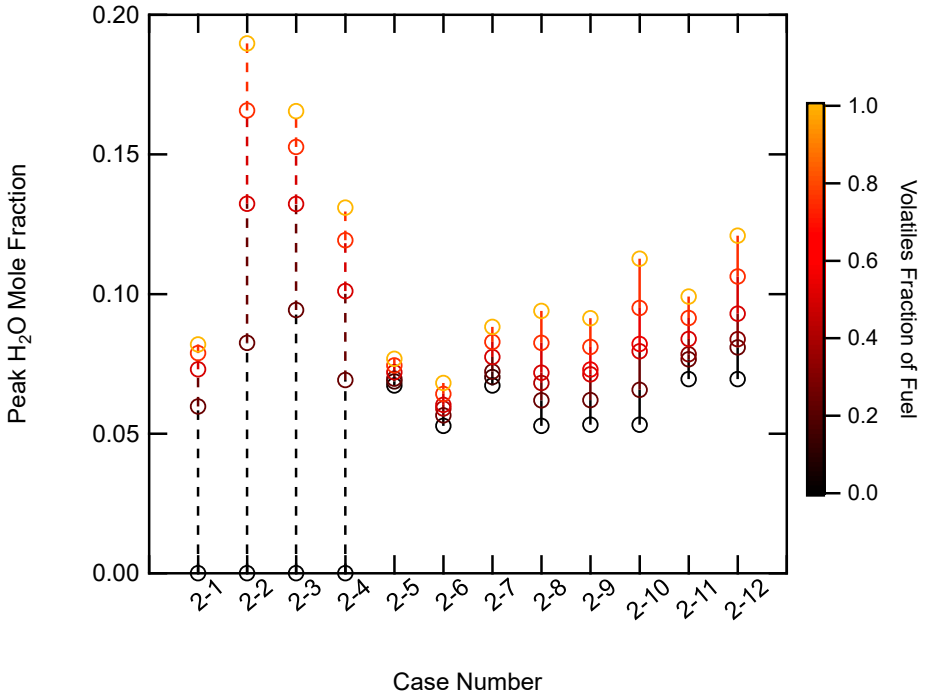

Figure 8-14. Peak H_2O mole fraction ranges for all two-mixture fraction fuel cases.

The peak H_2O mole fraction is highly dependent on the fuel chosen (similar to the one-mixture fraction results) and can range from no H_2O produced (graphite) to almost 20 mol% produced (methane). Fuels with a higher hydrogen fraction end up with a higher equilibrium moisture content than fuels with less hydrogen. In coal pyrolysis, the volatiles tend to become enriched in hydrogen, especially in the light gas species that include compounds like methane

(CH_4), ethane (C_2H_6), ethylene (C_2H_4) and other simple hydrocarbons. Accurately determining where fuel hydrogen is and when it is accessible to gas-phase chemistry is very important in determining other heterogeneous reactions as well as radiative heat transfer. This is not as important with a one-mixture fraction system but becomes more important in two- or three-mixture fraction systems.

8.3.2.6 Graphite Mole Fraction

Graphite (solid carbon) was shown in the one-mixture fraction approach to only matter in fuel-rich conditions. Industrial combustion applications usually do not operate in such conditions because it usually means some of the original fuel is not being completely burned, which can greatly impact many aspects of a combustion apparatus. The graphite mole fraction contours for cases 2-1 and 2-8 are shown in Figure 8-15.

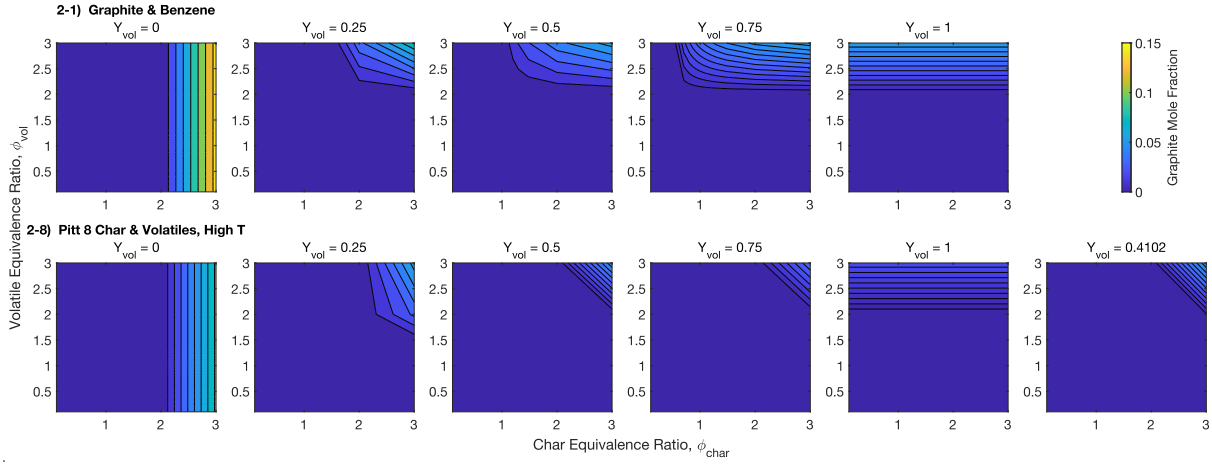

Figure 8-15. Equilibrium graphite mole fractions as calculated by Cantera.

Like the one-mixture fraction comparison, very little graphite is formed only in the fuel-rich cases for all two-mixture fraction fuel cases. The peak graphite mole fraction ranges for each two-mixture fraction case are shown in Figure 8-16.

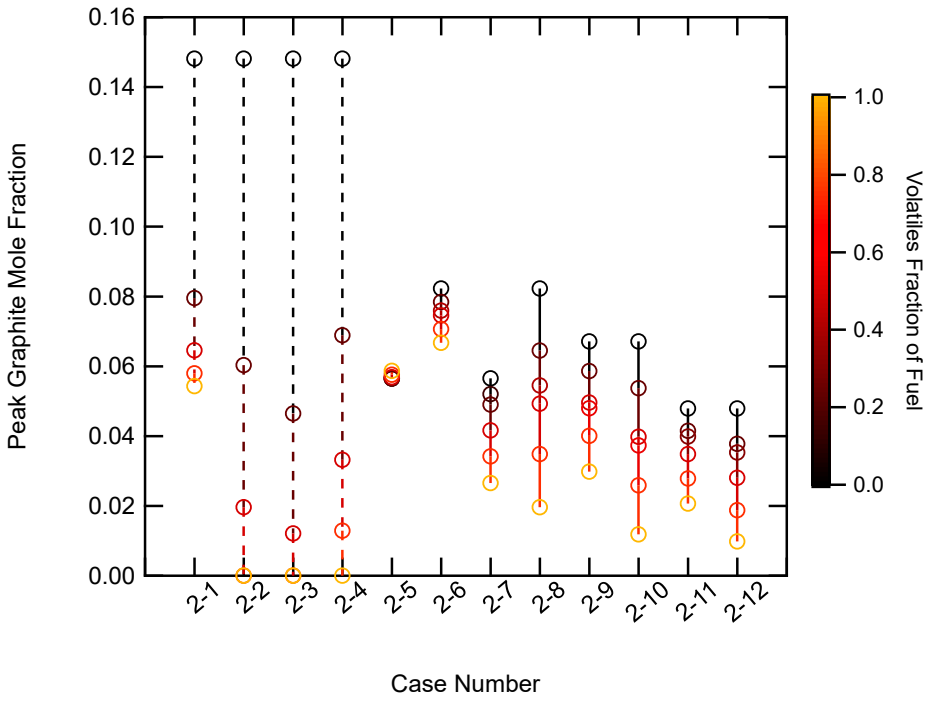

Figure 8-16. Peak graphite mole fraction ranges for all two-mixture fraction fuel cases.

The ranges of peak graphite mole fractions are quite varied, with the largest ranges in the surrogate gases, ranging between no equilibrium graphite to 15 mol% in the pure graphite fuel mixtures. None of the coal-based fuels exceed 9 mol% graphite at equilibrium, and many of the fuel cases fall well below that percentage. Incorrectly calculating solid carbon at equilibrium could cause major errors in large-scale simulations, particularly in deciding how much over-fire air might be needed to completely burn out the original fuel.

8.3.2.7 Discussion

A two-mixture fraction approach seems to be more appropriate for coal-based fuels than a one-mixture fraction approach. In an industrial coal boiler, the coal particles enter the hot environment (typically in slightly fuel rich conditions) and almost immediately begin to pyrolyze. The whole pyrolysis process typically lasts milliseconds with the high particle heating

rates of pulverized coal particles. This means that the local gas composition is a mix of oxidizer and volatile gases from the coal. The char remains a solid until the reactive gases can make it to the char surface and begin to react, adding mass from the char into the gas mixture. This means that coal pyrolysis and char conversion can be easily described using separate mixture fractions. Care must be taken when choosing the compositions and heating values of the volatiles and char. The results here indicate that choosing a simple volatile or char surrogate gas as a direct replacement for measured coal properties results in large differences in the equilibrium mole fractions of CO_2, CO, and H_2O. Much of this difference in equilibrium composition can be traced back to the difference in elemental compositions between fuels, as illustrated in Table 8-2. This is one of the key reasons why more than one mixture fraction is needed to accurately describe coal combustion reactions.

8.3.3 Three Mixture Fractions

Because coal pyrolysis results in three main products (char, tar, and light gas), coal pyrolysis can be easily divided into a three-mixture fraction approach. There was only one coal that included enough information to calculate an average light gas composition and heating value—the Pitt 8 coal, specifically with low temperature pyrolysis products (char, tar, and light gases). Because only one fuel was used to calculate equilibrium states based on a three-mixture fraction system, the results for this fuel were compared against the results for the same fuel using both one and two mixture fractions.

The procedure used to set up the three-mixture fraction comparison is described in greater detail in the introduction and approach sections; however, it is similar to the approach used in the two-mixture fraction comparisons, with the fuel mixing conditions being slightly more complex. In this case, the fractions of char and tar were allowed to vary between 0 and 1,

including the measured fractions of each at the reported pyrolysis conditions. The fraction of light gas was the remainder of the fuel mixture, and the sum of the three fuel fractions was constrained to sum to one. This approach allows for the testing of different local eddy compositions that would occur experimentally and in large-scale simulations. The oxidizer was handled the same way here as in the one- and two-mixture fraction approaches. The oxidizer contribution for each fuel stream was allowed to vary independently in an equivalence ratio between 0.1 and 3, with all stream contributions weighted by the fractions of each fuel stream.

The one-mixture fraction approach calculated at about 20 different equilibrium states over the whole range of equivalence ratios for each fuel; the two-mixture fraction approach calculated around 2,000 equilibrium states for each fuel; and the three-mixture fraction approach calculated almost 150,000 equilibrium states for a single fuel. The one-mixture fraction approach finished in generally under a minute for each fuel; the two-mixture fraction approach took anywhere from an hour to a couple of days in Cantera; and the three-mixture fraction approach took four or more days on a single processor.

Because of the large amount of data generated in the three-mixture fraction comparison, it would be difficult to compare the results of the coal-based fuels to the simple surrogate gases in any meaningful way. A more meaningful approach compares the results of all three mixture fraction approaches for one fuel. The same key variables were used to compare all three mixture fractions together, starting with the equilibrium temperature and H_2O mole fraction shown in Figure 8-17. To compare similar values, all of these comparison plots are made with respect to the carbon mixture fraction (Z_c) rather than any of the component mixture fractions (f_i) or equivalence ratios. For comparisons using the same parent fuel, any individual elemental mixture fraction, Z_j, would have the same range regardless of the number of component mixture fractions

used, while allowing for a comparison of all mixture fraction approaches on one figure in one mixture fraction dimension. In this comparison, the carbon mixture fraction seemed to be the most appropriate to use since the bulk of the fuel is comprised of carbon.

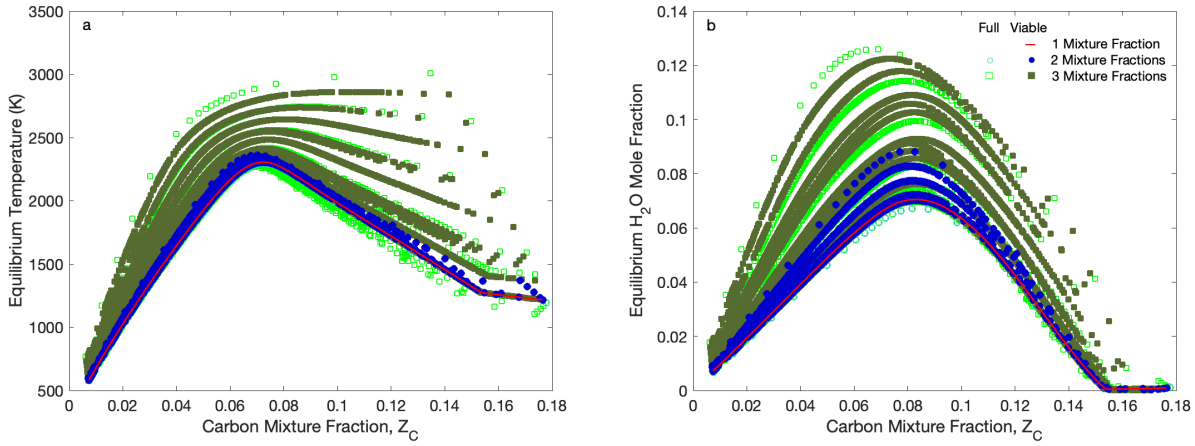

Figure 8-17. (a) Equilibrium temperature and (b) H_2O mole fraction calculations by Cantera for the Pitt 8 coal using one (case 1-6), two (case 2-7), and three mixture fractions.

Two sets of results are displayed for both the two- and three-mixture fraction approaches. The "full" results include all equilibrium states over the full range of fuel mixing conditions (the full range of eddy compositions, including the extremes of 100% mass from the char, 100% tar, and 100% light gases, along with everything in between) and the "viable" results limit the fuel mixing conditions to have a maximum char yield based on pyrolysis measurements. In combustion applications, the other pyrolysis products (tar and light gas) enter the gas phase before the solid char begins to react with the gas phase. For this reason, there are situations where there might be equilibrium between the volatile gases (tar and light gases) before any material from the char mixes in with the gas phase, but the reverse situation (i.e., all char and no pyrolysis gases) would not occur unless the starting fuel was only char.

The peak temperature changes with the fuel mixing condition, especially in the three-mixture fraction approach. Each distinct "line" of data points in the three-mixture fraction results corresponds to a different fuel mixing condition (i.e., a different set of f_i's). The temperatures for the one- and two-mixture fraction approaches (Figure 8-17a) are very close to each other, with the two-mixture fraction temperatures having a slightly increased range (shown here as a wider temperature band). The three-mixture fraction approach, however, allows for much hotter temperatures (up to almost 3,000 K) in addition to some fuel mixtures with similar temperatures to both the one- and two-mixture fraction approaches. The hotter temperatures achieved by the three-mixture fraction approach correspond to mixtures with greater percentages of the light gas species, which would include some of the same simple hydrocarbon surrogates with much higher temperatures shown in the one-mixture fraction comparison. Both the two- and three-mixture fraction results include many more equilibrium states than the one-mixture fraction results.

In the one- and two-mixture fraction approaches, the H_2O mole fraction was highly dependent on the fuel used. This result was also seen in the three-mixture fraction approach (see Appendix E), although the only case shown in Figure 8-17 is for a coal with realistic compositions and heating values of char, tar, and light gas. Note that this set of data was from a low temperature pyrolysis experiment. The H_2O mole fraction is highly dependent on the fuel mixing conditions (how much of char, tar, and light gases are mixed into the overall reactant mix). The peak H_2O mole fraction in Figure 8-17 varies between 6 and 13 mol% for the three-mixture fraction approach and between 6 and 8 mol% using two mixture fractions. This large variability might be enough to cause large errors in large-scale simulations if fewer mixture fractions or even simple coal surrogate gases are used in the place of more complex mixture fraction approaches.

Moisture can play a large role in large-scale combustion simulations, contributing to additional chemical reactions (mainly gasification) and impacting radiative heat transfer calculations. This was discussed to some extent in the two-mixture fraction comparison, however, in a three-mixture fraction system, knowing where hydrogen is in a system is even more important. The light gas components tend to be much more enriched in hydrogen than either the char or the tar. This is one of the reasons for the large variability in the equilibrium H_2O mole fraction in a three-mixture fraction system as opposed to a one- or two-mixture fraction system.

The equilibrium O_2 mole fraction was very similar over all fuel mixing conditions even in the three-mixture fraction calculations and are not shown here (see Appendix E). The CO_2 mole fraction had a wide range in both the one- and two-mixture fraction comparisons, depending on the fuel choice. Figure 8-18 shows the comparison of the one-, two-, and three-mixture fraction calculations of the mole fractions of CO_2 and CO for the Pitt 8 coal. The carbon in the fuel is the only source of carbon in these equilibrium calculations, so small changes in the total amount of each fuel component greatly influence the overall amount of CO_2 formed at equilibrium. Including light gases as a separate fuel stream changes the amount of CO_2 even more since the carbon content is greatly reduced in light gas components that tend to be enriched in hydrogen (e.g., methane) or oxygen (like CO or CO_2). The three-mixture fraction calculations show that CO becomes more prominent in fuel-rich conditions where the carbon cannot fully oxidize to CO_2. This result is similar to the findings from the one- and two-mixture fraction calculations. However, the CO mole fraction also tends to be a little more spread out in the three-mixture fraction approach for Z_c values ranging from 0.04 to 0.09.

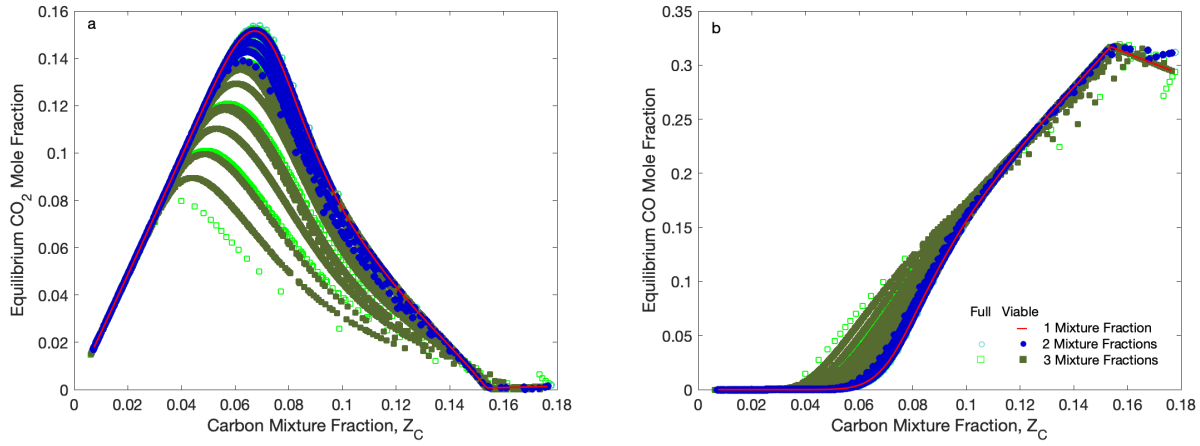

Figure 8-18. (a) Equilibrium CO_2 and (b) CO mole fraction calculations by Cantera for the Pitt 8 coal using one, two, and three mixture fractions.

In summary, the three-mixture fraction approach results in much more variety in equilibrium states than a simpler one- or two-mixture fraction approach, which would likely increase overall accuracy of coal combustor simulations using gas-phase equilibrium calculations. However, this greater variety would of necessity include significantly greater computational time and complexity. A two-mixture fraction approach that combines the tar and light gases into a single "volatiles" mixture fraction would give greater variability and accuracy than a single coal mixture fraction while not greatly increasing computational complexity.

8.3.4 Implications for Large Simulations

Carbon dioxide and water are two gases that greatly impact radiative heat transfer. Both of these gases are highly influenced by both the original fuel used and the number of mixture fractions used. The equilibrium H_2O mole fraction in particular varies widely from zero with pure graphite in the one- and two-mixture fraction approaches to almost 20 mol% when using only methane as a surrogate gas in place of coal. Even when using measured values from coal

and coal-based fuels there is a moderate amount of variability in both CO_2 and H_2O mole fractions, regardless of the number of mixture fractions used.

While a three-mixture fraction approach increases the variability of equilibrium states, it also greatly increases the computational time and complexity, often more than is desirable for large-scale simulations. In large-scale simulations, equilibrium calculations are often used to generate lookup tables to use in calculating the gas chemistry reactions, which means most of the time spent on equilibrium calculations would be incurred at the beginning of a simulation. When parallelized, the equilibrium calculations likely would not be significant compared to the overall simulation time, potentially only being an issue in smaller simulations. A two-mixture fraction approach that splits coal fuels into char and total volatiles can strike a better compromise between increased variability and accuracy while keeping the computational complexity low. In industrial applications, pyrolysis often occurs so fast that it is hard to distinguish a difference in when tars and light gases enter the gas phase.

One of the conclusions from Flores and Fletcher (2000) was that their two-mixture fraction approach would be better than a one-mixture fraction analysis in accurately accounting for soot precursors. Tar was modeled as a constant fraction of the volatiles. In coal combustion systems, the primary source of soot precursors is the tar (Fletcher et al., 1997; Brown and Fletcher, 1998; Josephson et al., 2017). A two-mixture fraction approach would be much better than a one-mixture fraction approach for modeling tar precursors, but a three-mixture fraction approach that models tar separately from light gases would seem to be most beneficial in calculating soot precursors. Hybrid approaches have been used where a mixture fraction of tar is solved for soot formation purposes but not fully integrated into the gas-phase chemistry calculations (Fletcher et al., 1997; Brown and Fletcher, 1998; Josephson et al., 2017).

The use of two or three fuel mixture fractions would not affect the outlet equilibrium composition of a combustor or gasifier if the coal achieved 100% conversion. The region of the combustor that would be most affected would be near the burner after pyrolysis but before significant char combustion or gasification occurred. This near-burner region plays a significant role in the formation of pollutants such as NO_x and soot, and therefore accurate calculations in this region are very important.

All mixture fraction methods used here were based on complete equilibrium. While equilibrium can be a useful assumption in combustion systems, it might not be the best assumption to use in coal-based systems. Other such assumptions might include only products of complete combustion, or by substituting the water-gas shift reaction in place of complete equilibrium. It would be appropriate to test these different reaction assumptions using the mixture fraction methods discussed here in order to quantify any uncertainty in reaction assumptions, especially when applied to coal-based fuels.

8.4 Conclusions

The one-mixture fraction comparison showed that the NASA-CEA and Cantera equilibrium programs generally agree when using both simple hydrocarbon surrogate gases and more complex coal-based fuels. However, there was some significant deviation between the two programs with some of the high-rank coals (some anthracites and semi-anthracites) in very fuel-rich conditions ($\phi > 2$). These deviations occur due to the way Cantera was set up to handle unreacted fuel in order to minimize numerical instabilities in the equilibrium calculations. Both NASA-CEA and most of the Cantera equilibrium states convert the unreacted fuel to graphite, but in the few cases where deviation occurred, Cantera instead left the unreacted fuel with the same composition and properties of the original fuel. These deviations might be made smaller

with improvements to the solid coal Cantera mechanism subroutine to better account for higher rank coals. While most industrial combustion applications do not use either high rank coals or such fuel-rich conditions on an overall basis, the local stoichiometry likely will fall to the fuel-rich extreme, especially in pyrolysis or gasification conditions. This means that more accurate modeling of fuel-rich conditions will be necessary for highly detailed, large-scale simulations of coal combustion systems.

In addition, the one-mixture fraction comparison showed that the equilibrium temperature and mole fractions of CO_2 and H_2O are highly dependent on the fuel used, and the CO mole fraction is highly dependent on the fuel only in fuel-rich conditions. In a one-mixture fraction system, this difference is nothing more than the difference in the elemental compositions of the original fuels, and this might be largely mitigated by using a combination of different surrogate gases and reference temperatures to match both composition and enthalpy of measured coal-based fuels. This procedure might cause the gas temperature to be out of the range of normal combustion conditions or even to be an impossible temperature. However, using the surrogate gases individually as direct replacements for coal-based fuels will make large-scale simulations inaccurate for any combination of mixture fractions. This is especially true when trying to accurately model gas compositions for radiative heat transfer calculations, which are greatly influenced by both CO_2 and H_2O compositions. Not only do the gas compositions greatly affect the heat transfer processes, but also impact many heterogeneous and homogenous reaction rates, both in terms of actual reaction speed and diffusion speed. As a final note on the one-mixture fraction analysis, the equilibrium oxygen content was not significantly influenced by fuel choice, but more by the ratio of air to fuel. The O_2 content plotted vs. equivalence ratio did not

significantly change even for coal-based fuels that can include a moderate amount of oxygen bound in the organic matrix.

The two-mixture fraction comparison showed similar results to the one-mixture fraction approach for equilibrium temperature and mole fractions of CO_2, H_2O, and CO, especially in the limiting cases of using only one fuel. Both the CO and H_2O peak mole fractions varied by up to 20 mol% based on fuel type, while the peak CO_2 mole fraction varied by closer to 10 mol%. The peak temperature varied between 2,200 and 2,400 K, depending on the fuel. In addition, the two-mixture fraction approach offers a broader range of values for the equilibrium temperature and mole fractions for the different combinations of component mixture fractions than the one-mixture fraction approach. While the two-mixture fraction approach does take more time, this approach is closer to what occurs in a real coal combustion system during devolatilization. The total volatiles enter the gas phase earlier than gases from the char reactions, and the tar and the light gases seem to be released at similar times in the pyrolysis process which is consistent with a two-mixture fraction approach. The plots of mole fractions of O_2 vs. equivalence ratio at equilibrium did not change much with respect to fuel choice in a manner similar to the one-mixture fraction approach. The peak O_2 mole fraction only varied by just over 0.2 mol% across all fuels in the two-mixture fraction comparison, with most of that variability in the coal surrogate fuels.

While none of the mixture fraction methods used here were validated against experimental data in this application, the one- and two-mixture fraction calculations indicated that using measured coal-based fuel properties will always be more accurate than using coal surrogate gases (like graphite, benzene, methane, or other simple hydrocarbons or their combinations) as a direct substitution for coal-based fuels, especially in accurately modeling the

CO_2, CO and H_2O mole fractions. Using surrogate compounds in the place of coal-based fuels might simplify gas-phase chemistry calculations (depending on the reaction scheme used), but the surrogate gases would have to be finely calibrated to achieve similar results to measured, coal-based fuels. This is typically accomplished by tuning the compound ratios and enthalpies of the surrogate gas, which can lead to gas temperatures that are either improbable in a real combustion application or that are physically impossible.

While the three-mixture fraction method offers a broader range of values in equilibrium temperatures and gas compositions than either the one- or two-mixture fraction methods, it is unclear whether a three-mixture fraction system is more realistic than a well-designed two-mixture fraction method. The two-mixture fraction method, if well designed, will allow for enough variability in fuel properties to come close to real coal reactions without adding too much complexity. Since the tar and light gases are released at similar times during coal pyrolysis, it is easy to justify a two-mixture fraction method, especially in simulations that do not have small enough time steps to differentiate between tar and light gas release. There is potential benefit, however, in using a three-mixture fraction approach in modeling coal combustion when trying to accurately model soot and soot precursors, since most of the soot in coal systems comes from the tar.

9 SUMMARY AND CONCLUSIONS

The purpose of this project was to investigate ways to improve submodels of coal pyrolysis and volatiles combustion in large-scale simulations of coal combustors without adding significant computational burden. Research included analysis of simple pyrolysis rate models, elemental compositions of pyrolysis products (tar and char), heating values of tar and char, and mixture fraction approaches with equilibrium chemistry. This chapter starts with a summary of the work performed for this dissertation, followed by the conclusions from each preceding chapter, and finally a description of potential future work based on the findings presented here.

9.1 Summary

This work was intended to explore and improve various aspects of the modeling of the coal pyrolysis reactions in large-scale simulations. Simple models of the rate/yield of pyrolysis products were explored first, comparing the simple model predictions to the predictions of a more complex, trusted coal devolatilization model—the CPD model. Two simple pyrolysis rate/yield models were developed to improve model accuracy and utility over a wider range of conditions.

Next, correlations describing carbon aromaticity of coal based on several coal-specific structural and chemical parameters were explored by comparing the calculated aromaticity values to a large data set of measured carbon aromaticity values. Some improvement of

correlations found in the literature were made by re-fitting the suggested model coefficients using the aromaticity data set, and a new and better model was proposed (see Figure 5-1). The elemental composition (CHONS) of coal char and tar after pyrolysis was studied, and correlations describing the elemental composition of char and tar were developed (with the measured and correlated aromaticity along with other coal- and reaction-specific parameters) using a complex cross-validation and model refinement procedure.

After studying the chemical composition of pyrolysis products, the thermodynamic properties (fuel heating values, or enthalpies of combustion) of char, tar, and other hydrocarbon-based fuels were explored, and several heating value correlations based on the chemical composition of the fuel were found in the literature. These literature correlations were tested using a very large data set of measured heating values of various fuels, and improved model coefficients were suggested to use for different fuel types.

The heating value correlations were used in conjunction with the experimentally measured heating values and chemical compositions of several coal-based fuels to test some simplifying assumptions made in calculating equilibrium states of coal-based fuels. Three levels of fuel mixture fractions were used to quantify uncertainty among different methods of equilibrium, different fuels used (including simple hydrocarbon coal surrogates), and two common equilibrium programs (NASA-CEA and Cantera).

9.2 Conclusions

The main conclusions for each of these projects are summarized below, in the following order: (1) pyrolysis rate/yield models, (2) carbon aromaticity of coal, (3) the elemental composition of coal pyrolysis products, (4) the heating value of coal, char, tar, and other fuels, and (5) mixture fraction equilibrium of coal-based fuels. Following the summary of key

conclusions of each project is a summary of potential areas of future work expanding on these research projects.

9.2.1 Pyrolysis Rate/Yield Models

Several existing pyrolysis rate/yield models were tested by comparing their predictions to predictions made by a more accurate but computationally complex model—the CPD model. While most of these models can adequately predict coal pyrolysis rates and yields for one coal and reaction system, all fall short in using a single set of fitted coefficients to describe multiple reaction conditions simultaneously, with many failing spectacularly. Some models come close to exhibiting some key pyrolysis trends with respect to differing particle heating rates, but none were able to match all observed trends (see Table 4-10). One of the new models (called the RF model here) matched all trends and the CPD predictions nearly perfectly, however, with 18 fitted coefficients, it is potentially too computationally expensive for some large-scale simulations. The second model developed here (the RFE) was slightly less accurate with respect to the CPD calculations than the RF model, however, with only eight fitted coefficients, it could prove more computationally efficient in large-scale simulations.

9.2.2 Carbon Aromaticity of Coal

Several literature correlations describing carbon aromaticity were tested against a well-defined coal aromaticity data set along with many new model forms based on coal-specific parameters. While there was some promise with the literature models, especially after re-fitting the coefficients to the new data set, the proposed model presented in Chapter 5 performed the best. The proposed model had an R^2 value of almost 0.8, while the closest literature model had a value of 0.77, which means that the proposed model will likely calculate the aromaticity more

accurately but many other of the re-fit literature models will be almost as accurate. These correlations can be used to limit the amount of expensive and often time-consuming NMR characterization of different coals. The correlations can even be used in other coal models or to predict other structural parameters generally only available from NMR characterizations.

9.2.3 Elemental Composition of Coal Pyrolysis Products

Almost 200 different model forms were tested to develop correlations to calculate the elemental composition (CHONS) of coal char and tar after pyrolysis. Two sets of models were chosen for each of the elements in both the char and the tar—one with the best overall fit (according to the R^2 value) and a second with the best "utility" (the best R^2/N_{coeff} value). While some correlations were both the best overall fit and the best utility (carbon and hydrogen in the tar and hydrogen and oxygen in the char), most elements had two unique model forms. In most cases, the best overall fit is expected to give the most accurate prediction of each elemental composition, however, the correlations with the best utility will be almost as accurate with fewer fitted coefficients, making them perhaps more computationally efficient in large-scale simulations.

Each elemental correlation generally agrees with the observed trends in experimental data, with some elements performing better than others. The correlations for the elements in the tar generally performed well when tested with the elemental composition data set, with most models showing an R^2 value of 0.75 or higher. The correlations for elemental composition of the char did not perform as well, with many correlations falling to an R^2 of between 0.45 and 0.55. While there is room for improvement in these correlations (particularly the char elemental

compositions), they can perhaps reduce overall uncertainty in large-scale simulations by more accurately predicting the local elemental compositions of coal pyrolysis products.

9.2.4 Heating Value of Coal, Char, Tar, and Other Fuels

Heating values are an important part of combustion experiments and modeling. While this analysis began as a study of coal, char, and tar heating values, it expanded to include a total of 11 major fuel types. Several correlations were found in the literature that predict fuel heating values based on the primary organic (CHONS) elemental composition of the fuel, including 10 mathematical forms with a total of 13 sets of unique fitted coefficients. Most of these literature correlations were originally developed to predict the heating values of the parent coal, with some applied to other fuels. In an effort to maximize the utility of these literature models and to minimize potential bias, both the original coefficients and coefficients re-fit to the heating value data sets were tested to determine the best possible fit. This was accomplished using two key statistical parameters: the mean square error (MSE) and the Akaike Information Criterion (AIC).

In most cases, many of the literature models with re-fit coefficients can adequately predict the fuel heating value based on primary elemental composition, however, the AIC method helped to identify which models might be the most correct choice by limiting the potential for overfitting. The literature correlation coefficients were re-fit to each data set with varying accuracy, with the fits to the char-only data set being the best overall fit (see Figure 7-4), with the best two models having a mean-square-error value of just under 0.4. Interestingly, the model with the best MSE value was over 80% less likely to be the correct fit according to the AIC probability. This is likely due to a larger potential for overfitting from the larger number of fitted coefficients, which is penalized in the AIC method.

The other coal-based data sets also showed good agreement between the experimental and predicted heating values, which is not surprising since over 60% of the data were coal-based fuels (including coal, char, and tar samples). For the coal-based fuels, the predictions are the most accurate using the correlations re-fit to the individual data sets (i.e., using the coefficients fit to the coal-only data set to predict the heating value of coal). However, the coefficients re-fit to the combined coal-char-tar data set should allow for only slightly less accurate heating values of most coal-based fuels.

Out of all the coal-based fuels, the tar-only data set performed the worst with an R^2 value of under 0.4 (see Appendix D) for the best literature model with re-fit coefficients. The tar samples have potential uncertainty because of the inherent difficulties in capturing and analyzing of coal tar in pyrolysis reactions.

In addition to coal-based fuels, the literature correlations presented in Chapter 7 can predict the heating value of other fuels (including biomass samples and other non-traditional fuels) with varying degrees of accuracy. The accuracy is much better when using coefficients fit to individual data sets rather than to combined data sets (see Table 7-21). In other words, a correlation with coefficients fit to a biomass-only data set would calculate heating values much more accurately than a correlation with coefficients fit to the full data set (which includes non-biomass fuels). The best model fit to the full data set (the re-fit Given model) had an R^2 value of just under 0.9 and an average relative error of around 7% (see Appendix D). This means that the fit in general is pretty good, however, with a maximum relative error of over 300%, there are a few outliers in the experimental data.

Some of the fuels fit very well (coal char-only) whereas others did not perform as well (coal tar-only); however, with the exception of a few outlier samples, the fits for all data sets

were good. While the correlations presented in Chapter 7 might be improved in the future with better and more accurate data, they can be used in large-scale simulations to aid in the calculation of chemistry-turbulence interactions without the need to perform calorimetry experiments.

9.2.5 Mixture Fraction Equilibrium of Coal-Based Fuels

Turbulence-chemistry interactions are an important part of combustion modeling and have been widely studied as part of coal combustion modeling. While a lot of improvement has been made over the years as computing resources advance, most large-scale simulations still use simplifying assumptions to make calculations faster and easier. Two simplifying assumptions are commonly made in modeling the gas-phase turbulent-chemistry interactions in large-scale simulations of coal combustion applications. The first assumption is made using a surrogate gas in the place of measured coal-gas properties. The second assumption is made by simplifying the mixing conditions of the fuel and oxidizing gases. A common way of representing the mixing conditions of a reacting system in large-scale combustion simulations is by using a mixture fraction method. The mixture fraction analysis presented here addressed both of these common simplifying assumptions.

Several conclusions were discussed in Section 8.4 with regards to the two common assumptions, however, several other conclusions were also made about the modeling of chemical interactions in coal combustion simulations. One of the first conclusions was based on a comparison between equilibrium states calculated by both NASA-CEA and Cantera equilibrium solvers. In a combustion system described by one fuel mixture fraction, the equilibrium states calculated by both the NASA-CEA and Cantera programs generally agree for both simple hydrocarbon surrogate gases as well as the more complex coal-based fuels. Some deviation

occurred between the two programs with some of the high-rank coals (some anthracites and semi-anthracites) in very fuel-rich conditions ($\phi > 2$). It is likely that these deviations occur due to the way Cantera was set up to handle solid, unreacted fuel in order to minimize numerical instabilities in the equilibrium calculations. While most industrial combustion applications do not use either high rank coals or such fuel-rich conditions on an overall basis, local stoichiometry will likely fall in the fuel-rich extreme conditions, especially in pyrolysis or gasification conditions.

The mixture fraction comparison also showed that several key variables in combustion modeling depend highly on the fuel that is used, specifically the equilibrium temperature and the mole fractions of CO_2 and H_2O, with the CO mole fraction being highly dependent only in fuel-rich conditions. In one-mixture fraction systems, this difference is likely nothing more than the difference in elemental compositions of the fuels used. In fact, most of this deviation between simple surrogate gases and coal-based fuels might be mitigated by using a combination of different surrogate gases and reference temperatures to match both composition and enthalpy of measured coal-based fuels. While this procedure might improve numerical agreement with measured coal-based fuel properties, a well-defined surrogate gas might have an equilibrium gas temperature out of the range of normal combustion conditions or might even result in an impossible temperature. In other words, using a surrogate gas in the place of measured coal-based fuel properties can make certain calculations in a large-scale simulation easier, but it can make others much harder and potentially introduce a large amount of uncertainty.

The results of the two-mixture fraction comparison supported those of the one-mixture fraction comparison and also allowed for additional insight into coal combustion reactions. While a two-mixture fraction method is computationally more complex than a one-mixture

fraction method, a two-mixture fraction system is much better for describing the products of coal pyrolysis than a simple one-mixture fraction system. A two-mixture fraction approach offers a broader range of values for the equilibrium temperature and mole fractions for the different combinations of component mixture fractions than a one-mixture fraction approach. For coal combustion applications, this additional range of equilibrium states appears to match the physical processes of coal pyrolysis reactions much better than a one-mixture fraction approach. Both one- and two-mixture fraction methods demonstrate that using measured coal-based fuel properties will always be more accurate than using coal surrogate gases as a direct substitution for coal-based fuels.

A three-mixture fraction method is even more computationally expensive than the two-mixture fraction method, generating almost 150,000 equilibrium states for a single fuel (one coal type, split into char, tar, and light gas components) compared to about 2,000 equilibrium states of the two-mixture fraction method. In addition, it is unclear whether a three-mixture fraction system is more realistic than a well-designed two-mixture fraction system because tar and light gases are released at similar times during coal pyrolysis. It is easy to justify using a simpler two-mixture fraction method in simulations that do not have small enough time steps to differentiate between the tar and light gas release during pyrolysis. There is, however, a potential benefit to using a three-mixture fraction method in coal combustion simulations—when trying to accurately model soot and soot precursors. In coal systems, most of the soot comes from the tar, so it might be beneficial to separate the tar and light gases in these cases.

9.3 Future Work

While the results and conclusions presented here detail the best models, applications, and results possible using current experimental data and methods, improvements can always be made

with improvements in both experimental data and validation methods. Most of the models discussed here can and should be improved with careful study of the data sets and methods used, including the addition of more reliable data, removal of bad or unreliable data, and by improving the model with better model forms using existing independent variables or adding new variables that potentially affect the different aspects of the models.

A number of avenues of future work can be explored with the pyrolysis rate/yield models. These models can be improved by increasing the number of coal samples used to validate the models, both in terms of experimental data as well as CPD (or other network model) predictions. In addition to using more coals to validate the pyrolysis rate models, these models can also be applied to both tar and total volatiles. While some of the simple model forms are closer to modeling expected physical and chemical characteristics of coal pyrolysis, the model forms might be improved by looking at additional processes that occur in coal pyrolysis reactions. Another avenue of future work would be to correlate model coefficients with various coal- and condition-specific parameters, like Biagini and Tognotti (2014) did with their model. If this correlation of model coefficients is done well, it could help to bridge the gap between the flexibility and accuracy of network models and the computational efficiency of the simpler global kinetic models. The last avenue of future work for pyrolysis rate/yield models comes in the form of practical application. These models were tested against CPD model predictions, but a greater amount of validation and uncertainty quantification could be performed by incorporating these simple pyrolysis models into large-scale simulations and testing them for computational time, accuracy, and other related parameters.

The correlations describing the carbon aromaticity of coal can be extended or improved in a couple of ways. While the data set used to test and develop the correlations described here

was fairly well-rounded, including a wide variety of different coals and coal ranks, a greater analysis of model bias and uncertainty would be helped with the addition of more aromaticity samples. In addition, it may be possible to extend the carbon aromaticity correlations to other fuels such as coal char and tar or biomass and other non-coal fuels. This type of extension would require the careful measurement of carbon aromaticity of these different fuels, which would potentially be very expensive. The coal tar aromaticities would likely be very difficult to measure since it is difficult to collect sufficient quantities in most coal pyrolysis equipment.

The correlations of the elemental compositions of tar and char could be improved in two ways: (1) by increasing the amount of good data used to fit and test the correlations, and (2) by exploring additional variables that might affect the composition of pyrolysis products. There is room for significant improvement with the char elemental compositions. Either the data are inaccurate or incomplete, or there may be additional variables affecting char composition that were not explored here.

The heating value correlations have a lot of potential for improvement in a lot of ways. The analysis described here used a data set where almost 65 percent of samples were coal-based fuels. While this was important for the research described here, the addition of many more samples of other fuels, including more biomass and other non-traditional fuels, may lead to many avenues of future work, especially as some of the non-traditional fuels become more widely used in industrial applications. Additionally, the mixture fraction analysis revealed that the coal-based heating value correlations could use some improvement with the lowest- and highest-rank coals—lignites and anthracites. Equilibrium states using the correlated heating values for some lignites and anthracites were a poor replacement for equilibrium states using experimentally measured heating values.

The mixture fraction analysis here used air as the oxidizer in calculating equilibrium states, however, this analysis could be extended to oxy-fuel conditions, which typically use various mixtures of O_2 and CO_2 as an oxidizer. Using a different oxidizer gas profile could change the equilibrium temperature and main compounds present at equilibrium, especially the CO_2 and CO mole fractions. Additionally, the analysis can also be extended using the elemental composition correlations. This could reveal a few potential areas of future research, including quantifying uncertainty between the correlated and experimental elemental composition cases as well as identifying additional areas of improvement with the elemental composition correlations.

While the mixture fraction analysis attempted to quantify uncertainty when using several common simplifying assumptions, it only addressed these concerns on a very basic level. Several assumptions were used in this analysis that may or may not be strong. One key assumption was that the coal-gas combustion reaction followed equilibrium chemistry. Several other reaction schemes can be used in the place of equilibrium, including the water-gas shift reaction and products of complete combustion. While these reaction schemes are perhaps simpler than full equilibrium, they might allow for simplification without sacrificing accuracy. Another logical follow-up to this work would be to apply it to several simulations (from small- to large-scale) in order to ascertain just how much uncertainty there is in the simulations, like Flores and Fletcher (2000) did for their two-mixture fraction method.

All models and methods presented here can be combined for use in large-scale simulations, which would aid in determining the overall uncertainty in the pyrolysis processes. The following order would be perhaps the most logical, assuming the coal- and process-specific parameters (e.g., proximate and ultimate analysis, temperatures, residence times, etc.) are known or can be approximated a priori:

1. Use the proximate and ultimate analysis of the coal along with the process conditions with the elemental composition correlations (Chapter 6) to calculate the elemental compositions of the char and tar (and the average light gas composition by difference).
2. Use the calculated elemental compositions of the char and tar to calculate the heating values (Chapter 7).
3. Use the calculated elemental compositions and heating values of the char and tar with the two-mixture fraction model (Chapter 8).
4. Use the new pyrolysis rate model(s) for the volatiles and tar yields as a function of time (Chapter 4) in conjunction with the two-mixture fraction model in a large simulation.
5. Track a third non-participating mixture fraction to separate the light gas and tar yields and compositions so that the local tar information can be used to model soot formation and destruction.

Using the research presented in this dissertation will likely reveal additional avenues of future improvements to the modeling of coal pyrolysis reactions in large-scale simulations.

REFERENCES

Abraham, B. M., J. G. Asbury, E. P. Lynch and A. P. S. Teotia, "Coal-oxygen Process Provides CO_2 for Enhanced Recovery," *Oil & Gas Journal,* **80**(11), 68 (1982).

Ahmed, M. A., M. J. Blesa, R. Juan and R. E. Vandenberghe, "Characterisation of an Egyptian Coal by Mössbauer and FT-IR Spectroscopy," *Fuel,* **82**(14), 1825-1829 (2003).

Ahmed, M. A., M. J. Blesa and J. L. Miranda, "Maria Coal Pyrolysis Studied by Fourier Transform Infrared and Mössbauer Spectroscopy," *Energy Sources, Part A: Recovery, Utilization and Environmental Effects,* **32**(18), 1747-1755 (2010).

Al-Abbas, A. H., J. Naser and E. K. Hussein, "Numerical Simulation of Brown Coal Combustion in a 550 MW Tangentially-fired Furnace Under Different Operating Conditions," *Fuel,* **107**, 688-698 (2013).

Alvarez, L., M. Gharebaghi, J. M. Jones, M. Pourkashanian, A. Williams, J. Riaza, C. Pevida, J. J. Pis and F. Rubiera, "CFD Modeling of Oxy-coal Combustion: Prediction of Burnout, Volatile and NO Precursors Release," *Applied Energy,* **104**, 653-665 (2013).

Annamalai, K., J. M. Sweeten and S. C. Ramalingam, "Estimation of Gross Heating Values of Biomass Fuels," *Transactions of the ASAE,* **30**(4), 1205-1208 (1987).

Anthony, D. B., J. B. Howard, H. C. Hottel and H. P. Meissner, "Rapid Devolatilization of Pulverized Coal," *Symposium (International) on Combustion,* **15**(1), 1303-1317 (1975).

Anthony, D. B. and J. B. Howard, "Coal Devolatilization and Hydrogasification," *Aiche Journal,* **22**(4), 625-656 (1976).

Arenillas, A., F. Rubiera, J. J. Pis, M. J. Cuesta, M. J. Iglesias, A. Jimenez and I. Suarez-Ruis, "Thermal Behaviour During the Pyrolysis of Low Rank Perhydrous Coals," *Journal of Analytical and Applied Pyrolysis,* **68-9**, 371-385 (2003).

Authier, O., E. Thunin, P. Plion, C. Schonnenbeck, G. Leyssens, J. F. Brilhac and L. Porcheron, "Kinetic Study of Pulverized Coal Devolatilization for Boiler CFD Modeling," *Fuel,* **122**, 254-260 (2014).

Babcock and Wilcox, "Studies on Coal Devolatilization and Char Reactivity Under PFBC Conditions: Final Report," DOE/MC/23247—2985, Alliance, OH**:** 117 (1990).

Backreedy, R. I., R. Habib, J. M. Jones, M. Pourkashanian and A. Williams, "An Extended Coal Combustion Model," *Fuel,* **78**(14), 1745-1754 (1999).

Backreedy, R. I., L. M. Fletcher, L. Ma, M. Pourkashanian and A. Williams, "Modelling Pulverised Coal Combustion Using a Detailed Coal Combustion Model," *Combustion Science and Technology,* **178**(4), 763-787 (2006).

Badzioch, S. and P. G. W. Hawksley, "Kinetics of Thermal Decomposition of Pulverized Coal Particles," *Industrial & Engineering Chemistry Process Design and Development,* **9**(4), 521-530 (1970).

Barnhart, J. S. and N. M. Laurendeau, "Pulverized Coal Combustion and Gasification in a Cyclone Reactor .1. Experiment," *Industrial & Engineering Chemistry Process Design and Development,* **21**(4), 671-680 (1982).

Barnhart, J. S., J. F. Thomas and N. M. Laurendeau, "Pulverized Coal Combustion and Gasification in a Cyclone Reactor .2. Model and Comparison With Experiment," *Industrial & Engineering Chemistry Process Design and Development,* **21**(4), 681-689 (1982).

Benito, A., V. Cebolla, I. Fernandez, M. T. Martinez, J. L. Miranda, H. Oelert and J. G. Prado, "Transport Fuels From 2-stage Coal-liquefaction," *International Journal of Energy Research,* **18**(2), 257-265 (1994).

Bharadwaj, A., L. L. Baxter and A. L. Robinson, "Effects of Intraparticle Heat and Mass Transfer on Biomass Devolatilization: Experimental Results and Model Predictions," *Energy & Fuels,* **18**(4), 1021-1031 (2004).

Bhuiyan, A. A. and J. Naser, "Numerical Modelling of Oxy Fuel Combustion, the Effect of Radiative and Convective Heat Transfer and Burnout," *Fuel,* **139**, 268-284 (2015).

Bhunia, S., A. K. Sadhukhan, S. Haldar, P. P. Mondal, A. Prabhakar and P. Gupta, "Devolatilization and Combustion of Coarse-sized Coal Particles in Oxy–fuel Conditions: Experimental and Modeling Studies," *Energy & Fuels,* **32**(1), 839-854 (2018).

Biagini, E. and L. Tognotti, "A Generalized Correlation for Coal Devolatilization Kinetics at High Temperature," *Fuel Processing Technology,* **126**, 513-520 (2014).

Bilger, R. W., S. H. Stårner and R. J. Kee, "On Reduced Mechanisms for Methane-air Combustion in Nonpremixed Flames," *Combustion and Flame,* **80**(2), 135-149 (1990).

Bilger, R. W., "Conditional Moment Closure for Turbulent Reacting Flow," *Physics of Fluids a-Fluid Dynamics,* **5**(2), 436-444 (1993).

Bird, R. B., W. E. Stewart and E. N. Lightfoot, Transport Phenomena, Revised 2nd, New York, John Wiley & Sons, Inc. (2007).

Boie, W., " Fuel Technology Calculations," *Energietechnik,* **3**, 309-316 (1953).

Borghi, G., A. F. Sarofim and J. M. Beér, "A Model of Coal Devolatilization and Combustion in Fluidized Beds," *Combustion and Flame,* **61**(1), 1-16 (1985).

Bradley, D., M. Lawes, H. Y. Park and N. Usta, "Modeling of Laminar Pulverized Coal Flames With Speciated Devolatilization and Comparisons With Experiments," *Combustion and Flame,* **144**(1-2), 190-204 (2006).

Brewster, B. S., L. L. Baxter and L. D. Smoot, "Treatment of Coal Devolatilization in Comprehensive Combustion Modeling," *Energy & Fuels,* **2**(4), 362-370 (1988).

Brewster, B. S., L. D. Smoot, S. H. Barthelson and D. E. Thornock, "Model Comparisons With Drop Tube Combustion Data for Various Devolatilization Submodels," *Energy & Fuels,* **9**(5), 870-879 (1995).

Brown, A. L. and T. H. Fletcher, "Modeling Soot Derived from Pulverized Coal," *Energy & Fuels,* **12**(4), 745-757 (1998).

Bryers, R. W., "Personal Communication," (1988).

Buhre, B. J. P., L. K. Elliott, C. D. Sheng, R. P. Gupta and T. F. Wall, "Oxy-fuel Combustion Technology for Coal-fired Power Generation," *Progress in Energy and Combustion Science,* **31**(4), 283-307 (2005).

Burke, S. P. and T. E. W. Schumann, "Diffusion Flames," *Industrial & Engineering Chemistry,* **20**(10), 998-1004 (1928).

Burnham, K. P. and D. R. Anderson, Model Selection and Multimodel Interference: A Practical Information-theoretic Approach, 2nd, New York, Springer (2002).

Cai, H. Y., A. J. Guell, D. R. Dugwell and R. Kandiyoti, "Heteroatom Distribution in Pyrolysis Products as a Function of Heating Rate and Pressure," *Fuel,* **72**(3), 321-327 (1993).

Cai, J. M., W. X. Wu and R. H. Liu, "An Overview of Distributed Activation Energy Model and its Application in the Pyrolysis of Lignocellulosic Biomass," *Renewable & Sustainable Energy Reviews,* **36**, 236-246 (2014).

Carr, A. D. and J. E. Williamson, "The Relationship Between Aromaticity, Vitrinite Reflectance and Maceral Composition of Coals: Implications for the Use of Vitrinite Reflectance as a Maturation Parameter," *Organic Geochemistry,* **16**(1-3), 313-323 (1990).

Chakravarty, T., M. R. Khan and H. L. C. Meuzelaar, "Modeling and Predicting the Composition of Fossil Fuel Derived Pyrolysis Liquids by Using Low-voltage Mass Spectrometry and Canonical Correlation Analysis," *Industrial and Engineering Chemistry Research,* **29**(11), 2173-2180 (1990).

Channiwala, S. A. and P. P. Parikh, "A Unified Correlation for Estimating HHV of Solid, Liquid and Gaseous Fuels," *Fuel,* **81**(8), 1051-1063 (2002).

Chen, C. X., X. Q. Ma and Y. He, "Co-pyrolysis Characteristics of Microalgae *Chlorella vulgaris* and Coal Through TGA," *Bioresource Technology,* **117**, 264-273 (2012a).

Chen, L. and A. F. Ghoniem, "Simulation of Oxy-coal Combustion in a 100 kW_{th} Test Facility Using RANS and LES: A Validation Study," *Energy & Fuels,* **26**(8), 4783-4798 (2012).

Chen, L., S. Z. Yong and A. F. Ghoniem, "Oxy-fuel Combustion of Pulverized Coal: Characterization, Fundamentals, Stabilization and CFD Modeling," *Progress in Energy and Combustion Science,* **38**(2), 156-214 (2012b).

Chen, Y., G. L. Wang and C. D. Sheng, "Comparison of Particle Size Evolution during Pulverized Coal Combustion in O_2/CO_2 and O_2/N_2 Atmospheres," *Energy & Fuels,* **28**(1), 136-145 (2014).

Chern, J. S. and A. N. Hayhurst, "Morphological Changes and Fragmentation of a Coal Particle During Pyrolysis in a Hot Bed of Sand Fluidised by Nitrogen," *Journal of the Energy Institute,* **78**(2), 62-75 (2005).

Cope, R. F., L. D. Smoot and P. O. Hedman, "Effects of Pressure and Coal Rank on Carbon Conversion in an Entrained-coal Gasifier," *Fuel,* **68**(6), 806-808 (1989).

Costa, M., P. Costen and F. C. Lockwood, "Burner Stability Limits and Gas Species Measurement for Lignite Pulverized Fuel in a Cylindrical Furnace," *Fuel,* **69**(3), 403-406 (1990).

Costa, V. J., V. G. Krioukov and C. R. Maliska, "Numerical Simulation of Pulverized Wet Coal Combustion Using Detailed Chemical Kinetics," *Journal of the Brazilian Society of Mechanical Sciences and Engineering,* **36**(4), 661-672 (2014).

Cui, K., B. Liu, Y. X. Wu, H. R. Yang, J. F. Lu and H. Zhang, "Numerical Simulation of Oxy-coal Combustion for a Swirl Burner With EDC Model," *Chinese Journal of Chemical Engineering,* **22**(2), 193-201 (2014).

Cui, X., H. Yan, P. Zhao, Y. Yang and Y. Xie, "Modeling of Molecular and Properties of Anthracite Base on Structural Accuracy Identification Methods," *Journal of Molecular Structure,* **1183**, 313-323 (2019).

D'Huart, K., *Die Warme,* **53**, 313-317 (1930).

Daood, S. S., W. Nimmo, P. Edge and B. M. Gibbs, "Deep-staged, Oxygen Enriched Combustion of Coal," *Fuel,* **101**, 187-196 (2012).

Demirbaş, A., "Calculation of Higher Heating Values of Biomass Fuels," *Fuel,* **76**(5), 431-434 (1997).

Demirbaş, A., "Combustion Properties and Calculation Higher Heating Values of Diesel Fuels," *Petroleum Science and Technology,* **16**(7-8), 785-795 (1998).

Demirbaş, A., "Relationships Between Lignin Contents and Heating Values of Biomass," *Energy Conversion and Management,* **42**(2), 183-188 (2001).

Ding, L., J. Wei, Z. Dai, Q. Guo and G. Yu, "Study on Rapid Pyrolysis and In-situ Char Gasification Characteristics of Coal and Petroleum Coke," *International Journal of Hydrogen Energy,* **41**(38), 16823-16834 (2016).

Eatough, C. N. and L. D. Smoot, "Devolatilization of Large Coal Particles at High Pressure," *Fuel,* **75**(13), 1601-1605 (1996).

Edwards, J. H., I. W. Smith and R. J. Tyler, "CSIRO Flash Pyrolysis Project: Compendium of Data," Commonwealth Scientific and Industrial Research Organization, North Ryde (Australia). Div. of Fossil Fuel**:** 35 (1983).

EIA, "October 2020 Monthly Energy Review," U. S. E. I. Administration, U.S. Energy Information Administration (2020).

Esbensen, K. H. and P. Geladi, "Principles of Proper Validation: Use and Abuse of Re-sampling for Validation," *Journal of Chemometrics,* **24**(3-4), 168-187 (2010).

Ferrara, F., A. Orsini, A. Plaisant and A. Pettinau, "Pyrolysis of Coal, Biomass and Their Blends: Performance Assessment by Thermogravimetric Analysis," *Bioresource Technology,* **171**, 433-441 (2014).

Fletcher, T. H., M. S. Solum, D. M. Grant, S. Critchfield and R. J. Pugmire, "Solid State ^{13}C and ^{1}H NMR Studies of the Evolution of the Chemical Structure of Coal Char and Tar During Devolatilization," *Twenty-Third Symposium (International) on Combustion/The Combustion Institute*, 1231-1237 (1990).

Fletcher, T. H. and D. R. Hardesty, "Compilation of Sandia Coal Devolatilization Data: Milestone Report," Livermore, CA, Sandia National Laboratories**:** 362 (1992).

Fletcher, T. H., A. R. Kerstein, R. J. Pugmire, M. Solum and D. M. Grant, "A Chemical Percolation Model for Devolatilization: Milestone Report," Sandia National Laboratories**:** 1-66 (1992a).

Fletcher, T. H., A. R. Kerstein, R. J. Pugmire, M. S. Solum and D. M. Grant, "Chemical Percolation Model for Devolatilization. 3. Direct Use of ^{13}C NMR Data to Predict Effects of Coal Type," *Energy & Fuels,* **6**(4), 414-431 (1992b).

Fletcher, T. H., J. Ma, J. R. Rigby, A. L. Brown and B. W. Webb, "Soot in Coal Combustion Systems," *Progress in Energy and Combustion Science,* **23**(3), 283-301 (1997).

Fletcher, T. H., H. R. Pond, J. Webster, J. Wooters and L. L. Baxter, "Prediction of Tar and Light Gas During Pyrolysis of Black Liquor and Biomass," *Energy & Fuels,* **26**(6), 3381-3387 (2012).

Fletcher, T. H., D. Barfuss and R. J. Pugmire, "Modeling Light Gas and Tar Yields from Pyrolysis of Green River Oil Shale Demineralized Kerogen Using the Chemical Percolation Devolatilization Model," *Energy & Fuels,* **29**(8), 4921-4926 (2015).

Fletcher, T. H., "Review of 30 Years of Research Using the Chemical Percolation Devolatilization Model," *Energy and Fuels,* **33**(12), 12123-12153 (2019).

Flores, D. V. and T. H. Fletcher, "The Use of Two Mixture Fractions to Treat Coal Combustion Products in Turbulent Pulverized-coal Flames," *Combustion Science and Technology,* **150**(1-6), 1-26 (2000).

Fox, R. O., Computational Models for Turbulent Reacting Flows, Cambridge, Cambridge University Press (2003).

Franchetti, B. M., F. C. Marincola, S. Navarro-Martinez and A. M. Kempf, "Large Eddy Simulation of a Pulverised Coal Jet Flame," *Proceedings of the Combustion Institute,* **34**, 2419-2426 (2013).

Freihaut, J. D., W. Proscia, B. Knight, A. Vranos, H. Hollick and K. Wicks, "Combustion Properties of Micronized Coal for High Intensity Combustion Applications," United Technologies Research Center, East Hartford, CT (USA)**:** 257 (1989a).

Freihaut, J. D., W. M. Proscia and D. J. Seery, "Chemical Characteristics of Tars Produced in a Novel Low-severity, Entrained-flow Reactor," *Energy & Fuels,* **3**(6), 692-703 (1989b).

Gale, T. K., C. H. Bartholomew and T. H. Fletcher, "Comparison of Reactivity and Physical Structure of Chars Prepared Under Different Pyrolysis Conditions, i.e. Temperature, Gas Atmosphere, and Heating Rate," 7th International Conference on Coal Science, 2 (1993).

Gale, T. K., C. H. Bartholomew and T. H. Fletcher, "Decreases in the Swelling and Porosity of Bituminous Coals During Devolatilization at High Heating Rates," *Combustion and Flame,* **100**(1-2), 94-100 (1995a).

Gale, T. K., T. H. Fletcher and C. H. Bartholomew, "Effects of Pyrolysis Conditions on Internal Surface Areas and Densities of Coal Chars Prepared at High Heating Rates in Reactive and Nonreactive Atmospheres," *Energy & Fuels,* **9**(3), 513-24 (1995b).

Gale, T. K., C. H. Bartholomew and T. H. Fletcher, "Effects of Pyrolysis Heating Rate on Intrinsic Reactivities of Coal Chars," *Energy & Fuels,* **10**(3), 766-75 (1996).

Genetti, D. and T. H. Fletcher, "Modeling Nitrogen Release During Devolatilization on the Basis of Chemical Structure of Coal," *Energy & Fuels,* **13**(5), 1082-1091 (1999).

Genetti, D., T. H. Fletcher and R. J. Pugmire, "Development and Application of a Correlation of ^{13}C NMR Chemical Structural Analyses of Coal Based on Elemental Composition and Volatile Matter Content," *Energy & Fuels,* **13**(1), 60-68 (1999).

Genetti, D. B., "An Advanced Model of Coal Devolatilization Based on Chemical Structure," M.S. Thesis, Chemical Engineering, Brigham Young University (1999).

Gerschel, H. and M. Schmidt, "Modelling the Relationship Between Carbon Aromaticity of Lignite Pyrolysis Chars and the Process Temperature With Petrographic Parameters," *International Journal of Oil Gas and Coal Technology,* **11**(3), 290-307 (2016).

Gerstein, B. C., P. D. Murphy and L. M. Ryan, "Aromaticity in Coal," Coal Structure, Eds. R. A. Meyers, New York, Academic Press (1982).

Gibbins-Matham, J. and R. Kandiyoti, "Coal Pyrolysis Yields From Fast and Slow Heating in a Wire-mesh Apparatus With a Gas Sweep," *Energy & Fuels,* **2**(4), 505-511 (1988).

Given, P. H., D. Weldon and J. H. Zoeller, "Calculation of Calorific Values of Coals from Ultimate Analyses: Theoretical Basis and Geochemical Implications," *Fuel,* **65**(6), 849-854 (1986).

Glick, D. C. and A. Davis, "Operation and Composition of the Penn State Coal Sample Bank and Data Base," *Organic Geochemistry,* **17**(4), 421-430 (1991).

Go, A. W. and A. T. Conag, "A Unified Semi-empirical Model for Estimating the Higher Heating Value of Coals Based on Proximate Analysis," *Combustion Science and Technology,* **190**(12), 2203-2223 (2018).

Goodwin, D. G., R. L. Speth, H. K. Moffat and B. W. Weber, "Cantera: An Object-oriented Software Toolkit for Chemical Kinetics, Thermodynamics, and Transport Processes," https://www.cantera.org (2018).

Gordon, S. and B. J. McBride, "Computer Program for Calculation of Complex Chemical Equilibrium Compositions and Applications I. Analysis.," USA, NASA**:** 64 (1994).

Goshayeshi, B. and J. C. Sutherland, "A Comparison of Various Models in Predicting Ignition Delay in Single-particle Coal Combustion," *Combustion and Flame,* **161**(7), 1900-1910 (2014).

Gövert, B., S. Pielsticker, T. Kreitzberg, M. Habermehl, O. Hatzfeld and R. Kneer, "Measurement of Reaction Rates for Pulverized Fuel Combustion in Air and Oxyfuel Atmosphere Using a Novel Fluidized Bed Reactor Setup," *Fuel,* **201**, 81-92 (2017).

Grabosky, M. and R. Bain, "Properties of Biomass Relevant to Gasification," Biomass Gasification – Principles and Technology, Eds. T. B. Reed, New Jersey, Noyes Data Corporation**:** 41 (1981).

Grant, D. M., R. J. Pugmire, T. H. Fletcher and A. R. Kerstein, "Chemical-model of Coal Devolatilization Using Percolation Lattice Statistics," *Energy & Fuels,* **3**(2), 175-186 (1989).

Green, D. W., Ed. Perry's Chemical Engineers' Handbook, New York, McGraw Hill (1984).

Gumz, W., *Feuerungstech,* **26**, 322 (1938).

Guo, J. J., Z. H. Liu, P. Wang, X. H. Huang, J. Li, P. Xu and C. G. Zheng, "Numerical Investigation on Oxy-combustion Characteristics of a 200 MW_e Tangentially Fired Boiler," *Fuel,* **140**, 660-668 (2015).

Hambly, E. M., "The Chemical Structure of Coal Tar and Char During Devolatilization," M.S. Thesis, Chemical Engineering, Brigham Young University (1998).

Hambly, E. M., T. H. Fletcher, M. Solum and R. J. Pugmire, "Solid-state ^{13}C NMR Analysis of Coal Tar and Char," *Abstracts of Papers of the American Chemical Society,* **215**, U607-U607 (1998).

Hashimoto, N. and H. Shirai, "Numerical Simulation of Sub-bituminous Coal and Bituminous Coal Mixed Combustion Employing Tabulated-devolatilization-process Model," *Energy,* **71**, 399-413 (2014).

Hees, J., D. Zabrodiec, A. Massmeyer, S. Pielsticker, B. Gövert, M. Habermehl, O. Hatzfeld and R. Kneer, "Detailed Analyzes of Pulverized Coal Swirl Flames in Oxy-fuel Atmospheres," *Combustion and Flame,* **172**, 289-301 (2016).

Herce, C., B. de Caprariis, S. Stendardo, N. Verdone and P. De Filippis, "Comparison of Global Models of Sub-bituminous Coal Devolatilization by Means of Thermogravimetric Analysis," *Journal of Thermal Analysis and Calorimetry,* **117**(1), 507-516 (2014).

Hillier, J. L. and T. H. Fletcher, "Pyrolysis Kinetics of a Green River Oil Shale Using a Pressurized TGA," *Energy & Fuels,* **25**, 232-239 (2011).

Huéscar Medina, C., H. N. Phylaktou, G. E. Andrews and B. M. Gibbs, "Explosion Characteristics of Pulverised Torrefied and Raw Norway Spruce (*Picea abies*) and Southern Pine (*Pinus palustris*) in Comparison to Bituminous Coal," *Biomass and Bioenergy,* **79**, 116-127 (2014).

Ibarra, J. V., I. Cervero, J. L. Miranda and R. Moliner, "Structural Rank Parameters of Spanish Low Rank Coals and Their Influence on Pyrolysis Yields," *Fuel Processing Technology,* **28**(3), 259-273 (1991).

Idris, S. S., N. A. Rahman and K. Ismail, "Combustion Characteristics of Malaysian Oil Palm Biomass, Sub-bituminous Coal and Their Respective Blends via Thermogravimetric Analysis (TGA)," *Bioresource Technology,* **123**, 581-591 (2012).

IGT, "Coal Conversion Systems Technical Data Book," Springfield, VA, IGT (1978).

Jamaluddin, A. S., J. S. Truelove and T. F. Wall, "Devolatilization of Bituminous Coals at Medium to High Heating Rates," *Combustion and Flame,* **63**(3), 329-337 (1986).

Jayaraman, K., I. Gokalp and S. Bostyn, "High Ash Coal Pyrolysis at Different Heating Rates to Analyze its Char Structure, Kinetics and Evolved Species," *Journal of Analytical and Applied Pyrolysis,* **113**, 426-433 (2015).

Jin, Y. Q., L. Lu, X. J. Ma, H. M. Liu, Y. Chi and K. Yoshikawa, "Effects of Blending Hydrothermally Treated Municipal Solid Waste With Coal on Co-combustion Characteristics in a Lab-scale Fluidized Bed Reactor," *Applied Energy,* **102**, 563-570 (2013).

Josephson, A. J., N. D. Gaffin, S. T. Smith, T. H. Fletcher and D. O. Lignell, "Modeling Soot Oxidation and Gasification with Bayesian Statistics," *Energy & Fuels,* **31**(10), 11291-11303 (2017).

Jovanovic, R., A. Milewska, B. Swiatkowski, A. Goanta and H. Spliethoff, "Sensitivity Analysis of Different Devolatilisation Models on Predicting Ignition Point Position During Pulverized Coal Combustion in O_2/N_2 and O_2/CO_2 Atmospheres," *Fuel,* **101**, 23-37 (2012).

Jupudi, R. S., V. Zamansky and T. H. Fletcher, "Prediction of Light Gas Composition in Coal Devolatilization," *Energy & Fuels,* **23**, 3063-3067 (2009).

Kaiho, M., Y. Kodera and O. Yamada, "Estimation of Heats of Formation and Combustion of Coal," *Fuel,* **237**, 536-544 (2019).

Kajitani, S., S. Hara and H. Matsuda, "Gasification Rate Analysis of Coal Char With a Pressurized Drop Tube Furnace," *Fuel,* **81**(5), 539-546 (2002).

Khan, M. R., "Production of High Quality Liquid Fuels From Coal by Mild Pyrolysis of Coal-lime Mixtures," *Fuel Science and Technology International,* **5**(2), 185-231 (1987).

Khatami, R., C. Stivers and Y. A. Levendis, "Ignition Characteristics of Single Coal Particles From Three Different Ranks in O_2/N_2 and O_2/CO_2 Atmospheres," *Combustion and Flame,* **159**(12), 3554-3568 (2012).

Knappstein, R., G. Kuenne, T. Meier, A. Sadiki and J. Janicka, "Evaluation of Coal Particle Volatiles Reaction by Using Detailed Kinetics and FGM Tabulated Chemistry," *Fuel,* **201**, 39-52 (2017).

Ko, G. H., D. M. Sanchez, W. A. Peters and J. B. Howard, "Application of First-order Single Reaction Model for Coal Devolatilization Over a Wide Range of Heating Rates," American Chemical Society, Division of Fuel Chemistry Preprints, 33 (1988).

Ko, G. H., D. M. Sanchez, W. A. Peters and J. B. Howard, "Correlations for Effects of Coal Type and Pressure on Tar Yields From Rapid Devolatilization," *Symposium (International) on Combustion,* **22**(1), 115-124 (1989).

Kobayashi, H., J. B. Howard and A. F. Sarofim, "Coal Devolatilization at High Temperatures," *Sixteenth Symposium (International) on Combustion/The Combustion Institute*, 411-425 (1977).

Lakshmanan, C. C. and N. White, "A New Distributed Activation-energy Model Using Weibull Distribution for the Representation of Complex Kinetics," *Energy & Fuels,* **8**(6), 1158-1167 (1994).

Lazaro, M. J., R. Moliner and I. Suelves, "Non-isothermal Versus Isothermal Technique to Evaluate Kinetic Parameters of Coal Pyrolysis," *Journal of Analytical and Applied Pyrolysis,* **47**(2), 111-125 (1998).

Lee, A., C. K. Law and A. Makino, "Aerothermochemical Studies of Energetic Liquid Materials .3. Approximate Determination of Some Thermophysical and Thermochemical Properties of Organic Azides," *Combustion and Flame,* **78**(3-4), 263-274 (1989).

Lei, M., C. B. Wang and S. L. Wang, "Effect of Pyrolysis Characteristics on Ignition Mechanism and NO Emission of Pulverized Coal During Oxy-fuel Combustion," *Journal of Thermal Analysis and Calorimetry,* **117**(2), 665-673 (2014).

Lemaire, R., C. Bruhier, D. Menage, E. Therssen and P. Seers, "Study of the High Heating Rate Devolatilization of a Pulverized Bituminous Coal Under Oxygen-containing Atmospheres," *Journal of Analytical and Applied Pyrolysis,* **114**, 22-31 (2015).

Lewis, A. D. and T. H. Fletcher, "Prediction of Sawdust Pyrolysis Yields from a Flat-flame Burner Using the CPD Model," *Energy & Fuels,* **27**(2), 942-953 (2013).

Li, S. F., H. Yang, T. H. Fletcher and M. Dong, "Model for the Evolution of Pore Structure in a Lignite Particle During Pyrolysis," *Energy & Fuels,* **29**(8), 5322-5333 (2015).

Li, T. W., K. Chaudhari, D. VanEssendelft, R. Turton, P. Nicoletti, M. Shahnam and C. Guenther, "Computational Fluid Dynamic Simulations of a Pilot-scale Transport Coal Gasifier: Evaluation of Reaction Kinetics," *Energy & Fuels,* **27**(12), 7896-7904 (2013).

Lin, H. L., K. J. Li, X. W. Zhang and H. X. Wang, "Structure Characterization and Model Construction of Indonesian Brown Coal," *Energy & Fuels,* **30**(5), 3809-3814 (2016).

Lisandy, K. Y., R. G. Kim, C. W. Hwang and C. H. Jeon, "Sensitivity Test of Low Rank Indonesian Coal Utilization Using Steady State and Dynamic Simulations of Entrained-type Gasifier," *Applied Thermal Engineering,* **102**, 1433-1450 (2016).

Liu, G. S. and S. Niksa, "Coal Conversion Submodels for Design Applications at Elevated Pressures. Part II. Char Gasification," *Progress in Energy and Combustion Science,* **30**(6), 679-717 (2004).

Liu, J., Y. Ma, L. Luo, J. Ma, H. Zhang and X. Jiang, "Pyrolysis of Superfine Pulverized Coal. Part 4. Evolution of Functionalities in Chars," *Energy Conversion and Management,* **134**, 32-46 (2017).

Liu, J. X., X. M. Jiang, J. Shen and H. Zhang, "Pyrolysis of Superfine Pulverized Coal. Part 2. Mechanisms of Carbon Monoxide Formation," *Energy Conversion and Management,* **87**, 1039-1049 (2014a).

Liu, J. X., X. M. Jiang, J. Shen and H. Zhang, "Pyrolysis of Superfine Pulverized Coal. Part 1. Mechanisms of Methane Formation," *Energy Conversion and Management,* **87**, 1027-1038 (2014b).

Liu, J. X., X. M. Jiang, J. Shen and H. Zhang, "Pyrolysis of Superfine Pulverized Coal. Part 3. Mechanisms of Nitrogen-containing Species Formation," *Energy Conversion and Management,* **94**, 130-138 (2015).

Lloyd, W. G., J. W. Reasoner, J. C. Hower and L. P. Yates, "Effects of Pressure Upon the Isothermal Plastic Behavior of High-volatile Bituminous Kentucky Coals," *Energy & Fuels,* **3**(5), 585-589 (1989).

Lu, K. M., W. J. Lee, W. H. Chen and T. C. Lin, "Thermogravimetric Analysis and Kinetics of Co-pyrolysis of Raw/Torrefied Wood and Coal Blends," *Applied Energy,* **105**, 57-65 (2013).

Ma, J., "Soot Formation During Coal Pyrolysis," Ph.D. Dissertation, Chemical Engineering, Brigham Young University (1996).

Magnussen, B. F. and B. H. Hjertager, "On Mathematical Modeling of Turbulent Combustion with Special Emphasis on Soot Formation and Combustion," *Symposium (International) on Combustion,* **16**(1), 719-729 (1977).

Maloney, D. J., E. R. Monazam, S. D. Woodruff and L. O. Lawson, "Measurements and Analysis of Temperature Histories and Size Changes for Single Carbon and Coal Particles During the Early Stages of Heating and Devolatilization," *Combustion and Flame,* **84**(1-2), 210-220 (1991).

Man, C. K. and J. R. Gibbins, "Factors Affecting Coal Particle Ignition Under Oxyfuel Combustion Atmospheres," *Fuel,* **90**(1), 294-304 (2011).

Maroto-Valer, M. M., J. M. Andresen and C. E. Snape, "Verification of the Linear Relationship Between Carbon Aromaticities and H/C Ratios for Bituminous Coals," *Fuel,* **77**(7), 783-785 (1998).

Matali, S., N. A. Rahman, S. S. Idris, A. B. Alias and M. R. Mohatar, "Co-pyrolysis and Characteristics of Malaysian Sub-bituminous Coal and Waste HDPE Blends via TGA," *Jurnal Teknologi,* **76**(10), 21-26 (2015).

Mathews, J. P., V. Krishnamoorthy, E. Louw, A. H. N. Tchapda, F. Castro-Marcano, V. Karri, D. A. Alexis and G. D. Mitchell, "A Review of the Correlations of Coal Properties With Elemental Composition," *Fuel Processing Technology,* **121**, 104-113 (2014).

McBride, B. J. and S. Gordon, "Computer Program for Calculation of Complex Chemical Equilibrium Compositions and Applications II. Users Manual and Program Description.," USA, NASA**:** 177 (1996).

Merrick, D., "Mathematical Models of the Thermal Decomposition of Coal. 2. Specific Heats and Heats of Reaction," *Fuel,* **62**(5), 540-546 (1983).

Messig, D., M. Vascellari and C. Hasse, "Flame Structure Analysis and Flamelet Progress Variable Modelling of Strained Coal Flames," *Combustion Theory and Modelling,* **21**(4), 700-721 (2017).

Miller, B. G., "1 - The Chemical and Physical Characteristics of Coal," Clean Coal Engineering Technology (Second Edition), Eds., Butterworth-Heinemann**:** 3-60 (2017a).

Miller, B. G., "2 - Coal as Fuel," Clean Coal Engineering Technology (Second Edition), Eds., Butterworth-Heinemann**:** 61-104 (2017b).

Muto, M., H. Watanabe, R. Kurose, S. Komori, S. Balusamy and S. Hochgreb, "Large-eddy Simulation of Pulverized Coal Jet Flame - Effect of Oxygen Concentration on NO_x Formation," *Fuel,* **142**, 152-163 (2015).

Niessen, W. R., Combustion and Incineration Processes, 3, New York, Marcel Dekker, Inc. (2002).

Niksa, S., "Rapid Coal Devolatilization as an Equilibrium Flash Distillation," *Aiche Journal,* **34**(5), 790-802 (1988).

Niksa, S., G. S. Liu and R. H. Hurt, "Coal Conversion Submodels for Design Applications at Elevated Pressures. Part I. Devolatilization and Char Oxidation," *Progress in Energy and Combustion Science,* **29**(5), 425-477 (2003).

Nugroho, Y. S., A. C. McIntosh and B. M. Gibbs, "Low-temperature Oxidation of Single and Blended Coals," *Fuel,* **79**(15), 1951-1961 (2000).

Oberkampf, W. L. and M. F. Barone, "Measures of Agreement Between Computation and Experiment: Validation Metrics," *Journal of Computational Physics,* **217**(1), 5-36 (2006).

Oberkampf, W. L. and C. J. Roy, Verification and Validation in Scientific Computing, New York, Cambridge University Press (2010).

Ocheduszko, S., Applied Thermodynamics (Termodynamika Stosowana – in Polish), Warszawa, WNT (1967).

Park, D. K. and E. Song, "Pressurized Pyrolysis Characteristics of Two Ranks of Coal in a Thermogravimetric Analyzer," *Journal of Energy Engineering,* **143**(5) (2017).

Parkash, S., "True Density and Elemental Composition of Subbituminous Coals," *Fuel,* **64**(5), 631-634 (1985).

Parkash, S. and S. K. Chakrabartty, "Microporosity in Alberta Plains Coals," *International Journal of Coal Geology,* **6**(1), 55-70 (1986).

Pedel, J., "Large Eddy Simulations of Coal Jet Flame Ignition Using the Direct Quadrature Method of Moments," Ph.D. Dissertation, Chemical Engineering, University of Utah (2012).

Pedel, J., J. N. Thornock and P. J. Smith, "Large Eddy Simulation of Pulverized Coal Jet Flame Ignition Using the Direct Quadrature Method of Moments," *Energy & Fuels,* **26**(11), 6686-6694 (2012).

Pedel, J., J. N. Thornock and P. J. Smith, "Ignition of Co-axial Turbulent Diffusion Oxy-coal Jet Flames: Experiments and Simulations Collaboration," *Combustion and Flame,* **160**(6), 1112-1128 (2013).

Perry, S. T., "A Global Free-radical Mechanism for Nitrogen Release During Coal Devolatilization Based on Chemical Structure," Ph.D. Dissertation, Chemical Engineering, Brigham Young University (1999).

Perry, S. T., E. M. Hambly, T. H. Fletcher, M. S. Solum and R. J. Pugmire, "Solid-State ^{13}C NMR Characterization of Matched Tars and Chars From Rapid Coal Devolatilization," *Proceedings of the Combustion Institute,* **28**, 2313-2319 (2000).

Peters, N., Turbulent Combustion, Cambridge, Cambridge University Press (2000).

Pielsticker, S., B. Gövert, T. Kreitzberg, M. Habermehl, O. Hatzfeld and R. Kneer, "Simultaneous Investigation Into the Yields of 22 Pyrolysis Gases From Coal and Biomass in a Small-scale Fluidized Bed Reactor," *Fuel,* **190**, 420-434 (2017a).

Pielsticker, S., S. Heuer, O. Senneca, F. Cerciello, P. Salatino, L. Cortese, B. Gövert, O. Hatzfeld, M. Schiemann, V. Scherer and R. Kneer, "Comparison of Pyrolysis Test Rigs for Oxy-fuel Conditions," *Fuel Processing Technology,* **156**, 461-472 (2017b).

Poinsot, T. and D. Veynante, Theoretical and Numerical Combustion, 2nd, Philadelphia, Edwards (2005).

Proscia, W. M., J. D. Freihaut, S. Rastogi and G. E. Klinzing, "Thermodynamic Properties of Pulverized Coal During Rapid Heating Devolatilization Processes," East Hartford, Connecticut (United States), United States Office of the Assistant Secretary for Fossil Energy, USDOE**:** 232 (1994).

Pugmire, R. J., M. S. Solum, D. M. Grant, S. Critchfield and T. H. Fletcher, "Structural Evolution of Matched Tar-char Pairs in Rapid Pyrolysis Experiments," *Fuel,* **70**(3), 414-423 (1991).

Ra, H. W., M. W. Seo, S. J. Yoon, S. M. Yoon, J. K. Kim, J. G. Lee and S. B. Park, "Devolatilization Characteristics of High Volatile Coal in a Wire Mesh Reactor," *Korean Journal of Chemical Engineering,* **31**(9), 1570-1576 (2014).

Rabaçal, M., B. M. Franchetti, F. C. Marincola, F. Proch, M. Costa, C. Hasse and A. M. Kempf, "Large Eddy Simulation of Coal Combustion in a Large-scale Laboratory Furnace," *Proceedings of the Combustion Institute,* **35**, 3609-3617 (2015).

Radulovic, P. T., M. U. Ghani and L. D. Smoot, "An Improved Model for Fixed Bed Coal Combustion and Gasification," *Fuel,* **74**(4), 582-594 (1995).

Rebola, A. and J. L. T. Azevedo, "Modelling Pulverized Coal Combustion Using Air and O_2^+ Recirculated Flue Gas as Oxidant," *Applied Thermal Engineering,* **83**, 1-7 (2015).

Reichel, D., S. Siegl, C. Neubert and S. Krzack, "Determination of Pyrolysis Behavior of Brown Coal in a Pressurized Drop Tube Reactor," *Fuel,* **158**, 983-998 (2015).

Riaza, J., R. Khatami, Y. A. Levendis, L. Alvarez, M. V. Gil, C. Pevida, F. Rubiera and J. J. Pis, "Single Particle Ignition and Combustion of Anthracite, Semi-anthracite and Bituminous Coals in Air and Simulated Oxy-fuel Conditions," *Combustion and Flame,* **161**(4), 1096-1108 (2014).

Riaza, J., M. Ajmi, J. Gibbins and H. Chalmers, "Ignition and Combustion of Single Particles of Coal and Biomass Under O_2/CO_2 Atmospheres," 13th International Conference on Greenhouse Gas Control Technologies, GHGT 2016, 114 (2017a).

Riaza, J., J. Gibbins and H. Chalmers, "Ignition and Combustion of Single Particles of Coal and Biomass," *Fuel,* **202**, 650-655 (2017b).

Richards, A. P. and T. H. Fletcher, "A Comparison of Simple Global Kinetic Models for Coal Devolatilization With the CPD Model," *Fuel,* **185**, 171-180 (2016).

Richards, A. P., C. Johnson and T. H. Fletcher, "Correlations of the Elemental Compositions of Primary Coal Tar and Char," *Energy & Fuels,* **33**(10), 9520-9537 (2019).

Richards, A. P., D. O. Lignell and T. H. Fletcher, "A Comparison of Mixture Fraction Approaches for Coal Combustion Simulations," *Fuel*, submitted (2020).

Richards, A. P., D. Haycock, J. Frandsen and T. H. Fletcher, "A Review of Coal Heating Value Correlations With Application to Coal Char, Tar, and Other Fuels," *Fuel,* **283**, 118942 (2021).

Rieth, M., F. Proch, M. Rabaçal, B. M. Franchetti, F. C. Marincola and A. M. Kempf, "Flamelet LES of a Semi-industrial Pulverized Coal Furnace," *Combustion and Flame,* **173**, 39-56 (2016).

Rieth, M., A. G. Clements, M. Rabaçal, F. Proch, O. T. Stein and A. M. Kempf, "Flamelet LES Modeling of Coal Combustion With Detailed Devolatilization by Directly Coupled CPD," *Proceedings of the Combustion Institute,* **36**(2), 2181-2189 (2017a).

Rieth, M., F. Proch, A. G. Clements, M. Rabaçal and A. M. Kempf, "Highly Resolved Flamelet LES of a Semi-industrial Scale Coal Furnace," *Proceedings of the Combustion Institute,* **36**(3), 3371-3379 (2017b).

Rieth, M., A. M. Kempf, O. T. Stein, A. Kronenburg, C. Hasse and M. Vascellari, "Evaluation of a Flamelet/Progress Variable Approach for Pulverized Coal Combustion in a Turbulent Mixing Layer," *Proceedings of the Combustion Institute,* **37**(3), 2927-2934 (2019).

Ringen, S., J. Lanum and F. P. Miknis, "Calculating Heating Values From Elemental Compositions of Fossil Fuels," *Fuel,* **58**(1), 69-71 (1979).

Roberts, D. G., D. J. Harris and T. F. Wall, "On the Effects of High Pressure and Heating Rate During Coal Pyrolysis on Char Gasification Reactivity," *Energy & Fuels,* **17**(4), 887-895 (2003).

Russell, N. J., M. A. Wilson, R. J. Pugmire and D. M. Grant, "Preliminary Sudies on the Aromaticity of Australian Coals - Solid-state NMR Techniques," *Fuel,* **62**(5), 601-605 (1983).

Sadhukhan, A. K., P. Gupta and R. K. Saha, "Modeling and Experimental Investigations on the Pyrolysis of Large Coal Particles," *Energy & Fuels,* **25**(12), 5573-5583 (2011).

Sahu, R., Y. A. Levendis, R. C. Flagan and G. R. Gavalas, "Physical Properties and Oxidation Rates of Chars From Three Bituminous Coals," *Fuel,* **67**(2), 275-283 (1988).

Saito, M., M. Sato, H. Murata and M. Sadakata, "Combustion Behavior of Pulverized Coal Particles in a High-temperature and High Oxygen Concentration Atmosphere," *Fuel,* **70**(6), 709-712 (1991).

Saxena, S. C., "Devolatilization and Combustion Characteristics of Coal Particles," *Progress in Energy and Combustion Science,* **16**(1), 55-94 (1990).

Schaffer, C., "Selecting a Classification Method by Cross-validation," *Machine Learning,* **13**(1), 135-143 (1993).

Schroeder, B. B., "Scale-bridging Model Development and Increased Model Credibility," PhD Dissertation, Chemical Engineering Department, University of Utah (2015).

Sciazko, M., "Rank-dependent Formation Enthalpy of Coal," *Fuel,* **114**, 2-9 (2013).

Seo, D. K., S. S. Park, Y. T. Kim, J. Hwang and T.-U. Yu, "Study of Coal Pyrolysis by Thermogravimetric Analysis (TGA) and Concentration Measurements of the Evolved Species," *Journal of Analytical and Applied Pyrolysis,* **92**(1), 209-216 (2011).

Serio, M. A., D. G. Hamblen, J. R. Markham and P. R. Solomon, "Kinetics of Volatile Product Evolution in Coal Pyrolysis - Experiment and Theory," *Energy & Fuels,* **1**(2), 138-152 (1987).

Seylor, A. C., *Proc S Wales Inst Engrs,* **53**, 254 (1938).

Shadle, L. J., E. R. Monazam and M. L. Swanson, "Coal Gasification in a Transport Reactor," *Industrial & Engineering Chemistry Research,* **40**(13), 2782-2792 (2001).

Shamsi, A., L. J. Shadle and K. S. Seshadri, "Study of Low-temperature Oxidation of Buckskin Subbituminous Coal and Derived Chars Produced in ENCOAL Process," *Fuel Processing Technology,* **86**(3), 275-292 (2004).

Shaw, D. W., X. Zhu, M. K. Misra and R. H. Essenhigh, "Determination of Global Kinetics of Coal Volatiles Combustion," *Symposium (International) on Combustion,* **23**(1), 1155-1162 (1991).

Sheng, C. D. and J. L. T. Azevedo, "Modeling the Evolution of Particle Morphology During Coal Devolatilization," *Proceedings of the Combustion Institute,* **28**, 2225-2232 (2000).

Singh, K. P. and M. C. Kakati, "Comprehensive Models for Predicting Aromaticity of Coals," *Chemical Engineering Communications,* **190**(10), 1335-1347 (2003).

Smith, K. L., L. D. Smoot, T. H. Fletcher and R. J. Pugmire, The Structure and Reaction Processes of Coal, New York, Plenum Press (1994).

Smith, P. J., T. H. Fletcher and L. D. Smoot, "Model for Pulverized Coal-fired Reactors," *Symposium (International) on Combustion,* **18**(1), 1285-1293 (1981).

Smoot, L. D., "Pulverized Coal Diffusion Flames: A Perspective Through Modeling," *Symposium (International) on Combustion,* **18**(1), 1185-1202 (1981).

Smoot, L. D., P. O. Hedman and P. J. Smith, "Pulverized-coal Combustion Research at Brigham Young University," *Progress in Energy and Combustion Science,* **10**(4), 359-441 (1984).

Smoot, L. D. and P. J. Smith, Coal Combustion and Gasification, New York, Plenum Press (1985).

Solomon, P. R. and M. B. Colket, "Coal Devolatilization," *Symposium (International) on Combustion,* **17**(1), 131-143 (1979).

Solomon, P. R., D. G. Hamblen, R. M. Carangelo, M. A. Serio and G. V. Deshpande, "General-model of Coal Devolatilization," *Energy & Fuels,* **2**(4), 405-422 (1988).

Solomon, P. R., M. A. Serio and E. M. Suuberg, "Coal Pyrolysis - Experiments, Kinetic Rates and Mechanisms," *Progress in Energy and Combustion Science,* **18**(2), 133-220 (1992).

Solomon, P. R., T. H. Fletcher and R. J. Pugmire, "Progress in Coal Pyrolysis," *Fuel,* **72**(5), 587-597 (1993).

Solum, M. S., R. J. Pugmire and D. M. Grant, "^{13}C Solid-state NMR of Argonne Premium Coals," *Energy & Fuels,* **3**(2), 187-193 (1989).

Sorensen, L. H., J. Saastamoinen and J. E. Hustad, "Evaluation of Char Reactivity Data by Different Shrinking-core Models," *Fuel,* **75**(11), 1294-1300 (1996).

Soria-Verdugo, A., L. M. Garcia-Gutierrez, L. Blanco-Cano, N. Garcia-Hernando and U. Ruiz-Rivas, "Evaluating the Accuracy of the Distributed Activation Energy Model for Biomass Devolatilization Curves Obtained at High Heating Rates," *Energy Conversion and Management,* **86**, 1045-1049 (2014).

Steinberg, M., "History of CO_2 Greenhouse Gas Mitigation Technologies," *Energy Conversion and Management,* **33**(5–8), 311-315 (1992).

Steuer, W., *Brennstoff-Chem,*(7), 344-347 (1926).

Stollinger, M., B. Naud, D. Roekaerts, N. Beishuizen and S. Heinz, "PDF Modeling and Simulations of Pulverized Coal Combustion - Part 1: Theory and Modeling," *Combustion and Flame,* **160**(2), 384-395 (2013a).

Stollinger, M., B. Naud, D. Roekaerts, N. Beishuizen and S. Heinz, "PDF Modeling and Simulations of Pulverized Coal Combustion - Part 2: Application," *Combustion and Flame,* **160**(2), 396-410 (2013b).

Stone, J. V., Information Theory: A Tutorial Introduction, Sebtel Press (2015).

Stournas, S., M. Papachristos and G. B. Kyriakopoulos, "Copper Catalyzed Low-temperature Pyrolysis as a Means for Upgrading Low-rank Solid Fuels," *Abstracts of Papers of the American Chemical Society,* **194**, 227-233 (1987).

Strache, H. and R. Lant, Kohlenchemie, Leipzig, Akademische Verlag G.m.b.H. (1924).

Suggate, R. P. and W. W. Dickinson, "Carbon NMR of Coals: The Effects of Coal Type and Rank," *International Journal of Coal Geology,* **57**(1), 1-22 (2004).

Sun, Q., Y. Zhang, K. Z. Xu, Z. Y. Ren, J. R. Song and F. Q. Zhao, "Studies on Thermodynamic Properties of FOX-7 and Its Five Closed-loop Derivatives," *Journal of Chemical and Engineering Data,* **60**(7), 2057-2061 (2015).

Suuberg, E. M., W. A. Peters and J. B. Howard, "Product Composition and Kinetics of Lignite Pyrolysis," *Industrial & Engineering Chemistry Process Design and Development,* **17**(1), 37-46 (1978).

Theron, J. A. and E. le Roux, "Representation of Coal and Coal Derivatives in Process Modelling," *Journal of the Southern African Institute of Mining and Metallurgy,* **115**(5), 339-348 (2015).

Therssen, E., L. Gourichon and L. Delfosse, "Devolatilization of Coal Particles in a Flat Flame - Experimental and Modeling Study," *Combustion and Flame,* **103**(1-2), 115-128 (1995).

Tian, Y. J., K. C. Xie, S. Y. Zhu and T. H. Fletcher, "Simulation of Coal Pyrolysis in Plasma Jet by CPD Model," *Energy & Fuels,* **15**(6), 1354-1358 (2001).

Toftegaard, M. B., J. Brix, P. A. Jensen, P. Glarborg and A. D. Jensen, "Oxy-fuel Combustion of Solid Fuels," *Progress in Energy and Combustion Science,* **36**(5), 581-625 (2010).

Tolvanen, H., L. Kokko and R. Raiko, "Fast Pyrolysis of Coal, Peat, and Torrefied Wood: Mass Loss Study With a Drop-tube Reactor, Particle Geometry Analysis, and Kinetics Modeling," *Fuel,* **111**, 148-156 (2013).

Tomaszewicz, M. and A. Mianowski, "Char Structure Dependence on Formation Enthalpy of Parent Coal," *Fuel,* **199**, 380-393 (2017).

Tourunen, A., J. Saastamoinen and H. Nevalainen, "Experimental Trends of NO in Circulating Fluidized Bed Combustion," *Fuel,* **88**(7), 1333-1341 (2009).

Tufano, G. L., O. T. Stein, A. Kronenburg, A. Frassoldati, T. Faravelli, L. Deng, A. M. Kempf, M. Vascellari and C. Hasse, "Resolved Flow Simulation of Pulverized Coal Particle Devolatilization and Ignition in Air- and O_2/CO_2-atmospheres," *Fuel,* **186**, 285-292 (2016).

Tufano, G. L., O. T. Stein, A. Kronenburg, G. Gentile, A. Stagni, A. Frassoldati, T. Faravelli, A. M. Kempf, M. Vascellari and C. Hasse, "Fully-resolved Simulations of Coal Particle Combustion Using a Detailed Multi-step Approach for Heterogeneous Kinetics," *Fuel,* **240**, 75-83 (2019).

Turns, S. R., An Introduction to Combustion: Concepts and Applications, 3rd, New York, McGraw Hill (2012).

Tyler, R. J., "Flash Pyrolysis of Coals. Devolatilization of Bituminous Coals in a Small Fluidized-bed Reactor," *Fuel,* **59**(4), 218-226 (1980).

Ubhayakar, S. K., D. B. Stickler, C. W. Von Rosenberg Jr and R. E. Gannon, "Rapid Devolatilization of Pulverized Coal in Hot Combustion Gases," *Symposium (International) on Combustion,* **16**(1), 427-436 (1977).

Van Essendelft, D., T. W. Li, P. Nicoletti and T. Jordan, "Advanced Chemistry Surrogate Model Development within C3M for CFD Modeling, Part 1: Methodology Development for Coal Pyrolysis," *Industrial & Engineering Chemistry Research,* **53**(18), 7780-7796 (2014).

Van Krevelen, D. W., "Graphical-statistical Method for the Study of Structure and Reaction Processes of Coal," *Fuel,* **29**, 269-284 (1950).

Van Krevelen, D. W., Coal: Typology - Physics - Chemistry - Constitution, 3, Amsterdam, Elsevier Science (1993).

Vascellari, M., D. G. Roberts, S. S. Hla, D. J. Harris and C. Hasse, "From Laboratory-scale Experiments to Industrial-scale CFD Simulations of Entrained Flow Coal Gasification," *Fuel,* **152**, 58-73 (2015).

Vascellari, M., G. L. Tufano, O. T. Stein, A. Kronenburg, A. M. Kempf, A. Scholtissek and C. Hasse, "A Flamelet/Progress Variable Approach for Modeling Coal Particle Ignition," *Fuel,* **201**, 29-38 (2017).

Veras, C. A. G., J. Saastamoinen, J. A. Carvalho and N. Aho, "Overlapping of the Devolatilization and Char Combustion Stages in the Burning of Coal Particles," *Combustion and Flame,* **116**(4), 567-579 (1999).

Veras, C. A. G., J. A. Carvalho and M. A. Ferreira, "The Chemical Percolation Devolatilization Model Applied to the Devolatilization of Coal in High Intensity Acoustic Fields," *Journal of the Brazilian Chemical Society,* **13**(3), 358-367 (2002).

Vorres, K. S., "The Argonne Premium Coal Sample Program," *Energy & Fuels,* **4**(5), 420-426 (1990).

Walpole, R. E. and R. H. Myers, Probability and Statistics for Engineers and Scientists, 2nd, New York, Macmillan Publishing Co., Inc. (1978).

Wang, G. L., R. Zander and M. Costa, "Oxy-fuel Combustion Characteristics of Pulverized-coal in a Drop Tube Furnace," *Fuel,* **115**, 452-460 (2014).

Wang, J. H., J. Du, L. P. Chang and K. C. Xie, "Study on the Structure and Pyrolysis Characteristics of Chinese Western Coals," *Fuel Processing Technology,* **91**(4), 430-433 (2010).

Wang, Z. H., K. D. Wan, J. Xia, Y. He, Y. Z. Liu and J. Z. Liu, "Pyrolysis Characteristics of Coal, Biomass, and Coal-biomass Blends under High Heating Rate Conditions: Effects of Particle Diameter, Fuel Type, and Mixing Conditions," *Energy & Fuels,* **29**(8), 5036-5046 (2015).

Warzecha, P. and A. Boguslawski, "LES and RANS Modeling of Pulverized Coal Combustion in Swirl Burner for Air and Oxy-combustion Technologies," *Energy,* **66**, 732-743 (2014).

Watanabe, J. and K. Yamamoto, "Flamelet Model for Pulverized Coal Combustion," *Proceedings of the Combustion Institute,* **35**, 2315-2322 (2015).

Watanabe, J., T. Okazaki, K. Yamamoto, K. Kuramashi and A. Baba, "Large-eddy Simulation of Pulverized Coal Combustion Using Flamelet Model," *Proceedings of the Combustion Institute,* **36**(2), 2155-2163 (2017).

Watt, M., "The Chemical Structure of Coal Tar and Char During Devolatilization," M.S. Thesis, Chemical Engineering, Brigham Young University (1996).

Watt, M., T. H. Fletcher, S. Bai, M. S. Solum and R. J. Pugmire, "Chemical Structure of Coal Tar During Devolatilization," *Symposium (International) on Combustion,* **26**(2), 3153-3160 (1996).

Weiland, N. T., N. C. Means and B. D. Morreale, "Product Distributions From Isothermal Co-pyrolysis of Coal and Biomass," *Fuel,* **94**(1), 563-570 (2012).

Weinberg, F. J., "The First Half-million Years of Combustion Research and Today's Burning Problems," *Symposium (International) on Combustion,* **15**(1), 1-17 (1975).

Wen, X., K. Luo, Y. J. Luo, H. I. Kassem, H. H. Jin and J. R. Fan, "Large Eddy Simulation of a Semi-industrial Scale Coal Furnace Using Non-adiabatic Three-stream Flamelet/Progress Variable Model," *Applied Energy,* **183**, 1086-1097 (2016).

Wen, X., K. Luo, H. H. Jin and J. R. Fan, "Large Eddy Simulation of Piloted Pulverised Coal Combustion Using Extended Flamelet/Progress Variable Model," *Combustion Theory and Modelling,* **21**(5), 925-953 (2017a).

Wen, X., K. Luo, H. H. Jin and J. R. Fan, "Numerical Investigation of Coal Flamelet Characteristics in a Laminar Counterflow With Detailed Chemistry," *Fuel,* **195**, 232-242 (2017b).

Wen, X., H. O. Wang, Y. J. Luo, K. Luo and J. R. Fan, "Evaluation of Flamelet/Progress Variable Model for Laminar Pulverized Coal Combustion," *Physics of Fluids,* **29**(8), 18 (2017c).

Wen, X., K. Luo, H. O. Wang, Y. J. Luo and J. R. Fan, "Analysis of Pulverized Coal Flame Stabilized in a 3D Laminar Counterflow," *Combustion and Flame,* **189**, 106-125 (2018).

Wen, X., Y. J. Luo, H. O. Wang, K. Luo, H. H. Jin and J. R. Fan, "A Three Mixture Fraction Flamelet Model for Multi-stream Laminar Pulverized Coal Combustion," *Proceedings of the Combustion Institute,* **37**(3), 2901-2910 (2019).

Williams, A., R. Backreedy, R. Habib, J. M. Jones and M. Pourkashanian, "Modelling Coal Combustion: The Current Position," *Fuel,* **81**(5), 605-618 (2002).

Wu, D. M. P. and D. P. Harrison, "Volatile Products From Lignite Pyrolysis and Hydropyrolysis," *Fuel,* **65**(6), 747-751 (1986).

Xu, H. B., F. Hunger, M. Vascellari and C. Hasse, "A Consistent Flamelet Formulation for a Reacting Char Particle Considering Curvature Effects," *Combustion and Flame,* **160**(11), 2540-2558 (2013).

Xu, W.-C. and A. Tomita, "Effect of Coal Type on the Flash Pyrolysis of Various Coals," *Fuel,* **66**(5), 627-631 (1987a).

Xu, W.-C. and A. Tomita, "Effect of Temperature on the Flash Pyrolysis of Various Coals," *Fuel,* **66**(5), 632-636 (1987b).

Yamamoto, K., T. Murota, T. Okazaki and M. Taniguchi, "Large Eddy Simulation of a Pulverized Coal Jet Flame Ignited by a Preheated Gas Flow," *Proceedings of the Combustion Institute,* **33**(2), 1771-1778 (2011).

Yan, B. H., C. X. Cao, Y. Cheng, Y. Jin and Y. Cheng, "Experimental Investigation on Coal Devolatilization at High Temperatures With Different Heating Rates," *Fuel,* **117**, 1215-1222 (2014a).

Yan, B. H., Y. Cheng, P. C. Xu, C. X. Cao and Y. Cheng, "Generalized Model of Heat Transfer and Volatiles Evolution Inside Particles for Coal Devolatilization," *Aiche Journal,* **60**(8), 2893-2906 (2014b).

Yang, H., S. F. Li, T. H. Fletcher and M. Dong, "Simulation of the Swelling of High-volatile Bituminous Coal During Pyrolysis," *Energy & Fuels,* **28**(11), 7216-7226 (2014a).

Yang, H., S. F. Li, T. H. Fletcher, M. Dong and W. S. Zhou, "Simulation of the Evolution of Pressure in a Lignite Particle During Pyrolysis," *Energy & Fuels,* **28**(5), 3511-3518 (2014b).

Yang, H., S. F. Li, T. H. Fletcher and M. Dong, "Simulation of the Swelling of High-volatile Bituminous Coal During Pyrolysis. Part 2: Influence of the Maximum Particle Temperature," *Energy & Fuels,* **29**(6), 3953-3962 (2015).

Yang, X., A. Clements, J. Szuhánszki, X. Huang, O. Farias Moguel, J. Li, J. Gibbins, Z. Liu, C. Zheng, D. Ingham, L. Ma, B. Nimmo and M. Pourkashanian, "Prediction of the Radiative Heat Transfer in Small and Large Scale Oxy-coal Furnaces," *Applied Energy,* **211**, 523-537 (2018).

Yi, B. J., L. Q. Zhang, Z. H. Mao, F. Huang and C. G. Zheng, "Effect of the Particle Size on Combustion Characteristics of Pulverized Coal in an O_2/CO_2 Atmosphere," *Fuel Processing Technology,* **128**, 17-27 (2014).

Zhang, J. W., T. Ito, S. Ito, D. Riechelmann and T. Fujimori, "Numerical Investigation of Oxy-coal Combustion in a Large-scale Furnace: Non-gray Effect of Gas and Role of Particle Radiation," *Fuel,* **139**, 87-93 (2015).

Zhang, K., Y. Li, Z. Wang, Q. Li, R. Whiddon, Y. He and K. Cen, "Pyrolysis Behavior of a Typical Chinese Sub-bituminous Zhundong Coal From Moderate to High Temperatures," *Fuel,* **185**, 701-708 (2016).

Zhang, P. Z., L. Y. Li and C. H. Ye, "Solid State ^{13}C NMR Study of Chinese Coals," *Fuel Science & Technology International,* **13**(4), 467-481 (1995).

Zhao, Y., Y. Chen, D. G. Hamblen and M. Serio, "Coal Devolatilization Submodel for Comprehensive Combustion and Gasification Codes," 9th International Conference on Coal Science, Essen, Germany, 2 (1997).

APPENDIX

A. Computational Tools

B. Experimental Data Sets

C. Additional Elemental Composition Analysis

D. Additional Heating Value Analysis

E. Additional Mixture Fraction Analysis

APPENDIX A. COMPUTATIONAL METHODS

This appendix chapter summarizes some of the computational tools and methods used in this dissertation. Included in this chapter are summaries of the MATLAB optimizers, equilibrium codes, and statistical toolkits used in the main chapters of this dissertation.

A.1 MATLAB Tools

Most of the build-in MATLAB tools used in this dissertation are six optimizer algorithms: (1) *fminunc*, (2) *fmincon*, (3) MultiStart algorithm, (4) GlobalSearch algorithm, (5) particle swarm algorithm, and (6) genetic algorithm. MATLAB is organized into several libraries of built-in tools, called toolboxes. The six main optimization algorithms are found in two of these toolboxes—the Optimization Toolbox and the Global Optimization Toolbox. The first two optimizers (*fminunc* and *fmincon*) fall into the Optimization Toolbox and the others are in the Global Optimization Toolbox. The following sections summarize the key similarities and differences between the different optimizer algorithms. Most of these summaries include information directly from the documentation of MATLAB from MathWorks.com.

A.1.1 *fminunc* Optimization Algorithm

The *fminunc* optimizer is one of the simpler algorithms designed to find the minimum of an unconstrained function. This function must have one output that is being minimized (usually some sort of error function, like SSE, when comparing a model to experimental data). This

function can have any number of variables and fitted coefficients. This optimizer has several algorithm choices built-in, including quasi-newton and trust-region. The quasi-newton is the default algorithm, not requiring user-defined gradients, whereas the trust-region algorithm does require an input of gradients. All analyses in this dissertation that used the *fminunc* optimizer used the default optimization algorithm. In addition to an input of the function to be minimized, the *fminunc* optimizer also requires an initial guess value for the fitted coefficients. Ideally, the guess values should be relatively close to the global minimum values for *fminunc* to find the global minimum rather than a local minimum.

A.1.2 *fmincon* Optimization Algorithm

The *fmincon* optimizer is very similar in many ways to the *fminunc* optimizer, however, *fmincon* can include constraints (both linear and non-linear) on the multivariable function to be minimized. In addition to linear and non-linear constraints on the function, upper and lower bounds can be placed on the model coefficients. This can be useful if coefficients must conform to specific regions of numbers (e.g., non-negative values, some coefficients must be larger/smaller than others, etc.). This optimization algorithm also requires an initial guess value in addition to the optimized function and any constraints. The *fmincon* optimizer also includes some different optimization algorithms than *fminunc*, many of which can only be applied in certain situations and have their own dependencies (such as a user-defined gradient). Like the *fminunc* optimizer, the analyses that used *fmincon* in this dissertation used the default optimization algorithm (interior-point).

A.1.3 GlobalSearch and MultiStart

One of the key disadvantages of both *fminunc* and *fmincon* optimizers is the need to supply an initial condition, which could inadvertently result in either optimizer finding a local minimum rather than the global (or overall) minimum value. The optimizers from the Global Optimization Toolkit are designed to get around this problem in a couple of ways. The GlobalSearch and MultiStart algorithms are similar in the way they approach an optimization problem but can be used in slightly different ways. GlobalSearch tends to be better at finding the global minimum of a function, whereas MultiStart can be used to find multiple local minima. GlobalSearch uses *fmincon* as its main optimizer while MultiStart can use either *fmincon* or *fminunc*. Both algorithms use an initial guess value to run several iterations of the simpler optimizers in order to find either the global minimum or multiple local minima. Essentially, both optimization algorithms rely on multiple runs of the simpler optimization programs from slightly different starting values. If both *fminunc* and *fmincon* find the global minimum, it is likely both GlobalSearch and MultiStart algorithms will also find the same solutions.

A.1.4 Particle Swarm Algorithm

Particle swarm algorithms are inspired by swarming insects, hence the name. The particle swarm algorithms can be either constrained or unconstrained. Another disadvantage of the simpler *fminunc* and *fmincon* optimizers is that the objective function must be continuous, otherwise the optimization algorithm generally will not work. A particle swarm algorithm can optimize an objective function that is neither differentiable nor continuous, although, it could optimize a function that is differentiable and continuous as well. In a particle swarm algorithm, the optimizer starts with a certain specified number of "particles," or points in the optimization field. Each particle moves with a velocity and direction that is influenced by the best location

found by each individual particle as well as the best found by the swarm in general. Ideally, at the end of the optimization, all particles will end up in the same location—that of the global minimum. Applying a particle swarm algorithm to VUQ is advantageous because experimental data are often very noisy and comparing real-world values to model predictions results in objective functions that are not very smooth, meaning simpler optimizers often get stuck in local minima rather than the global minimum.

A.1.5 Genetic Algorithm

Genetic algorithms are another optimization scheme that mimic biological systems, this time modeling principles of biological evolution. Like the particle swarm algorithm, genetic algorithms can be applied to continuous or non-continuous objective functions. The genetic algorithm introduces several different "steps" of evolution in the "population" of individual points, including selection of the best points, random mutations, and cross-over of different points. The genetic algorithm is a little more difficult to understand on the surface than other similar optimization schemes (such as particle swarm). Ideally, genetic algorithms will also find the global minimum.

A.1.6 Optimization Algorithm Summary

MATLAB's built-in optimization algorithms were very useful in the research detailed in this dissertation. Most of the research here used one or more of these optimizers to fit model coefficients to a supplied data set using a simple least-squares analysis. In several instances, multiple optimizer algorithms were applied to the same problem in the hope that one or more would find the global minimum, which would be the best possible fit of the model coefficients to each data set. While this generates a lot more data than using one optimizer, it helps to inspire

confidence in the model fits, that they are the best possible using the model forms and data sets in each analysis.

A.2 Statistical Tools

As discussed in the main body of the dissertation, the optimization of the model coefficients used a simple minimization of the sum-of-squared-errors (SSE), also called a least-squares analysis. While this is useful in finding the best fit for each model form, the SSE does not give a complete picture of the error between the model and experimental data. The statistical branch of VUQ (discussed in greater detail in Section 2.4) is full of different techniques and tools that can be used to paint a picture of the error between model predictions and real-world values. Several techniques and tools were considered as part of this dissertation, however, ultimately the set of validation metrics and techniques detailed in Section 2.4 were ultimately used here. The validation metrics (among other statistical measures such as standard deviation, confidence intervals, T-tests, etc.) were coded into a statistical package (written in MATLAB but can be applied to any number of other coding platforms) for use in conjunction with any of the built-in optimization algorithms. This package compares the experimental values to the model predictions and outputs all statistical values for each comparison in one concise package that can be further manipulated to find the best fits of multiple models.

A.3 Equilibrium Solvers

The mixture fraction analysis (Chapter 8) used two equilibrium codes: NASA-CEA and Cantera. While a summary of each program is found in that chapter, this section deals more with how each program was used and the motivation behind using either solver over the other.

A.3.1 NASA-CEA

The NASA-CEA equilibrium solver has been widely used in combustion calculations for years, being especially useful in the coal community for its ability to use non-standard compounds that are not included in the provided thermodynamic properties libraries. This code has several different problem types it can solve, depending on what conditions are known of the equilibrium state. One of the most common in many combustion applications is the problem type called HP, where the reactant enthalpies and system pressure are known. User-defined compounds are defined with an elemental composition (either on a mass or molar basis) and an enthalpy of formation. This is enough information along with the system pressure and all other reactants to calculate an equilibrium state of the mixture using Gibbs energy minimization. The code also allows for multiple independent equilibria based on multiple mixtures of reactants, which is useful when completing large numbers of equilibrium states. However, this is limited to a relatively small number of about 15 maximum equilibrium states for a single run of the NASA-CEA code.

The original NASA-CEA code was freely available in a downloadable file with a graphical user interface allowing for programming of inputs and visualization of outputs, however, recent versions of the code are no longer freely available, with permission needed to access and download the code. There is currently a browser-based version of the CEA code, however, it does not currently have the same capabilities with user-defined compounds as the original code.

A.3.2 Cantera

Cantera acts as a plug-in of libraries mainly for MATLAB or Python (and can also be used with C/C++ or Fortran 90) and is becoming more popular in combustion applications.

Cantera can be integrated into existing research codes for a wide variety of applications. This can make Cantera much more flexible than the stand-alone NASA-CEA code. The main equilibrium solver used in this dissertation also relies on Gibbs energy minimization to solve the equilibrium states based on an input of reactant information and system pressure. This application of Cantera even includes some of the same equations used by the NASA-CEA code to generate thermodynamic properties of user-defined compounds. Integrating directly into MATLAB or Python also allows for immediate numerical manipulation and even plotting of useful information in the same code as the equilibrium calculations.

Unlike the NASA-CEA code, Cantera does not include built-in thermodynamic libraries from which to draw reactant and product information. Cantera instead relies either on complex mechanisms (such as GRI3.0) or thermodynamic files (extension .cti) that include all relevant chemical and thermodynamic information for each compound, including user-defined and other common compounds (methane, ethane, etc.).

While there are a number of advantages to using Cantera, there are also a number of disadvantages. One of the main disadvantages is the learning curve necessary to know how to work with Cantera. Cantera includes extensive documentation, but it can be difficult to navigate when using Cantera for the first time. Another key disadvantage of Cantera is that it tends to take much longer to calculate some equilibrium states that the NASA-CEA code, which calculates most equilibrium states almost instantly. As discussed in Chapter 8, some of the more complex equilibrium calculations in Cantera took days to run on a single processor. The equilibrium calculations could be sped up using parallel computing, but that is beyond the scope of many small research projects that rely on single processors.

A.4 Code Availability

The research detailed in this dissertation generated a large amount of computer code. It would be impossible to include all of this code in the pages of this dissertation, even in an appendix format. For this reason, the key codes used in this research have been consolidated and are available free of charge by email (andrewprichards1@gmail.com). All codes are supplied as-is, many likely not providing much documentation on how to use the codes.

APPENDIX B. EXPERIMENTAL DATA

This appendix chapter details the entirety of the experimental data sets used in the elemental composition analysis, the aromaticity correlation analysis, and the fuel heating value analysis. The descriptions of these data sets are included in Section 2.5, which describes the criteria for the selection process for each data set.

B.1 Elemental Composition Data Set

The elemental composition analysis was divided into two parts: elemental composition of coal char and coal tar at different residence times and reaction temperatures. The coal char data set is found in Table B-1 and the coal tar data set is found in Table B-2. The sources in each table are listed as follows, as described in Table 2-4:

1. Freihaut et al. (1989b)
2. Hambly (1998)
3. Perry (Perry, 1999; Perry et al., 2000)
4. Sandia, Fletcher and Hardesty (1992)
5. Watt (1996)
6. Tyler (1980)
7. Freihaut et al. #2* (1989a)
8. Parkash (1985)

The second Freihaut source (source 7, marked with a *) is a DOE technical report that was only found in print, and not available online. Because of this, some of the information is missing from this report, namely the coal names and rank. Some of the tar values reported in this report were the same as in the first Freihaut source, however, some were different coals. It is likely that all were standard research coals from the Pennsylvania State Coal Databank, but the original report would be necessary to determine that information. In addition to the tar and parent coal information, the Freihaut technical report also contains char elemental compositions, whereas the first Freihaut source (an article from Energy & Fuels) only contains information on tars and their parent coal.

The elemental compositions are on a dry, ash-free wt.% basis, as are the volatiles yield V_i and the ASTM volatile matter. Maximum gas temperature ($T_{gas,max}$) is in K, residence time (t_{res}) is in milliseconds, and the particle diameter (d_p) is in microns. Oxygen is measured by difference, so some values are negative (colored red in the following tables). Note that some sources did not report some information, including oxygen and sulfur compositions of the coal, char, or tar, particle diameters, or volatiles yield. The volatiles yield is assumed to be the maximum for that particular residence time, so the ratio of V_i/V_{max} is equal to 1 for those samples. The particle diameter was not included in any of the correlations, and as such is unnecessary for the elemental composition analysis. It was briefly considered as an additional variable, but in the end was not included due to the lack of diverse particle size data reported. For those samples that did not report oxygen and sulfur contents, those samples were not included in the optimization of the correlation coefficients for correlations using those variables.

Table B-1. Char Elemental Composition Data

Source	Coal	Rank	Char Composition					Parent Coal Composition					$T_{gas,max}$	t_{res}	d_p	V_i	V_{ASTM}
			C	H	O	N	S	C	H	O	N	S					
2			71.73	4.49	21.44	1.04	1.3	64.16	4.78	28.32	0.94	1.81	820	170	69	29.4	49
2			81.61	3.34	12.59	1.26	1.2	64.16	4.78	28.32	0.94	1.81	1080	285	69	51.9	49
2			78.53	5.3	14.02	1.33	0.81	74.23	5.48	18.35	1.3	0.65	820	170	69	10.7	45.68
2			84.97	3.35	9.37	1.67	0.64	74.23	5.48	18.35	1.3	0.65	1080	285	69	51.2	45.68
2			78.36	5.1	10.56	1.57	4.42	74.81	5.33	13.54	1.48	4.85	820	170	69	10.6	45.59
2			86.25	3.43	4.75	1.86	3.7	74.81	5.33	13.54	1.48	4.85	1080	285	69	59.2	45.59
2			84.9	5.49	6.58	1.8	1.24	82.77	5.61	8.9	1.74	0.98	820	170	69	10.3	38.69
2			89.83	3.6	3.63	2.1	0.84	82.77	5.61	8.9	1.74	0.98	1080	285	69	47.9	38.69
2			90.95	4.47	2.46	1.28	0.84	90.92	4.51	2.41	1.34	0.82	820	170	69	5.1	18.01
2			96.62	3.7	-2.42	1.4	0.7	90.92	4.51	2.41	1.34	0.82	1080	285	69	27.1	18.01
3			75.32	3.33	20.49	0.68	0.18	65.31	4.76	29.22	0.52	0.18	895	263	60	46	53.1
3			84.09	2.95	12.09	0.73	0.14	65.31	4.76	29.22	0.52	0.18	1000	252	60	55	53.1
3			87.65	2.57	8.94	0.7	0.13	65.31	4.76	29.22	0.52	0.18	1085	234	60	57.8	53.1
3			78.25	3.77	16	1.52	0.46	71.37	5.36	21.55	1.18	0.55	895	263	60	41.6	51.3
3			81.61	3.16	13.35	1.59	0.3	71.37	5.36	21.55	1.18	0.55	1000	252	60	51.1	51.3
3			84.18	2.91	11.09	1.58	0.24	71.37	5.36	21.55	1.18	0.55	1085	234	60	54.4	51.3
3			84.25	3.34	10.74	1.49	0.18	76.72	6.35	15.59	1.13	0.21	1000	252	60	58.3	54.7
3			85.16	3.04	10.13	1.49	0.18	76.72	6.35	15.59	1.13	0.21	1085	234	60	60.4	54.7
3			82.48	3.44	5.46	1.48	7.15	79.91	6.13	8.3	1.18	4.48	895	263	60	66.8	53
3			85.28	3.42	4.08	1.44	5.78	79.91	6.13	8.3	1.18	4.48	1000	252	60	63.9	53
3			89.97	3	1.13	1.4	4.49	79.91	6.13	8.3	1.18	4.48	1085	234	60	64.7	53
3			87.18	4.08	5.92	2.35	0.46	82.82	5.43	9.18	2.08	0.48	895	263	60	38.6	37.2
3			88.05	3.42	5.74	2.47	0.31	82.82	5.43	9.18	2.08	0.48	1000	252	60	43.8	37.2
3			89.94	2.84	4.41	2.48	0.34	82.82	5.43	9.18	2.08	0.48	1085	234	60	47.9	37.2
3			80.91	4.15	7.14	1.72	6.08	82.77	5.48	6.73	1.64	3.38	895	263	60	45.1	42.5
3			82.46	4.06	5.73	1.78	5.97	82.77	5.48	6.73	1.64	3.38	960	263	60	47.2	42.5
3			82.51	4.02	6.31	1.78	5.38	82.77	5.48	6.73	1.64	3.38	960	263	60	46.4	42.5
3			87.49	3.37	3.41	1.92	3.82	82.77	5.48	6.73	1.64	3.38	1000	252	60	50.7	42.5
3			87.99	3.08	3.43	1.78	3.72	82.77	5.48	6.73	1.64	3.38	1085	234	60	54.4	42.5

Table B-1. Char Elemental Composition Data, CONTINUED

Source	Coal	Rank	Char Composition					Parent Coal Composition					$T_{gas,max}$	t_{res}	d_p	V_i	V_{ASTM}
			C	H	O	N	S	C	H	O	N	S					
3			85.47	3.09	5.01	1.61	4.82	84.15	5.13	4.6	1.55	4.56	895	263	60	42.9	33.4
3			85.99	3.31	0.77	1.62	8.32	84.15	5.13	4.6	1.55	4.56	1000	252	60	49	33.4
3			89.21	2.81	1.17	1.69	5.13	84.15	5.13	4.6	1.55	4.56	1085	234	60	45.2	33.4
3			91.54	4.32	2.05	1.35	0.73	91.57	4.57	1.74	1.36	0.76	895	263	60	13.4	20.1
3			93.31	3.45	1.14	1.43	0.67	91.57	4.57	1.74	1.36	0.76	1000	252	60	21.7	20.1
3			92.45	2.96	2.56	1.42	0.61	91.57	4.57	1.74	1.36	0.76	1085	234	60	25.8	20.1
4			77.29	5.56	15.11	1.35	0.69	75.6	5.26	17.33	1.32	0.49	1050	0	115.5	0	46.77
4			73.16	4.92	20	1.3	0.62	75.6	5.26	17.33	1.32	0.49	1050	59	115.5	0	46.77
4			79.55	5.11	13.2	1.45	0.68	75.6	5.26	17.33	1.32	0.49	1050	88	115.5	6.1	46.77
4			79.39	4.63	13.75	1.53	0.7	75.6	5.26	17.33	1.32	0.49	1050	123	115.5	30.8	46.77
4			79.02	4.98	13.87	1.47	0.66	75.6	5.26	17.33	1.32	0.49	1050	120	115.5	22	46.77
4			79.42	4.13	14.15	1.59	0.71	75.6	5.26	17.33	1.32	0.49	1050	180	115.5	39	46.77
4			83.01	3.75	10.85	1.74	0.65	75.6	5.26	17.33	1.32	0.49	1050	253	115.5	46.9	46.77
4			81.92	6.45	8.72	1.65	1.26	81.92	6.45	8.72	1.65	1.26	1050	0	115.5	0	39.83
4			82.96	5.53	8.91	1.49	1.12	81.92	6.45	8.72	1.65	1.26	1050	54	115.5	0	39.83
4			82.22	5.49	9.43	1.7	1.16	81.92	6.45	8.72	1.65	1.26	1050	112	115.5	1.1	39.83
4			82.67	5.14	9.79	1.26	1.15	81.92	6.45	8.72	1.65	1.26	1050	167	115.5	19	39.83
4			81.75	4.94	10.14	1.82	1.36	81.92	6.45	8.72	1.65	1.26	1050	231	115.5	37.7	39.83
4			82.49	4.09	10.26	1.87	1.29	81.92	6.45	8.72	1.65	1.26	1050	337	115.5	43.8	39.83
4			84.23	5.54	7.56	1.65	1.01	84.23	5.54	7.56	1.65	1.01	1050	0	69	0	38.7
4			84.32	5.4	8.06	1.64	0.58	84.23	5.54	7.56	1.65	1.01	1050	63	69	0	38.7
4			84.36	5.44	7.92	1.64	0.64	84.23	5.54	7.56	1.65	1.01	1050	95	69	12.5	38.7
4			83.28	4.82	9.14	1.7	1.07	84.23	5.54	7.56	1.65	1.01	1050	136	69	25.1	38.7
4			84.66	4.43	8.2	1.78	0.94	84.23	5.54	7.56	1.65	1.01	1050	167	69	33.7	38.7
4			83.37	3.98	9.61	1.82	1.22	84.23	5.54	7.56	1.65	1.01	1050	200	69	33.2	38.7
4			86.29	3.79	7.03	1.89	1	84.23	5.54	7.56	1.65	1.01	1050	287	69	55.5	38.7
4			74.12	4.96	13.08	1.45	6.29	74.12	4.96	13.18	1.45	6.29	1050	0	115.5	0	43.4
4			73.98	4.76	13.07	1.38	6.8	74.12	4.96	13.18	1.45	6.29	1050	61	115.5	1.8	43.4
4			75.34	4.99	12.18	1.42	6.07	74.12	4.96	13.18	1.45	6.29	1050	91	115.5	27.9	43.4

Table B-1. Char Elemental Composition Data, CONTINUED

Source	Coal	Rank	Char Composition					Parent Coal Composition					$T_{gas,max}$	t_{res}	d_p	V_i	V_{ASTM}
			C	H	O	N	S	C	H	O	N	S					
4			75.49	4.35	12.16	1.59	6.41	74.12	4.96	13.18	1.45	6.29	1050	127	115.5	29.3	43.4
4			74.36	4.01	11.72	1.54	8.37	74.12	4.96	13.18	1.45	6.29	1050	156	115.5	36.7	43.4
4			73.45	3.67	11.95	1.43	9.49	74.12	4.96	13.18	1.45	6.29	1050	186	115.5	38.3	43.4
4			75.22	3.28	10.53	1.42	9.55	74.12	4.96	13.18	1.45	6.29	1050	266	115.5	43.5	43.4
4			66.56	4.26	25.16	1.12	2.89	66.56	4.26	25.16	1.12	2.89	1050	0	90.5	0.0	49.6
4			64.41	4.07	24.75	1.13	5.64	66.56	4.26	25.16	1.12	2.89	1050	60	90.5	0.0	49.6
4			64.83	3.97	24.82	1.1	5.28	66.56	4.26	25.16	1.12	2.89	1050	90	90.5	0.0	49.6
4			68.7	3.41	21.7	1.2	5	66.56	4.26	25.16	1.12	2.89	1050	109	90.5	21.5	49.6
4			67.26	2.63	22.88	1.32	5.92	66.56	4.26	25.16	1.12	2.89	1050	160	90.5	47.3	49.6
4			69.43	2.69	21.32	1.37	5.19	66.56	4.26	25.16	1.12	2.89	1050	193	90.5	30.4	49.6
4			74.6	2.77	17.62	1.36	3.65	66.56	4.26	25.16	1.12	2.89	1050	278	90.5	52.5	49.6
4			67.99	4.24	24.83	0.99	1.95	66.56	4.26	25.16	1.12	2.89	1050	0	90.5	0.0	49.6
4			72.79	3.15	19.58	1.16	3.32	66.56	4.26	25.16	1.12	2.89	1050	160	90.5	29.0	49.6
4			71.39	2.98	19.79	1.11	4.73	66.56	4.26	25.16	1.12	2.89	1050	193	90.5	37.8	49.6
4			73.32	3.17	19.11	1.21	3.19	66.56	4.26	25.16	1.12	2.89	1050	278	90.5	30.5	49.6
4			88.83	4.37	5.14	1.06	0.6	88.83	4.37	5.14	1.06	0.60	1050	0	115.5	0.0	17.18
4			88.56	4.39	5.41	1.04	0.6	88.83	4.37	5.14	1.06	0.60	1050	60	115.5	0.0	17.18
4			87.66	4.3	6.49	0.98	0.58	88.83	4.37	5.14	1.06	0.60	1050	89	115.5	0.0	17.18
4			88.78	4.34	5.32	0.98	0.57	88.83	4.37	5.14	1.06	0.60	1050	127	115.5	0.0	17.18
4			90.06	4.34	4.06	1	0.53	88.83	4.37	5.14	1.06	0.60	1050	155	115.5	3.0	17.18
4			90.29	4.31	3.76	1.06	0.58	88.83	4.37	5.14	1.06	0.60	1050	185	115.5	5.3	17.18
4			89.24	4.12	5.04	1.01	0.59	88.83	4.37	5.14	1.06	0.60	1050	269	115.5	6.6	17.18
5			73.79	4.35	-[a]	0.92	-	69.99	5.59	21.19	1.17	2.08	850	140	69	23.0	49
5			76.34	3.62	-	1.29	-	69.99	5.59	21.19	1.17	2.08	900	160	69	38.2	49
5			80.89	3.01	-	1.49	-	69.99	5.59	21.19	1.17	2.08	1050	210	69	44.8	49
5			75.34	4.78	-	1.34	-	75.03	5.35	18.03	1.12	0.47	850	110	69	17.9	17.92
5			76.86	4.34	-	1.49	-	75.03	5.35	18.03	1.12	0.47	900	130	69	26.2	26.15
5			76.7	4.74	-	1.23	-	75.03	5.35	18.03	1.12	0.47	920	110	69	31.7	31.67
5			78.98	5.05	-	1.44	-	77.29	5.69	14.96	1.27	0.79	850	140	69	17.7	45.68

Table B-1. Char Elemental Composition Data, CONTINUED

Source	Coal	Rank	Char Composition					Parent Coal Composition					$T_{gas,max}$	t_{res}	d_p	V_i	V_{ASTM}
			C	H	O	N	S	C	H	O	N	S					
5			79.3	4.83	-	1.28	-	77.29	5.69	14.96	1.27	0.79	900	160	69	23.2	45.68
5			83.8	3.24	-	1.83	-	77.29	5.69	14.96	1.27	0.79	1050	210	69	47.1	45.68
5			76.77	4.67	-	1.9	-	76.65	4.93	10.01	1.47	6.93	850	140	69	9.0	45.59
5			77.21	4.39	-	1.56	-	76.65	4.93	10.01	1.47	6.93	900	160	69	37.5	45.59
5			82.16	3.26	-	1.93	-	76.65	4.93	10.01	1.47	6.93	1050	210	69	45.5	45.59
5			84.93	5.43	-	1.25	-	84.7	5.4	7.26	1.71	0.92	850	140	69	21.5	38.69
5			83.73	3.9	-	1.86	-	84.7	5.4	7.26	1.71	0.92	900	160	69	45.9	38.69
5			88.11	3.32	-	1.91	-	84.7	5.4	7.26	1.71	0.92	1050	210	69	45.0	38.69
5			93.46	4.38	-	1.14	-	90.52	4.6	2.52	1.6	0.77	850	140	69	6.6	18.01
5			89.89	4.25	-	1.13	-	90.52	4.6	2.52	1.6	0.77	900	160	69	11.8	18.01
5			90.16	3.35	-	1.18	-	90.52	4.6	2.52	1.6	0.77	1050	210	69	13.0	18.01
7			82.82	5.15	-	1.56	-	83.98	5.48	7.41	1.67	1.46	780.2	580	25	15.0	37.76
7			82.6	5.05	-	1.55	-	83.98	5.48	7.41	1.67	1.46	842.2	545	25	22.0	37.76
7			82.77	4.96	-	1.63	-	83.98	5.48	7.41	1.67	1.46	933.2	515	25	24.0	37.76
7			82.68	4.76	-	1.63	-	83.98	5.48	7.41	1.67	1.46	1069	450	25	26.0	37.76
7			64	4.05	-	1.22	-	71.42	5.17	21.01	1.35	1.06	1098	450	25	-[a]	57.5
7			65.02	3.3	-	0.9	-	72.49	4.32	20.22	1.09	1.88	1098	450	25	-	50.45
7			66.46	4.08	-	0.95	-	73.67	5.9	18.22	1.11	1.1	1098	450	25	-	48.18
7			74.16	4.35	-	1.27	-	76.72	5.44	15.65	1.28	0.91	1098	450	25	-	44.4
7			73.72	4.33	-	1.35	-	78.79	5.16	10.15	1.48	4.42	1098	450	25	-	43.9
7			82.77	4.96	-	1.63	-	83.98	5.48	7.41	1.67	1.46	1098	450	25	-	37.76
7			85.82	4.45	-	1.43	-	80.53	5.11	1.5	1.59	1.26	1098	450	25	-	19.58
8			78.2	3	17.1	1.5	0.2	75	4.4	19.3	1.1	0.2	823.2	575	-[a]	-	39.6
8			79.6	2.8	16.2	1.2	0.2	75	4.4	19.3	1.1	0.2	923.2	608	-	-	39.6
8			83.9	2.2	12.3	1.5	0.1	75	4.4	19.3	1.1	0.2	973.2	625	-	-	39.6
8			78.5	2.9	16.1	1.7	0.8	74.1	4.3	19.1	2	0.5	823.2	575	-	-	43
8			83.7	2.4	11.3	1.9	0.7	74.1	4.3	19.1	2	0.5	923.2	608	-	-	43
8			86.3	2.2	8.7	2.2	0.6	74.1	4.3	19.1	2	0.5	973.2	625	-	-	43
8			80.5	3.2	13	2.3	1	75.8	5.4	16.1	1.8	0.9	823.2	575	-	-	47.1

Table B-1. Char Elemental Composition Data, CONTINUED

Source	Coal	Rank	Char Composition					Parent Coal Composition					$T_{gas,max}$	t_{res}	d_p	V_i	V_{ASTM}
			C	H	O	N	S	C	H	O	N	S					
8			85.4	2.5	8.7	2.5	0.9	75.8	5.4	16.1	1.8	0.9	923.2	608	-[a]	-	47.1
8			88.3	2.2	6	2.7	0.8	75.8	5.4	16.1	1.8	0.9	973.2	625	-	-	47.1

[a] These values were not reported in the cited sources and were not included in the respective correlations.

Table B-2. Tar Elemental Composition Data

Source	Coal	Rank	Tar Composition					Parent Coal Composition					$T_{gas,max}$	t_{res}	d_p	V_i	V_{ASTM}
			C	H	O	N	S	C	H	O	N	S					
1			84.05	6.07	-[a]	1.64	-	83.98	5.48	7.41	1.67	1.46	780	580	25	-	37.76
1			84.07	5.94	-	1.67	-	83.98	5.48	7.41	1.67	1.46	842	545	25	-	37.76
1			84.37	5.86	-	1.68	-	83.98	5.48	7.41	1.67	1.46	933	515	25	-	37.76
1			84.46	5.93	-	1.76	-	83.98	5.48	7.41	1.67	1.46	933	515	25	-	37.76
1			84.62	5.55	-	1.69	-	83.98	5.48	7.41	1.67	1.46	1069	450	25	-	37.76
1			83.97	6.22	-	1.64	-	84.7	5.4	7.26	1.71	0.92	780	580	69	-	38.69
1			84.47	5.83	-	1.72	-	84.7	5.4	7.26	1.71	0.92	933	515	69	-	38.69
1			84.16	5.79	-	1.74	-	84.7	5.4	7.26	1.71	0.92	933	515	69	-	38.69
1			78.21	8.43	-	0.63	-	73.67	5.9	18.22	1.11	1.1	780	580	25	-	48.18
1			78.53	8.19	-	0.68	-	73.67	5.9	18.22	1.11	1.1	842	545	25	-	48.18
1			78.15	7.83	-	0.79	-	73.67	5.9	18.22	1.11	1.1	933	515	25	-	48.18
1			77.78	7.63	-	0.81	-	73.67	5.9	18.22	1.11	1.1	933	515	25	-	48.18
1			89.38	5.6	-	1.39	-	88.88	4.71	4.3	1.49	1.25	842	569	25	-	19.58
1			88.78	5.25	-	1.29	-	88.88	4.71	4.3	1.49	1.25	933	660	25	-	19.58
1			89.6	5.24	-	1.44	-	88.88	4.71	4.3	1.49	1.25	1069	450	25	-	19.58
1			89.75	5.23	-	1.46	-	88.88	4.71	4.3	1.49	1.25	1069	450	25	-	19.58
2			71.02	8.71	18.19	0.38	1.71	64.16	4.78	28.32	0.94	1.81	820	170	69	29.4	49
2			78.71	4.9	12.71	1.3	2.38	64.16	4.78	28.32	0.94	1.81	1080	285	69	51.9	49
2			78.39	6.59	13.3	1.2	0.52	74.23	5.48	18.35	1.3	0.65	820	170	69	10.7	45.68
2			83.61	4.85	9.2	1.68	0.66	74.23	5.48	18.35	1.3	0.65	1080	285	69	51.2	45.68
2			78.88	5.96	11.05	1.51	2.6	74.81	5.33	13.54	1.48	4.85	820	170	69	10.6	45.59

Table B-2. Tar Elemental Composition Data, CONTINUED

Source	Coal	Rank	Tar Composition					Parent Coal Composition					$T_{gas,max}$	t_{res}	d_p	V_i	V_{ASTM}
			C	H	O	N	S	C	H	O	N	S					
2			85.23	4.89	5	1.8	3.08	74.81	5.33	13.54	1.48	4.85	1080	285	69	59.2	45.59
2			83.39	6	8.04	1.74	0.83	82.77	5.61	8.9	1.74	0.98	820	170	69	10.3	38.69
2			87.68	4.94	4.55	1.96	0.88	82.77	5.61	8.9	1.74	0.98	1080	285	69	47.9	38.69
2			92.13	4.86	0.73	1.34	0.93	90.92	4.51	2.41	1.34	0.82	1080	285	69	27.1	18.01
3			73.25	5.79	20.3	0.54	0.12	65.31	4.76	29.22	0.52	0.18	895	263	60	46	53.1
3			79.19	4.64	15.22	0.78	0.17	65.31	4.76	29.22	0.52	0.18	1000	252	60	55	53.1
3			86.37	4.58	7.9	0.91	0.23	65.31	4.76	29.22	0.52	0.18	1085	234	60	57.8	53.1
3			78.82	6.69	16	1.18	0.41	71.37	5.36	21.55	1.18	0.55	895	263	60	41.6	51.3
3			81.48	4.82	11.46	1.69	0.54	71.37	5.36	21.55	1.18	0.55	1000	252	60	51.1	51.3
3			84.66	4.65	8.35	1.77	0.58	71.37	5.36	21.55	1.18	0.55	1085	234	60	54.4	51.3
3			85.55	5.75	6.84	1.63	0.23	76.72	6.35	15.59	1.13	0.21	1000	252	60	58.3	54.7
3			87.51	4.76	5.76	1.72	0.25	76.72	6.35	15.59	1.13	0.21	1085	234	60	60.4	54.7
3			85.42	6.06	4.47	1.38	2.68	79.91	6.13	8.3	1.18	4.48	895	263	60	66.8	53
3			86.99	4.76	3.6	1.59	3.07	79.91	6.13	8.3	1.18	4.48	1000	252	60	63.9	53
3			89.89	4.36	1.69	1.65	2.4	79.91	6.13	8.3	1.18	4.48	1085	234	60	64.7	53
3			84.62	6.02	6.86	2.07	0.43	82.82	5.43	9.18	2.08	0.48	895	263	60	38.6	37.2
3			86.54	4.92	5.67	2.38	0.48	82.82	5.43	9.18	2.08	0.48	1000	252	60	43.8	37.2
3			91.12	4.44	1.42	2.54	0.48	82.82	5.43	9.18	2.08	0.48	1085	234	60	47.9	37.2
3			84.12	5.87	7.33	1.71	0.97	82.77	5.48	6.73	1.64	3.38	895	263	60	45.1	42.5
3			85.5	5.65	6.08	1.76	1.02	82.77	5.48	6.73	1.64	3.38	960	263	60	47.2	42.5
3			86.55	5.66	4.94	1.81	1.03	82.77	5.48	6.73	1.64	3.38	960	263	60	46.4	42.5
3			86.5	4.85	5.36	1.91	1.38	82.77	5.48	6.73	1.64	3.38	1000	252	60	50.7	42.5
3			88.92	4.43	3.2	1.99	1.47	82.77	5.48	6.73	1.64	3.38	1085	234	60	54.4	42.5
3			87.95	5.53	3.94	1.6	0.97	84.15	5.13	4.6	1.55	4.56	895	263	60	42.9	33.4
3			89.51	4.73	2.82	1.79	1.15	84.15	5.13	4.6	1.55	4.56	1000	252	60	49	33.4
3			92.25	4.24	0.27	1.93	1.31	84.15	5.13	4.6	1.55	4.56	1085	234	60	45.2	33.4
3			90.8	5.26	1.91	1.34	0.69	91.57	4.57	1.74	1.36	0.76	895	263	60	13.4	20.1
3			92.32	4.78	0.81	1.41	0.69	91.57	4.57	1.74	1.36	0.76	1000	252	60	21.7	20.1
3			92.64	4.5	0.74	1.45	0.67	91.57	4.57	1.74	1.36	0.76	1085	234	60	25.8	20.1

Table B-2. Tar Elemental Composition Data, CONTINUED

Source	Coal	Rank	Tar Composition					Parent Coal Composition					$T_{gas,max}$	t_{res}	d_p	V_i	V_{ASTM}
			C	H	O	N	S	C	H	O	N	S					
5			70.4	8.17	-[a]	0.4	-	69.99	5.59	21.19	1.17	2.08	850	140	69	23.01	49
5			76.29	6.95	-	0.94	-	69.99	5.59	21.19	1.17	2.08	900	160	69	38.18	49
5			73.61	5.02	-	1.23	-	69.99	5.59	21.19	1.17	2.08	1050	210	69	44.75	49
5			77.93	7.62	-	0.9	-	77.29	5.69	14.96	1.27	0.79	850	140	69	17.68	45.68
5			79.07	7.07	-	1.22	-	77.29	5.69	14.96	1.27	0.79	900	160	69	23.16	45.68
5			80.49	4.98	-	1.74	-	77.29	5.69	14.96	1.27	0.79	1050	210	69	47.06	45.68
5			68.54	5.35	-	1.38	-	76.65	4.93	10.01	1.47	6.93	850	140	69	8.95	45.59
5			79.36	5.66	-	1.27	-	76.65	4.93	10.01	1.47	6.93	900	160	69	37.5	45.59
5			81.645	4.92	-	1.77	-	76.65	4.93	10.01	1.47	6.93	1050	210	69	45.51	45.59
5			82.5	6.13	-	1.5	-	84.7	5.4	7.26	1.71	0.92	850	140	69	21.5	38.69
5			86.61	5.48	-	2.12	-	84.7	5.4	7.26	1.71	0.92	900	160	69	45.9	38.69
5			85.46	4.95	-	1.94	-	84.7	5.4	7.26	1.71	0.92	1050	210	69	45.03	38.69
5			74	7	-	0.4	-	90.52	4.6	2.52	1.6	0.77	850	140	69	6.6	18.01
5			80.63	4.97	-	1.05	-	90.52	4.6	2.52	1.6	0.77	900	160	69	11.84	18.01
5			89.98	4.9	-	1.25	-	90.52	4.6	2.52	1.6	0.77	1050	210	69	12.96	18.01
6			81	6.4	-	-[a]	-	80.5	4.9	-[a]	1.9	-	873.15	700	-[a]	38	34.4
6			83.2	6.3	-	-	-	85.9	4.7	-	1.9	-	873.15	700	-	30	26.3
6			78.8	6	-	-	-	81.6	4.7	-	1.9	-	873.15	700	-	36	33.2
6			77.5	6.3	-	-	-	77.9	5.1	-	1.6	-	873.15	700	-	45	40
6			80.1	6.3	-	-	-	82.1	5.3	-	1.7	-	873.15	700	-	50	37.3
6			80.3	7	-	-	-	80.5	5.7	-	2	-	873.15	700	-	61	41.6
6			81.4	6.8	-	-	-	80.3	5.8	-	2	-	873.15	700	-	52	45.6
6			80.3	7.6	-	-	-	78.4	6.4	-	1.2	-	873.15	700	-	54	51.4
6			80.2	6.5	-	-	-	77.7	5.6	-	0	-	873.15	700	-	60	44.6
6			80.3	6.6	-	-	-	81.3	5.3	-	0	-	873.15	700	-	41	-[a]
7			84.05	6.07	-	1.64	-	83.98	5.48	7.41	1.67	1.46	780.15	580	25	15	37.76
7			84.07	5.94	-	1.67	-	83.98	5.48	7.41	1.67	1.46	842.15	545	25	22	37.76
7			84.37	5.86	-	1.68	-	83.98	5.48	7.41	1.67	1.46	933.15	515	25	24	37.76
7			84.62	5.55	-	1.69	-	83.98	5.48	7.41	1.67	1.46	1069.15	450	25	26	37.76

Table B-2. Tar Elemental Composition Data, CONTINUED

Source	Coal	Rank	Tar Composition					Parent Coal Composition					$T_{gas,max}$	t_{res}	d_p	V_i	V_{ASTM}
			C	H	O	N	S	C	H	O	N	S					
7			80.27	8.88	-[a]	0.76	-	71.42	5.17	21.01	1.35	1.06	1098.15	450	25	-	57.5
7			77.58	7.86	-	0.73	-	72.49	4.32	20.22	1.09	1.88	1098.15	450	25	-	50.45
7			77.78	7.63	-	0.81	-	73.67	5.9	18.22	1.11	1.1	1098.15	450	25	-	48.18
7			78.15	7.83	-	0.79	-	73.67	5.9	18.22	1.11	1.1	1098.15	450	25	-	48.18
7			78.56	6.24	-	1.27	-	76.72	5.44	15.65	1.28	0.91	1098.15	450	25	-	44.4
7			79.52	5.51	-	1.44	-	78.79	5.16	10.15	1.48	4.42	1098.15	450	25	-	43.9
7			84.37	5.86	-	1.68	-	83.98	5.48	7.41	1.67	1.46	1098.15	450	25	-	39.98
7			89.18	5.18	-	0.96	-	89.71	4.29	4.27	1.1	0.63	1098.15	450	25	-	16.91
7			88.78	5.25	-	1.29	-	88.88	4.71	4.3	1.49	1.25	1098.15	450	25	-	19.58

[a] These values were not reported in the cited sources and were not included in the respective correlations.

B.2 Aromaticity Data Set

The aromaticity data set is described in Section 2.5 and all sources used in the aromaticity data set are shown in Table B-3. The sources are as follows:

1. Genetti et al. (Genetti et al., 1999; Genetti, 1999)
2. Solum et al. (1989)
3. Hambly/Watt (Watt, 1996; Hambly, 1998)
4. Sandia, Fletcher and Hardesty (1992)
5. Perry (1999)
6. Gerschel and Schmidt (2016)
7. Cui et al. (2019)
8. Ahmed et al. (2003)
9. Ibarra et al. (1991)
10. Lin et al. (2016)
11. Russell et al. (1983)
12. Suggate and Dickinson (2004)
13. Wang et al. (2010)
14. Zhang et al. (1995)

The elemental composition values listed here are on a DAF wt.% basis. The aromaticity values (f_a') are the corrected aromaticity, without the carbonyl contributions. The other NMR parameters are actual measured values. ASTM volatile matter is also on a DAF wt.% basis. If no ASTM volatile matter is reported for a specific sample, that sample was excluded from the analysis if the model form of interest used the ASTM volatile matter as a variable.

Table B-3. Coal Aromaticity Data Set

Source	Coal	Rank	Elemental Composition					V_{ASTM}	M_δ	M_{cl}	p_0	$\sigma+1$	f_a'
			C	H	O	N	S						
1, 2	Beulah-Zap	ligA	72.9	4.83	20.34	1.15	0.7	49.8	40	269	0.64	4.1	0.54
1, 2	Wyodak	subC	75	5.35	18.02	1.12	0.47	49	42	408	0.55	5.6	0.55
1, 2	Blind Canyon	hvBb	80.7	5.76	11.58	1.57	0.37	48.1	36	366	0.49	5.1	0.64
1, 2	Illinois #6	hvCb	77.7	5	13.51	1.37	2.38	47.4	27	322	0.63	5	0.72
1, 2	Pittsburgh #8	hvAb	83.2	5.32	8.83	1.64	0.89	41.7	28	330	0.64	4.7	0.72
1, 2	Stockton	hvAb	82.6	5.25	9.83	1.56	0.65	37.6	20	272	0.69	4.8	0.75
1, 2	Upper Freeport	mvb	85.5	4.7	7.51	1.55	0.74	31.6	17	312	0.67	5.3	0.81
1, 2	Pocahontas #3	lvb	91.1	4.44	2.47	1.33	0.5	19.5	13	307	0.74	4.4	0.86
2	Zap	lig	66.5	4.8	26.5	1.1	1.1	-[a]	46	339	0.63	4.5	0.58
2	Rosebud	subB	72.1	4.9	20.3	1.2	1.2	-	48	459	0.57	5.8	0.53
2	Illinois #6	hvBb	73.9	5.1	15.4	1.4	4.2	-	29	267	0.61	4.6	0.67
1, 3	Lower Wilcox	ligA	72.3	5.21	20.11	1.35	0.94	78.7	36	297	0.59	4.8	0.56
1, 3	Dietz	subB	76	5.23	17.27	0.94	0.53	44.2	37	310	0.54	4.7	0.56
1, 3	Buck Mountain	an	95.4	1.38	1.86	0.84	0.53	3.9	7.5	661.5	1	4.7	0.94
1, 4	Blue #1	hvCb	75.6	5.26	17.33	1.32	0.49	48.2	47	410	0.42	5.0	0.53
1, 4	Pittsburgh #8	hvAb	84.2	5.54	7.56	1.65	1.01	38.7	34	356	0.45	5.0	0.6
1, 4	Illinois #6	hvAb	74.1	4.96	13.18	1.45	6.29	43.4	34	270	0.56	4.1	0.67
1, 4	Beulah-Zap	ligA	66.6	4.26	25.16	1.12	2.89	49.6	52	440	0.48	5.2	0.57
1, 4	Pocahontas #3	mvb	88.8	4.37	5.14	1.06	0.6	17.2	23	316	0.59	4.0	0.77
1	not named	hvb	87.9	3.77	4.65	1.31	2.37	36.9	21	264	0.64	4.8	-[a]
1	not named	lvb	88.5	4.94	1.4	-[a]	1.75	19.3	19	295	0.65	5.0	-
1	Bottom	subC	70.7	5.83	20.83	1.47	1.18	53.6	55	505	0.42	5.8	-
1	Adaville #1	hvCb	72.5	5.22	20.09	1.17	1.04	45.6	43	381	0.55	5.1	-
1	Beulah-Zap	ligA	68.5	4.94	24.96	1	0.64	61.7	42	329	0.68	4.6	-
1	Sewell	mvb	85.5	4.91	7.12	1.72	0.72	33.2	72	483	0.72	4.5	-
1	Kentucky #9	hvBb	79.4	5.62	8.57	1.74	4.71	44.6	35	370	0.48	5.3	-
1	Elkhorn #3	hvAb	82.7	5.73	8.76	1.78	0.99	40.5	21	247	0.64	4.7	-
1	Lykens Valley #2	an	93.8	2.72	1.96	0.92	0.62	5.1	13	216	1	3.8	-
1	Deadman	subA	76.5	5.24	15.95	1.53	0.76	40.6	34	361	0.55	5.2	-

Table B-3. Coal Aromaticity Data Set, CONTINUED

Source	Coal	Rank	Elemental Composition					V_{ASTM}	M_δ	M_{cl}	p_0	$\sigma+1$	f_a'
			C	H	O	N	S						
1	Penna. Semian. C	sa	88.4	4.02	5.47	1.24	0.86	11.8	4	231	1	6.0	-[a]
1	Lower Kittanning	lvb	86.2	4.86	4.64	1.81	2.45	21.6	21	354	0.35	4.5	-
1	Smith-Roland	subC	67.4	5.37	24.39	1	1.84	53.4	46	282	0.64	3.7	-
1	Lower Hartshorne	lvb	91.2	4.56	1.53	1.82	0.89	23.5	14	225	0.69	4.4	-
5	Yallourn	brown	65.31	4.76	29.22	0.52	0.18	53.1	46	452	0.6	6.1	0.57
5	South Banko	brown	71.37	5.36	21.55	1.18	0.55	51.3	46	405	0.55	5.3	0.54
5	Taiheiyo	sub	76.72	6.35	15.59	1.13	0.21	54.7	47	430	0.4	5.5	0.51
5	Miike	hvb	79.91	6.13	8.3	1.18	4.48	53	31	329	0.57	5.0	0.64
5	Hunter Valley	hvb	82.82	5.43	9.18	2.08	0.48	37.2	21	266	0.67	4.9	0.71
5	Pittsburgh	hvb	82.77	5.48	6.73	1.64	3.38	42.5	28	311	0.62	4.5	0.7
5	Upper Freeport	mvb	84.15	5.13	4.6	1.55	4.56	33.4	18	317	0.67	5.3	0.81
5	Pocahontas	lvb	91.57	4.57	1.74	1.36	0.76	20.1	13	305	0.74	4.4	0.86
6	Schoningen	lig	70.8	5.53	15.75	0.4	7.51	58.59	-[a]	-	-	-	0.67
7		an	81.4	3.51	11.12	1.16	2.81	-[a]	-	-	-	-	0.7368
8			74.52	5.07	16.77	1.6	2.04	-	-	-	-	-	0.59
8			75.14	5.81	15.16	1.43	2.46	-	-	-	-	-	0.58
8			77.18	6.45	13.42	1.33	1.62	-	-	-	-	-	0.47
8			74.53	6.36	13.17	1.25	4.69	-	-	-	-	-	0.46
8			75.33	6.47	13.94	1.26	3	-	-	-	-	-	0.46
8			73.15	5.79	15.85	1.47	3.74	-	-	-	-	-	0.47
9	Arino		69.8	3.3	21.7	0.3	4.9	40.7	-	-	-	-	0.58
9	Canizar		65.3	3.3	26.6	0.2	4.6	42.5	-	-	-	-	0.6
9	Arino		67.2	3.5	23.1	0.5	5.7	42.2	-	-	-	-	0.59
9	Castellote		73.4	3.8	19.9	0.5	2.4	39.7	-	-	-	-	0.61
9	Utrillas		68.8	4.5	24.1	0.5	2.1	40.4	-	-	-	-	0.58
9	Estercuel		59.7	3.3	33	0.6	4.3	40.3	-	-	-	-	0.58
9	Torrelapaja		73.7	4.2	19.1	0.5	2.5	40.1	-	-	-	-	0.6
9	Corta Alloza		63.8	3	28.4	0.6	4.2	43.3	-	-	-	-	0.53
9	Mequinenza		69.2	4.7	16.9	0.7	8.5	57.5	-	-	-	-	0.43

Table B-3. Coal Aromaticity Data Set, CONTINUED

Source	Coal	Rank	Elemental Composition					V_{ASTM}	M_δ	M_{cl}	p_0	$\sigma + 1$	f_a'
			C	H	O	N	S						
10		brown	69.2	5.14	24.49	0.89	0.28	54.63	-[a]	-	-	-	0.3412
11	Loy Yang		70	4.9	23.4	0.6	0.4	-[a]	-	-	-	-	0.53
11	Callide		68.3	4.5	22.6	0.8	0.2	-	-	-	-	-	0.76
11	Wambo		76	5.3	12.7	2.9	0.4	-	-	-	-	-	0.61
11	Liddell		74.7	4.9	10.7	1.9	0.4	-	-	-	-	-	0.68
11	Bayswater		72.3	4.9	8	1.8	0.3	-	-	-	-	-	0.64
11	Bulli		77.8	4.4	3.2	2.4	0.3	-	-	-	-	-	0.74
12	d1385		80	5.9	10.2	1.4	2	46.35	-	-	-	-	0.609
12	d1385		81.7	5.7	10.8	1.3	0.5	41.95	-	-	-	-	0.628
12	d1281		80.5	5.6	9.5	1.2	3.2	42.75	-	-	-	-	0.643
12	d1281		82.2	5.8	10.2	1.2	0.6	41.21	-	-	-	-	0.677
12	PR d2		84	6.3	5.6	1.2	3	49.26	-	-	-	-	0.588
12	PR d2		83.6	6	8.5	1	0.8	45.62	-	-	-	-	0.708
12	d1334		79.2	5.9	8.2	0.9	5.7	47.72	-	-	-	-	0.666
12	PR d6		81.8	6	4.6	0.8	6.9	48.26	-	-	-	-	0.625
12	PR d6		84.7	6.1	5.9	1	2.4	46.25	-	-	-	-	0.638
12	PR d6		84.6	6.2	7.7	0.9	0.7	44.50	-	-	-	-	0.675
12	d1215		85	5.3	6	1.1	2.7	33.71	-	-	-	-	0.695
12	d1222		85.7	5.4	4.8	1.2	3	33.37	-	-	-	-	0.728
12	d1222		87.4	5.2	5	1.2	1.2	29.92	-	-	-	-	0.752
12	d1222		85.2	5.1	4.7	1	4	29.34	-	-	-	-	0.758
12	d1241		87.6	5.2	4.7	1.3	1.2	30.76	-	-	-	-	0.745
12	d1241		86.2	4.9	3.8	1.1	4	28.25	-	-	-	-	0.769
12	Cape		76.7	4.9	17	0.7	0.7	36.27	-	-	-	-	0.711
12	Farewell-1		79.8	6.4	9.2	1.1	3.5	50.84	-	-	-	-	0.598
12	Farewell-1		81.9	6.1	8.5	1.3	2.2	43.51	-	-	-	-	0.684
12	Farewell-1		83.6	6.4	7.3	1.4	1.3	45.85	-	-	-	-	0.652
12	Farewell-1		84.7	6.1	6.9	1.4	0.9	42.79	-	-	-	-	0.691
12	Kupe		71.1	5.1	18.9	1.2	3.8	49	-	-	-	-	0.617

Table B-3. Coal Aromaticity Data Set, CONTINUED

Source	Coal	Rank	Elemental Composition					V_{ASTM}	M_δ	M_{cl}	p_0	$\sigma+1$	f_a'
			C	H	O	N	S						
12	South-4		76.9	5.6	15.3	1.7	0.6	41.81	-[a]	-	-	-	0.653
12	Tahi-1		73.9	5.6	18.7	1.2	0.7	48.14	-	-	-	-	0.552
12	Tahi-1		72.7	5	20.5	1.1	0.8	42.34	-	-	-	-	0.641
12	North		77.8	5.7	14.3	1.2	1	43.35	-	-	-	-	0.653
12	Tasman-1		80	6	11.8	1.4	1.2	45.03	-	-	-	-	0.633
12	Tasman-1		80.7	6.4	10.7	1.3	1	46.82	-	-	-	-	0.63
12	Tasman-1		80.9	6	10.7	1.4	1.1	43.78	-	-	-	-	0.664
12	Toru-1		73	5.3	18.2	1.4	2.1	46.67	-	-	-	-	0.567
12	Toru-1		79.5	5.5	12.1	1.4	1.6	42.31	-	-	-	-	0.695
12	Tane-1		79.9	5.7	12	1.3	1	41.71	-	-	-	-	0.656
12	Tane-1		81.7	6.1	9.6	1.2	1.5	43.78	-	-	-	-	0.671
12	Tane-1		83.5	5.9	8.7	1.3	0.7	38.28	-	-	-	-	0.706
12	Tane-1		83.4	6.3	8.2	1.3	0.8	42.19	-	-	-	-	0.665
13	HM		83.26	3.44	12.2	0.77	0.33	24.52	-	-	-	-	0.877
13	LW		79.71	3.84	15.28	0.71	0.46	30.91	-	-	-	-	0.839
13	SD		79.53	4.16	14.92	0.91	0.48	33.72	-	-	-	-	0.807
13	PS		80.41	5.2	11.95	1.38	1.06	37.19	-	-	-	-	0.756
14	Xundian	lig	66.08	5.21	26.46	0.96	1.29	-	-	-	-	-	0.65
14	Huelinhe	lig	71.08	4.75	21.96	1.09	1.12	-	-	-	-	-	0.75
14	Fushun		76.6	5.44	16.3	1.15	0.5	-	-	-	-	-	0.77
14	Laohutai		79.02	5.58	13.45	1.3	0.64	-	-	-	-	-	0.8
14	Fengfeng fat		87.8	5.15	4.77	1.11	1.16	-	-	-	-	-	0.85
14	Fengfeng coking		88.03	5.27	4.59	1.64	0.49	-	-	-	-	-	0.85
14	Fengfeng lean		89.29	4.07	3.67	1.14	1.83	-	-	-	-	-	0.9
14	Shanxi Meagre		90.6	3.72	2.36	0.85	2.46	-	-	-	-	-	0.93
14	Jincheng	an	92.79	2.79	3.06	0.99	0.38	-	-	-	-	-	0.96

[a] Some sources did not report information including V_{ASTM} and NMR parameters (including aromaticity). These samples were not used in correlations where this information was necessary. Some sources also did not include coal name or rank information.

B.3 Fuel Heating Value Data Set

The sources for this data set are detailed in Table 2-5. Table B-4 details the entire heating value data set. Included in Table B-4 are the following columns: (1) source, which is either the institution or primary author of the cited paper, (2) the fuel type or major fuel group from Table 7-1, (3) coal rank (if the fuel is coal and rank was reported), (4) the country of origin (mostly coals with reported countries of origin), (5) the CHONS wt.% on a dry, ash-free basis, and (6) the higher heating value (HHV) in MJ/kg and also on a dry, ash-free basis. Appropriate abbreviations are defined both in the nomenclature section. Sources are in the same order in this table as in Table 2-5.

Table B-4. Heating Value of Various Fuels

Source	Fuel Type	Coal Rank	Country	C	H	O	N	S	HHV
Argonne	Coal	MVB	US	85.50	4.70	7.51	1.55	0.74	36.08
	Coal	SUB	US	75.03	5.35	18.03	1.12	0.47	29.88
	Coal	HVB	US	77.72	5.00	13.52	1.37	2.38	32.91
	Coal	HVB	US	83.30	5.33	8.84	1.64	0.89	34.97
	Coal	LVB	US	91.23	4.45	2.47	1.33	0.50	36.77
	Coal	HVB	US	80.71	5.76	11.58	1.57	0.37	34.00
	Coal	HVB	US	82.68	5.26	9.84	1.56	0.65	34.31
	Coal	Lig	US	72.97	4.83	20.35	1.15	0.70	28.35
Penn State Coal Data Bank	Coal	LVB	US	91.53	4.38	2.10	1.10	0.63	36.56
	Coal	HVC	US	74.99	5.64	17.21	1.40	0.75	32.14
	Coal	HVA	US	83.34	5.41	8.11	1.58	1.58	34.67
	Coal	subB	US	76.03	5.23	17.28	0.94	0.53	30.78
	Coal	HVC	US	78.10	4.92	9.61	1.50	5.87	32.82
	Coal	HVC	US	80.06	5.26	12.89	1.23	0.56	32.33
	Coal	LigA	US	71.57	5.04	20.81	0.95	1.63	28.25
	Coal	LVB	US	88.83	4.68	3.29	1.64	1.56	35.96
	Coal	LigA	US	72.39	5.21	20.12	1.35	0.94	29.27
	Coal	subB	US	73.78	2.77	20.95	1.11	1.38	30.54
	Coal	HVA	US	84.04	5.58	7.82	1.54	1.01	35.04
	Coal	an	US	95.42	1.38	1.86	0.84	0.53	34.33
	Coal	MVB	US	88.85	5.12	3.17	1.87	0.99	36.39
	Coal	MVB	US	81.85	5.50	10.29	1.66	0.71	34.05

Table B-4. Heating Value of Various Fuels, CONTINUED

Source	Fuel Type	Coal Rank	Country	C	H	O	N	S	HHV
Penn State, cont.	Coal	LigA	US	72.57	4.71	20.76	1.10	0.86	27.88
Foster Wheeler	Coal	MVB	US	84.67	5.34	5.14	2.14	2.71	34.75
	Coal	LigA	US	68.60	4.85	23.00	1.37	2.18	26.82
	Coal	Sub	US	71.83	5.39	20.85	1.44	0.49	29.03
	Coal	HVB	US	77.54	5.52	10.23	2.11	4.60	32.46
	Coal	lig	US	59.58	6.89	28.94	1.06	3.53	24.19
	Coal	HVA	US	76.71	5.83	10.22	1.56	5.68	31.46
	Coal	HVB	US	76.68	5.83	10.91	1.75	4.82	31.86
Ahmed	Coal	sub	Spain	71.17	3.38	17.12	0.90	7.43	28.04
	Char	-	Spain	86.85	2.38	4.88	1.13	4.76	29.70
Proscia	Coal	HVA	US	82.36	5.51	8.56	1.65	1.92	33.92
	Coal	LVB	US	86.47	4.75	4.85	1.63	2.30	35.14
	Char	-	US	83.01	5.24	8.23	1.68	1.84	33.56
	Char	-	US	83.03	4.68	8.64	1.71	1.94	32.85
	Char	-	US	85.22	4.41	6.96	1.85	1.56	32.75
	Char	-	US	85.42	4.03	7.13	1.81	1.60	31.73
	Char	-	US	88.44	4.73	3.55	1.61	1.69	35.39
	Char	-	US	88.20	4.50	3.84	1.64	1.82	33.65
	Char	-	US	88.62	4.21	3.76	1.62	1.79	34.99
	Char	-	US	89.52	3.50	3.62	1.65	1.72	35.64
	Tar	-	US	85.02	6.40	5.68	1.63	1.27	35.12
	Tar	-	US	85.12	5.91	5.88	1.77	1.32	35.22
	Tar	-	US	85.70	5.82	5.47	1.78	1.23	35.24
	Tar	-	US	86.38	5.60	5.08	1.80	1.14	34.65
Shamsi	Coal	sub	US	53.21	4.28	40.92	0.72	0.87	21.15
	Char	-	US	69.32	3.52	25.03	1.08	1.05	27.34
	Char	-	US	69.51	3.61	24.76	1.03	1.09	27.50
	Char	-	US	65.61	3.49	29.09	0.96	0.85	25.34
	Char	-	US	63.79	3.68	30.48	1.00	1.05	24.93
Lazaro	Coal	lig	Spain	68.70	5.39	13.85	0.96	11.10	23.23
	Coal	lig	Spain	75.90	5.34	12.27	0.71	5.78	20.21
Ferrara	Coal	bit	S. Africa	93.46	3.09	1.21	1.63	0.61	34.57
	Coal	sub	Italy	73.67	5.16	11.00	1.85	8.32	29.49
	biomass	-	Italy	58.15	6.25	35.53	0.07	0.00	20.79
Tomasz.	coal	LigB	Poland	64.68	5.05	27.70	0.69	1.88	25.20
	coal	LigB	Poland	67.31	4.97	24.96	0.84	1.92	26.17
	coal	LigB	Poland	68.27	5.02	25.15	0.75	0.80	26.41
	coal	LigA	Poland	70.33	6.19	21.64	0.69	1.15	29.37
	coal	SubB	Poland	78.19	4.48	14.54	1.22	1.58	30.94

Table B-4. Heating Value of Various Fuels, CONTINUED

Source	Fuel Type	Coal Rank	Country	C	H	O	N	S	HHV
Tomasz., cont.	coal	SubA	Poland	78.65	5.08	13.62	1.21	1.45	31.63
	coal	hvCb	Poland	80.81	4.76	11.77	1.26	1.39	31.55
	coal	hvCb	Poland	83.75	5.11	9.12	1.43	0.59	33.94
	coal	hvAb	Poland	84.04	5.00	8.32	1.47	1.17	33.86
	coal	hvCb	Poland	82.92	5.21	8.50	1.69	1.68	33.14
	coal	hvAb	Poland	85.44	4.82	7.92	1.46	0.36	33.89
Tourunen	coal	bit	Poland	81.51	5.04	11.14	1.40	0.91	33.60
Ding	coal	lig	China	71.40	2.74	23.70	1.41	0.75	33.10
	coal	bit	China	84.45	2.48	11.06	1.20	0.82	30.26
	petcoke	-	China	89.39	3.73	4.04	0.75	2.09	36.18
	petcoke	-	China	88.23	3.79	1.35	0.36	6.27	36.88
Kajitani	Coal	bit	Aus.	82.50	5.10	10.50	1.40	0.50	34.69
	Coal	bit	China	78.40	5.60	14.90	1.00	0.10	30.81
Roberts	Coal	-	Aus.	82.00	5.23	10.80	1.70	0.27	37.84
	Coal	-	Aus.	82.90	5.95	8.40	1.83	0.88	31.33
	Coal	-	Aus.	76.00	5.85	16.50	1.15	0.49	31.88
Wang	Coal	bit	UK	82.60	6.15	8.75	1.98	0.52	36.46
	Coal	bit	UK	79.77	5.29	12.55	1.66	0.73	35.17
Franchetti	Coal	bit	Aus.	84.79	5.19	7.70	1.77	0.52	34.32
Suggate	Coal	-	New Zealand	80.60	5.90	10.20	1.40	2.00	33.96
	Coal	-	New Zealand	81.70	5.70	10.80	1.30	0.50	34.10
	Coal	-	New Zealand	80.50	5.60	9.50	1.20	3.20	34.09
	Coal	-	New Zealand	82.20	5.80	10.20	1.20	0.60	34.66
	Coal	-	New Zealand	84.00	6.30	5.60	1.20	3.00	35.78
	Coal	-	New Zealand	83.60	6.00	8.50	1.00	0.80	35.18
	Coal	-	New Zealand	79.20	5.90	8.20	0.90	5.70	34.01
	Coal	-	New Zealand	81.80	6.00	4.60	0.80	6.90	35.32
	Coal	-	New Zealand	84.70	6.10	5.90	1.00	2.40	36.10
	Coal	-	New Zealand	84.60	6.20	7.70	0.90	0.70	36.24
	Coal	-	New Zealand	85.00	5.30	6.00	1.10	2.70	35.70

Table B-4. Heating Value of Various Fuels, CONTINUED

Source	Fuel Type	Coal Rank	Country	C	H	O	N	S	HHV
Suggate, cont.	Coal	-	New Zealand	85.70	5.40	4.80	1.20	3.00	36.12
	Coal	-	New Zealand	87.40	5.20	5.00	1.20	1.20	36.38
	Coal	-	New Zealand	85.20	5.10	4.70	1.00	4.00	35.73
	Coal	-	New Zealand	87.60	5.20	4.70	1.30	1.20	36.63
	Coal	-	New Zealand	86.20	4.90	3.80	0.10	4.00	35.65
	Coal	-	New Zealand	76.70	4.90	17.00	0.70	0.70	30.40
	Coal	-	New Zealand	79.80	6.40	9.20	1.10	3.50	34.12
	Coal	-	New Zealand	81.90	6.10	8.50	1.30	2.20	34.36
	Coal	-	New Zealand	83.60	6.40	7.30	1.40	1.30	35.23
	Coal	-	New Zealand	84.70	6.10	6.90	1.40	0.90	35.37
	Coal	-	New Zealand	71.10	5.10	18.90	1.20	3.80	28.01
	Coal	-	New Zealand	76.90	5.60	15.30	0.70	0.60	31.31
	Coal	-	New Zealand	73.90	5.60	18.70	1.20	0.70	29.93
	Coal	-	New Zealand	72.70	5.00	20.50	1.10	0.80	28.62
	Coal	-	New Zealand	77.80	5.70	14.30	1.20	1.00	31.82
	Coal	-	New Zealand	80.00	6.00	11.80	1.40	1.20	33.28
	Coal	-	New Zealand	80.70	6.40	10.70	1.30	1.00	33.89
	Coal	-	New Zealand	80.90	6.00	10.70	1.40	1.10	33.52
	Coal	-	New Zealand	73.00	5.30	18.20	1.40	2.10	29.18
	Coal	-	New Zealand	79.50	5.50	12.10	1.40	1.60	32.74
	Coal	-	New Zealand	79.90	5.70	12.00	1.30	1.00	33.04

Table B-4. Heating Value of Various Fuels, CONTINUED

Source	Fuel Type	Coal Rank	Country	C	H	O	N	S	HHV
Suggate, cont.	Coal	-	New Zealand	81.70	6.10	9.60	1.20	1.50	34.15
	Coal	-	New Zealand	83.50	5.90	8.70	1.30	0.70	34.79
	Coal	-	New Zealand	83.40	6.30	8.20	1.30	0.80	35.26
	Peat	-	New Zealand	61.10	5.50	32.20	0.70	0.50	22.00
	Peat	-	New Zealand	63.70	5.70	29.40	0.70	0.50	22.92
	Peat	-	New Zealand	62.40	5.20	31.20	0.60	0.60	21.56
	Peat	-	New Zealand	63.50	5.30	30.20	0.50	0.50	22.37
	Peat	-	New Zealand	63.70	5.40	30.00	0.50	0.50	22.37
	Peat	-	New Zealand	62.40	5.10	31.10	0.50	1.10	20.02
	Peat	-	New Zealand	61.80	5.00	31.60	0.60	1.20	21.12
	Peat	-	New Zealand	65.00	6.20	27.50	0.70	0.70	24.97
Ra	Coal	hvBb	Indo	71.13	5.04	14.85	1.68	1.38	28.50
Reichel	Coal	lig	Germ	67.50	4.80	26.60	0.80	0.30	26.45
Riaza	Coal	an	Spain	94.70	1.60	2.00	1.00	0.70	34.03
	Coal	semi-an	Spain	91.70	3.50	1.30	1.90	1.60	35.61
	Coal	MVB	Mexico	86.20	5.50	5.90	1.60	0.80	35.23
	Coal	HVB	S. Africa	81.50	5.00	10.50	2.10	0.90	32.71
Riaza	Coal	HVB	Col	73.00	5.20	18.60	2.20	1.00	33.10
	Biomass	-	UK	51.49	3.14	44.70	0.55	0.12	17.93
Riaza	Biomass	-	UK	52.80	6.50	39.10	1.60	0.00	21.75
	Biomass	-	UK	52.70	5.80	41.20	0.20	0.10	20.88
Seo	Coal	-	China	82.68	4.87	11.26	1.08	0.11	33.69
Shadle	Coal	sub	US	73.34	5.51	19.79	0.89	0.47	28.91
	Coal	bit	US	78.46	5.70	10.58	1.25	4.02	31.82
	Coal	bit	US	84.12	5.03	9.05	1.41	0.39	30.98
Shaw	Coal	-	-	84.42	5.45	7.06	1.69	1.38	34.98
	Coal	-	-	82.37	5.52	9.07	1.86	1.18	33.99
	Coal	-	-	84.12	5.77	5.92	1.73	2.46	35.44
	Coal	lig	US	58.91	6.76	33.21	0.91	0.21	30.00

Table B-4. Heating Value of Various Fuels, CONTINUED

Source	Fuel Type	Coal Rank	Country	C	H	O	N	S	HHV
Shaw, cont.	Coal	hvAb	US	82.69	5.85	7.81	1.65	2.00	34.28
	Coal	SubB	US	76.00	5.27	17.27	0.94	0.53	30.76
	Coal	hvBb	US	78.07	4.92	9.65	1.50	5.87	32.80
	Coal	hvCb	US	80.04	5.26	12.91	1.23	0.56	32.33
	Coal	lig	US	71.55	5.04	20.83	0.95	1.63	28.25
	Coal	hvCb	US	74.97	5.64	17.23	1.40	0.75	32.13
	Coal	-	-	79.09	5.45	10.60	1.34	3.52	32.22
	Coal	lig	-	70.05	5.21	21.55	1.01	1.35	27.64
	Coal	lig	US	70.30	5.23	20.02	0.75	3.67	28.45
	Coal	lig	US	72.34	5.21	20.18	1.35	0.94	29.25
Tufano	Coal	HVB	US	81.26	5.57	10.62	1.54	2.16	33.42
Vascellari	Coal	sub	Aus.	75.80	4.98	16.73	1.38	1.12	29.17
	Coal	bit	Aus.	86.35	5.22	7.70	1.89	1.20	34.01
	Coal	Semi-an	Aus.	92.81	3.69	0.89	1.90	0.71	35.83
	Coal + Limestone	Semi-an	Aus.	93.41	3.96	0.00	1.92	0.70	35.28
	Coal	sub	Aus.	78.80	5.80	14.04	1.01	0.35	32.01
Weiland	Coal	HVB	US	72.10	5.40	15.66	1.35	5.50	27.19
	Biomass	-	US	49.16	6.36	43.73	0.63	0.13	20.14
Wen	Coal	bit	Aus.	84.79	5.19	7.70	1.77	0.52	34.32
Wu	Coal	lig	US	69.21	5.47	21.76	2.04	0.76	28.12
	Coal	lig	US	73.29	5.16	19.19	1.46	0.90	28.57
Sahu	Coal	hvBb	-	80.47	5.69	9.33	1.82	1.72	33.25
	Coal	hvBb	-	83.85	5.78	5.88	1.39	3.10	35.40
	Coal	hvAb	-	82.66	5.43	8.09	1.50	1.50	33.69
Parkash	Coal	sub	Canada	75.80	5.10	16.90	1.70	0.50	29.80
	Coal	sub	Canada	75.80	4.20	18.40	1.10	0.50	29.70
	Coal	sub	Canada	75.10	4.10	19.50	0.90	0.40	28.40
	Coal	sub	Canada	75.00	4.40	19.30	1.10	0.20	28.80
	Coal	sub	Canada	75.70	4.10	18.50	1.20	0.50	29.20
	Coal	sub	Canada	74.20	4.50	19.30	1.60	0.40	28.30
	Coal	sub	Canada	73.40	4.40	19.20	1.60	1.20	27.90
	Coal	sub	Canada	74.40	5.00	18.50	1.50	0.60	29.40
	Coal	sub	Canada	73.70	4.60	19.20	1.70	0.80	28.10
	Coal	sub	Canada	76.80	5.10	15.60	1.70	0.80	28.70
	Coal	sub	Canada	75.80	5.40	16.10	1.80	0.90	30.60
Babcock & Wilcox	Coal	HVB	US	81.44	5.68	8.57	1.80	2.51	33.84
	Coal	lig	US	71.93	5.33	20.02	1.52	1.21	28.67
Miller	Coal	an	US	93.50	1.90	2.40	1.20	1.00	25.26
	Coal	an	US	90.80	2.60	5.20	0.80	0.60	29.31

Table B-4. Heating Value of Various Fuels, CONTINUED

Source	Fuel Type	Coal Rank	Country	C	H	O	N	S	HHV
Miller, cont.	Coal	an	US	91.30	3.90	3.00	0.60	1.20	32.85
	Coal	semi-an	US	89.60	3.80	3.60	1.40	1.60	26.04
	Coal	semi-an	US	91.50	3.40	2.70	1.60	0.80	32.79
	Coal	semi-an	US	92.20	3.90	1.00	2.10	0.80	33.43
	Coal	LVB	US	88.80	4.70	3.20	1.60	1.60	32.62
	Coal	LVB	US	87.20	4.70	3.30	1.50	3.30	29.16
	Coal	MVB	US	87.00	5.50	2.90	1.70	2.90	32.58
	Coal	MVB	US	87.40	5.90	4.30	1.70	0.70	34.63
	Coal	MVB	US	88.20	5.00	4.60	1.50	0.70	34.59
	Coal	hvAb	US	83.30	5.70	8.30	1.40	1.30	31.48
	Coal	hvAb	US	84.50	5.60	7.50	1.40	1.00	30.87
	Coal	hvAb	US	85.20	5.50	5.80	1.50	2.00	31.82
	Coal	hvAb	US	81.30	6.20	10.50	1.60	0.40	32.38
	Coal	hvAb	US	86.50	5.50	6.00	1.40	0.60	32.32
	Coal	hvBb	US	82.80	5.50	9.30	1.60	0.80	31.10
	Coal	hvBb	US	80.60	5.70	11.40	1.40	0.90	30.85
	Coal	hvBb	US	79.10	5.80	8.90	1.40	4.80	29.51
	Coal	hvBb	US	79.90	5.60	8.30	1.60	4.60	29.38
	Coal	hvCb	US	77.50	5.50	14.60	1.80	0.60	29.68
	Coal	hvCb	US	78.40	5.20	10.10	1.40	4.90	29.59
	Coal	hvCb	US	79.70	4.90	10.40	1.60	3.40	28.59
	Coal	subB	US	75.50	6.10	16.90	1.00	0.50	28.25
	Coal	subB	US	75.30	5.10	17.60	1.10	0.90	27.18
	Coal	subB	US	75.50	6.20	16.90	1.00	0.40	28.42
	Coal	subB	US	75.10	5.20	18.50	0.90	0.30	27.35
	Coal	LigA	US	73.10	4.50	20.60	1.00	0.80	25.73
	Coal	lig	US	72.30	5.20	20.20	1.40	0.90	22.99
	Coal	an	Germ	91.80	3.60	2.60	1.40	0.70	35.91
	Coal	an	Spain	87.20	2.50	8.00	0.90	1.40	32.77
	Coal	an	Russia	94.60	1.80	1.80	1.00	0.80	33.94
	Coal	semi-an	Russia	90.00	4.20	2.10	1.50	2.20	35.77
	Coal	brown	Germ	68.30	5.00	27.50	0.50	0.50	26.38
	Coal	lig	Germ	74.00	5.50	14.50	1.40	4.60	29.73
	Coal	lig	Greece	60.50	6.20	30.60	1.30	1.40	24.45
	Coal	brown	Yugoslavia	61.90	4.30	29.80	0.90	3.10	21.98
	Coal	brown	Turkey	61.40	5.10	29.60	0.80	5.10	23.70
	Coal	lig	Poland	71.40	5.80	20.20	0.60	2.00	29.10
	Coal	lig	Russia	72.20	4.30	22.10	1.10	0.30	26.03

Table B-4. Heating Value of Various Fuels, CONTINUED

Source	Fuel Type	Coal Rank	Country	C	H	O	N	S	HHV
Miller, cont.	Coal	hvAb	Poland	82.90	5.20	9.90	1.00	1.00	33.84
	Coal	lvb	Russia	88.00	4.50	2.90	1.50	3.10	35.82
	Coal	hvAb	Russia	83.00	5.10	5.60	1.50	4.80	35.22
	Coal	hvBb	Russia	82.00	5.50	8.50	1.50	2.50	33.96
	Coal	hvCb	Russia	77.00	5.60	12.30	1.60	3.50	32.33
	Coal	mvb	India	83.60	4.50	9.90	1.30	0.70	34.04
	Coal	MVB	S. Africa	84.60	4.90	7.20	2.20	1.10	32.73
	Coal	hvAb	Aus.	81.20	6.10	11.00	1.10	0.60	34.03
	Coal	hvBb	Aus.	77.40	5.50	15.30	1.20	0.60	31.38
Al-Abbas	Coal	brown	Aus.	69.00	4.72	25.44	0.53	0.31	28.13
Alvarez	Coal	an	Spain	94.70	1.60	2.00	1.00	0.70	34.03
	Coal	hvb	S. Africa	81.50	5.00	10.50	2.10	0.90	32.71
Benito	Coal	lig	Spain	65.30	5.50	17.00	0.60	11.50	29.24
	Coal	lig	Spain	64.90	4.90	18.40	0.50	11.30	29.01
	Coal	lig	Spain	65.60	4.30	24.90	0.30	4.90	27.94
	Coal	lig	Spain	64.60	4.30	27.60	0.40	3.10	27.45
Bharadwaj	Biomass	-	US	49.01	6.07	44.82	0.07	0.01	19.43
	Biomass	-	US	48.80	6.09	42.47	2.40	0.23	19.52
Brewster	Coal	hvAb	-	84.00	6.00	7.70	1.80	0.60	35.10
	Coal	hvBb	-	80.00	5.90	8.70	2.10	3.40	33.90
	Coal	subC	-	72.60	5.50	20.10	1.10	0.60	29.80
Chakravarty	Tar	hvAb	US	74.70	8.90	12.10	2.20	2.10	36.53
	Tar	mvb	US	83.90	8.60	3.90	1.00	2.60	40.56
	Tar	hvAb	US	79.40	8.70	9.20	1.70	1.00	36.74
	Tar	hvAb	US	85.00	8.90	3.60	1.70	0.80	39.60
	Tar	hvAb	US	86.00	9.40	2.30	2.10	0.20	39.12
	Tar	subC	US	78.60	9.70	9.20	2.00	0.50	37.50
	Tar	hvAb	US	80.70	9.10	7.90	1.60	0.70	36.58
	Tar	hvAb	US	84.00	9.10	3.40	3.00	0.50	39.08
	Tar	hvAb	US	84.90	10.20	2.20	2.00	0.70	40.59
	Tar	-	US	78.70	11.70	7.10	1.80	0.70	38.88
	Tar	hvAb	US	79.70	8.70	8.10	3.00	0.50	34.97
	Oil shale tar	-	US	84.40	11.30	1.60	2.00	0.70	42.57
	Tar	hvCb	US	76.20	9.00	12.60	1.70	0.50	33.80
	Tar	hvAb	US	80.30	8.70	6.60	2.90	1.50	33.00
	Tar	hvAb	US	83.90	9.40	4.20	1.80	0.70	39.35
	Tar	subA	US	83.00	9.40	5.20	1.90	0.50	38.99
	Tar	hvCb	US	66.70	9.10	19.50	2.50	2.20	35.57

Table B-4. Heating Value of Various Fuels, CONTINUED

Source	Fuel Type	Coal Rank	Country	C	H	O	N	S	HHV
Chakravarty, cont.	Resinite tar	-	US	87.70	11.10	0.00	1.00	0.20	42.86
	Tar	hvAb	US	84.60	10.10	2.90	2.00	0.40	35.75
	Tar sand tar	-	US	87.30	11.30	0.00	1.70	0.30	44.14
	Tar	hvBb	US	73.10	8.60	14.30	1.60	2.40	36.61
	Tar	hvAb	US	82.40	9.60	4.40	2.40	1.20	31.93
	Oil shale tar	-	US	82.30	9.90	4.40	1.50	1.90	40.79
Channiwala	Biomass	-	-	50.58	5.74	43.68	0.00	0.00	20.64
	Biomass	-	-	50.41	5.71	43.46	0.41	0.00	20.25
	Biomass	-	-	51.53	5.98	41.88	0.62	0.00	21.05
	Biomass	-	-	46.76	5.87	47.12	0.25	0.00	19.92
	Biomass	-	-	48.73	5.94	45.29	0.03	0.00	20.02
	Biomass	-	-	47.64	6.02	46.03	0.31	0.00	19.29
	Biomass	-	-	49.40	6.36	43.92	0.32	0.00	19.12
	Biomass	-	-	49.73	6.45	43.62	0.20	0.00	20.96
	Biomass	-	-	49.21	6.39	44.32	0.08	0.00	20.66
	Biomass	-	-	47.66	6.27	45.78	0.29	0.00	19.76
	Biomass	-	-	48.76	6.27	44.82	0.15	0.00	20.24
	Biomass	-	-	49.16	6.00	43.37	1.48	0.00	19.40
	Biomass	-	-	47.90	6.20	44.93	0.97	0.00	18.65
	Biomass	-	-	46.14	6.18	47.67	0.01	0.00	20.00
	Biomass	-	-	46.13	5.75	50.47	0.00	0.00	19.32
	Biomass	-	-	46.20	6.15	47.61	0.04	0.00	19.70
	Biomass	-	-	44.81	5.80	49.16	0.35	0.00	18.65
	Biomass	-	-	48.88	6.60	43.94	0.57	0.00	18.66
	Biomass	-	-	47.84	6.29	45.19	0.68	0.00	18.79
	Biomass	-	-	45.72	5.25	47.31	1.72	0.00	19.05
	Biomass	-	-	46.98	6.16	46.70	0.15	0.00	19.35
	Biomass	-	-	44.28	5.72	49.67	0.44	0.00	16.60
	Biomass	-	-	43.36	6.15	50.31	0.18	0.00	17.77
	Biomass char	-	-	87.05	2.03	10.91	0.01	0.00	31.60
	Biomass char	-	-	89.37	1.07	6.48	3.08	0.00	31.26
	Biomass char	-	-	84.98	1.49	12.40	1.14	0.00	30.82
	Biomass char	-	-	91.61	0.75	6.22	1.42	0.00	32.05
	Biomass char	-	-	57.50	4.56	35.29	2.65	0.00	19.95

Table B-4. Heating Value of Various Fuels, CONTINUED

Source	Fuel Type	Coal Rank	Country	C	H	O	N	S	HHV
Channiwala, cont.	Liq Gas	-	-	74.85	25.15	0.00	0.00	0.00	55.35
	Liq Gas	-	-	81.70	18.30	0.00	0.00	0.00	50.24
	Liq Gas	-	-	82.40	17.60	0.00	0.00	0.00	49.60
	Liq Gas	-	-	0.00	5.92	0.00	0.00	94.08	16.41
	Liq Gas	-	-	83.22	16.78	0.00	0.00	0.00	48.54
	Liq Gas	-	-	85.01	14.99	0.00	0.00	0.00	47.04
	Liq Gas	-	-	92.25	7.75	0.00	0.00	0.00	41.79
	Liq Gas	-	-	88.34	11.66	0.00	0.00	0.00	44.53
	Liq Gas	-	-	85.10	14.90	0.00	0.00	0.00	47.30
	Liq Gas	-	-	86.50	13.20	0.00	0.00	0.00	45.70
	Liq Gas	-	-	85.43	11.40	0.20	0.16	2.80	42.92
	Liq Gas	-	-	37.50	12.50	50.00	0.00	0.00	22.69
	Liq Gas	-	-	57.29	7.74	33.37	1.11	0.20	24.82
	Liq Gas	-	-	76.72	6.46	14.68	2.14	0.00	31.31
	Liq Gas	-	-	71.40	8.90	14.20	5.60	0.00	34.30
	Coal	an	-	94.39	1.77	2.13	0.71	1.00	34.63
	Coal	hvb	US	84.17	5.57	5.46	1.34	3.46	35.40
	Coal	an	UK	91.26	3.88	3.10	0.60	1.15	35.84
	Coal	semi-an	UK	86.42	3.92	5.29	1.30	3.00	34.22
	Coal	hvBb	Germ	81.80	5.10	11.60	0.58	0.45	33.08
	Coal	mvb	US	89.70	4.77	3.31	1.52	1.01	36.25
	Coal	hvBb	US	76.05	5.87	7.63	1.65	8.70	33.18
	Coal	subC	US	69.87	5.38	23.08	0.72	0.95	28.53
	Coal	-	India	79.08	4.90	13.47	1.88	0.57	32.08
	Coal	lig	Germ	66.90	5.20	25.70	0.60	0.50	26.28
	Coke	-	-	96.47	0.47	1.06	0.92	1.08	33.69
	Charcoal	-	-	92.99	2.48	2.99	0.54	1.01	34.74
	Peat	-	-	57.73	5.15	36.08	1.03	0.00	21.31
	Biomass	-	-	50.58	5.74	43.68	0.00	0.00	20.64
	Biomass	-	-	52.48	5.70	41.50	0.21	0.11	20.51
	Biomass	-	-	51.53	5.93	42.33	0.10	0.10	20.50
	Biomass	-	-	50.69	6.19	43.04	0.06	0.02	20.40
	Biomass	-	-	49.96	5.41	42.79	0.58	0.03	19.83
	Biomass	-	-	48.72	5.99	44.67	0.39	0.01	19.44
	Biomass	-	-	47.67	6.12	46.00	1.51	0.02	19.12
	Biomass	-	-	50.49	6.03	44.57	0.43	0.01	19.53
	Biomass	-	-	46.22	6.06	45.00	2.58	0.14	18.61
	Biomass	-	-	48.73	5.94	45.29	0.03	0.00	20.02
	Biomass	-	-	49.16	6.00	43.37	1.48	0.00	19.36
	Biomass	-	-	50.05	6.22	42.85	0.69	0.17	21.21

Table B-4. Heating Value of Various Fuels, CONTINUED

Source	Fuel Type	Coal Rank	Country	C	H	O	N	S	HHV
Channiwala, cont.	Biomass	-	-	48.01	6.44	40.92	2.82	1.83	18.56
	Other	-	-	54.09	6.82	37.39	1.36	0.34	22.59
	Other	-	-	49.65	7.34	36.71	3.85	2.45	16.59
	Other	-	-	52.22	6.29	38.22	3.26	0.00	20.23
	Other	-	-	49.91	6.93	42.81	0.77	0.00	21.76
	Other	-	-	45.88	6.93	50.59	3.27	0.52	17.52
	Biomass char	-	-	82.17	3.65	13.76	0.21	0.21	31.77
	Other	-	-	93.37	1.36	3.06	1.87	0.34	31.73
	Other	-	-	80.57	3.14	15.66	0.49	0.12	29.56
	Char	lig	-	89.00	1.10	8.90	0.70	0.30	31.30
	Other	-	-	100.00	0.00	0.00	0.00	0.00	33.82
	Other	-	-	50.21	6.76	41.57	1.25	0.20	20.28
	Other	-	-	53.56	7.65	34.24	3.93	0.62	23.49
	Other	-	-	51.58	6.96	39.48	1.77	0.21	20.22
	Other	-	-	46.18	6.19	47.15	0.27	0.21	18.74
	Other	-	-	47.74	6.62	45.01	0.53	0.11	18.14
	Other	-	-	58.29	6.72	26.31	9.81	2.35	24.49
	Other	-	-	59.99	8.33	25.91	4.29	1.75	25.48
	Other	-	-	68.22	7.14	19.03	6.46	0.02	28.14
	Other	-	-	85.93	10.68	2.97	0.15	0.27	43.28
	Other	-	-	85.56	14.35	0.00	0.06	0.03	46.44
	Other	-	-	54.47	6.90	29.60	7.75	1.30	23.60
	Other	-	-	86.28	11.50	0.00	0.00	2.22	29.27
	Other	-	-	79.87	11.51	6.21	2.39	0.00	37.23
	Other	-	-	84.71	7.28	6.32	0.11	1.61	34.63
	Other	-	-	72.05	10.42	16.96	0.49	0.08	34.52
Chern	Coal	an	UK	95.20	2.90	0.30	1.00	0.60	35.64
	Coal	bit	UK	81.30	4.80	11.50	1.28	1.12	32.82
	Coal	bit	UK	80.40	5.70	10.90	1.37	1.63	33.00
	Coal	bit	UK	84.30	4.60	7.90	1.80	1.40	34.68
Cope	Coal	ligA	US	69.44	4.56	23.89	0.89	1.22	26.33
	Coal	subC	US	74.78	5.33	18.70	0.87	0.33	30.11
	Coal	hvCb	US	75.37	5.38	13.29	1.37	4.58	31.27
Costa	Coal	lig	Greece	58.24	6.12	28.89	1.88	4.87	23.31
	Coal	lig	S. Africa	70.48	4.41	22.62	1.79	0.69	26.07
	Coal	bit	UK	75.78	5.27	15.98	1.35	1.62	30.57
Daood	Coal	-	Russia	80.80	5.35	10.91	2.55	0.42	33.27
Eatough	Coal	hvBb	US	80.24	5.23	12.75	1.22	0.56	29.28
	Coal	lig	US	74.57	5.01	20.28	1.24	0.73	23.37

Table B-4. Heating Value of Various Fuels, CONTINUED

Source	Fuel Type	Coal Rank	Country	C	H	O	N	S	HHV
Hees	Coal	lig	Germ	69.05	4.83	25.13	0.69	0.30	26.88
Huéscar Medina	Biomass	-	Norway	53.39	6.22	40.29	0.00	0.00	21.31
	Biomass	-	Norway	59.89	5.68	33.55	0.77	0.00	22.51
	Biomass	-	-	53.36	5.95	42.01	0.66	0.00	21.39
	Biomass	-	-	58.44	5.63	35.17	0.76	0.00	23.38
	Coal	bit	UK	82.07	5.18	6.94	3.03	2.78	34.34
Ibarra	Coal	sub	Spain	69.80	3.30	21.70	0.30	4.90	21.10
	Coal	sub	Spain	65.30	3.30	26.60	0.20	4.60	20.60
	Coal	sub	Spain	67.20	3.50	23.10	0.50	5.70	22.30
	Coal	sub	Spain	73.40	3.80	19.90	0.50	2.40	22.10
	Coal	sub	Spain	68.80	4.50	24.10	0.50	2.10	23.70
	Coal	sub	Spain	59.70	3.30	33.00	0.60	4.30	21.60
	Coal	sub	Spain	73.70	4.20	19.10	0.50	2.50	24.70
	Coal	sub	Spain	63.80	3.00	28.40	0.60	4.20	22.00
	Coal	sub	Spain	69.20	4.70	16.90	0.70	8.50	22.00
Idris	Coal	sub	Malaysia	60.04	5.06	32.62	1.93	0.28	24.60
	Biomass	-	Malaysia	51.52	5.45	40.91	1.89	0.23	19.00
	Biomass	-	Malaysia	48.68	4.77	45.27	1.17	0.20	16.30
	Biomass	-	Malaysia	47.65	5.20	44.97	1.82	0.36	16.80
Arenillas	Coal	sub	US	77.30	5.90	13.70	0.70	2.30	30.81
	Coal	sub	Spain	79.70	6.20	11.30	0.50	2.30	28.41
	Coal	hvb	Aus.	84.80	5.90	7.50	0.90	1.00	34.15
	Coal	hvb	Portugal	80.50	5.70	11.00	0.90	1.90	32.73
	Coal	hvb	UK	82.40	5.70	10.10	1.20	0.60	32.26
	Coal	sub	UK	82.60	7.40	6.60	1.20	2.20	36.97
Jayaraman	Coal	-	India	72.82	4.65	19.91	1.79	0.83	28.14
Jin	Coal	bit	China	71.74	4.64	22.24	0.88	0.50	23.08
	Other	-	-	69.91	5.02	23.72	0.90	0.45	22.62
	Other	-	-	68.23	5.37	25.11	0.91	0.40	22.21
	Other	-	-	66.66	5.70	26.38	0.92	0.35	21.80
	Other	-	-	63.83	6.29	28.69	0.94	0.26	21.05
	Other	-	-	58.12	7.49	33.32	0.99	0.08	19.47
Khan	Coal	hvb	US	77.18	5.03	14.36	1.44	1.98	35.27
	Coal	hvb	US	69.30	4.75	21.43	1.32	3.20	33.27
Khatami	Coal	hvAb	US	83.31	5.45	8.00	1.62	1.62	36.50
	Coal	subB	US	75.54	6.17	16.88	0.97	0.43	30.52
	Coal	ligA	US	73.23	4.42	20.58	1.00	0.77	28.43
	Coal	ligA	US	72.26	5.22	20.10	1.40	0.89	29.26
Lemaire	Coal	hvb	France	86.24	5.15	6.89	0.85	0.87	34.82
Lloyd	Coal	hvb	US	84.46	5.53	5.66	2.17	2.18	35.32
	Coal	hvb	US	81.53	5.75	7.90	1.85	2.98	34.48

Table B-4. Heating Value of Various Fuels, CONTINUED

Source	Fuel Type	Coal Rank	Country	C	H	O	N	S	HHV
Lloyd, cont.	Coal	hvb	US	83.35	5.54	6.18	1.77	3.15	35.16
	Coal	hvb	US	80.26	5.39	8.92	1.59	3.84	33.48
	Coal	hvb	US	80.51	5.48	8.21	1.78	4.02	33.93
	Coal	hvb	US	83.62	5.51	8.19	1.84	0.83	34.78
Lu	Biomass	-	Taiwan	51.73	5.30	42.80	0.17	0.00	20.29
	Biomass char	-	Taiwan	58.16	5.19	36.65	0.00	0.00	22.55
	Biomass char	-	Taiwan	73.30	4.35	22.35	0.00	0.00	26.60
	Coal	an	Aus.	86.56	4.93	6.20	1.70	0.61	27.34
Man	Coal	-	China	90.10	4.30	3.40	1.70	0.40	30.10
	Coal	an	Vietnam	93.30	3.50	1.50	0.90	0.70	26.10
	Coal	bit	UK	83.43	5.32	7.23	1.81	2.31	28.11
	Coal	mvb	S. Africa	83.90	5.00	9.00	1.70	0.40	25.80
	Coal	lvb	China	89.55	4.52	4.22	1.41	0.30	28.54
	Coal	-	UK	91.80	3.90	1.90	1.30	0.90	33.40
	Coal	-	UK	92.50	3.80	1.40	1.30	0.90	33.40
Matali	Coal	sub	Malaysia	72.80	4.60	20.30	1.90	0.40	24.60
	Other	-	Malaysia	80.60	14.00	5.20	0.60	0.10	45.10
Nugroho	Coal	lig	Indo	62.54	4.20	32.01	1.25	0.00	23.00
	Coal	sub	Indo	65.36	4.51	29.08	1.05	0.00	28.70
	Coal	bit	Indo	76.78	5.50	15.96	1.76	0.00	31.90
	Coal	bit	Indo	72.02	4.99	21.44	1.55	0.00	29.00
Park	Coal	bit	Russia	88.52	5.29	2.96	2.54	0.68	34.27
	Coal	bit	Aus.	88.00	5.69	3.03	1.94	1.32	34.34
	Coal	sub	Indo	75.61	5.36	15.79	1.79	1.47	30.29
	Coal	sub	Indo	76.16	5.29	16.79	1.27	0.49	29.18
Pielsticker	Coal	hvb	Col	78.99	5.36	12.92	1.79	0.88	32.56
Saito	Coal	sub	Japan	77.67	6.53	14.61	0.95	0.24	31.52
CSIRO	Coal	sub	Aus.	78.40	6.70	13.10	1.20	0.60	33.42
	Coal	sub	Aus.	79.12	6.50	12.60	1.20	0.60	33.57
	Coal	sub	Aus.	79.00	6.30	12.80	1.20	0.70	33.01
	Coal	sub	Aus.	78.20	6.70	13.20	1.20	0.70	33.60
	Tar	-	Aus.	80.40	8.30	9.75	0.90	0.65	37.40
	Tar	-	Aus.	80.90	8.50	9.10	0.90	0.60	38.00
	Tar	-	Aus.	81.40	7.60	9.28	1.10	0.62	36.80
	Tar	-	Aus.	80.70	7.70	10.03	0.90	0.67	36.50
	Tar	-	Aus.	79.80	8.30	10.32	0.90	0.68	37.00
	Tar	-	Aus.	80.20	8.30	9.94	0.90	0.66	37.30
	Tar	-	Aus.	80.90	7.60	9.85	1.00	0.65	36.50
	Tar	-	Aus.	81.00	7.70	9.66	1.00	0.64	36.70

Table B-4. Heating Value of Various Fuels, CONTINUED

Source	Fuel Type	Coal Rank	Country	C	H	O	N	S	HHV
CSIRO, cont.	Tar	-	Aus.	81.20	7.90	9.28	1.00	0.62	37.20
	Tar	-	Aus.	80.50	7.60	10.22	1.00	0.68	36.30
	Tar	-	Aus.	79.80	7.90	10.69	0.90	0.71	36.40
	Tar	-	Aus.	80.80	7.90	9.66	1.00	0.64	36.90
	Tar	-	Aus.	81.50	7.50	9.38	1.00	0.62	36.60
	Tar	-	Aus.	81.10	7.10	10.22	0.90	0.68	35.80
	Char	-	Aus.	84.90	4.10	8.60	1.70	0.70	32.80
	Char	-	Aus.	83.20	3.89	10.60	1.60	0.70	31.76
	Char	-	Aus.	80.26	5.16	12.30	1.50	0.70	32.27
	Char	-	Aus.	86.76	3.39	7.40	1.80	0.60	32.80
	Char	-	Aus.	80.92	4.11	12.80	1.70	0.50	30.88
	Char	-	Aus.	90.40	2.86	3.10	3.20	0.60	34.04
	Char	-	Aus.	80.30	5.50	12.10	1.40	0.70	32.80
	Char	-	Aus.	82.20	4.00	11.50	1.60	0.70	31.42
	Char	-	Aus.	82.10	4.50	11.10	1.60	0.70	31.98
	Char	-	Aus.	82.00	4.10	11.60	1.60	0.70	31.63
	Char	-	Aus.	78.70	6.30	13.00	1.30	0.70	32.90
	Char	-	Aus.	80.30	4.40	13.00	1.60	0.70	31.04
	Char	-	Aus.	80.00	4.60	13.10	1.50	0.80	31.47
	Char	-	Aus.	77.20	4.80	15.47	1.50	1.03	30.10
	Char	-	Aus.	76.80	4.30	16.60	1.50	0.80	29.13
	Char	-	Aus.	89.60	2.50	5.91	1.60	0.39	32.60
	Char	-	Aus.	88.90	2.50	6.56	1.60	0.44	32.20
	Char	-	Aus.	89.20	2.60	6.10	1.70	0.40	32.60
	Char	-	Aus.	81.60	5.40	10.90	1.40	0.70	33.30
	Char	-	Aus.	83.00	4.40	10.30	1.60	0.70	32.50
	Char	-	Aus.	80.10	4.10	13.60	1.50	0.70	30.50
	Char	-	Aus.	83.60	3.00	11.00	1.60	1.80	30.60
	Char	-	Aus.	80.30	4.70	12.60	1.60	0.80	31.60
	Char	-	Aus.	83.90	3.80	10.00	1.70	0.60	32.00
	Char	-	Aus.	82.00	4.00	11.80	1.60	0.60	31.30
	Char	-	Aus.	81.70	4.00	12.10	1.60	0.60	31.10
	Coal	bit	Aus.	80.64	6.02	10.88	2.06	0.40	33.83
	Coal	bit	Aus.	82.80	5.90	8.80	2.10	0.40	34.00
	Tar	-	Aus.	83.20	6.90	7.60	1.90	0.40	36.60
	Tar	-	Aus.	83.10	7.10	7.51	1.90	0.39	36.90
	Tar	-	Aus.	82.20	7.10	8.46	1.80	0.44	36.40
	Tar	-	Aus.	83.10	6.10	8.17	2.20	0.43	35.30
	Tar	-	Aus.	83.20	6.30	7.98	2.10	0.42	35.70
	Tar	-	Aus.	83.20	7.70	7.03	1.70	0.37	37.80
	Tar	-	Aus.	82.70	7.60	8.17	1.10	0.43	37.30

Table B-4. Heating Value of Various Fuels, CONTINUED

Source	Fuel Type	Coal Rank	Country	C	H	O	N	S	HHV
CSIRO, cont.	Char	-	Aus.	82.50	3.70	10.70	2.30	0.80	31.30
	Char	-	Aus.	83.80	3.40	9.58	2.50	0.72	31.50
	Char	-	Aus.	84.90	2.80	9.21	2.40	0.69	31.00
	Char	-	Aus.	80.60	4.50	11.82	2.20	0.88	31.50
	Coal	brown	Aus.	71.00	4.80	23.30	0.60	0.30	27.10
Stournas	coal	lig	Greece	60.40	5.90	29.00	1.80	2.90	24.42
	peat	-	Greece	56.70	5.50	34.90	1.80	1.10	20.36
	coal	lig	Greece	63.20	5.20	28.40	1.60	1.60	23.43
Niessen	Other	-	-	46.18	6.19	47.15	0.27	0.21	18.72
	Other	-	-	49.90	6.19	43.69	0.05	0.16	19.99
	Other	-	-	45.39	6.15	47.85	0.00	0.11	18.13
	Other	-	-	42.98	6.46	50.35	0.09	0.12	16.62
	Other	-	-	46.20	6.02	47.46	0.10	0.22	18.25
	Other	-	-	46.59	6.35	46.80	0.19	0.08	18.46
	Other	-	-	59.91	9.36	30.50	0.12	0.10	27.64
	Other	-	-	48.07	6.55	45.04	0.16	0.17	19.18
	Other	-	-	43.89	6.27	49.54	0.20	0.10	17.20
	Biomass	-	-	51.58	6.96	39.48	1.77	0.21	20.22
	Biomass	-	-	49.68	5.88	43.16	1.15	0.12	19.29
	Other	-	-	62.78	9.98	25.97	1.07	0.20	30.47
	Other	-	-	73.14	11.54	14.82	0.43	0.07	38.28
	Other	-	-	53.56	7.65	34.24	3.93	0.62	23.48
	Other	-	-	53.40	7.36	35.35	3.80	0.32	21.52
	Biomass	-	-	50.63	6.46	42.69	0.14	0.08	9.88
	Biomass	-	-	53.81	5.66	40.12	0.21	1.23	15.25
	Biomass	-	-	51.41	6.25	42.14	0.10	0.10	18.59
	Biomass	-	-	49.70	6.14	43.96	0.10	0.10	17.06
	Biomass	-	-	50.41	6.19	43.20	0.10	0.10	18.46
	Biomass	-	-	49.81	6.72	41.52	1.76	0.20	20.83
	Biomass	-	-	55.05	6.88	36.33	1.54	0.21	22.89
	Biomass	-	-	49.15	6.96	42.33	1.27	0.27	19.66
	Biomass	-	-	49.42	6.38	38.98	4.77	0.45	20.69
	Biomass	-	-	46.47	6.48	44.70	2.31	0.05	19.18
	Biomass	-	-	54.46	6.38	31.69	7.30	0.17	21.55
	Biomass	-	-	44.12	6.48	49.13	0.22	0.05	17.90
	Biomass	-	-	50.97	6.03	42.80	0.15	0.05	20.22
	Biomass	-	-	46.38	6.44	44.94	2.18	0.05	19.99
	Biomass	-	-	46.33	6.48	44.83	2.30	0.06	18.91
	Biomass	-	-	51.77	6.79	38.06	3.00	0.37	20.89
	other	-	-	48.46	6.28	44.86	0.31	0.10	17.87
	other	-	-	84.69	7.28	6.32	0.11	1.61	34.64

Table B-4. Heating Value of Various Fuels, CONTINUED

Source	Fuel Type	Coal Rank	Country	C	H	O	N	S	HHV
Niessen, cont.	other	-	-	66.74	8.90	12.79	11.12	0.44	22.89
	other	-	-	54.46	6.90	29.60	7.75	1.30	23.59
	other	-	-	76.13	10.14	11.10	0.72	1.92	36.70
	other	-	-	86.28	11.50	0.00	0.00	2.22	29.29
	other	-	-	66.82	8.02	25.17	0.00	0.00	37.19
	other	-	-	72.05	10.42	16.96	0.49	0.08	34.56
	other	-	-	85.56	14.35	0.00	0.06	0.03	46.49
	other	-	-	87.49	8.49	3.98	0.21	0.02	38.38
	other	-	-	67.89	6.72	18.94	6.43	0.02	27.27
	other	-	-	85.93	10.68	2.97	0.15	0.27	23.25
	other	-	-	66.20	7.36	25.76	0.14	0.55	26.61
	other	-	-	56.38	6.77	31.98	4.22	0.13	18.23
	other	-	-	47.70	6.62	43.22	2.25	0.21	19.29
	other	-	-	79.87	11.51	6.21	2.39	0.00	37.19
	other	-	-	52.55	6.97	29.57	9.22	1.69	23.15
	other	-	-	74.44	9.28	14.44	1.81	0.04	31.73
	other	-	-	46.27	6.35	46.93	0.19	0.27	18.59
	other	-	-	47.74	6.62	45.01	0.53	0.11	18.13
	other	-	-	93.96	1.68	2.68	0.00	1.68	32.54
	Biomass	-	-	52.38	6.04	41.31	0.02	0.25	9.22
	Biomass	-	-	47.31	6.16	45.71	0.68	0.14	8.53
	Coal	meta-an	US	93.90	2.10	2.30	0.30	1.40	34.52
	Coal	an	US	93.50	2.60	2.30	0.90	0.70	35.10
	Coal	semi-an	US	90.70	4.20	3.30	1.00	0.80	35.62
	Coal	lvb	US	90.40	4.80	2.70	1.30	0.80	36.43
	Coal	lvb	US	89.40	4.80	2.40	1.50	1.90	36.30
	Coal	mvb	US	88.60	4.80	3.10	1.60	1.90	36.12
	Coal	mvb	US	87.60	5.20	3.30	1.40	2.50	36.33
	Coal	hvAb	US	85.00	5.40	5.80	1.70	2.10	35.48
	Coal	hvAb	US	85.50	5.50	6.70	1.60	0.70	35.73
	Coal	hvAb	US	80.90	5.70	7.40	1.40	4.60	34.24
	Coal	hvBb	US	80.50	5.50	9.10	1.60	3.30	33.54
	Coal	hvBb	US	79.80	5.60	11.80	1.70	1.10	33.15
	Coal	hvCb	US	79.20	5.70	9.50	1.50	4.10	33.47
	Coal	subA	US	80.90	5.10	12.20	1.30	0.50	32.80
	Coal	subB	US	75.90	5.10	17.00	1.60	0.40	30.45
	Coal	subC	US	74.00	5.60	18.60	0.90	0.90	30.15
	Coal	ligA	US	72.70	4.90	20.80	0.90	0.70	28.66
	Coal	hvBb	Aus.	81.90	5.10	10.80	1.80	0.40	32.50

Table B-4. Heating Value of Various Fuels, CONTINUED

Source	Fuel Type	Coal Rank	Country	C	H	O	N	S	HHV
Niessen, cont.	Coal	hvBb	China	80.20	4.90	13.20	1.10	0.60	31.94
	Coal	hvAb	France	81.90	5.30	10.30	1.50	1.00	33.55
	Coal	hvAb	S. Africa	81.40	5.30	10.60	1.90	0.80	33.05
	Coal	hvBb	Indo	76.10	5.60	16.90	1.20	0.20	30.77
	Coal	semi-an	Korea	90.10	1.20	5.80	0.30	2.60	28.87
	Coal	subB	Spain	62.20	4.60	19.10	1.50	12.60	23.82
	Liq Gas	-	-	85.90	13.30	0.00	0.00	0.01	45.72
	Liq Gas	-	-	86.10	11.80	0.00	0.00	0.05	44.56
	Liq Gas	-	-	86.50	10.60	0.00	0.00	0.20	42.49
	Liq Gas	-	-	86.50	10.50	0.00	0.00	0.50	42.07
	Liq Gas	-	-	86.51	9.50	0.00	0.00	0.70	40.47
	Liq Gas	-	-	86.70	14.10	0.00	0.10	0.50	46.16
	Liq Gas	-	-	88.20	13.90	0.00	0.10	1.00	45.91
	Liq Gas	-	-	89.29	13.01	0.00	0.00	2.00	45.18
	Liq Gas	-	-	89.29	12.01	0.00	0.00	3.00	44.26
	Liq Gas	-	-	90.65	12.06	0.00	0.00	3.52	44.36
	Liq Gas	-	-	75.25	23.53	0.00	1.22	0.00	53.86
	Liq Gas	-	-	74.72	23.30	1.22	0.76	0.00	53.24
	Liq Gas	-	-	69.12	23.20	1.58	5.76	0.34	51.30
	Liq Gas	-	-	69.26	22.68	0.00	8.06	0.00	50.73
	Liq Gas	-	-	64.84	20.85	1.41	12.90	0.00	46.86
Biagini	Coal	-	Col	77.75	5.46	14.29	1.68	0.82	28.71
	Coal	-	Germ	84.39	5.31	7.71	1.69	0.90	34.18
	Coal	bit	Col	78.90	5.20	13.73	1.49	0.68	29.86
	Coal	lig	Germ	79.20	5.20	12.86	1.48	1.26	29.66
	Coal	mvb	S. Africa	81.20	4.40	12.00	1.83	0.57	26.40
	Coal	-	US	83.70	5.30	8.50	1.60	0.90	30.78
	Coal	-	S. Africa	81.90	4.50	10.80	2.00	0.80	27.72
	Coal	-		80.20	4.70	12.50	1.80	0.80	28.36
	Coal	-	Poland	79.98	4.30	12.72	1.80	1.20	29.57
	Coal	-		80.60	4.69	12.06	1.73	0.92	27.15
	Coal	-	Egypt	73.55	6.03	16.35	1.23	2.84	30.33
	Coal	-	S. Africa	77.80	5.43	14.22	1.65	0.90	28.70
	Coal	mvb	S. Africa	81.31	4.27	12.03	1.83	0.56	29.17
	Coal	-	Poland	82.73	4.72	10.84	1.23	0.48	29.46
	Coal	-	Canada	84.80	4.10	9.50	1.20	0.40	32.23

Table B-4. Heating Value of Various Fuels, CONTINUED

Source	Fuel Type	Coal Rank	Country	C	H	O	N	S	HHV
Biagini, cont.	Coal	bit	UK	65.80	3.90	27.60	1.10	1.60	24.09
	Coal	bit	UK	63.40	3.50	30.50	1.10	1.50	22.21
	Coal	hvb	S. Africa	68.70	3.80	25.10	1.60	0.80	27.77
	Coal	sub	Canada	67.00	2.70	28.80	1.30	0.20	25.05
	Coal	bit	UK	80.36	5.18	9.99	1.81	2.66	28.75
Chen	Biomass	-	-	53.32	7.14	27.86	10.04	1.63	23.33
	Coal	semi-an	China	80.52	6.04	11.27	0.99	1.17	27.55
Gövert	Coal	bit	Col	78.72	5.26	12.82	2.11	1.09	32.32
Guo	Coal	bit	China	81.33	4.92	11.91	1.10	0.73	25.82
Hashimoto	Coal	bit	Aus.	82.27	5.67	9.69	1.89	0.48	28.28
	Coal	sub	Indo	68.44	5.31	24.41	1.23	0.64	26.28
	Coal	sub	Indo	71.56	5.26	22.06	0.97	0.09	28.15
Rabaçal	Coal	bit	UK	82.60	6.15	8.75	1.98	0.52	30.96
Rieth	Coal	bit	Aus.	84.79	5.19	7.70	1.77	0.52	29.16
	Coal	hvb	Germ	79.30	4.70	13.70	1.30	1.00	33.28
Sadhukhan	Coal	lig	India	78.53	5.26	14.74	1.12	0.35	30.00
	Coal	sub	India	78.34	4.26	13.70	1.94	1.76	23.63
	Coal	sub	India	86.46	4.51	7.06	1.82	0.51	30.29
Sorensen	Coke	-	Norway	97.00	0.20	0.80	0.90	1.10	29.59
Toftegaard	Coal	bit	Col	80.70	5.41	11.47	1.69	0.73	29.62
Tolvanen	Peat	-	-	56.62	5.92	35.97	1.33	0.15	22.16
	Coal	-	-	78.56	5.33	13.36	2.36	0.38	29.13
	Coal	-	-	76.60	5.32	14.02	2.45	1.62	29.28
	Biomass	-	-	53.31	6.01	40.46	0.20	0.02	22.29
Wen	Coal	hvb	Germ	80.36	5.08	12.17	1.45	0.94	33.35
Yang	Coal	-	China	83.10	5.02	10.04	0.66	1.17	25.17
	Coal	bit	Col	80.92	5.12	11.79	1.65	0.52	31.80
Zhang	Coal	sub	China	78.81	3.64	15.87	1.24	0.44	28.81
	Char	-	China	86.56	3.14	8.91	0.97	0.37	30.25
	Char	-	China	89.65	2.57	6.51	0.92	0.35	31.82
	Char	-	China	93.16	1.45	4.01	1.00	0.37	31.95
	Char	-	China	94.91	0.27	3.46	0.93	0.42	30.68
	Char	-	China	95.12	0.70	2.79	0.98	0.41	30.85
	Char	-	China	95.80	0.00	2.86	0.92	0.42	30.53
Zhang	Coal	-	-	78.13	4.10	16.41	1.11	0.25	23.43
Ringen	Oil Shale	-	Aus.	84.64	11.50	3.00	0.56	0.30	43.73
	Oil Shale	-	Aus.	84.44	11.98	2.62	0.57	0.43	44.19

Table B-4. Heating Value of Various Fuels, CONTINUED

Source	Fuel Type	Coal Rank	Country	C	H	O	N	S	HHV
Ringen, cont.	Oil Shale	-	Aus.	85.18	11.84	2.00	0.56	0.42	44.15
	Oil Shale	-	Aus.	85.56	12.02	1.51	0.52	0.39	44.38
	Oil Shale	-	Aus.	85.39	12.00	1.63	0.54	0.44	44.08
	Oil Shale	-	Aus.	84.37	12.04	2.63	0.48	0.48	44.24
	Oil Shale	-	Aus.	85.56	10.57	2.53	0.72	0.62	42.33
	Oil Shale	-	Brazil	83.32	11.73	3.79	0.97	0.24	43.87
	Oil Shale	-	Brazil	84.28	12.05	2.32	1.10	0.25	43.96
	Oil Shale	-	Brazil	85.66	11.53	2.21	0.00	0.60	43.29
	Oil Shale	-	Brazil	85.15	12.02	2.40	0.00	0.43	43.80
	Oil Shale	-	Brazil	85.08	12.44	2.10	0.00	0.38	44.26
	Oil Shale	-	France	84.88	11.36	2.61	0.84	0.31	43.43
	Oil Shale	-	France	85.07	11.43	2.06	1.12	0.32	43.22
	Oil Shale	-	France	84.56	11.28	2.63	1.18	0.35	43.12
	Oil Shale	-	France	85.24	11.58	1.67	1.00	0.21	44.01
	Oil Shale	-	France	83.74	10.54	2.30	0.66	2.76	42.47
	Oil Shale	-	France	85.16	11.26	2.53	0.59	0.46	43.22
	Oil Shale	-	Man	81.24	11.91	5.82	0.84	0.19	42.43
	Oil Shale	-	New Zealand	83.35	11.80	3.61	0.60	0.64	43.36
	Oil Shale	-	Sweden	84.96	9.00	3.61	0.71	1.72	40.61
	Oil Shale	-	Sweden	85.87	9.76	2.33	0.72	1.32	41.82
	Oil Shale	-	Thailand	84.42	12.44	1.63	1.10	0.41	44.01
	Oil Shale	-	South Africa	84.98	10.82	3.53	0.00	0.67	41.82
	Oil Shale	-	South Africa	84.84	11.13	3.39	0.00	0.64	42.22
	Oil Shale	-	South Africa	84.99	11.11	3.27	0.00	0.63	42.31
	Oil Shale	-	South Africa	85.13	11.46	2.82	0.00	0.59	42.73
	Oil Shale	-	South Africa	84.99	11.55	2.93	0.00	0.53	43.12
Annamalai	Other	-	-	54.71	6.45	37.34	1.16	0.35	17.36
	Other	-	-	58.01	8.63	30.77	1.21	1.37	15.12
	Other	-	-	56.35	7.58	34.10	1.15	0.82	18.54
	Other	-	-	52.90	5.96	35.96	4.01	1.16	12.49
	Other	-	-	52.88	5.97	35.99	4.01	1.16	11.30
	Other	-	-	49.35	5.52	38.39	5.56	1.18	4.40
Sun	Prop	-	-	16.22	2.72	43.22	37.84	0.00	7.83
	Prop	-	-	27.59	3.47	36.75	32.18	0.00	12.60
	Prop	-	-	31.92	4.29	34.01	29.78	0.00	14.78
	Prop	-	-	31.92	4.29	34.01	29.78	0.00	15.07

Table B-4. Heating Value of Various Fuels, CONTINUED

Source	Fuel Type	Coal Rank	Country	C	H	O	N	S	HHV
Sun, cont.	Prop	-	-	27.59	3.47	36.75	32.18	0.00	8.91
	Prop	-	-	35.64	4.99	31.65	27.72	0.00	16.92
Lee	Liq Gas	-	-	82.66	17.34	0.00	0.00	0.00	46.05
	Liq Gas	-	-	83.23	16.77	0.00	0.00	0.00	45.35
	Liq Gas	-	-	83.62	16.38	0.00	0.00	0.00	45.10
	Liq Gas	-	-	83.90	16.10	0.00	0.00	0.00	44.92
	Liq Gas	-	-	84.12	15.88	0.00	0.00	0.00	44.78
	Liq Gas	-	-	84.28	15.72	0.00	0.00	0.00	44.68
	Liq Gas	-	-	84.41	15.59	0.00	0.00	0.00	44.60
	Prop	-	-	48.46	9.15	0.00	42.39	0.00	29.38
	Prop	-	-	53.06	9.80	0.00	37.14	0.00	31.17
	Prop	-	-	56.65	10.30	0.00	33.04	0.00	32.55
	Prop	-	-	59.53	10.71	0.00	29.76	0.00	33.67
	Prop	-	-	61.89	11.04	0.00	27.07	0.00	34.59
	Prop	-	-	63.86	11.31	0.00	24.83	0.00	35.36
	Prop	-	-	65.52	11.55	0.00	22.93	0.00	36.01
	Prop	-	-	28.56	4.79	0.00	66.64	0.00	20.24
	Prop	-	-	34.27	5.75	0.00	59.97	0.00	22.60
	Prop	-	-	38.95	6.54	0.00	54.52	0.00	24.53
	Prop	-	-	42.84	7.19	0.00	49.97	0.00	26.14
	Prop	-	-	46.13	7.74	0.00	46.13	0.00	27.50
	Prop	-	-	48.95	8.22	0.00	42.83	0.00	28.67
	Prop	-	-	51.40	8.63	0.00	39.97	0.00	29.68
	Prop	-	-	53.54	8.99	0.00	37.47	0.00	30.56

APPENDIX C. ADDITIONAL ELEMENTAL COMPOSITION ANALYSIS

This appendix contains extra analysis information for the aromaticity (Chapter 5) and elemental composition (Chapter 6) correlations. The majority of the information here is taken from the supplemental material section of Richards et al. (2019), starting with the aromaticity analysis followed by the elemental composition analysis.

C.1 Coal Aromaticity

The experimental data used in the coal aromaticity analysis is found in Table B-3. This appendix chapter includes all aromaticity correlation model forms tested as part of the analysis, the original and re-fit coefficients of the literature models (see Table 2-2 for the mathematical forms), and the complete statistical results of the aromaticity correlation tests. All variables are defined in the nomenclature section.

Table C-1 includes all model forms tested in the aromaticity analysis. Table C-2 shows both the original and re-fit coefficients of the literature correlations (Models 37-44 in Table C-1). All elemental compositions are on a mass basis, unless otherwise stated. Table C-3 shows the complete statistical results of the aromaticity correlation analysis. Model 4 is the proposed aromaticity correlation in Chapter 5. Looking at Table C-3, there are a few models with better statistical results, however, these models were not chosen for the proposed correlation because they require measured NMR parameters, which require a measured carbon aromaticity to calculate, effectively making the aromaticity correlation unnecessary.

Table C-1. Aromaticity Model Forms

Model	Equation
1	$f_a' = a + b \cdot M_{cl,Genetti}$
2	$f_a' = a + b \cdot M_{cl,re-fit}$
3	$f_a' = a + b \cdot C_{coal} + c \cdot C_{coal}^2 + d \cdot H_{coal} + e \cdot H_{coal}^2 + f \cdot O_{coal} + g \cdot O_{coal}^2 + h \cdot (100 - V_{ASTM}) + i \cdot (100 - V_{ASTM})^2$
4*	$f_a' = a + b \cdot C_{coal} + c \cdot C_{coal}^2 + d \cdot H_{coal} + e \cdot H_{coal}^2 + f \cdot O_{coal} + g \cdot O_{coal}^2 + h \cdot V_{ASTM} + i \cdot V_{ASTM}^2$
5	$f_a' = a + b \cdot M_{\delta,Genetti}$
6	$f_a' = a + b \cdot M_{\delta,re-fit}$
7	$f_a' = a + b \cdot M_{\delta,Genetti} + c \cdot V_{ASTM}$
8	$f_a' = a + b \cdot M_{\delta,re-fit} + c \cdot V_{ASTM}$
9	$f_a' = a + b \cdot M_{\delta,meas} + c \cdot V_{ASTM}$
10	$f_a' = a + b \cdot M_{\delta,Genetti} + c \cdot C_{coal}$
11	$f_a' = a + b \cdot M_{\delta,re-fit} + c \cdot C_{coal}$
12	$f_a' = a + b \cdot M_{\delta,meas} + c \cdot C_{coal}$
13	$f_a' = a + b \cdot M_{\delta,Genetti} + c \cdot C_{coal} + d \cdot V_{ASTM}$
14	$f_a' = a + b \cdot M_{\delta,re-fit} + c \cdot C_{coal} + d \cdot V_{ASTM}$
15	$f_a' = a + b \cdot M_{\delta,meas} + c \cdot C_{coal} + d \cdot V_{ASTM}$
16	$f_a' = a + b \cdot M_{\delta,Genetti} + c \cdot C_{coal} + d \cdot V_{ASTM} + e \cdot O_{coal}$
17	$f_a' = a + b \cdot M_{\delta,re-fit} + c \cdot C_{coal} + d \cdot V_{ASTM} + e \cdot O_{coal}$
18	$f_a' = a + b \cdot M_{\delta,meas} + c \cdot C_{coal} + d \cdot V_{ASTM} + e \cdot O_{coal}$
19	$f_a' = a + b \cdot M_{\delta,Genetti} + c \cdot C_{coal} + d \cdot V_{ASTM} + e \cdot H_{coal}$
20	$f_a' = a + b \cdot M_{\delta,re-fit} + c \cdot C_{coal} + d \cdot V_{ASTM} + e \cdot H_{coal}$
21	$f_a' = a + b \cdot M_{\delta,meas} + c \cdot C_{coal} + d \cdot V_{ASTM} + e \cdot H_{coal}$
22	$f_a' = a + b \cdot M_{\delta,Genetti} + c \cdot \frac{H_{coal}}{C_{coal}}$
23	$f_a' = a + b \cdot M_{\delta,re-fit} + c \cdot \frac{H_{coal}}{C_{coal}}$
24	$f_a' = a + b \cdot M_{\delta,meas} + c \cdot \frac{H_{coal}}{C_{coal}}$

Table C-1. Aromaticity Model Forms, CONTINUED

Model	Equation
25	$f_a' = a + b \cdot M_{\delta,Genetti} + c \cdot \frac{H_{coal}}{C_{coal}} + d \cdot \left(\frac{H_{coal}}{C_{coal}}\right)^2$
26	$f_a' = a + b \cdot M_{\delta,re-fit} + c \cdot \frac{H_{coal}}{C_{coal}} + d \cdot \left(\frac{H_{coal}}{C_{coal}}\right)^2$
27	$f_a' = a + b \cdot M_{\delta,meas} + c \cdot \frac{H_{coal}}{C_{coal}} + d \cdot \left(\frac{H_{coal}}{C_{coal}}\right)^2$
28	$f_a' = a + b \cdot M_{\delta,Genetti} + c \cdot C_{coal} + d \cdot C_{coal}^2$
29	$f_a' = a + b \cdot M_{\delta,re-fit} + c \cdot C_{coal} + d \cdot C_{coal}^2$
30	$f_a' = a + b \cdot M_{\delta meas} + c \cdot C_{coal} + d \cdot C_{coal}^2$
31	$f_a' = a + b \cdot M_{\delta,Genetti} + c \cdot \frac{H_{coal}}{C_{coal}} + d \cdot \frac{O_{coal}}{C_{coal}}$
32	$f_a' = a + b \cdot M_{\delta,re-fit} + c \cdot \frac{H_{coal}}{C_{coal}} + d \cdot \frac{O_{coal}}{C_{coal}}$
33	$f_a' = a + b \cdot M_{\delta,meas} + c \cdot \frac{H_{coal}}{C_{coal}} + d \cdot \frac{O_{coal}}{C_{coal}}$
34	$f_a' = a + b \cdot M_{\delta,Genetti} + c \cdot \frac{H_{coal}}{C_{coal}} + d \cdot \frac{O_{coal}}{C_{coal}} + e \cdot V_{ASTM}$
35	$f_a' = a + b \cdot M_{\delta,re-fit} + c \cdot \frac{H_{coal}}{C_{coal}} + d \cdot \frac{O_{coal}}{C_{coal}} + e \cdot V_{ASTM}$
36	$f_a' = a + b \cdot M_{\delta,meas} + c \cdot \frac{H_{coal}}{C_{coal}} + d \cdot \frac{O_{coal}}{C_{coal}} + e \cdot V_{ASTM}$
37 (Ko)	$f_a' = a + b \cdot \left(\frac{C_{coal}}{100}\right) + c \cdot \left(\frac{C_{coal}}{100}\right)^2$
38 (Gerstein)	$f_a' = a + b \cdot C_{coal}$
39 (Maroto-Valer)	$f_a' = a + b \cdot H_{coal}/C_{coal}$ H_{coal}/C_{coal} on a mass fraction basis

Table C-1. Aromaticity Model Forms, CONTINUED

Model	Equation
40 (Maroto-Valer)	$f_a' = a + b \cdot H_{coal}/C_{coal}$ H_{coal}/C_{coal} on an atomic basis
41 (SK 1)	$f_a' = a + b \cdot V_{ASTM}$
42 (SK 2)	$f_a' = a + b \cdot O_{coal}/C_{coal} + c \cdot H_{coal}/C_{coal}$ Elemental ratios on atomic basis
43 (SK 3)	$f_a' = a + b \cdot O_{coal}/C_{coal} + c \cdot O_{coal}/H_{coal} + d \cdot H_{coal}/C_{coal}$ Elemental ratios on atomic basis
44 (SK 4)	$f_a' = a + b \cdot O_{coal}/C_{coal} + c \cdot O_{coal}/H_{coal} + d \cdot H_{coal}/C_{coal} + e \cdot V_{ASTM}$ Elemental ratios on atomic basis

Table C-2. Original and Re-Fit Coefficients for Aromaticity Literature Correlations

Model	Name	Coefficients	a	b	c	d	e
37	Ko et al.	Original	0.8305	-2.0081	2.2412		
		Re-fit	3.7746	-9.2248	6.6376		
38	Gerstein et al.	Original	-0.564	0.0159			
		Re-fit	-0.3944	0.0133			
40	Maroto-Valer et al.	Original	1.22	-0.58			
		Re-fit	1.2075	-0.6711			
41	Singh & Kakati 1	Original	1.2029	-0.0126			
		Re-fit	0.9714	-0.0073			
42	Singh & Kakati 2	Original	1.364	-0.5372	-0.7846		
		Re-fit	1.1667	-0.5567	-0.5395		
43	Singh & Kakati 3	Original	1.3656	-0.5119	-0.0211	-0.7865	
		Re-fit	1.2582	0.6547	-1.0025	-0.6532	
44	Singh & Kakati 4	Original	174.4405	621.6823	-856.495	-629.617	9.1339
		Re-fit	1.0513	-1.0735	0.3826	-0.3099	-0.017

Table C-3. Statistical Results for Each Aromaticity Correlation

Model	N_{coeff}	N_{var}	R^2	L_1 Norm	L_2 Norm	Infinity Norm	SSE
Original Coefficients							
Ko	3	1	0.595	0.058	0.076	0.215	0.458
Gerstein	2	1	0.549	0.075	0.089	0.195	0.626
Maroto-Valer	2	1	0.626	0.091	0.113	0.367	1.012
SK 1	2	1	0.649	0.055	0.082	0.349	0.406
SK 2	3	2	0.716	0.053	0.070	0.231	0.394
SK 3	4	3	0.716	0.053	0.070	0.231	0.393
SK 4	5	4	0.057	27.473	45.616	274.318	1.269×10^5
Fitted Models							
1	2	1	0.018	0.068	0.097	0.369	0.570
2	2	1	0.030	0.067	0.096	0.402	0.563
3	9	4	0.791	0.034	0.045	0.170	0.122
4	9	4	0.797	0.033	0.044	0.166	0.118
5	2	1	0.660	0.042	0.057	0.209	0.197
6	2	1	0.697	0.043	0.054	0.193	0.176
7	3	2	0.724	0.037	0.051	0.209	0.160
8	3	2	0.748	0.037	0.049	0.198	0.146
9	3	2	0.933	0.026	0.033	0.073	0.026
10	3	2	0.662	0.042	0.057	0.202	0.196
11	3	2	0.699	0.042	0.053	0.189	0.174
12	3	2	0.896	0.031	0.040	0.094	0.043
13	4	3	0.725	0.037	0.051	0.203	0.159
14	4	3	0.749	0.037	0.049	0.196	0.146
15	4	3	0.941	0.023	0.031	0.066	0.023
16	5	4	0.746	0.037	0.049	0.188	0.148
17	5	4	0.753	0.037	0.048	0.187	0.143
18	5	4	0.941	0.023	0.031	0.066	0.023
19	5	4	0.744	0.036	0.049	0.204	0.149
20	5	4	0.755	0.036	0.048	0.200	0.142
21	5	4	0.953	0.021	0.027	0.061	0.018
22	3	2	0.707	0.039	0.053	0.223	0.170
23	3	2	0.727	0.040	0.051	0.209	0.158
24	3	2	0.945	0.023	0.029	0.063	0.022
25	4	2	0.708	0.039	0.053	0.223	0.170
26	4	2	0.727	0.040	0.051	0.209	0.158
27	4	2	0.945	0.023	0.029	0.064	0.022
28	4	2	0.682	0.040	0.055	0.217	0.184
29	4	2	0.715	0.040	0.052	0.202	0.166
30	4	2	0.950	0.022	0.027	0.059	0.020
31	4	3	0.774	0.035	0.046	0.172	0.131
32	4	3	0.772	0.034	0.047	0.175	0.132

Table C-3. Statistical Results for Each Aromaticity Correlation, CONTINUED

Model	N_{coeff}	N_{var}	R^2	L_1 Norm	L_2 Norm	Infinity Norm	SSE
33	4	3	0.946	0.023	0.029	0.064	0.022
34	5	4	0.780	0.034	0.046	0.174	0.128
35	5	4	0.777	0.034	0.046	0.177	0.129
36	5	4	0.950	0.023	0.028	0.060	0.019
37	3	1	0.641	0.053	0.070	0.228	0.395
38	2	1	0.549	0.063	0.079	0.198	0.497
39	2	1	0.626	0.056	0.072	0.274	0.411
40	2	1	0.626	0.056	0.072	0.273	0.411
41	2	1	0.649	0.040	0.058	0.232	0.204
42	3	2	0.724	0.047	0.062	0.201	0.304
43	4	3	0.729	0.046	0.061	0.212	0.298
44	5	4	0.777	0.034	0.046	0.176	0.129

C.2 Elemental Composition Analysis

This section contains all the extra material for the elemental composition analysis, including all tested model forms and the R^2 values for each completed test. This section also includes all the average statistical values for the initial cross-validation analysis. Next are the results of the final training step, which details the results using the complete data set (see Table B-1 and Table B-2 for complete data sets for char and tar, respectively).The final training results include the complete statistical values for each test in table format and in figures to better show trends. Finally, this appendix details the complete results of the model refinement step with an additional cross-validation and final training cycle.

C.2.1 Elemental Correlation Summary

Table C-4 contains the totality of the tested composition model forms. This table is broken into two main sections: models used in the initial cross-validation analysis and models developed through model refinement. Also included in the table are the total number of coefficients and the number of variables in each tested model form.

Table C-4. Elemental Composition Model Forms

Model	N_{coeff}	N_{var}	Equation
1	12	4	$\frac{X_i}{X_{i0}} = a + b \cdot T_{gas,max} + c \cdot T_{gas,max}^2 + d \cdot T_{gas,max}^3 + e \cdot \exp(f \cdot t_{res}) + g \cdot V_{norm} + h \cdot V_{norm}^2 + i \cdot V_{norm}^3 + j \cdot X_{i0} + k \cdot X_{i0}^2 + l \cdot X_{i0}^3$
2	9	4	$\frac{X_i}{X_{i0}} = a + b \cdot T_{gas,max}^c + d \cdot t_{res}^e + f \cdot V_{norm}^g + h \cdot X_{i0}^i$
3	17	4	$\frac{X_i}{X_{i0}} = a + b \cdot T_{gas,max} + c \cdot T_{gas,max}^2 + d \cdot T_{gas,max}^3 + e \cdot T_{gas,max}^4 + f \cdot t_{res} + g \cdot t_{res}^2 + h \cdot t_{res}^3 + i \cdot t_{res}^4 + j \cdot V_{norm} + k \cdot V_{norm}^2 + l \cdot V_{norm}^3 + m \cdot V_{norm}^4 + n \cdot X_{i0} + o \cdot X_{i0}^2 + p \cdot X_{i0}^3 + q \cdot X_{io}^4$
4	5	4	$\frac{X_i}{X_{i0}} = a + b \cdot \ln(T_{gas,max}) + c \cdot \ln(t_{res}) + d \cdot \ln(V_{norm}) + e \cdot \ln(X_{i0})$
5	5	4	$\frac{X_i}{X_{i0}} = a + b \cdot \log_{10}(T_{gas,max}) + c \cdot \log_{10}(t_{res}) + d \cdot \log_{10}(V_{norm}) + e \cdot \log_{10}(X_{i0})$
6	9	4	$\frac{X_i}{X_{i0}} = a + b \cdot \exp(c \cdot T_{gas,max}) + d \cdot \exp(e \cdot t_{res}) + f \cdot \exp(g \cdot V_{norm}) + h \cdot \exp(i \cdot X_{i0})$
7	5	4	$\frac{X_i}{X_{i0}} = a + \frac{b}{T_{gas,max}} + \frac{c}{t_{res}} + \frac{d}{V_{norm}} + \frac{e}{X_{i0}}$
8	17	4	$\frac{X_i}{X_{i0}} = a + b \cdot T_{gas,max} + c \cdot T_{gas,max}^{1/2} + d \cdot T_{gas,max}^{1/3} + e \cdot T_{gas,max}^{1/4} + f \cdot t_{res} + g \cdot t_{res}^{1/2} + h \cdot t_{res}^{1/3} + i \cdot t_{res}^{1/4} + j \cdot V_{norm} + k \cdot V_{norm}^{1/2} + l \cdot V_{norm}^{1/3} + m \cdot V_{norm}^{1/4} + n \cdot X_{i0} + o \cdot X_{i0}^{1/2} + p \cdot X_{i0}^{1/3} + q \cdot X_{io}^{1/4}$
9	13	5	$\frac{X_i}{X_{i0}} = a + b \cdot T_{gas,max} + c \cdot T_{gas,max}^2 + d \cdot T_{gas,max}^3 + e \cdot \exp(f \cdot t_{res}) + g \cdot V_{norm} + h \cdot V_{norm}^2 + i \cdot V_{norm}^3 + j \cdot X_{i0} + k \cdot X_{i0}^2 + l \cdot X_{i0}^3 + m \cdot f_a'$
10	14	5	$\frac{X_i}{X_{i0}} = a + b \cdot T_{gas,max} + c \cdot T_{gas,max}^2 + d \cdot T_{gas,max}^3 + e \cdot \exp(f \cdot t_{res}) + g \cdot V_{norm} + h \cdot V_{norm}^2 + i \cdot V_{norm}^3 + j \cdot X_{i0} + k \cdot X_{i0}^2 + l \cdot X_{i0}^3 + m \cdot f_a' + n \cdot f_a'^2$
11	13	5	$\frac{X_i}{X_{i0}} = a + b \cdot T_{gas,max} + c \cdot T_{gas,max}^2 + d \cdot T_{gas,max}^3 + e \cdot \exp(f \cdot t_{res}) + g \cdot V_{norm} + h \cdot V_{norm}^2 + i \cdot V_{norm}^3 + j \cdot X_{i0} + k \cdot X_{i0}^2 + l \cdot X_{i0}^3 + m \cdot \ln(f_a')$

Table C-4. Elemental Composition Model Forms, CONTINUED

Model	N_{coeff}	N_{var}	Equation
12	14	5	$\frac{X_i}{X_{i0}} = a + b \cdot T_{gas,max} + c \cdot T_{gas,max}^2 + d \cdot T_{gas,max}^3 + e \cdot \exp(f \cdot t_{res}) + g \cdot V_{norm} + h \cdot V_{norm}^2 + i \cdot V_{norm}^3 + j \cdot X_{i0} + k \cdot X_{i0}^2 + l \cdot X_{i0}^3 + m \cdot c_0 + n \cdot c_0^2$
13	14	5	$\frac{X_i}{X_{i0}} = a + b \cdot T_{gas,max} + c \cdot T_{gas,max}^2 + d \cdot T_{gas,max}^3 + e \cdot \exp(f \cdot t_{res}) + g \cdot V_{norm} + h \cdot V_{norm}^2 + i \cdot V_{norm}^3 + j \cdot X_{i0} + k \cdot X_{i0}^2 + l \cdot X_{i0}^3 + m \cdot M_{\delta,Genetti} + n \cdot M_{\delta,Genetti}^2$
14	14	5	$\frac{X_i}{X_{i0}} = a + b \cdot T_{gas,max} + c \cdot T_{gas,max}^2 + d \cdot T_{gas,max}^3 + e \cdot \exp(f \cdot t_{res}) + g \cdot V_{norm} + h \cdot V_{norm}^2 + i \cdot V_{norm}^3 + j \cdot X_{i0} + k \cdot X_{i0}^2 + l \cdot X_{i0}^3 + m \cdot M_{\delta,Genetti}^n$
15	13	5	$\frac{X_i}{X_{i0}} = a + b \cdot T_{gas,max} + c \cdot T_{gas,max}^2 + d \cdot T_{gas,max}^3 + e \cdot \exp(f \cdot t_{res}) + g \cdot V_{norm} + h \cdot V_{norm}^2 + i \cdot V_{norm}^3 + j \cdot X_{i0} + k \cdot X_{i0}^2 + l \cdot X_{i0}^3 + m \cdot O_{coal}$
16	14	5	$\frac{X_i}{X_{i0}} = a + b \cdot T_{gas,max} + c \cdot T_{gas,max}^2 + d \cdot T_{gas,max}^3 + e \cdot \exp(f \cdot t_{res}) + g \cdot V_{norm} + h \cdot V_{norm}^2 + i \cdot V_{norm}^3 + j \cdot X_{i0} + k \cdot X_{i0}^2 + l \cdot X_{i0}^3 + m \cdot O_{coal} + n \cdot O_{coal}^2$
17	13	5	$\frac{X_i}{X_{i0}} = a + b \cdot T_{gas,max} + c \cdot T_{gas,max}^2 + d \cdot T_{gas,max}^3 + e \cdot \exp(f \cdot t_{res}) + g \cdot V_{norm} + h \cdot V_{norm}^2 + i \cdot V_{norm}^3 + j \cdot X_{i0} + k \cdot X_{i0}^2 + l \cdot X_{i0}^3 + m \cdot V_{ASTM}$
18	14	5	$\frac{X_i}{X_{i0}} = a + b \cdot T_{gas,max} + c \cdot T_{gas,max}^2 + d \cdot T_{gas,max}^3 + e \cdot \exp(f \cdot t_{res}) + g \cdot V_{norm} + h \cdot V_{norm}^2 + i \cdot V_{norm}^3 + j \cdot X_{i0} + k \cdot X_{i0}^2 + l \cdot X_{i0}^3 + m \cdot V_{ASTM} + n \cdot V_{ASTM}^2$
19	14	5	$\frac{X_i}{X_{i0}} = a + b \cdot T_{gas,max} + c \cdot T_{gas,max}^2 + d \cdot T_{gas,max}^3 + e \cdot \exp(f \cdot t_{res}) + g \cdot V_{norm} + h \cdot V_{norm}^2 + i \cdot V_{norm}^3 + j \cdot X_{i0} + k \cdot X_{i0}^2 + l \cdot X_{i0}^3 + m \cdot V_{ASTM}^n$
20	20	9	$\frac{X_i}{X_{i0}} = a + b \cdot T_{gas,max} + c \cdot T_{gas,max}^2 + d \cdot T_{gas,max}^3 + e \cdot \exp(f \cdot t_{res}) + g \cdot V_{norm} + h \cdot V_{norm}^2 + i \cdot V_{norm}^3 + j \cdot X_{i0} + k \cdot X_{i0}^2 + l \cdot X_{i0}^3 + m \cdot c_0 + n \cdot c_0^2 + o \cdot \ln(f_a') + p \cdot M_{\delta,Genetti}^q + r \cdot O_{coal} + s \cdot V_{ASTM}^t$

Table C-4. Elemental Composition Model Forms, CONTINUED

Model	N_{coeff}	N_{var}	Equation
21	17	4	$\frac{X_i}{X_{i0}} = a + b \cdot T_{gas,max} + \frac{1}{c \cdot T_{gas,max}^2 + d \cdot T_{gas,max}^3 + e \cdot T_{gas,max}^4} + f \cdot t_{res} + \frac{1}{g \cdot t_{res}^2 + h \cdot t_{res}^3 + i \cdot t_{res}^4} + j \cdot V_{norm} + \frac{1}{1 + k \cdot V_{norm}^2 + l \cdot V_{norm}^3 + m \cdot V_{norm}^4} + n \cdot X_{i0} + \frac{1}{o \cdot X_{i0}^2 + p \cdot X_{i0}^3 + q \cdot X_{i0}^4}$
22	13	4	$\frac{X_i}{X_{i0}} = a + b \cdot T_{gas,max} + c \cdot T_{gas,max}^2 + d \cdot T_{gas,max}^3 + e \cdot t_{res} + f \cdot t_{res}^2 + g \cdot t_{res}^3 + h \cdot V_{norm} + i \cdot V_{norm}^2 + j \cdot V_{norm}^3 + k \cdot X_{i0} + l \cdot X_{i0}^2 + m \cdot X_{i0}^3$
23	14	5	$\frac{X_i}{X_{i0}} = a + b \cdot T_{gas,max} + c \cdot T_{gas,max}^2 + d \cdot T_{gas,max}^3 + e \cdot t_{res} + f \cdot t_{res}^2 + g \cdot t_{res}^3 + h \cdot V_{norm} + i \cdot V_{norm}^2 + j \cdot V_{norm}^3 + k \cdot X_{i0} + l \cdot X_{i0}^2 + m \cdot X_{i0}^3 + n \cdot c_0$
24	14	5	$\frac{X_i}{X_{i0}} = a + b \cdot T_{gas,max} + c \cdot T_{gas,max}^2 + d \cdot T_{gas,max}^3 + e \cdot t_{res} + f \cdot t_{res}^2 + g \cdot t_{res}^3 + h \cdot V_{norm} + i \cdot V_{norm}^2 + j \cdot V_{norm}^3 + k \cdot X_{i0} + l \cdot X_{i0}^2 + m \cdot X_{i0}^3 + n \cdot \ln(c_0)$
25	14	5	$\frac{X_i}{X_{i0}} = a + b \cdot T_{gas,max} + c \cdot T_{gas,max}^2 + d \cdot T_{gas,max}^3 + e \cdot t_{res} + f \cdot t_{res}^2 + g \cdot t_{res}^3 + h \cdot V_{norm} + i \cdot V_{norm}^2 + j \cdot V_{norm}^3 + k \cdot X_{i0} + l \cdot X_{i0}^2 + m \cdot X_{i0}^3 + n \cdot f_a'$
26	15	5	$\frac{X_i}{X_{i0}} = a + b \cdot T_{gas,max} + c \cdot T_{gas,max}^2 + d \cdot T_{gas,max}^3 + e \cdot t_{res} + f \cdot t_{res}^2 + g \cdot t_{res}^3 + h \cdot V_{norm} + i \cdot V_{norm}^2 + j \cdot V_{norm}^3 + k \cdot X_{i0} + l \cdot X_{i0}^2 + m \cdot X_{i0}^3 + n \cdot f_a' + o \cdot f_a'^2$
27	14	5	$\frac{X_i}{X_{i0}} = a + b \cdot T_{gas,max} + c \cdot T_{gas,max}^2 + d \cdot T_{gas,max}^3 + e \cdot t_{res} + f \cdot t_{res}^2 + g \cdot t_{res}^3 + h \cdot V_{norm} + i \cdot V_{norm}^2 + j \cdot V_{norm}^3 + k \cdot X_{i0} + l \cdot X_{i0}^2 + m \cdot X_{i0}^3 + n \cdot \ln(f_a')$
28	14	5	$\frac{X_i}{X_{i0}} = a + b \cdot T_{gas,max} + c \cdot T_{gas,max}^2 + d \cdot T_{gas,max}^3 + e \cdot t_{res} + f \cdot t_{res}^2 + g \cdot t_{res}^3 + h \cdot V_{norm} + i \cdot V_{norm}^2 + j \cdot V_{norm}^3 + k \cdot X_{i0} + l \cdot X_{i0}^2 + m \cdot X_{i0}^3 + n \cdot M_{\delta,Genetti}$
29	15	5	$\frac{X_i}{X_{i0}} = a + b \cdot T_{gas,max} + c \cdot T_{gas,max}^2 + d \cdot T_{gas,max}^3 + e \cdot t_{res} + f \cdot t_{res}^2 + g \cdot t_{res}^3 + h \cdot V_{norm} + i \cdot V_{norm}^2 + j \cdot V_{norm}^3 + k \cdot X_{i0} + l \cdot X_{i0}^2 + m \cdot X_{i0}^3 + n \cdot M_{\delta,Genetti} + o \cdot M_{\delta,Genetti}^2$

Table C-4. Elemental Composition Model Forms, CONTINUED

Model	N_{coeff}	N_{var}	Equation
30	14	5	$\frac{X_i}{X_{i0}} = a + b \cdot T_{gas,max} + c \cdot T_{gas,max}^2 + d \cdot T_{gas,max}^3 + e \cdot t_{res} + f \cdot t_{res}^2 + g \cdot t_{res}^3 + h \cdot V_{norm} + i \cdot V_{norm}^2 + j \cdot V_{norm}^3 + k \cdot X_{i0} + l \cdot X_{i0}^2 + m \cdot X_{i0}^3 + n \cdot V_{ASTM}$
31	15	5	$\frac{X_i}{X_{i0}} = a + b \cdot T_{gas,max} + c \cdot T_{gas,max}^2 + d \cdot T_{gas,max}^3 + e \cdot t_{res} + f \cdot t_{res}^2 + g \cdot t_{res}^3 + h \cdot V_{norm} + i \cdot V_{norm}^2 + j \cdot V_{norm}^3 + k \cdot X_{i0} + l \cdot X_{i0}^2 + m \cdot X_{i0}^3 + n \cdot V_{ASTM} + o \cdot V_{ASTM}^2$
32	16	7	$\frac{X_i}{X_{i0}} = a + b \cdot T_{gas,max} + c \cdot T_{gas,max}^2 + d \cdot T_{gas,max}^3 + e \cdot t_{res} + f \cdot t_{res}^2 + g \cdot t_{res}^3 + h \cdot V_{norm} + i \cdot V_{norm}^2 + j \cdot V_{norm}^3 + k \cdot X_{i0} + l \cdot X_{i0}^2 + m \cdot X_{i0}^3 + n \cdot c_0 + o \cdot M_{\delta,Genetti} + p \cdot V_{ASTM}$
33	15	5	$\frac{X_i}{X_{i0}} = a + b \cdot T_{gas,max} + c \cdot T_{gas,max}^2 + d \cdot T_{gas,max}^3 + e \cdot t_{res} + f \cdot t_{res}^2 + g \cdot t_{res}^3 + h \cdot V_{norm} + i \cdot V_{norm}^2 + j \cdot V_{norm}^3 + k \cdot X_{i0} + l \cdot X_{i0}^2 + m \cdot X_{i0}^3 + n \cdot c_0 + o \cdot c_0^2$
34	16	5	$\frac{X_i}{X_{i0}} = a + b \cdot T_{gas,max} + c \cdot T_{gas,max}^2 + d \cdot T_{gas,max}^3 + e \cdot t_{res} + f \cdot t_{res}^2 + g \cdot t_{res}^3 + h \cdot V_{norm} + i \cdot V_{norm}^2 + j \cdot V_{norm}^3 + k \cdot X_{i0} + l \cdot X_{i0}^2 + m \cdot X_{i0}^3 + n \cdot c_0 + o \cdot c_0^2 + p \cdot c_0^3$
35	15	5	$\frac{X_i}{X_{i0}} = a + b \cdot T_{gas,max} + c \cdot T_{gas,max}^2 + d \cdot T_{gas,max}^3 + e \cdot t_{res} + f \cdot t_{res}^2 + g \cdot t_{res}^3 + h \cdot V_{norm} + i \cdot V_{norm}^2 + j \cdot V_{norm}^3 + k \cdot X_{i0} + l \cdot X_{i0}^2 + m \cdot X_{i0}^3 + n \cdot M_{\delta,Genetti}^o$
36	14	5	$\frac{X_i}{X_{i0}} = a + b \cdot T_{gas,max} + c \cdot T_{gas,max}^2 + d \cdot T_{gas,max}^3 + e \cdot t_{res} + f \cdot t_{res}^2 + g \cdot t_{res}^3 + h \cdot V_{norm} + i \cdot V_{norm}^2 + j \cdot V_{norm}^3 + k \cdot X_{i0} + l \cdot X_{i0}^2 + m \cdot X_{i0}^3 + n \cdot O_{coal}$
37	15	5	$\frac{X_i}{X_{i0}} = a + b \cdot T_{gas,max} + c \cdot T_{gas,max}^2 + d \cdot T_{gas,max}^3 + e \cdot t_{res} + f \cdot t_{res}^2 + g \cdot t_{res}^3 + h \cdot V_{norm} + i \cdot V_{norm}^2 + j \cdot V_{norm}^3 + k \cdot X_{i0} + l \cdot X_{i0}^2 + m \cdot X_{i0}^3 + n \cdot V_{ASTM}^o$
38	19	9	$\frac{X_i}{X_{i0}} = a + b \cdot T_{gas,max} + c \cdot T_{gas,max}^2 + d \cdot T_{gas,max}^3 + e \cdot t_{res} + f \cdot t_{res}^2 + g \cdot t_{res}^3 + h \cdot V_{norm} + i \cdot V_{norm}^2 + j \cdot V_{norm}^3 + k \cdot X_{i0} + l \cdot X_{i0}^2 + m \cdot X_{i0}^3 + n \cdot c_0 + o \cdot c_0^2 + p \cdot f_a' + q \cdot M_{\delta,Genetti} + r \cdot O_{coal} + s \cdot V_{ASTM}$

Table C-4. Elemental Composition Model Forms, CONTINUED

Model	N_{coeff}	N_{var}	Equation
39	16	5	$\frac{X_i}{X_{i0}} = a + b \cdot T_{gas,max} + c \cdot T_{gas,max}^2 + d \cdot T_{gas,max}^3 + e \cdot t_{res} + f \cdot t_{res}^2 + g \cdot t_{res}^3 + h \cdot V_{norm} + i \cdot V_{norm}^2 + j \cdot V_{norm}^3 + k \cdot X_{i0} + l \cdot X_{i0}^2 + m \cdot X_{i0}^3 + n \cdot f_a' + o \cdot f_a'^2 + p \cdot f_a'^3$
40	14	5	$\frac{X_i}{X_{i0}} = a + b \cdot T_{gas,max} + c \cdot T_{gas,max}^2 + d \cdot T_{gas,max}^3 + e \cdot t_{res} + f \cdot t_{res}^2 + g \cdot t_{res}^3 + h \cdot V_{norm} + i \cdot V_{norm}^2 + j \cdot V_{norm}^3 + k \cdot X_{i0} + l \cdot X_{i0}^2 + m \cdot X_{i0}^3 + n \cdot (\sigma + 1)_{Genetti}$
41	15	5	$\frac{X_i}{X_{i0}} = a + b \cdot T_{gas,max} + c \cdot T_{gas,max}^2 + d \cdot T_{gas,max}^3 + e \cdot t_{res} + f \cdot t_{res}^2 + g \cdot t_{res}^3 + h \cdot V_{norm} + i \cdot V_{norm}^2 + j \cdot V_{norm}^3 + k \cdot X_{i0} + l \cdot X_{i0}^2 + m \cdot X_{i0}^3 + n \cdot (\sigma + 1)_{Genetti} + o \cdot (\sigma + 1)_{Genetti}^2$
42	15	5	$\frac{X_i}{X_{i0}} = a + b \cdot T_{gas,max} + c \cdot T_{gas,max}^2 + d \cdot T_{gas,max}^3 + e \cdot t_{res} + f \cdot t_{res}^2 + g \cdot t_{res}^3 + h \cdot V_{norm} + i \cdot V_{norm}^2 + j \cdot V_{norm}^3 + k \cdot X_{i0} + l \cdot X_{i0}^2 + m \cdot X_{i0}^3 + n \cdot (\sigma + 1)_{Genetti}^o$
43	16	7	$\frac{X_i}{X_{i0}} = a + b \cdot T_{gas,max} + c \cdot T_{gas,max}^2 + d \cdot T_{gas,max}^3 + e \cdot t_{res} + f \cdot t_{res}^2 + g \cdot t_{res}^3 + h \cdot V_{norm} + i \cdot V_{norm}^2 + j \cdot V_{norm}^3 + k \cdot X_{i0} + l \cdot X_{i0}^2 + m \cdot X_{i0}^3 + n \cdot c_0 + o \cdot f_a' + p \cdot (\sigma + 1)_{Genetti}$
44	12	4	$\frac{X_i}{X_{i0}} = a + b \cdot T_{gas,max} + c \cdot T_{gas,max}^2 + d \cdot T_{gas,max}^3 + e \cdot t_{res} + f \cdot t_{res}^2 + g \cdot t_{res}^3 + h \cdot V_{norm} + i \cdot V_{norm}^2 + j \cdot X_{i0} + k \cdot X_{i0}^2 + l \cdot x_{i0}^3$
45	13	5	$\frac{X_i}{X_{i0}} = a + b \cdot T_{gas,max} + c \cdot T_{gas,max}^2 + d \cdot T_{gas,max}^3 + e \cdot t_{res} + f \cdot t_{res}^2 + g \cdot t_{res}^3 + h \cdot V_{norm} + i \cdot V_{norm}^2 + j \cdot X_{i0} + k \cdot X_{i0}^2 + l \cdot x_{i0}^3 + m \cdot c_0$
46	15	5	$\frac{X_i}{X_{i0}} = a + b \cdot T_{gas,max} + c \cdot T_{gas,max}^2 + d \cdot T_{gas,max}^3 + e \cdot t_{res} + f \cdot t_{res}^2 + g \cdot t_{res}^3 + h \cdot V_{norm} + i \cdot V_{norm}^2 + j \cdot X_{i0} + k \cdot X_{i0}^2 + l \cdot x_{i0}^3 + m \cdot c_0 + n \cdot c_0^2 + o \cdot c_0^3$
47	13	5	$\frac{X_i}{X_{i0}} = a + b \cdot T_{gas,max} + c \cdot T_{gas,max}^2 + d \cdot T_{gas,max}^3 + e \cdot t_{res} + f \cdot t_{res}^2 + g \cdot t_{res}^3 + h \cdot V_{norm} + i \cdot V_{norm}^2 + j \cdot X_{i0} + k \cdot X_{i0}^2 + l \cdot x_{i0}^3 + m \cdot f_a'$

Table C-4. Elemental Composition Model Forms, CONTINUED

Model	N_{coeff}	N_{var}	Equation
48	14	5	$\frac{X_i}{X_{i0}} = a + b \cdot T_{gas,max} + c \cdot T_{gas,max}^2 + d \cdot T_{gas,max}^3 + e \cdot t_{res} + f \cdot t_{res}^2 + g \cdot t_{res}^3 + h \cdot V_{norm} + i \cdot V_{norm}^2 + j \cdot X_{i0} + k \cdot X_{i0}^2 + l \cdot x_{i0}^3 + m \cdot f_a' + n \cdot f_a'^2$
49	13	5	$\frac{X_i}{X_{i0}} = a + b \cdot T_{gas,max} + c \cdot T_{gas,max}^2 + d \cdot T_{gas,max}^3 + e \cdot t_{res} + f \cdot t_{res}^2 + g \cdot t_{res}^3 + h \cdot V_{norm} + i \cdot V_{norm}^2 + j \cdot X_{i0} + k \cdot X_{i0}^2 + l \cdot x_{i0}^3 + m \cdot M_{\delta,Genetti}$
50	13	5	$\frac{X_i}{X_{i0}} = a + b \cdot T_{gas,max} + c \cdot T_{gas,max}^2 + d \cdot T_{gas,max}^3 + e \cdot t_{res} + f \cdot t_{res}^2 + g \cdot t_{res}^3 + h \cdot V_{norm} + i \cdot V_{norm}^2 + j \cdot X_{i0} + k \cdot X_{i0}^2 + l \cdot x_{i0}^3 + m \cdot S_{coal}$
51	15	5	$\frac{X_i}{X_{i0}} = a + b \cdot T_{gas,max} + c \cdot T_{gas,max}^2 + d \cdot T_{gas,max}^3 + e \cdot t_{res} + f \cdot t_{res}^2 + g \cdot t_{res}^3 + h \cdot V_{norm} + i \cdot V_{norm}^2 + j \cdot X_{i0} + k \cdot X_{i0}^2 + l \cdot x_{i0}^3 + m \cdot S_{coal} + n \cdot S_{coal}^2 + o \cdot S_{coal}^3$
52	13	5	$\frac{X_i}{X_{i0}} = a + b \cdot T_{gas,max} + c \cdot T_{gas,max}^2 + d \cdot T_{gas,max}^3 + e \cdot t_{res} + f \cdot t_{res}^2 + g \cdot t_{res}^3 + h \cdot V_{norm} + i \cdot V_{norm}^2 + j \cdot X_{i0} + k \cdot X_{i0}^2 + l \cdot x_{i0}^3 + m \cdot V_{ASTM}$
53	15	5	$\frac{X_i}{X_{i0}} = a + b \cdot T_{gas,max} + c \cdot T_{gas,max}^2 + d \cdot T_{gas,max}^3 + e \cdot t_{res} + f \cdot t_{res}^2 + g \cdot t_{res}^3 + h \cdot V_{norm} + i \cdot V_{norm}^2 + j \cdot X_{i0} + k \cdot X_{i0}^2 + l \cdot x_{i0}^3 + m \cdot V_{ASTM} + n \cdot V_{ASTM}^2 + o \cdot V_{ASTM}^3$
54	21	9	$\frac{X_i}{X_{i0}} = a + b \cdot T_{gas,max} + c \cdot T_{gas,max}^2 + d \cdot T_{gas,max}^3 + e \cdot t_{res} + f \cdot t_{res}^2 + g \cdot t_{res}^3 + h \cdot V_{norm} + i \cdot V_{norm}^2 + j \cdot X_{i0} + k \cdot X_{i0}^2 + l \cdot x_{i0}^3 + m \cdot c_0 + n \cdot c_0^2 + o \cdot c_0^3 + p \cdot f_a' + q \cdot M_{\delta,Genetti} + r \cdot S_{coal} + s \cdot S_{coal}^2 + t \cdot S_{coal}^3 + u \cdot V_{ASTM}$
55	12	4	$\frac{X_i}{X_{i0}} = a + b \cdot T_{gas,max}^c + d \cdot t_{res} + e \cdot t_{res}^2 + f \cdot t_{res}^3 + g \cdot V_{norm} + h \cdot V_{norm}^2 + i \cdot V_{norm}^3 + j \cdot X_{i0} + k \cdot X_{i0}^2 + l \cdot X_{i0}^3$
56	14	5	$\frac{X_i}{X_{i0}} = a + b \cdot T_{gas,max}^c + d \cdot t_{res} + e \cdot t_{res}^2 + f \cdot t_{res}^3 + g \cdot V_{norm} + h \cdot V_{norm}^2 + i \cdot V_{norm}^3 + j \cdot X_{i0} + k \cdot X_{i0}^2 + l \cdot X_{i0}^3 + m \cdot c_0 + n \cdot c_0^2$

Table C-4. Elemental Composition Model Forms, CONTINUED

Model	N_{coeff}	N_{var}	Equation
57	15	5	$\frac{X_i}{X_{i0}} = a + b \cdot T_{gas,max}^{c} + d \cdot t_{res} + e \cdot t_{res}^2 + f \cdot t_{res}^3 + g \cdot V_{norm} + h \cdot V_{norm}^2 + i \cdot V_{norm}^3 + j \cdot X_{i0} + k \cdot X_{i0}^2 + l \cdot X_{i0}^3 + m \cdot c_0 + n \cdot c_0^2 + o \cdot c_0^3$
58	13	5	$\frac{X_i}{X_{i0}} = a + b \cdot T_{gas,max}^{c} + d \cdot t_{res} + e \cdot t_{res}^2 + f \cdot t_{res}^3 + g \cdot V_{norm} + h \cdot V_{norm}^2 + i \cdot V_{norm}^3 + j \cdot X_{i0} + k \cdot X_{i0}^2 + l \cdot X_{i0}^3 + m \cdot \ln(c_0)$
59	14	5	$\frac{X_i}{X_{i0}} = a + b \cdot T_{gas,max}^{c} + d \cdot t_{res} + e \cdot t_{res}^2 + f \cdot t_{res}^3 + g \cdot V_{norm} + h \cdot V_{norm}^2 + i \cdot V_{norm}^3 + j \cdot X_{i0} + k \cdot X_{i0}^2 + l \cdot X_{i0}^3 + m \cdot f_a' + n \cdot f_a'^2$
60	15	5	$\frac{X_i}{X_{i0}} = a + b \cdot T_{gas,max}^{c} + d \cdot t_{res} + e \cdot t_{res}^2 + f \cdot t_{res}^3 + g \cdot V_{norm} + h \cdot V_{norm}^2 + i \cdot V_{norm}^3 + j \cdot X_{i0} + k \cdot X_{i0}^2 + l \cdot X_{i0}^3 + m \cdot f_a' + n \cdot f_a'^2 + o \cdot f_a'^3$
61	13	5	$\frac{X_i}{X_{i0}} = a + b \cdot T_{gas,max}^{c} + d \cdot t_{res} + e \cdot t_{res}^2 + f \cdot t_{res}^3 + g \cdot V_{norm} + h \cdot V_{norm}^2 + i \cdot V_{norm}^3 + j \cdot X_{i0} + k \cdot X_{i0}^2 + l \cdot X_{i0}^3 + m \cdot M_{\delta,Genetti}$
62	14	5	$\frac{X_i}{X_{i0}} = a + b \cdot T_{gas,max}^{c} + d \cdot t_{res} + e \cdot t_{res}^2 + f \cdot t_{res}^3 + g \cdot V_{norm} + h \cdot V_{norm}^2 + i \cdot V_{norm}^3 + j \cdot X_{i0} + k \cdot X_{i0}^2 + l \cdot X_{i0}^3 + m \cdot M_{\delta,Genetti} + n \cdot M_{\delta,Genetti}^2$
63	15	5	$\frac{X_i}{X_{i0}} = a + b \cdot T_{gas,max}^{c} + d \cdot t_{res} + e \cdot t_{res}^2 + f \cdot t_{res}^3 + g \cdot V_{norm} + h \cdot V_{norm}^2 + i \cdot V_{norm}^3 + j \cdot X_{i0} + k \cdot X_{i0}^2 + l \cdot X_{i0}^3 + m \cdot M_{\delta,Genetti} + n \cdot M_{\delta,Genetti}^2 + o \cdot M_{\delta,Genetti}^3$
64	14	5	$\frac{X_i}{X_{i0}} = a + b \cdot T_{gas,max}^{c} + d \cdot t_{res} + e \cdot t_{res}^2 + f \cdot t_{res}^3 + g \cdot V_{norm} + h \cdot V_{norm}^2 + i \cdot V_{norm}^3 + j \cdot X_{i0} + k \cdot X_{i0}^2 + l \cdot X_{i0}^3 + m \cdot M_{\delta,Genetti}^n$
65	13	5	$\frac{X_i}{X_{i0}} = a + b \cdot T_{gas,max}^{c} + d \cdot t_{res} + e \cdot t_{res}^2 + f \cdot t_{res}^3 + g \cdot V_{norm} + h \cdot V_{norm}^2 + i \cdot V_{norm}^3 + j \cdot X_{i0} + k \cdot X_{i0}^2 + l \cdot X_{i0}^3 + m \cdot C_{coal}$

Table C-4. Elemental Composition Model Forms, CONTINUED

Model	N_{coeff}	N_{var}	Equation
66	14	5	$\frac{X_i}{X_{i0}} = a + b \cdot T_{gas,max}^{c} + d \cdot t_{res} + e \cdot t_{res}^2 + f \cdot t_{res}^3 + g \cdot V_{norm} + h \cdot V_{norm}^2 + i \cdot V_{norm}^3 + j \cdot X_{i0} + k \cdot X_{i0}^2 + l \cdot X_{i0}^3 + m \cdot C_{coal} + n \cdot C_{coal}^2$
67	15	5	$\frac{X_i}{X_{i0}} = a + b \cdot T_{gas,max}^{c} + d \cdot t_{res} + e \cdot t_{res}^2 + f \cdot t_{res}^3 + g \cdot V_{norm} + h \cdot V_{norm}^2 + i \cdot V_{norm}^3 + j \cdot X_{i0} + k \cdot X_{i0}^2 + l \cdot X_{i0}^3 + m \cdot C_{coal} + n \cdot C_{coal}^2 + o \cdot C_{coal}^3$
68	13	5	$\frac{X_i}{X_{i0}} = a + b \cdot T_{gas,max}^{c} + d \cdot t_{res} + e \cdot t_{res}^2 + f \cdot t_{res}^3 + g \cdot V_{norm} + h \cdot V_{norm}^2 + i \cdot V_{norm}^3 + j \cdot X_{i0} + k \cdot X_{i0}^2 + l \cdot X_{i0}^3 + m \cdot O_{coal}$
69	15	5	$\frac{X_i}{X_{i0}} = a + b \cdot T_{gas,max}^{c} + d \cdot t_{res} + e \cdot t_{res}^2 + f \cdot t_{res}^3 + g \cdot V_{norm} + h \cdot V_{norm}^2 + i \cdot V_{norm}^3 + j \cdot X_{i0} + k \cdot X_{i0}^2 + l \cdot X_{i0}^3 + m \cdot O_{coal} + n \cdot O_{coal}^2 + o \cdot O_{coal}^3$
70	15	5	$\frac{X_i}{X_{i0}} = a + b \cdot T_{gas,max}^{c} + d \cdot t_{res} + e \cdot t_{res}^2 + f \cdot t_{res}^3 + g \cdot V_{norm} + h \cdot V_{norm}^2 + i \cdot V_{norm}^3 + j \cdot X_{i0} + k \cdot X_{i0}^2 + l \cdot X_{i0}^3 + m \cdot S_{coal} + n \cdot S_{coal}^2 + o \cdot S_{coal}^3$
71	13	5	$\frac{X_i}{X_{i0}} = a + b \cdot T_{gas,max}^{c} + d \cdot t_{res} + e \cdot t_{res}^2 + f \cdot t_{res}^3 + g \cdot V_{norm} + h \cdot V_{norm}^2 + i \cdot V_{norm}^3 + j \cdot X_{i0} + k \cdot X_{i0}^2 + l \cdot X_{i0}^3 + m \cdot V_{ASTM}$
72	14	5	$\frac{X_i}{X_{i0}} = a + b \cdot T_{gas,max}^{c} + d \cdot t_{res} + e \cdot t_{res}^2 + f \cdot t_{res}^3 + g \cdot V_{norm} + h \cdot V_{norm}^2 + i \cdot V_{norm}^3 + j \cdot X_{i0} + k \cdot X_{i0}^2 + l \cdot X_{i0}^3 + m \cdot V_{ASTM} + n \cdot V_{ASTM}^2$
73	15	5	$\frac{X_i}{X_{i0}} = a + b \cdot T_{gas,max}^{c} + d \cdot t_{res} + e \cdot t_{res}^2 + f \cdot t_{res}^3 + g \cdot V_{norm} + h \cdot V_{norm}^2 + i \cdot V_{norm}^3 + j \cdot X_{i0} + k \cdot X_{i0}^2 + l \cdot X_{i0}^3 + m \cdot V_{ASTM} + n \cdot V_{ASTM}^2 + o \cdot V_{ASTM}^3$
74	14	5	$\frac{X_i}{X_{i0}} = a + b \cdot T_{gas,max}^{c} + d \cdot t_{res} + e \cdot t_{res}^2 + f \cdot t_{res}^3 + g \cdot V_{norm} + h \cdot V_{norm}^2 + i \cdot V_{norm}^3 + j \cdot X_{i0} + k \cdot X_{i0}^2 + l \cdot X_{i0}^3 + m \cdot V_{ASTM}^n$

Table C-4. Elemental Composition Model Forms, CONTINUED

Model	N_{coeff}	N_{var}	Equation
75	13	5	$\frac{X_i}{X_{i0}} = a + b \cdot T_{gas,max}^{c} + d \cdot t_{res} + e \cdot t_{res}^2 + f \cdot t_{res}^3 + g \cdot V_{norm} + h \cdot V_{norm}^2 + i \cdot V_{norm}^3 + j \cdot X_{i0} + k \cdot X_{i0}^2 + l \cdot X_{i0}^3 + m \cdot \frac{O_{coal}}{C_{coal}}$
76	14	5	$\frac{X_i}{X_{i0}} = a + b \cdot T_{gas,max}^{c} + d \cdot t_{res} + e \cdot t_{res}^2 + f \cdot t_{res}^3 + g \cdot V_{norm} + h \cdot V_{norm}^2 + i \cdot V_{norm}^3 + j \cdot X_{i0} + k \cdot X_{i0}^2 + l \cdot X_{i0}^3 + m \cdot \frac{O_{coal}}{C_{coal}} + n \cdot \left(\frac{O_{coal}}{C_{coal}}\right)^2$
77	15	5	$\frac{X_i}{X_{i0}} = a + b \cdot T_{gas,max}^{c} + d \cdot t_{res} + e \cdot t_{res}^2 + f \cdot t_{res}^3 + g \cdot V_{norm} + h \cdot V_{norm}^2 + i \cdot V_{norm}^3 + j \cdot X_{i0} + k \cdot X_{i0}^2 + l \cdot X_{i0}^3 + m \cdot \frac{O_{coal}}{C_{coal}} + n \cdot \left(\frac{O_{coal}}{C_{coal}}\right)^2 + o \cdot \left(\frac{O_{coal}}{C_{coal}}\right)^3$
78	13	5	$\frac{X_i}{X_{i0}} = a + b \cdot T_{gas,max}^{c} + d \cdot t_{res} + e \cdot t_{res}^2 + f \cdot t_{res}^3 + g \cdot V_{norm} + h \cdot V_{norm}^2 + i \cdot V_{norm}^3 + j \cdot X_{i0} + k \cdot X_{i0}^2 + l \cdot X_{i0}^3 + m \cdot \ln\left(\frac{O_{coal}}{C_{coal}}\right)$
79	22	9	$\frac{X_i}{X_{i0}} = a + b \cdot T_{gas,max}^{c} + d \cdot t_{res} + e \cdot t_{res}^2 + f \cdot t_{res}^3 + g \cdot V_{norm} + h \cdot V_{norm}^2 + i \cdot V_{norm}^3 + j \cdot X_{i0} + k \cdot X_{i0}^2 + l \cdot X_{i0}^3 + m \cdot c_0 + n \cdot c_0^2 + o \cdot c_0^3 + p \cdot f_a' + q \cdot f_a'^2 + r \cdot f_a'^3 + s \cdot M_{\delta,Genetti} + t \cdot \ln\left(\frac{O_{coal}}{C_{coal}}\right) + u \cdot V_{ASTM}^{v}$
80	26	10	$\frac{X_i}{X_{i0}} = a + b \cdot T_{gas,max}^{c} + d \cdot t_{res} + e \cdot t_{res}^2 + f \cdot t_{res}^3 + g \cdot V_{norm} + h \cdot V_{norm}^2 + i \cdot V_{norm}^3 + j \cdot X_{i0} + k \cdot X_{i0}^2 + l \cdot X_{i0}^3 + m \cdot c_0 + n \cdot f_a' + o \cdot f_a'^2 + p \cdot M_{\delta,Genetti} + q \cdot M_{\delta,Genetti}^2 + r \cdot S_{coal} + s \cdot S_{coal}^2 + t \cdot S_{coal}^3 + u \cdot V_{ASTM} + v \cdot V_{ASTM}^2 + w \cdot V_{ASTM}^3 + x \cdot \frac{O_{coal}}{C_{coal}} + y \cdot \left(\frac{O_{coal}}{C_{coal}}\right)^2 + z \cdot \left(\frac{O_{coal}}{C_{coal}}\right)^3$

Table C-4. Elemental Composition Model Forms, CONTINUED

Model	N_{coeff}	N_{var}	Equation
81	13	4	$\frac{X_i}{X_{i0}} = a + b \cdot T_{gas,max} + c \cdot T_{gas,max}^2 + d \cdot T_{gas,max}^3 + e \cdot T_{gas,max}^4 + f \cdot t_{res} + g \cdot t_{res}^2 + h \cdot t_{res}^3 + i \cdot t_{res}^4 + j \cdot V_{norm} + k \cdot V_{norm}^2 + l \cdot X_{i0} + m \cdot X_{i0}^2$
82	14	5	$\frac{X_i}{X_{i0}} = a + b \cdot T_{gas,max} + c \cdot T_{gas,max}^2 + d \cdot T_{gas,max}^3 + e \cdot T_{gas,max}^4 + f \cdot t_{res} + g \cdot t_{res}^2 + h \cdot t_{res}^3 + i \cdot t_{res}^4 + j \cdot V_{norm} + k \cdot V_{norm}^2 + l \cdot X_{i0} + m \cdot X_{i0}^2 + n \cdot f_a'$
83	15	5	$\frac{X_i}{X_{i0}} = a + b \cdot T_{gas,max} + c \cdot T_{gas,max}^2 + d \cdot T_{gas,max}^3 + e \cdot T_{gas,max}^4 + f \cdot t_{res} + g \cdot t_{res}^2 + h \cdot t_{res}^3 + i \cdot t_{res}^4 + j \cdot V_{norm} + k \cdot V_{norm}^2 + l \cdot X_{i0} + m \cdot X_{i0}^2 + n \cdot f_a' + o \cdot f_a'^2$
84	14	5	$\frac{X_i}{X_{i0}} = a + b \cdot T_{gas,max} + c \cdot T_{gas,max}^2 + d \cdot T_{gas,max}^3 + e \cdot T_{gas,max}^4 + f \cdot t_{res} + g \cdot t_{res}^2 + h \cdot t_{res}^3 + i \cdot t_{res}^4 + j \cdot V_{norm} + k \cdot V_{norm}^2 + l \cdot X_{i0} + m \cdot X_{i0}^2 + n \cdot \ln(f_a')$
85	15	5	$\frac{X_i}{X_{i0}} = a + b \cdot T_{gas,max} + c \cdot T_{gas,max}^2 + d \cdot T_{gas,max}^3 + e \cdot T_{gas,max}^4 + f \cdot t_{res} + g \cdot t_{res}^2 + h \cdot t_{res}^3 + i \cdot t_{res}^4 + j \cdot V_{norm} + k \cdot V_{norm}^2 + l \cdot X_{i0} + m \cdot X_{i0}^2 + n \cdot O_{coal} + o \cdot O_{coal}^2$
86	16	5	$\frac{X_i}{X_{i0}} = a + b \cdot T_{gas,max} + c \cdot T_{gas,max}^2 + d \cdot T_{gas,max}^3 + e \cdot T_{gas,max}^4 + f \cdot t_{res} + g \cdot t_{res}^2 + h \cdot t_{res}^3 + i \cdot t_{res}^4 + j \cdot V_{norm} + k \cdot V_{norm}^2 + l \cdot X_{i0} + m \cdot X_{i0}^2 + n \cdot O_{coal} + o \cdot O_{coal}^2 + p \cdot O_{coal}^3$
87	14	5	$\frac{X_i}{X_{i0}} = a + b \cdot T_{gas,max} + c \cdot T_{gas,max}^2 + d \cdot T_{gas,max}^3 + e \cdot T_{gas,max}^4 + f \cdot t_{res} + g \cdot t_{res}^2 + h \cdot t_{res}^3 + i \cdot t_{res}^4 + j \cdot V_{norm} + k \cdot V_{norm}^2 + l \cdot X_{i0} + m \cdot X_{i0}^2 + n \cdot (\sigma + 1)_{Genetti}$
88	15	5	$\frac{X_i}{X_{i0}} = a + b \cdot T_{gas,max} + c \cdot T_{gas,max}^2 + d \cdot T_{gas,max}^3 + e \cdot T_{gas,max}^4 + f \cdot t_{res} + g \cdot t_{res}^2 + h \cdot t_{res}^3 + i \cdot t_{res}^4 + j \cdot V_{norm} + k \cdot V_{norm}^2 + l \cdot X_{i0} + m \cdot X_{i0}^2 + n \cdot (\sigma + 1)_{Genetti} + o \cdot (\sigma + 1)_{Genetti}^2$
89	14	5	$\frac{X_i}{X_{i0}} = a + b \cdot T_{gas,max} + c \cdot T_{gas,max}^2 + d \cdot T_{gas,max}^3 + e \cdot T_{gas,max}^4 + f \cdot t_{res} + g \cdot t_{res}^2 + h \cdot t_{res}^3 + i \cdot t_{res}^4 + j \cdot V_{norm} + k \cdot V_{norm}^2 + l \cdot X_{i0} + m \cdot X_{i0}^2 + n \cdot \ln(\sigma + 1)_{Genetti}$

Table C-4. Elemental Composition Model Forms, CONTINUED

Model	N_{coeff}	N_{var}	Equation
90	17	7	$\frac{X_i}{X_{i0}} = a + b \cdot T_{gas,max} + c \cdot T_{gas,max}^2 + d \cdot T_{gas,max}^3 + e \cdot T_{gas,max}^4 + f \cdot t_{res} + g \cdot t_{res}^2 + h \cdot t_{res}^3 + i \cdot t_{res}^4 + j \cdot V_{norm} + k \cdot V_{norm}^2 + l \cdot X_{i0} + m \cdot X_{i0}^2 + n \cdot \ln(f_a') + o \cdot O_{coal} + p \cdot (\sigma + 1)_{Genetti} + q \cdot (\sigma + 1)_{Genetti}^2$
91	9	4	$\frac{X_i}{X_{i0}} = a + b \cdot T_{gas,max} + c \cdot T_{gas,max}^2 + d \cdot t_{res} + e \cdot t_{res}^2 + f \cdot V_{norm} + g \cdot V_{norm}^2 + h \cdot V_{norm}^3 + i \cdot X_{i0}$
92	10	5	$\frac{X_i}{X_{i0}} = a + b \cdot T_{gas,max} + c \cdot T_{gas,max}^2 + d \cdot t_{res} + e \cdot t_{res}^2 + f \cdot V_{norm} + g \cdot V_{norm}^2 + h \cdot V_{norm}^3 + i \cdot X_{i0} + j \cdot c_0$
93	11	5	$\frac{X_i}{X_{i0}} = a + b \cdot T_{gas,max} + c \cdot T_{gas,max}^2 + d \cdot t_{res} + e \cdot t_{res}^2 + f \cdot V_{norm} + g \cdot V_{norm}^2 + h \cdot V_{norm}^3 + i \cdot X_{i0} + j \cdot c_0 + k \cdot c_0^2$
94	12	5	$\frac{X_i}{X_{i0}} = a + b \cdot T_{gas,max} + c \cdot T_{gas,max}^2 + d \cdot t_{res} + e \cdot t_{res}^2 + f \cdot V_{norm} + g \cdot V_{norm}^2 + h \cdot V_{norm}^3 + i \cdot X_{i0} + j \cdot c_0 + k \cdot c_0^2 + l \cdot c_0^3$
95	10	5	$\frac{X_i}{X_{i0}} = a + b \cdot T_{gas,max} + c \cdot T_{gas,max}^2 + d \cdot t_{res} + e \cdot t_{res}^2 + f \cdot V_{norm} + g \cdot V_{norm}^2 + h \cdot V_{norm}^3 + i \cdot X_{i0} + j \cdot \ln(c_0)$
96	11	5	$\frac{X_i}{X_{i0}} = a + b \cdot T_{gas,max} + c \cdot T_{gas,max}^2 + d \cdot t_{res} + e \cdot t_{res}^2 + f \cdot V_{norm} + g \cdot V_{norm}^2 + h \cdot V_{norm}^3 + i \cdot X_{i0} + j \cdot S_{coal} + k \cdot S_{coal}^2$
97	12	5	$\frac{X_i}{X_{i0}} = a + b \cdot T_{gas,max} + c \cdot T_{gas,max}^2 + d \cdot t_{res} + e \cdot t_{res}^2 + f \cdot V_{norm} + g \cdot V_{norm}^2 + h \cdot V_{norm}^3 + i \cdot X_{i0} + j \cdot S_{coal} + k \cdot S_{coal}^2 + l \cdot S_{coal}^3$
98	12	6	$\frac{X_i}{X_{i0}} = a + b \cdot T_{gas,max} + c \cdot T_{gas,max}^2 + d \cdot t_{res} + e \cdot t_{res}^2 + f \cdot V_{norm} + g \cdot V_{norm}^2 + h \cdot V_{norm}^3 + i \cdot X_{i0} + j \cdot c_0 + k \cdot S_{coal} + l \cdot S_{coal}^2$

Table C-4. Elemental Composition Model Forms, CONTINUED

Model	N_{coeff}	N_{var}	Equation
99	14	5	$\frac{X_i}{X_{i0}} = a + b \cdot T_{gas,max} + c \cdot T_{gas,max}^2 + d \cdot T_{gas,max}^3 + e \cdot t_{res} + f \cdot t_{res}^2 + g \cdot t_{res}^3 + h \cdot V_{norm} + i \cdot V_{norm}^2 + j \cdot V_{norm}^3 + k \cdot X_{i0} + l \cdot X_{i0}^2 + m \cdot X_{i0}^3 + n \cdot X_{i0}^4$
100	16	5	$\frac{X_i}{X_{i0}} = a + b \cdot T_{gas,max} + c \cdot T_{gas,max}^2 + d \cdot T_{gas,max}^3 + e \cdot t_{res} + f \cdot t_{res}^2 + g \cdot t_{res}^3 + h \cdot V_{norm} + i \cdot V_{norm}^2 + j \cdot V_{norm}^3 + k \cdot X_{i0} + l \cdot X_{i0}^2 + m \cdot X_{i0}^3 + n \cdot X_{i0}^4 + o \cdot c_0 + p \cdot c_0^2$
101	17	5	$\frac{X_i}{X_{i0}} = a + b \cdot T_{gas,max} + c \cdot T_{gas,max}^2 + d \cdot T_{gas,max}^3 + e \cdot t_{res} + f \cdot t_{res}^2 + g \cdot t_{res}^3 + h \cdot V_{norm} + i \cdot V_{norm}^2 + j \cdot V_{norm}^3 + k \cdot X_{i0} + l \cdot X_{i0}^2 + m \cdot X_{i0}^3 + n \cdot X_{i0}^4 + o \cdot c_0 + p \cdot c_0^2 + q \cdot c_0^3$
102	15	5	$\frac{X_i}{X_{i0}} = a + b \cdot T_{gas,max} + c \cdot T_{gas,max}^2 + d \cdot T_{gas,max}^3 + e \cdot t_{res} + f \cdot t_{res}^2 + g \cdot t_{res}^3 + h \cdot V_{norm} + i \cdot V_{norm}^2 + j \cdot V_{norm}^3 + k \cdot X_{i0} + l \cdot X_{i0}^2 + m \cdot X_{i0}^3 + n \cdot X_{i0}^4 + o \cdot f_a'$
103	16	5	$\frac{X_i}{X_{i0}} = a + b \cdot T_{gas,max} + c \cdot T_{gas,max}^2 + d \cdot T_{gas,max}^3 + e \cdot t_{res} + f \cdot t_{res}^2 + g \cdot t_{res}^3 + h \cdot V_{norm} + i \cdot V_{norm}^2 + j \cdot V_{norm}^3 + k \cdot X_{i0} + l \cdot X_{i0}^2 + m \cdot X_{i0}^3 + n \cdot X_{i0}^4 + o \cdot f_a' + p \cdot f_a'^2$
104	17	5	$\frac{X_i}{X_{i0}} = a + b \cdot T_{gas,max} + c \cdot T_{gas,max}^2 + d \cdot T_{gas,max}^3 + e \cdot t_{res} + f \cdot t_{res}^2 + g \cdot t_{res}^3 + h \cdot V_{norm} + i \cdot V_{norm}^2 + j \cdot V_{norm}^3 + k \cdot X_{i0} + l \cdot X_{i0}^2 + m \cdot X_{i0}^3 + n \cdot X_{i0}^4 + o \cdot f_a' + p \cdot f_a'^2 + q \cdot f_a'^3$
105	15	5	$\frac{X_i}{X_{i0}} = a + b \cdot T_{gas,max} + c \cdot T_{gas,max}^2 + d \cdot T_{gas,max}^3 + e \cdot t_{res} + f \cdot t_{res}^2 + g \cdot t_{res}^3 + h \cdot V_{norm} + i \cdot V_{norm}^2 + j \cdot V_{norm}^3 + k \cdot X_{i0} + l \cdot X_{i0}^2 + m \cdot X_{i0}^3 + n \cdot X_{i0}^4 + o \cdot M_{\delta,Genetti}$
106	16	5	$\frac{X_i}{X_{i0}} = a + b \cdot T_{gas,max} + c \cdot T_{gas,max}^2 + d \cdot T_{gas,max}^3 + e \cdot t_{res} + f \cdot t_{res}^2 + g \cdot t_{res}^3 + h \cdot V_{norm} + i \cdot V_{norm}^2 + j \cdot V_{norm}^3 + k \cdot X_{i0} + l \cdot X_{i0}^2 + m \cdot X_{i0}^3 + n \cdot X_{i0}^4 + o \cdot M_{\delta,Genetti} + p \cdot M_{\delta,Genetti}^2$
107	17	5	$\frac{X_i}{X_{i0}} = a + b \cdot T_{gas,max} + c \cdot T_{gas,max}^2 + d \cdot T_{gas,max}^3 + e \cdot t_{res} + f \cdot t_{res}^2 + g \cdot t_{res}^3 + h \cdot V_{norm} + i \cdot V_{norm}^2 + j \cdot V_{norm}^3 + k \cdot X_{i0} + l \cdot X_{i0}^2 + m \cdot X_{i0}^3 + n \cdot X_{i0}^4 + o \cdot M_{\delta,Genetti} + p \cdot M_{\delta,Genetti}^2 + q \cdot M_{\delta,Genetti}^3$

Table C-4. Elemental Composition Model Forms, CONTINUED

Model	N_{coeff}	N_{var}	Equation
108	15	5	$\frac{X_i}{X_{i0}} = a + b \cdot T_{gas,max} + c \cdot T_{gas,max}^2 + d \cdot T_{gas,max}^3 + e \cdot t_{res} + f \cdot t_{res}^2 + g \cdot t_{res}^3 + h \cdot V_{norm} + i \cdot V_{norm}^2 + j \cdot V_{norm}^3 + k \cdot X_{i0} + l \cdot X_{i0}^2 + m \cdot X_{i0}^3 + n \cdot X_{i0}^4 + o \cdot C_{coal}$
109	17	5	$\frac{X_i}{X_{i0}} = a + b \cdot T_{gas,max} + c \cdot T_{gas,max}^2 + d \cdot T_{gas,max}^3 + e \cdot t_{res} + f \cdot t_{res}^2 + g \cdot t_{res}^3 + h \cdot V_{norm} + i \cdot V_{norm}^2 + j \cdot V_{norm}^3 + k \cdot X_{i0} + l \cdot X_{i0}^2 + m \cdot X_{i0}^3 + n \cdot X_{i0}^4 + o \cdot C_{coal} + p \cdot C_{coal}^2 + q \cdot C_{coal}^3$
110	16	5	$\frac{X_i}{X_{i0}} = a + b \cdot T_{gas,max} + c \cdot T_{gas,max}^2 + d \cdot T_{gas,max}^3 + e \cdot t_{res} + f \cdot t_{res}^2 + g \cdot t_{res}^3 + h \cdot V_{norm} + i \cdot V_{norm}^2 + j \cdot V_{norm}^3 + k \cdot X_{i0} + l \cdot X_{i0}^2 + m \cdot X_{i0}^3 + n \cdot X_{i0}^4 + o \cdot O_{coal} + p \cdot O_{coal}^2$
111	17	5	$\frac{X_i}{X_{i0}} = a + b \cdot T_{gas,max} + c \cdot T_{gas,max}^2 + d \cdot T_{gas,max}^3 + e \cdot t_{res} + f \cdot t_{res}^2 + g \cdot t_{res}^3 + h \cdot V_{norm} + i \cdot V_{norm}^2 + j \cdot V_{norm}^3 + k \cdot X_{i0} + l \cdot X_{i0}^2 + m \cdot X_{i0}^3 + n \cdot X_{i0}^4 + o \cdot O_{coal} + p \cdot O_{coal}^2 + q \cdot O_{coal}^3$
112	15	5	$\frac{X_i}{X_{i0}} = a + b \cdot T_{gas,max} + c \cdot T_{gas,max}^2 + d \cdot T_{gas,max}^3 + e \cdot t_{res} + f \cdot t_{res}^2 + g \cdot t_{res}^3 + h \cdot V_{norm} + i \cdot V_{norm}^2 + j \cdot V_{norm}^3 + k \cdot X_{i0} + l \cdot X_{i0}^2 + m \cdot X_{i0}^3 + n \cdot X_{i0}^4 + o \cdot \ln(O_{coal})$
113	17	5	$\frac{X_i}{X_{i0}} = a + b \cdot T_{gas,max} + c \cdot T_{gas,max}^2 + d \cdot T_{gas,max}^3 + e \cdot t_{res} + f \cdot t_{res}^2 + g \cdot t_{res}^3 + h \cdot V_{norm} + i \cdot V_{norm}^2 + j \cdot V_{norm}^3 + k \cdot X_{i0} + l \cdot X_{i0}^2 + m \cdot X_{i0}^3 + n \cdot X_{i0}^4 + o \cdot S_{coal} + p \cdot S_{coal}^2 + q \cdot S_{coal}^3$
114	15	5	$\frac{X_i}{X_{i0}} = a + b \cdot T_{gas,max} + c \cdot T_{gas,max}^2 + d \cdot T_{gas,max}^3 + e \cdot t_{res} + f \cdot t_{res}^2 + g \cdot t_{res}^3 + h \cdot V_{norm} + i \cdot V_{norm}^2 + j \cdot V_{norm}^3 + k \cdot X_{i0} + l \cdot X_{i0}^2 + m \cdot X_{i0}^3 + n \cdot X_{i0}^4 + o \cdot V_{ASTM}$
115	16	5	$\frac{X_i}{X_{i0}} = a + b \cdot T_{gas,max} + c \cdot T_{gas,max}^2 + d \cdot T_{gas,max}^3 + e \cdot t_{res} + f \cdot t_{res}^2 + g \cdot t_{res}^3 + h \cdot V_{norm} + i \cdot V_{norm}^2 + j \cdot V_{norm}^3 + k \cdot X_{i0} + l \cdot X_{i0}^2 + m \cdot X_{i0}^3 + n \cdot X_{i0}^4 + o \cdot V_{ASTM} + p \cdot V_{ASTM}^2$
116	15	5	$\frac{X_i}{X_{i0}} = a + b \cdot T_{gas,max} + c \cdot T_{gas,max}^2 + d \cdot T_{gas,max}^3 + e \cdot t_{res} + f \cdot t_{res}^2 + g \cdot t_{res}^3 + h \cdot V_{norm} + i \cdot V_{norm}^2 + j \cdot V_{norm}^3 + k \cdot X_{i0} + l \cdot X_{i0}^2 + m \cdot X_{i0}^3 + n \cdot X_{i0}^4 + o \cdot \ln(V_{ASTM})$

Table C-4. Elemental Composition Model Forms, CONTINUED

Model	N_{coeff}	N_{var}	Equation
117	17	5	$\frac{X_i}{X_{i0}} = a + b \cdot T_{gas,max} + c \cdot T_{gas,max}^2 + d \cdot T_{gas,max}^3 + e \cdot t_{res} + f \cdot t_{res}^2 + g \cdot t_{res}^3 + h \cdot V_{norm} + i \cdot V_{norm}^2 + j \cdot V_{norm}^3 + k \cdot X_{i0} + l \cdot X_{i0}^2 + m \cdot X_{i0}^3 + n \cdot X_{i0}^4 + o \cdot \frac{O_{coal}}{C_{coal}} + p \cdot \left(\frac{O_{coal}}{C_{coal}}\right)^2 + q \cdot \left(\frac{O_{coal}}{C_{coal}}\right)^3$
118	28	10	$\frac{X_i}{X_{i0}} = a + b \cdot T_{gas,max} + c \cdot T_{gas,max}^2 + d \cdot T_{gas,max}^3 + e \cdot t_{res} + f \cdot t_{res}^2 + g \cdot t_{res}^3 + h \cdot V_{norm} + i \cdot V_{norm}^2 + j \cdot V_{norm}^3 + k \cdot X_{i0} + l \cdot X_{i0}^2 + m \cdot X_{i0}^3 + n \cdot X_{i0}^4 + o \cdot c_0 + p \cdot c_0^2 + q \cdot c_0^3 + r \cdot f_a' + s \cdot f_a'^2 + t \cdot M_{\delta,Genetti} + u \cdot M_{\delta,Genetti}^2 + v \cdot S_{coal} + w \cdot S_{coal}^2 + x \cdot S_{coal}^3 + y \cdot V_{ASTM} + z \cdot \frac{O_{coal}}{C_{coal}} + aa \cdot \left(\frac{O_{coal}}{C_{coal}}\right)^2 + bb \cdot \left(\frac{O_{coal}}{C_{coal}}\right)^3$
119	16	8	$\frac{X_i}{X_{i0}} = a + b \cdot T_{gas,max} + c \cdot T_{gas,max}^2 + d \cdot t_{res} + e \cdot V_{norm} + f \cdot V_{norm}^2 + g \cdot V_{norm}^3 + h \cdot N_{coal}^3 + i \cdot N_{coal}^4 + j \cdot c_0 + k \cdot M_{\delta,Genetti} + l \cdot M_{\delta,Genetti}^2 + m \cdot S_{coal} + n \cdot S_{coal}^2 + o \cdot S_{coal}^3 + p \cdot V_{ASTM}$
120	15	5	$\frac{X_i}{X_{i0}} = a + b \cdot T_{gas,max} + c \cdot T_{gas,max}^2 + d \cdot T_{gas,max}^3 + e \cdot t_{res} + f \cdot t_{res}^2 + g \cdot t_{res}^3 + h \cdot V_{norm} + i \cdot V_{norm}^2 + j \cdot X_{i0} + k \cdot X_{i0}^2 + l \cdot X_{i0}^3 + m \cdot V_{ASTM} + n \cdot V_{ASTM}^2 + o \cdot V_{ASTM}^3$
Model Refinement			
121	16	4	$\frac{X_i}{X_{i0}} = a + b \cdot T_{gas,max} + c \cdot T_{gas,max}^{1/2} + d \cdot T_{gas,max}^{1/3} + e \cdot T_{gas,max}^{1/4} + f \cdot t_{res} + g \cdot t_{res}^{1/2} + h \cdot t_{res}^{1/3} + i \cdot t_{res}^{1/4} + j \cdot V_{norm} + k \cdot V_{norm}^{1/2} + l \cdot V_{norm}^{1/3} + m \cdot V_{norm}^{1/4} + n \cdot X_{i0} + o \cdot X_{i0}^{1/2} + p \cdot X_{io}^{1/4}$
122	15	4	$\frac{X_i}{X_{i0}} = a + b \cdot T_{gas,max} + c \cdot T_{gas,max}^{1/2} + d \cdot T_{gas,max}^{1/4} + e \cdot t_{res} + f \cdot t_{res}^{1/2} + g \cdot t_{res}^{1/3} + h \cdot t_{res}^{1/4} + i \cdot V_{norm} + j \cdot V_{norm}^{1/2} + k \cdot V_{norm}^{1/3} + l \cdot V_{norm}^{1/4} + m \cdot X_{i0} + n \cdot X_{i0}^{1/2} + o \cdot X_{io}^{1/4}$
123	14	4	$\frac{X_i}{X_{i0}} = a + b \cdot T_{gas,max} + c \cdot T_{gas,max}^{1/2} + d \cdot T_{gas,max}^{1/4} + e \cdot t_{res} + f \cdot t_{res}^{1/2} + g \cdot t_{res}^{1/3} + h \cdot t_{res}^{1/4} + i \cdot V_{norm} + j \cdot V_{norm}^{1/2} + k \cdot V_{norm}^{1/3} + l \cdot V_{norm}^{1/4} + m \cdot X_{i0} + n \cdot X_{i0}^{1/2}$

Table C-4. Elemental Composition Model Forms, CONTINUED

Model	N_{coeff}	N_{var}	Equation
124	13	4	$\frac{X_i}{X_{i0}} = a + b \cdot T_{gas,max} + c \cdot T_{gas,max}^{1/2} + d \cdot T_{gas,max}^{1/4} + e \cdot t_{res} + f \cdot t_{res}^{1/2} + g \cdot t_{res}^{1/3} + h \cdot t_{res}^{1/4} + i \cdot V_{norm}^{1/2} + j \cdot V_{norm}^{1/3} + k \cdot V_{norm}^{1/4} + l \cdot X_{i0} + m \cdot X_{i0}^{1/2}$
125	12	4	$\frac{X_i}{X_{i0}} = a + b \cdot T_{gas,max} + c \cdot T_{gas,max}^{\frac{1}{2}} + d \cdot T_{gas,max}^{\frac{1}{4}} + e \cdot t_{res} + f \cdot t_{res}^{\frac{1}{2}} + g \cdot t_{res}^{\frac{1}{3}} + h \cdot t_{res}^{\frac{1}{4}} + i \cdot \exp(j \cdot V_{norm}) + k \cdot X_{i0} + l \cdot X_{i0}^{\frac{1}{2}}$
126	11	4	$\frac{X_i}{X_{i0}} = a + b \cdot T_{gas,max} + c \cdot T_{gas,max}^{\frac{1}{2}} + d \cdot T_{gas,max}^{\frac{1}{4}} + e \cdot t_{res} + f \cdot t_{res}^{\frac{1}{2}} + g \cdot t_{res}^{\frac{1}{3}} + h \cdot t_{res}^{\frac{1}{4}} + i \cdot \exp(V_{norm}) + j \cdot X_{i0} + k \cdot X_{i0}^{\frac{1}{2}}$
127	11	5	$\frac{X_i}{X_{i0}} = a + b \cdot T_{gas,max}^{c} + d \cdot t_{res}^{e} + f \cdot V_{norm}^{g} + h \cdot X_{i0}^{i} + j \cdot V_{ASTM}^{k}$
128	9	4	$\frac{X_i}{X_{i0}} = a + b \cdot T_{gas,max}^{c} + d \cdot t_{res}^{e} + f \cdot X_{i0}^{g} + h \cdot V_{ASTM}^{i}$
129	10	5	$\frac{X_i}{X_{i0}} = a + b \cdot T_{gas,max}^{c} + d \cdot t_{res}^{e} + f \cdot V_{norm}^{g} + h \cdot X_{i0} + i \cdot V_{ASTM}^{j}$
130	8	4	$\frac{X_i}{X_{i0}} = a + b \cdot T_{gas,max}^{c} + d \cdot t_{res}^{e} + f \cdot X_{i0} + g \cdot V_{ASTM}^{h}$
131	9	5	$\frac{X_i}{X_{i0}} = a + b \cdot T_{gas,max}^{c} + d \cdot t_{res}^{e} + f \cdot V_{norm} + g \cdot X_{i0} + h \cdot V_{ASTM}^{i}$
132	14	5	$\frac{X_i}{X_{i0}} = a + b \cdot T_{gas,max} + c \cdot T_{gas,max}^{2} + d \cdot t_{res} + e \cdot t_{res}^{2} + f \cdot t_{res}^{3} + g \cdot V_{norm} + h \cdot V_{norm}^{2} + i \cdot X_{i0} + j \cdot X_{i0}^{2} + k \cdot X_{i0}^{3} + l \cdot V_{ASTM} + m \cdot V_{ASTM}^{2} + n \cdot V_{ASTM}^{3}$
133	13	5	$\frac{X_i}{X_{i0}} = a \cdot T_{gas,max} + b \cdot T_{gas,max}^{2} + c \cdot t_{res} + d \cdot t_{res}^{2} + e \cdot t_{res}^{3} + f \cdot V_{norm} + g \cdot V_{norm}^{2} + h \cdot X_{i0} + i \cdot X_{i0}^{2} + j \cdot X_{i0}^{3} + k \cdot V_{ASTM} + l \cdot V_{ASTM}^{2} + m \cdot V_{ASTM}^{3}$

Table C-4. Elemental Composition Model Forms, CONTINUED

Model	N_{coeff}	N_{var}	Equation
134	12	5	$\frac{X_i}{X_{i0}} = a \cdot T_{gas,max} + b \cdot T_{gas,max}^2 + c \cdot t_{res} + d \cdot t_{res}^2 + e \cdot t_{res}^3 + f \cdot V_{norm} + g \cdot V_{norm}^2 + h \cdot \exp(i \cdot X_{i0}) + j \cdot V_{ASTM} + k \cdot V_{ASTM}^2 + l \cdot V_{ASTM}^3$
135	11	5	$\frac{X_i}{X_{i0}} = a \cdot T_{gas,max} + b \cdot T_{gas,max}^2 + c \cdot t_{res} + d \cdot t_{res}^2 + e \cdot t_{res}^3 + f \cdot V_{norm}^2 + g \cdot \exp(h \cdot X_{i0}) + i \cdot V_{ASTM} + j \cdot V_{ASTM}^2 + k \cdot V_{ASTM}^3$
136	10	4	$\frac{X_i}{X_{i0}} = a \cdot T_{gas,max} + b \cdot T_{gas,max}^2 + c \cdot t_{res} + d \cdot t_{res}^2 + e \cdot t_{res}^3 + f \cdot V_{norm} + g \cdot V_{norm}^2 + h \cdot V_{ASTM} + i \cdot V_{ASTM}^2 + j \cdot V_{ASTM}^3$
137	13	5	$\frac{X_i}{X_{i0}} = a + b \cdot T_{gas,max}^c + d \cdot t_{res} + e \cdot t_{res}^2 + f \cdot t_{res}^3 + g \cdot V_{norm} + h \cdot V_{norm}^2 + i \cdot V_{norm}^3 + j \cdot X_{i0}^2 + k \cdot X_{i0}^3 + l \cdot M_{\delta,Genetti} + m \cdot M_{\delta,Genetti}^2$
138	12	5	$\frac{X_i}{X_{i0}} = a \cdot T_{gas,max}^b + c \cdot t_{res} + d \cdot t_{res}^2 + e \cdot t_{res}^3 + f \cdot V_{norm} + g \cdot V_{norm}^2 + h \cdot V_{norm}^3 + i \cdot X_{i0}^2 + j \cdot X_{i0}^3 + k \cdot M_{\delta,Genetti} + l \cdot M_{\delta,Genetti}^2$
139	11	4	$\frac{X_i}{X_{i0}} = a + b \cdot t_{res} + c \cdot t_{res}^2 + d \cdot t_{res}^3 + e \cdot V_{norm} + f \cdot V_{norm}^2 + g \cdot V_{norm}^3 + h \cdot X_{i0}^2 + i \cdot X_{i0}^3 + j \cdot M_{\delta,Genetti} + k \cdot M_{\delta,Genetti}^2$
140	12	5	$\frac{X_i}{X_{i0}} = a + b \cdot T_{gas,max} + c \cdot t_{res} + d \cdot t_{res}^2 + e \cdot t_{res}^3 + f \cdot V_{norm} + g \cdot V_{norm}^2 + h \cdot V_{norm}^3 + i \cdot X_{i0}^2 + j \cdot X_{i0}^3 + k \cdot M_{\delta,Genetti} + l \cdot M_{\delta,Genetti}^2$
141	11	5	$\frac{X_i}{X_{i0}} = a \cdot T_{gas,max} + b \cdot t_{res} + c \cdot t_{res}^2 + d \cdot t_{res}^3 + e \cdot V_{norm} + f \cdot V_{norm}^2 + g \cdot V_{norm}^3 + h \cdot X_{i0}^2 + i \cdot X_{i0}^3 + j \cdot M_{\delta,Genetti} + k \cdot M_{\delta,Genetti}^2$
142	10	5	$\frac{X_i}{X_{i0}} = a \cdot T_{gas,max} + b \cdot t_{res} + c \cdot t_{res}^2 + d \cdot V_{norm} + e \cdot V_{norm}^2 + f \cdot V_{norm}^3 + g \cdot X_{i0}^2 + h \cdot X_{i0}^3 + i \cdot M_{\delta,Genetti} + j \cdot M_{\delta,Genetti}^2$

Table C-4. Elemental Composition Model Forms, CONTINUED

Model	N_{coeff}	N_{var}	Equation
143	16	4	$\frac{X_i}{X_{i0}} = a \cdot T_{gas,max} + \frac{1}{b \cdot T_{gas,max}^2 + c \cdot T_{gas,max}^3 + d \cdot T_{gas,max}^4} + e \cdot t_{res} + \frac{1}{f \cdot t_{res}^2 + g \cdot t_{res}^3 + h \cdot t_{res}^4} + i \cdot V_{norm} + \frac{1}{1 + j \cdot V_{norm}^2 + k \cdot V_{norm}^3 + l \cdot V_{norm}^4} + m \cdot X_{i0} + \frac{1}{n \cdot X_{i0}^2 + o \cdot X_{i0}^3 + p \cdot X_{i0}^4}$
144	15	4	$\frac{X_i}{X_{i0}} = a \cdot T_{gas,max} + \frac{1}{b \cdot T_{gas,max}^2 + c \cdot T_{gas,max}^3 + d \cdot T_{gas,max}^4} + e \cdot t_{res} + \frac{1}{f \cdot t_{res}^2 + g \cdot t_{res}^4} + h \cdot V_{norm} + \frac{1}{1 + i \cdot V_{norm}^2 + j \cdot V_{norm}^3 + k \cdot V_{norm}^4} + l \cdot X_{i0} + \frac{1}{m \cdot X_{i0}^2 + n \cdot X_{i0}^3 + o \cdot X_{i0}^4}$
145	14	4	$\frac{X_i}{X_{i0}} = a \cdot T_{gas,max} + \frac{1}{b \cdot T_{gas,max}^2 + c \cdot T_{gas,max}^3} + d \cdot t_{res} + \frac{1}{e \cdot t_{res}^2 + f \cdot t_{res}^4} + g \cdot V_{norm} + \frac{1}{1 + h \cdot V_{norm}^2 + i \cdot V_{norm}^3 + j \cdot V_{norm}^4} + k \cdot X_{i0} + \frac{1}{l \cdot X_{i0}^2 + m \cdot X_{i0}^3 + n \cdot X_{i0}^4}$
146	13	4	$\frac{X_i}{X_{i0}} = a \cdot T_{gas,max} + \frac{1}{b \cdot T_{gas,max}^3} + c \cdot t_{res} + \frac{1}{d \cdot t_{res}^2 + e \cdot t_{res}^4} + f \cdot V_{norm} + \frac{1}{1 + g \cdot V_{norm}^2 + h \cdot V_{norm}^3 + i \cdot V_{norm}^4} + j \cdot X_{i0} + \frac{1}{k \cdot X_{i0}^2 + l \cdot X_{i0}^3 + m \cdot X_{i0}^4}$
147	12	4	$\frac{X_i}{X_{i0}} = a \cdot T_{gas,max} + b \cdot t_{res} + \frac{1}{c \cdot t_{res}^2 + d \cdot t_{res}^4} + e \cdot V_{norm} + \frac{1}{1 + f \cdot V_{norm}^2 + g \cdot V_{norm}^3 + h \cdot V_{norm}^4} + i \cdot X_{i0} + \frac{1}{j \cdot X_{i0}^2 + k \cdot X_{i0}^3 + l \cdot X_{i0}^4}$
148	11	4	$\frac{X_i}{X_{i0}} = a \cdot T_{gas,max} + \frac{1}{b \cdot T_{gas,max}^3} + c \cdot t_{res} + \frac{1}{d \cdot t_{res}^2 + e \cdot t_{res}^4} + f \cdot \exp(g \cdot V_{norm}) + h \cdot X_{i0} + \frac{1}{i \cdot X_{i0}^2 + j \cdot X_{i0}^3 + k \cdot X_{i0}^4}$

Table C-4. Elemental Composition Model Forms, CONTINUED

Model	N_{coeff}	N_{var}	Equation
149	16	4	$\frac{X_i}{X_{i0}} = a + b \cdot T_{gas,max} + \frac{1}{c \cdot T_{gas,max}^2 + d \cdot T_{gas,max}^3 + e \cdot T_{gas,max}^4} + f \cdot t_{res} + \frac{1}{g \cdot t_{res}^2 + h \cdot t_{res}^3 + i \cdot t_{res}^4} + j \cdot V_{norm} + \frac{1}{1 + k \cdot V_{norm}^2 + l \cdot V_{norm}^3 + m \cdot V_{norm}^4} + n \cdot X_{i0} + \frac{1}{o \cdot X_{i0}^2 + p \cdot X_{i0}^4}$
150	15	4	$\frac{X_i}{X_{i0}} = a + b \cdot T_{gas,max} + \frac{1}{c \cdot T_{gas,max}^2 + d \cdot T_{gas,max}^3 + e \cdot T_{gas,max}^4} + f \cdot t_{res} + \frac{1}{g \cdot t_{res}^2 + h \cdot t_{res}^4} + i \cdot V_{norm} + \frac{1}{1 + j \cdot V_{norm}^2 + k \cdot V_{norm}^3 + l \cdot V_{norm}^4} + m \cdot X_{i0} + \frac{1}{n \cdot X_{i0}^2 + o \cdot X_{i0}^4}$
151	14	4	$\frac{X_i}{X_{i0}} = a + b \cdot T_{gas,max} + \frac{1}{c \cdot T_{gas,max}^2 + d \cdot T_{gas,max}^3 + e \cdot T_{gas,max}^4} + f \cdot t_{res} + \frac{1}{g \cdot t_{res}^2 + h \cdot t_{res}^4} + \frac{1}{1 + i \cdot V_{norm}^2 + j \cdot V_{norm}^3 + k \cdot V_{norm}^4} + l \cdot X_{i0} + \frac{1}{m \cdot X_{i0}^2 + n \cdot X_{i0}^4}$
152	13	4	$\frac{X_i}{X_{i0}} = a + b \cdot T_{gas,max} + \frac{1}{c \cdot T_{gas,max}^2 + d \cdot T_{gas,max}^3 + e \cdot T_{gas,max}^4} + f \cdot t_{res} + \frac{1}{g \cdot t_{res}^2 + h \cdot t_{res}^4} + \frac{1}{1 + i \cdot V_{norm}^3 + j \cdot V_{norm}^4} + k \cdot X_{i0} + \frac{1}{l \cdot X_{i0}^2 + m \cdot X_{i0}^4}$
153	12	4	$\frac{X_i}{X_{i0}} = a + b \cdot T_{gas,max} + \frac{1}{c \cdot T_{gas,max}^2 + d \cdot T_{gas,max}^3 + e \cdot T_{gas,max}^4} + f \cdot t_{res} + \frac{1}{g \cdot t_{res}^2 + h \cdot t_{res}^4} + \frac{1}{1 + i \cdot V_{norm}^3} + j \cdot X_{i0} + \frac{1}{k \cdot X_{i0}^2 + l \cdot X_{i0}^4}$
154	11	4	$\frac{X_i}{X_{i0}} = a + b \cdot T_{gas,max} + \frac{1}{c \cdot T_{gas,max}^3 + d \cdot T_{gas,max}^4} + e \cdot t_{res} + \frac{1}{f \cdot t_{res}^2 + g \cdot t_{res}^4} + \frac{1}{1 + h \cdot V_{norm}^3} + i \cdot X_{i0} + \frac{1}{j \cdot X_{i0}^2 + k \cdot X_{i0}^4}$
155	12	5	$\frac{X_i}{X_{i0}} = a + b \cdot T_{gas,max}^c + d \cdot t_{res} + e \cdot t_{res}^2 + f \cdot t_{res}^3 + g \cdot V_{norm} + h \cdot V_{norm}^2 + i \cdot V_{norm}^3 + \frac{j}{X_{i0}} + k \cdot M_{\delta,Genetti} + l \cdot M_{\delta,Genetti}^2$

Table C-4. Elemental Composition Model Forms, CONTINUED

Model	N_{coeff}	N_{var}	Equation
156	11	5	$\frac{X_i}{X_{i0}} = a + b \cdot T_{gas,max} + c \cdot t_{res} + d \cdot t_{res}^2 + e \cdot t_{res}^3 + f \cdot V_{norm} + g \cdot V_{norm}^2 + h \cdot V_{norm}^3 + \frac{i}{X_{i0}} + j \cdot M_{\delta,Genetti} + k \cdot M_{\delta,Genetti}^2$
157	10	4	$\frac{X_i}{X_{i0}} = a + b \cdot T_{gas,max} + c \cdot t_{res} + d \cdot t_{res}^2 + e \cdot t_{res}^3 + f \cdot V_{norm} + g \cdot V_{norm}^2 + h \cdot V_{norm}^3 + i \cdot M_{\delta,Genetti} + j \cdot M_{\delta,Genetti}^2$
158	9	4	$\frac{X_i}{X_{i0}} = a + b \cdot T_{gas,max} + c \cdot t_{res}^2 + d \cdot t_{res}^3 + e \cdot V_{norm} + f \cdot V_{norm}^2 + g \cdot V_{norm}^3 + h \cdot M_{\delta,Genetti} + i \cdot M_{\delta,Genetti}^2$
159	11	5	$\frac{X_i}{X_{i0}} = a + b \cdot T_{gas,max} + c \cdot T_{gas,max}^2 + d \cdot t_{res} + e \cdot t_{res}^2 + f \cdot V_{norm} + g \cdot V_{norm}^2 + h \cdot V_{norm}^3 + i \cdot X_{i0} + j \cdot S_{coal}^2 + k \cdot S_{coal}^3$
160	11	5	$\frac{X_i}{X_{i0}} = a + b \cdot T_{gas,max} + c \cdot T_{gas,max}^2 + d \cdot t_{res} + e \cdot t_{res}^2 + f \cdot V_{norm} + g \cdot V_{norm}^2 + h \cdot V_{norm}^3 + i \cdot \log_{10} X_{i0} + j \cdot S_{coal}^2 + k \cdot S_{coal}^3$
161	10	5	$\frac{X_i}{X_{i0}} = a + b \cdot T_{gas,max} + c \cdot T_{gas,max}^2 + d \cdot t_{res} + e \cdot t_{res}^2 + f \cdot V_{norm}^2 + g \cdot V_{norm}^3 + h \cdot \log_{10} X_{i0} + i \cdot S_{coal}^2 + j \cdot S_{coal}^3$
162	9	5	$\frac{X_i}{X_{i0}} = a \cdot T_{gas,max} + b \cdot T_{gas,max}^2 + c \cdot t_{res} + d \cdot t_{res}^2 + e \cdot V_{norm}^2 + f \cdot V_{norm}^3 + g \cdot \log_{10} X_{i0} + h \cdot S_{coal}^2 + i \cdot S_{coal}^3$
163	16	8	$\frac{X_i}{X_{i0}} = a + b \cdot T_{gas,max} + c \cdot T_{gas,max}^2 + d \cdot t_{res} + e \cdot V_{norm} + f \cdot V_{norm}^2 + g \cdot V_{norm}^3 + h \cdot N_{coal}^3 + i \cdot N_{coal}^4 + \frac{j}{1 + c_0} + k \cdot M_{\delta,Genetti} + l \cdot M_{\delta,Genetti}^2 + m \cdot S_{coal} + n \cdot S_{coal}^2 + o \cdot S_{coal}^3 + p \cdot V_{ASTM}$

Table C-4. Elemental Composition Model Forms, CONTINUED

Model	N_{coeff}	N_{var}	Equation
164	15	8	$\frac{X_i}{X_{i0}} = a \cdot T_{gas,max} + b \cdot T_{gas,max}^2 + c \cdot t_{res} + d \cdot V_{norm} + e \cdot V_{norm}^2 + f \cdot V_{norm}^3 + g \cdot N_{coal}^3 + h \cdot N_{coal}^4 + \frac{i}{1+c_0} + j \cdot M_{\delta,Genetti} + k \cdot M_{\delta,Genetti}^2 + l \cdot S_{coal} + m \cdot S_{coal}^2 + n \cdot S_{coal}^3 + o \cdot V_{ASTM}$
165	14	8	$\frac{X_i}{X_{i0}} = a \cdot T_{gas,max} + b \cdot T_{gas,max}^2 + c \cdot t_{res} + d \cdot V_{norm} + e \cdot V_{norm}^2 + f \cdot V_{norm}^3 + \frac{g}{N_{coal}} + \frac{h}{1+c_0} + i \cdot M_{\delta,Genetti} + j \cdot M_{\delta,Genetti} + k \cdot S_{coal} + l \cdot S_{coal}^2 + m \cdot S_{coal}^3 + n \cdot V_{ASTM}$
166	13	8	$\frac{X_i}{X_{i0}} = a \cdot T_{gas,max} + b \cdot T_{gas,max}^2 + c \cdot t_{res} + d \cdot V_{norm} + e \cdot V_{norm}^2 + f \cdot V_{norm}^3 + \frac{g}{N_{coal}} + \frac{h}{1+c_0} + i \cdot M_{\delta,Genetti} + j \cdot M_{\delta,Genetti} + k \cdot S_{coal} + l \cdot S_{coal}^2 + m \cdot V_{ASTM}$
167	12	8	$\frac{X_i}{X_{i0}} = a \cdot T_{gas,max} + b \cdot T_{gas,max}^2 + c \cdot t_{res} + d \cdot V_{norm} + e \cdot V_{norm}^2 + f \cdot V_{norm}^3 + \frac{g}{N_{coal}} + \frac{h}{1+c_0} + i \cdot M_{\delta,Genetti} + j \cdot M_{\delta,Genetti} + \frac{k}{S_{coal}} + l \cdot V_{ASTM}$
168	11	7	$\frac{X_i}{X_{i0}} = a \cdot T_{gas,max} + b \cdot T_{gas,max}^2 + c \cdot t_{res} + d \cdot V_{norm} + e \cdot V_{norm}^2 + f \cdot V_{norm}^3 + \frac{g}{N_{coal}} + h \cdot M_{\delta,Genetti} + i \cdot M_{\delta,Genetti} + \frac{j}{S_{coal}} + k \cdot V_{ASTM}$
169	8	4	$\frac{X_i}{X_{i0}} = a + b \cdot T_{gas,max}^c + d \cdot t_{res}^e + f \cdot V_{norm}^g + h \cdot X_{i0}$
170	7	4	$\frac{X_i}{X_{i0}} = a \cdot T_{gas,max}^b + c \cdot t_{res}^d + e \cdot V_{norm}^f + g \cdot X_{i0}$
171	6	3	$\frac{X_i}{X_{i0}} = a + b \cdot t_{res}^c + d \cdot V_{norm}^e + f \cdot X_{i0}$
172	7	4	$\frac{X_i}{X_{i0}} = a + b \cdot \ln(T_{gas,max}) + c \cdot t_{res}^d + e \cdot V_{norm}^f + g \cdot X_{i0}$

Table C-5 contains the R^2 values from the final training step of both the initial cross-validation cycle and the model refinement analysis. There are different text colors corresponding to which models are used for which part of the analysis: blue is the best R^2 value from the initial cross-validation cycle, red is the best R^2/N_{coeff} value from the initial cross-validation cycle, orange is the best overall R^2 value post model refinement, and green is the model with the best utility post model refinement (the best possible R^2 value with the fewest possible coefficients). This table also shows which model form was used for each element in both the char and the tar.

Table C-5. Complete R^2 Values for Each Model Form

Model	Char					Tar				
	C	H	O	N	S	C	H	O	N	S
1	0.232									
2	0.500	0.743	0.327	0.368	0.297	0.752	0.631	0.764	0.490	0.765
3	0.470	0.681	0.362	0.234	0.073	0.692	0.549	0.565	0.330	0.607
4	nw[a]	nw	nw	nw	nw	0.743	0.596	0.733	0.424	0.626
5	nw	nw	nw	nw	nw	0.743	0.596	0.733	0.424	0.626
6	0.505	0.699	0.329	0.359	0.319	0.775	0.538	0.612	0.473	0.726
7	nw	nw	nw	nw	nw	0.598	0.607	0.308	0.452	0.318
8	0.541	0.748	0.342	0.378	0.378	0.807	0.626	0.766	0.570	0.737
9	0.272									
10	0.193									
11	0.340									
12	0.239									
13	0.292									
14	0.229									
15	0.220									
16	0.414									
17	0.286									
18	0.243									
19	0.357									
20	0.340									
21	0.527	0.746	0.323	0.401	0.565	0.824	0.649	0.750	0.582	0.736
22		0.691				0.693				0.642
23		0.679				0.712				
24		nw				nw				nw
25		0.685				0.712				0.642

Table C-5. Complete R^2 Values for Each Model Form, CONTINUED

Model	Char					Tar				
	C	H	O	N	S	C	H	O	N	S
26		0.684				0.633				
27		0.683								0.642
28		0.740				0.659				
29		0.731				0.698				
30		0.741				0.642				
31		0.753				0.721				
32		0.723								
33						0.633				
34						0.683				0.644
35						0.670				
36						0.718				
37						0.642				
38						0.640				
39										0.643
40										0.642
41										0.654
42										0.642
43										0.643
44			0.322							
45			0.282							
46			0.323							
47			0.282							
48			0.279							
49			0.279							
50			0.279							
51			0.349							
52			0.371							
53			0.316							
54			0.349							
55				0.385			0.317			
56				0.589			0.047			
57				0.589						
58				nw			nw			
59				0.564			0.047			
60				0.130			0.047			
61				0.501						
62				0.597			0.697			
63				0.514			0.676			
64							0.372			
65				0.474						
66							0.443			

Table C-5. Complete R^2 Values for Each Model Form, CONTINUED

Model	Char					Tar				
	C	H	O	N	S	C	H	O	N	S
67				0.510						
68				0.468						
69				0.573			0.383			
70							0.488			
71				0.513						
72				0.518			0.420			
73							0.003			
74				0.129						
75				0.450						
76				0.551						
77							0.685			
78				0.520						
79				0.392						
80							0.151			
81					0.051					
82					0.034					
83					0.051					
84					0.034					
85					0.095					
86					0.086					
87					0.034					
88					0.051					
89					0.063					
90					0.052					
91								0.773		
92								0.764		
93								0.774		
94								0.772		
95								nw		
96								0.837		
97								0.842		
98								0.834		
99									0.439	
100									0.434	
101									0.506	
102									0.430	
103									0.435	
104									0.440	
105									0.535	
106									0.540	
107									0.651	

Table C-5. Complete R^2 Values for Each Model Form, CONTINUED

Model	Char					Tar				
	C	H	O	N	S	C	H	O	N	S
108									0.540	
109									0.502	
110									0.460	
111									0.444	
112									0.436	
113									0.517	
114									0.582	
115									0.602	
116									0.512	
117									0.442	
118									0.687	
119									0.717	
120			0.438							
Model Refinement										
121	0.551									
122	0.541									
123	0.543									
124	0.544									
125	0.541									
126	0.548									
127		0.800								
128		0.758								
129		0.787								
130		0.757								
131		0.773								
132			0.435							
133			0.437							
134			0.447							
135			0.445							
136			0.411							
137				0.595						
138				0.587						
139				0.588						
140				0.595						
141				0.592						
142				0.585						
143					0.605					
144					0.570					
145					0.560					
146					0.562					
147					0.570					

Table C-5. Complete R^2 Values for Each Model Form, CONTINUED

Model	Char					Tar				
	C	H	O	N	S	C	H	O	N	S
148					0.605					
149						0.822				
150						0.823				
151						0.822				
152						0.823				
153						0.824				
154						0.825				
155							0.796			
156							0.799			
157							0.800			
158							0.786			
159								0.843		
160								0.842		
161								0.842		
162								0.841		
163									0.738	
164									0.746	
165									0.729	
166									0.747	
167									0.746	
168									0.747	
169										0.764
170										0.750
171										0.760
172										0.763

[a] nw refers to model forms that did not work. This was because of an undefined value, either log(0) or 1/0.
[b] blank spaces in this table indicate model forms that were not tested for those elements
[c] colors indicate the following: best R^2, best R^2/N_{coeff}, best overall post model refinement, and best utility (four colors for most elements, except for char nitrogen model 62 having the best R^2 and R^2/N_{coeff}, and best overall post model refinement, tar sulfur model 2 having the best R^2 value pre- and post-model refinement, and tar carbon and hydrogen and char hydrogen and oxygen only having a best overall post model refinement)
[d] blank spaces in this table indicate model forms that were not tested for those elements

C.2.2 Cross-Validation Results

The following tables show the complete cross-validation results for the C, H, O, N, and S in the tar and the char. The results include the average values of each of the five validation

metrics and the average R^2/N_{coeff} values. Higher values for the R^2 values and lower values for the remaining validation metrics indicate that the tested model form has a better ability to predict "new" data, meaning that the tested model form likely has less overall bias.

Table C-6 includes the results for carbon in the tar and is an exact copy of Table 6-1 in the main elemental analysis chapter. All the model forms performed well. Of note are model forms 4, 6, and 20, all having very high R^2 values as well as the lowest values for each of the other statistical values.

Table C-6. Tar Carbon Cross-Validation Results

Model	N_{coeff}	R^2	R^2/N_{coeff}	L_1 Norm	L_2 Norm	Infinity Norm	SSE
22	13	0.573	0.044	0.028	0.035	0.067	0.010
4	5	0.914	0.183	0.034	0.046	0.106	0.017
5	5	0.914	0.183	0.034	0.046	0.106	0.017
6	9	0.922	0.102	0.032	0.044	0.105	0.016
7	5	0.887	0.177	0.044	0.060	0.135	0.028
8	17	0.886	0.052	0.032	0.043	0.102	0.016
23	14	0.791	0.057	0.024	0.028	0.051	0.006
34	16	0.794	0.050	0.023	0.027	0.053	0.006
25	14	0.843	0.060	0.022	0.027	0.050	0.006
26	14	0.785	0.056	0.025	0.030	0.057	0.007
28	14	0.823	0.059	0.022	0.027	0.051	0.006
29	15	0.814	0.054	0.023	0.027	0.051	0.006
35	15	0.819	0.055	0.023	0.028	0.052	0.006
36	14	0.804	0.057	0.022	0.028	0.053	0.006
30	14	0.826	0.059	0.031	0.039	0.076	0.013
31	15	0.847	0.056	0.029	0.038	0.079	0.012
37	15	0.836	0.056	0.031	0.040	0.079	0.013
38	19	0.791	0.042	0.024	0.030	0.054	0.007
21	17	0.869	0.051	0.045	0.059	0.131	0.031
2	9	0.908	0.101	0.034	0.046	0.104	0.017
3	17	0.586	0.034	0.027	0.034	0.062	0.010
33	15	0.854	0.057	0.021	0.029	0.056	0.006

The results for the cross-validation of hydrogen in the tar are included in Table C-7. Most of the tested model forms performed poorly, but the best of these were 2, 3, 19, 21, and 22. Each

of these model forms had an R^2 value of above 0.65, combined with better than average values for the remaining statistical parameters.

Table C-7. Tar Hydrogen Cross-Validation Results

Model	N_{coeff}	R^2	R^2/N_{coeff}	L_1 Norm	L_2 Norm	Infinity Norm	SSE
55	12	0.439	0.037	0.164	0.210	0.388	0.414
4	5	0.689	0.138	0.090	0.120	0.246	0.125
5	5	0.728	0.146	0.091	0.117	0.228	0.117
6	9	0.786	0.087	0.077	0.097	0.189	0.081
8	17	0.812	0.048	0.087	0.104	0.189	0.087
56	14	0.429	0.031	0.156	0.190	0.339	0.236
59	14	0.396	0.028	0.143	0.178	0.320	0.205
60	15	0.361	0.024	0.193	0.252	0.460	0.492
62	14	0.528	0.038	0.129	0.150	0.244	0.141
53	15	0.589	0.039	0.110	0.131	0.223	0.109
54	14	0.389	0.028	0.149	0.181	0.323	0.223
66	14	0.582	0.042	0.116	0.147	0.288	0.185
69	15	0.555	0.037	0.120	0.133	0.206	0.112
70	15	0.480	0.032	0.132	0.163	0.297	0.173
72	14	0.333	0.024	0.156	0.181	0.290	0.231
73	15	0.370	0.025	0.129	0.155	0.262	0.180
77	15	0.360	0.024	0.193	0.252	0.459	0.491
80	26	0.492	0.019	0.125	0.149	0.271	0.137
21	17	0.873	0.051	0.084	0.099	0.172	0.085
2	9	0.584	0.065	0.128	0.181	0.395	0.259
3	17	0.782	0.046	0.101	0.119	0.197	0.116
7	5	0.728	0.146	0.067	0.083	0.142	0.062

Table C-8 shows the results for oxygen in the tar. While most of the tested model forms performed well, 2, 3, 10, and 14 performed the best overall, with R^2 values over 0.8.

Table C-8. Tar Oxygen Cross-Validation Results

Model	N_{coeff}	R^2	R^2/N_{coeff}	L_1 Norm	L_2 Norm	Infinity Norm	SSE
91	9	0.744	0.083	0.114	0.143	0.263	0.144
4	5	0.755	0.151	0.134	0.157	0.266	0.151
5	5	0.755	0.151	0.134	0.157	0.266	0.151

Table C-8. Tar Oxygen Cross-Validation Results, CONTINUED

Model	N_{coeff}	R^2	R^2/N_{coeff}	L_1 Norm	L_2 Norm	Infinity Norm	SSE
6	9	0.668	0.074	0.137	0.166	0.284	0.196
7	5	0.480	0.096	0.100	0.123	0.243	0.106
8	17	0.798	0.047	0.128	0.146	0.245	0.129
92	10	0.744	0.074	0.114	0.143	0.262	0.144
93	11	0.744	0.068	0.114	0.143	0.262	0.144
94	12	0.744	0.062	0.114	0.143	0.262	0.144
96	11	0.819	0.074	0.096	0.117	0.229	0.097
97	12	0.820	0.068	0.099	0.116	0.206	0.100
98	12	0.817	0.068	0.096	0.117	0.229	0.098
21	17	0.831	0.049	0.124	0.142	0.222	0.121
2	9	0.833	0.093	0.117	0.136	0.231	0.112
3	17	0.734	0.043	0.122	0.147	0.254	0.152

Table C-9 contains the cross-validation data for nitrogen in the tar. All models did relatively well with R^2 values over 0.65. Tar nitrogen had the most models tested with a total of 29 models. The best performer in the cross-validation analysis was model 7 with an R^2 value of 0.807.

Table C-9. Tar Nitrogen Cross-Validation Results

Model	N_{coeff}	R^2	R^2/N_{coeff}	L_1 Norm	L_2 Norm	Infinity Norm	SSE
99	14	0.690	0.049	0.133	0.159	0.257	0.179
2	9	0.782	0.087	0.134	0.169	0.305	0.202
4	5	0.754	0.151	0.124	0.147	0.245	0.157
5	5	0.754	0.151	0.124	0.147	0.245	0.157
6	9	0.765	0.085	0.123	0.143	0.237	0.134
7	5	0.807	0.161	0.105	0.121	0.208	0.103
8	17	0.703	0.041	0.201	0.237	0.432	0.400
100	16	0.673	0.042	0.136	0.162	0.255	0.187
101	17	0.690	0.041	0.135	0.158	0.246	0.177
102	15	0.702	0.047	0.134	0.159	0.253	0.178
103	16	0.709	0.044	0.132	0.158	0.255	0.178
104	17	0.670	0.039	0.136	0.160	0.247	0.181
105	15	0.740	0.049	0.121	0.149	0.258	0.157
106	16	0.725	0.045	0.122	0.159	0.282	0.178
107	17	0.763	0.045	0.130	0.155	0.281	0.165
108	15	0.739	0.049	0.122	0.154	0.259	0.166

Table C-9. Tar Nitrogen Cross-Validation Results, CONTINUED

Model	N_{coeff}	R^2	R^2/N_{coeff}	L_1 Norm	L_2 Norm	Infinity Norm	SSE
109	17	0.758	0.045	0.127	0.148	0.258	0.153
110	16	0.697	0.044	0.128	0.160	0.265	0.182
111	17	0.698	0.041	0.130	0.158	0.255	0.175
112	15	0.715	0.048	0.131	0.158	0.253	0.176
113	17	0.690	0.041	0.135	0.161	0.255	0.184
114	15	0.756	0.050	0.119	0.147	0.270	0.152
115	16	0.771	0.048	0.111	0.139	0.258	0.136
116	15	0.700	0.047	0.132	0.156	0.251	0.172
117	17	0.781	0.046	0.118	0.136	0.237	0.132
118	28	0.663	0.024	0.140	0.173	0.306	0.211
21	17	0.760	0.045	0.148	0.182	0.348	0.259
119	16	0.777	0.049	0.093	0.114	0.199	0.088
3	17	0.671	0.039	0.134	0.158	0.243	0.180

Table C-10 includes the cross-validation results for sulfur in the tar. Most of these models performed well with R^2 values over 0.6, and some over 0.9. The best of these models were 8 with an R^2 of 0.943 and 6 with 0.918.

Table C-10. Tar Sulfur Cross-Validation Results

Model	N_{coeff}	R^2	R^2/N_{coeff}	L_1 Norm	L_2 Norm	Infinity Norm	SSE
22	13	0.690	0.053	0.213	0.237	0.348	0.395
2	9	0.880	0.098	0.083	0.105	0.201	0.086
4	5	0.796	0.159	0.100	0.126	0.256	0.112
5	5	0.709	0.142	0.117	0.145	0.293	0.150
6	9	0.918	0.102	0.074	0.099	0.203	0.069
7	5	0.642	0.128	0.157	0.190	0.367	0.252
8	17	0.943	0.055	0.075	0.093	0.162	0.063
34	16	0.692	0.043	0.213	0.233	0.330	0.381
25	14	0.684	0.049	0.219	0.240	0.334	0.407
39	16	0.672	0.042	0.216	0.240	0.354	0.407
27	14	0.686	0.049	0.216	0.241	0.360	0.409
40	14	0.684	0.049	0.218	0.241	0.343	0.410
41	15	0.700	0.047	0.209	0.226	0.316	0.359
42	15	0.689	0.046	0.217	0.239	0.346	0.404
43	16	0.698	0.044	0.209	0.229	0.338	0.366
21	17	0.875	0.051	0.092	0.110	0.184	0.092
3	17	0.711	0.042	0.220	0.244	0.365	0.420

Table C-11 shows the cross-validation results for carbon in the char. Most of the tested models performed poorly with R^2 values well below 0.5. The best performers were models 8 and 21, with R^2 values of 0.662 and 0.6, respectively.

Table C-11. Char Carbon Cross-Validation Results

Model	N_{coeff}	R^2	R^2/N_{coeff}	L_1 Norm	L_2 Norm	Infinity Norm	SSE
1	12	0.306	0.026	0.048	0.068	0.156	0.046
6	9	0.593	0.066	0.048	0.064	0.154	0.041
8	17	0.662	0.039	0.037	0.049	0.108	0.025
9	13	0.324	0.025	0.049	0.066	0.152	0.044
10	14	0.323	0.023	0.050	0.068	0.156	0.047
11	13	0.390	0.030	0.047	0.065	0.146	0.042
12	14	0.257	0.018	0.051	0.071	0.164	0.050
13	14	0.238	0.017	0.050	0.071	0.163	0.051
14	14	0.303	0.022	0.049	0.068	0.157	0.046
15	13	0.346	0.027	0.051	0.068	0.159	0.047
16	14	0.427	0.030	0.046	0.063	0.131	0.040
17	13	0.271	0.021	0.050	0.069	0.162	0.048
18	14	0.292	0.021	0.047	0.067	0.156	0.045
19	14	0.264	0.019	0.050	0.070	0.164	0.049
20	20	0.344	0.017	0.049	0.066	0.154	0.044
21	17	0.600	0.035	0.045	0.063	0.142	0.038
2	9	0.560	0.062	0.049	0.067	0.165	0.043
3	17	0.489	0.029	0.027	0.036	0.082	0.013

Table C-12 details the averaged cross-validation results for hydrogen in the char. All the models performed reasonably well, with all having R^2 values over 0.65. The best performers were models 8, 21, and 2, with R^2 values of 0.877, 0.871, and 0.852, respectively.

Table C-12. Char Hydrogen Cross-Validation Results

Model	N_{coeff}	R^2	R^2/N_{coeff}	L_1 Norm	L_2 Norm	Infinity Norm	SSE
22	13	0.679	0.052	0.078	0.096	0.209	0.094
6	9	0.795	0.088	0.065	0.076	0.132	0.060
8	17	0.877	0.052	0.050	0.058	0.112	0.034

Table C-12. Char Hydrogen Cross-Validation Results, CONTINUED

Model	N_{coeff}	R^2	R^2/N_{coeff}	L_1 Norm	L_2 Norm	Infinity Norm	SSE
23	14	0.669	0.048	0.081	0.098	0.207	0.098
25	14	0.681	0.049	0.078	0.095	0.207	0.092
26	15	0.664	0.044	0.079	0.097	0.212	0.096
27	14	0.661	0.047	0.083	0.099	0.199	0.100
28	14	0.711	0.051	0.077	0.092	0.177	0.086
29	15	0.722	0.048	0.078	0.092	0.155	0.085
30	14	0.710	0.051	0.079	0.091	0.160	0.083
31	15	0.706	0.047	0.079	0.091	0.154	0.084
32	16	0.727	0.045	0.075	0.088	0.166	0.078
21	17	0.871	0.051	0.047	0.055	0.095	0.030
2	9	0.852	0.050	0.057	0.066	0.105	0.044
3	17	0.685	0.076	0.080	0.098	0.202	0.100

Table C-13 includes the averaged cross-validation results for oxygen in the char. The char oxygen models were average performers, with R^2 values mostly around 0.5. Models 53 and 120 performed the best with R^2 values of 0.666 and 0.601, respectively.

Table C-13. Char Oxygen Cross-Validation Results

Model	N_{coeff}	R^2	R^2/N_{coeff}	L_1 Norm	L_2 Norm	Infinity Norm	SSE
44	12	0.564	0.047	0.144	0.184	0.350	0.281
6	9	0.563	0.063	0.196	0.224	0.373	0.491
8	17	0.562	0.033	0.158	0.193	0.360	0.310
45	13	0.587	0.045	0.136	0.179	0.348	0.265
46	15	0.585	0.039	0.139	0.179	0.341	0.266
47	13	0.582	0.045	0.137	0.178	0.351	0.263
48	14	0.569	0.041	0.141	0.180	0.347	0.268
49	13	0.592	0.046	0.138	0.180	0.350	0.269
50	13	0.581	0.045	0.138	0.180	0.349	0.267
51	15	0.544	0.036	0.159	0.190	0.348	0.294
52	13	0.584	0.045	0.143	0.183	0.352	0.281
53	15	0.666	0.044	0.130	0.168	0.327	0.236
54	21	0.517	0.025	0.164	0.195	0.364	0.310
21	17	0.493	0.029	0.158	0.197	0.360	0.318
2	9	0.428	0.048	0.169	0.209	0.368	0.360
3	17	0.545	0.032	0.152	0.187	0.361	0.290
120	15	0.601	0.040	0.132	0.174	0.351	0.252

Table C-14 shows the cross-validation results for nitrogen in the char. Most of the models performed poorly, with R^2 values under 0.5, with many below 0.4. The best performers were models 8, 62, and 2, with R^2 values of 0.666, 0.6, and 0.6, respectively.

Table C-14. Char Nitrogen Cross-Validation Results

Model	N_{coeff}	R^2	R^2/N_{coeff}	L_1 Norm	L_2 Norm	Infinity Norm	SSE
55	12	0.338	0.028	0.809	0.840	1.033	7.475
6	9	0.585	0.065	0.094	0.120	0.258	0.138
8	17	0.666	0.039	0.092	0.117	0.247	0.132
56	14	0.331	0.024	0.883	0.914	1.114	8.394
57	15	0.345	0.023	0.667	0.698	0.883	5.771
59	14	0.351	0.025	0.594	0.622	0.800	4.833
60	15	0.353	0.024	0.525	0.556	0.735	4.078
61	13	0.518	0.040	0.101	0.135	0.317	0.203
62	14	0.600	0.043	0.077	0.097	0.185	0.097
63	15	0.571	0.038	0.085	0.111	0.228	0.142
65	13	0.344	0.026	0.736	0.763	0.949	6.523
67	15	0.571	0.038	0.080	0.099	0.201	0.102
68	13	0.517	0.040	0.103	0.136	0.291	0.223
69	15	0.480	0.032	0.103	0.145	0.319	0.233
71	13	0.483	0.037	0.108	0.133	0.232	0.178
72	14	0.470	0.034	0.099	0.132	0.293	0.188
74	14	0.332	0.024	0.815	0.849	1.049	7.646
75	13	0.344	0.026	0.735	0.765	0.951	6.556
76	14	0.330	0.024	0.952	0.981	1.179	9.154
78	13	0.350	0.027	0.662	0.688	0.866	5.588
79	22	0.519	0.024	0.099	0.130	0.300	0.192
21	17	0.440	0.026	0.107	0.146	0.341	0.212
2	9	0.600	0.067	0.095	0.120	0.248	0.138
3	17	0.322	0.019	0.093	0.122	0.258	0.151

Table C-15 contains the cross-validation results for sulfur in the char. Most of these models performed very poorly, having R^2 values below 0.3. In addition, most of these had incredibly large values for the other validation metrics. The best performers were models 6, 8, and 2, with R^2 values of 0.511, 0.543, and 0.549, respectively.

Table C-15. Char Sulfur Cross-Validation Results

Model	N_{coeff}	R^2	R^2/N_{coeff}	L_1 Norm	L_2 Norm	Infinity Norm	SSE
81	13	0.274	0.021	5.53×10^{1}	6.81×10^{1}	1.30×10^{2}	7.23×10^{4}
6	9	0.511	0.057	0.256	0.321	0.573	0.895
8	17	0.543	0.032	0.236	0.277	0.481	0.663
82	14	0.261	0.019	1.65×10^{2}	2.00×10^{2}	3.76×10^{2}	5.82×10^{5}
83	15	0.197	0.013	1.38×10^{2}	1.83×10^{2}	3.99×10^{2}	5.46×10^{5}
84	14	0.181	0.013	1.49×10^{2}	1.98×10^{2}	4.21×10^{2}	6.14×10^{5}
85	15	0.226	0.015	1.46×10^{2}	1.72×10^{2}	2.84×10^{2}	3.08×10^{5}
86	16	0.105	0.007	1.54×10^{2}	1.95×10^{2}	3.77×10^{2}	7.27×10^{5}
87	14	0.184	0.013	8.35×10^{1}	9.51×10^{1}	1.54×10^{2}	2.63×10^{5}
88	15	0.226	0.015	1.58×10^{4}	1.90×10^{4}	3.42×10^{4}	6.03×10^{9}
89	14	0.247	0.018	1.45×10^{2}	1.78×10^{2}	3.34×10^{2}	5.87×10^{5}
90	17	0.275	0.016	8.90×10^{3}	1.11×10^{3}	2.01×10^{4}	1.54×10^{9}
21	17	0.400	0.024	0.229	0.290	0.535	0.677
2	9	0.549	0.061	0.250	0.303	0.502	0.798
3	17	0.310	0.018	0.308	0.360	0.615	1.117

C.2.3 Model Training Using Complete Data Set

The last step in the cross-validation procedure is to train the model(s) of interest on all the experimental data. This is described as "final" training, which can be a misleading title. The word "final" does not indicate that these are the final correlation fits shown in Section 6.3, but indicates that this is the training using the entire data set rather than splitting the data set into groups and testing on each group. The tar correlations are discussed first, followed by the char correlations. All the discussed model forms in this section are included in Table C-4. The model forms with the best R^2 values and the model forms with the best R^2/N_{coeff} values are presented here, as well as tables of all model form results. The two best models for each element were used as a basis for model refinement.

C.2.3.1 Tar Carbon

The cross-validation process determined that Model 21 had the highest R^2 value, and Model 5 had the highest R^2/N_{coeff}. The best results for both cross-validation and final training are included in Table C-16.

Table C-16. Best Tar Carbon Final Training Results

Step	**Model**	**N_{coeff}**	**R^2**	**R^2/N_{coeff}**	**L_1 Norm**	**L_2 Norm**	**Infinity Norm**	**SSE**
Cross-validation, best R^2	21	17	0.869	0.051	0.045	0.059	0.131	0.031
Final training, best R^2	21	17	0.824	0.048	0.021	0.031	0.108	0.070
Cross-validation, best R^2/N_{coeff}	5	5	0.914	0.183	0.034	0.046	0.106	0.017
Final training, best R^2/N_{coeff}	5	5	0.743	0.149	0.027	0.037	0.117	0.103

Model 21 fit the complete data set very well, with a very high R^2 value of 0.824 in the final training step, as well as an average value of 0.869 in the cross-validation step. This indicates that model 21 has a high certainty of predicting new information accurately. Model 5 had the highest R^2/N_{coeff} value, with an R^2 value of 0.743 in final training and an average value of 0.914 in cross- validation, which means it did an even better job of predicting new information. Both model 5 and model 21 were used to refine a final correlation for carbon in the tar. This is discussed in more detail in Section 6.3.3.

Figure C-1 shows the parity plots from all tar elemental composition models using the parameters found from final training. Plot a shows the carbon in the tar. Note that the carbon in the tar generally ranges from 1 to about 1.15, meaning that the carbon content of the tar increases by up to 15% above the carbon content in the parent coal (dry, ash-free basis). Most of the data for the normalized hydrogen in the tar ranges from 0.8 to about 1.5, whereas the normalized oxygen in the tar ranges from 0.1 to 1.1, the normalized nitrogen ranges from 0.3 to 1.7, and the normalized sulfur ranges from 0.2 to 1.4.

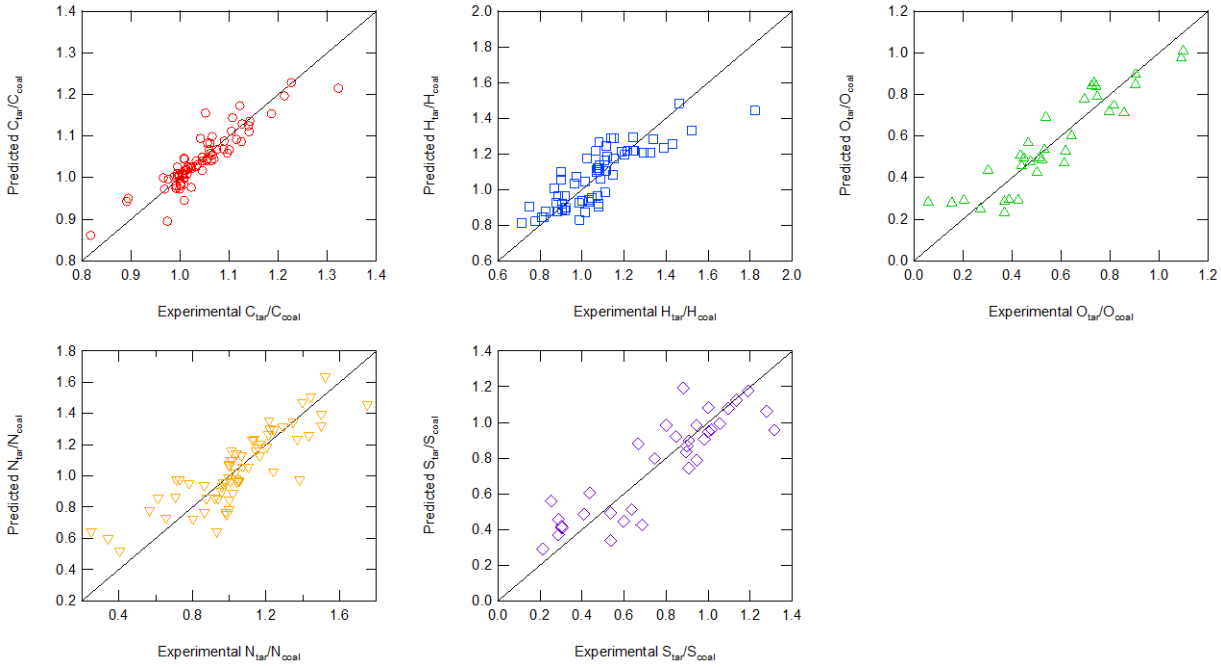

Figure C-1. Final training parity plots of CHONS in the tar.

Table C-17 details the complete "final" training results for carbon in the tar. The best of these results are summarized in Table C-16. All of the tested models performed well with R^2 values over 0.6 for all except Model 7 with a value of 0.598.

Table C-17. Complete Tar Carbon Final Training Results

Model	N_{coeff}	R^2	R^2/N_{coeff}	L_1 Norm	L_2 Norm	Infinity Norm	SSE
22	13	0.693	0.053	0.031	0.041	0.156	0.124
4	5	0.743	0.149	0.027	0.037	0.117	0.103
5	5	0.743	0.149	0.027	0.037	0.117	0.103
6	9	0.775	0.086	0.025	0.035	0.106	0.090
7	5	0.598	0.120	0.037	0.046	0.146	0.161
8	17	0.807	0.047	0.023	0.032	0.123	0.077
23	14	0.712	0.051	0.032	0.041	0.140	0.107
34	16	0.683	0.043	0.032	0.043	0.178	0.122
25	14	0.712	0.051	0.031	0.041	0.140	0.107
26	14	0.633	0.045	0.033	0.046	0.159	0.140
28	14	0.659	0.047	0.034	0.044	0.152	0.128
29	15	0.698	0.047	0.031	0.042	0.156	0.113
35	15	0.670	0.045	0.033	0.043	0.154	0.123
36	14	0.718	0.051	0.031	0.040	0.145	0.105
30	14	0.642	0.046	0.033	0.044	0.171	0.145
31	15	0.721	0.048	0.030	0.039	0.138	0.112
37	15	0.642	0.043	0.033	0.044	0.169	0.146
38	19	0.640	0.034	0.033	0.044	0.171	0.146
21	17	0.824	0.048	0.021	0.031	0.108	0.070
2	9	0.752	0.084	0.027	0.036	0.113	0.099
3	17	0.692	0.041	0.029	0.041	0.163	0.126
33	15	0.633	0.042	0.033	0.046	0.159	0.140

It is difficult to observe trends from tables of data. All of the validation metrics were plotted against the number of model coefficients, and are shown in the following figures, starting with the L_1 norm (Figure C-2), the L_2 norm (Figure C-3), the infinity norm (Figure C-4), the SSE (Figure C-5), and finally the R^2 values (Figure C-6). These figures include plots for all elements (CHONS) in the tar.

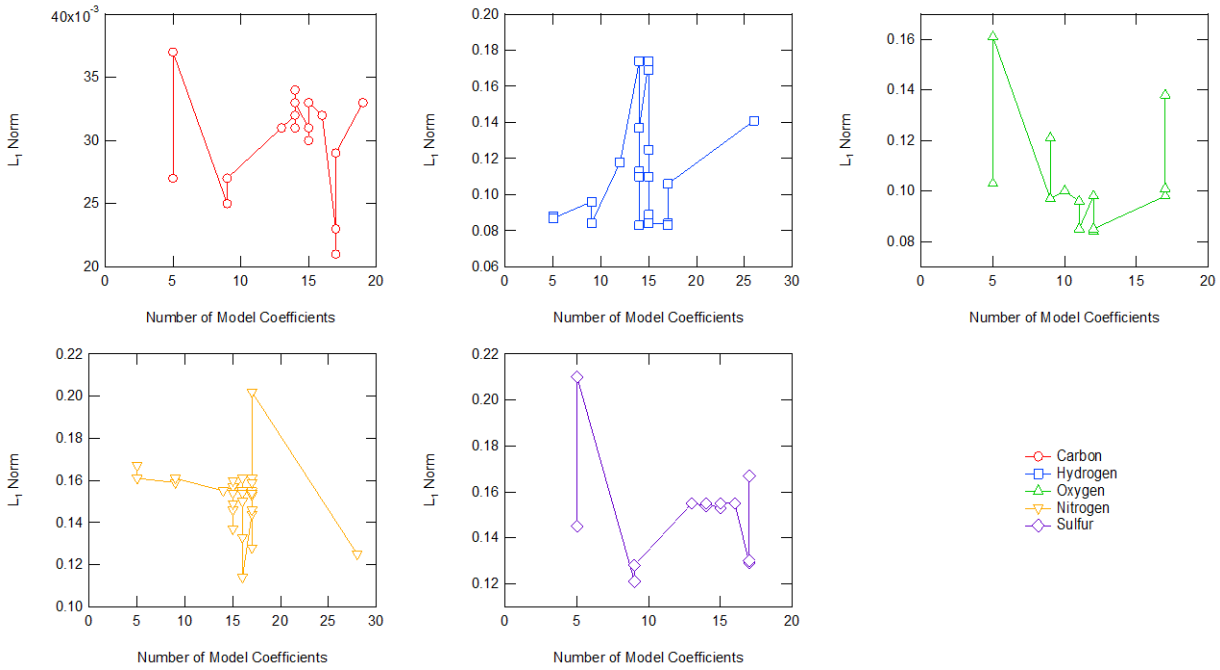

Figure C-2. L_1 norm for each model of each element in the tar, plotted against number of model coefficients.

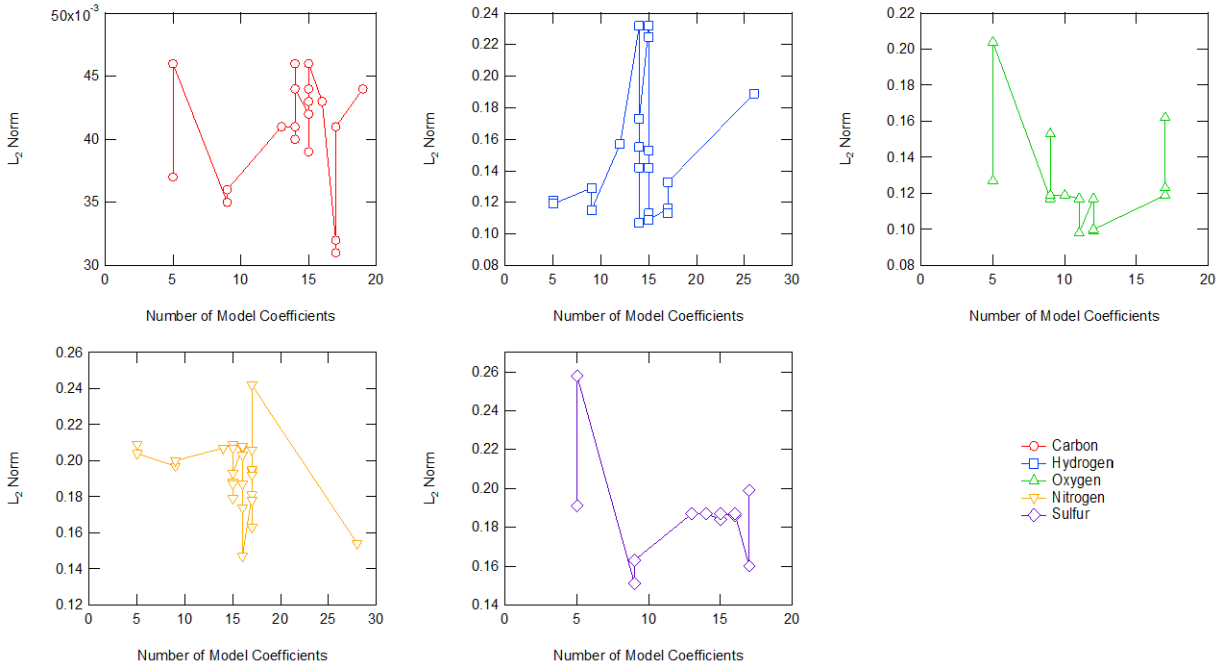

Figure C-3. L_2 norm for each model of each element in the tar, plotted against number of model coefficients

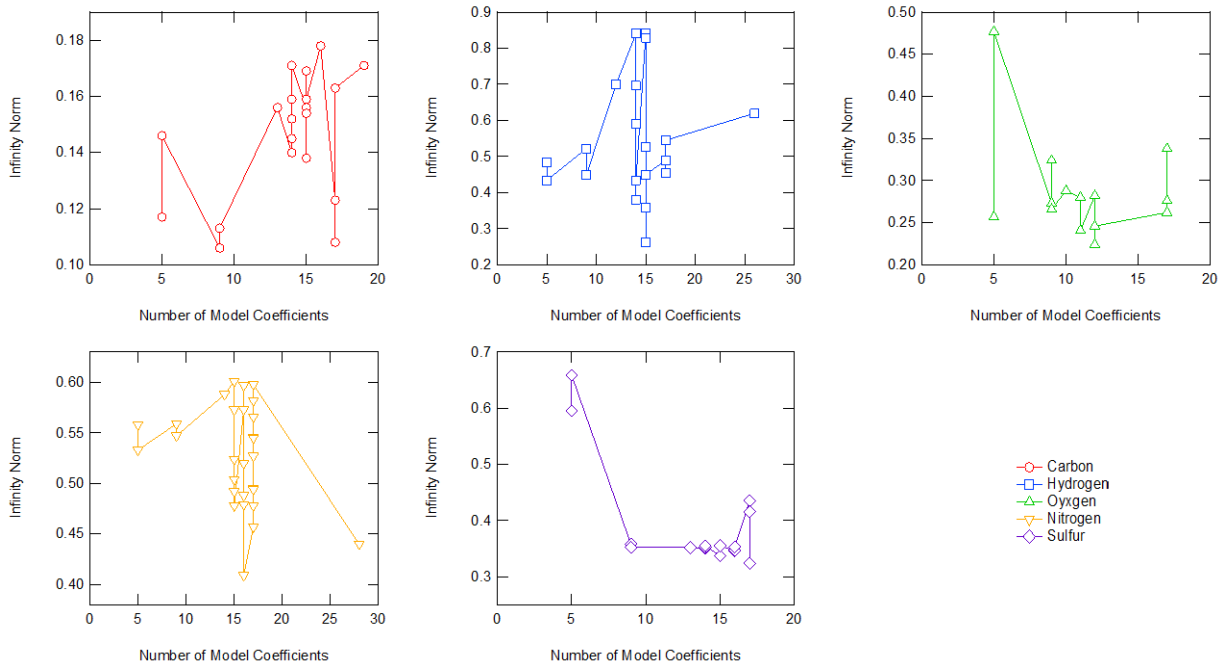

Figure C-4. Infinity norm for each model of each element in the tar, plotted against number of model coefficients.

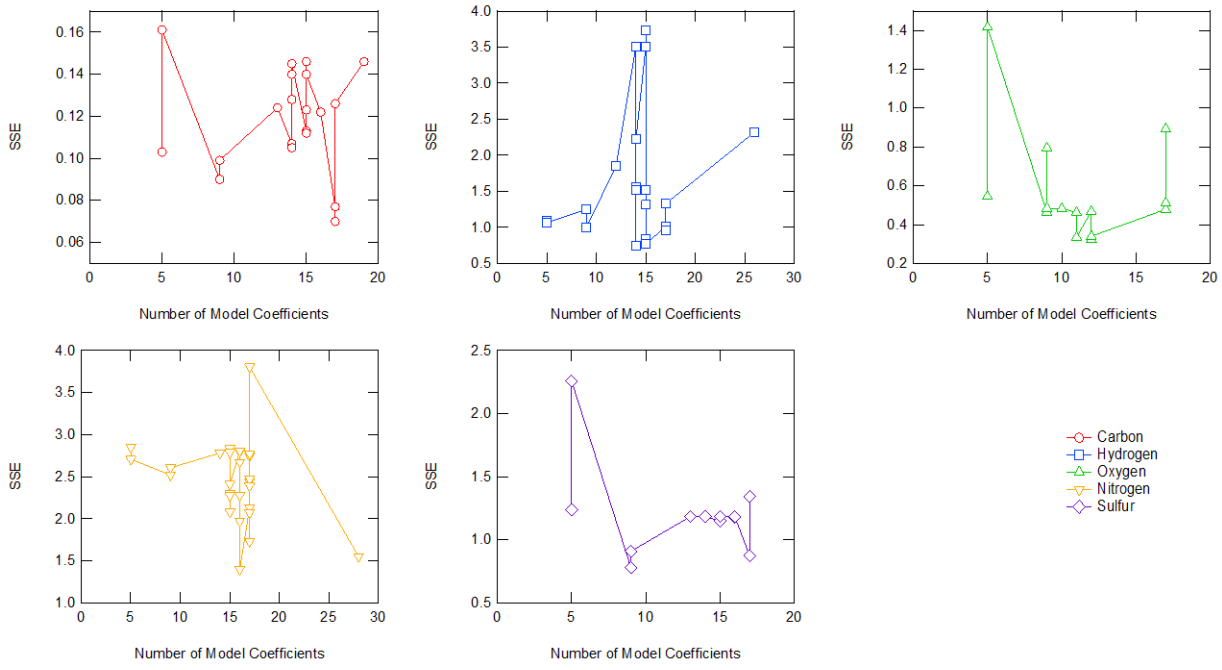

Figure C-5. SSE for each model of each element in the tar, plotted against number of model coefficients.

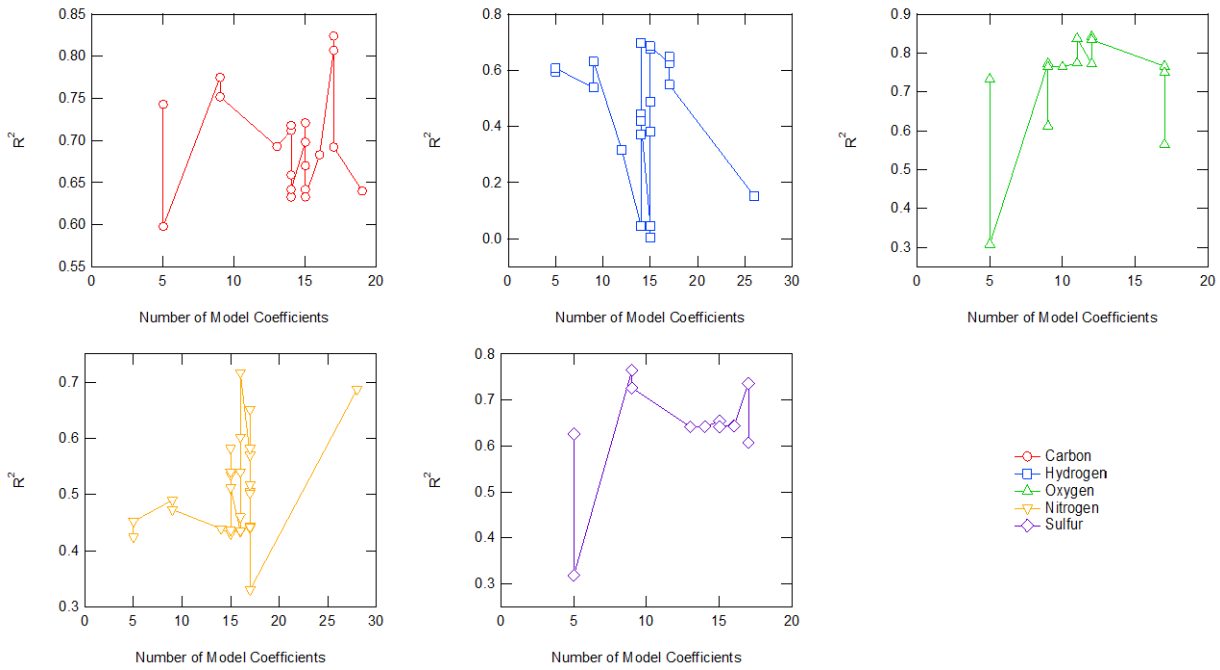

Figure C-6. R^2 for each model of each element in the tar, plotted against number of model coefficients.

C.2.3.2 Tar Hydrogen

Model form 62 had the best R^2 value for the hydrogen in the tar, and Model 7 had the best R^2/N_{coeff} value. Their statistical values for both cross-validation and final training are included in Table C-18.

Model 62 performed moderately well with an R^2 value of 0.697 in final training and an average value of 0.528 in cross-validation. Figure C-1 shows the parity relationship for model 62 using the fitted coefficients found during the final training step. Model 7 had a moderate final training R^2 value of 0.607 and an average of 0.728 in cross-validation, indicating that Model 7 was better at predicting new data than model 62. This may indicate that Model 62 is overfit. Both Model 7 and Model 62 were used to refine a final correlation for hydrogen in the tar, shown in Section 6.3.4. Table C-19 includes the complete final training results for tar hydrogen, and Figure C-2 to Figure C-6 show the trends associated with these results.

Table C-18. Best Tar Hydrogen Final Training Results

Step	Model	N_{coeff}	R^2	R^2/N_{coeff}	L_1 Norm	L_2 Norm	Infinity Norm	SSE
Cross-validation, best R^2	62	14	0.528	0.038	0.129	0.150	0.244	0.141
Final training, best R^2	62	14	0.697	0.050	0.083	0.107	0.381	0.742
Cross-validation, best R^2/N_{coeff}	7	5	0.728	0.146	0.067	0.083	0.142	0.062
Final training, best R^2/N_{coeff}	7	5	0.607	0.121	0.087	0.119	0.434	1.064

Table C-19. Complete Tar Hydrogen Final Training Results

Model	N_{coeff}	R^2	R^2/N_{coeff}	L_1 Norm	L_2 Norm	Infinity Norm	SSE
55	12	0.317	0.026	0.118	0.157	0.700	1.851
4	5	0.596	0.119	0.088	0.121	0.485	1.095
5	5	0.596	0.119	0.088	0.121	0.484	1.095
6	9	0.538	0.060	0.096	0.129	0.522	1.252
8	17	0.626	0.037	0.084	0.116	0.490	1.012
56	14	0.047	0.003	0.174	0.232	0.841	3.511
59	14	0.047	0.003	0.174	0.232	0.841	3.511
60	15	0.047	0.003	0.174	0.232	0.841	3.511
62	14	0.697	0.050	0.083	0.107	0.381	0.742
53	15	0.676	0.045	0.089	0.113	0.262	0.835
54	14	0.372	0.027	0.113	0.155	0.696	1.555
66	14	0.443	0.032	0.110	0.142	0.590	1.517
69	15	0.383	0.026	0.125	0.153	0.526	1.517
70	15	0.488	0.033	0.110	0.142	0.358	1.313
72	14	0.420	0.030	0.137	0.173	0.434	2.226
73	15	0.003	0.000	0.169	0.225	0.829	3.737
77	15	0.685	0.046	0.084	0.109	0.450	0.770
80	26	0.151	0.006	0.141	0.189	0.620	2.322
21	17	0.649	0.038	0.083	0.113	0.454	0.954
2	9	0.631	0.070	0.084	0.115	0.449	1.000
3	17	0.549	0.032	0.106	0.133	0.545	1.328
7	5	0.607	0.121	0.087	0.119	0.434	1.064

C.2.3.3 Tar Oxygen

All the tested models for oxygen in the tar performed well in cross-validation, but the model with the highest R^2 value was Model 97, and Model 5 had the highest R^2/N_{coeff}. The statistical values calculated during final training and cross-validation for these models are found in Table C-20.

Table C-20. Best Tar Oxygen Final Training Results

Step	**Model**	**N_{coeff}**	**R^2**	**R^2/N_{coeff}**	**L_1 Norm**	**L_2 Norm**	**Infinity Norm**	**SSE**
Cross-validation, best R^2	97	12	0.820	0.068	0.099	0.116	0.206	0.100
Final training, best R^2	97	12	0.842	0.070	0.084	0.098	0.224	0.324
Cross-validation, best R^2/N_{coeff}	5	5	0.755	0.151	0.134	0.157	0.266	0.151
Final training, best R^2/N_{coeff}	5	5	0.733	0.147	0.103	0.127	0.257	0.546

Model 97 performed well in final training with an R^2 value of 0.842 and a cross-validation average R^2 value of 0.820, indicating that this model fit the entire data set very well and predicted new data well. Model 5 didn't have quite as high of an R^2 value for either final training (0.733) or during cross-validation (0.755), however, it had an R^2/N_{coeff} value more than twice as high as model 97. Both these models were used to refine a final correlation detailed in Section 6.3.5. Figure C-1 shows the parity plot of the normalized mass fraction of oxygen in the tar, as predicted by Model 97 when compared to experimentally measured values. Table C-21

includes all the data from the final training step of the initial cross-validation cycle, and Figure C-2 to Figure C-6 show the trends associated with these results.

Table C-21. Complete Tar Oxygen Final Training Results

Model	N_{coeff}	R^2	R^2/N_{coeff}	L_1 Norm	L_2 Norm	Infinity Norm	SSE
91	9	0.773	0.086	0.097	0.117	0.273	0.465
4	5	0.733	0.147	0.103	0.127	0.257	0.546
5	5	0.733	0.147	0.103	0.127	0.257	0.546
6	9	0.612	0.068	0.121	0.153	0.324	0.795
7	5	0.308	0.062	0.161	0.204	0.477	1.417
8	17	0.766	0.045	0.098	0.119	0.262	0.479
92	10	0.764	0.076	0.100	0.119	0.288	0.483
93	11	0.774	0.070	0.096	0.117	0.280	0.463
94	12	0.772	0.064	0.098	0.117	0.282	0.468
96	11	0.837	0.076	0.085	0.099	0.241	0.335
97	12	0.842	0.070	0.084	0.098	0.224	0.324
98	12	0.834	0.070	0.085	0.100	0.246	0.340
21	17	0.750	0.044	0.101	0.123	0.276	0.513
2	9	0.764	0.085	0.097	0.119	0.266	0.484
3	17	0.565	0.033	0.138	0.162	0.338	0.894

C.2.3.4 Tar Nitrogen

Tar nitrogen Model 119 had the highest R^2 value and Model 7 had the highest R^2/N_{coeff} value. Their final training statistical values are in Table C-22.

Model 119 performed moderately well with a final training R^2 value of 0.717 and an average cross-validation R^2 value of 0.777. The model with the highest R^2/N_{coeff} value was model 7, which did not have a high R^2 value (0.452). The higher R^2/N_{coeff} value comes from the fewer number of coefficients.

Table C-22. Best Tar Nitrogen Final Training Results

Step	Model	N_{coeff}	R^2	R^2/N_{coeff}	L_1 Norm	L_2 Norm	Infinity Norm	SSE
Cross-validation, best R^2	119	16	0.777	0.049	0.093	0.114	0.199	0.088
Final training, best R^2	119	16	0.717	0.045	0.114	0.147	0.409	1.397
Cross-validation, best R^2/N_{coeff}	7	5	0.807	0.161	0.105	0.121	0.208	0.103
Final training, best R^2/N_{coeff}	7	5	0.452	0.090	0.161	0.204	0.533	2.706

Figure C-1 shows the parity plot comparing the predicted value (from model 119) of the normalized mass fraction of nitrogen in the tar with the experimentally measured value. Table C-23 shows all validation metrics for the complete set of model forms tested for nitrogen in the tar. Figure C-2 to Figure C-6 show the trends associated with these validation metrics.

Table C-23. Complete Tar Nitrogen Final Training Results

Model	N_{coeff}	R^2	R^2/N_{coeff}	L_1 Norm	L_2 Norm	Infinity Norm	SSE
99	14	0.439	0.031	0.155	0.207	0.588	2.780
2	9	0.490	0.054	0.159	0.197	0.559	2.519
4	5	0.424	0.085	0.167	0.209	0.558	2.848
5	5	0.424	0.085	0.167	0.209	0.558	2.848
6	9	0.473	0.053	0.161	0.200	0.547	2.606
7	5	0.452	0.090	0.161	0.204	0.533	2.706
8	17	0.570	0.034	0.144	0.181	0.457	2.132
100	16	0.434	0.027	0.161	0.207	0.573	2.796
101	17	0.506	0.030	0.155	0.194	0.495	2.443
102	15	0.430	0.029	0.157	0.209	0.601	2.834
103	16	0.435	0.027	0.155	0.208	0.597	2.803
104	17	0.440	0.026	0.161	0.206	0.566	2.769
105	15	0.535	0.036	0.146	0.188	0.524	2.302

Table C-23. Complete Tar Nitrogen Final Training Results, CONTINUED

Model	N_{coeff}	R^2	R^2/N_{coeff}	L_1 Norm	L_2 Norm	Infinity Norm	SSE
106	16	0.540	0.034	0.150	0.187	0.488	2.276
107	17	0.651	0.038	0.128	0.163	0.478	1.727
108	15	0.540	0.036	0.149	0.187	0.492	2.272
109	17	0.502	0.030	0.155	0.195	0.546	2.470
110	16	0.460	0.029	0.154	0.203	0.520	2.671
111	17	0.444	0.026	0.159	0.206	0.545	2.745
112	15	0.436	0.029	0.160	0.207	0.573	2.787
113	17	0.517	0.030	0.153	0.192	0.494	2.388
114	15	0.582	0.039	0.137	0.179	0.504	2.080
115	16	0.602	0.038	0.133	0.174	0.479	1.972
116	15	0.512	0.034	0.154	0.193	0.478	2.411
117	17	0.442	0.026	0.154	0.206	0.582	2.770
118	28	0.687	0.025	0.125	0.154	0.440	1.551
21	17	0.582	0.034	0.146	0.178	0.527	2.070
119	16	0.717	0.045	0.114	0.147	0.409	1.397
3	17	0.330	0.019	0.202	0.242	0.598	3.805

C.2.3.5 Tar Sulfur

Many of the tested models for sulfur in the tar performed very well. Model 2 had the highest R^2 value and model 4 the highest R^2/N_{coeff} value. The statistical values for both these models from cross-validation and final training are detailed in Table C-24.

For being a relatively small, and many times inaccurate, contribution, the correlations predicting the sulfur composition of the tar performed well. Model 2 had the highest R^2 value of 0.765 in final training and an average value of 0.880 in cross-validation, indicating a good ability to predict new data. Model 4 had the highest R^2/N_{coeff} value and did reasonably well in cross-validation. Both models were used to refine the final correlation in Section 6.3.7.

The parity plot showing the normalized mass fraction of sulfur in the tar predicted by model 2 compared to the same values measured experimentally is found in Figure C-1. The results for the complete set of tested tar sulfur models are found in Table C-25. Figure C-2 to Figure C-6 show the trends of these results.

Table C-24. Best Tar Sulfur Final Training Results

Step	Model	N_{coeff}	R^2	R^2/N_{coeff}	L_1 Norm	L_2 Norm	Infinity Norm	SSE
Cross-validation, best R^2	2	9	0.880	0.098	0.083	0.105	0.201	0.086
Final training, best R^2	2	9	0.765	0.085	0.121	0.151	0.358	0.779
Cross-validation, best R^2/N_{coeff}	4	5	0.796	0.159	0.100	0.126	0.256	0.112
Final training, best R^2/N_{coeff}	4	5	0.626	0.125	0.145	0.191	0.595	1.239

Table C-25. Complete Tar Sulfur Final Training Results

Model	N_{coeff}	R^2	R^2/N_{coeff}	L_1 Norm	L_2 Norm	Infinity Norm	SSE
22	13	0.642	0.049	0.155	0.187	0.352	1.184
2	9	0.765	0.085	0.121	0.151	0.358	0.780
4	5	0.626	0.125	0.145	0.191	0.595	1.239
5	5	0.626	0.125	0.145	0.191	0.595	1.239
6	9	0.726	0.081	0.128	0.163	0.352	0.908
7	5	0.318	0.064	0.210	0.258	0.659	2.257
8	17	0.737	0.043	0.129	0.160	0.435	0.873
34	16	0.644	0.040	0.155	0.186	0.346	1.180
25	14	0.642	0.046	0.154	0.187	0.350	1.186
39	16	0.643	0.040	0.155	0.186	0.347	1.181
27	14	0.642	0.046	0.155	0.187	0.353	1.184
40	14	0.642	0.046	0.155	0.187	0.355	1.184
41	15	0.654	0.044	0.153	0.184	0.337	1.148
42	15	0.642	0.043	0.155	0.187	0.355	1.185
43	16	0.643	0.040	0.155	0.187	0.353	1.184
21	17	0.736	0.043	0.130	0.160	0.324	0.873
3	17	0.607	0.036	0.167	0.199	0.416	1.341

2.2.3.6 Char Carbon

Char carbon models 6 and 8 performed the best in cross-validation and final training, with model 8 having the highest R^2 value and 6 having the highest R^2/N_{coeff} value. The statistical values for these models are included in Table C-26.

Table C-26. Best Char Carbon Final Training Results

Step	**Model**	**N_{coeff}**	**R^2**	**R^2/N_{coeff}**	**L_1 Norm**	**L_2 Norm**	**Infinity Norm**	**SSE**
Cross-validation, best R^2	8	17	0.662	0.039	0.037	0.049	0.108	0.025
Final training, best R^2	8	17	0.541	0.032	0.034	0.046	0.189	0.208
Cross-validation, best R^2/N_{coeff}	6	9	0.593	0.066	0.048	0.064	0.154	0.041
Final training, best R^2/N_{coeff}	6	9	0.505	0.056	0.034	0.048	0.192	0.225

Even though model 8 performed the best in final training, with an R^2 value of 0.541, it doesn't fit all the data well. Both model 8 and 6 were used to develop the final char carbon correlation found in Section 6.3.8. The parity plot showing the predictive capabilities of model 8 against the experimental data set is in Figure C-7.

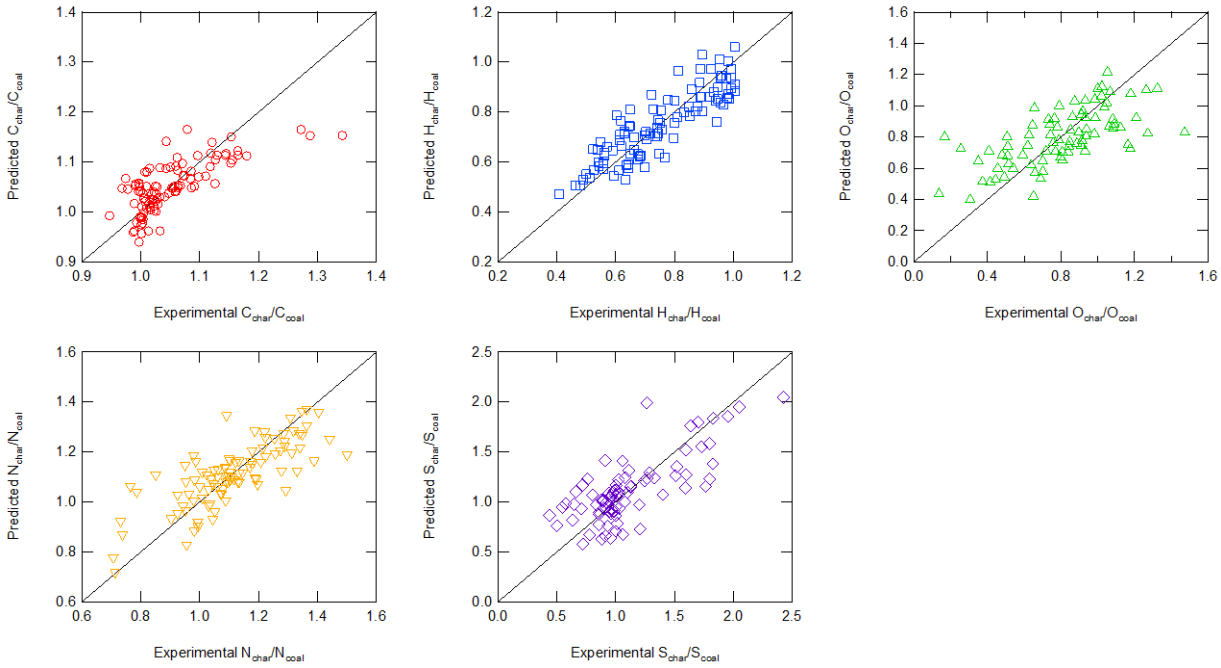

Figure C-7. Final training parity plots of CHONS in the char.

Table C-27 shows the complete set of "final training" validation metrics for carbon in the char. The following figures include the same values as Table C-27 but are included to better show the trends. Figure C-8 shows the L_1 norm, Figure C-9 shows the L_2 norm, Figure C-10 shows the infinity norm, Figure C-11 shows the SSE, and Figure C-12 shows the R^2 values. These figures include plots for all five elements (CHONS) in the char.

Table C-27. Complete Char Carbon Final Training Results

Model	N_{coeff}	R^2	R^2/N_{coeff}	L_1 Norm	L_2 Norm	Infinity Norm	SSE
1	12	0.232	0.019	0.044	0.059	0.245	0.349
6	9	0.505	0.056	0.034	0.048	0.192	0.225
8	17	0.541	0.032	0.034	0.046	0.189	0.208
9	13	0.272	0.021	0.043	0.058	0.214	0.331
10	14	0.193	0.014	0.046	0.061	0.251	0.369
11	13	0.340	0.026	0.040	0.055	0.216	0.301
12	14	0.239	0.017	0.044	0.059	0.227	0.349
13	14	0.292	0.021	0.043	0.057	0.205	0.324
14	14	0.229	0.016	0.045	0.060	0.241	0.353

Table C-27. Complete Char Carbon Final Training Results, CONTINUED

Model	N_{coeff}	R^2	R^2/N_{coeff}	L_1 Norm	L_2 Norm	Infinity Norm	SSE
15	13	0.220	0.017	0.045	0.060	0.236	0.354
16	14	0.414	0.030	0.039	0.052	0.146	0.266
17	13	0.286	0.022	0.042	0.057	0.227	0.325
18	14	0.243	0.017	0.044	0.059	0.227	0.346
19	14	0.357	0.026	0.039	0.054	0.229	0.292
20	20	0.340	0.017	0.041	0.055	0.207	0.303
21	17	0.527	0.031	0.034	0.047	0.190	0.215
2	9	0.500	0.056	0.034	0.048	0.208	0.227
3	17	0.470	0.028	0.038	0.051	0.188	0.262

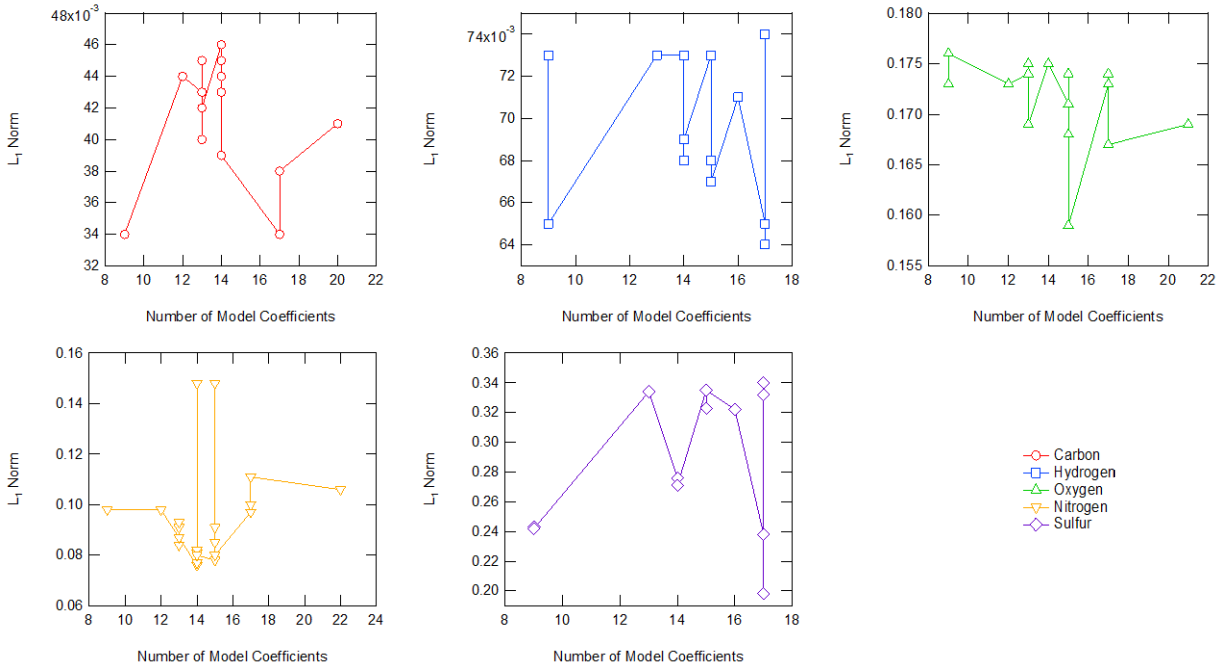

Figure C-8. L_1 norm for each model of each element in the char, plotted against number of model coefficients.

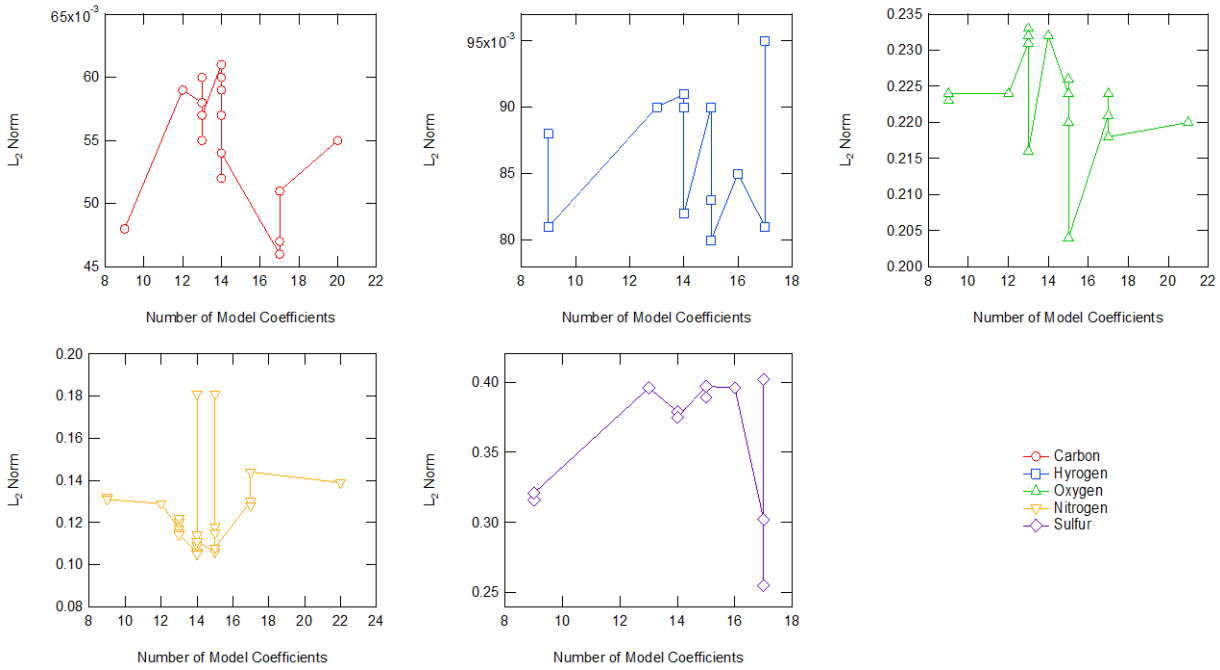

Figure C-9. L_2 norm for each model of each element in the char, plotted against number of model coefficients.

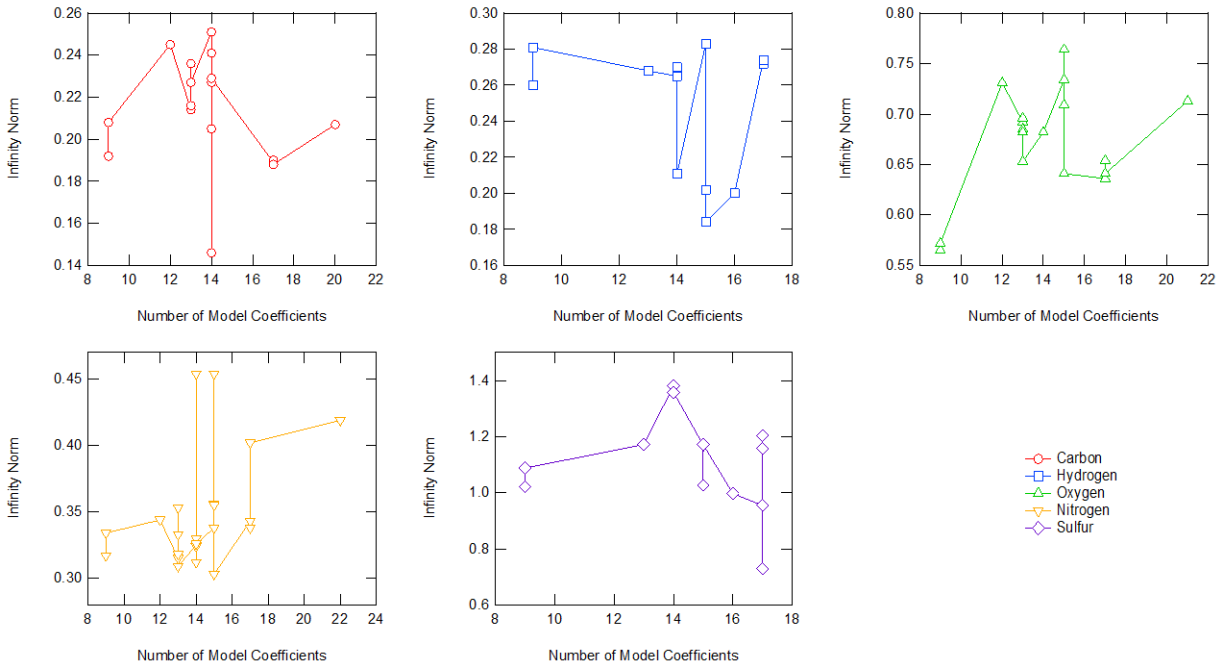

Figure C-10. Infinity norm for each model of each element in the char, plotted against number of model coefficients.

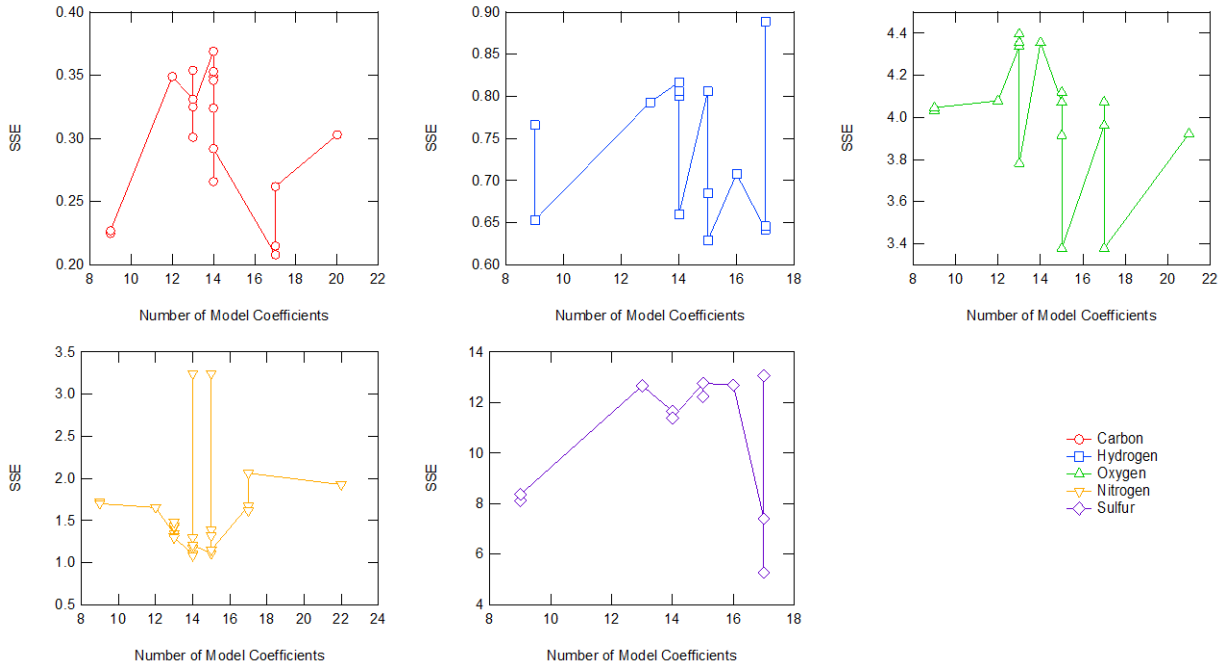

Figure C-11. SSE for each model of each element in the char, plotted against number of model coefficients.

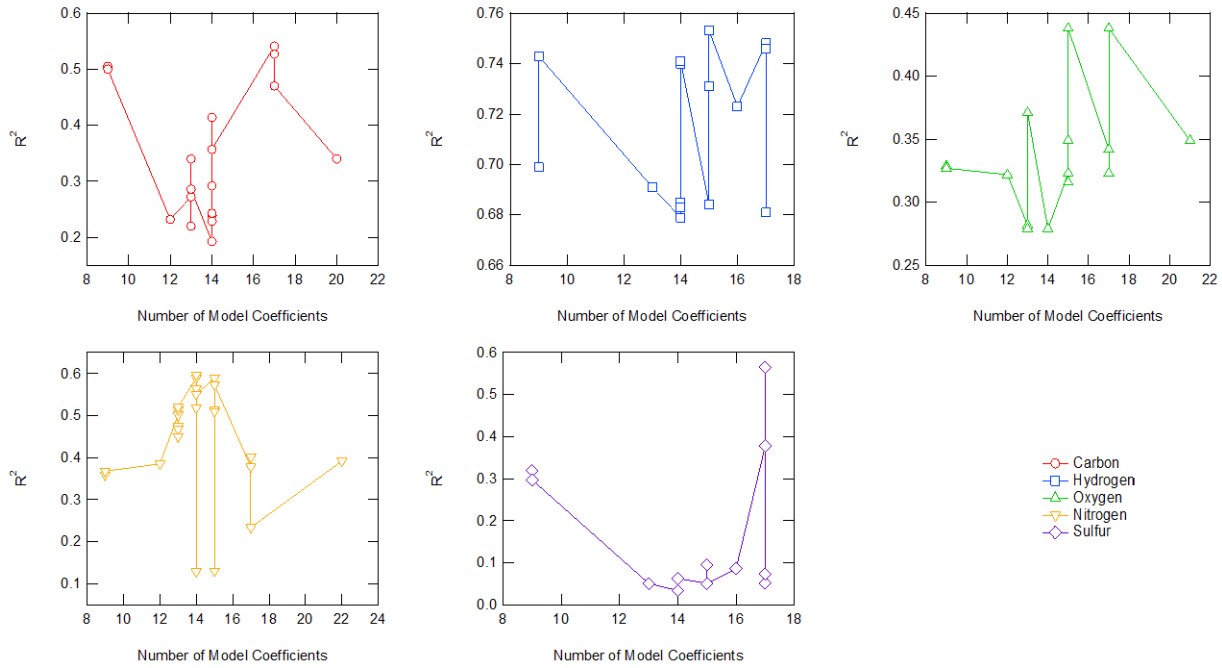

Figure C-12. R^2 for each model of each element in the char, plotted against number of model coefficients.

C.2.3.7 Char Hydrogen

The cross-validation and final training analysis indicated that char hydrogen models 2 and 31 performed the best, with model 31 having the highest R^2 value and model 2 having the highest R^2/N_{coeff} value. The results for these models from cross-validation and final training are included in Table C-28.

Table C-28. Best Char Hydrogen Final Training Results

Step	**Model**	**N_{coeff}**	**R^2**	**R^2/N_{coeff}**	**L_1 Norm**	**L_2 Norm**	**Infinity Norm**	**SSE**
Cross-validation, best R^2	31	15	0.706	0.047	0.079	0.091	0.154	0.084
Final training, best R^2	31	15	0.753	0.050	0.067	0.080	0.184	0.629
Cross-validation, best R^2/N_{coeff}	2	9	0.852	0.050	0.057	0.066	0.105	0.044
Final training, best R^2/N_{coeff}	2	9	0.743	0.083	0.065	0.081	0.281	0.653

Model 31 performed well with a final training R^2 value of 0.753 and an average R^2 value of 0.706 in cross-validation. As this was the best fit of the initial cross-validation analysis, figure S7 shows the predictive capabilities of model 31. Model 2 also did well with a slightly lower R^2 value of 0.743 in final training and an even higher average R^2 value of 0.852. Both these models were used to develop the final char hydrogen correlation in Section 6.3.9. Table C-29 shows the final training results of all tested char hydrogen models, and Figure C-8 to Figure C-12 show the same results plotted to better show the trends.

Table C-29. Complete Char Hydrogen Final Training Results

Model	N_{coeff}	R^2	R^2/N_{coeff}	L_1 Norm	L_2 Norm	Infinity Norm	SSE
22	13	0.691	0.053	0.073	0.090	0.268	0.793
6	9	0.699	0.078	0.073	0.088	0.260	0.766
8	17	0.748	0.044	0.065	0.081	0.274	0.642
23	14	0.679	0.048	0.073	0.091	0.265	0.817
25	14	0.685	0.049	0.073	0.090	0.270	0.800
26	15	0.684	0.046	0.073	0.090	0.283	0.806
27	14	0.683	0.049	0.073	0.090	0.270	0.806
28	14	0.740	0.053	0.068	0.082	0.211	0.660
29	15	0.731	0.049	0.068	0.083	0.202	0.685
30	14	0.741	0.053	0.069	0.082	0.211	0.660
31	15	0.753	0.050	0.067	0.080	0.184	0.629
32	16	0.723	0.045	0.071	0.085	0.200	0.708
21	17	0.746	0.044	0.064	0.081	0.272	0.646
2	9	0.743	0.083	0.065	0.081	0.281	0.653
3	17	0.681	0.040	0.074	0.095	0.274	0.889

C.2.3.8 Char Oxygen

Char oxygen model 6 had the highest R^2/N_{coeff} value and model 120 had the highest R^2 value. The statistical values for these models are found in Table C-30.

Table C-30. Best Char Oxygen Final Training Results

Step	Model	N_{coeff}	R^2	R^2/N_{coeff}	L_1 Norm	L_2 Norm	Infinity Norm	SSE
Cross-validation, best R^2	120	15	0.601	0.040	0.132	0.174	0.351	0.252
Final training, best R^2	120	15	0.438	0.029	0.159	0.204	0.641	3.378
Cross-validation, best R^2/N_{coeff}	6	9	0.563	0.063	0.196	0.224	0.373	0.491
Final training, best R^2/N_{coeff}	6	9	0.329	0.037	0.173	0.223	0.565	4.034

None of the char oxygen models tested performed well, with model 120 having the highest R^2 value of 0.438. The final training fit of model 120 is shown in Figure C-7. Model 6 performed only a little worse overall but had the highest R^2/N_{coeff} value of 0.037. Both model 6 and model 120 were used to refine the final correlation shown in Section 6.3.10. Table C-31 contains the validation metrics for all tested char oxygen models, with the same data shown in graphical form in Figure C-8 to Figure C-12.

Table C-31. Complete Char Oxygen Final Training Results

Model	N_{coeff}	R^2	R^2/N_{coeff}	L_1 Norm	L_2 Norm	Infinity Norm	SSE
44	12	0.322	0.027	0.171	0.224	0.731	4.079
6	9	0.329	0.037	0.173	0.223	0.565	4.034
8	17	0.342	0.020	0.173	0.221	0.636	3.961
45	13	0.282	0.022	0.174	0.231	0.692	4.337
46	15	0.323	0.022	0.171	0.224	0.734	4.072
47	13	0.282	0.022	0.174	0.233	0.696	4.396
48	14	0.279	0.020	0.175	0.232	0.682	4.355
49	13	0.279	0.021	0.175	0.232	0.685	4.357
50	13	0.279	0.021	0.175	0.232	0.682	4.355
51	15	0.349	0.023	0.174	0.220	0.709	3.914
52	13	0.371	0.029	0.169	0.216	0.653	3.782
53	15	0.316	0.021	0.168	0.226	0.764	4.119
54	21	0.349	0.017	0.169	0.220	0.713	3.923
21	17	0.323	0.019	0.174	0.224	0.654	4.073
2	9	0.327	0.036	0.176	0.224	0.572	4.047
3	17	0.362	0.021	0.167	0.218	0.683	3.840
120	15	0.438	0.029	0.159	0.204	0.641	3.378

C.2.3.9 Char Nitrogen

The nitrogen in the char was unique among all the other elements because one model had both the best R^2 value and the best R^2/N_{coeff} value: Model 62. This models' statistical values from final training and cross-validation are included in Table C-32.

Table C-32. Best Char Nitrogen Final Training Results

Step	Model	N_{coeff}	R^2	R^2/N_{coeff}	L_1 Norm	L_2 Norm	Infinity Norm	SSE
Cross-validation	62	14	0.600	0.043	0.077	0.097	0.185	0.097
Final training	62	14	0.597	0.043	0.077	0.105	0.312	1.084

Model 62 performed the best of all tested char nitrogen models with an R^2 value of 0.597 in final training and an average value of 0.600 in cross-validation. Its predictive capabilities are shown in Figure C-7. Model 62 was the only model used to refine the final correlation discussed in Section 6.3.11. Table C-33 includes all validation metrics for all tested char nitrogen model forms. This same data is in Figure C-8 to Figure C-12 to show the trends.

Table C-33. Complete Char Nitrogen Final Training Results

Model	N_{coeff}	R^2	R^2/N_{coeff}	L_1 Norm	L_2 Norm	Infinity Norm	SSE
55	12	0.385	0.032	0.098	0.129	0.344	1.654
6	9	0.359	0.040	0.098	0.132	0.317	1.725
8	17	0.378	0.022	0.097	0.130	0.343	1.674
56	14	0.589	0.042	0.076	0.106	0.325	1.106
57	15	0.589	0.039	0.078	0.106	0.338	1.108
59	14	0.564	0.040	0.081	0.109	0.324	1.172
60	15	0.130	0.009	0.148	0.181	0.454	3.245
61	13	0.501	0.039	0.087	0.117	0.315	1.344
62	14	0.597	0.043	0.077	0.105	0.312	1.084
63	15	0.514	0.034	0.091	0.118	0.356	1.386
65	13	0.474	0.036	0.091	0.120	0.315	1.417
67	15	0.510	0.034	0.085	0.115	0.355	1.319
68	13	0.468	0.036	0.091	0.120	0.318	1.431
69	15	0.573	0.038	0.080	0.108	0.303	1.150
71	13	0.513	0.039	0.084	0.115	0.353	1.311
72	14	0.518	0.037	0.082	0.114	0.330	1.296
74	14	0.129	0.009	0.148	0.181	0.454	3.244
75	13	0.450	0.035	0.093	0.122	0.333	1.480
76	14	0.551	0.039	0.080	0.111	0.326	1.210
78	13	0.520	0.040	0.087	0.114	0.309	1.293
79	22	0.392	0.018	0.106	0.139	0.419	1.926

Table C-33. Complete Char Nitrogen Final Training Results, CONTINUED

Model	N_{coeff}	R^2	R^2/N_{coeff}	L_1 Norm	L_2 Norm	Infinity Norm	SSE
21	17	0.401	0.024	0.100	0.128	0.338	1.615
2	9	0.368	0.041	0.098	0.131	0.334	1.701
3	17	0.234	0.014	0.111	0.144	0.402	2.063

C.2.3.10 Char Sulfur

The models that performed the best during the char sulfur cross-validation and final training were 6 (best R^2/N_{coeff}) and 21 (best R^2). The statistical values from cross-validation and final training are included in Table C-34.

Table C-34. Best Char Sulfur Final Training Results

Step	Model	N_{coeff}	R^2	R^2/N_{coeff}	L_1 Norm	L_2 Norm	Infinity Norm	SSE
Cross-validation, best R^2	21	17	0.400	0.024	0.229	0.290	0.535	0.677
Final training, best R^2	21	17	0.565	0.033	0.198	0.255	0.728	5.277
Cross-validation, best R^2/N_{coeff}	6	9	0.511	0.057	0.256	0.321	0.573	0.895
Final training, best R^2/N_{coeff}	6	9	0.319	0.035	0.243	0.316	1.021	8.110

None of the tested char sulfur models performed well in either final training or cross-validation. This is not surprising as sulfur is a relatively small composition overall, it is hard to measure accurately, and many researchers do not distinguish between the types of sulfur contributions. The best model tested was model 21 with an R^2 value of 0.565 for final training and an average value of 0.400 in cross-validation. The parity plot comparing the model values

predicted by model 21 to the experimental values is found in Figure C-7. Both model 21 and model 6 were used to develop the final correlation in Section 6.3.12. Table C-35 contains the complete results for "final training" for the tested char sulfur models. Figure C-8 to Figure C-12 show plots of these data.

Table C-35. Complete Char Sulfur Final Training Results

Model	N_{coeff}	R^2	R^2/N_{coeff}	L_1 Norm	L_2 Norm	Infinity Norm	SSE
81	13	0.051	0.004	0.334	0.396	1.172	12.670
6	9	0.319	0.035	0.243	0.316	1.020	8.108
8	17	0.378	0.022	0.238	0.302	0.955	7.407
82	14	0.034	0.002	0.276	0.379	1.381	11.661
83	15	0.051	0.003	0.335	0.397	1.170	12.768
84	14	0.034	0.002	0.276	0.379	1.381	11.661
85	15	0.095	0.006	0.323	0.389	1.026	12.238
86	16	0.086	0.005	0.322	0.396	0.997	12.688
87	14	0.034	0.002	0.276	0.379	1.381	11.662
88	15	0.051	0.003	0.335	0.397	1.172	12.768
89	14	0.063	0.005	0.271	0.375	1.358	11.392
90	17	0.052	0.003	0.340	0.402	1.158	13.088
21	17	0.565	0.033	0.198	0.255	0.728	5.277
2	9	0.297	0.033	0.242	0.321	1.088	8.366
3	17	0.073	0.004	0.332	0.402	1.204	13.059

C.3 Model Refinement

This section contains the complete results of the model refinement analysis. The best models are detailed in Section 6.3. This section details both a cross-validation analysis as well as a "final training" analysis over the complete data set. The "final training" results in this case are the same values as the final correlations reported in Section 6.3, for the best performers. This section starts with the cross-validation results followed by the final training results. The final training results include both a tabular presentation and the same data in graphical presentation. The figures are to better show the trends in the data.

C.3.1 Model Refinement Cross-Validation

As with the initial cross-validation procedure described above, better average validation metric values (higher for R^2, lower for the other validation metrics) mean that model is better at predicting "new" data and will be better at predicting new data after the final correlations are found. Table C-36 shows the cross-validation results for carbon in the tar, Table C-37 contains the cross-validation results for hydrogen in the tar, Table C-38 summarizes the cross-validation results for oxygen in the tar, Table C-39 includes the cross-validation results for nitrogen in the tar, and Table C-40 has the cross-validation results for sulfur in the tar.

Table C-36. Tar Carbon Model Refinement Cross-Validation Results

Model	N_{coeff}	R^2	R^2/N_{coeff}	L_1 Norm	L_2 Norm	Infinity Norm	SSE
21	17	0.869	0.051	0.045	0.059	0.131	0.031
5	5	0.914	0.183	0.034	0.046	0.106	0.017
149	16	0.886	0.055	0.041	0.051	0.110	0.020
150	15	0.886	0.059	0.041	0.050	0.109	0.020
151	14	0.883	0.063	0.041	0.052	0.116	0.021
152	13	0.885	0.068	0.041	0.050	0.110	0.020
153	12	0.884	0.074	0.041	0.050	0.110	0.020
154	11	0.884	0.080	0.041	0.050	0.110	0.020

Table C-37. Tar Hydrogen Model Refinement Cross-Validation Results

Model	N_{coeff}	R^2	R^2/N_{coeff}	L_1 Norm	L_2 Norm	Infinity Norm	SSE
62	14	0.528	0.038	0.129	0.150	0.244	0.141
7	5	0.728	0.146	0.067	0.083	0.142	0.062
155	12	0.717	0.060	0.088	0.104	0.173	0.074
156	11	0.489	0.044	0.121	0.146	0.265	0.145
157	10	0.465	0.047	0.118	0.147	0.281	0.147
158	9	0.781	0.087	0.076	0.093	0.162	0.054

Table C-38. Tar Oxygen Model Refinement Cross-Validation Results

Model	N_{coeff}	R^2	R^2/N_{coeff}	L_1 Norm	L_2 Norm	Infinity Norm	SSE
97	12	0.820	0.068	0.099	0.116	0.206	0.100
5	5	0.755	0.151	0.134	0.157	0.266	0.151
159	11	0.839	0.076	0.096	0.113	0.201	0.090
160	11	0.829	0.075	0.100	0.114	0.192	0.091
161	10	0.832	0.083	0.100	0.113	0.191	0.090
162	9	0.832	0.092	0.100	0.113	0.191	0.090

Table C-39. Tar Nitrogen Model Refinement Cross-Validation Results

Model	N_{coeff}	R^2	R^2/N_{coeff}	L_1 Norm	L_2 Norm	Infinity Norm	SSE
119	16	0.777	0.049	0.093	0.114	0.199	0.088
7	5	0.807	0.161	0.105	0.121	0.208	0.103
163	16	0.771	0.048	0.094	0.115	0.201	0.089
164	15	0.763	0.051	0.092	0.114	0.203	0.089
165	14	0.782	0.056	0.088	0.109	0.190	0.080
166	13	0.760	0.058	0.094	0.113	0.197	0.085
167	12	0.811	0.068	0.088	0.105	0.185	0.072
168	11	0.812	0.074	0.084	0.104	0.186	0.070

Table C-40. Tar Sulfur Model Refinement Cross-Validation Results

Model	N_{coeff}	R^2	R^2/N_{coeff}	L_1 Norm	L_2 Norm	Infinity Norm	SSE
2	9	0.880	0.098	0.083	0.105	0.201	0.086
4	5	0.796	0.159	0.100	0.126	0.256	0.112
169	8	0.952	0.119	0.062	0.078	0.154	0.050
170	7	0.942	0.135	0.074	0.095	0.184	0.068
171	6	0.953	0.159	0.067	0.082	0.152	0.052
172	7	0.955	0.136	0.062	0.076	0.147	0.042

Table C-41 includes the cross-validation results for carbon in the char, Table C-42 has the cross-validation results for hydrogen in the char, Table C-43 contains the cross-validation results for oxygen in the char, Table C-44 shows the results for cross-validation of nitrogen in the char, and Table C-45 detail the cross-validation results for sulfur in the char.

Table C-41. Char Carbon Model Refinement Cross-Validation Results

Model	N_{coeff}	R^2	R^2/N_{coeff}	L_1 Norm	L_2 Norm	Infinity Norm	SSE
8	17	0.662	0.039	0.037	0.049	0.108	0.025
6	9	0.593	0.066	0.048	0.064	0.154	0.041
121	16	0.663	0.041	0.037	0.049	0.108	0.025
122	15	0.665	0.044	0.036	0.049	0.107	0.025
123	14	0.666	0.048	0.036	0.049	0.107	0.025
124	13	0.660	0.051	0.037	0.049	0.108	0.025
125	12	0.655	0.055	0.037	0.049	0.110	0.025
126	11	0.671	0.061	0.036	0.049	0.107	0.025

Table C-42. Char Hydrogen Model Refinement Cross-Validation Results

Model	N_{coeff}	R^2	R^2/N_{coeff}	L_1 Norm	L_2 Norm	Infinity Norm	SSE
31	15	0.701	0.047	0.079	0.091	0.149	0.085
2	9	0.839	0.093	0.057	0.067	0.108	0.046
127	11	0.831	0.076	0.055	0.067	0.134	0.046
128	9	0.797	0.089	0.072	0.082	0.153	0.066
129	10	0.825	0.083	0.067	0.077	0.134	0.057
130	8	0.806	0.101	0.073	0.080	0.144	0.064
131	9	0.847	0.094	0.059	0.068	0.126	0.047

Table C-43. Char Oxygen Model Refinement Cross-Validation Results

Model	N_{coeff}	R^2	R^2/N_{coeff}	L_1 Norm	L_2 Norm	Infinity Norm	SSE
120	15	0.601	0.040	0.132	0.174	0.351	0.252
6	9	0.429	0.048	0.174	0.214	0.382	0.379
132	14	0.634	0.045	0.144	0.164	0.299	0.219
133	13	0.618	0.048	0.147	0.166	0.297	0.222
134	12	0.628	0.052	0.138	0.174	0.325	0.251
135	11	0.628	0.057	0.138	0.174	0.325	0.251
136	10	0.632	0.063	0.150	0.165	0.269	0.221

Table C-44. Char Nitrogen Model Refinement Cross-Validation Results

Model	N_{coeff}	R^2	R^2/N_{coeff}	L_1 Norm	L_2 Norm	Infinity Norm	SSE
62	14	0.600	0.043	0.077	0.097	0.185	0.097
137	13	0.600	0.046	0.077	0.097	0.185	0.097
138	12	0.601	0.050	0.077	0.097	0.185	0.097
139	11	0.619	0.056	0.074	0.091	0.174	0.085
140	12	0.645	0.054	0.067	0.085	0.172	0.077
141	11	0.648	0.059	0.067	0.085	0.172	0.076
142	10	0.682	0.068	0.076	0.090	0.156	0.079

Table C-45. Char Sulfur Model Refinement Cross-Validation Results

Model	N_{coeff}	R^2	R^2/N_{coeff}	L_1 Norm	L_2 Norm	Infinity Norm	SSE
21	17	0.381	0.022	0.295	0.388	0.759	1.361
6	9	0.511	0.057	0.256	0.321	0.573	0.895
143	16	0.428	0.027	0.214	0.272	0.512	0.597
144	15	0.378	0.025	0.227	0.288	0.538	0.670
145	14	0.421	0.030	0.229	0.288	0.535	0.677
146	13	0.388	0.030	0.226	0.284	0.526	0.649
147	12	0.425	0.035	0.224	0.279	0.512	0.642
148	11	0.417	0.038	0.261	0.322	0.581	0.903

C.3.2 Model Refinement Final Training

This section details the results of the "final training" of the models developed in model refinement. The best of these models are presented in Section 6.3. Table C-46 shows the results of the final training step of carbon in the tar after model refinement. Table C-47 contains the final training results of hydrogen in the tar after model refinement. Table C-48 includes final training results of oxygen in the tar after model refinement. Table C-49 summarizes final training validation metrics for nitrogen in the tar after model refinement. Table C-50 has the final training results for sulfur in the tar after model refinement. Figure C-13 to Figure C-17 include the same data as these tables to better show the trends observed in the model refinement analysis.

Table C-51 shows the results of the final training step of carbon in the char after model refinement. Table C-52 contains the final training results of hydrogen in the char after model refinement. Table C-53 includes final training results of oxygen in the char after model refinement. Table C-54 summarizes final training validation metrics for nitrogen in the char after model refinement. Table C-55 has the final training results for sulfur in the char after model refinement. Figure C-18 to Figure C-22 include the same data as these tables to better show the trends observed in the model refinement analysis.

Table C-46. Tar Carbon Model Refinement Final Training Results

Model	N_{coeff}	R^2	R^2/N_{coeff}	L_1 Norm	L_2 Norm	Infinity Norm	SSE
21	17	0.824	0.048	0.021	0.031	0.108	0.070
5	5	0.743	0.149	0.027	0.037	0.117	0.103
149	16	0.822	0.051	0.022	0.031	0.115	0.071
150	15	0.823	0.055	0.022	0.031	0.113	0.071
151	14	0.822	0.059	0.022	0.031	0.114	0.071
152	13	0.823	0.063	0.022	0.031	0.115	0.071
153	12	0.824	0.069	0.022	0.031	0.114	0.071
154	11	0.825	0.075	0.022	0.031	0.115	0.070

Table C-47. Tar Hydrogen Model Refinement Final Training Results

Model	N_{coeff}	R^2	R^2/N_{coeff}	L_1 Norm	L_2 Norm	Infinity Norm	SSE
62	14	0.697	0.050	0.083	0.107	0.381	0.742
7	5	0.607	0.121	0.087	0.119	0.434	1.064
155	12	0.796	0.066	0.067	0.088	0.295	0.499
156	11	0.799	0.073	0.066	0.087	0.299	0.491
157	10	0.800	0.080	0.067	0.087	0.305	0.490
158	9	0.786	0.087	0.069	0.090	0.312	0.524

Table C-48. Tar Oxygen Model Refinement Final Training Results

Model	N_{coeff}	R^2	R^2/N_{coeff}	L_1 Norm	L_2 Norm	Infinity Norm	SSE
97	12	0.842	0.070	0.084	0.098	0.224	0.324
5	5	0.733	0.147	0.103	0.127	0.257	0.546
159	11	0.843	0.077	0.082	0.097	0.229	0.322
160	11	0.842	0.077	0.083	0.098	0.227	0.324
161	10	0.842	0.084	0.082	0.097	0.235	0.323
162	9	0.841	0.093	0.082	0.098	0.240	0.325

Table C-49. Tar Nitrogen Model Refinement Final Training Results

Model	N_{coeff}	R^2	R^2/N_{coeff}	L_1 Norm	L_2 Norm	Infinity Norm	SSE
119	16	0.717	0.045	0.114	0.147	0.409	1.397
7	5	0.452	0.090	0.161	0.204	0.533	2.706
163	16	0.738	0.046	0.108	0.141	0.444	1.294
164	15	0.746	0.050	0.100	0.139	0.470	1.255
165	14	0.729	0.052	0.109	0.143	0.411	1.337
166	13	0.747	0.057	0.105	0.139	0.388	1.250
167	12	0.746	0.062	0.104	0.139	0.364	1.257
168	11	0.747	0.068	0.105	0.139	0.436	1.252

Table C-50. Tar Sulfur Model Refinement Final Training Results

Model	N_{coeff}	R^2	R^2/N_{coeff}	L_1 Norm	L_2 Norm	Infinity Norm	SSE
2	9	0.765	0.085	0.121	0.151	0.358	0.779
4	5	0.626	0.125	0.145	0.191	0.595	1.239
169	8	0.764	0.095	0.122	0.152	0.336	0.782
170	7	0.750	0.107	0.125	0.156	0.342	0.827
171	6	0.760	0.127	0.123	0.153	0.335	0.793
172	7	0.763	0.109	0.122	0.152	0.337	0.785

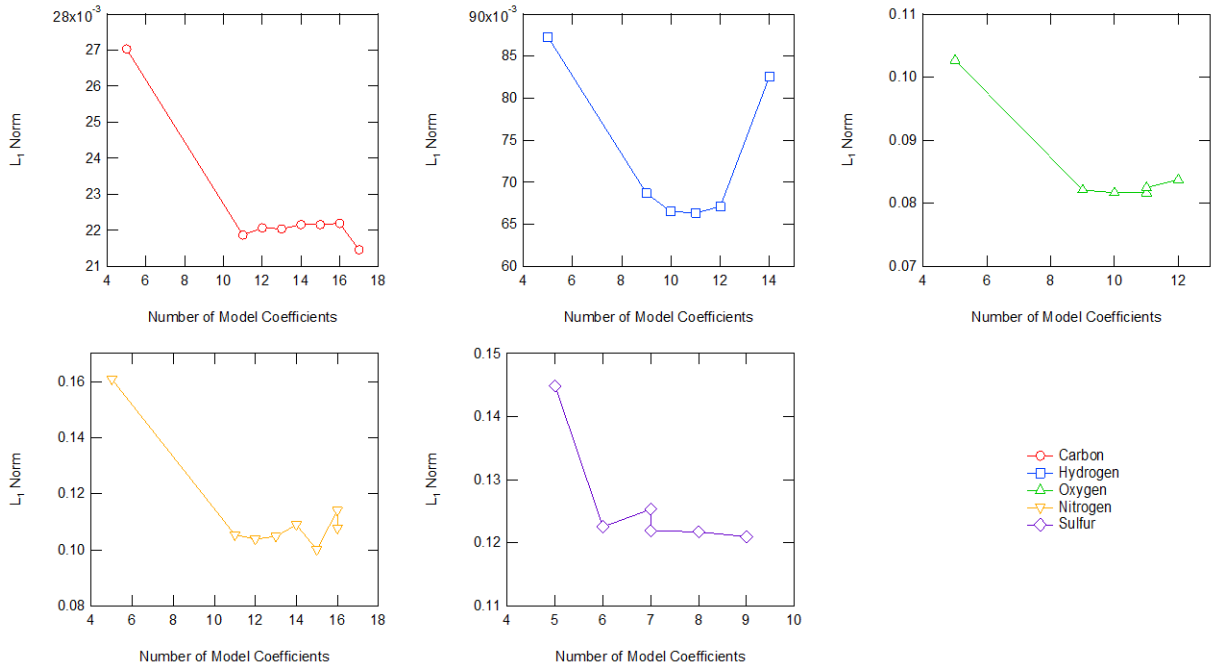

Figure C-13. L_1 norm for each model of each element in the tar, post model refinement.

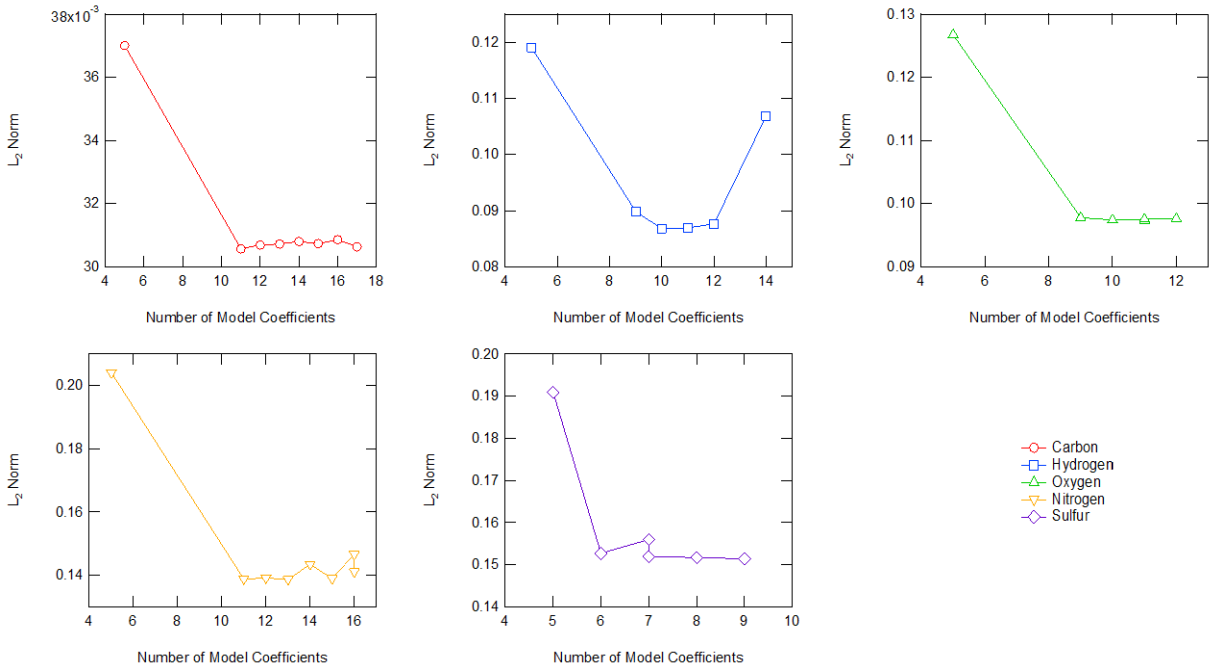

Figure C-14. L_2 norm for each model of each element in the tar, post model refinement.

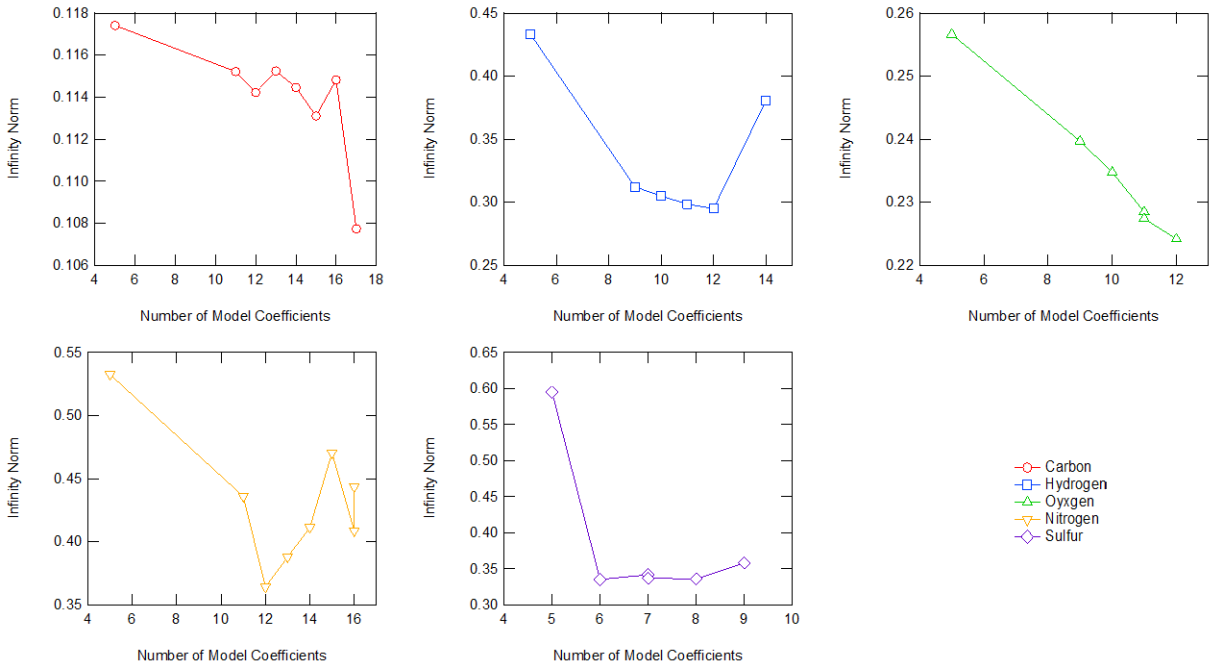

Figure C-15. Infinity norm for each model of each element in the tar, post model refinement.

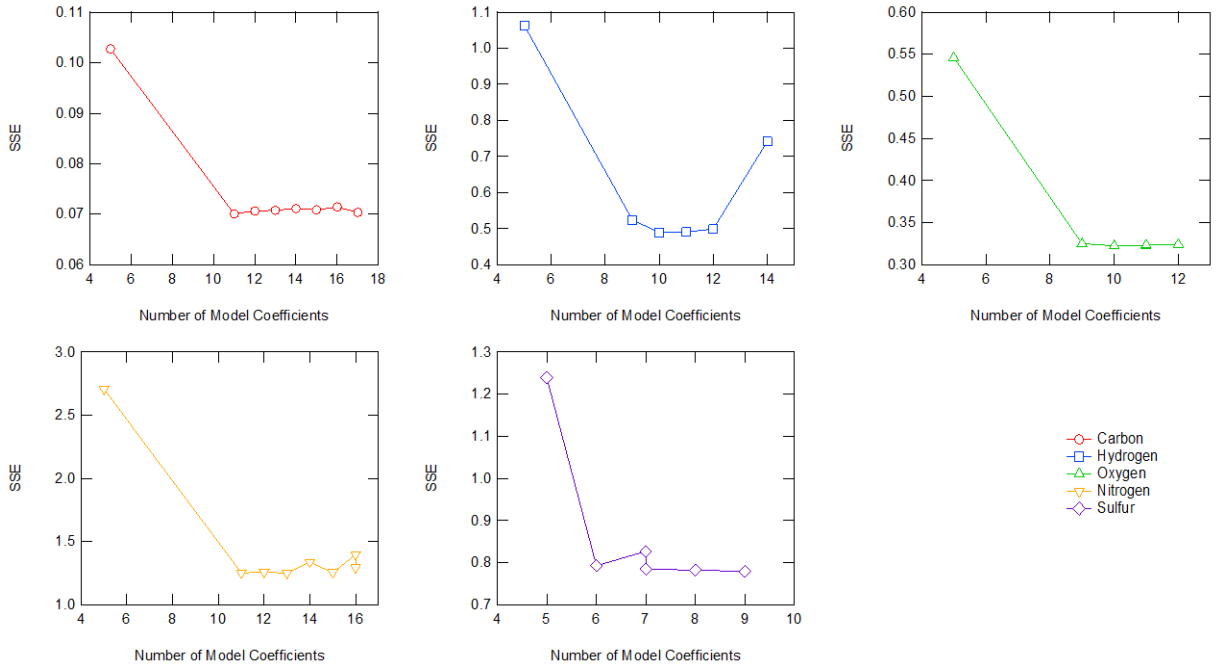

Figure C-16. SSE for each model of each element in the tar, post model refinement.

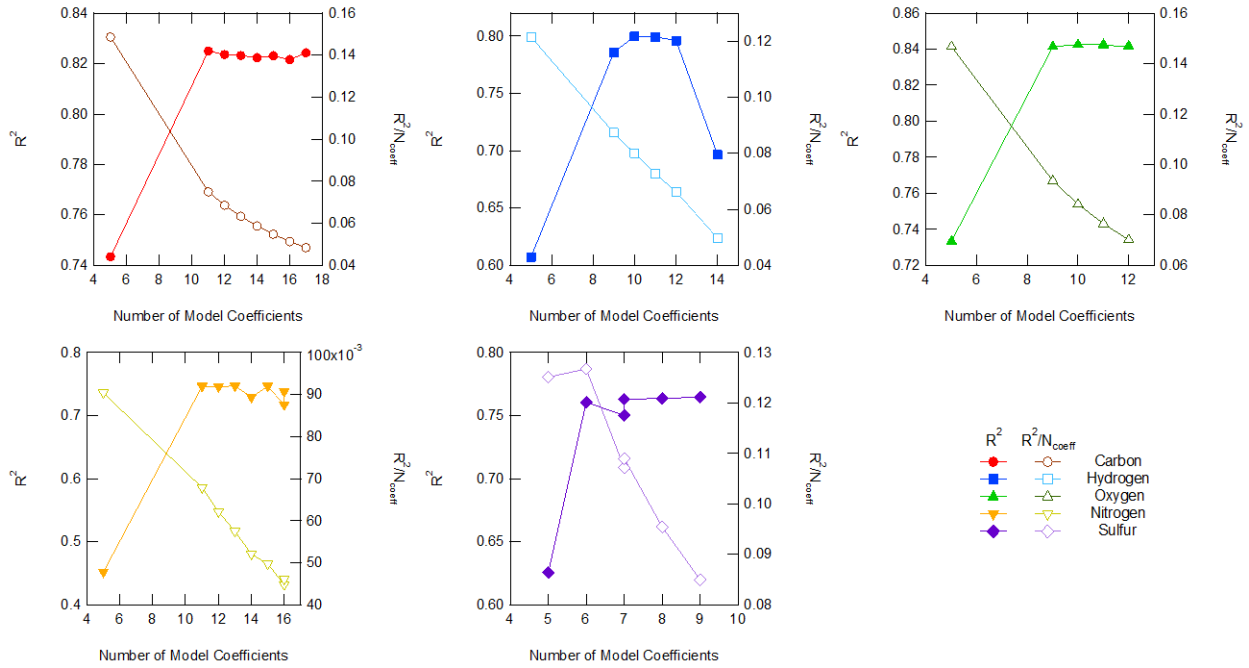

Figure C-17. R^2 for each model of each element in the tar, post model refinement.

Table C-51. Char Carbon Model Refinement Final Training Results

Model	N_{coeff}	R^2	R^2/N_{coeff}	L_1 Norm	L_2 Norm	Infinity Norm	SSE
8	17	0.541	0.032	0.034	0.046	0.189	0.208
6	9	0.505	0.056	0.034	0.048	0.192	0.225
121	16	0.551	0.034	0.033	0.045	0.188	0.204
122	15	0.541	0.036	0.034	0.046	0.193	0.209
123	14	0.543	0.039	0.034	0.046	0.192	0.207
124	13	0.544	0.042	0.034	0.046	0.182	0.207
125	12	0.541	0.045	0.034	0.046	0.192	0.208
126	11	0.548	0.050	0.033	0.046	0.190	0.205

Table C-52. Char Hydrogen Model Refinement Final Training Results

Model	N_{coeff}	R^2	R^2/N_{coeff}	L_1 Norm	L_2 Norm	Infinity Norm	SSE
31	15	0.753	0.050	0.067	0.080	0.184	0.629
2	9	0.743	0.083	0.065	0.081	0.281	0.653
127	11	0.800	0.073	0.058	0.072	0.221	0.509
128	9	0.758	0.084	0.068	0.079	0.169	0.617
129	10	0.787	0.079	0.059	0.074	0.237	0.542
130	8	0.757	0.095	0.068	0.079	0.170	0.618
131	9	0.773	0.086	0.065	0.076	0.195	0.576

Table C-53. Char Oxygen Model Refinement Final Training Results

Model	N_{coeff}	R^2	R^2/N_{coeff}	L_1 Norm	L_2 Norm	Infinity Norm	SSE
120	15	0.438	0.029	0.159	0.204	0.641	3.378
6	9	0.329	0.037	0.173	0.223	0.565	4.034
132	14	0.435	0.031	0.159	0.205	0.648	3.402
133	13	0.437	0.034	0.160	0.204	0.637	3.387
134	12	0.447	0.037	0.160	0.203	0.565	3.327
135	11	0.445	0.040	0.160	0.203	0.564	3.339
136	10	0.411	0.041	0.163	0.209	0.717	3.544

Table C-54. Char Nitrogen Model Refinement Final Training Results

Model	N_{coeff}	R^2	R^2/N_{coeff}	L_1 Norm	L_2 Norm	Infinity Norm	SSE
62	14	0.597	0.043	0.077	0.105	0.312	1.084
137	13	0.595	0.046	0.078	0.105	0.303	1.089
138	12	0.587	0.049	0.077	0.106	0.322	1.112
139	11	0.588	0.053	0.079	0.106	0.327	1.110
140	12	0.595	0.050	0.078	0.105	0.303	1.090
141	11	0.592	0.054	0.077	0.105	0.319	1.098
142	10	0.585	0.059	0.077	0.106	0.324	1.117

Table C-55. Char Sulfur Model Refinement Final Training Results

Model	N_{coeff}	R^2	R^2/N_{coeff}	L_1 Norm	L_2 Norm	Infinity Norm	SSE
21	17	0.565	0.033	0.198	0.255	0.728	5.277
6	9	0.319	0.035	0.243	0.316	1.021	8.110
143	16	0.605	0.038	0.180	0.241	0.620	4.703
144	15	0.570	0.038	0.194	0.251	0.604	5.119
145	14	0.560	0.040	0.188	0.254	0.666	5.237
146	13	0.562	0.043	0.200	0.254	0.624	5.229
147	12	0.570	0.048	0.190	0.251	0.634	5.121
148	11	0.605	0.055	0.182	0.241	0.601	4.702

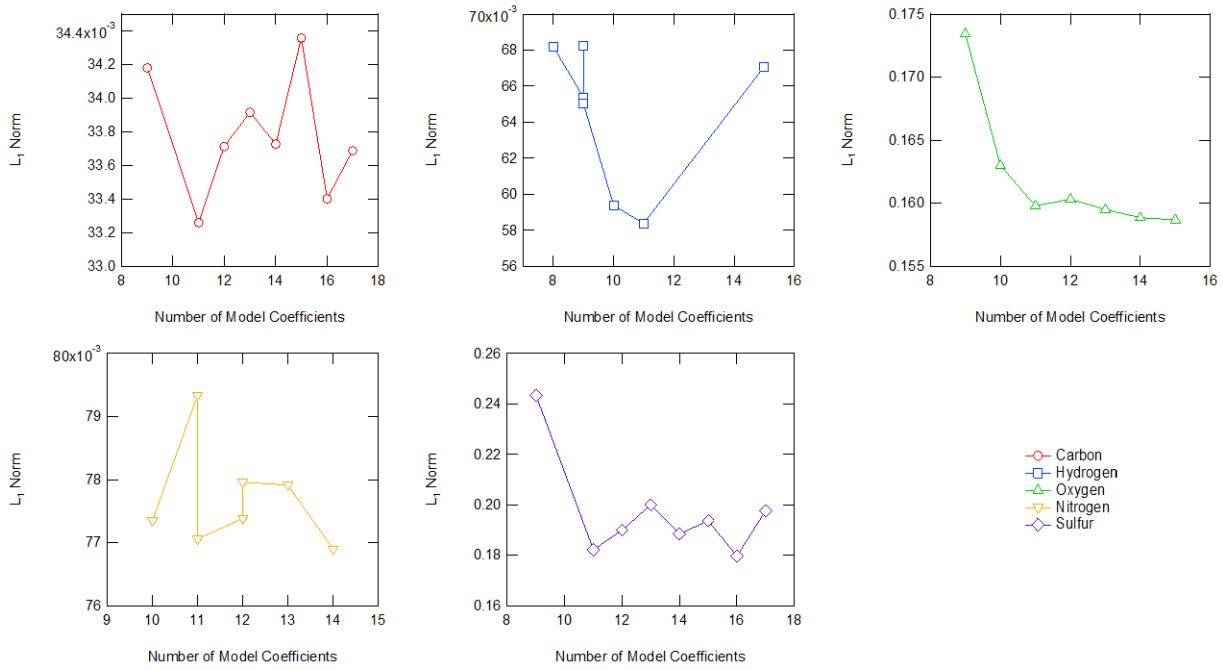

Figure C-18. L_1 norm for each model of each element in the char, post model refinement.

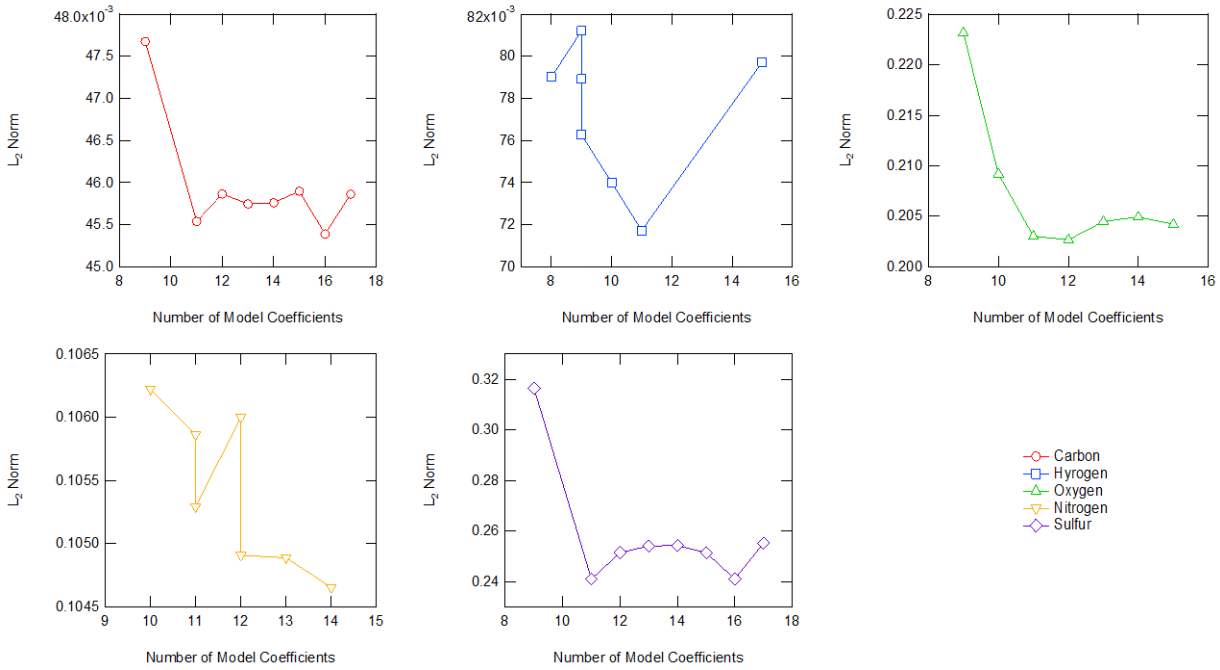

Figure C-19. L_2 norm for each model of each element in the char, post model refinement.

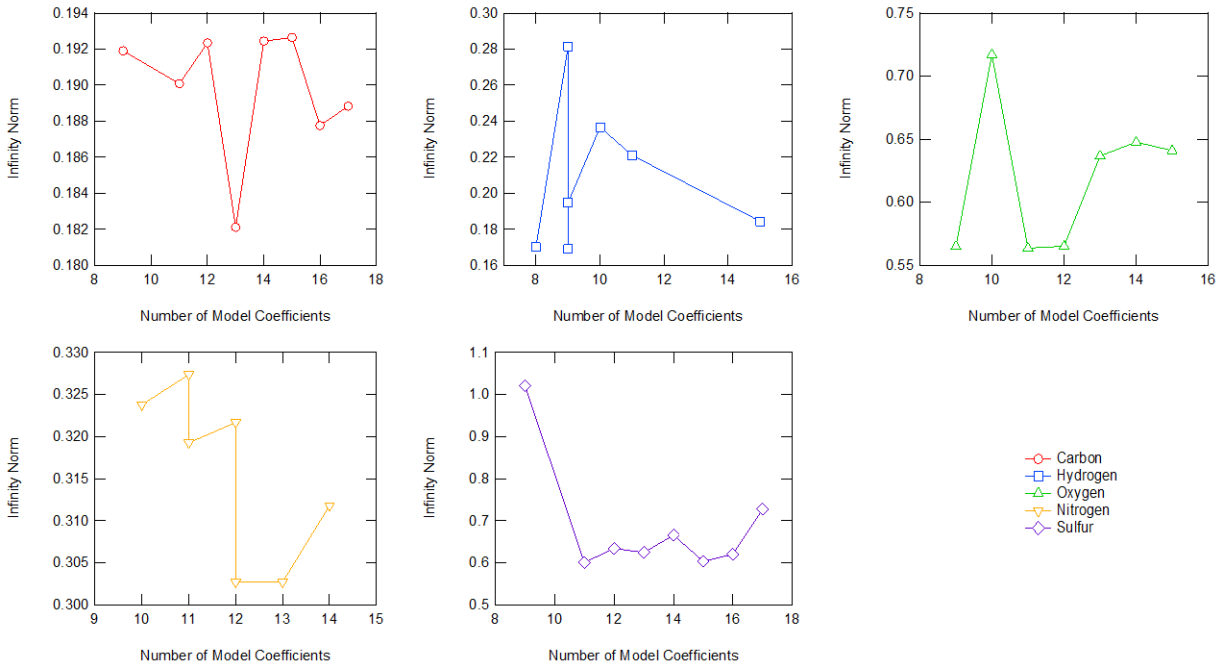

Figure C-20. Infinity norm for each model of each element in the char, post model refinement.

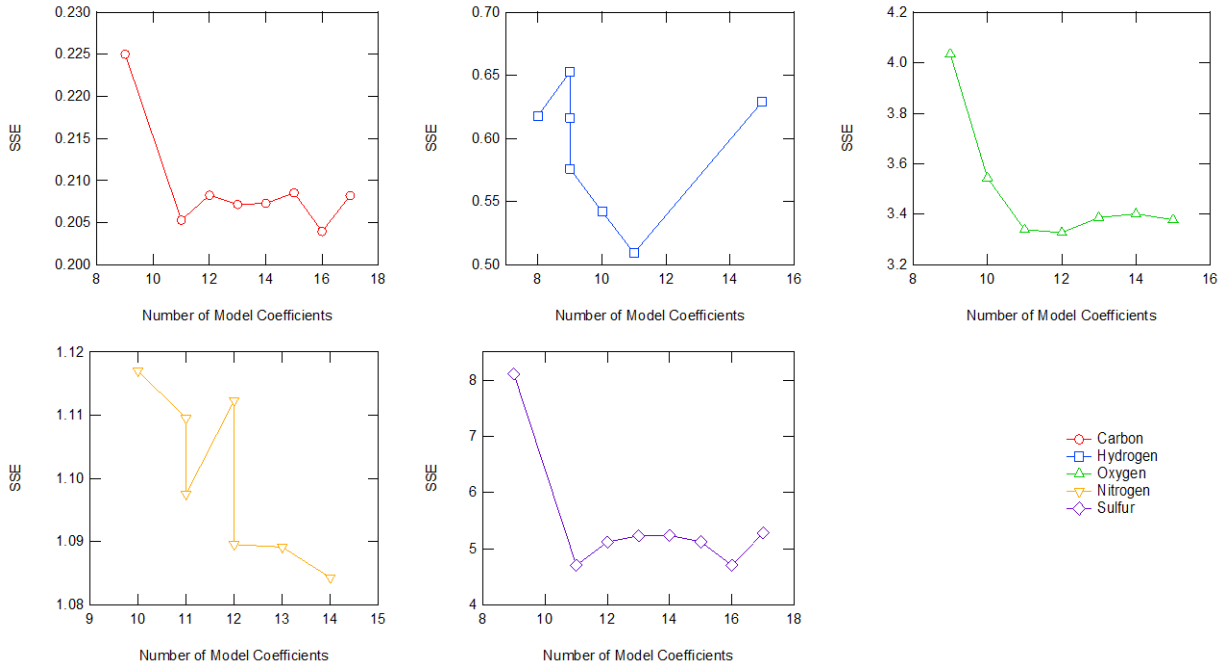

Figure C-21. SSE for each model of each element in the char, post model refinement.

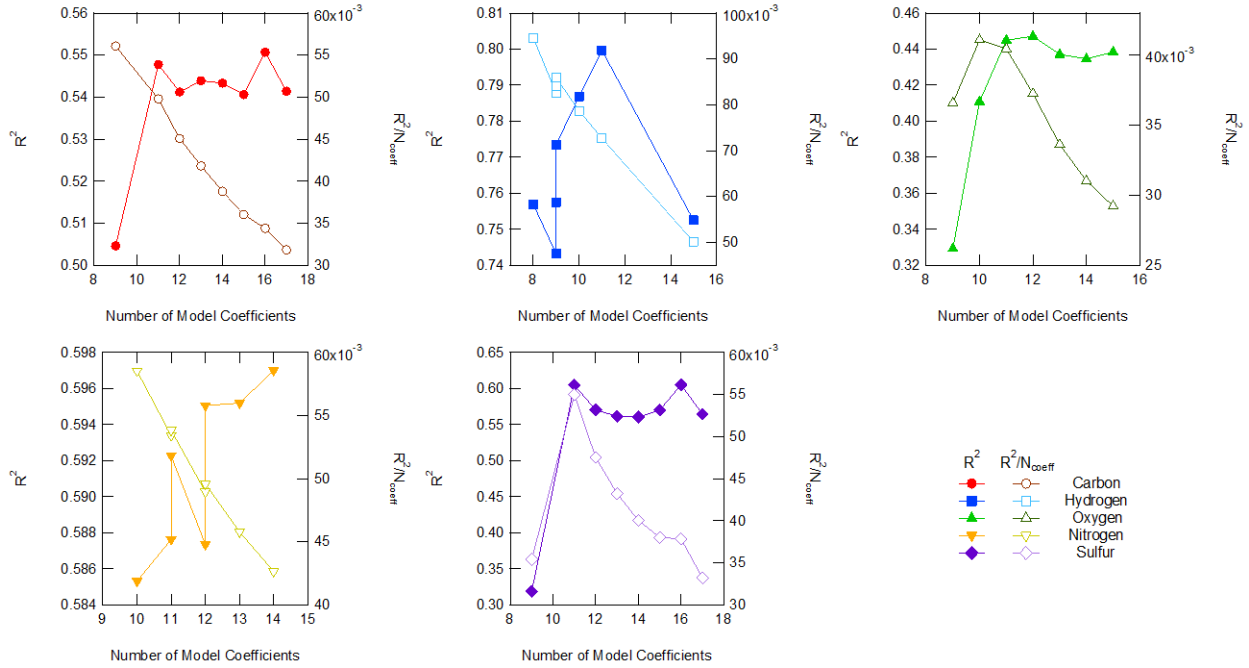

Figure C-22. R^2 for each model of each element in the char, post model refinement.

APPENDIX D. ADDITIONAL HEATING VALUE ANALYSIS

This appendix chapter details additional analysis for the heating value correlation comparison. Most of this appendix chapter comes directly from the supplemental material section of Richards et al. (2021). The complete analysis generated too much data to include in Chapter 7. The experimental data used in this analysis is found in Table B-4. This appendix chapter includes the following information:

- Description of additional statistical measures of fit
- All model forms (including "new" model forms explored and all original coefficients of the literature models)
- The complete results

D.1 Additional Statistical Measures of Fit

Chapter 7 details the primary comparison of literature heating value correlations using primarily the sum of squared errors (SSE), the mean squared error (MSE) and the Akaike Information Criterion (AIC), however, several additional measures of fit were used in the complete analysis to get a larger picture of the different facets of error when comparing all the correlations to the heating value data set. These statistical measures include: (1) The R^2 value (Equation 2-7 (2) the maximum relative error (maximum value from Equation 2-13), which helps to show the maximum "spread" of the model fit, (3) the average relative error (average of

Equation 2-13), which gives an indication of on average how closely the experimental and predicted data points are to each other, (4) the minimum relative error (minimum value from Equation 2-13), (5) the L_1 norm (Equation 2-14), which gives a measure of the average absolute error, (6) the L_2 norm (Equation 2-15), which gives the root-mean-squared error (RMSE), and (7) the infinity norm (Equation 2-16), which shows the maximum absolute error between the experimental and predicted heating values. Minimum relative error is included in this analysis, but the value is not as useful as the other measures. A minimum relative error gives an indication of the accuracy of the most accurate prediction. The R^2 value was not as helpful in this analysis, which is why it was not presented in Chapter 7. Many researchers use R^2 values to show the goodness-of-fit of a model, however, in many situations, R^2 can give a false sense of security, especially when the slopes of the models are high. In addition, R^2 is highly dependent on the number of points used in the comparison, so a high R^2 value does not automatically indicate a good model fit and a low R^2 value does not automatically indicate a bad model fit. An example to illustrate why the R^2 value was not considered as a main metric of goodness of fit is detailed in Table D-1. The values for each statistic are the "best" of all tested literature models (which are discussed at greater length in Chapter 7). Included with each of these "best" models is the AIC_c value (which is also discussed at greater length in Chapter 7). The AIC_c value gives an indication of how likely each model fit is to be the correct fit, with the lowest number being the most likely to be correct (including negative values).

Using the information in Table D-1, the "best" models indicated by the R^2 and minimum relative error statistics can be immediately rejected, since their AIC_c values are much higher than any of the other "best" models. This is the main reason R^2 in particular was dismissed as a reliable measure of goodness of fit. There is potential that an adjusted R^2 value could be more

Table D-1. Usefulness of Statistical Measures of Fit,
Using the Char-Only Data Set

Statistic	**Value**	**Model (Optimizer)**	**AIC_c**
R^2	0.915	Mott-Spooner (fmincon)	364.65
SSE	17.92	Mott-Spooner (fminunc)	-31.80
MSE	0.358	Mott-Spooner (fminunc)	-31.80
Max RE	0.055	Seylor	-35.04
Avg RE	0.013	Mott-Spooner (fminunc)	-31.80
Min RE	1.55e-5	Original Dulong	31.42
L_1 Norm	0.417	Mott-Spooner (fminunc)	-31.80
L_2 Norm	0.599	Mott-Spooner (fminunc)	-31.80
Infinity Norm	1.954	Seylor	-35.04

helpful since it has a correction both for the number of fitted model coefficients as well as the number of data points in the data base used to fit each model, however, an adjusted R^2 value was not used in this analysis. The AIC_c value contains an equivalent adjustment as part of its calculation, and it also gives an additional estimate of the likelihood of each model to be the correct model.

D.2 Model Forms

This analysis used the 10 model forms discussed in Section 2.3.3 and Chapter 7 (with 13 unique sets of suggested model coefficients cited in 13 original articles). These literature models are listed in Table D-2, which includes the original or suggested model coefficients. The sources in which these models are presented are detailed in Table 2-3 and are not repeated here. In addition to the literature models, this analysis also tested a set of "new" model forms to see if a better fit could be obtained. The new model forms are detailed in Table D-3, along with some

preliminary coefficients found from fitting an earlier (and much smaller) coal, char, and tar data set. The optimization used these "original" values (for both the literature and new models) as an initial guess value for the optimizations.

Table D-2. Literature Heating Value Model Forms

Number	Model	Units	Model Form
DM-1[a]	Dulong	kJ/kg	$\Delta H_c = 338.3C + 1443\left(H - \frac{O}{8}\right) + 94.2S$
DM-2	Strache-Lant[b]	kJ/kg	$\Delta H_c = 340.6C + 1432H - 153.2O + 104.7S$
DM-3	Steuer	kJ/kg	$\Delta H_c = 339.1\left(C - \frac{3}{8}O\right) + 238.6\left(\frac{3}{8}O\right) + 1444\left(H - \frac{1}{16}O\right) + 104.7S$
DM-4	D'Huart[b]	kJ/kg	$\Delta H_c = 339.1C + 1433.7H + 93.1S - 127.3O$
DM-5	Seylor	kJ/kg	$\Delta H_c = 519C + 1625H + O^2 - 17870$
DM-6	Gumz[c]	kJ/kg	$\Delta H_c = 340.3C + 1243.2H + 62.8N + 190.9S - 98.4O$
DM-7	Boie[b]	kJ/kg	$\Delta H_c = 351.7C + 1162.6H + 104.7S - 111O$
DM-8	Dulong-Berthelot	kJ/kg	$\Delta H_c = 341.4C + 1444.5H - \frac{1000(N + O - 1)}{8} + 93S$
DM-9	IGT	kJ/kg	$\Delta H_c = 341C + 1323H + 68.5 - 119.4(O + N)$
DM-10	Channiwala-Parikh[c]	kJ/kg	$\Delta H_c = 349.1C + 1178.3H + 100.5S - 103.4O - 15N$
DM-11	VDI	kJ/kg	$\Delta H_c = 339C + 1214\left(H - \frac{O}{8}\right) + 104S + 226H$
DM-12	Mott-Spooner	kJ/kg	$\Delta H_c = 336.5C + 1420H - 145.4O + 94.3S,$ $for\ coals\ with\ O < 15\%$ $\Delta H_c = 336.5C + 1420H - 153.4O + 0.71O^2 + 93.3S,$ $for\ coals\ with\ O > 15\%$
DM-13	Given, et al	kJ/kg	$\Delta H_c = 328.4C + 1422.0H - 138.0O + 92.7S + 636$

[a] The model numbers here are not the same as in the main paper. There are additional models shown here to give the "original" coefficients for each unique model found in literature.
[b] The Strache & Lant, D'Huart, and Boie models were combined in the main article since they have the same mathematical form but different fitted coefficients
[c] The Gumz and Channiwala & Parikh models were similarly combined in the main article

Table D-3. New Heating Value Model Forms

Number	Model	Units	Model Form
DM-14	Linear	Btu/lb	$\Delta H_c = 152.5C + 206.5H - 16.52O + 625.0N - 25.69S + 0.307$
DM-15	Second-Order	Btu/lb	$\Delta H_c = 522.0C - 3.739C^2 + 1.202H + 1.635H^2 - 320.6O + 2.584O^2 + 0.055N + 5.843N^2 - 229.0S - 0.262S^2 + 40.37$
DM-16	Polynomial	Btu/lb	$\Delta H_c = 154.5C + 41.68H^2 + 0.0019O^3 + 14.16N^4 - 0.262S^5 + 2.790$
DM-17	Power	Btu/lb	$\Delta H_c = 50.42C^{1.261} + 36.88H^{1.928} + 61.21O^{0.715} + 2.715N^{6.847} + 1.767S^{2.812} + 1.222$
DM-18	Exponential	Btu/lb	$\Delta H_c = 2658\exp(0.017C) + 2189\exp(0.094H) + 134.0\exp(-32.53O) + 21.23\exp(-57.22N) + 124.1\exp(-42.41S) + 9.719$
DM-19	Log10	Btu/lb	$\Delta H_c = 6626\log_{10} C + 1194\log_{10} H - 2720\log_{10} O + 954.3\log_{10} N - 858.7\log_{10} S + 3088$
DM-20	Natural Log	Btu/lb	$\Delta H_c = 3013\ln C + 2059\ln N$
DM-21	2nd-Order Root	Btu/lb	$\Delta H_c = -632.4C - 6.184C^{\frac{1}{2}} - 656.7H + 119.5H^{\frac{1}{2}} - 807.7O + 13.63O^{\frac{1}{2}} - 54.58N - 6.762N^{\frac{1}{2}} - 826.2S + 10.50S^{\frac{1}{2}} + 78747$
DM-22	Inverse	Btu/lb	$\Delta H_c = -\frac{815.5}{C} - \frac{4886}{H} + \frac{9480}{O} - \frac{210.4}{N} + \frac{71.89}{S} + 13590$
DM-23	Complex #1	Btu/lb	$\Delta H_c = 33.82C + 1.479C^2 + 216.1H + 959.3\ln O - \frac{1502}{N} - 557.8\exp(-1.247S) - 190.4$
DM-24	Complex #2	Btu/lb	$\Delta H_c = -181.4C + 3.123\times10^8C^2 + 869.0H - 76.44H^2 + 1389\ln O + 3226N - 897.5N^2 + 251.9S - 19.72S^2 - 106.1$

These “new” model forms were tested with the hope that they would give a much better fit than the literature model forms. This was not the case, since many did not offer enough improvement over the literature models, and some even performed worse for every data set. This is shown and discussed in the following section.

D.3 Complete Analysis Results

This section details the full results of the heating value analysis, including the statistical measures of fit in Chapter 7 as well as the additional statistical measures of fit described above. The full results of each set of analyses are detailed below. This section details the complete analysis, with all statistical measures of fit and the comparisons using the "new" model forms. The results are presented by the best of each data set, followed by a summary of the analysis using no cross-comparison. In the following sections, the choice of optimizer is listed as either *fminunc* or *fmincon*, depending on which was used to find the re-fit coefficients. If "original coefficients" is listed as the optimizer, this refers to the original coefficients found in Table D-2 and Table D-3, and are the suggested coefficients in the cited literature for the corresponding literature model or the original guess coefficients for the new models.

The following tables show the best performing models for all nine data sets in four categories: i) overall best (including literature and new models with original and re-fit coefficients), ii) best literature models using both re-fit and original coefficients, iii) best new models using both re-fit and original coefficients, and iv) best literature models using original coefficients only. These tables show only the best of the statistical measures of fit for all the studied cases. The full results for all fits and models are shown in figures below. Note that the values for MSE and AIC_c are shown in the main article for the best literature models (including both re-fit and original coefficients). The following sections are in the same order as in Section 7.3.

D.3.1 Parent Coal Only

Table D-4 shows the best fit statistics using the coal-only data set, including the results from Section 7.3.1.

Table D-4. Complete Best Model Calculations
Using the Coal-Only Data Set

	Statistic	Value	Model	Optimizer	AIC_c
Overall Best Performance	R^2	0.656	Second-Order	fmincon	590.5
	SSE $(MJ/kg)^2$	1752	Second-Order	fmincon	590.5
	MSE $(MJ/kg)^2$	4.964	Second-Order	fmincon	590.5
	Max RE (%)	43.32	Natural Log	Original coeff.	868.2
	Avg RE (%)	5.37	Seylor	Original coeff.	648.0
	Min RE (%)	3.78×10^{-4}	Dulong	Original coeff.	683.5
	L_1 (MJ/kg)	1.538	Seylor	Original coeff.	648.0
	L_2 (MJ/kg)	2.228	Second-Order	fmincon	590.5
	Infinity (MJ/kg)	9.645	Complex #2	fminunc	628.3
	AIC_c	590.5	Second-Order	fmincon	590.5
Best New Models	R^2	0.656	Second-Order	fmincon	590.5
	SSE $(MJ/kg)^2$	1752	Second-Order	fmincon	590.5
	MSE $(MJ/kg)^2$	4.964	Second-Order	fmincon	590.5
	Max RE (%)	43.32	Natural Log	Original coeff.	868.2
	Avg RE (%)	5.43	Second-Order	fmincon	590.5
	Min RE (%)	4.07×10^{-4}	Polynomial	fminunc	597.7
	L_1 (MJ/kg)	1.598	Second-Order	fmincon	590.5
	L_2 (MJ/kg)	2.228	Second-Order	fmincon	590.5
	Infinity (MJ/kg)	9.645	Complex #2	fminunc	628.3
	AIC_c	590.5	Second-Order	fmincon	590.5
Best Literature Models	R^2	0.644	Mott-Spooner	fminunc	594.1
	SSE $(MJ/kg)^2$	1813	Mott-Spooner	fmincon	594.1
	MSE $(MJ/kg)^2$	5.137	Mott-Spooner	fmincon	594.1
	Max RE (%)	49.02	Seylor	fmincon	593.7
	Avg RE (%)	5.37	Seylor	Original coeff.	648.0
	Min RE (%)	3.78×10^{-4}	Dulong	Original coeff.	583.5
	L_1 (MJ/kg)	1.538	Seylor	Original coeff.	648.0
	L_2 (MJ/kg)	2.266	Mott-Spooner	fmincon	594.1
	Infinity (MJ/kg)	9.908	Seylor	fmincon	593.7
	AIC_c	591.6	Strache-Lant	fmincon	591.6
Best Literature Models with Original Coefficients	R^2	0.639	D'Huart	Original coeff.	718.1
	SSE $(MJ/kg)^2$	2150	Seylor	Original coeff.	648.0
	MSE $(MJ/kg)^2$	6.091	Seylor	Original coeff.	648.0
	Max RE (%)	50.15	Seylor	Original coeff.	648.0
	Avg RE (%)	5.37	Seylor	Original coeff.	648.0
	Min RE (%)	3.78×10^{-4}	Dulong	Original coeff.	683.5
	L_1 (MJ/kg)	1.538	Seylor	Original coeff.	648.0
	L_2 (MJ/kg)	2.468	Seylor	Original coeff.	648.0
	Infinity (MJ/kg)	10.14	Seylor	Original coeff.	648.0
	AIC_c	648.0	Seylor	Original coeff.	648.0

The new models tended to perform slightly better than the re-fit literature models, but not enough improvement to make a difference statistically, with the potential exception of the second-order model (DM-15). Statistically speaking, the second-order model is very close to both the Mott-Spooner and Boie models (the best models suggested in Section 7.3.1). The conclusions and recommendations in Section 7.3.1 stand, however, using one of the best new models (the second-order model does the best for most statistical measures of fit) will likely give a slightly more accurate calculation for coal heating values. Figure D-1 to Figure D-10 show each of these statistical measures (in the same order as Table D-4) in the coal-only data set for the models using original coefficients and coefficients re-fit using *fmincon* and *fminunc*. In all these figures, a purple square indicates a better fit, according to each statistical measure, whereas a red square indicates a poor fit.

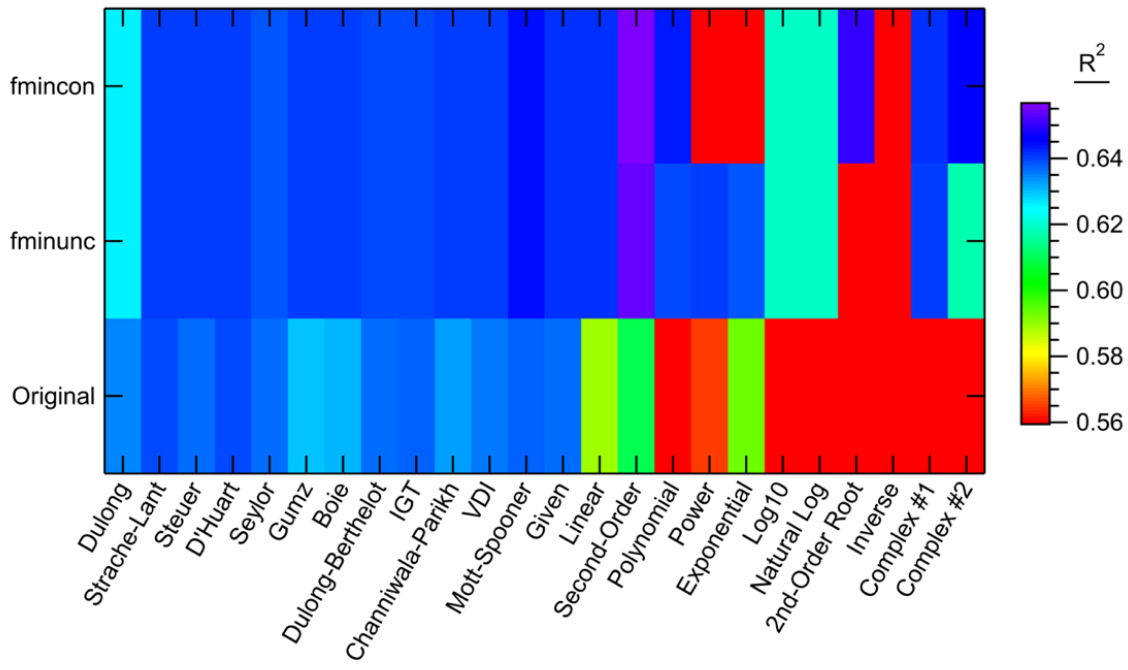

Figure D-1. R^2 values in the coal-only comparison for each model form.

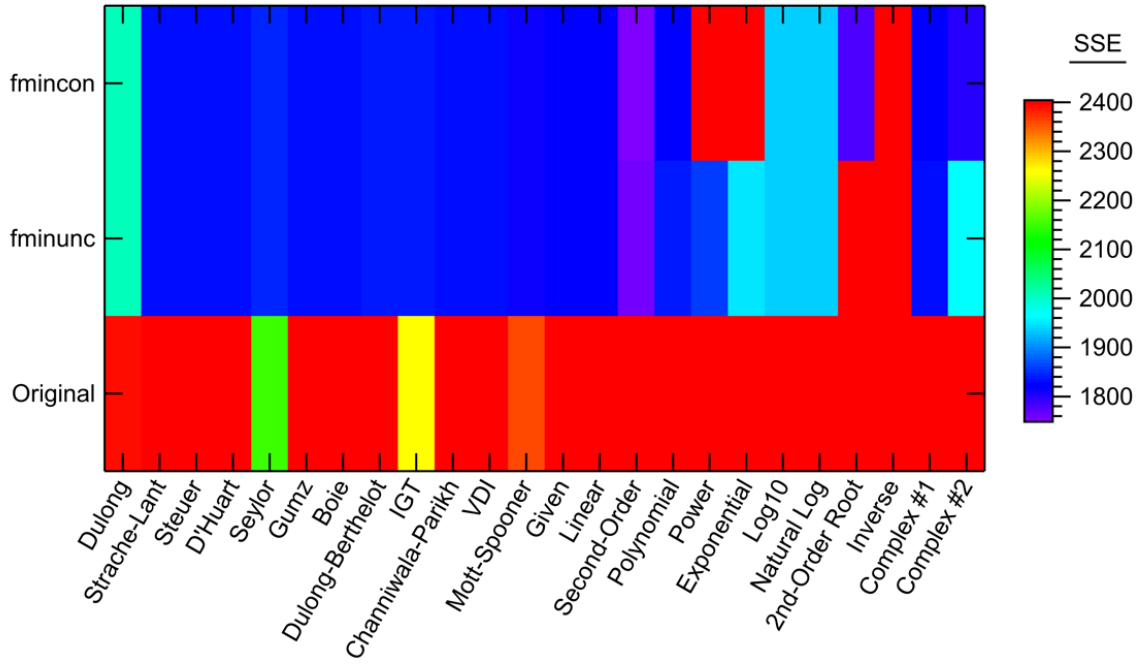

Figure D-2. SSE values in the coal-only comparison for each model form.

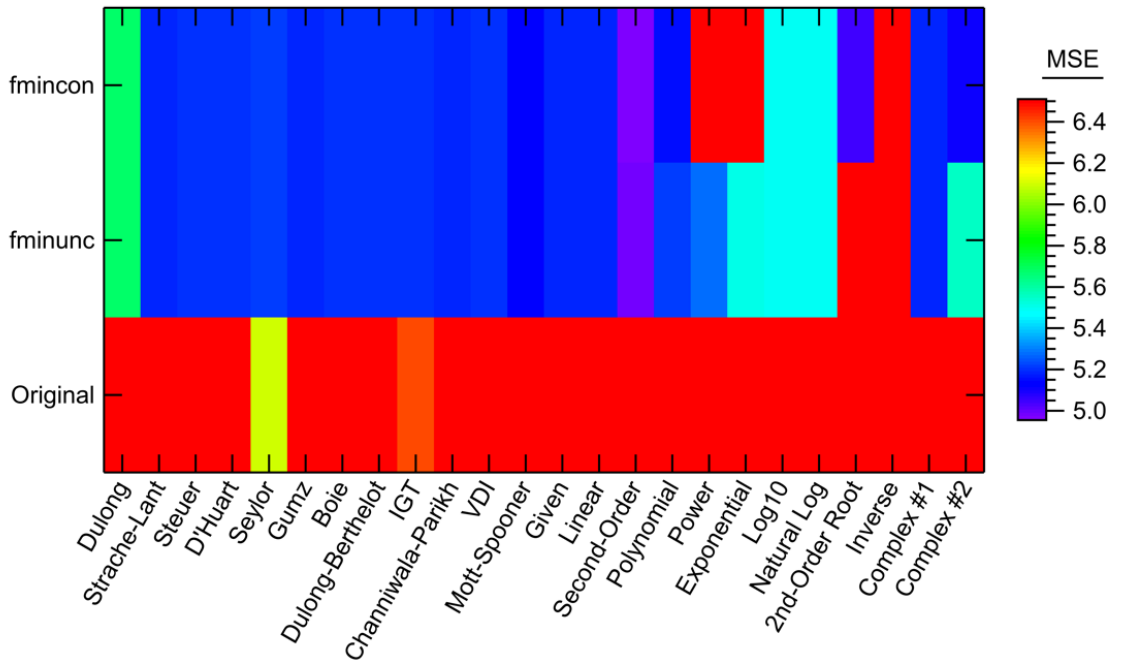

Figure D-3. MSE values in the coal-only comparison for each model form.

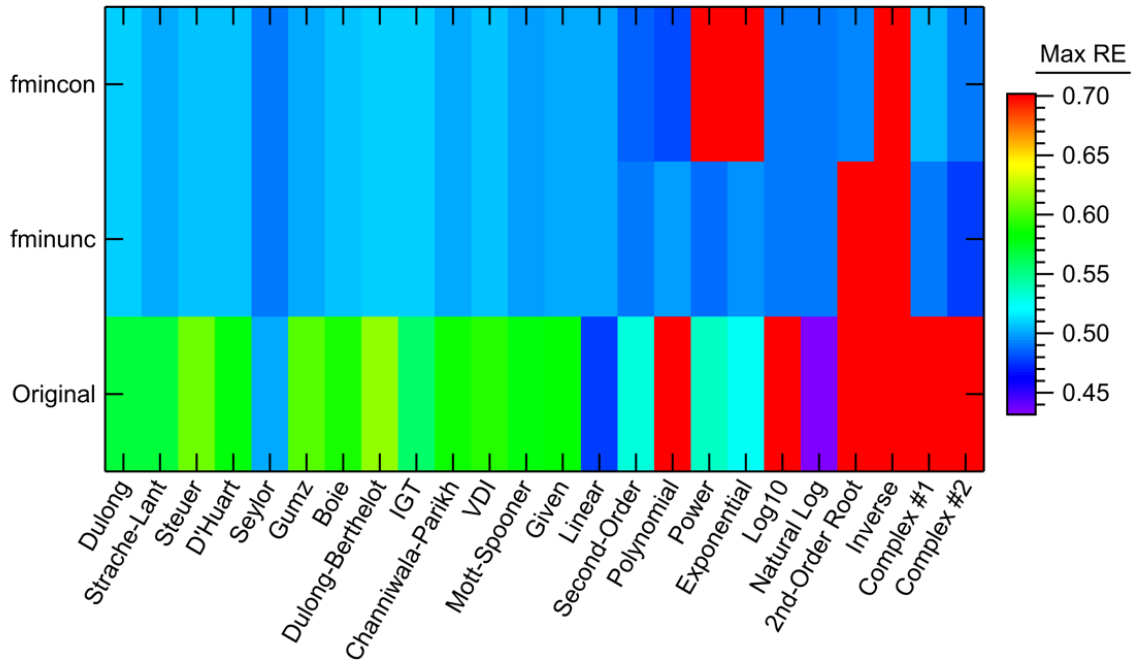

Figure D-4. Maximum relative error values in the coal-only comparison for each model form.

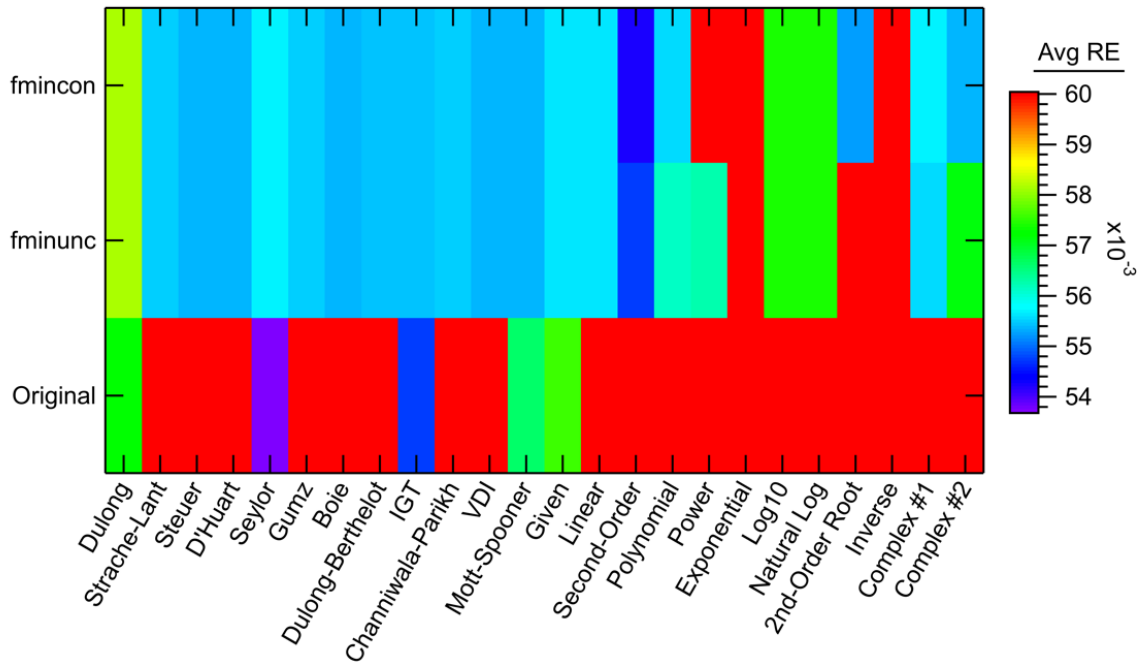

Figure D-5. Average relative error values in the coal-only comparison for each model form.

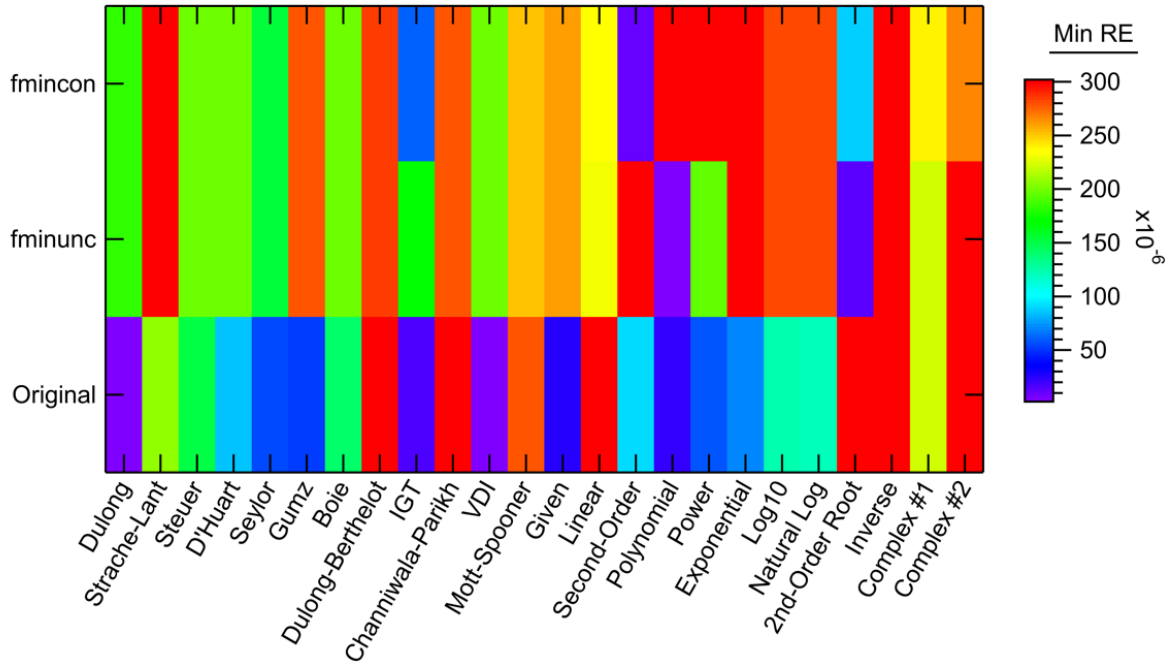

Figure D-6. Minimum relative error values in the coal-only comparison for each model form.

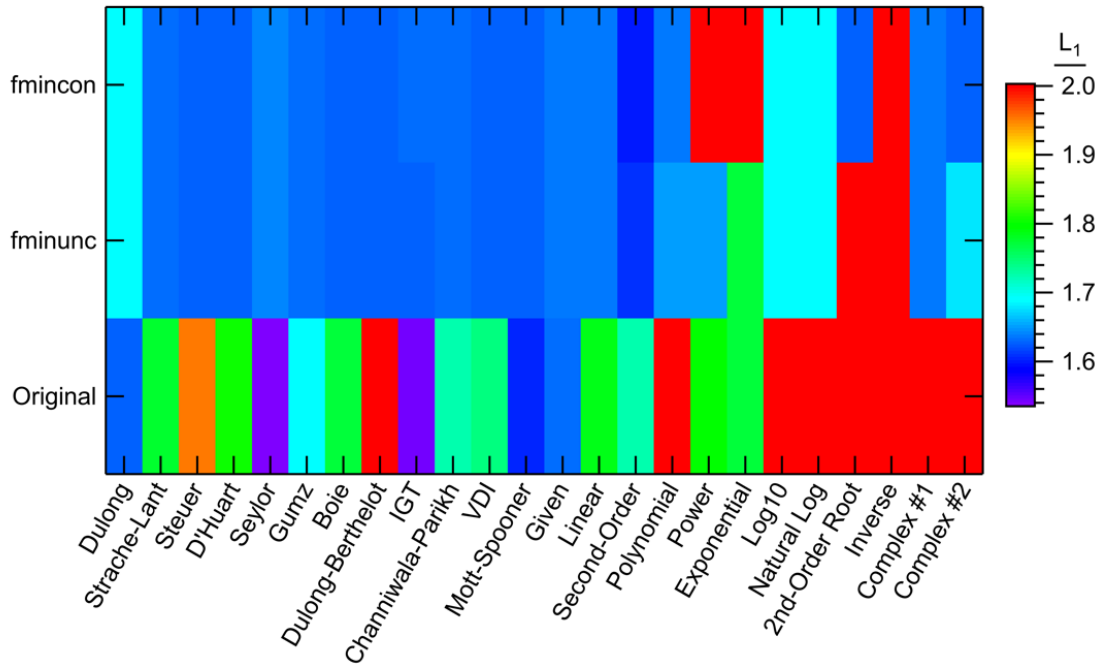

Figure D-7. L_1 norm values in the coal-only comparison for each model form.

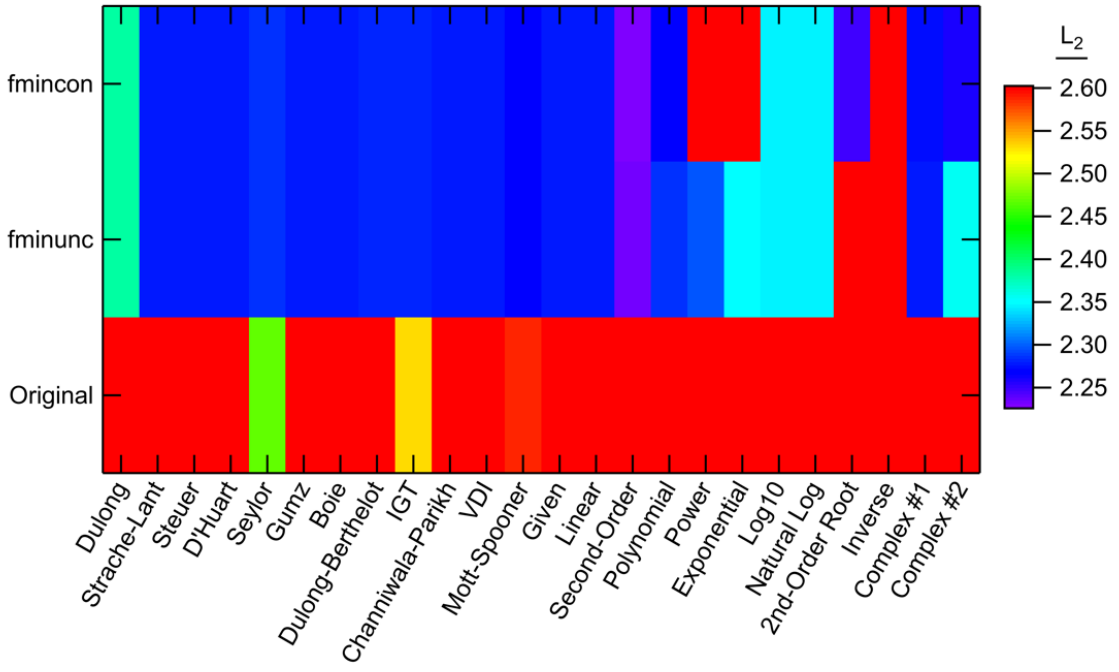

Figure D-8. L_2 norm values in the coal-only comparison for each model form.

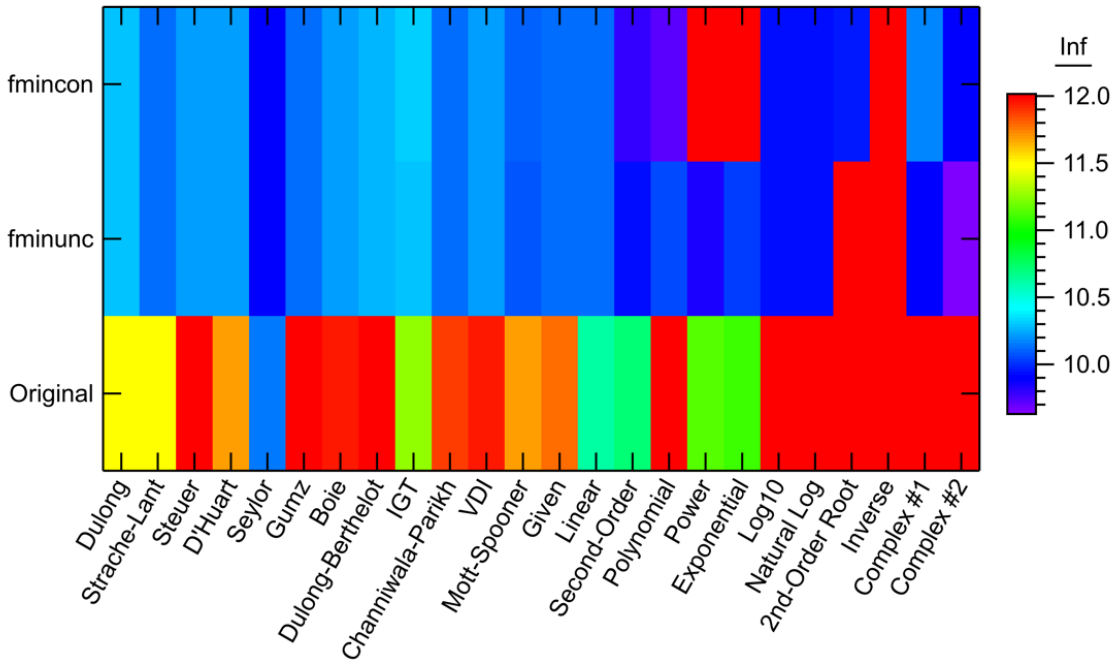

Figure D-9. Infinity norm values in the coal-only comparison for each model form.

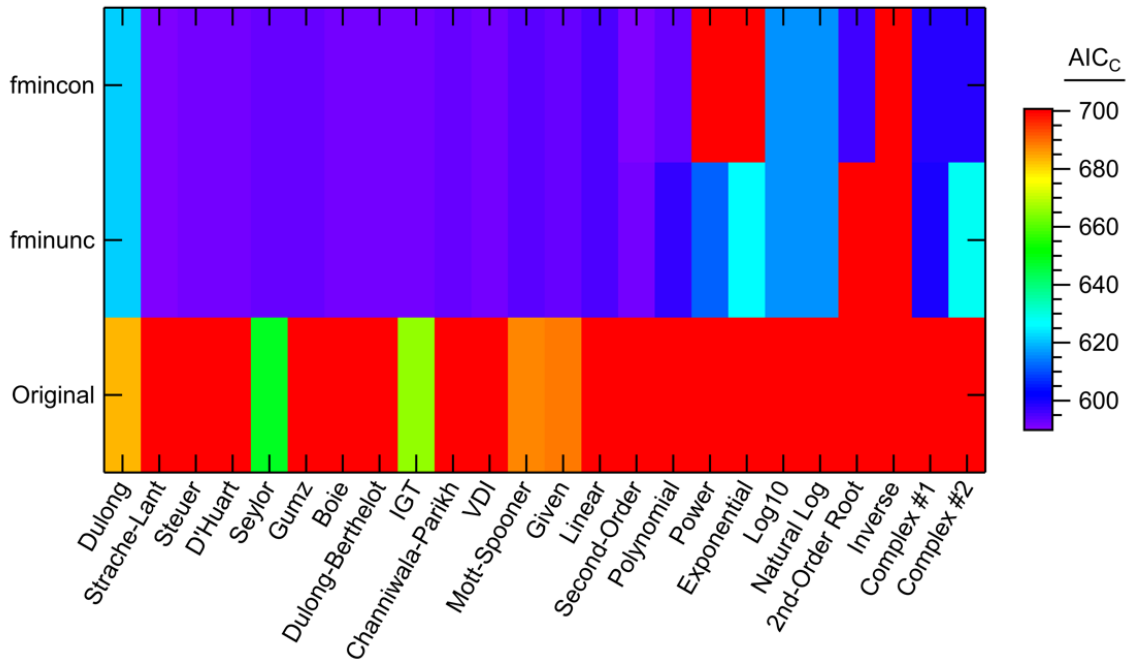

Figure D-10. AIC_c values in the coal-only comparison for each model form.

D.3.2 Coal Char Only

Table D-5 shows the complete results for the char-only data set analysis. There is some improvement in the "new" models compared to the literature models, however, it was pointed out in Section 7.3.1 that a visual inspection proves that the best fits of the literature models are very good, almost to the point of complete parity. This means that the improvement shown with the "new" models may make the heating value calculations for char more accurate, but it is hard to improve on excellent fits in the first place. Figure D-11 to Figure D-20 show plots of all statistical results for the char-only comparison.

Table D-5. Complete Best Model Calculations Using the Char-Only Data Set

	Statistic	Value	Model	Optimizer	AIC_c
Overall Best Performance	R^2	0.940	Second-Order	fmincon	-36.09
	SSE $(MJ/kg)^2$	12.70	Second-Order	fmincon	-36.09
	MSE $(MJ/kg)^2$	0.254	Second-Order	fmincon	-36.09
	Max RE (%)	4.76	Second-Order	fminunc	-28.59
	Avg RE (%)	1.07	Second-Order	fmincon	-36.09
	Min RE (%)	8.56×10^{-5}	Complex #1	fminunc	-23.70
	L_1 (MJ/kg)	0.337	Second-Order	fmincon	-36.09
	L_2 (MJ/kg)	0.504	Second-Order	fmincon	-36.09
	Infinity (MJ/kg)	1.573	2nd-Order Root	fmincon	-28.51
	AIC_c	-45.98	Complex #1	fmincon	-45.98
Best New Models	R^2	0.940	Second-Order	fmincon	-36.09
	SSE $(MJ/kg)^2$	12.70	Second-Order	fmincon	-36.09
	MSE $(MJ/kg)^2$	0.254	Second-Order	fmincon	-36.09
	Max RE (%)	4.76	Second-Order	fminunc	-28.59
	Avg RE (%)	1.07	Second-Order	fmincon	-36.09
	Min RE (%)	8.56×10^{-5}	Complex #1	fminunc	-23.70
	L_1 (MJ/kg)	0.337	Second-Order	fmincon	-36.09
	L_2 (MJ/kg)	0.504	Second-Order	fmincon	-36.09
	Infinity (MJ/kg)	1.573	2nd-Order Root	fmincon	-28.51
	AIC_c	-45.98	Complex #1	fmincon	-45.98
Best Literature Models	R^2	0.915	Mott-Spooner	fminunc	-31.80
	SSE $(MJ/kg)^2$	17.92	Mott-Spooner	fmincon	-31.80
	MSE $(MJ/kg)^2$	0.358	Mott-Spooner	fmincon	-31.80
	Max RE (%)	5.52	Seylor	fminunc	-35.04
	Avg RE (%)	1.33	Mott-Spooner	fminunc	-31.80
	Min RE (%)	1.55×10^{-3}	Dulong	Original coeff.	31.42
	L_1 (MJ/kg)	0.417	Mott-Spooner	fminunc	-31.80
	L_2 (MJ/kg)	0.599	Mott-Spooner	fmincon	-31.80
	Infinity (MJ/kg)	1.954	Seylor	fminunc	-35.04
	AIC_c	-35.42	Seylor	fmincon	-35.42
Best Literature Models with Original Coefficients	R^2	0.892	D'Huart	Original coeff.	29.95
	SSE $(MJ/kg)^2$	54.10	Seylor	Original coeff.	15.30
	MSE $(MJ/kg)^2$	1.082	Seylor	Original coeff.	15.30
	Max RE (%)	8.13	IGT	Original coeff.	16.48
	Avg RE (%)	2.12	Seylor	Original coeff.	15.30
	Min RE (%)	1.55×10^{-3}	Dulong	Original coeff.	31.42
	L_1 (MJ/kg)	0.625	Seylor	Original coeff.	15.30
	L_2 (MJ/kg)	1.040	Seylor	Original coeff.	15.30
	Infinity (MJ/kg)	2.415	IGT	Original coeff.	16.48
	AIC_c	15.30	Seylor	Original coeff.	15.30

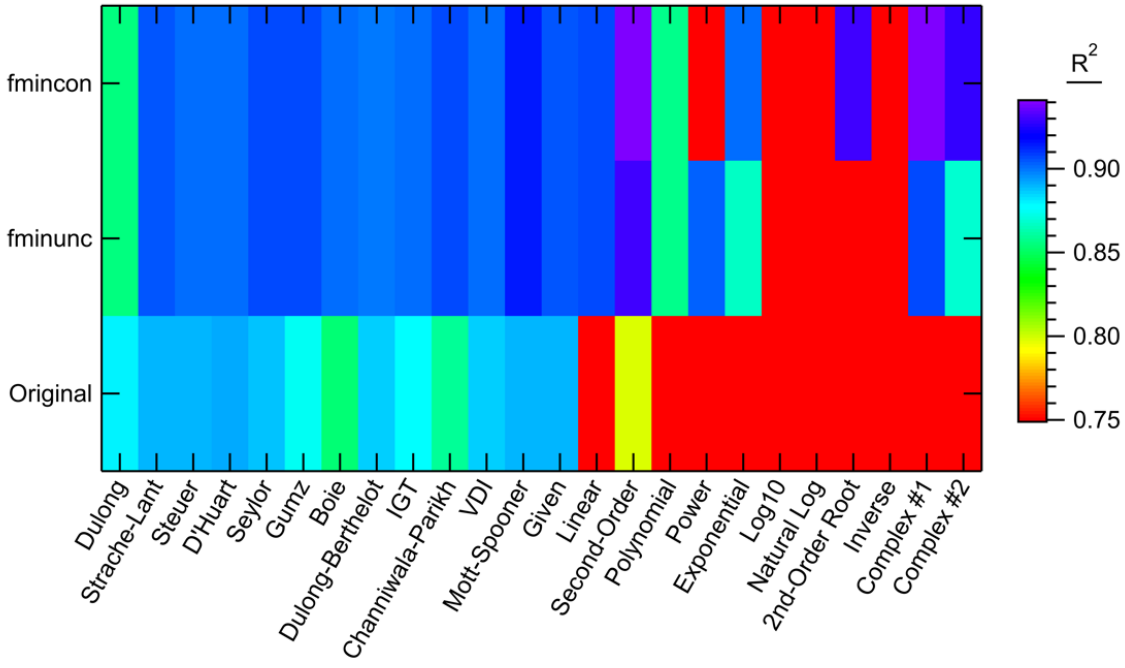

Figure D-11. R^2 values in the char-only comparison for each model form.

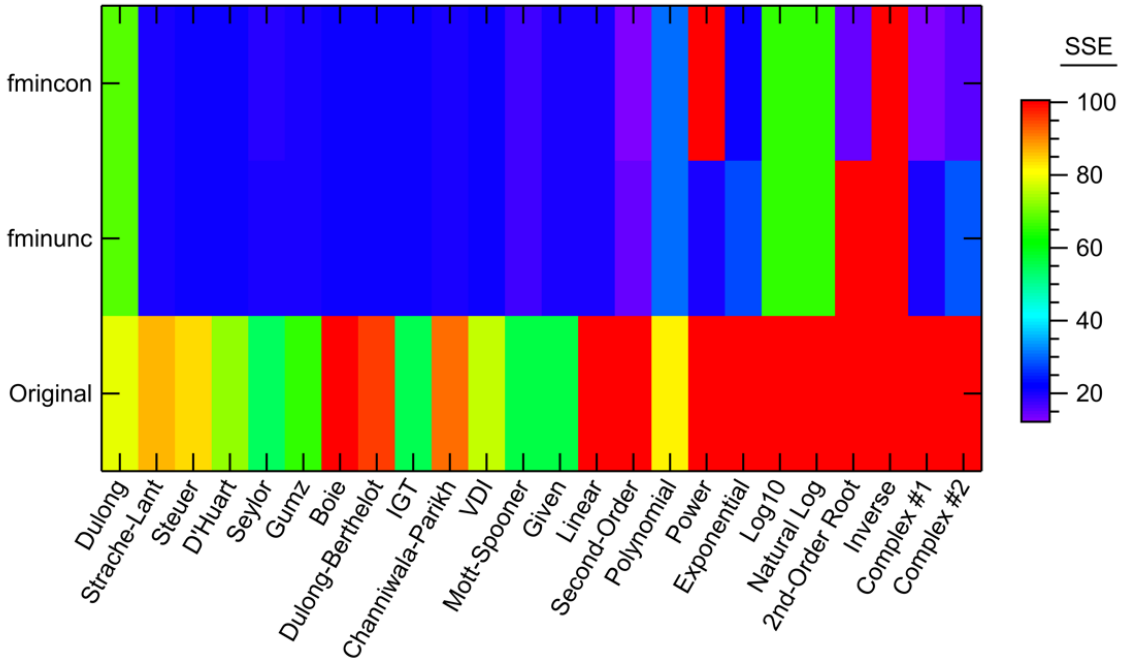

Figure D-12. SSE values in the char-only comparison for each model form.

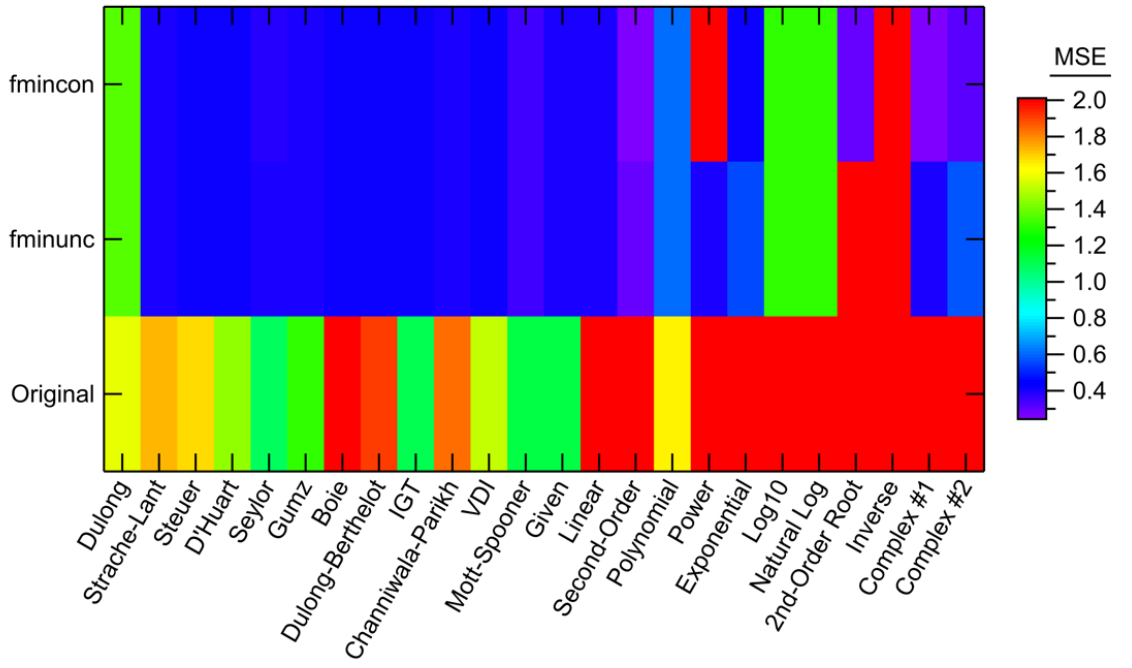

Figure D-13. MSE values in the char-only comparison for each model form.

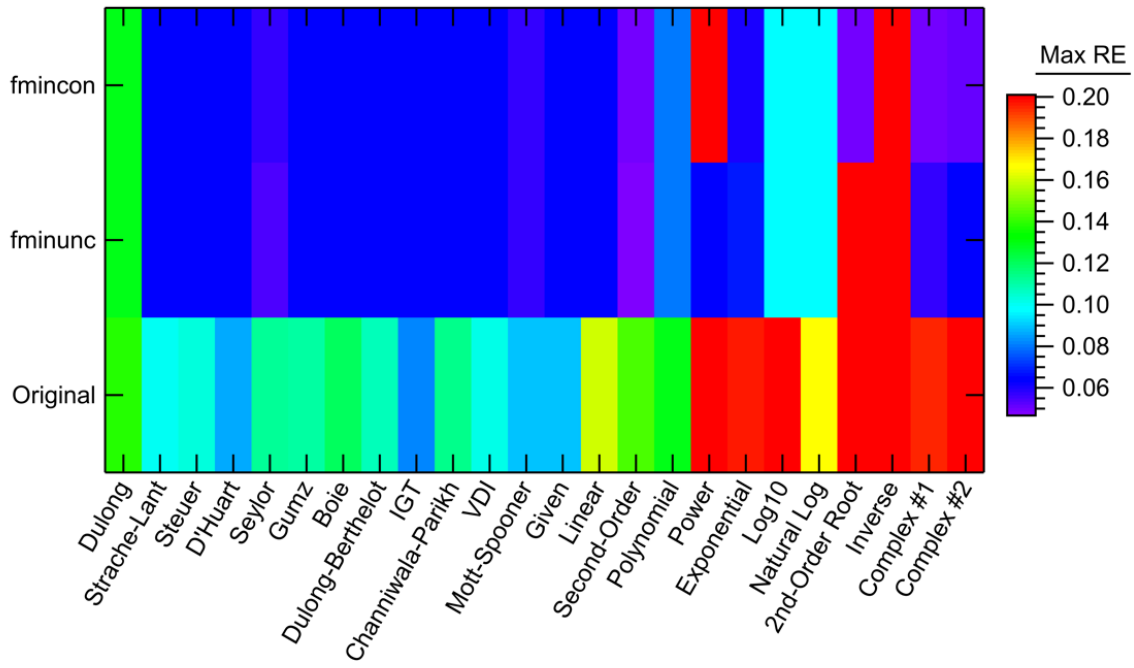

Figure D-14. Maximum relative error values in the char-only comparison for each model form.

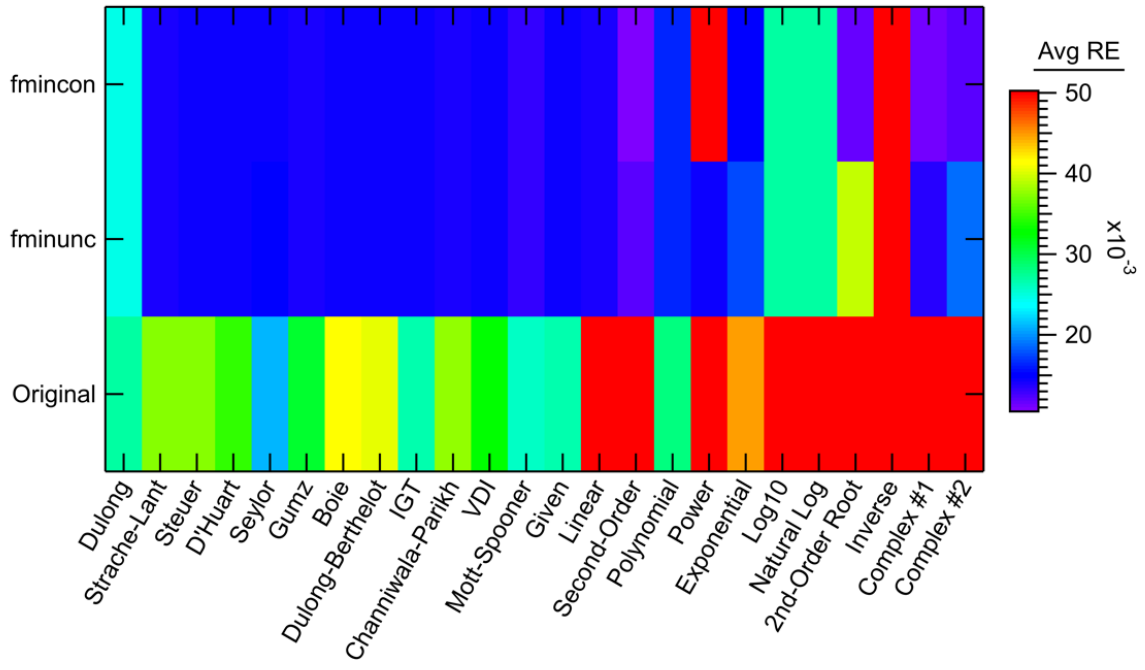

Figure D-15. Average relative error values in the char-only comparison for each model form.

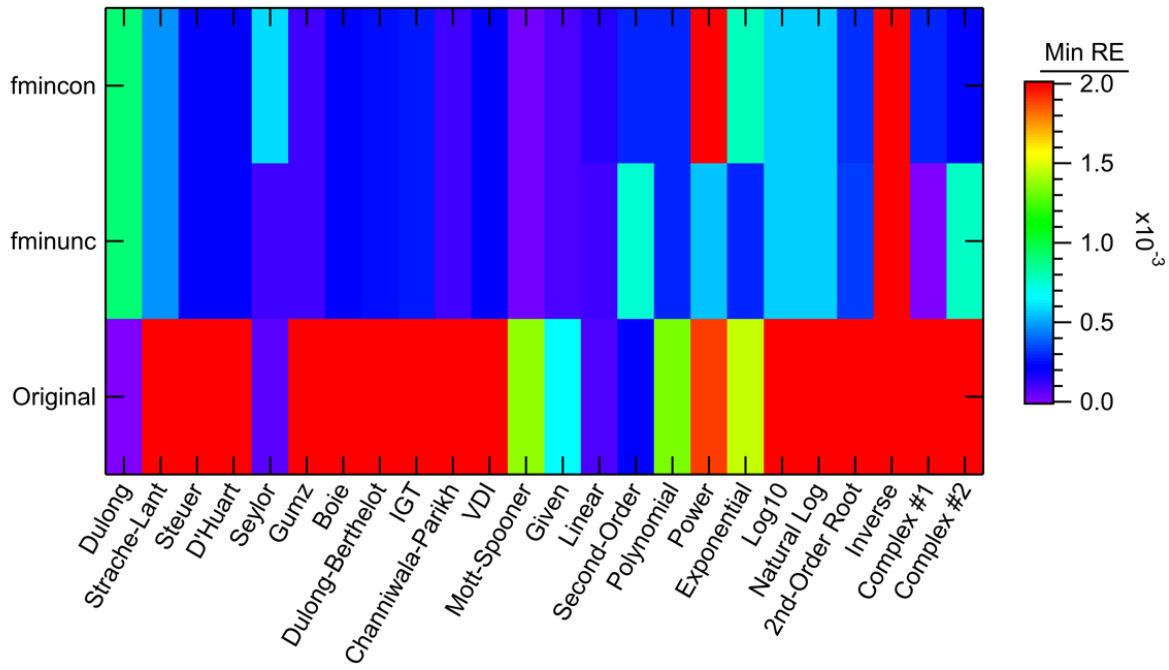

Figure D-16. Minimum relative error values in the char-only comparison for each model form.

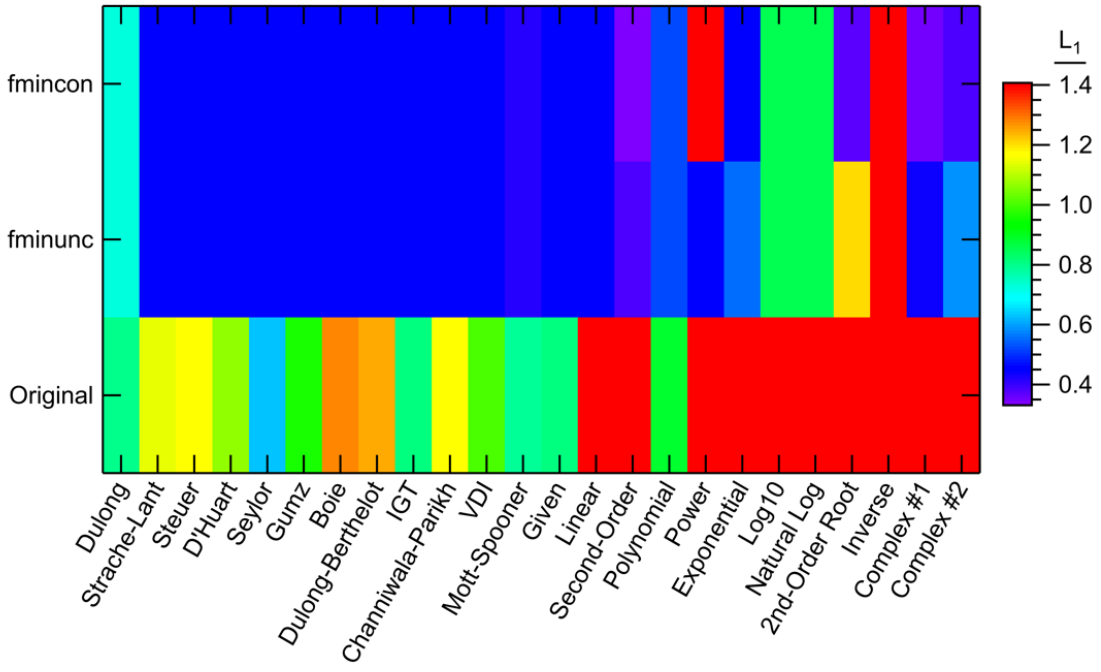

Figure D-17. L_1 norm values in the char-only comparison for each model form.

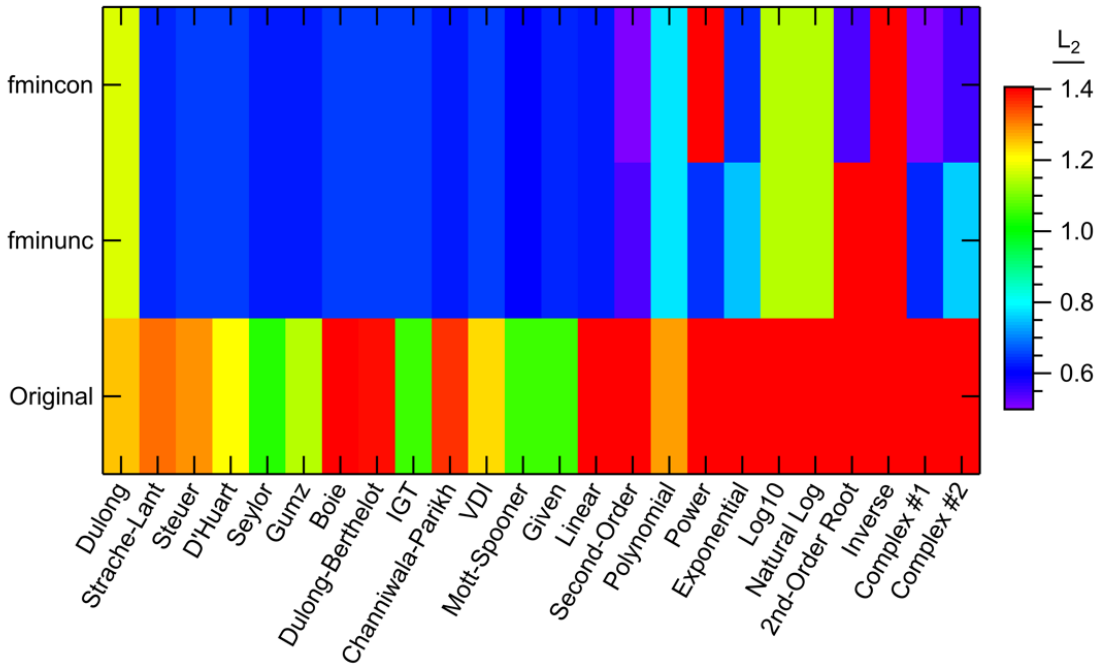

Figure D-18. L_2 norm values in the char-only comparison for each model form.

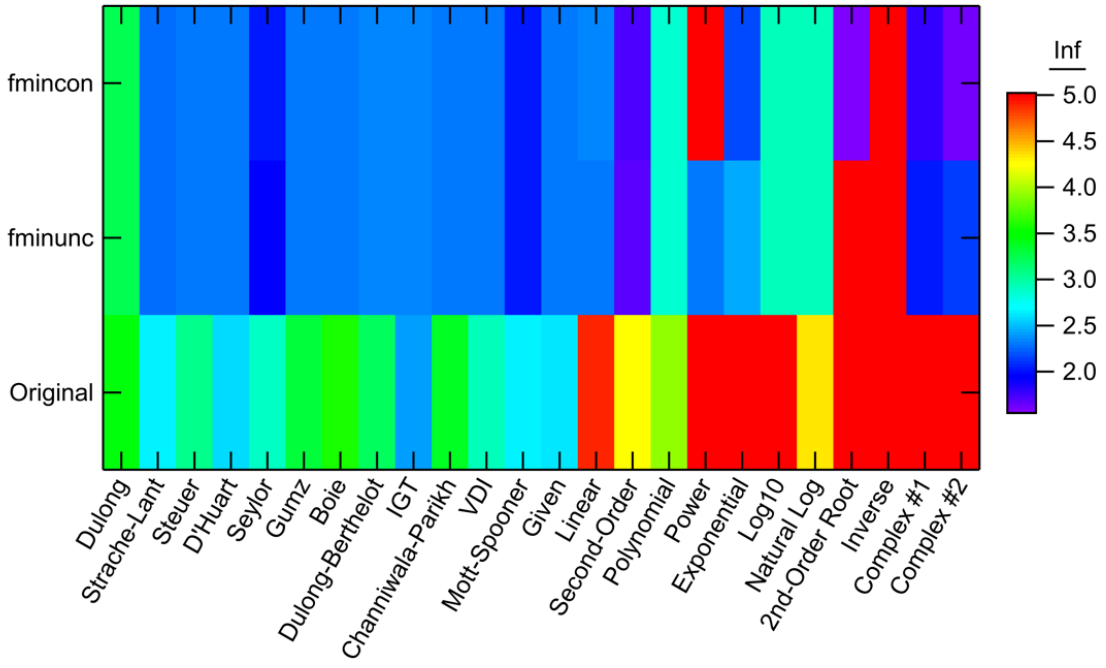

Figure D-19. Infinity norm values in the char-only comparison for each model form.

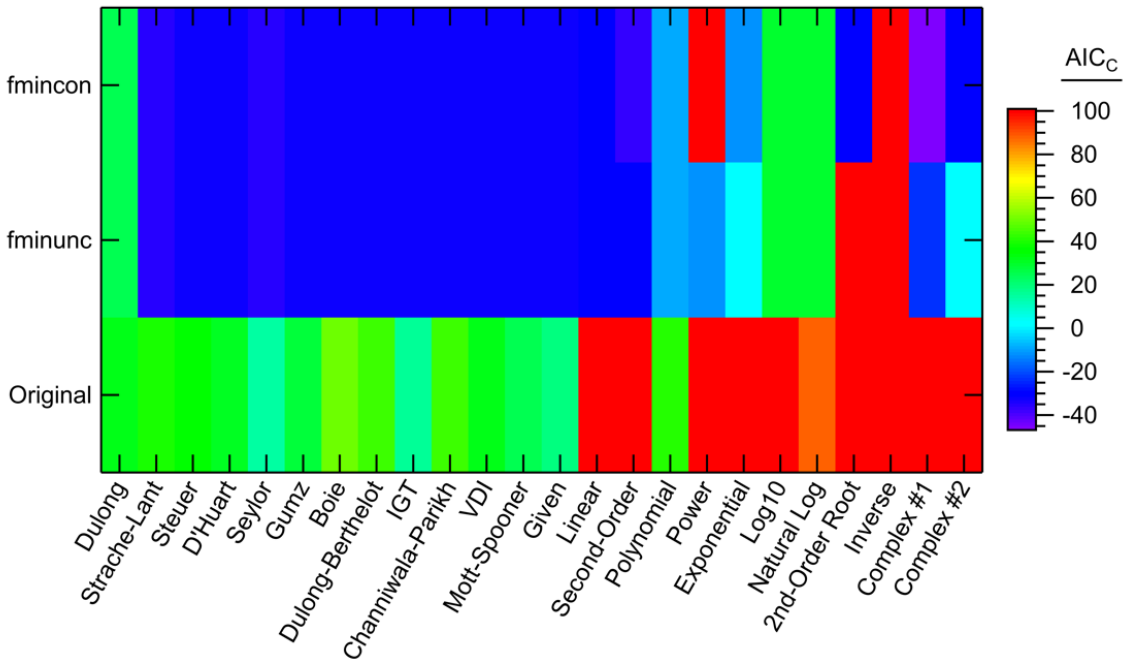

Figure D-20. AIC_c values in the char-only comparison for each model form.

D.3.3 Parent Coal and Coal Char Combined

Table D-6 shows the best measures of fit using the combined coal-char data set. Like the coal- and char-only data sets, the coal-char data set did show some slight improvement using the "new" models, but not enough improvement to justify using so many additional fitted coefficients. Figure D-21 to Figure D-30 show plots of the complete statistical results for the combined coal-char data set analysis.

Table D-6. Complete Best Model Calculations Using the Coal-Char Data Set

	Statistic	**Value**	**Model**	**Optimizer**	**AIC_c**
Overall Best Performance	R^2	0.676	Second-Order	fmincon	599.8
	SSE $(MJ/kg)^2$	1679	Second-Order	fmincon	599.8
	MSE $(MJ/kg)^2$	4.165	Second-Order	fmincon	599.8
	Max RE (%)	43.32	Natural Log	Original coeff.	930.9
	Avg RE (%)	4.75	Second-Order	fmincon	599.8
	Min RE (%)	3.78×10^{-4}	Dulong	Original coeff.	710.5
	L_1 (MJ/kg)	1.376	Seylor	Original coeff.	664.8
	L_2 (MJ/kg)	2.041	Second-Order	fmincon	599.8
	Infinity (MJ/kg)	9.391	Complex #2	fminunc	626.7
	AIC_c	599.8	Second-Order	fmincon	599.8
Best New Models	R^2	0.676	Second-Order	fmincon	599.8
	SSE $(MJ/kg)^2$	1679	Second-Order	fmincon	599.8
	MSE $(MJ/kg)^2$	4.165	Second-Order	fmincon	599.8
	Max RE (%)	43.32	Natural Log	Original coeff.	930.9
	Avg RE (%)	4.75	Second-Order	fmincon	599.8
	Min RE (%)	4.60×10^{-4}	Exponential	fminunc	643.4
	L_1 (MJ/kg)	1.407	Second-Order	fmincon	599.8
	L_2 (MJ/kg)	2.041	Second-Order	fmincon	599.8
	Infinity (MJ/kg)	9.391	Complex #2	fminunc	626.7
	AIC_c	599.8	Second-Order	fmincon	599.8
Best Literature Models	R^2	0.664	Mott-Spooner	fmincon	606.1
	SSE $(MJ/kg)^2$	1741	Mott-Spooner	fmincon	606.1
	MSE $(MJ/kg)^2$	4.321	Mott-Spooner	fmincon	606.1
	Max RE (%)	49.37	Channiwala-Parikh	fminunc	602.2
	Avg RE (%)	4.76	Seylor	Original coeff.	664.8
	Min RE (%)	3.78×10^{-4}	Dulong	Original coeff.	710.5
	L_1 (MJ/kg)	1.376	Seylor	Original coeff.	664.8
	L_2 (MJ/kg)	2.079	Mott-Spooner	fmincon	606.1
	Infinity (MJ/kg)	9.979	Channiwala-Parikh	fminunc	602.2
	AIC_c	600.3	Strache-Lant	fmincon	600.3

Table D-6. Complete Best Model Calculations Using the Coal-Char Data Set, CONTINUED

	Statistic	Value	Model	Optimizer	AIC_c
Best Literature Models with Original Coefficients	R^2	0.660	Strache-Lant	Original coeff.	745.9
	SSE $(MJ/kg)^2$	2046	Seylor	Original coeff.	664.8
	MSE $(MJ/kg)^2$	5.076	Seylor	Original coeff.	664.8
	Max RE (%)	50.15	Seylor	Original coeff.	664.8
	Avg RE (%)	4.76	Seylor	Original coeff.	664.8
	Min RE (%)	3.78×10^{-4}	Dulong	Original coeff.	710.5
	L_1 (MJ/kg)	1.376	Seylor	Original coeff.	664.8
	L_2 (MJ/kg)	2.253	Seylor	Original coeff.	664.8
	Infinity (MJ/kg)	10.14	Seylor	Original coeff.	664.8
	AIC_c	664.8	Seylor	Original coeff.	664.8

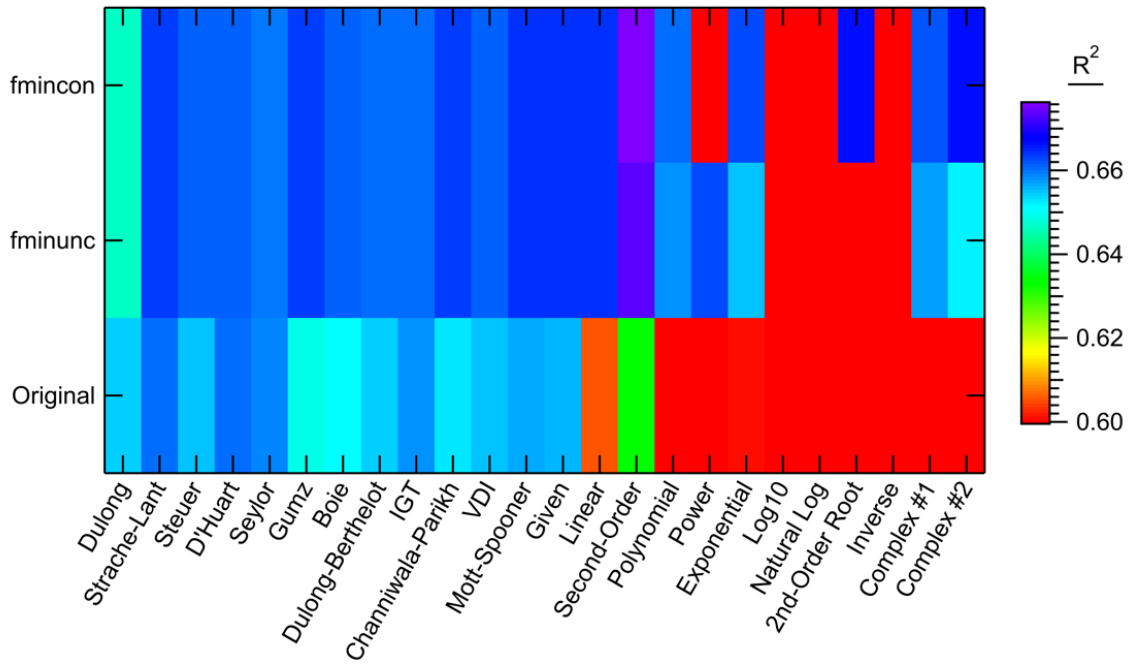

Figure D-21. R^2 values in the combined coal-char comparison for each model form.

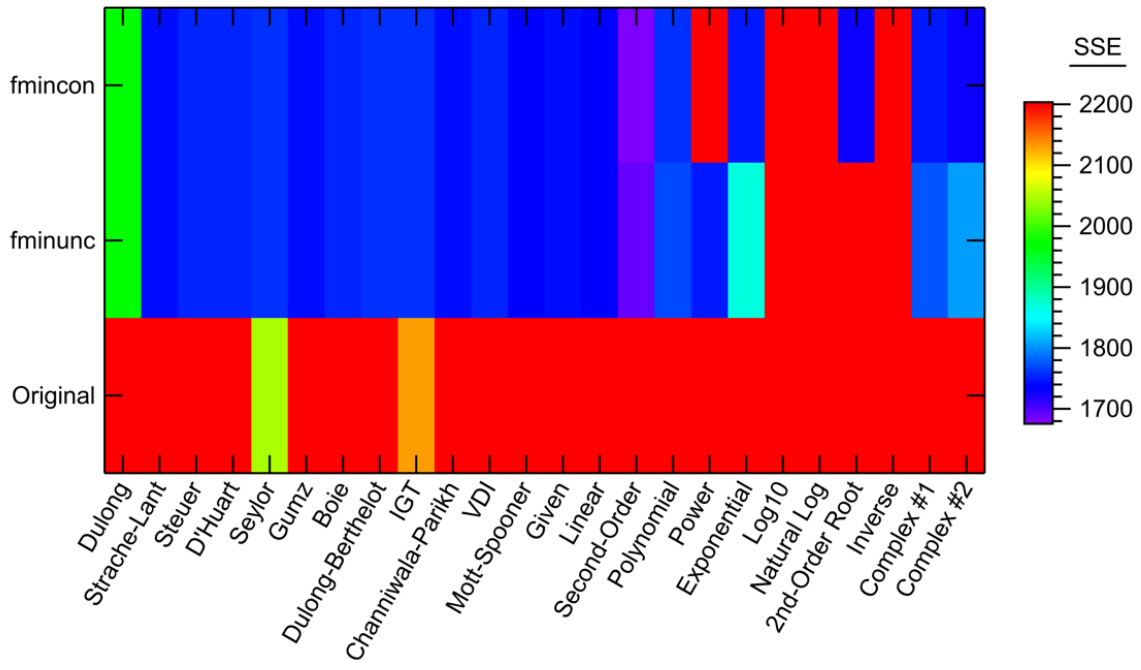

Figure D-22. SSE values in the combined coal-char comparison for each model form.

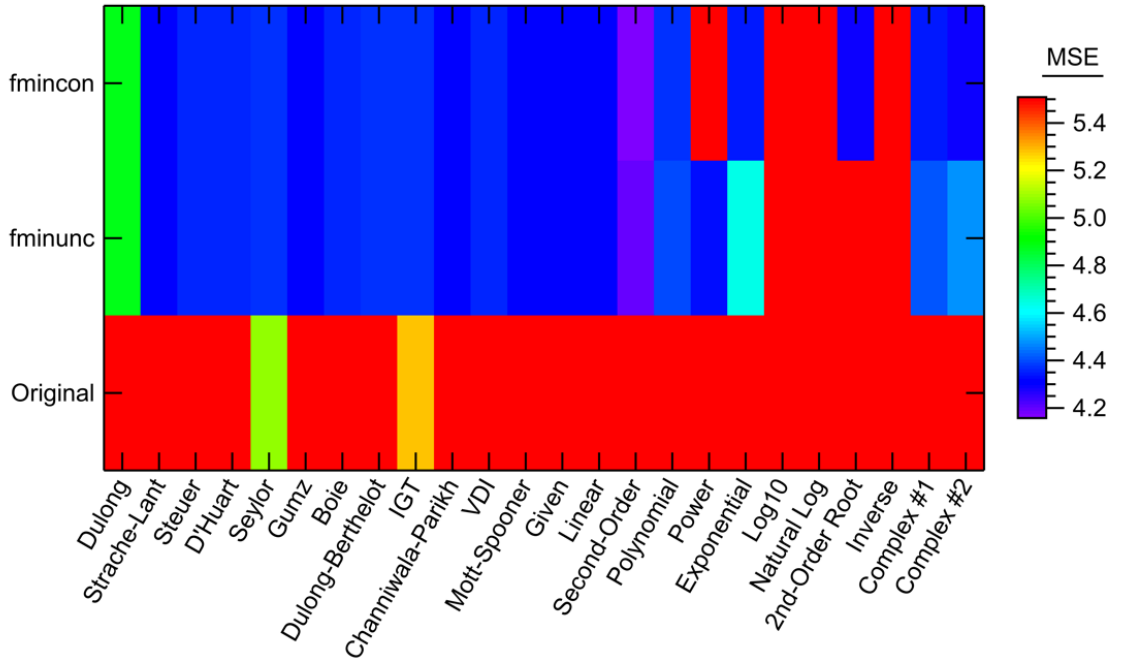

Figure D-23. MSE values in the combined coal-char comparison for each model form.

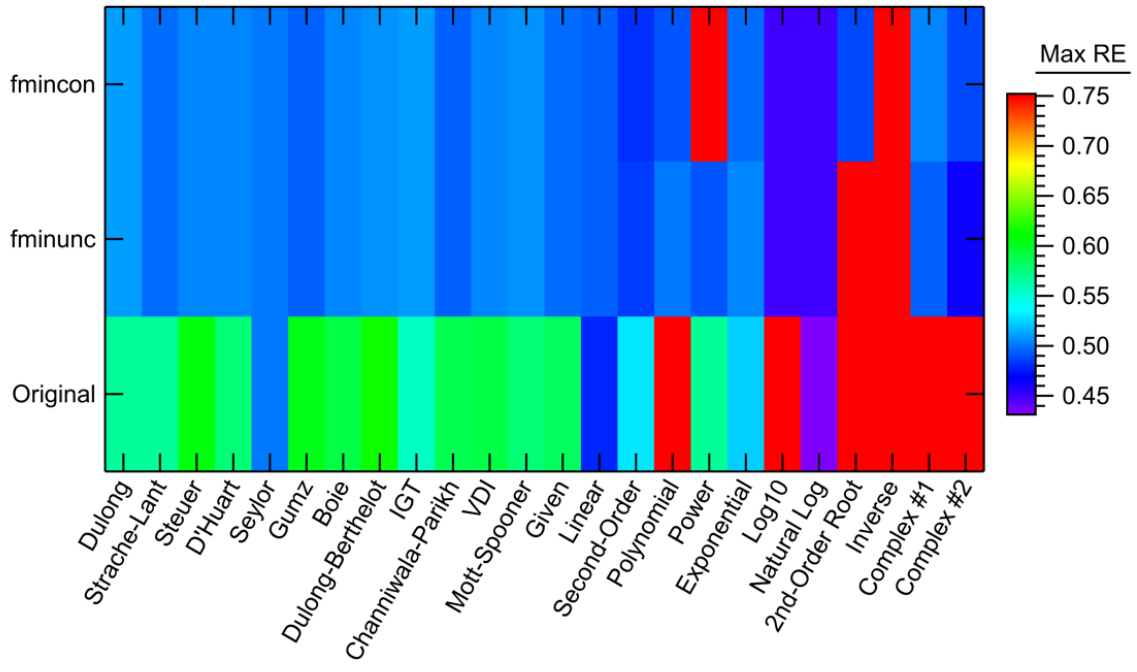

Figure D-24. Maximum relative error values in the combined coal-char comparison for each model form.

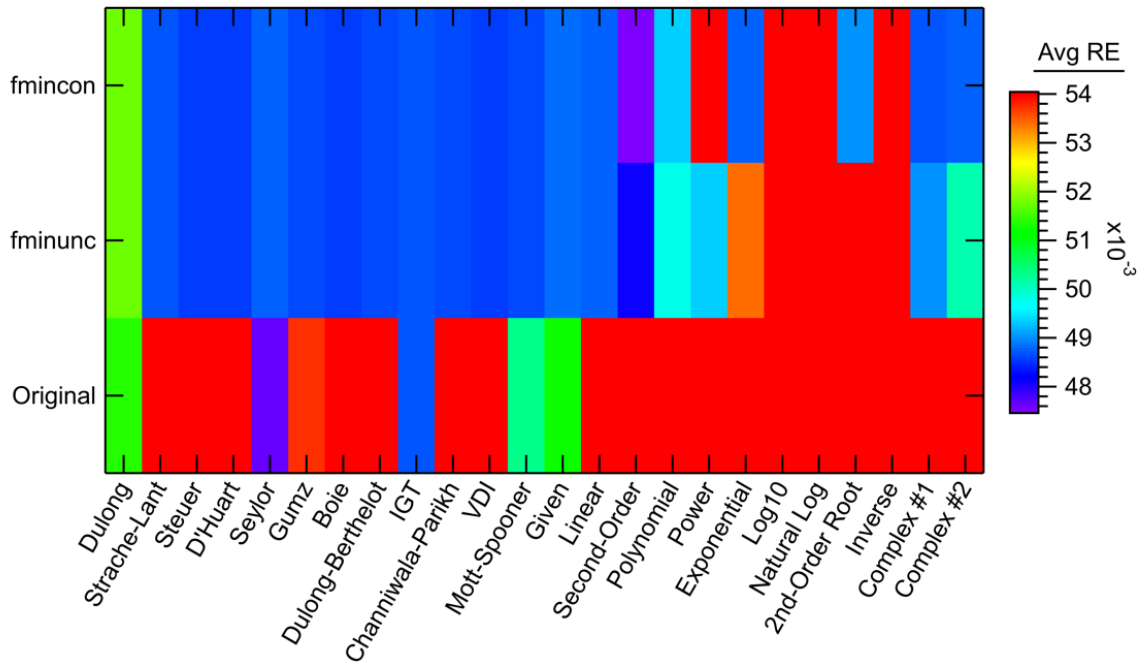

Figure D-25. Average relative error values in the combined coal-char comparison for each model form.

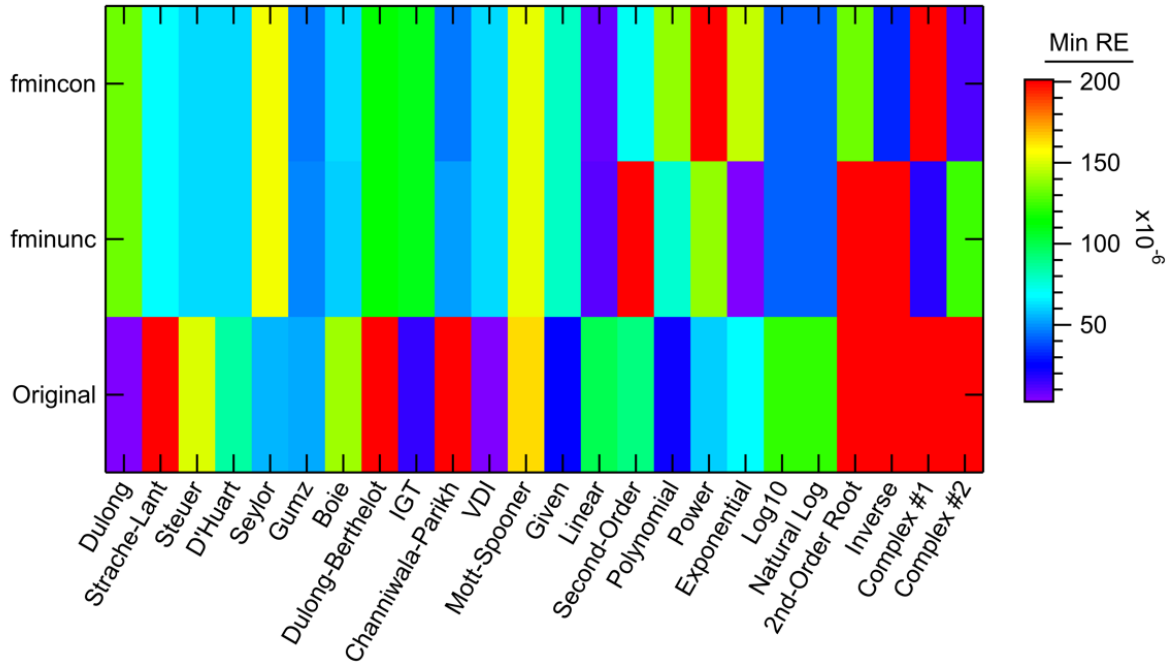

Figure D-26. Minimum relative error values in the combined coal-char comparison for each model form.

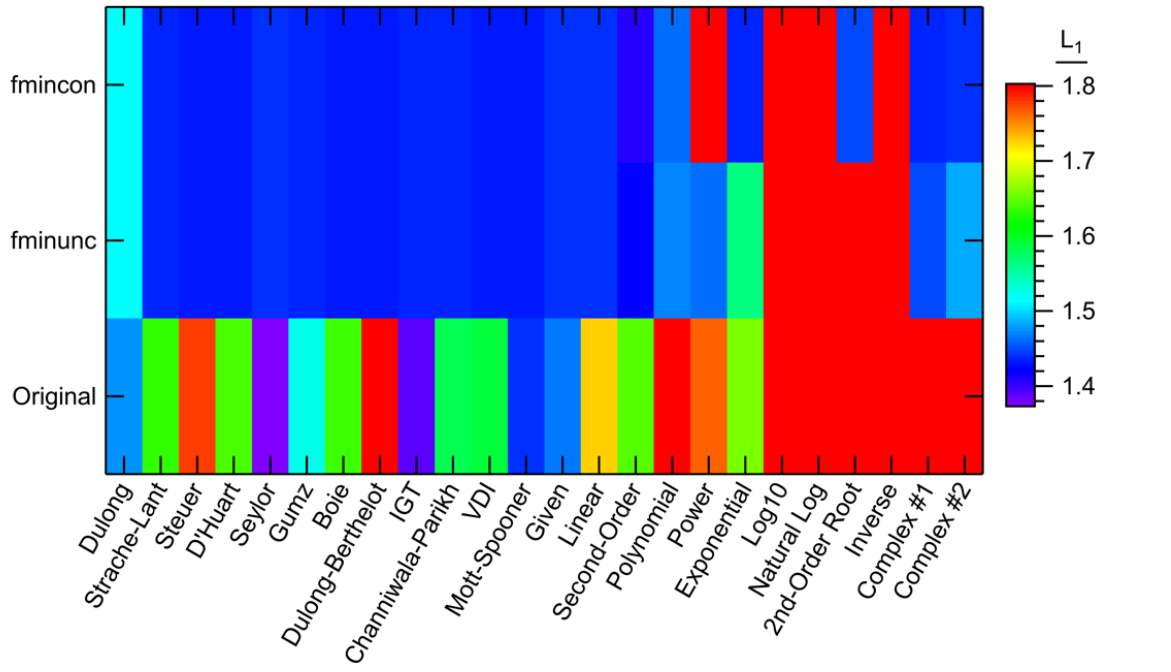

Figure D-27. L_1 norm values in the combined coal-char comparison for each model form.

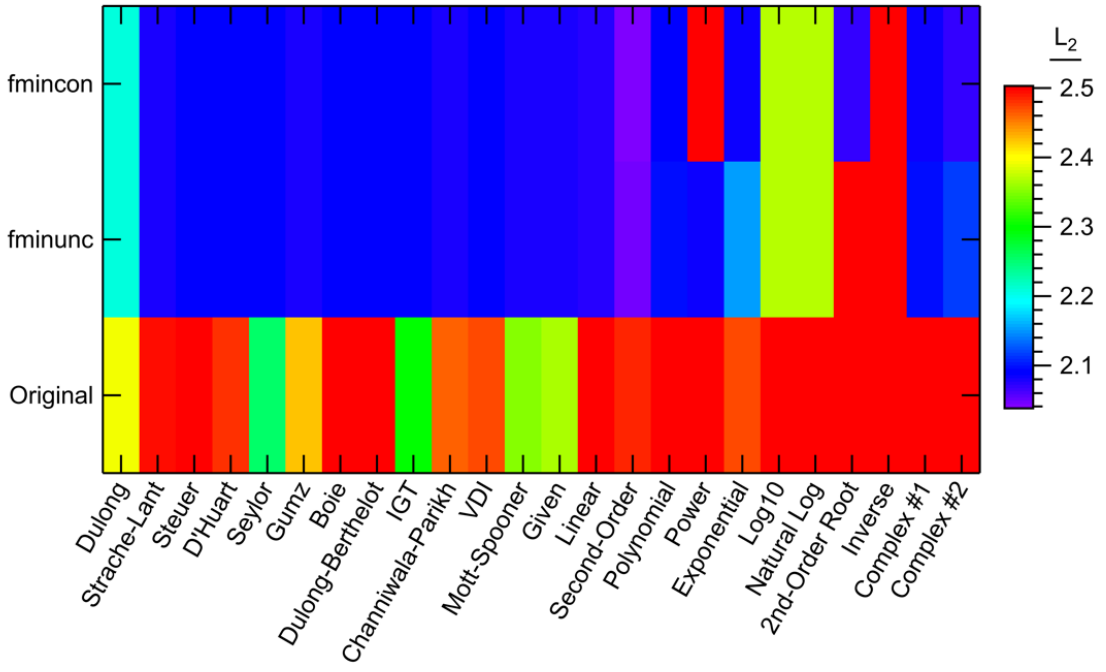

Figure D-28. L_2 norm values in the combined coal-char comparison for each model form.

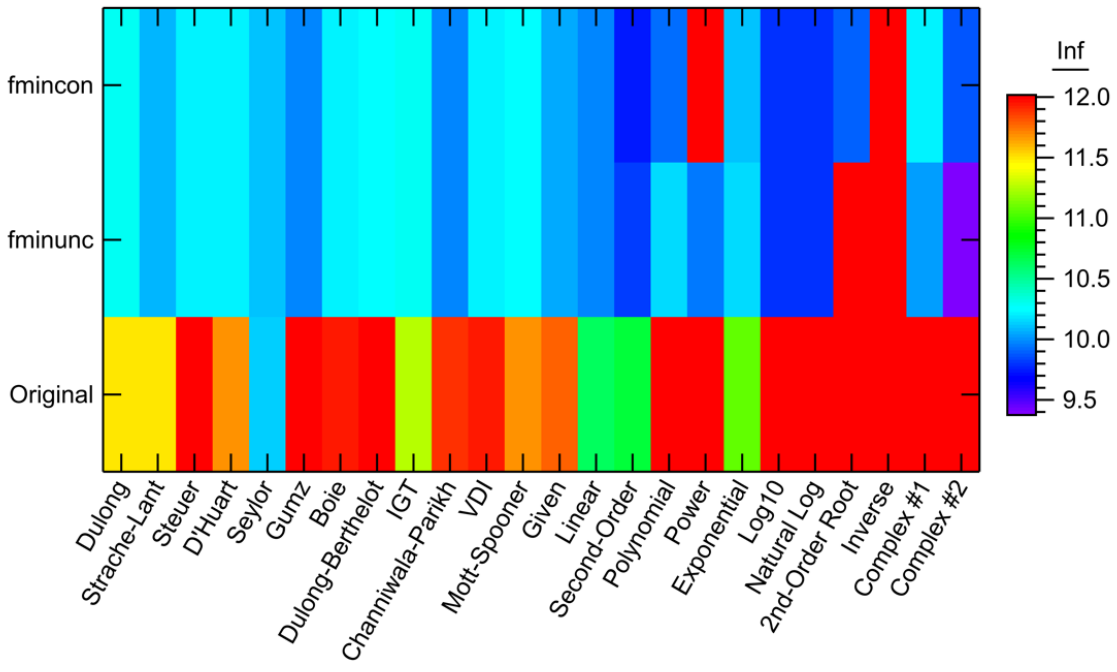

Figure D-29. Infinity norm values in the combined coal-char comparison for each model form.

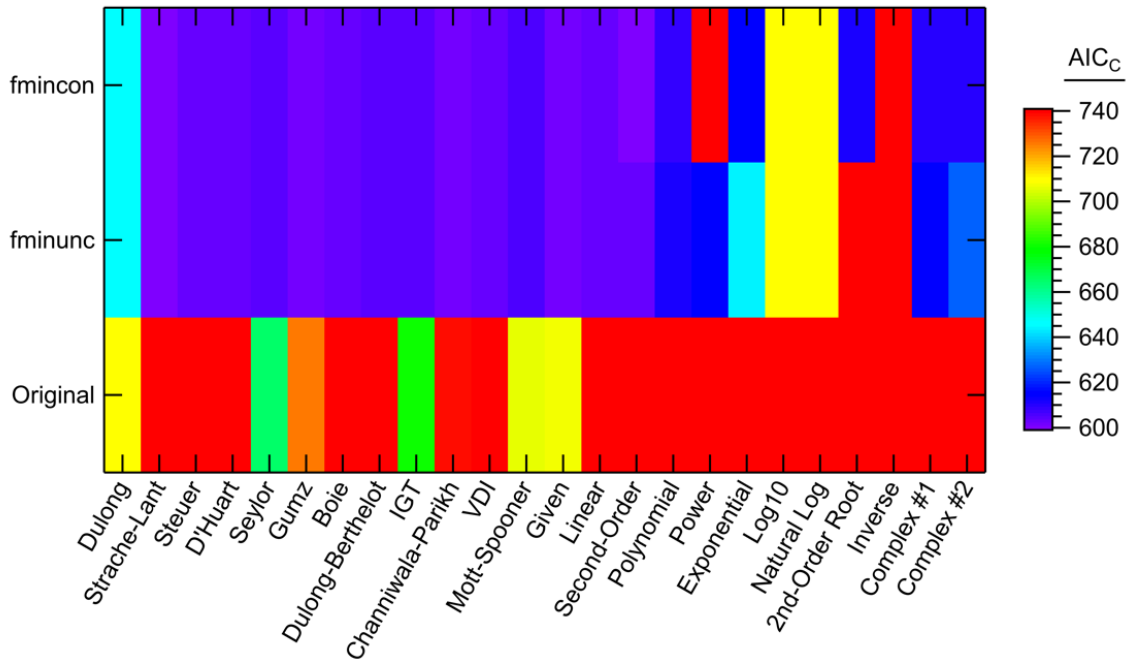

Figure D-30. AIC_c values in the combined coal-char comparison for each model form.

D.3.4 Coal Tar Only

Table D-7 shows the complete best results using the tar-only data set. This data set overall did not perform as well as the other coal-related data sets, and this was discussed at length in Section 7.3.1. The results of the tar data set showed the most difference between the literature model results and the new model results, which could indicate that tar heating values are more accurately calculated using the new model forms. However, there is so much variability in the tar heating value data set that these new model forms would not be any better than the literature models when comparing to a larger, more accurately measured tar heating value data set. Figure D-31 to Figure D-40 show the complete statistical results for the tar-only comparison.

Table D-7. Complete Best Model Calculations Using the Tar-Only Data Set

	Statistic	Value	Model	Optimizer	AIC_c
Overall Best Performance	R^2	0.601	Second-Order	fmincon	43.79
	SSE $(MJ/kg)^2$	54.89	Second-Order	fmincon	43.79
	MSE $(MJ/kg)^2$	1.247	Second-Order	fmincon	43.79
	Max RE (%)	11.43	Second-Order	fmincon	43.794
	Avg RE (%)	1.90	Second-Order	fmincon	43.79
	Min RE (%)	3.16×10^{-7}	Mott-Spooner	fmincon	54.66
	L_1 (MJ/kg)	0.692	Second-Order	fmincon	43.79
	L_2 (MJ/kg)	1.117	Second-Order	fmincon	43.79
	Infinity (MJ/kg)	3.650	Second-Order	fmincon	43.79
	AIC_c	41.91	Strache-Lant	fmincon	41.91
Best New Models	R^2	0.601	Second-Order	fmincon	43.79
	SSE $(MJ/kg)^2$	54.89	Second-Order	fmincon	43.79
	MSE $(MJ/kg)^2$	1.247	Second-Order	fmincon	43.79
	Max RE (%)	11.43	Second-Order	fmincon	43.794
	Avg RE (%)	1.90	Second-Order	fmincon	43.79
	Min RE (%)	1.26×10^{-3}	Complex #2	Original coeff.	163.3
	L_1 (MJ/kg)	0.692	Second-Order	fmincon	43.79
	L_2 (MJ/kg)	1.117	Second-Order	fmincon	43.79
	Infinity (MJ/kg)	3.650	Second-Order	fmincon	43.79
	AIC_c	42.42	Natural Log	fmincon	42.42
Best Literature Models	R^2	0.378	Channiwala-Parikh	fmincon	43.46
	SSE $(MJ/kg)^2$	85.43	Gumz	fmincon	43.46
	MSE $(MJ/kg)^2$	1.942	Gumz	fmincon	43.46
	Max RE (%)	16.67	Strache-Lant	fminunc	41.91
	Avg RE (%)	2.65	Given	fmincon	43.46
	Min RE (%)	3.16×10^{-7}	Mott-Spooner	fmincon	54.66
	L_1 (MJ/kg)	0.954	Given	fmincon	43.46
	L_2 (MJ/kg)	1.393	Gumz	fmincon	43.46
	Infinity (MJ/kg)	5.323	Strache-Lant	fminunc	41.91
	AIC_c	41.91	Strache-Lant	fmincon	41.91
Best Literature Models with Original Coefficients	R^2	0.256	Dulong-Berthelot	Original coeff.	98.09
	SSE $(MJ/kg)^2$	161.0	Channiwala-Parikh	Original coeff.	71.34
	MSE $(MJ/kg)^2$	3.658	Channiwala-Parikh	Original coeff.	71.34
	Max RE (%)	24.37	Channiwala-Parikh	Original coeff.	71.34
	Avg RE (%)	3.25	Channiwala-Parikh	Original coeff.	71.34
	Min RE (%)	2.37×10^{-3}	Seylor	Original coeff.	83.171
	L_1 (MJ/kg)	1.148	Channiwala-Parikh	Original coeff.	71.34
	L_2 (MJ/kg)	1.913	Channiwala-Parikh	Original coeff.	71.34
	Infinity (MJ/kg)	7.780	Channiwala-Parikh	Original coeff.	71.34
	AIC_c	69.990	Boie	Original coeff.	69.99

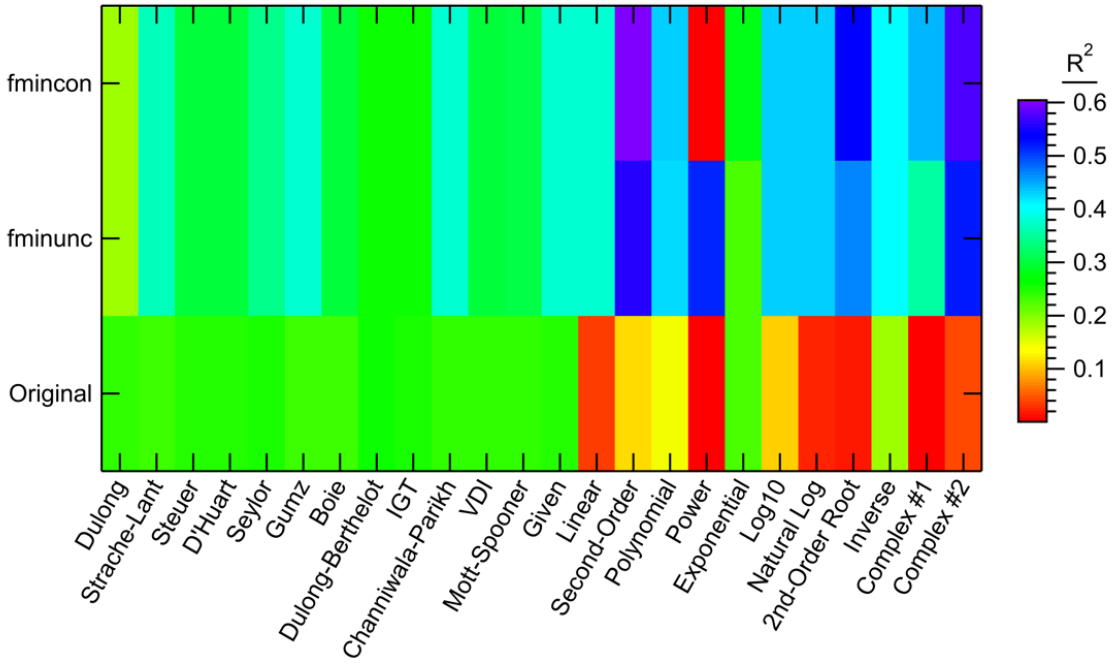

Figure D-31. R^2 values in the tar-only comparison for each model form.

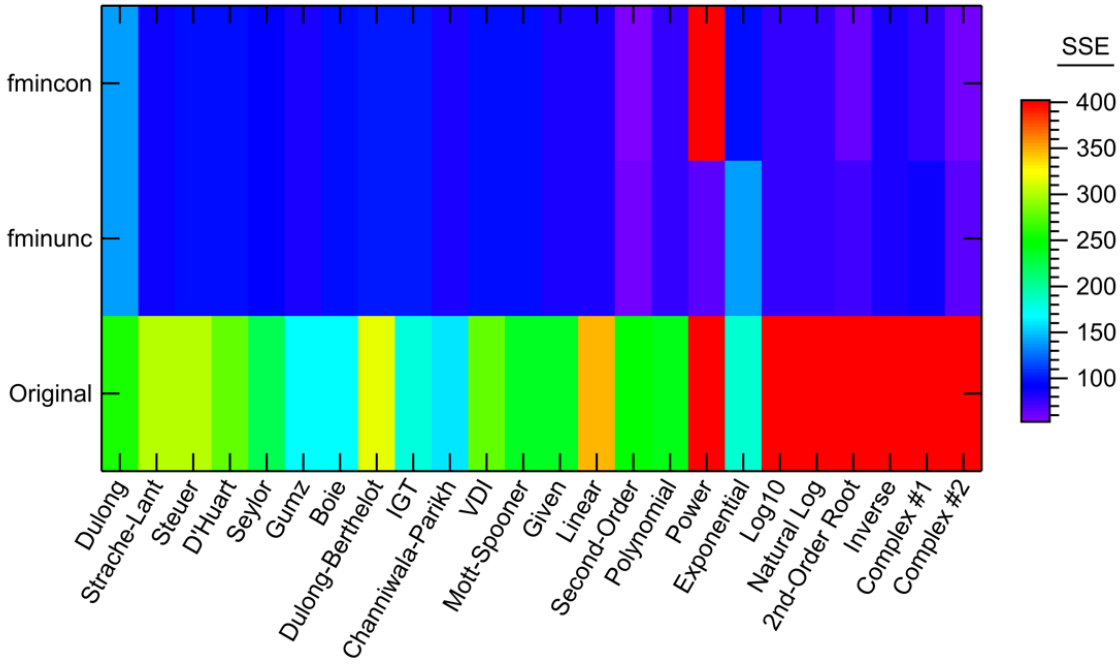

Figure D-32. SSE values in the tar-only comparison for each model form.

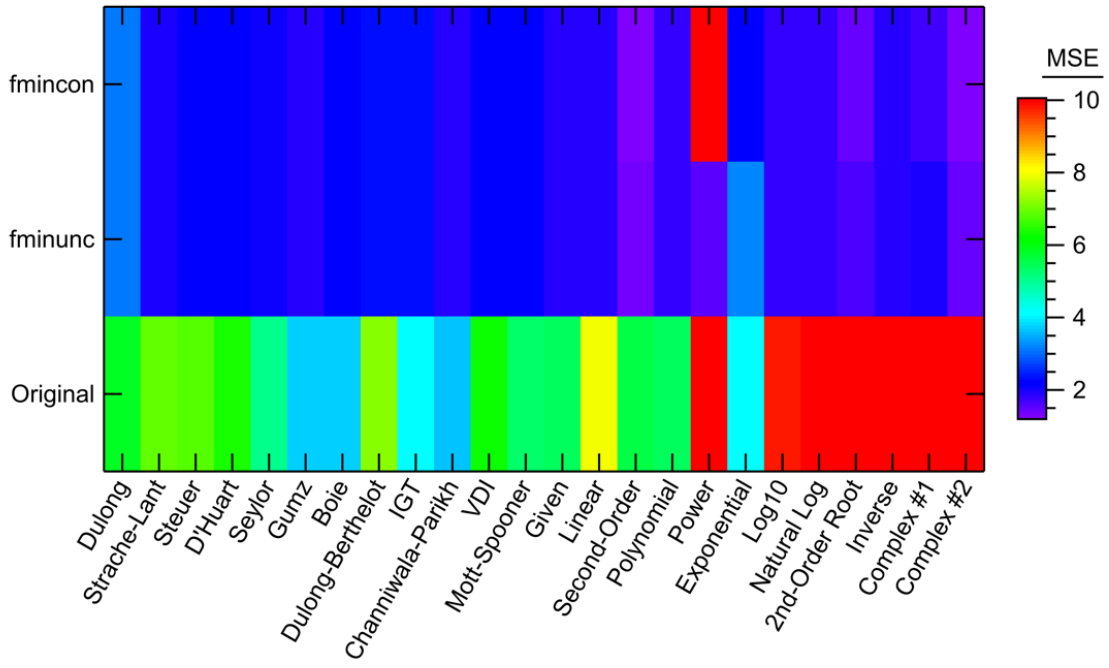

Figure D-33. MSE values in the tar-only comparison for each model form.

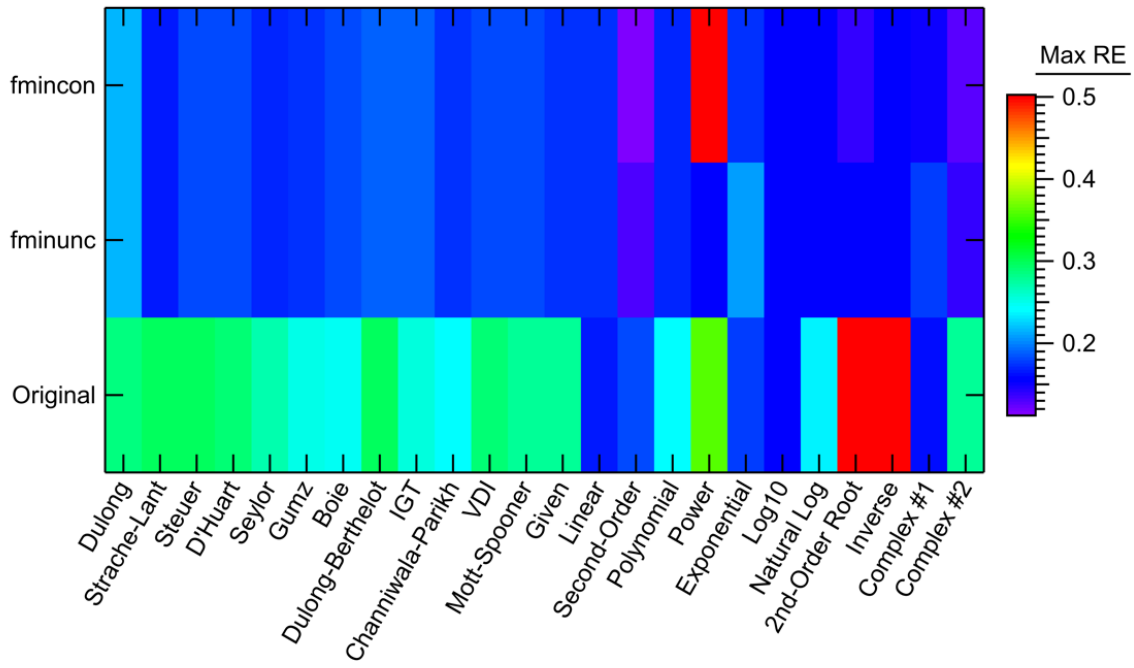

Figure D-34. Maximum relative error values in the tar-only comparison for each model form.

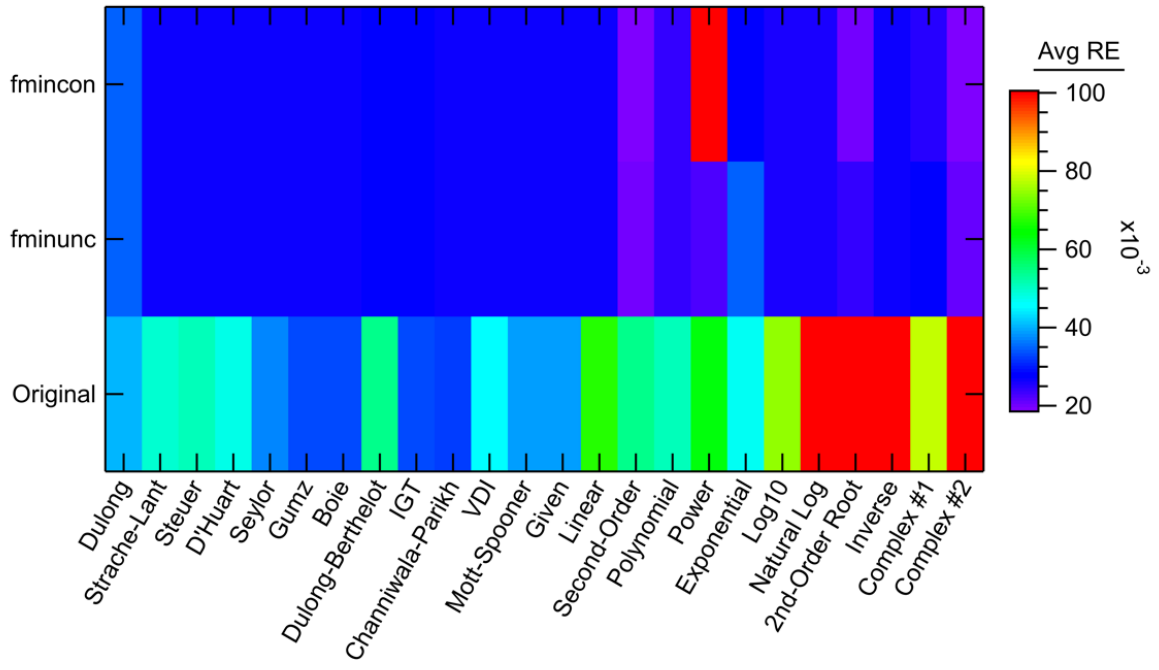

Figure D-35. Average relative error values in the tar-only comparison for each model form.

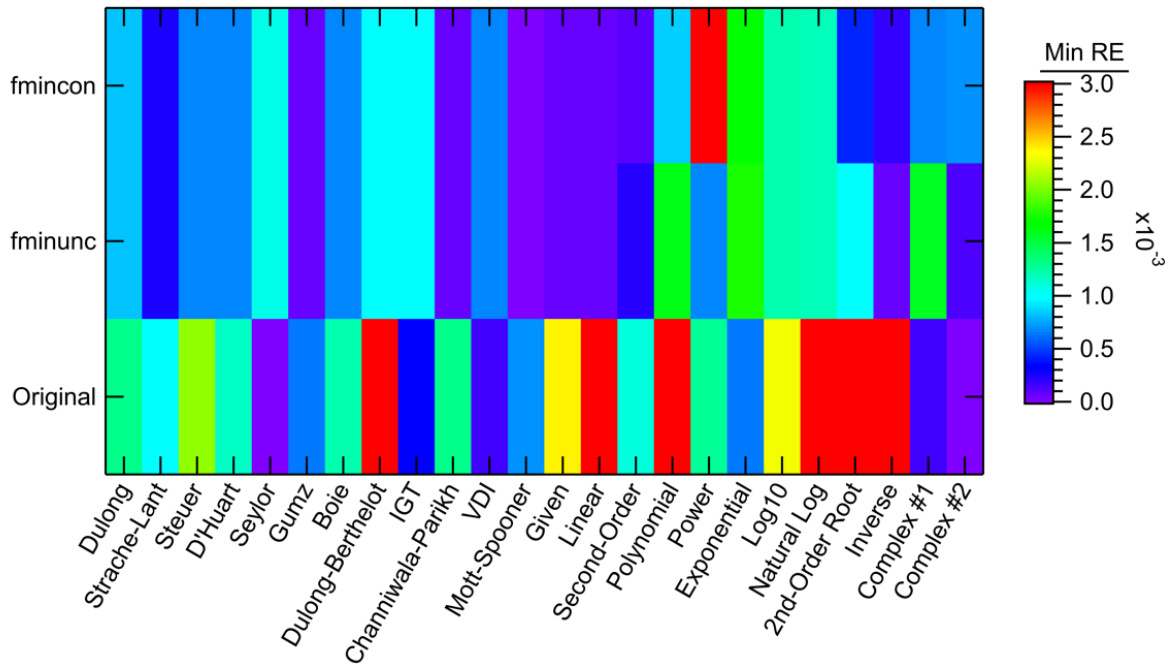

Figure D-36. Minimum relative error values in the tar-only comparison for each model form.

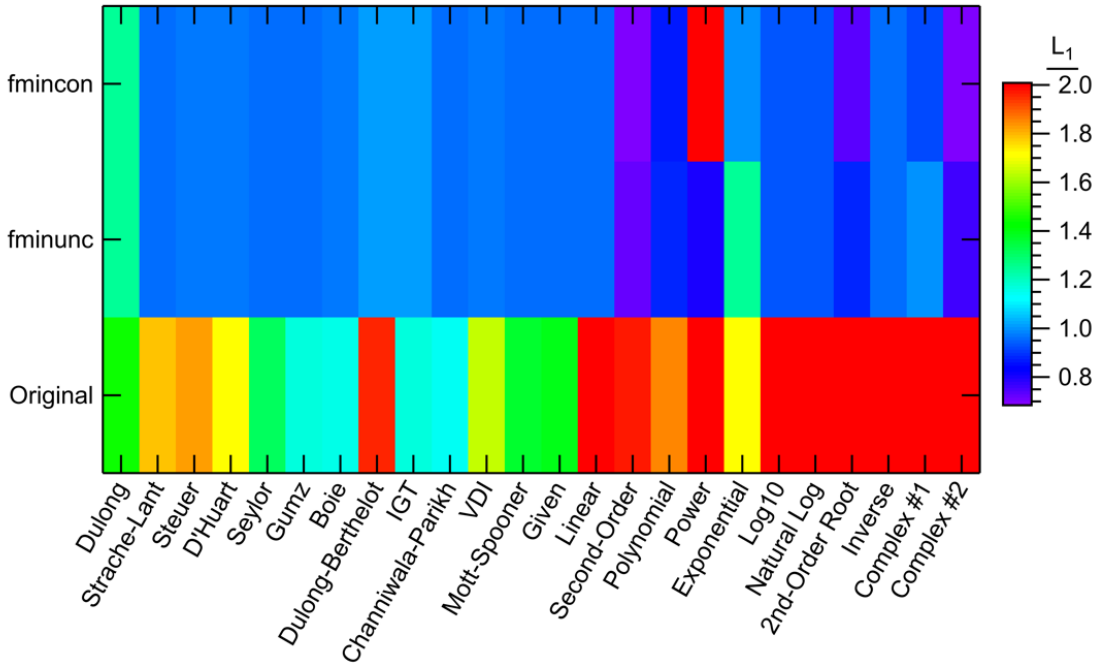

Figure D-37. L_1 norm values in the tar-only comparison for each model form.

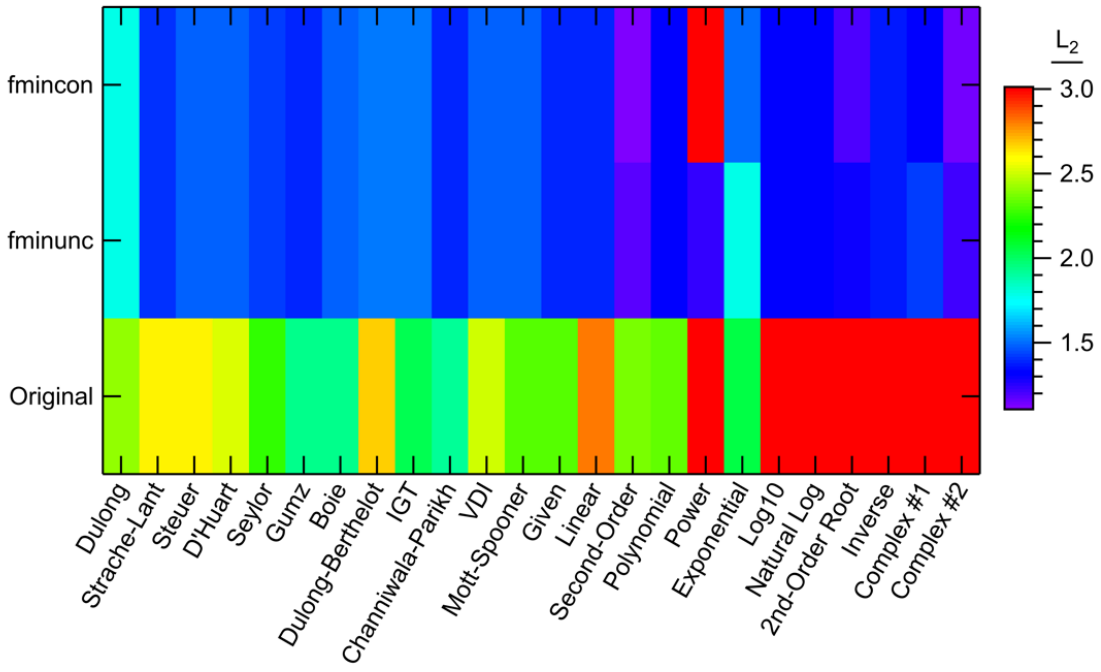

Figure D-38. L_2 norm values in the tar-only comparison for each model form.

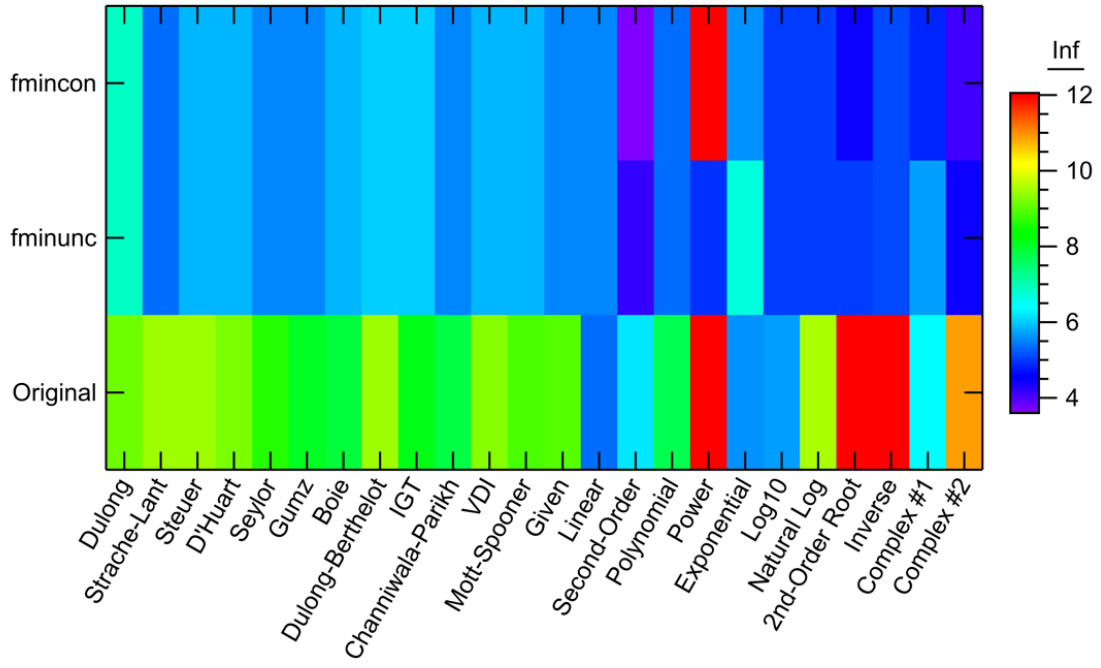

Figure D-39. Infinity norm values in the tar-only comparison for each model form.

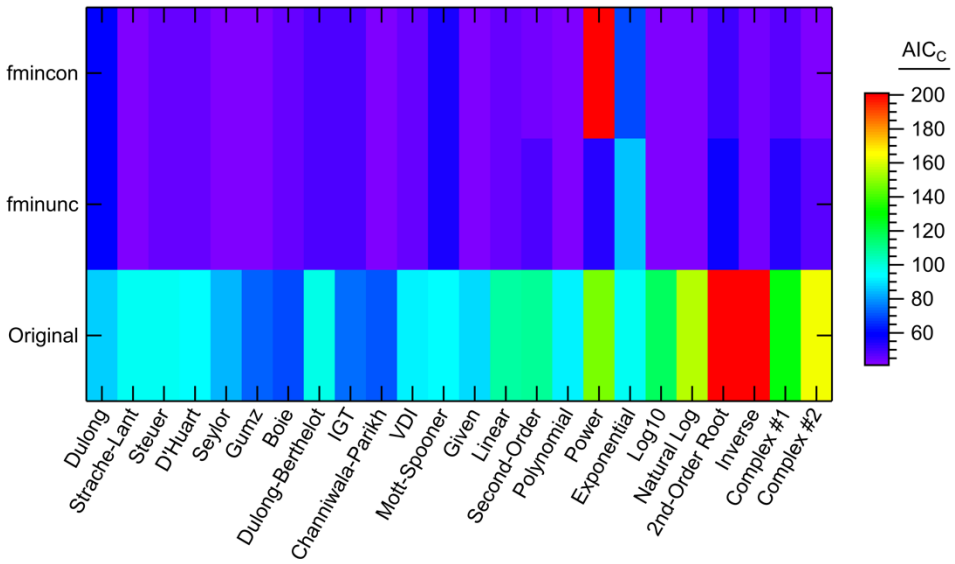

Figure D-40. AIC_c values in the tar-only comparison for each model form.

D.3.5 Combined Coal (Parent Coal, Char, and Tar)

Table D-8 shows the complete best model results for the combined coal, char, and tar data set comparison. The coal-char-tar comparison showed similar results to the other coal-based fuels comparisons. Like with the others, the new models showed a very slight improvement over the literature models, however, the improvement was not enough to justify the additional coefficients in the new models. Figure D-41 to Figure D-50 show the complete statistical results for the combined coal data set comparison.

Table D-8. Complete Best Model Calculations Using the Coal-Char-Tar Data Set

	Statistic	**Value**	**Model**	**Optimizer**	**AIC_c**
Overall Best Performance	R^2	0.701	Second-Order	fmincon	696.9
	SSE $(MJ/kg)^2$	2011	Second-Order	fmincon	696.9
	MSE $(MJ/kg)^2$	4.499	Second-Order	fmincon	696.9
	Max RE (%)	43.32	Natural Log	Original coeff.	1109
	Avg RE (%)	4.84	Seylor	Original coeff.	766.6
	Min RE (%)	3.16×10^{-4}	Complex #2	fminunc	728.8
	L_1 (MJ/kg)	1.414	Seylor	Original coeff.	766.6
	L_2 (MJ/kg)	2.121	Second-Order	fmincon	696.9
	Infinity (MJ/kg)	9.438	Complex #2	fminunc	728.8
	AIC_c	688.4	Boie	fmincon	688.4
Best New Models	R^2	0.701	Second-Order	fmincon	696.9
	SSE $(MJ/kg)^2$	2011	Second-Order	fmincon	696.9
	MSE $(MJ/kg)^2$	4.499	Second-Order	fmincon	696.9
	Max RE (%)	43.32	Natural Log	Original coeff.	1109
	Avg RE (%)	4.97	Second-Order	fmincon	696.9
	Min RE (%)	3.16×10^{-4}	Complex #2	fminunc	728.8
	L_1 (MJ/kg)	1.486	Second-Order	fmincon	696.9
	L_2 (MJ/kg)	2.121	Second-Order	fmincon	696.9
	Infinity (MJ/kg)	9.438	Complex #2	fminunc	728.8
	AIC_c	691.9	Linear	fmincon	691.9

Table D-8. Complete Best Model Calculations Using the Coal-Char-Tar Data Set, CONTINUED

	Statistic	Value	Model	Optimizer	AIC_c
Best Literature Models	R^2	0.699	Mott-Spooner	fmincon	691.7
	SSE $(MJ/kg)^2$	2025	Mott-Spooner	fmincon	691.7
	MSE $(MJ/kg)^2$	4.531	Mott-Spooner	fmincon	691.7
	Max RE (%)	49.73	Seylor	fmincon	689.3
	Avg RE (%)	4.84	Seylor	Original coeff.	766.6
	Min RE (%)	3.78×10^{-4}	Dulong	Original coeff.	816.2
	L_1 (MJ/kg)	1.414	Seylor	Original coeff.	766.6
	L_2 (MJ/kg)	2.129	Mott-Spooner	fmincon	691.7
	Infinity (MJ/kg)	10.05	Seylor	fmincon	689.3
	AIC_c	688.4	Boie	fmincon	688.4
Best Literature Models with Original Coefficients	R^2	0.696	D'Huart	Original coeff.	857.3
	SSE $(MJ/kg)^2$	2428	Seylor	Original coeff.	766.6
	MSE $(MJ/kg)^2$	5.432	Seylor	Original coeff.	766.6
	Max RE (%)	50.15	Seylor	Original coeff.	766.6
	Avg RE (%)	4.84	Seylor	Original coeff.	766.6
	Min RE (%)	3.78×10^{-4}	Dulong	Original coeff.	816.2
	L_1 (MJ/kg)	1.414	Seylor	Original coeff.	766.6
	L_2 (MJ/kg)	2.331	Seylor	Original coeff.	766.6
	Infinity (MJ/kg)	10.14	Seylor	Original coeff.	766.6
	AIC_c	766.6	Seylor	Original coeff.	766.6

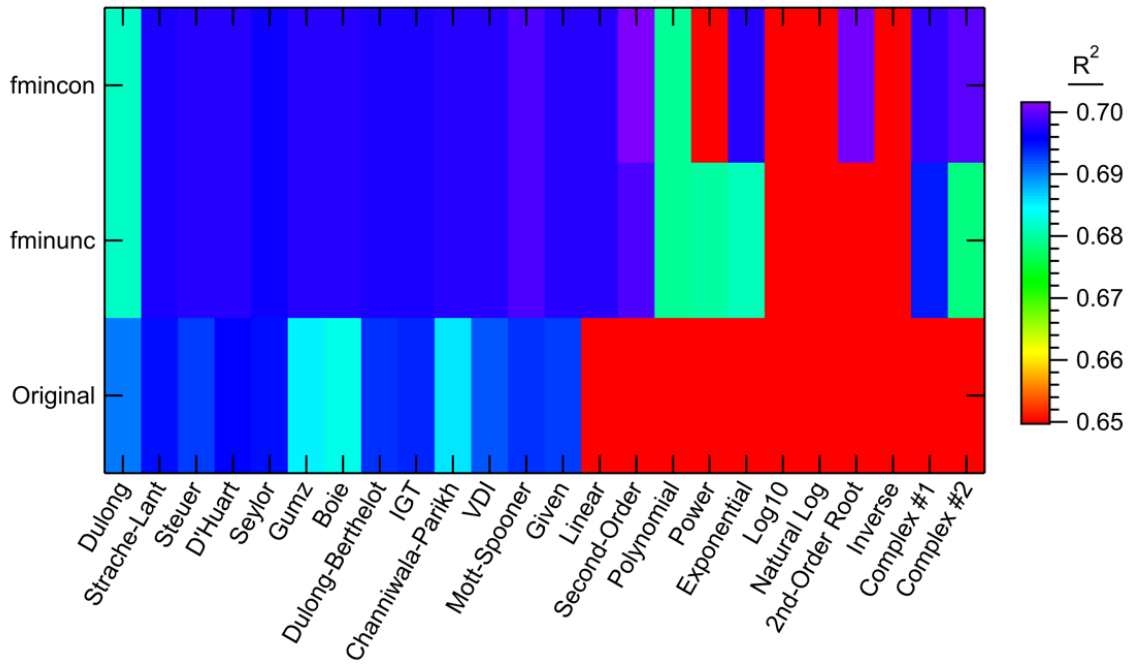

Figure D-41. R^2 values in the combined coal-char-tar comparison for each model form.

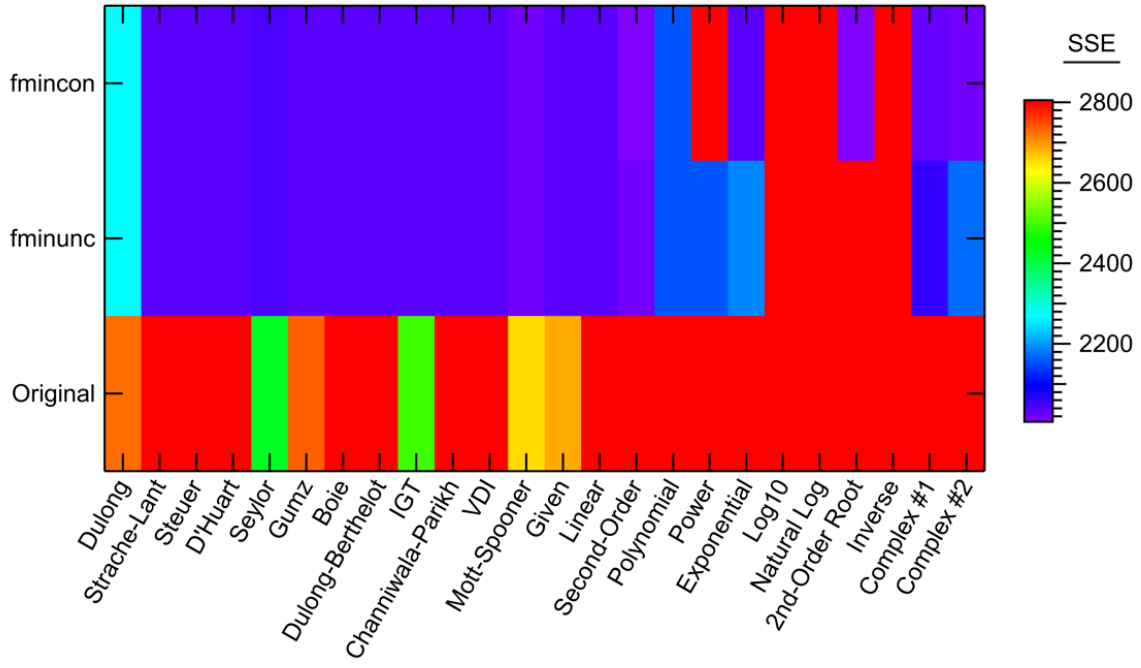

Figure D-42. SSE values in the combined coal-char-tar comparison for each model form.

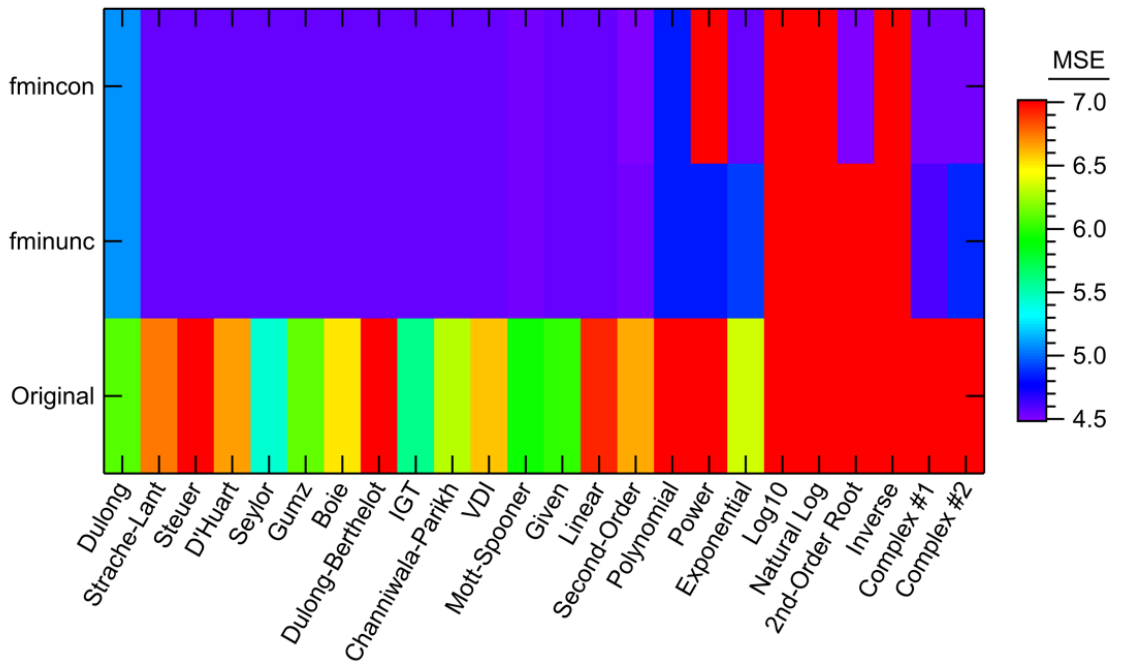

Figure D-43. MSE values in the combined coal-char-tar comparison for each model form.

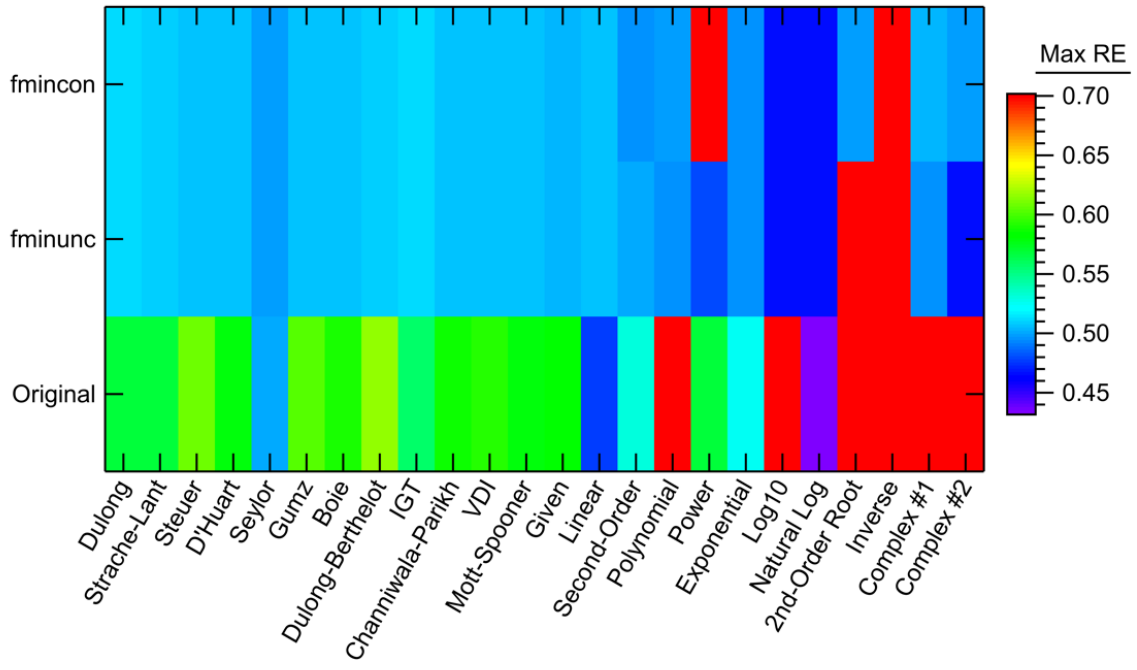

Figure D-44. Maximum relative error values in the combined coal-char-tar comparison for each model form.

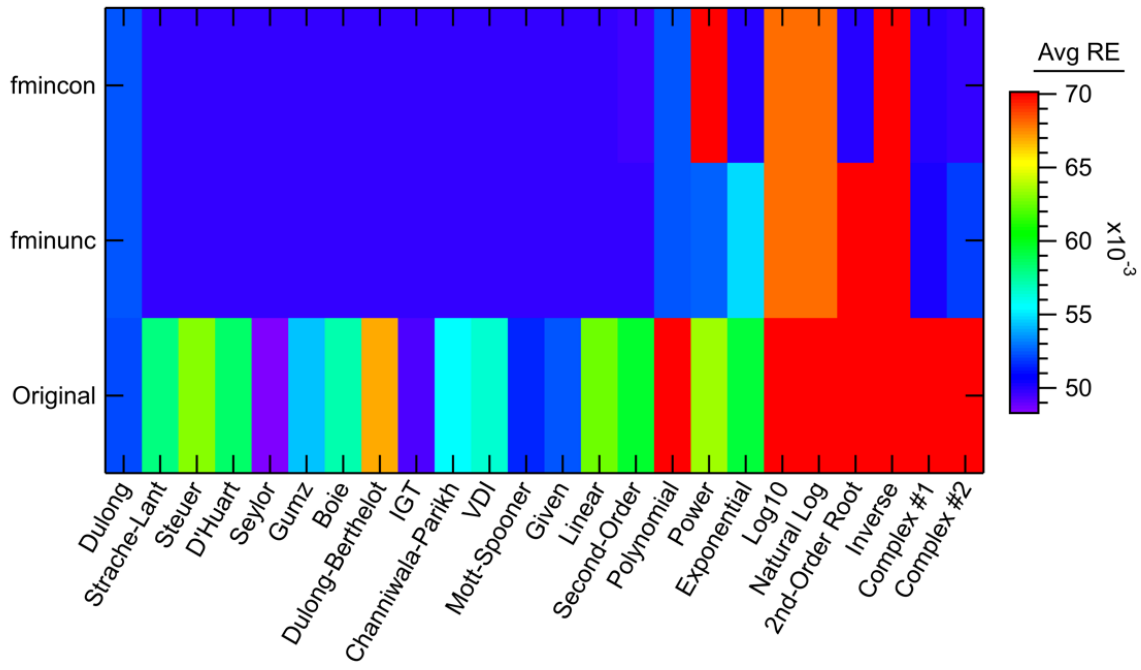

Figure D-45. Average relative error values in the combined coal-char-tar comparison for each model form.

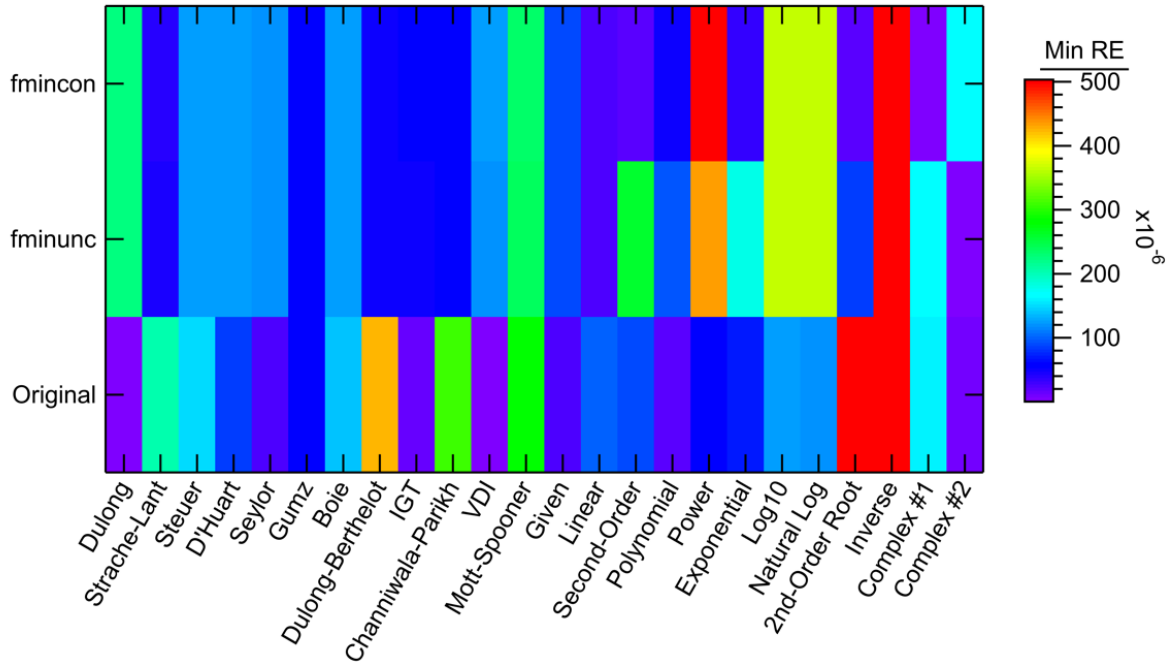

Figure D-46. Minimum relative error values in the combined coal-char-tar comparison for each model form.

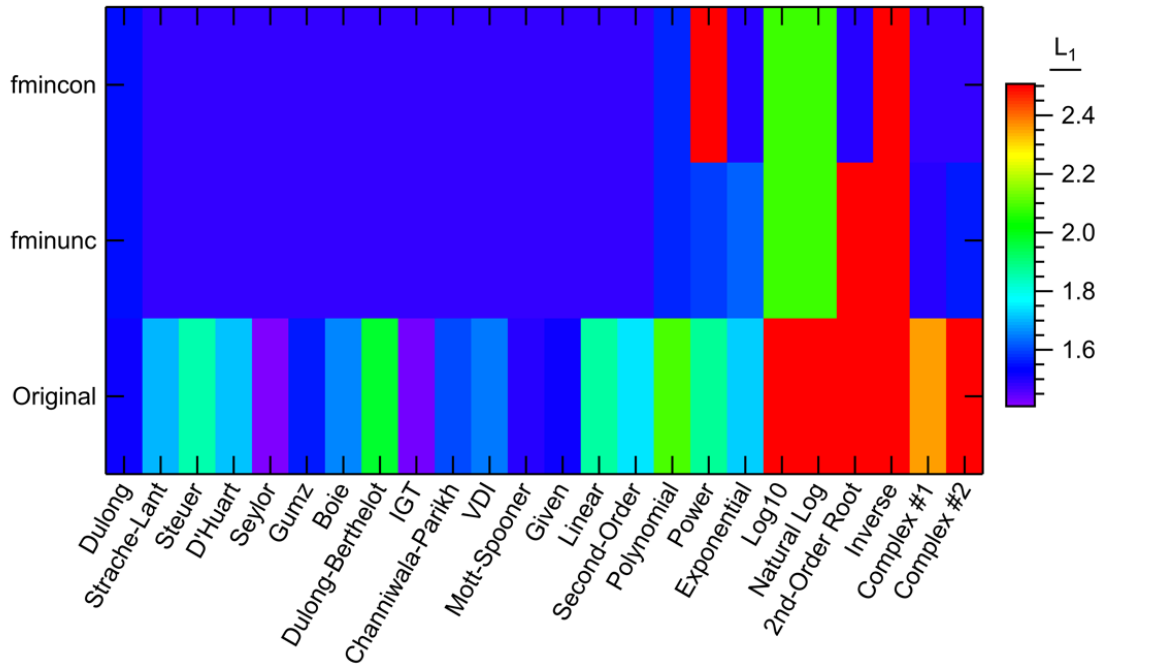

Figure D-47. L_1 norm values in the combined coal-char-tar comparison for each model form.

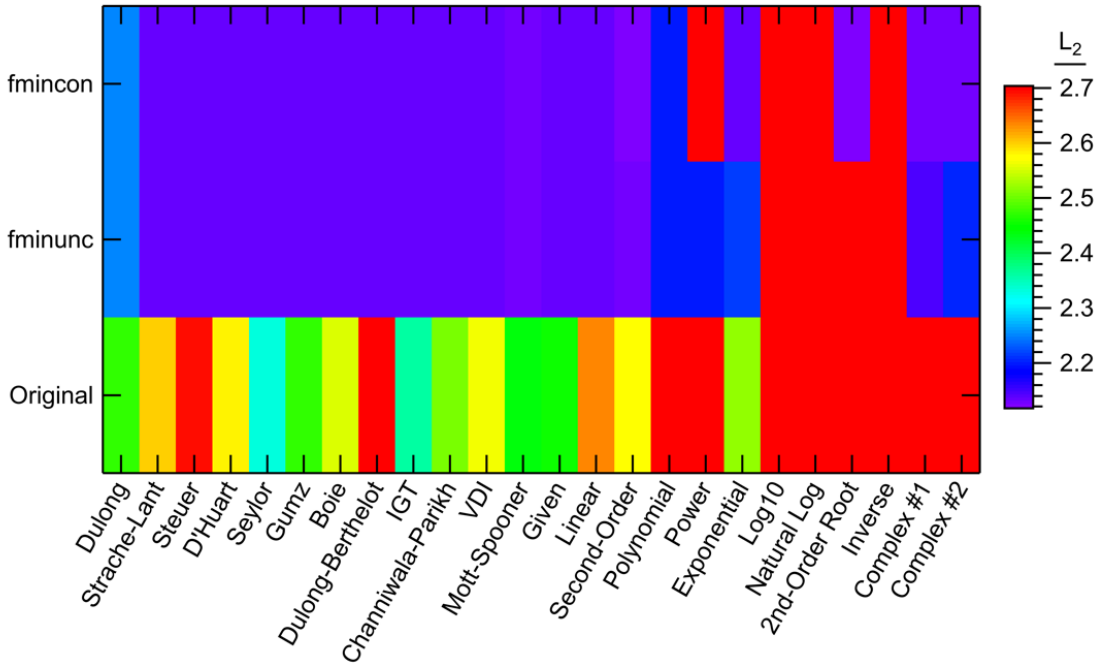

Figure D-48. L_2 norm values in the combined coal-char-tar comparison for each model form.

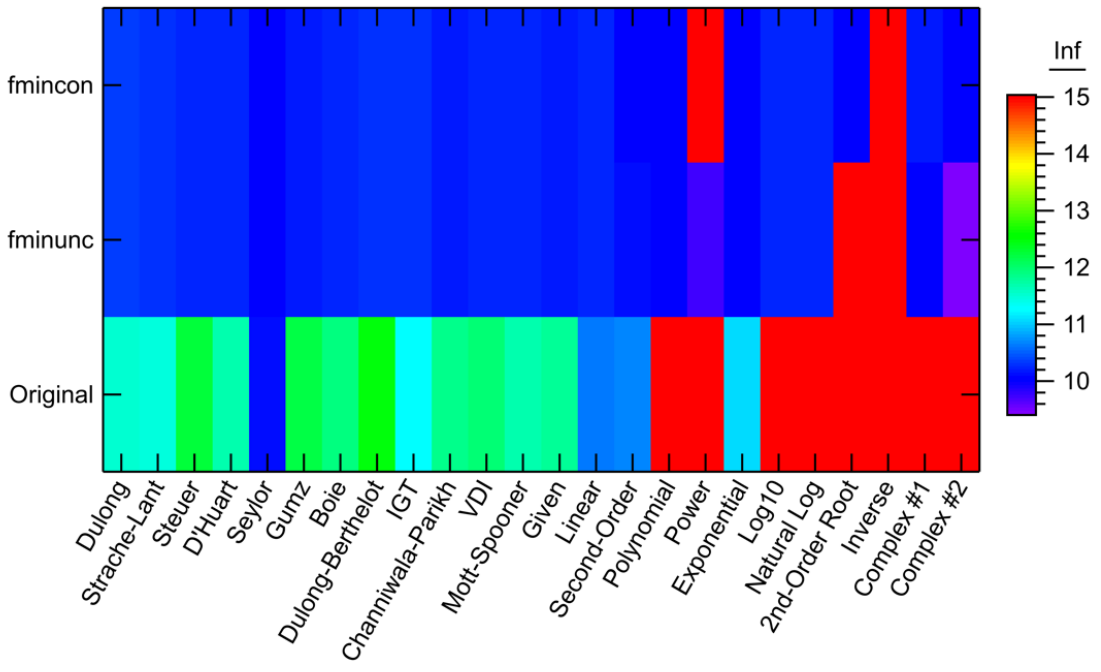

Figure D-49. Infinity norm values in the combined coal-char-tar comparison for each model form.

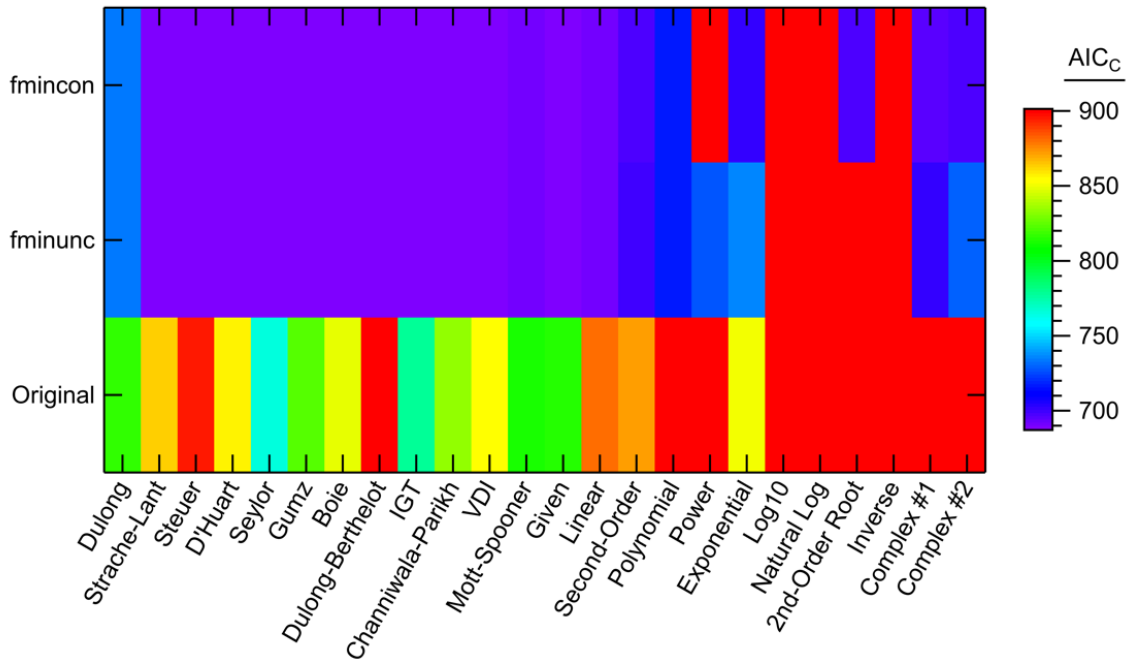

Figure D-50. AIC_c values in the combined coal-char-tar comparison for each model form.

D.3.6 Fossil Fuels Data Set

Table D-9 shows the best model results using the fossil fuel data set. Like most of the coal-based fuels comparisons, the fossil fuels comparison showed very little improvement using the new models over the literature models. This is not surprising since the combined data sets of coal, char, and tar are the bulk of the fossil fuels data set (447 samples out of 552). With a larger set of non-coal fossil fuels, the comparison might diverge even more from the coal-based fuels comparisons. Figure D-51 to Figure D-60 show the complete statistical results for the fossil fuels data set comparison.

Table D-9. Complete Best Model Calculations Using the Fossil Fuels Data Set

	Statistic	Value	Model	Optimizer	AIC_c
Overall Best Performance	R^2	0.897	Complex #2	fmincon	801.2
	SSE $(MJ/kg)^2$	2263	Complex #2	fmincon	801.2
	MSE $(MJ/kg)^2$	4.099	Complex #2	fmincon	801.2
	Max RE (%)	50.36	Polynomial	fmincon	1075
	Avg RE (%)	4.63	2nd-Order Root	fmincon	805.3
	Min RE (%)	1.91×10^{-4}	Power	fminunc	14991
	L_1 (MJ/kg)	1.380	2nd-Order Root	fmincon	805.3
	L_2 (MJ/kg)	2.025	Complex #2	fmincon	801.2
	Infinity (MJ/kg)	10.27	Complex #2	fminunc	813.6
	AIC_c	799.7	Given	fmincon	799.7
Best New Models	R^2	0.897	Complex #2	fmincon	801.2
	SSE $(MJ/kg)^2$	2263	Complex #2	fmincon	801.2
	MSE $(MJ/kg)^2$	4.099	Complex #2	fmincon	801.2
	Max RE (%)	50.36	Polynomial	fmincon	1075
	Avg RE (%)	4.63	2nd-Order Root	fmincon	805.3
	Min RE (%)	1.91×10^{-4}	Power	fminunc	14991
	L_1 (MJ/kg)	1.380	2nd-Order Root	fmincon	805.3
	L_2 (MJ/kg)	2.025	Complex #2	fmincon	801.2
	Infinity (MJ/kg)	10.27	Complex #2	fminunc	813.6
	AIC_c	801.1	Linear	fmincon	801.1
Best Literature Models	R^2	0.895	Given	fmincon	799.7
	SSE $(MJ/kg)^2$	2299	Given	fmincon	799.7
	MSE $(MJ/kg)^2$	4.165	Given	fmincon	799.7
	Max RE (%)	52.72	Gumz	fminunc	800.4
	Avg RE (%)	4.78	Given	fminunc	799.7
	Min RE (%)	3.78×10^{-4}	Dulong	Original coeff.	1057
	L_1 (MJ/kg)	1.427	Given	fminunc	799.7
	L_2 (MJ/kg)	2.041	Given	fmincon	799.7
	Infinity (MJ/kg)	10.29	Strache-Lant	fminunc	815.2
	AIC_c	799.7	Given	fmincon	799.7
Best Literature Models with Original Coefficients	R^2	0.894	Dulong	Original coeff.	1057
	SSE $(MJ/kg)^2$	3096	Gumz	Original coeff.	964.0
	MSE $(MJ/kg)^2$	5.609	Gumz	Original coeff.	964.0
	Max RE (%)	56.80	Strache-Lant	Original coeff.	1141
	Avg RE (%)	5.24	Gumz	Original coeff.	964.0
	Min RE (%)	3.78×10^{-4}	Dulong	Original coeff.	1057
	L_1 (MJ/kg)	1.500	Gumz	Original coeff.	964.0
	L_2 (MJ/kg)	2.368	Gumz	Original coeff.	964.0
	Infinity (MJ/kg)	11.48	Strache-Lant	Original coeff.	1141
	AIC_c	964.0	Gumz	Original coeff.	964.0

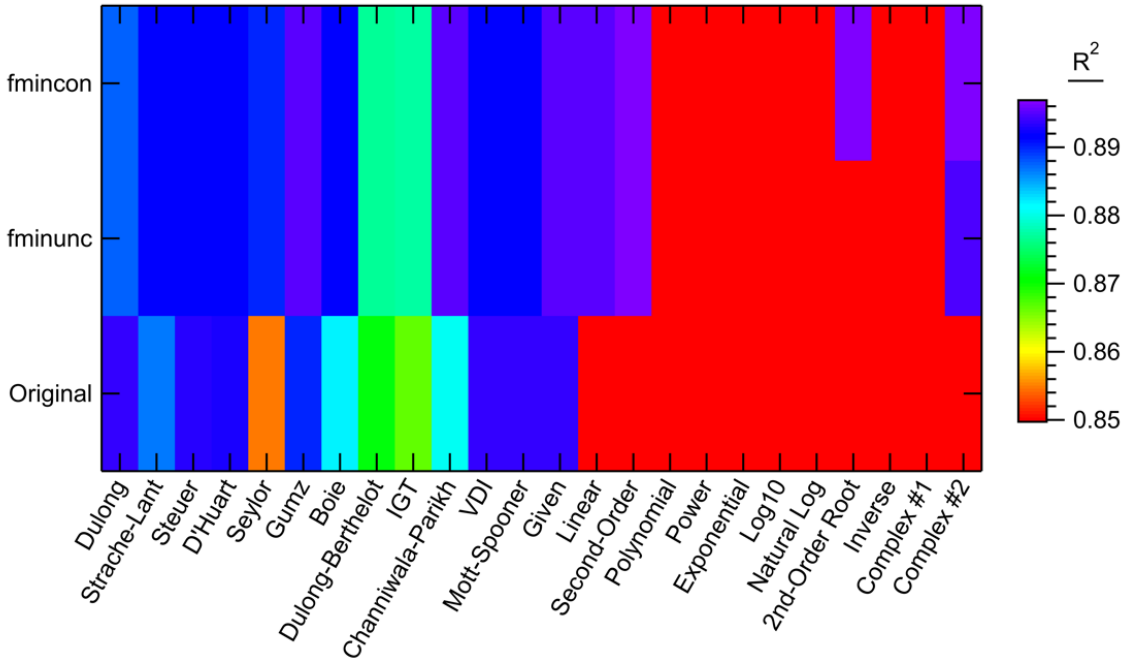

Figure D-51. R^2 values in the fossil fuels comparison for each model form.

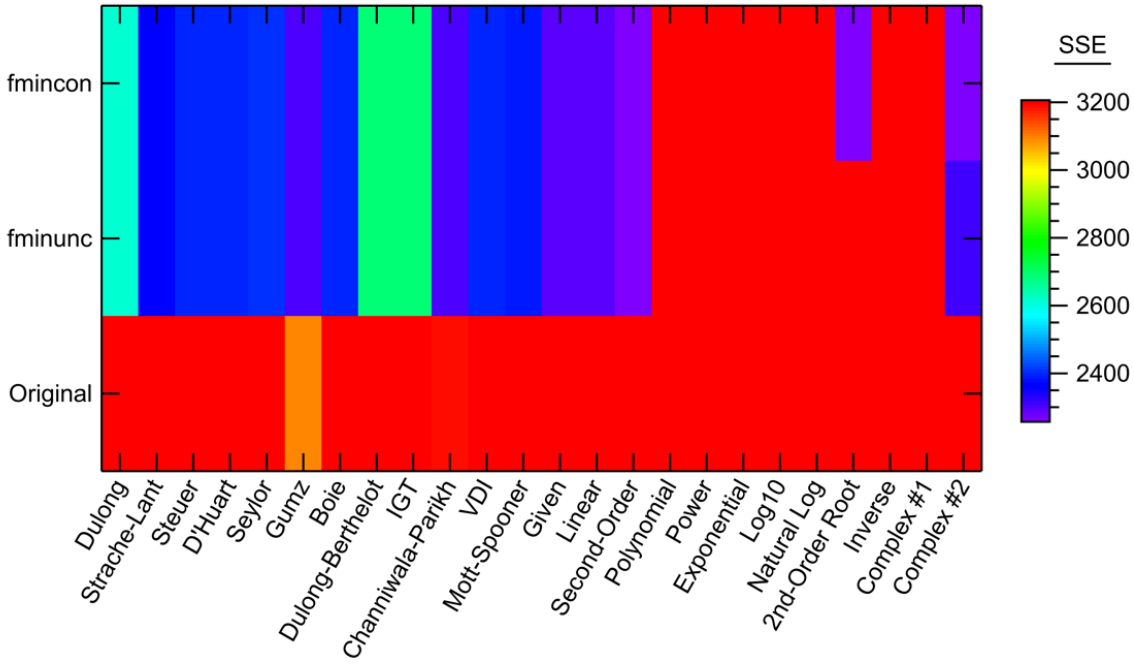

Figure D-52. SSE values in the fossil fuels comparison for each model form.

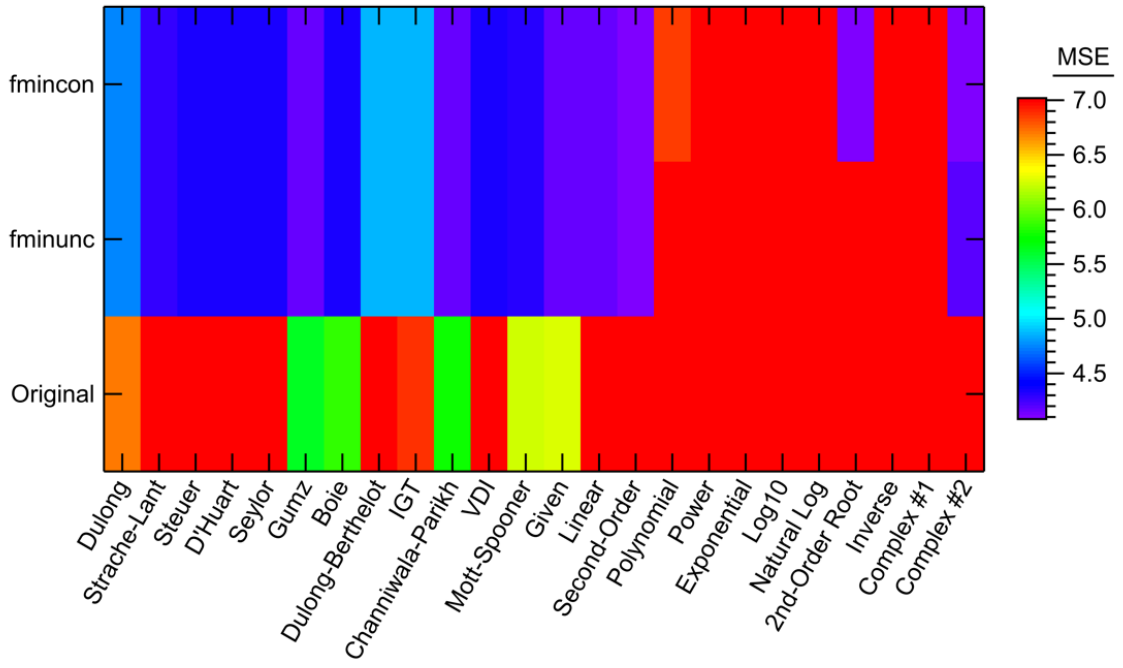

Figure D-53. MSE values in the fossil fuels comparison for each model form.

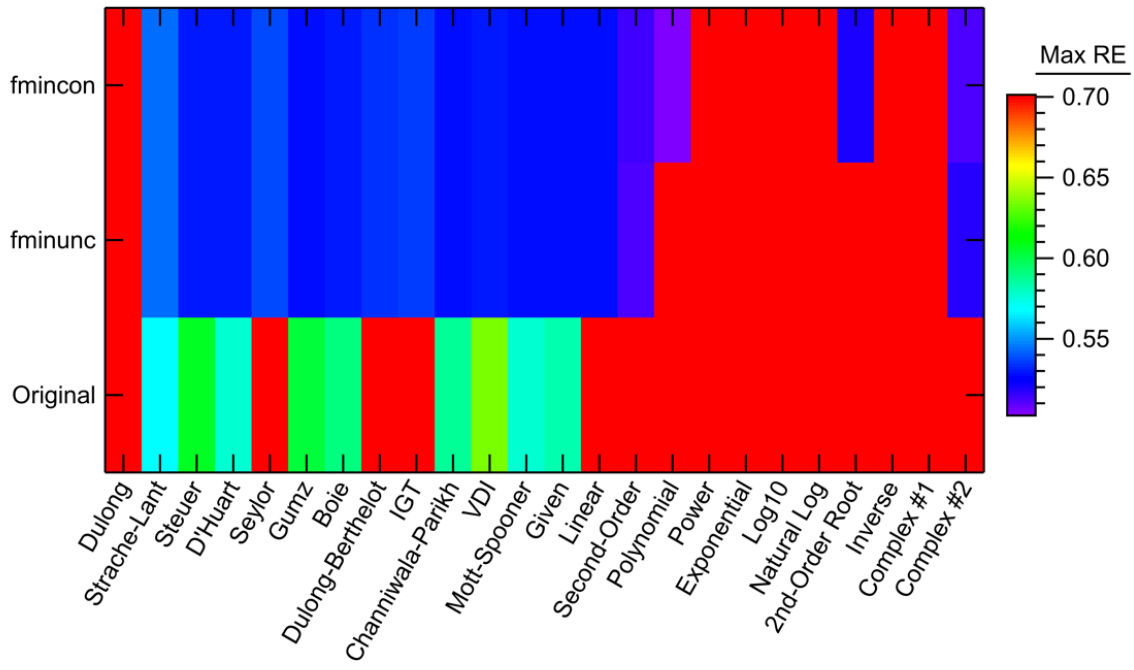

Figure D-54. Maximum relative error values in the fossil fuels comparison for each model form.

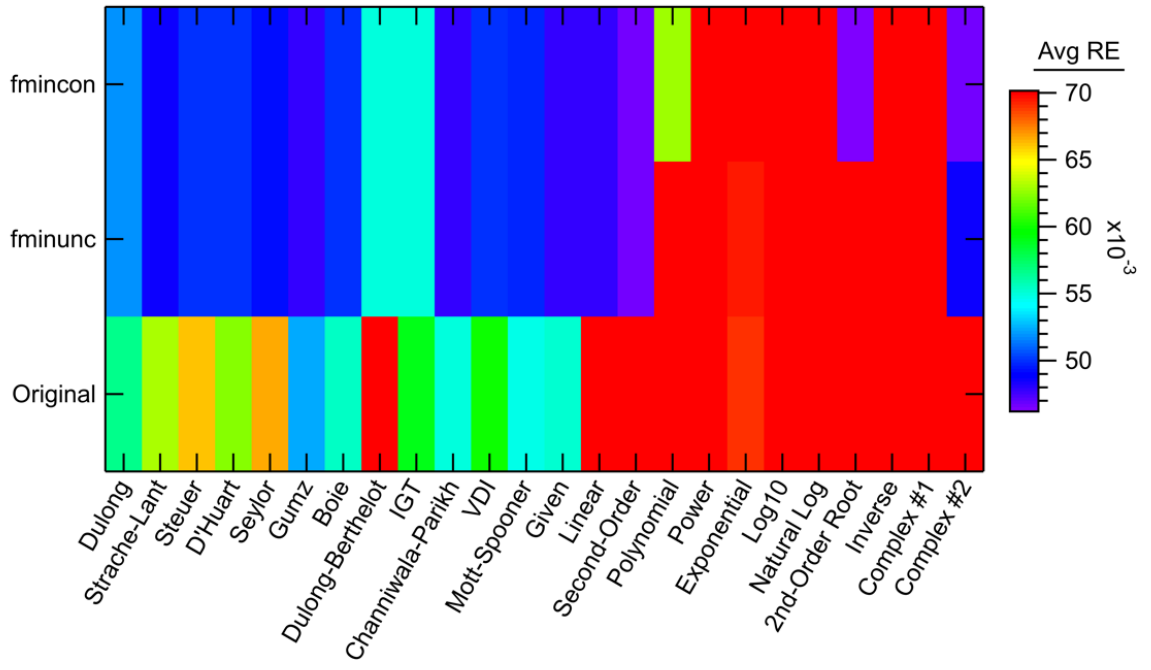

Figure D-55. Average relative error values in the fossil fuels comparison for each model form.

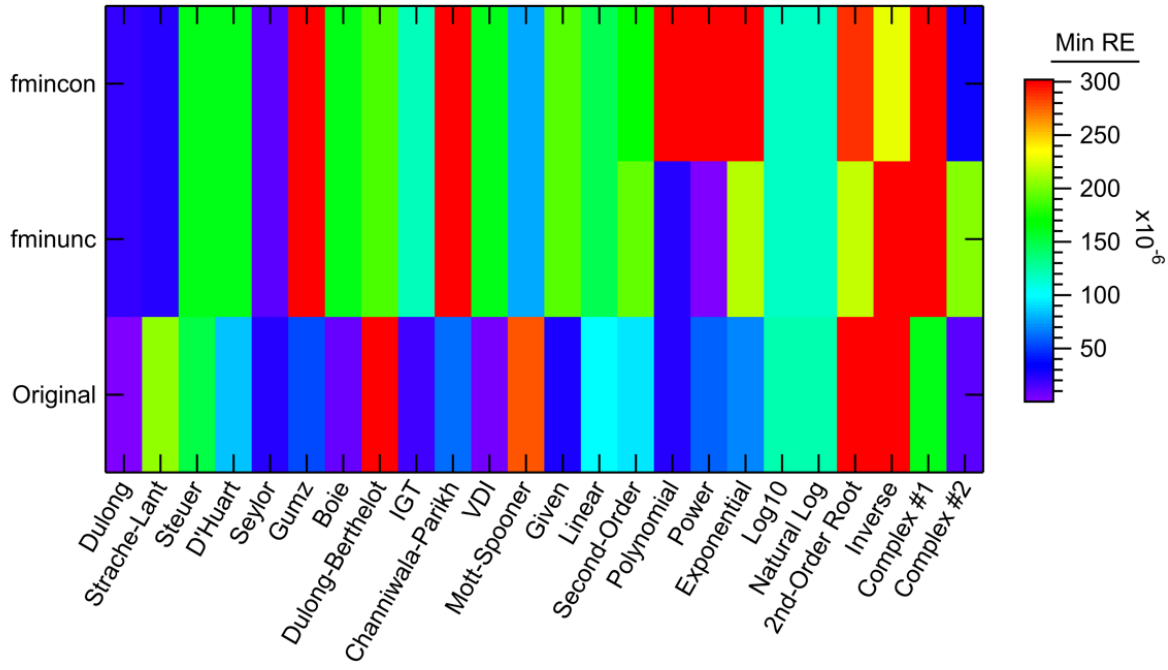

Figure D-56. Minimum relative error values in the fossil fuels comparison for each model form.

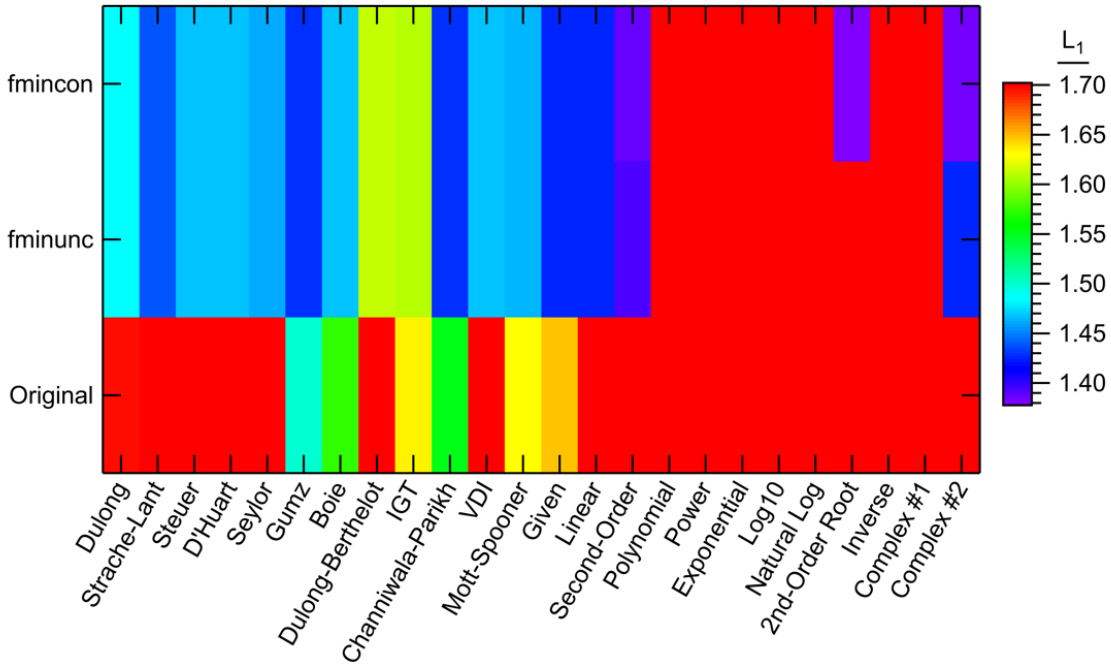

Figure D-57. L_1 norm values in the fossil fuels comparison for each model form.

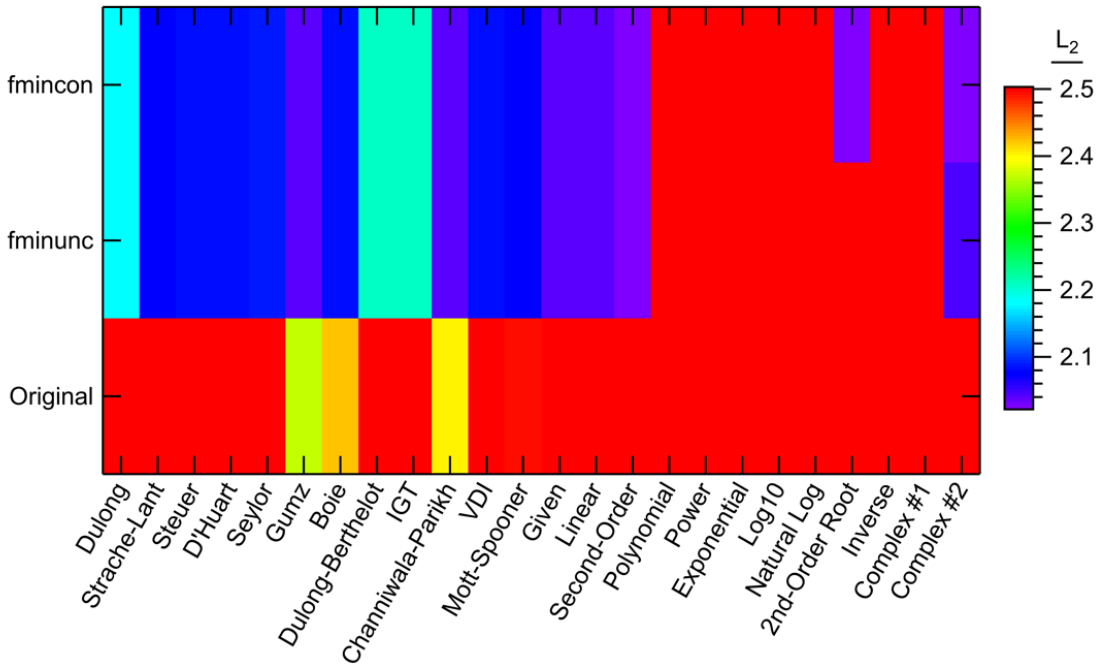

Figure D-58. L_2 norm values in the fossil fuels comparison for each model form.

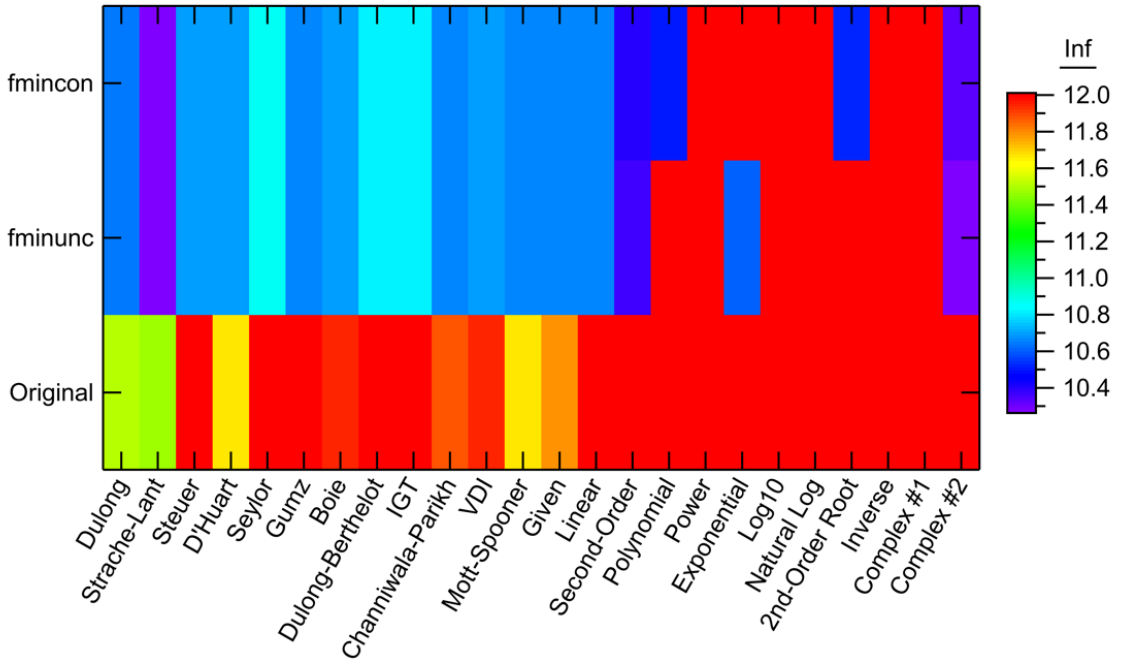

Figure D-59. Infinity norm values in the fossil fuels comparison for each model form.

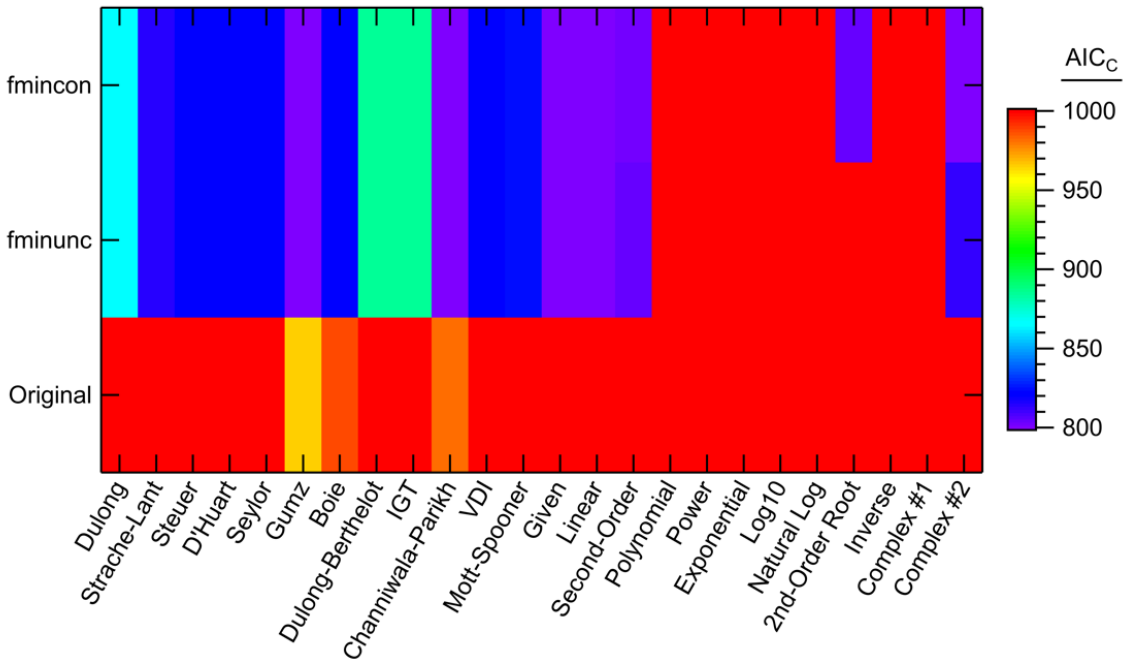

Figure D-60. AIC_c values in the fossil fuels comparison for each model form.

D.3.7 Biomass Data Set

Table D-10 gives the best results using the biomass data set. The biomass comparison found a greater difference using the new models compared to the literature models, however, just like the tar-only analysis, the biomass data set had a larger variability than the fossil fuels and other coal-based fuels. This is especially true of the three outlier samples discussed Section 7.3.3. A larger, more concise data set of biomass samples could bring the results of the literature and new models closer. Figure D-61 to Figure D-70 show the complete statistical results for the biomass data set comparison.

Table D-10. Complete Best Model Calculations Using the Biomass Data Set

	Statistic	**Value**	**Model**	**Optimizer**	**AIC_c**
Overall Best Performance	R^2	0.760	2nd-Order Root	fmincon	152.1
	SSE $(MJ/kg)^2$	353.5	2nd-Order Root	fmincon	152.1
	MSE $(MJ/kg)^2$	3.801	2nd-Order Root	fmincon	152.1
	Max RE (%)	106.2	Dulong	Original coeff.	194.9
	Avg RE (%)	7.41	2nd-Order Root	fmincon	152.1
	Min RE (%)	8.74×10^{-3}	Seylor	fmincon	159.6
	L_1 (MJ/kg)	1.123	Mott-Spooner	fminunc	157.3
	L_2 (MJ/kg)	1.950	2nd-Order Root	fmincon	152.1
	Infinity (MJ/kg)	9.231	2nd-Order Root	fmincon	152.1
	AIC_c	152.1	2nd-Order Root	fmincon	152.1
Best New Models	R^2	0.760	2nd-Order Root	fmincon	152.1
	SSE $(MJ/kg)^2$	353.5	2nd-Order Root	fmincon	152.1
	MSE $(MJ/kg)^2$	3.801	2nd-Order Root	fmincon	152.1
	Max RE (%)	108.2	2nd-Order Root	fmincon	152.1
	Avg RE (%)	7.41	2nd-Order Root	fmincon	152.1
	Min RE (%)	1.60×10^{-2}	Polynomial	fmincon	159.2
	L_1 (MJ/kg)	1.146	Exponential	fmincon	161.4
	L_2 (MJ/kg)	1.950	2nd-Order Root	fmincon	152.1
	Infinity (MJ/kg)	9.231	2nd-Order Root	fmincon	152.1
	AIC_c	152.1	2nd-Order Root	fmincon	152.1

Table D-10. Complete Best Model Calculations Using the Biomass Data Set, CONTINUED

	Statistic	Value	Model	Optimizer	AIC_c
Best Literature Models	R^2	0.717	Mott-Spooner	fminunc	157.3
	SSE $(MJ/kg)^2$	417.2	Mott-Spooner	fmincon	157.3
	MSE $(MJ/kg)^2$	4.486	Mott-Spooner	fmincon	157.3
	Max RE (%)	106.2	Dulong	Original coeff.	194.9
	Avg RE (%)	7.59	Mott-Spooner	fminunc	157.3
	Min RE (%)	8.74×10^{-3}	Seylor	fmincon	159.6
	L_1 (MJ/kg)	1.123	Mott-Spooner	fminunc	157.3
	L_2 (MJ/kg)	2.118	Mott-Spooner	fmincon	157.3
	Infinity (MJ/kg)	9.790	Dulong	Original coeff.	194.9
	AIC_c	153.0	Gumz	fmincon	153.0
Best Literature Models with Original Coefficients	R^2	0.666	Boie	Original coeff.	177.3
	SSE $(MJ/kg)^2$	522.8	Seylor	Original coeff.	171.3
	MSE $(MJ/kg)^2$	5.621	Seylor	Original coeff.	171.3
	Max RE (%)	106.2	Dulong	Original coeff.	194.9
	Avg RE (%)	8.60	Seylor	Original coeff.	171.3
	Min RE (%)	1.05×10^{-2}	VDI	Original coeff.	174.6
	L_1 (MJ/kg)	1.320	Seylor	Original coeff.	171.3
	L_2 (MJ/kg)	2.371	Seylor	Original coeff.	171.3
	Infinity (MJ/kg)	9.790	Dulong	Original coeff.	194.9
	AIC_c	171.3	Seylor	Original coeff.	171.3

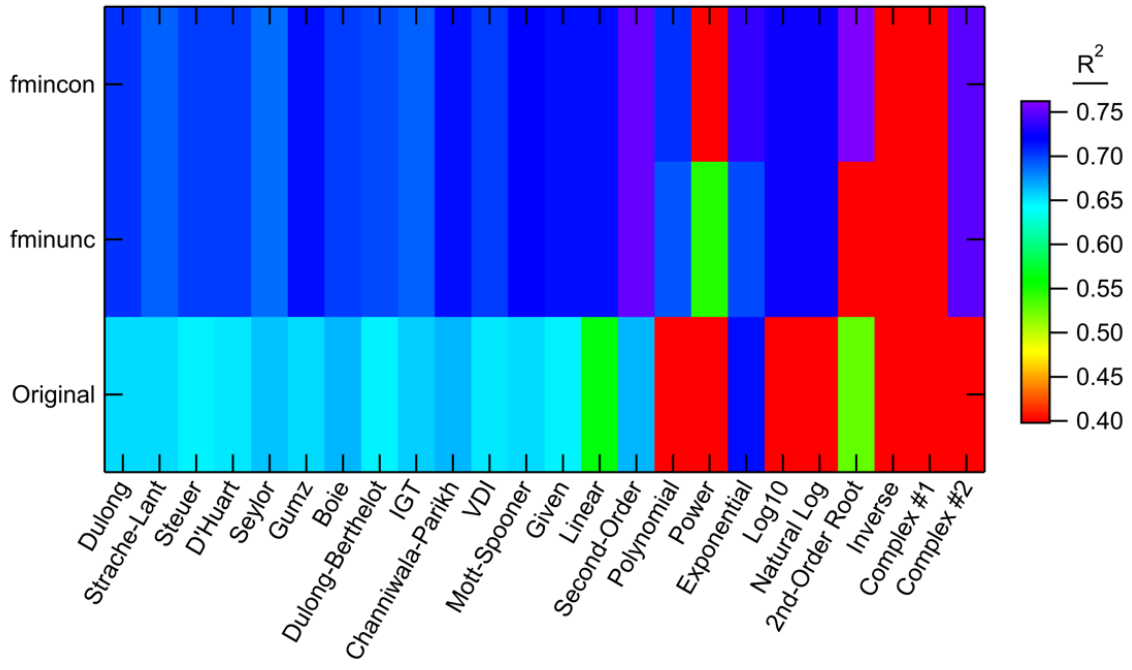

Figure D-61. R^2 values in the biomass comparison for each model form.

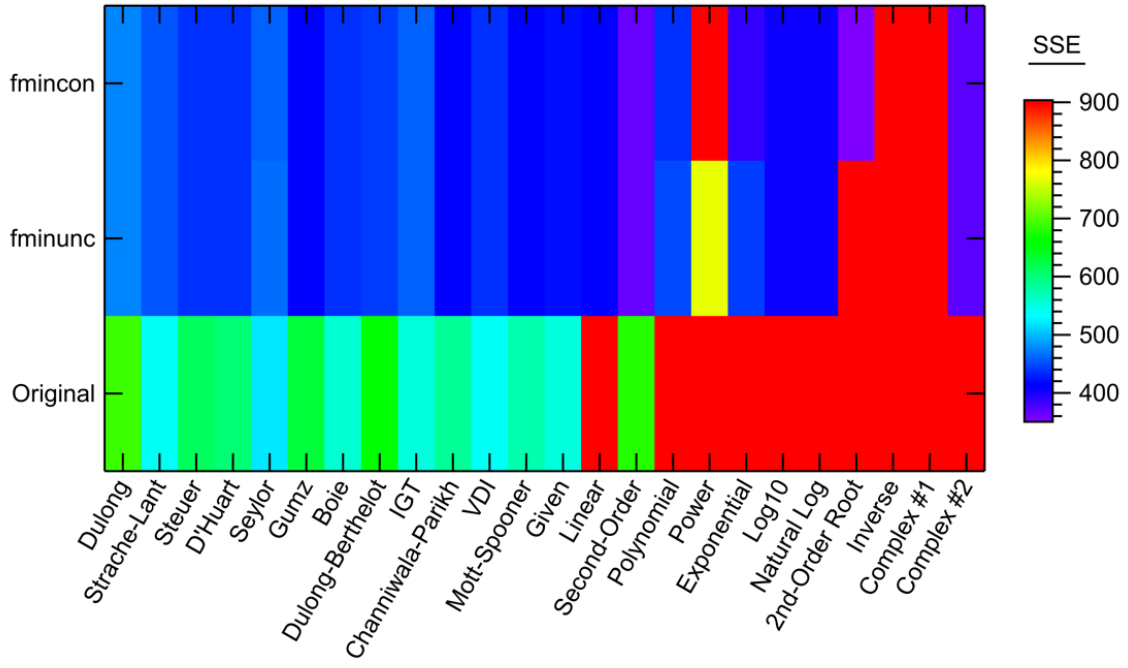

Figure D-62. SSE values in the biomass comparison for each model form.

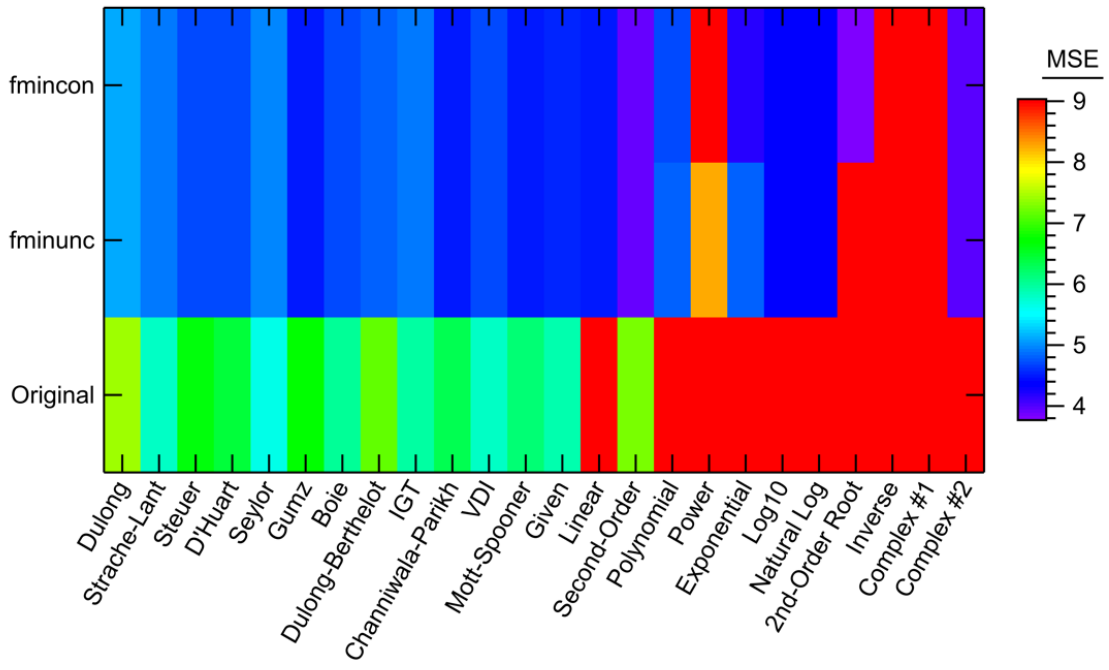

Figure D-63. MSE values in the biomass comparison for each model form.

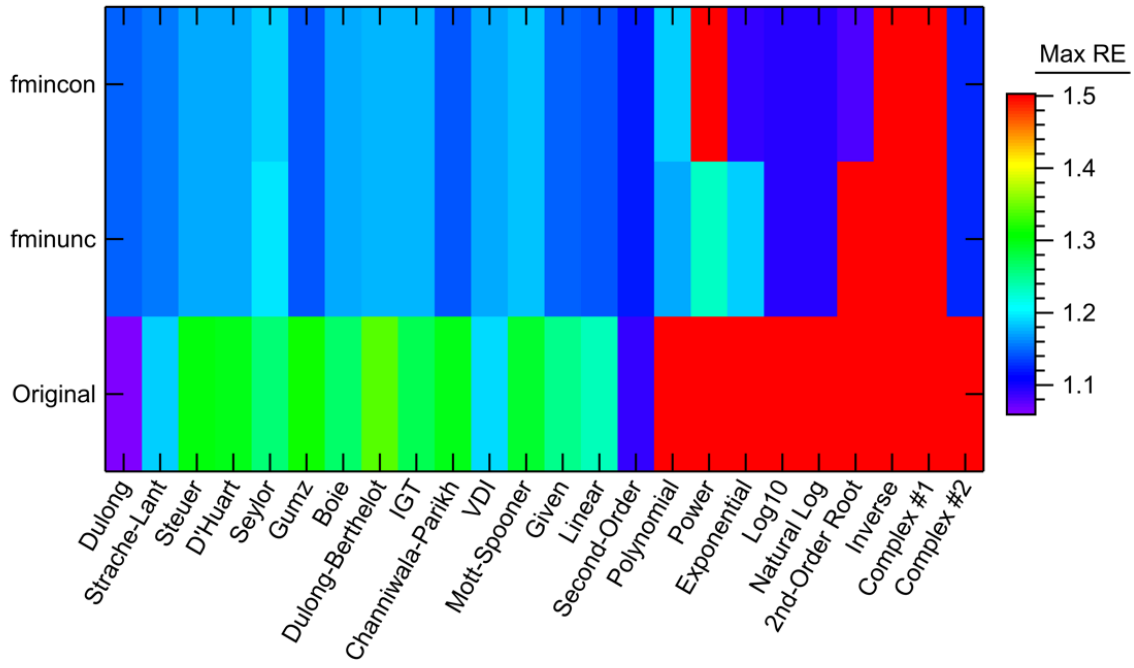

Figure D-64. Maximum relative error values in the biomass comparison for each model form.

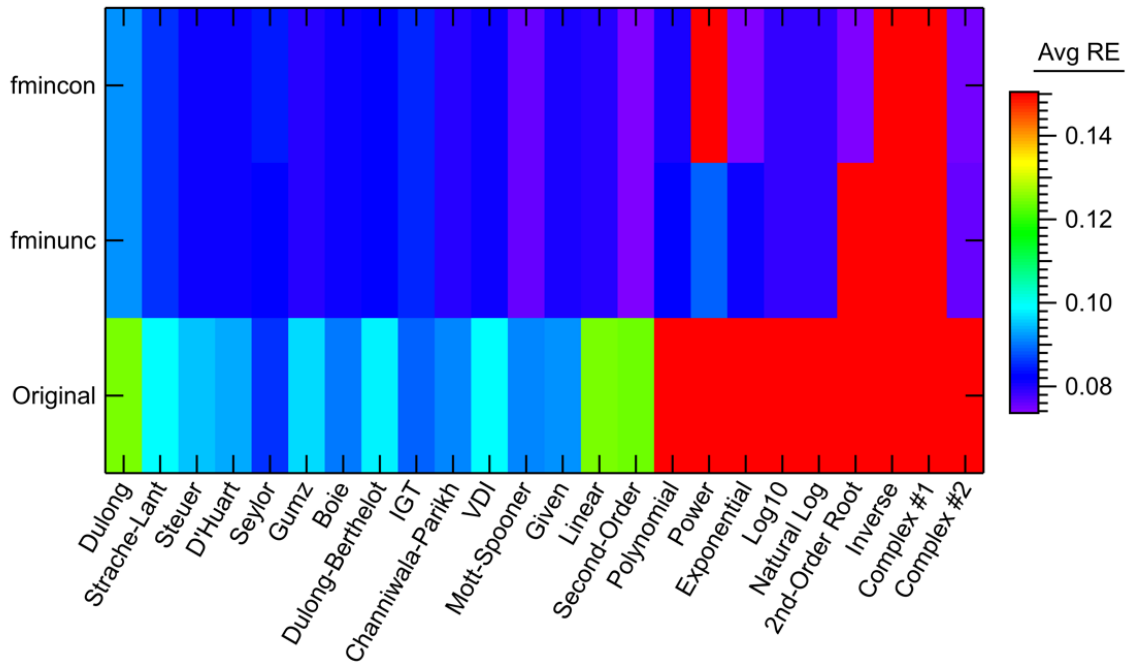

Figure D-65. Average relative error values in the biomass comparison for each model form.

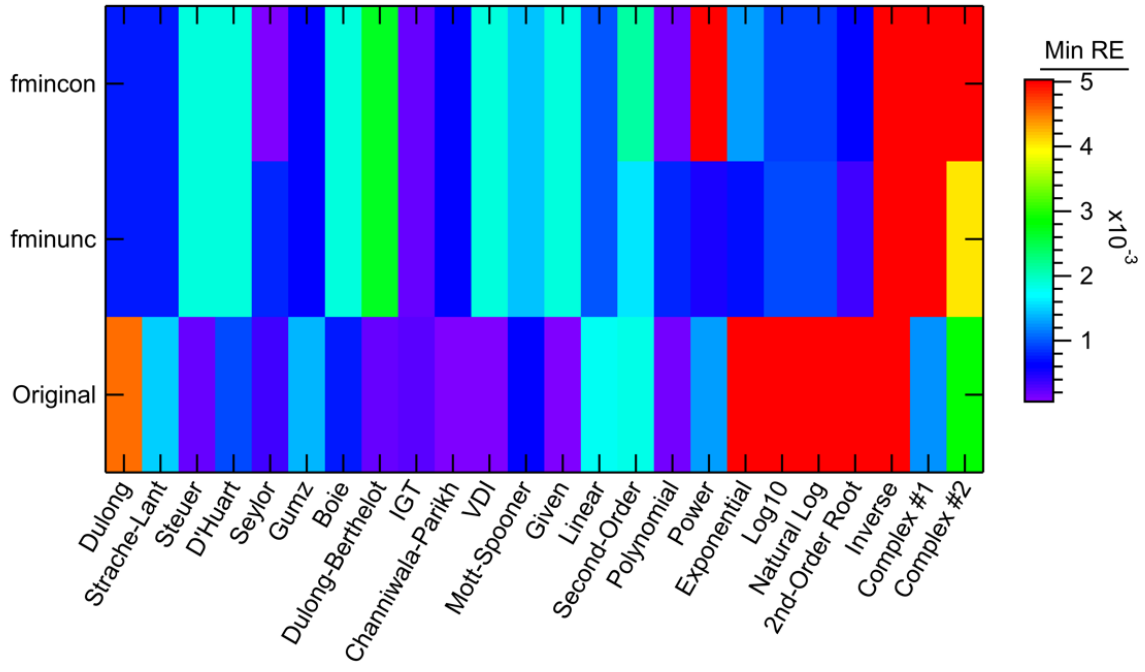

Figure D-66. Minimum relative error values in the biomass comparison for each model form.

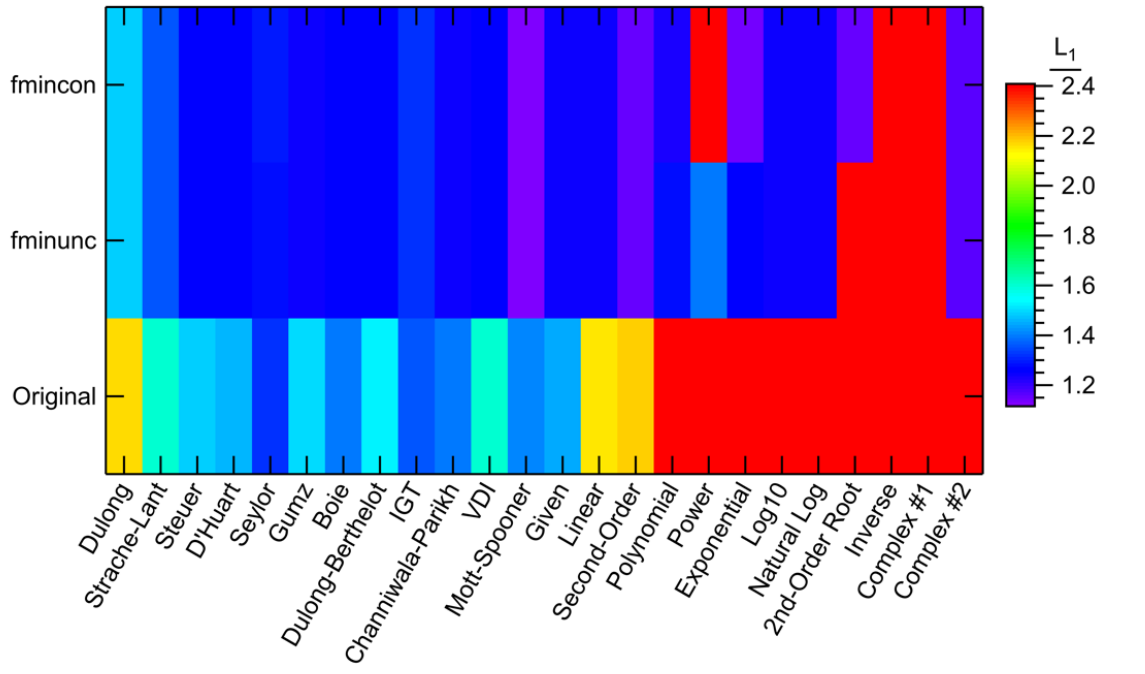

Figure D-67. L_1 norm values in the biomass comparison for each model form.

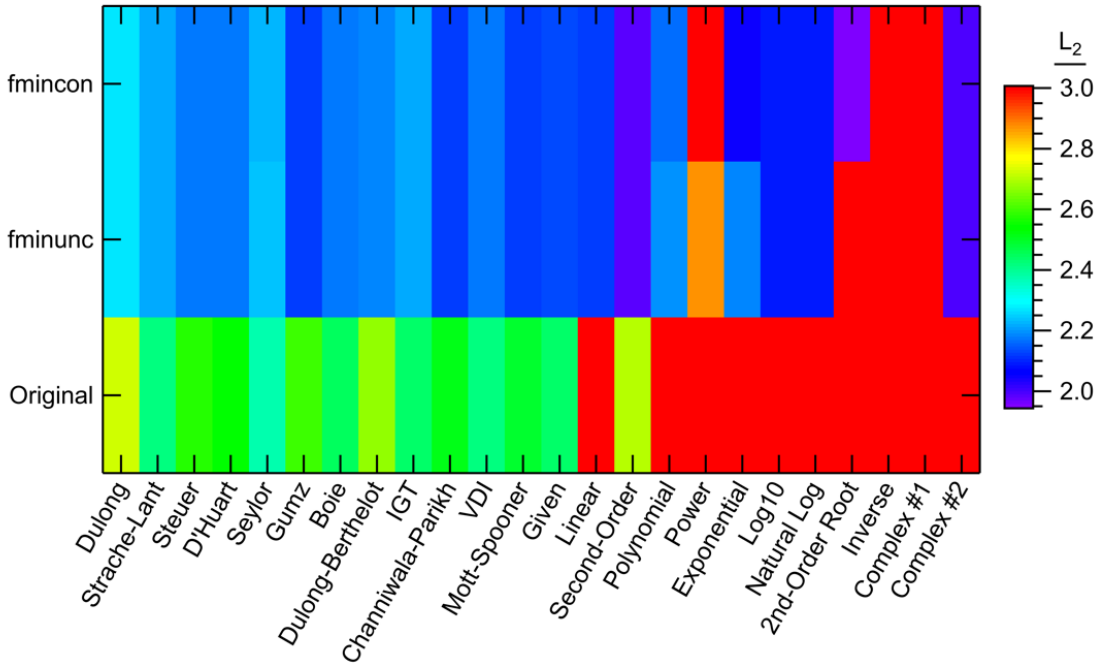

Figure D-68. L_2 norm values in the biomass comparison for each model form.

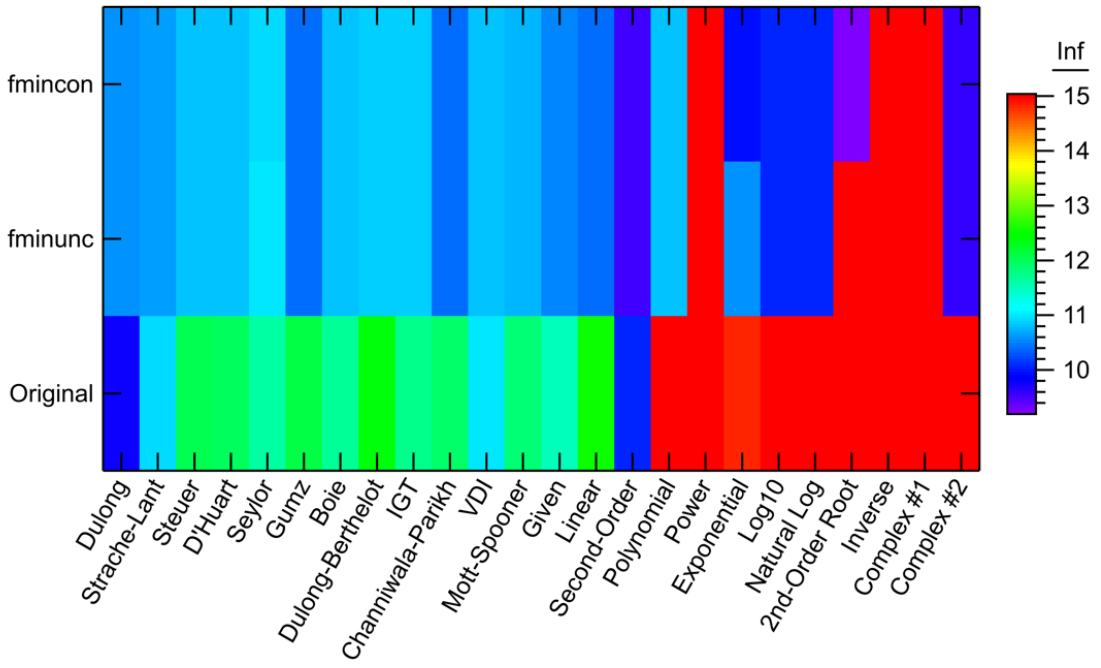

Figure D-69. Infinity norm values in the biomass comparison for each model form.

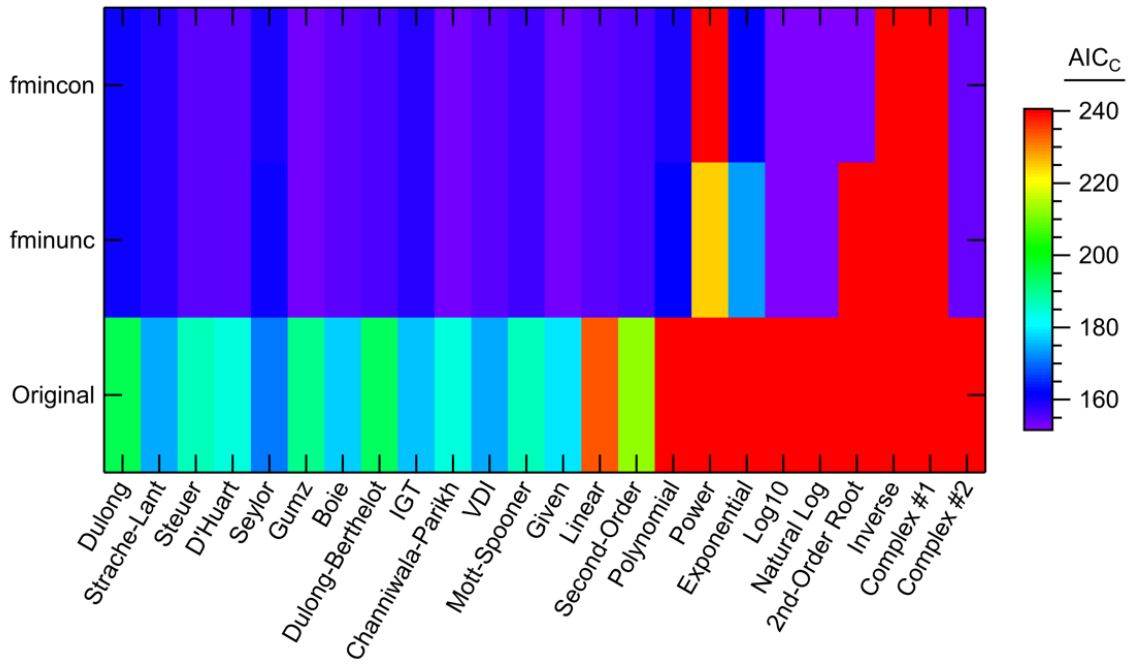

Figure D-70. AIC_c values in the biomass comparison for each model form.

D.3.8 Other Fuels Data Set

Table D-11 gives the best results using the "other" fuels data set. The other fuels data set was a bit of a catch-all subset which included the bulk of the non-traditional fuels. The extra variability in the chemical and structural composition of these non-traditional fuels compared to the fossil and biomass fuels leads to different model forms giving the best calculations for heating values. Like most of the other comparisons, however, there is not enough improvement using the new model forms over the literature model forms. Figure D-71 to Figure D-80 show the complete statistical results for the other fuels data set comparison.

Table D-11. Complete Best Model Calculations Using the Other Fuels Data Set

	Statistic	Value	Model	Optimizer	AIC_c
Overall Best Performance	R^2	0.861	2nd-Order Root	fmincon	240.1
	SSE $(MJ/kg)^2$	949.3	2nd-Order Root	fmincon	240.1
	MSE $(MJ/kg)^2$	10.55	2nd-Order Root	fmincon	240.1
	Max RE (%)	221.6	2nd-Order Root	fmincon	240.1
	Avg RE (%)	12.26	Second-Order	fmincon	247.3
	Min RE (%)	3.39×10^{-3}	Linear	fminunc	240.1
	L_1 (MJ/kg)	2.287	Second-Order	fminunc	248.5
	L_2 (MJ/kg)	3.248	2nd-Order Root	fmincon	240.1
	Infinity (MJ/kg)	13.81	2nd-Order Root	fminunc	245.9
	AIC_c	239.0	Channiwala-Parikh	fmincon	239.0
Best New Models	R^2	0.861	2nd-Order Root	fmincon	240.1
	SSE $(MJ/kg)^2$	949.3	2nd-Order Root	fmincon	240.1
	MSE $(MJ/kg)^2$	10.55	2nd-Order Root	fmincon	240.1
	Max RE (%)	221.6	2nd-Order Root	fmincon	240.1
	Avg RE (%)	12.26	Second-Order	fmincon	247.3
	Min RE (%)	3.39×10^{-3}	Linear	fminunc	240.1
	L_1 (MJ/kg)	2.287	Second-Order	fminunc	248.5
	L_2 (MJ/kg)	3.248	2nd-Order Root	fmincon	240.1
	Infinity (MJ/kg)	13.81	2nd-Order Root	fminunc	245.9
	AIC_c	240.1	2nd-Order Root	fmincon	240.1
Best Literature Models	R^2	0.838	Channiwala-Parikh	fminunc	239.0
	SSE $(MJ/kg)^2$	1108	Channiwala-Parikh	fmincon	239.0
	MSE $(MJ/kg)^2$	12.31	Channiwala-Parikh	fmincon	239.0
	Max RE (%)	241.0	Dulong	fmincon	252.2
	Avg RE (%)	12.61	Gumz	fmincon	239.0
	Min RE (%)	1.83×10^{-2}	Boie	Original coeff.	291.0
	L_1 (MJ/kg)	2.289	Gumz	fmincon	239.0
	L_2 (MJ/kg)	3.509	Channiwala-Parikh	fmincon	239.0
	Infinity (MJ/kg)	14.27	Seylor	fmincon	261.9
	AIC_c	239.0	Channiwala-Parikh	fmincon	239.0
Best Literature Models with Original Coefficients	R^2	0.806	Strache-Lant	Original coeff.	312.4
	SSE $(MJ/kg)^2$	2027	Boie	Original coeff.	291.0
	MSE $(MJ/kg)^2$	22.52	Boie	Original coeff.	291.0
	Max RE (%)	305.7	Dulong	Original coeff.	294.9
	Avg RE (%)	17.16	Boie	Original coeff.	291.0
	Min RE (%)	1.83×10^{-2}	Boie	Original coeff.	291.0
	L_1 (MJ/kg)	2.933	Boie	Original coeff.	291.0
	L_2 (MJ/kg)	4.746	Boie	Original coeff.	291.0
	Infinity (MJ/kg)	19.04	Gumz	Original coeff.	297.3
	AIC_c	291.0	Boie	Original coeff.	291.0

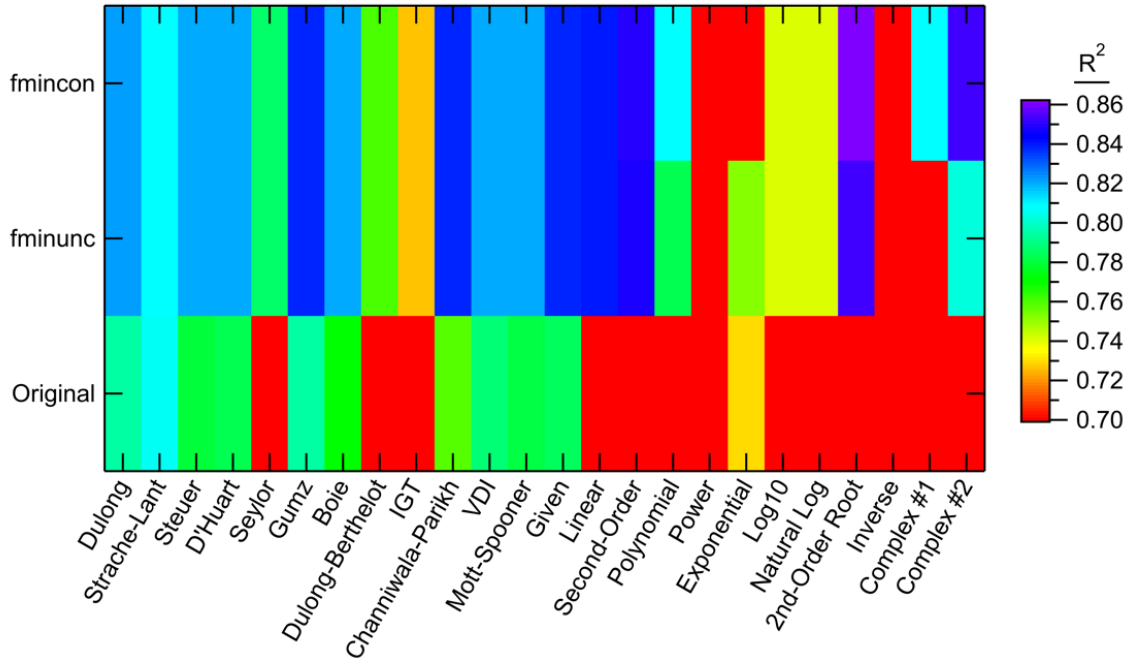

Figure D-71. R^2 values in the other fuels comparison for each model form.

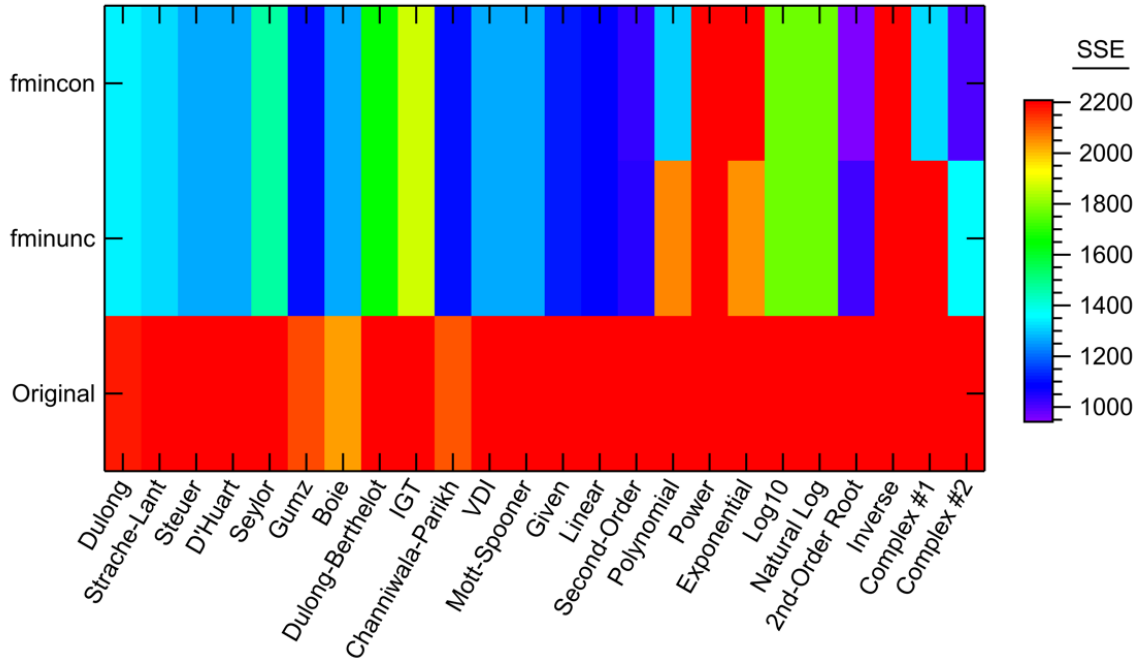

Figure D-72. SSE values in the other fuels comparison for each model form.

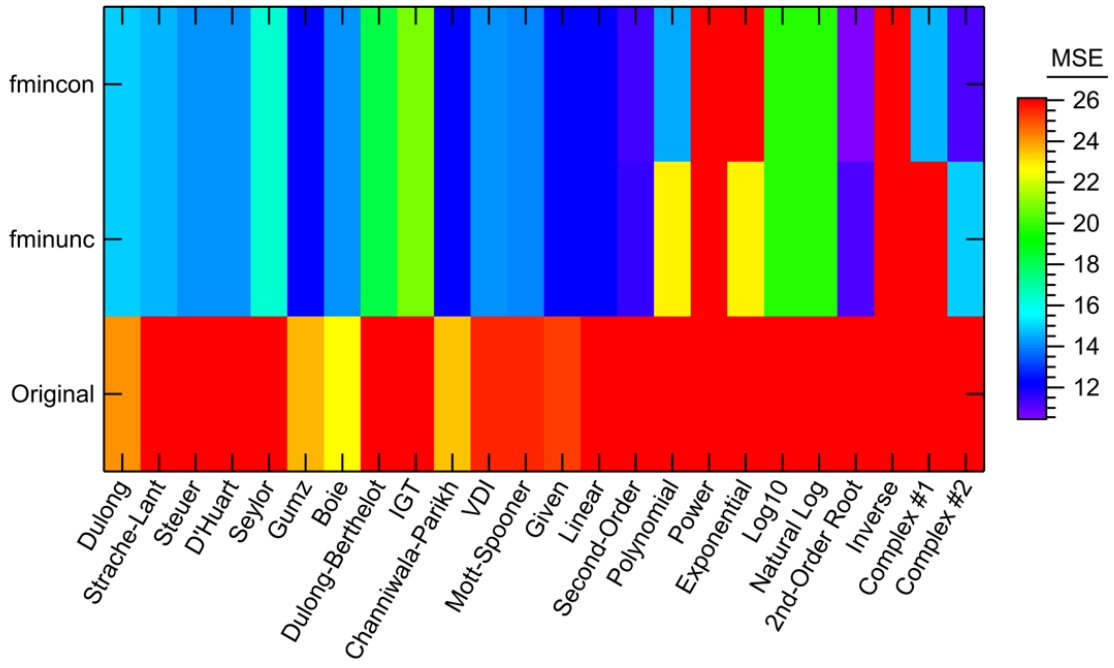

Figure D-73. MSE values in the other fuels comparison for each model form.

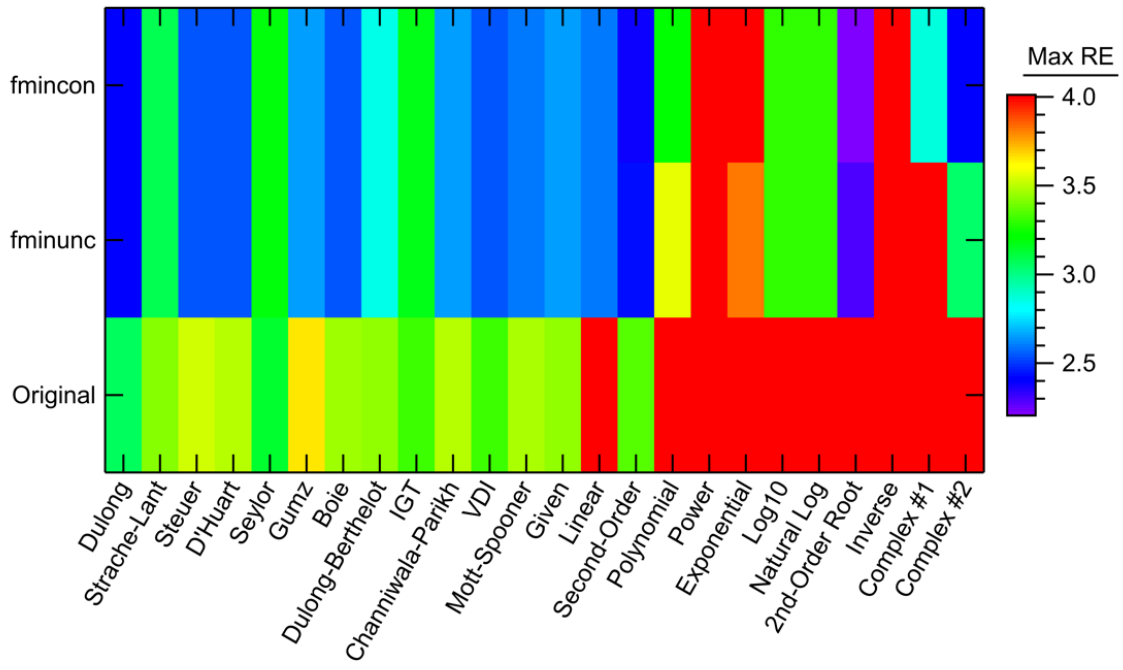

Figure D-74. Maximum relative error values in the other fuels comparison for each model form.

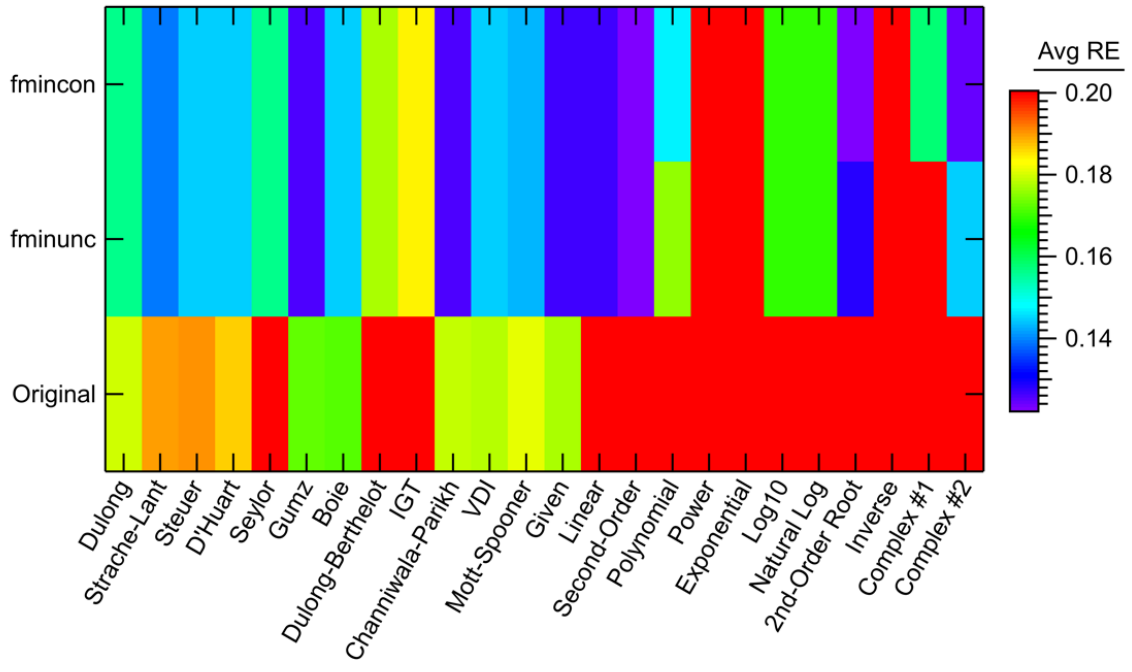

Figure D-75. Average relative error values in the other fuels comparison for each model form.

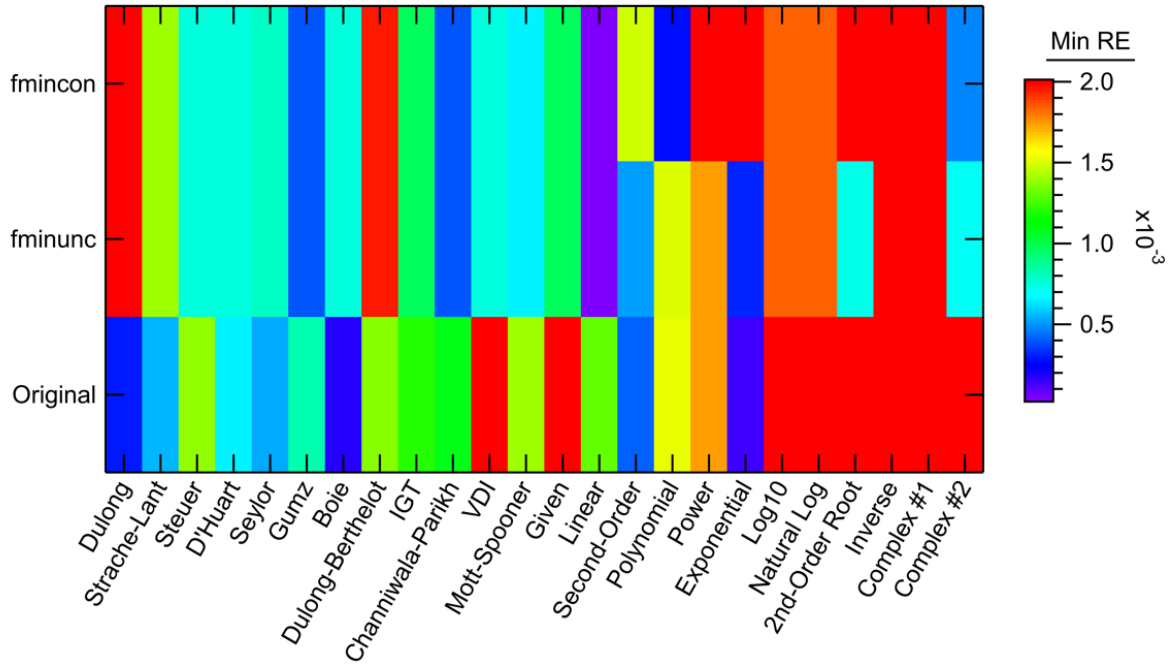

Figure D-76. Minimum relative error values in the other fuels comparison for each model form.

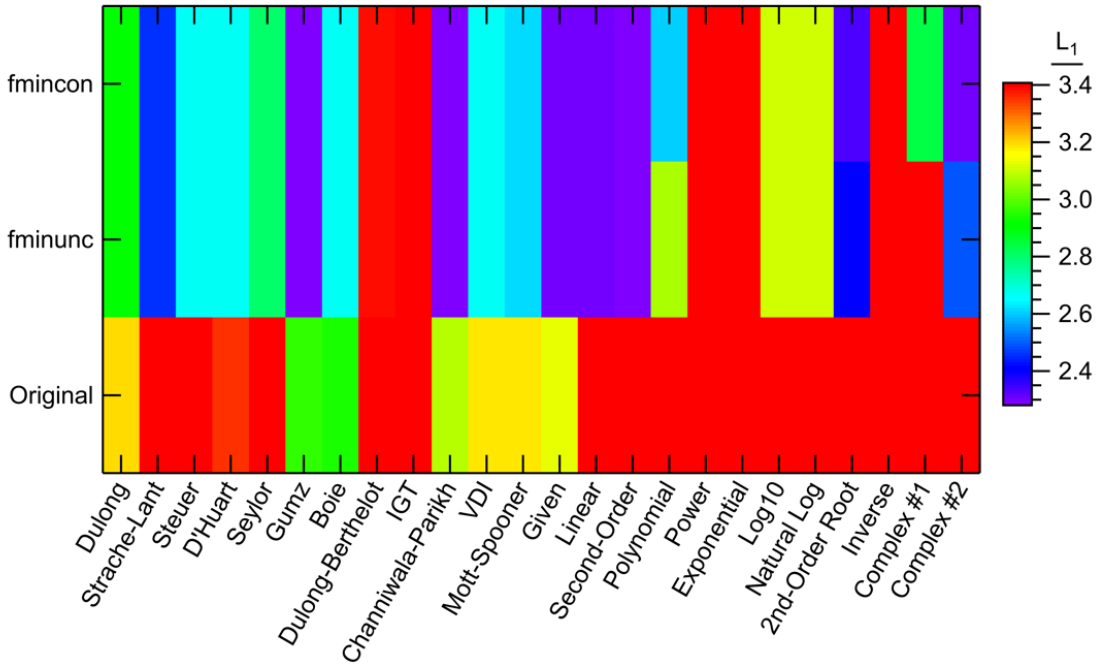

Figure D-77. L_1 norm values in the other fuels comparison for each model form.

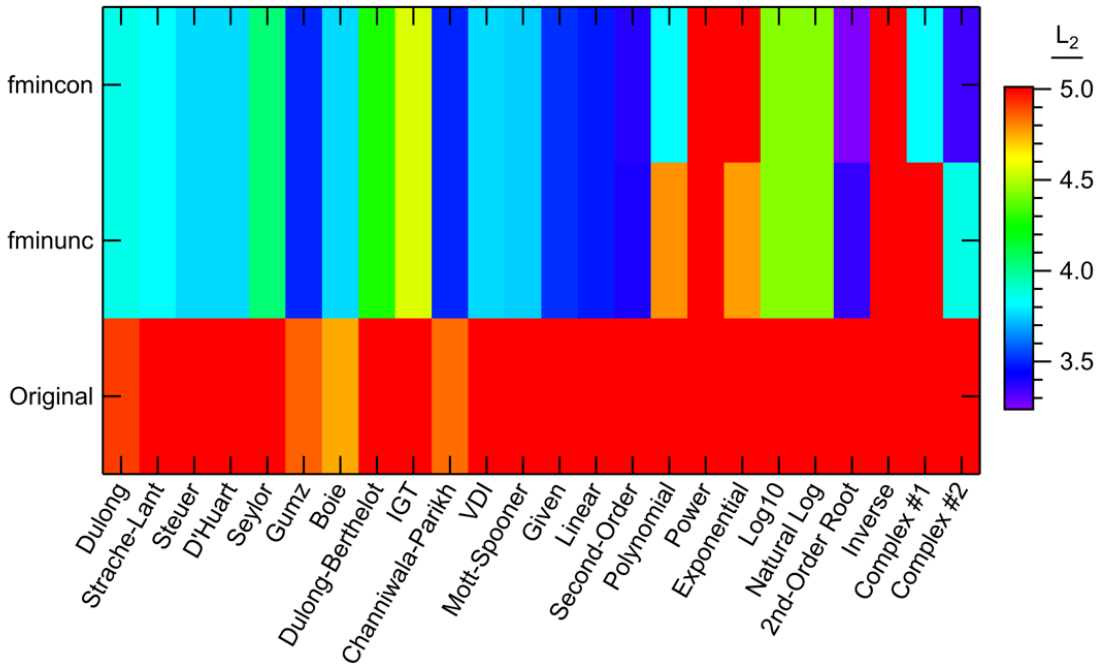

Figure D-78. L_2 norm values in the other fuels comparison for each model form.

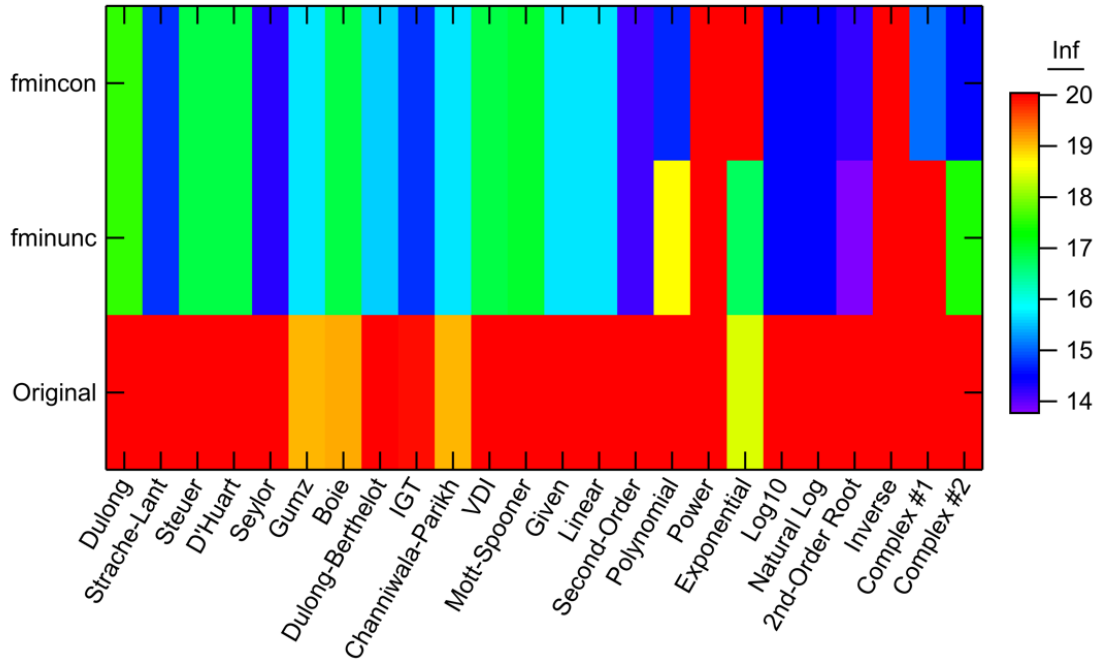

Figure D-79. Infinity norm values in the other fuels comparison for each model form.

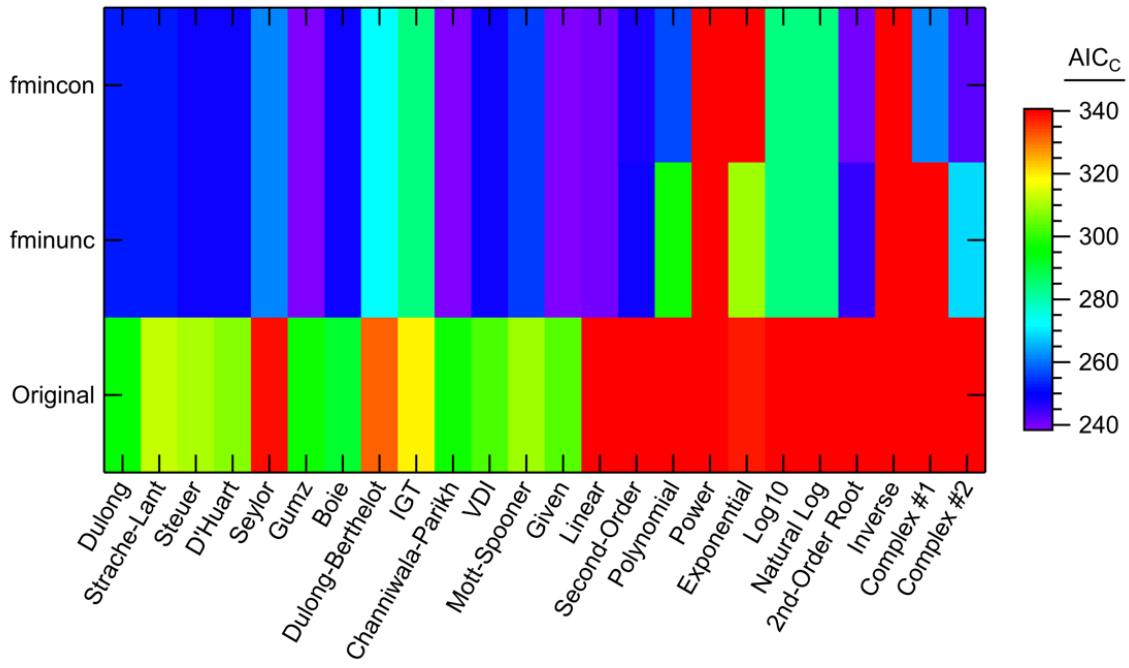

Figure D-80. AIC_c values in the other fuels comparison for each model form.

D.3.9 Full Data Set

Table D-12 shows the complete best results of the comparison using the full data set. Again, the full data set comparison showed some very slight improvement when using the new models over the literature models, but not enough to justify the extra fitted coefficients. For most of the data sets, there is little potential for great improvement using the new models instead of the literature models. This conclusion might change with a more extensive set of fuel samples. Figure D-81 to Figure D-90 show the complete statistical results of the full data set comparison.

Table D-12. Complete Best Model Calculations Using the Full Data Set

	Statistic	**Value**	**Model**	**Optimizer**	**AIC_c**
Overall Best Performance	R^2	0.896	2nd-Order Root	fmincon	1300
	SSE $(MJ/kg)^2$	4313	2nd-Order Root	fmincon	1300
	MSE $(MJ/kg)^2$	6.134	2nd-Order Root	fmincon	1300
	Max RE (%)	305.7	Dulong	Original coeff.	1557
	Avg RE (%)	6.59	2nd-Order Root	fmincon	1300
	Min RE (%)	1.59×10^{-4}	Seylor	fminunc	1347
	L_1 (MJ/kg)	1.605	Second-Order	fmincon	1309
	L_2 (MJ/kg)	2.477	2nd-Order Root	fmincon	1300
	Infinity (MJ/kg)	15.79	Polynomial	fmincon	1486
	AIC_c	1300	2nd-Order Root	fmincon	1300
Best New Models	R^2	0.896	2nd-Order Root	fmincon	1300
	SSE $(MJ/kg)^2$	4313	2nd-Order Root	fmincon	1300
	MSE $(MJ/kg)^2$	6.134	2nd-Order Root	fmincon	1300
	Max RE (%)	311.4	2nd-Order Root	fmincon	1300
	Avg RE (%)	6.59	2nd-Order Root	fmincon	1300
	Min RE (%)	1.92×10^{-4}	Power	fminunc	1892
	L_1 (MJ/kg)	1.605	Second-Order	fmincon	1309
	L_2 (MJ/kg)	2.477	2nd-Order Root	fmincon	1300
	Infinity (MJ/kg)	15.79	Polynomial	fmincon	1486
	AIC_c	1300	2nd-Order Root	fmincon	1300

Table D-12. Complete Best Model Calculations Using the Full Data Set, CONTINUED

	Statistic	Value	Model	Optimizer	AIC_c
Best Literature Models	R^2	0.893	Given	fmincon	1304
	SSE $(MJ/kg)^2$	4418	Given	fmincon	1304
	MSE $(MJ/kg)^2$	6.285	Given	fmincon	1304
	Max RE (%)	305.7	Dulong	Original coeff.	1557
	Avg RE (%)	6.71	Given	fminunc	1304
	Min RE (%)	1.59×10^{-4}	Seylor	fminunc	1347
	L_1 (MJ/kg)	1.622	Given	fminunc	1304
	L_2 (MJ/kg)	2.507	Given	fmincon	1304
	Infinity (MJ/kg)	17.52	Seylor	fmincon	1347
	AIC_c	1304	Given	fmincon	1304
Best Literature Models with Original Coefficients	R^2	0.892	Dulong	Original coeff.	1557
	SSE $(MJ/kg)^2$	5626	Boie	Original coeff.	1472
	MSE $(MJ/kg)^2$	8.003	Boie	Original coeff.	1472
	Max RE (%)	305.7	Dulong	Original coeff.	1557
	Avg RE (%)	7.24	Boie	Original coeff.	1472
	Min RE (%)	3.78×10^{-4}	Dulong	Original coeff.	1557
	L_1 (MJ/kg)	1.681	Gumz	Original coeff.	1485
	L_2 (MJ/kg)	2.829	Boie	Original coeff.	1472
	Infinity (MJ/kg)	19.04	Gumz	Original coeff.	1485
	AIC_c	1472	Boie	Original coeff.	1472

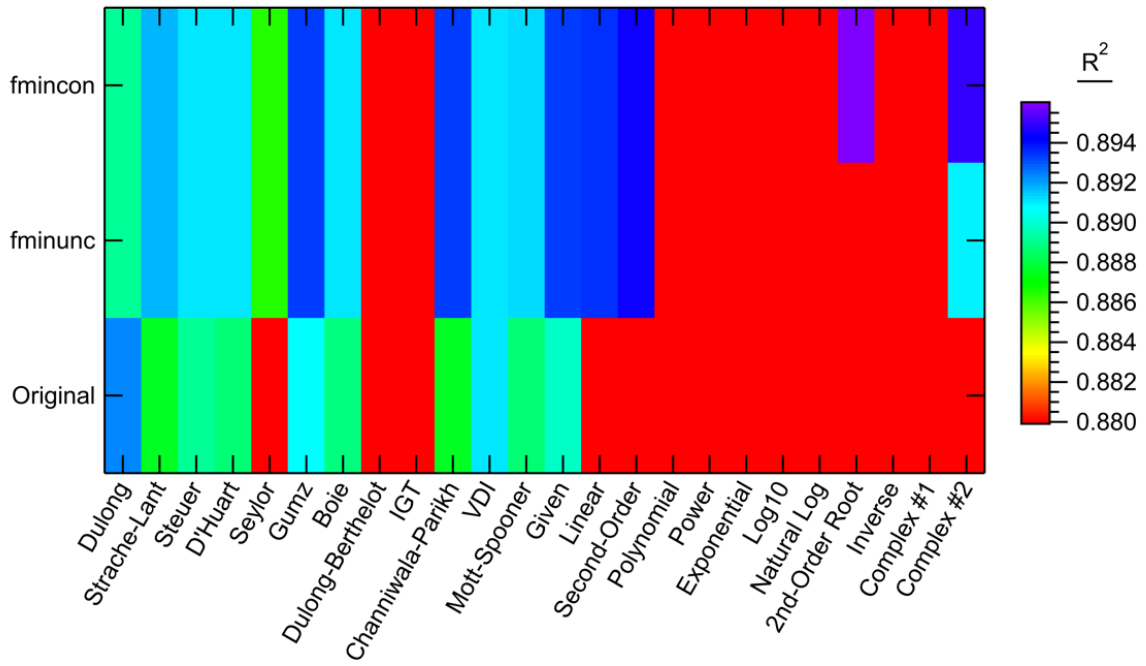

Figure D-81. R^2 values in the full data set comparison for each model form.

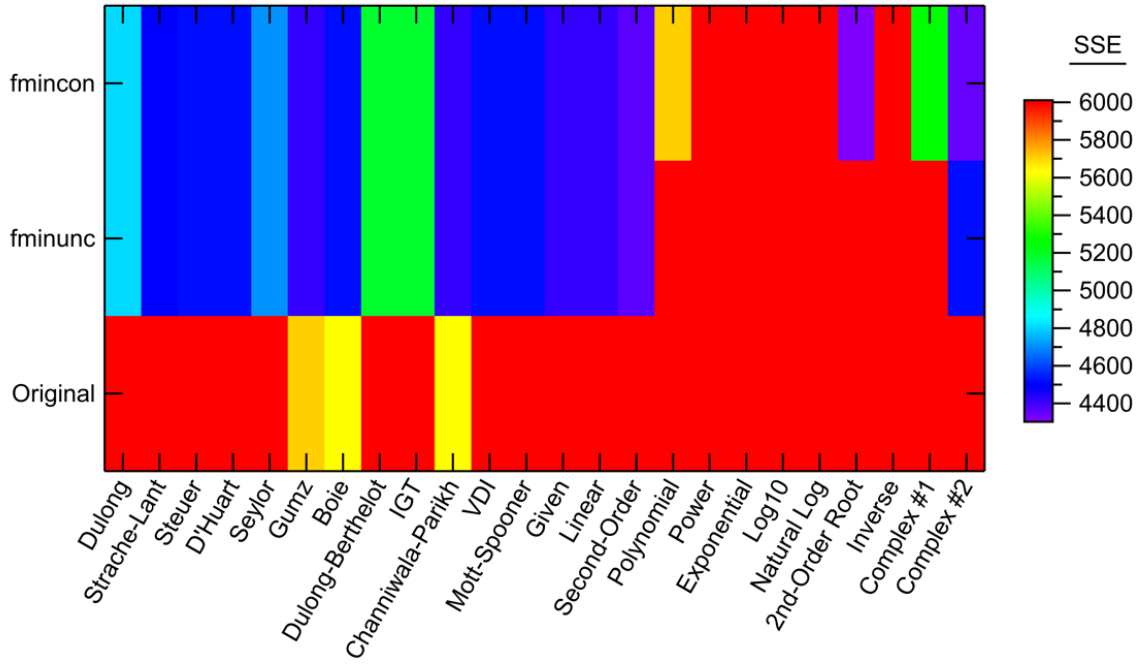

Figure D-82. SSE values in the full data set comparison for each model form.

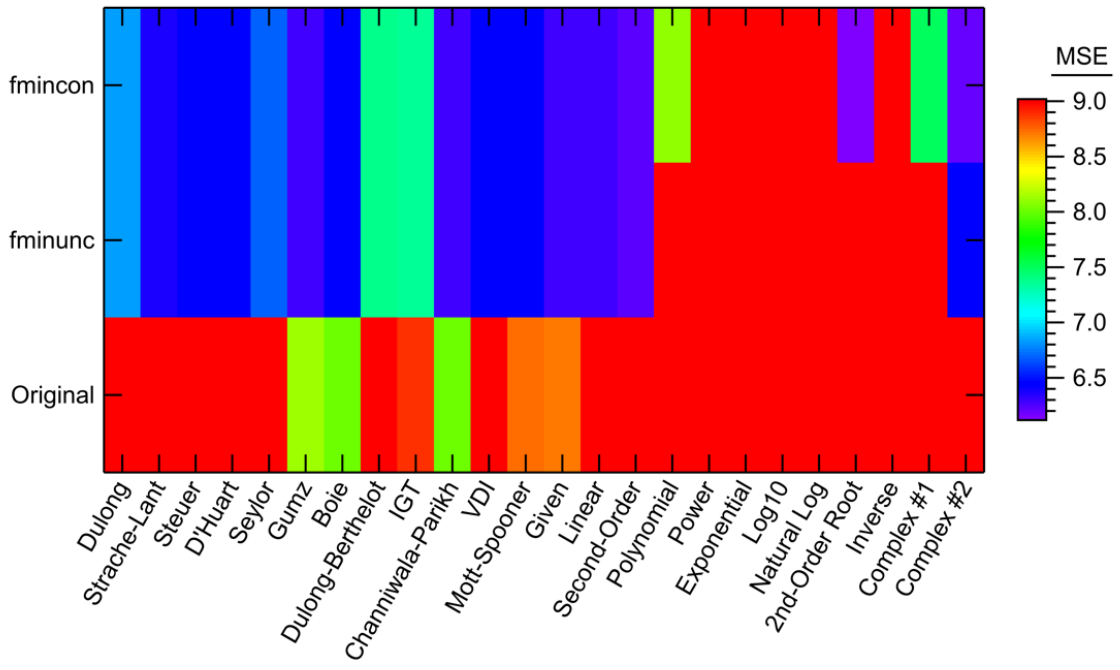

Figure D-83. MSE values in the full data set comparison for each model form.

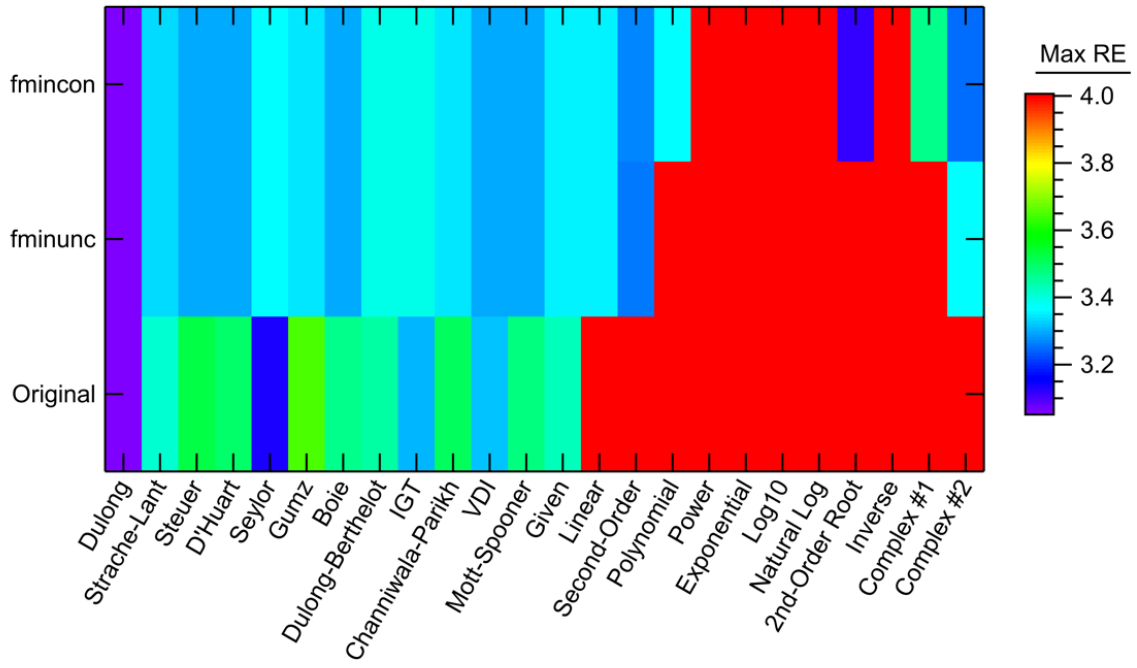

Figure D-84. Maximum relative error values in the full data set comparison for each model form.

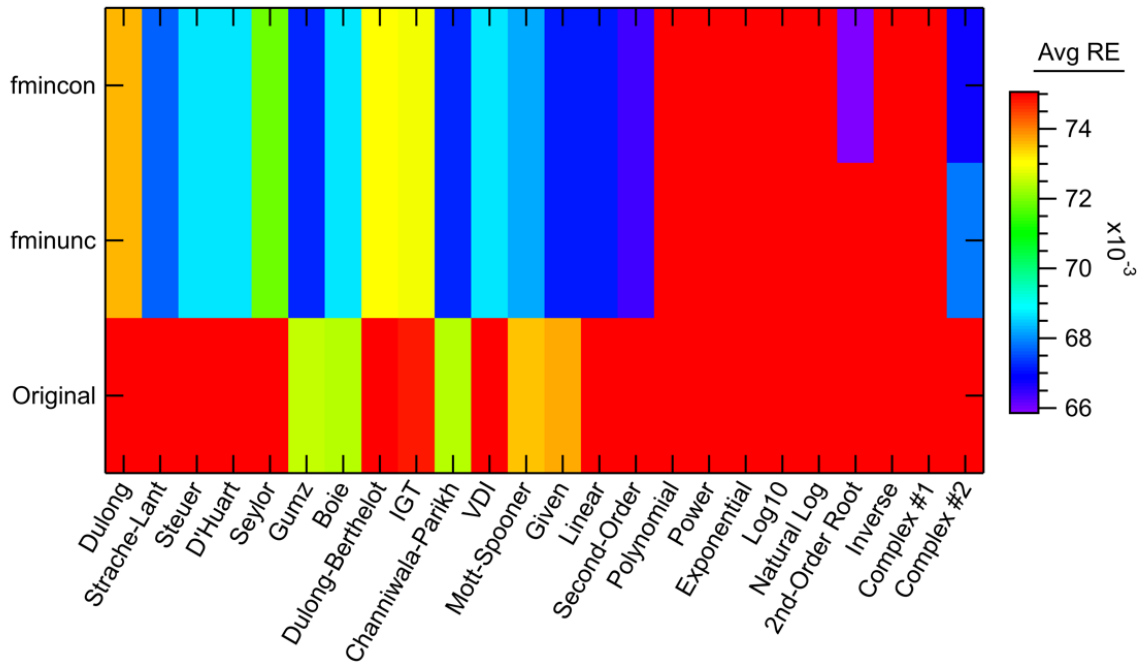

Figure D-85. Average relative error values in the full data set comparison for each model form.

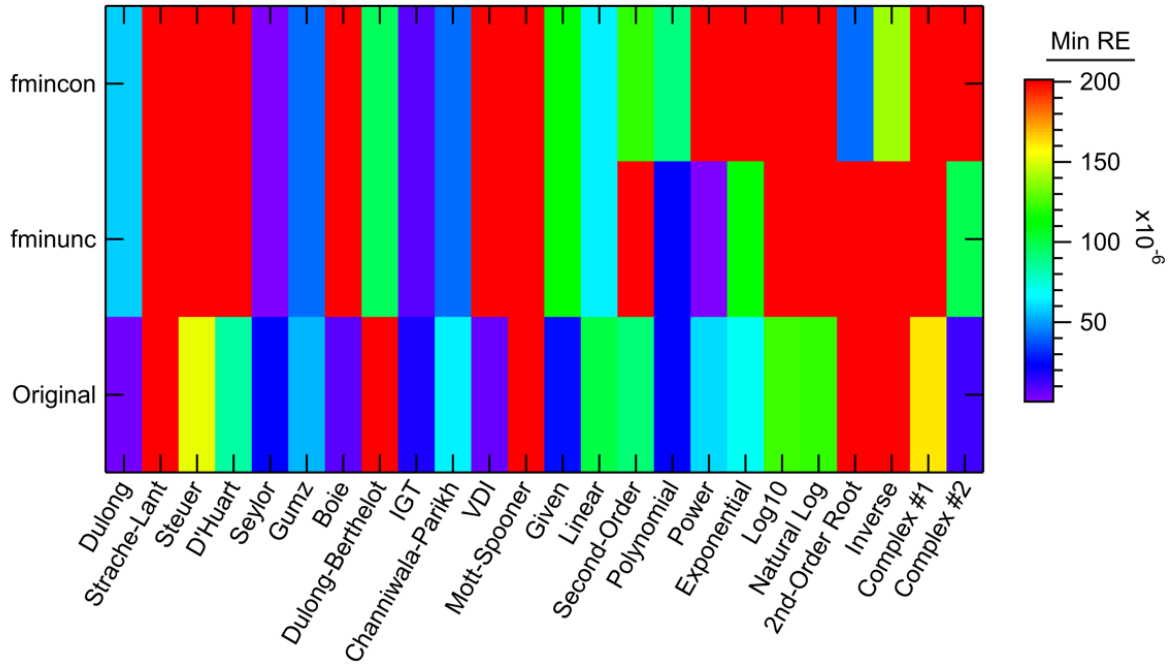

Figure D-86. Minimum relative error values in the full data set comparison for each model form.

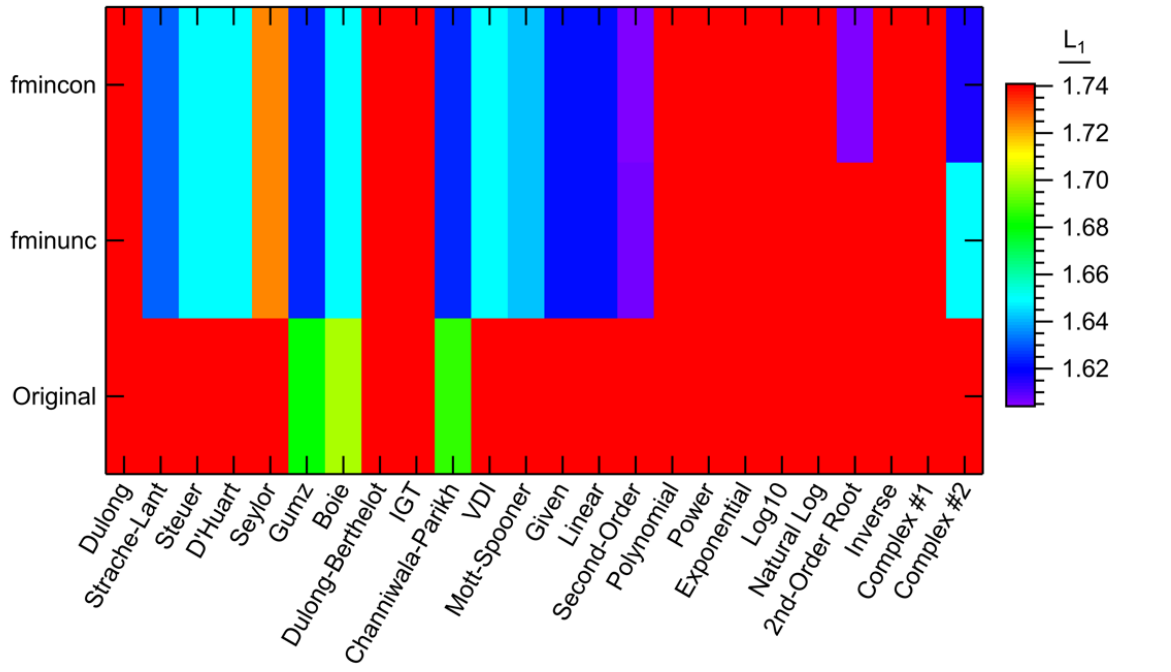

Figure D-87. L_1 norm values in the full data set comparison for each model form.

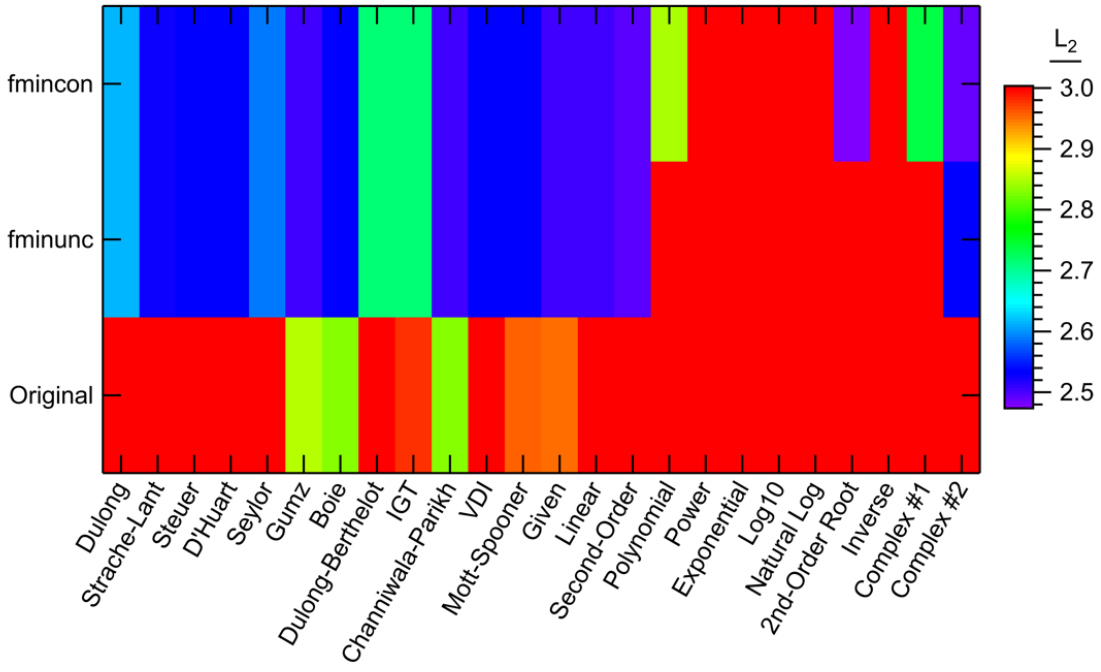

Figure D-88. L_2 norm values in the full data set comparison for each model form.

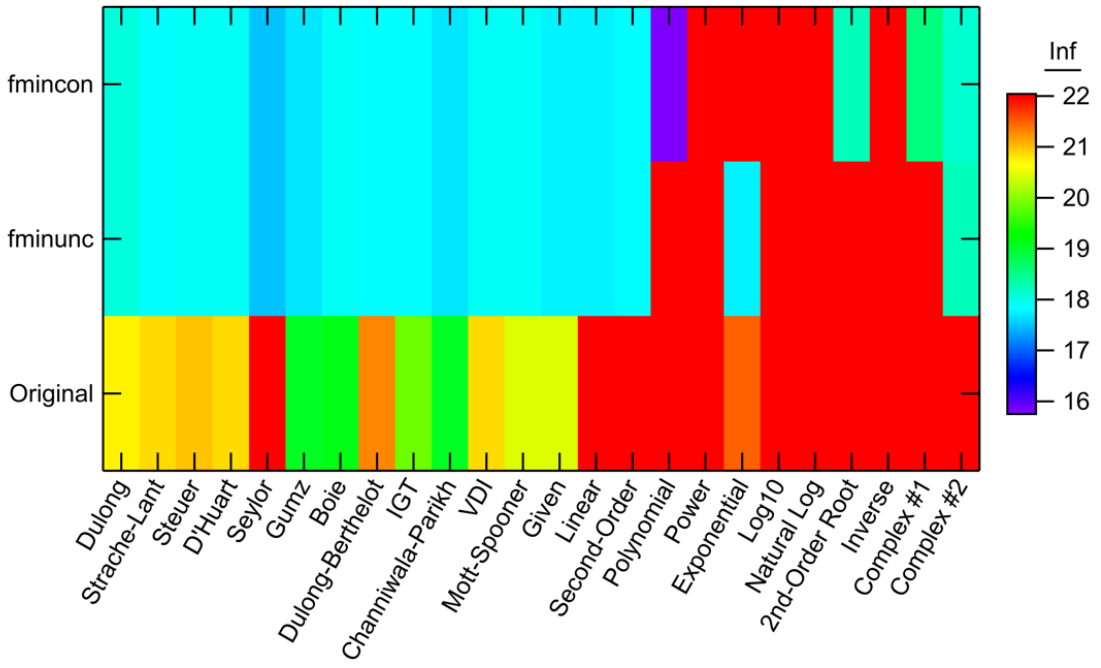

Figure D-89. Infinity norm values in the full data set comparison for each model form.

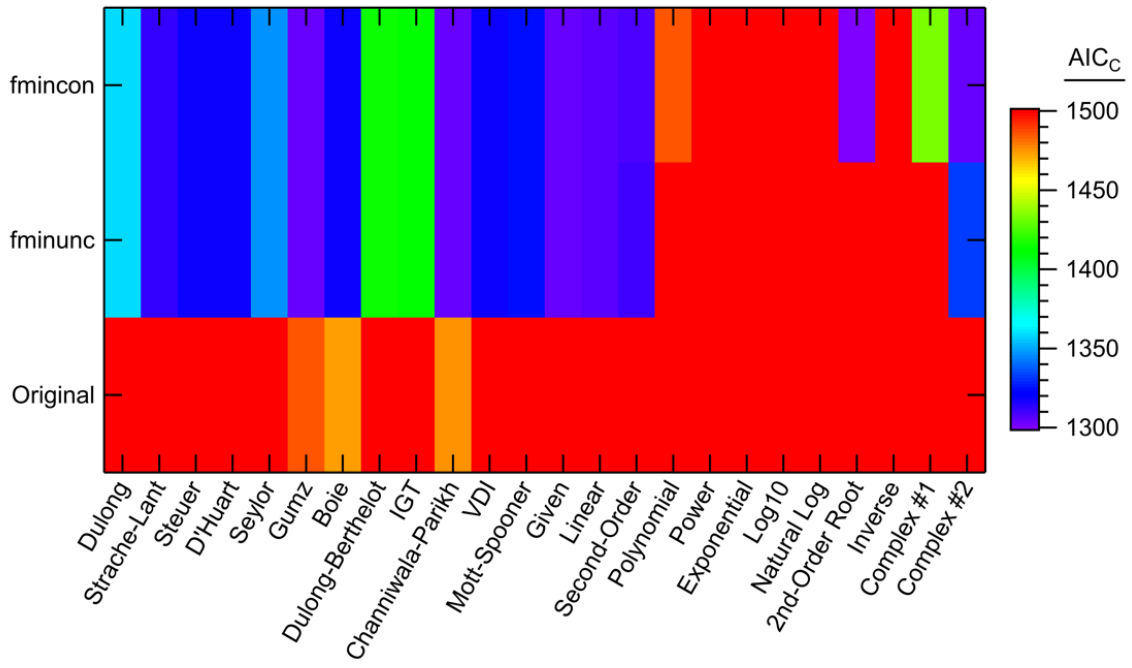

Figure D-90. AIC_c values in the full data set comparison for each model form.

D.4 Summary

In summary, the models presented in Section 7.3 are the best offered by this extensive analysis. The new models can generally increase the accuracy of heating value calculations; however, this analysis shows that this slight increase is not enough to justify using two or more times as many fitted coefficients as the literature models.

APPENDIX E. ADDITIONAL MIXTURE FRACTION ANALYSIS

This appendix chapter details additional mixture fraction analysis information not included in Chapter 8. The information here includes all information from the one-, two-, and three-mixture fraction results, using both experimentally determined heating values and heating values based on the correlations in Chapter 7. Chapter 8 shows the root-mean-square error (RMSE, see Equation 2-15) for some of the comparisons between the NASA-CEA and Cantera program results. This appendix chapter discusses these results along with several other statistical measures, including the L_1 norm (see Equation 2-14), the infinity norm (see Equation 2-16), and the average and maximum relative error values (see Equation 2-13).

E.1 One-Mixture Fraction Results

The one-mixture fraction analysis included three main comparisons: (1) NASA-CEA to Cantera, (2) comparison of different fuels, and (3) experimental to correlated fuel heating values. Chapter 8 discusses the main results of the first two comparisons but leaves out the third. The third comparison attempted to link the work discussed in Chapter 7 with the practical applications in Chapter 8. This appendix section will be divided into the same order, starting with the complete NASA-CEA to Cantera comparison, followed by the complete comparison of different fuels, and finally the complete comparison of experimental to correlated heating values.

E.1.1 Complete NASA-CEA to Cantera Comparison

Chapter 8 discusses the key results in the NASA-CEA to Cantera comparison. This section details the complete analysis, including the five statistical measures of fit between the NASA-CEA results and the Cantera results: L_1 norm, L_2 norm or RMSE, infinity norm, average relative error, and maximum relative error. This section also includes a few additional fuel results using a correlated heating value instead of an experimentally observed heating value. The complete list of fuel cases is found in Table E-1. Note that while there is some overlap from Table 8-3, the fuel cases in Table E-1 are different, since there are a few new cases.

Table E-1. Complete One-Mixture Fraction Fuel Cases

Case No.	Fuel	Coal Rank	ΔH_f
E1-1	Graphite		
E1-2	Benzene		
E1-3	Methane		
E1-4	Ethane		
E1-5	Ethylene		
E1-6	Pitt 8 coal	HVA	Exp.
E1-7	Pitt 8 char	HVA char	Exp.
E1-8	Pitt 8 tar	HVA tar	Exp.
E1-9	Lower Kittanning coal	LVB	Exp.
E1-10	Millmerran coal	sub	Exp.
E1-11	Liddell coal	bit	Exp.
E1-12	Mammoth coal	an	Exp.
E1-13	Beulah coal	ligA	Exp.
E1-14	Pitt 8 coal	HVA	Corr.
E1-15	Pitt 8 char	HVA char	Corr.
E1-16	Pitt 8 tar	HVA tar	Corr.
E1-17	Lower Kittanning coal	LVB	Corr.
E1-18	Millmerran coal	sub	Corr.
E1-19	Liddell coal	bit	Corr.
E1-20	Mammoth coal	an	Corr.
E1-21	Beulah coal	ligA	Corr.
E1-22	Buck Mountain coal	an	Exp.
E1-23	#8 Leader coal	an	Exp.
E1-24	#8 coal	semi-an	Exp.
E1-25	Gunnison coal	semi-an	Exp.
E1-26	L. Spadra coal	semi-an	Exp.

Chapter 8 uses the root-mean-square error along with a couple of simplified figures of H_2O and graphite mole fractions to illustrate the key similarities and differences between the NASA-CEA and Cantera results. While this is a good way of distilling the key results of this comparison, all 26 fuel cases in Table E-1 were equilibrated using both NASA-CEA and Cantera programs, using the procedure discussed in Chapter 8. This comparison is easily displayed in plots called "dashboards." These dashboards compare the six variables of interest (equilibrium temperature and mole fractions of O_2, CO_2, CO, H_2O, and graphite) vs equivalence ratio and fuel mixture fraction for both NASA-CEA and Cantera, as well as the residuals and relative errors between NASA-CEA and Cantera at each equivalence ratio. The dashboards are in Figure E-1 to Figure E-26, shown in order as listed in Table E-1. Discussion of these dashboard comparisons are found after all 26 figures. Note, NASA-CEA is abbreviated as "NASA" in these figures to save space in the figure legends.

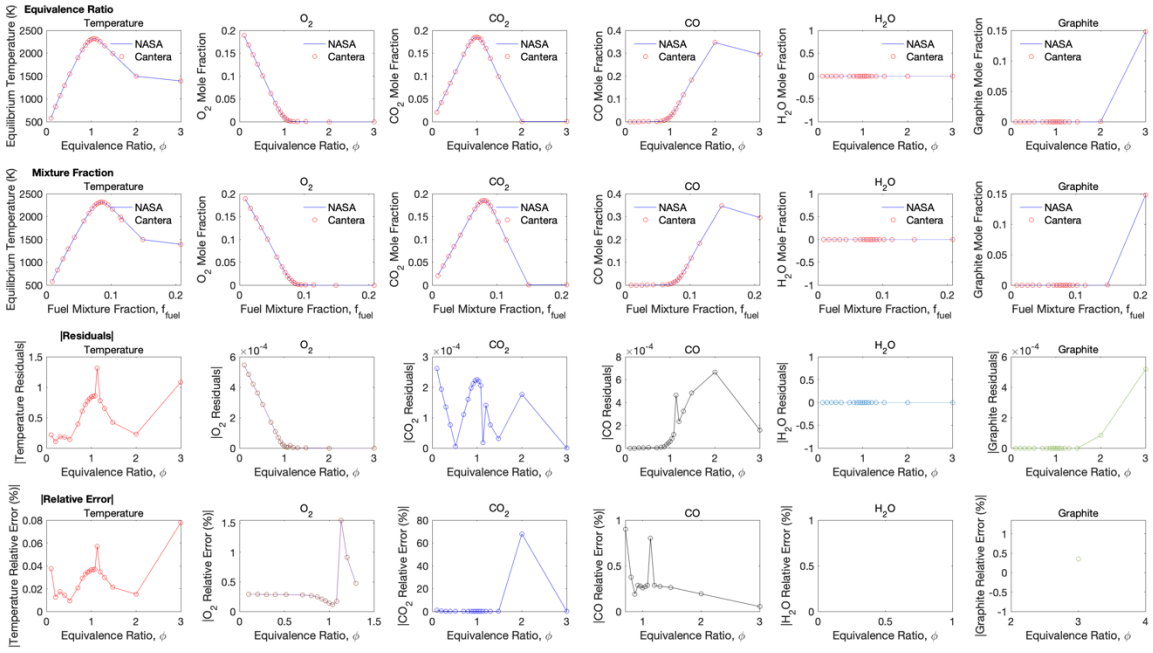

Figure E-1. Case E1-1 (graphite) NASA-CEA to Cantera comparison.

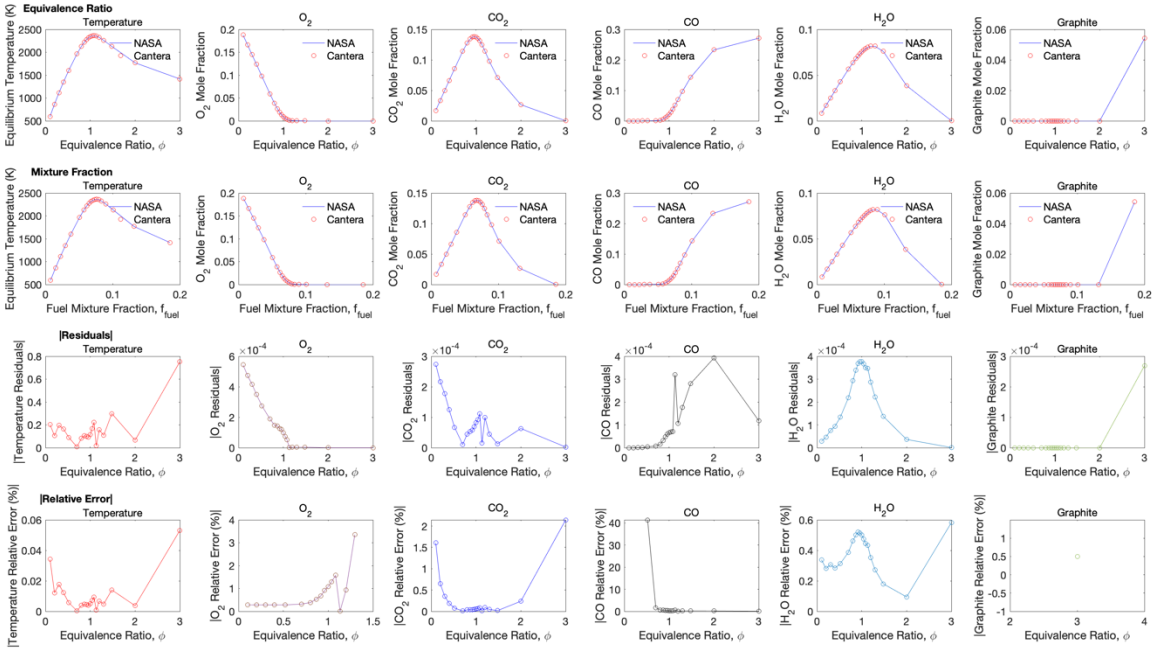

Figure E-2. Case E1-2 (benzene) NASA-CEA to Cantera comparison.

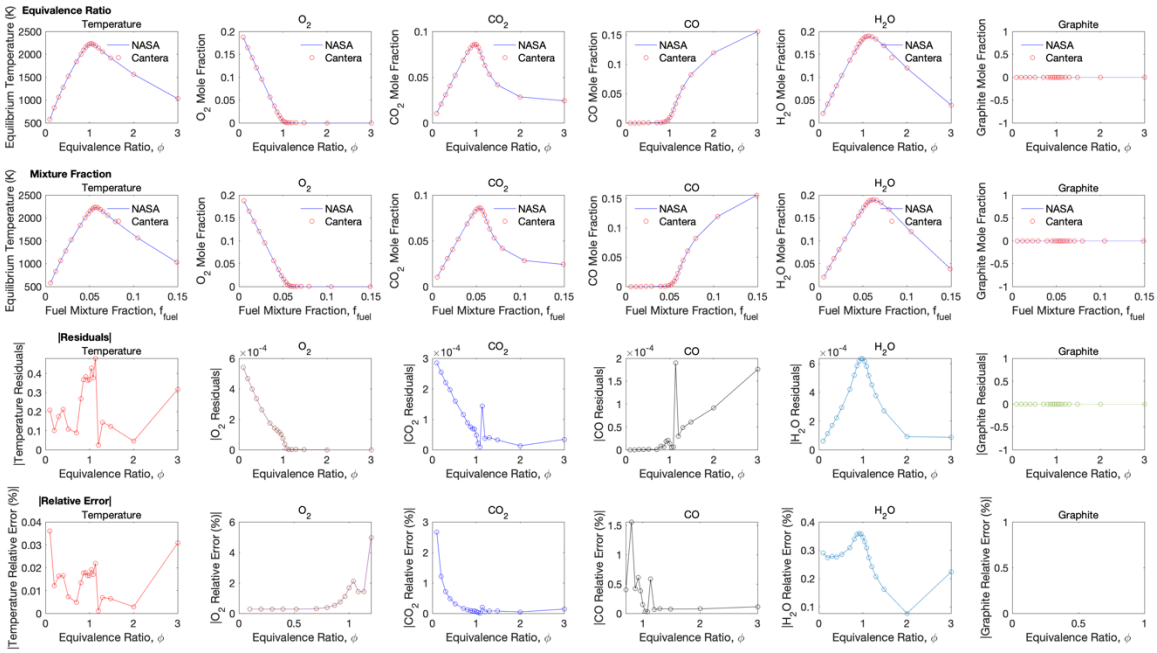

Figure E-3. Case E1-3 (methane) NASA-CEA to Cantera comparison.

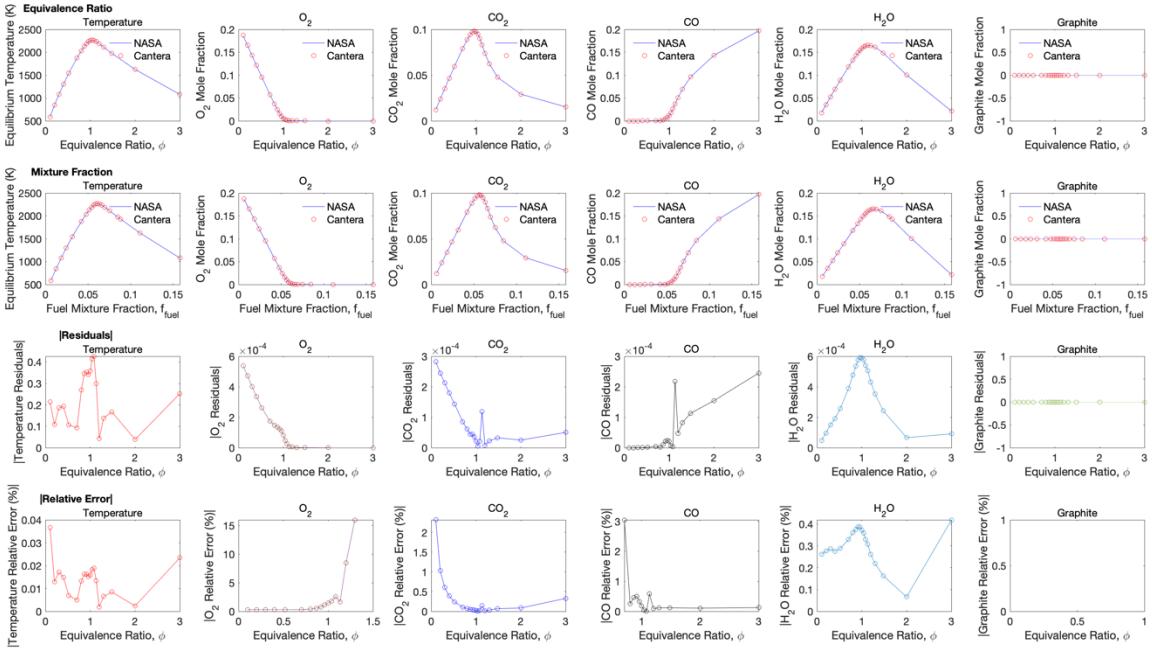

Figure E-4. Case E1-4 (ethane) NASA-CEA to Cantera comparison.

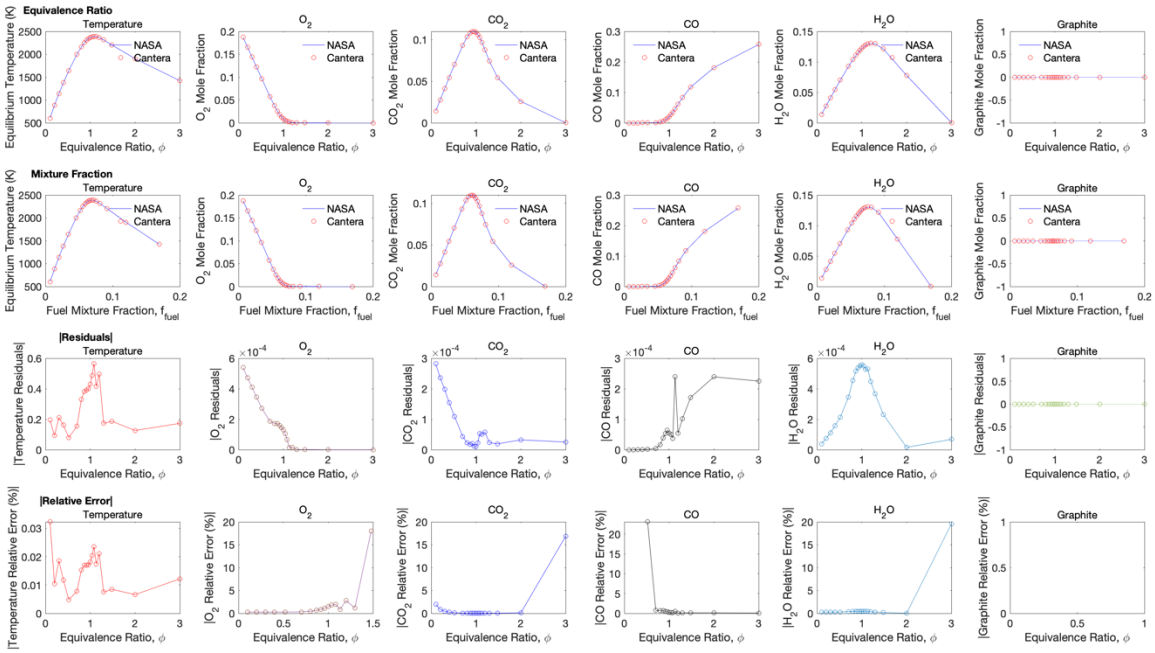

Figure E-5. Case E1-5 (ethylene) NASA-CEA to Cantera comparison.

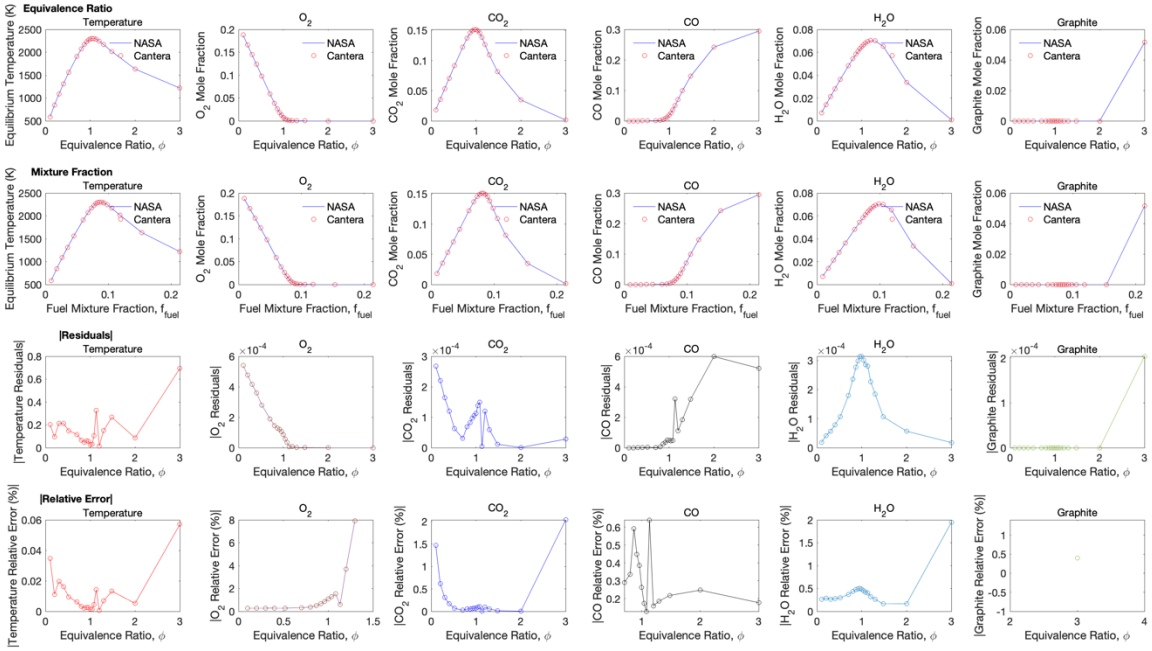

Figure E-6. Case E1-6 (Pitt 8 coal, exp.) NASA-CEA to Cantera comparison.

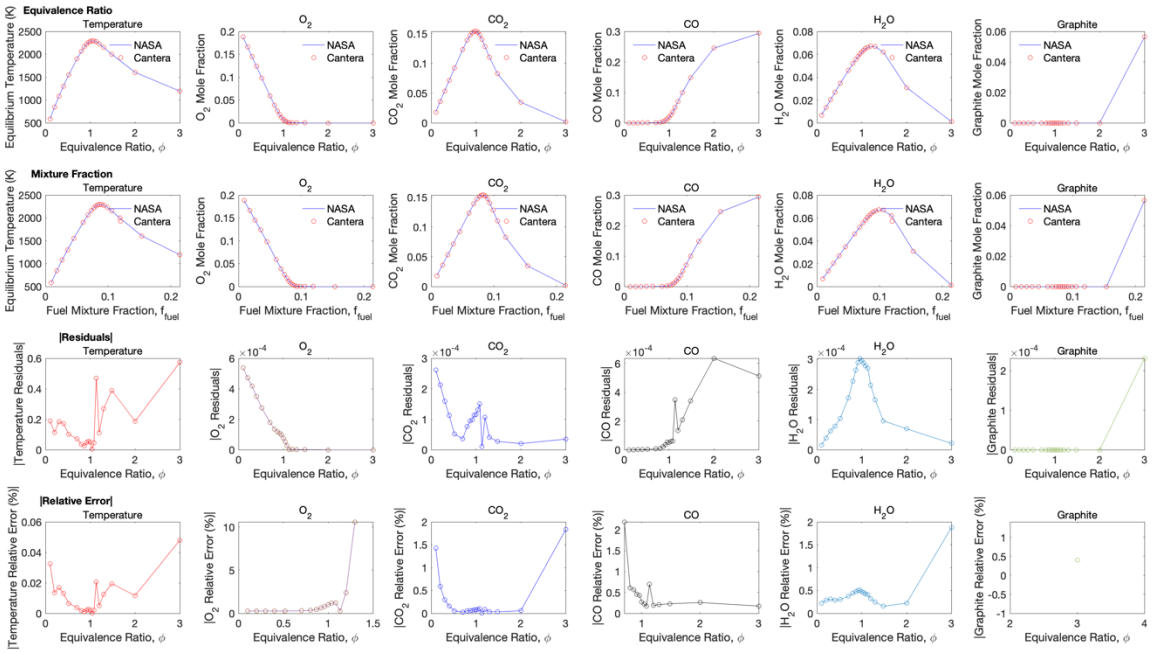

Figure E-7. Case E1-7 (Pitt 8 char, exp.) NASA-CEA to Cantera comparison.

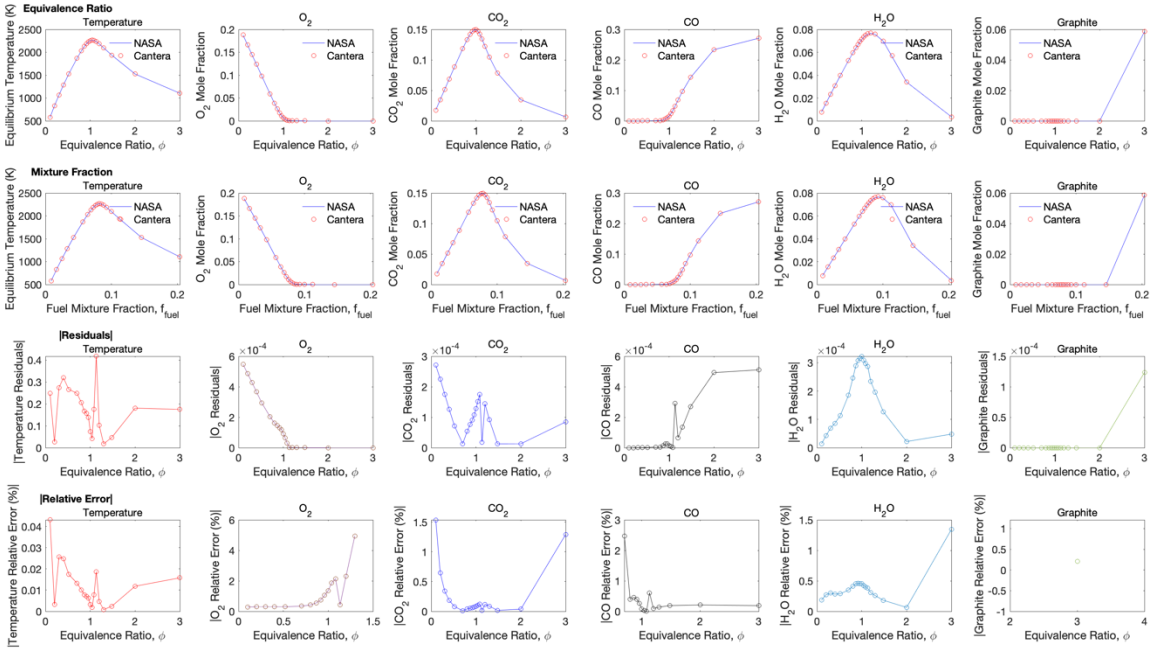

Figure E-8. Case E1-8 (Pitt 8 tar, exp.) NASA-CEA to Cantera comparison.

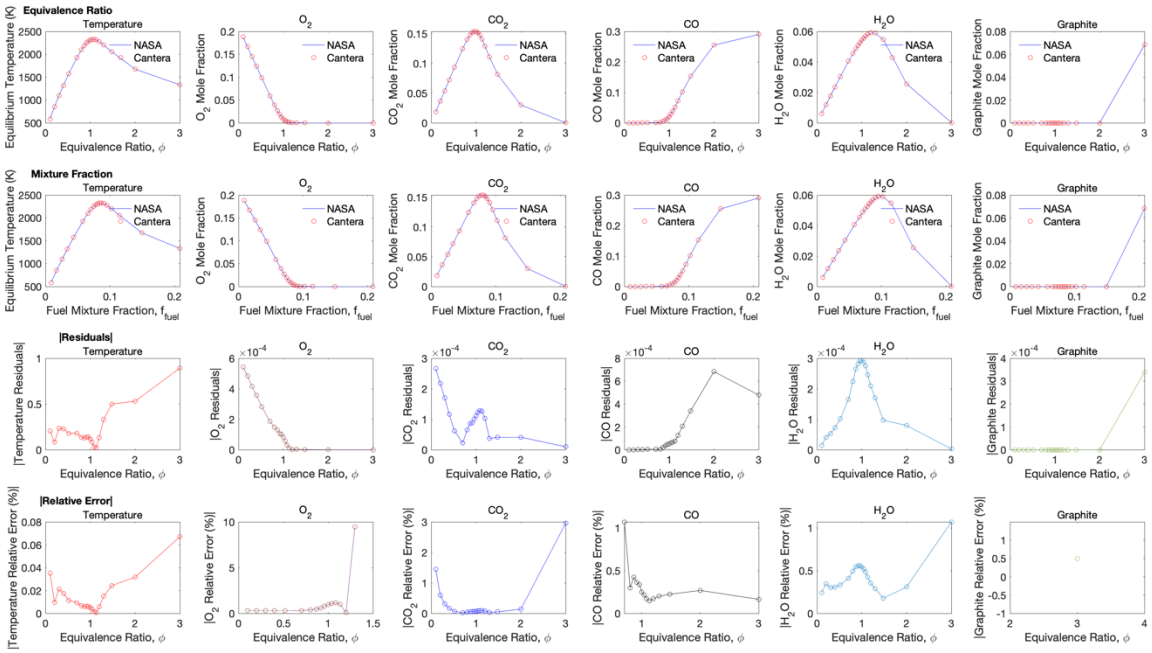

Figure E-9. Case E1-9 (Lower Kittanning coal, exp.) NASA-CEA to Cantera comparison.

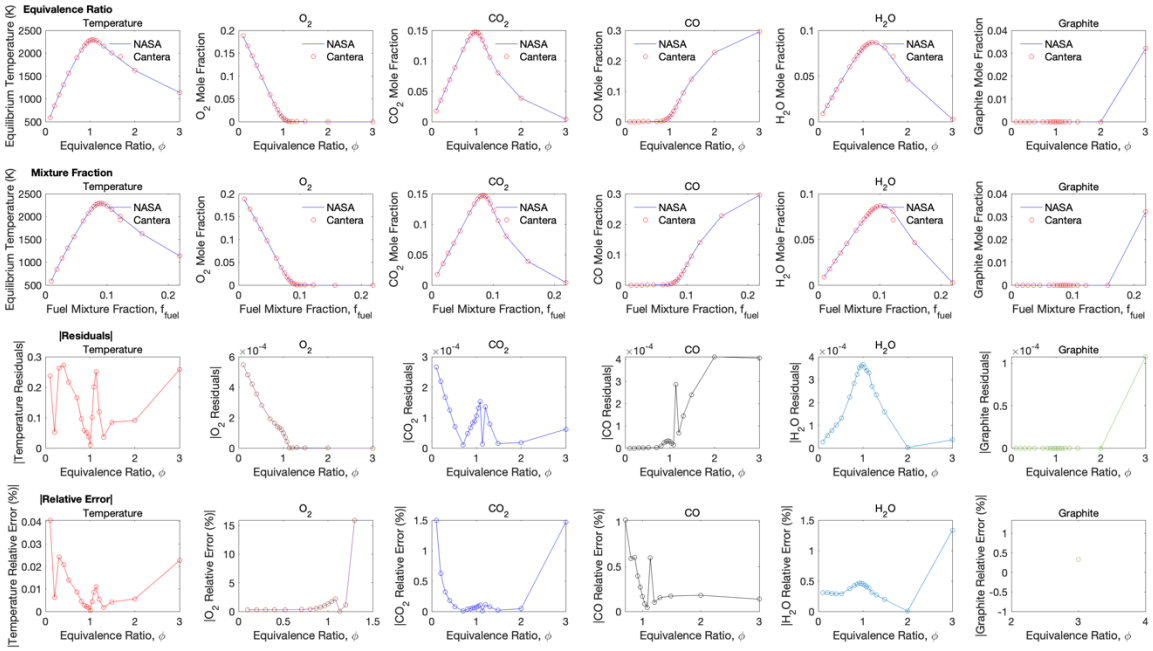

Figure E-10. Case E1-10 (Millmerran coal, exp.) NASA-CEA to Cantera comparison.

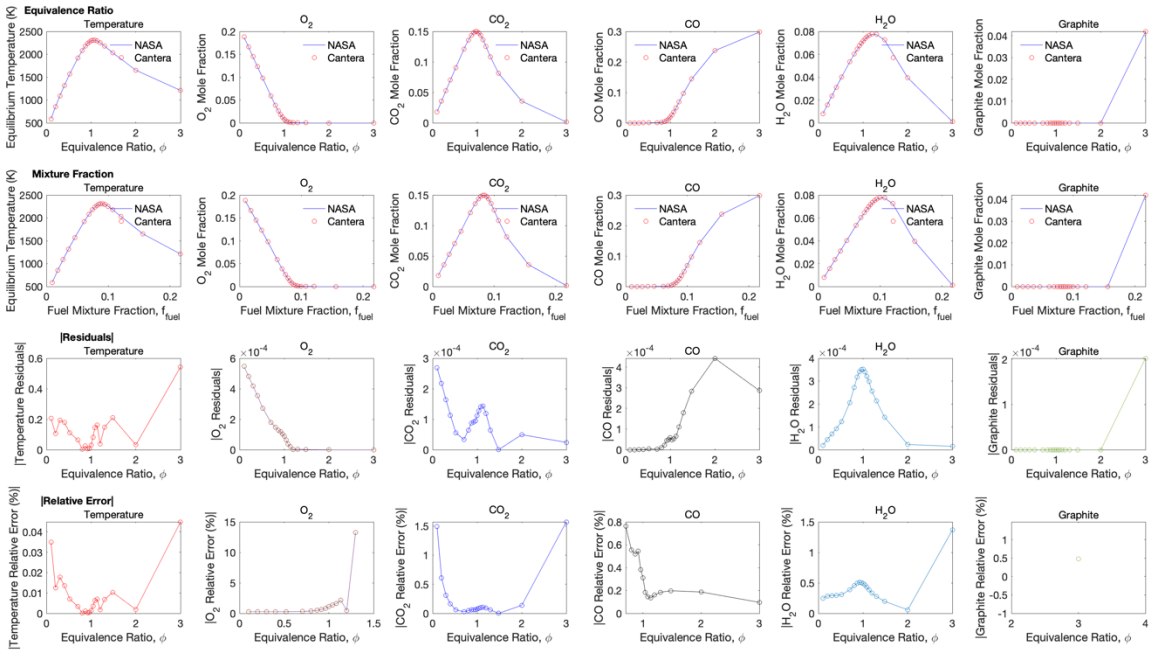

Figure E-11. Case E1-11 (Liddell coal, exp.) NASA-CEA to Cantera comparison.

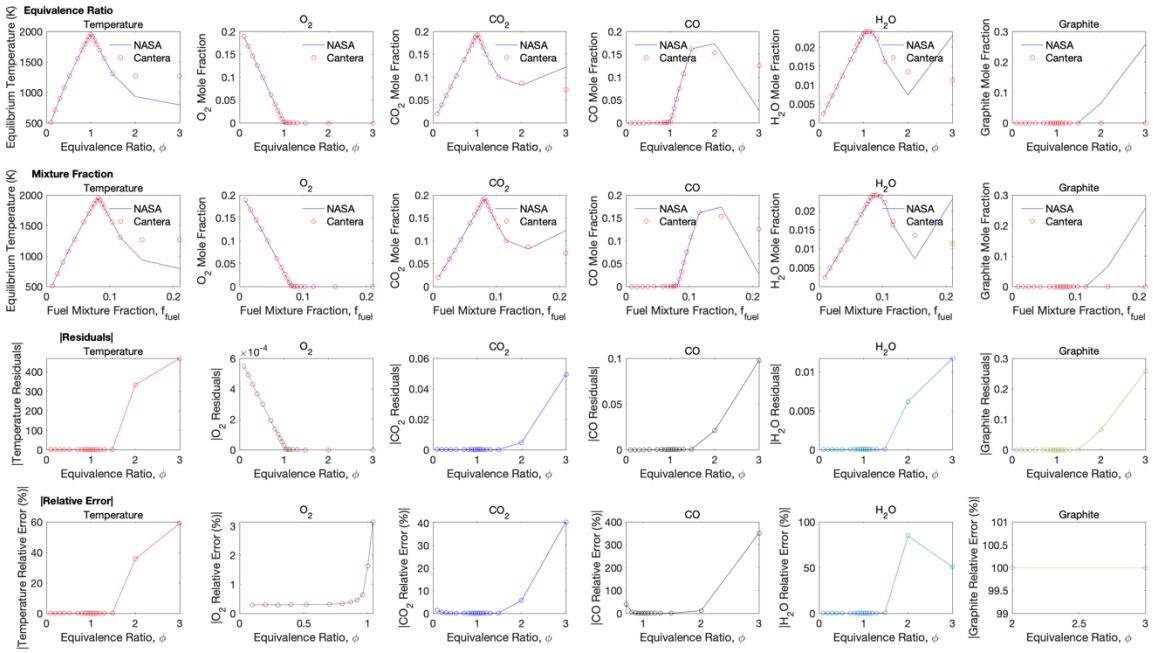

Figure E-12. Case E1-12 (Mammoth coal, exp.) NASA-CEA to Cantera comparison.

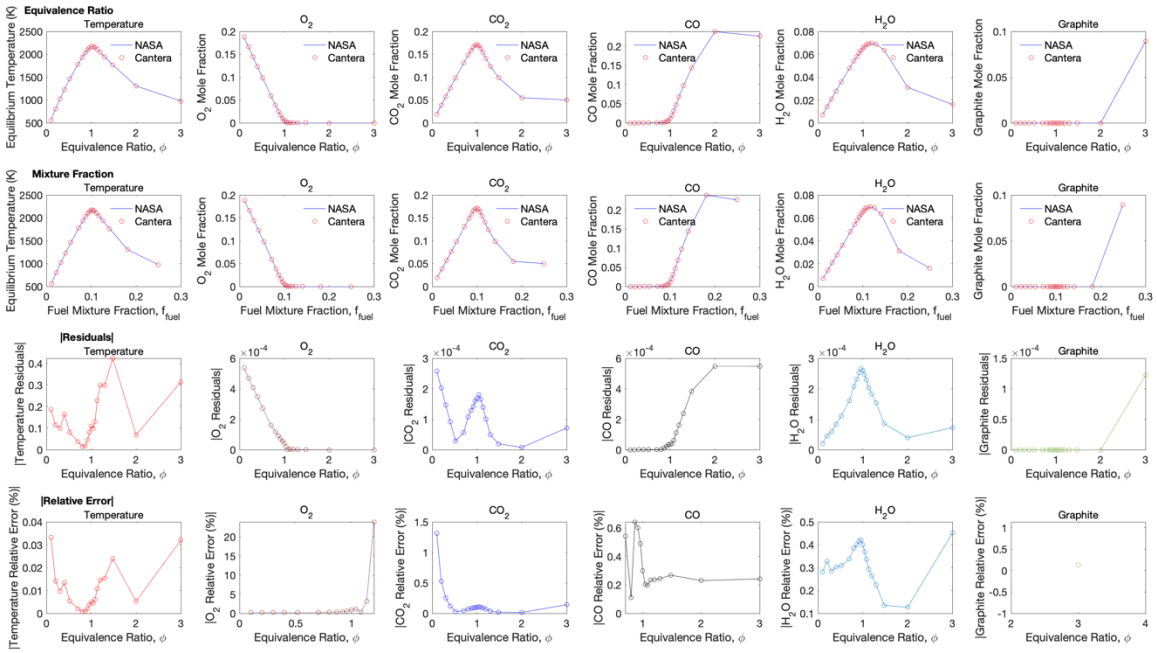

Figure E-13. Case E1-13 (Beulah coal, exp.) NASA-CEA to Cantera comparison.

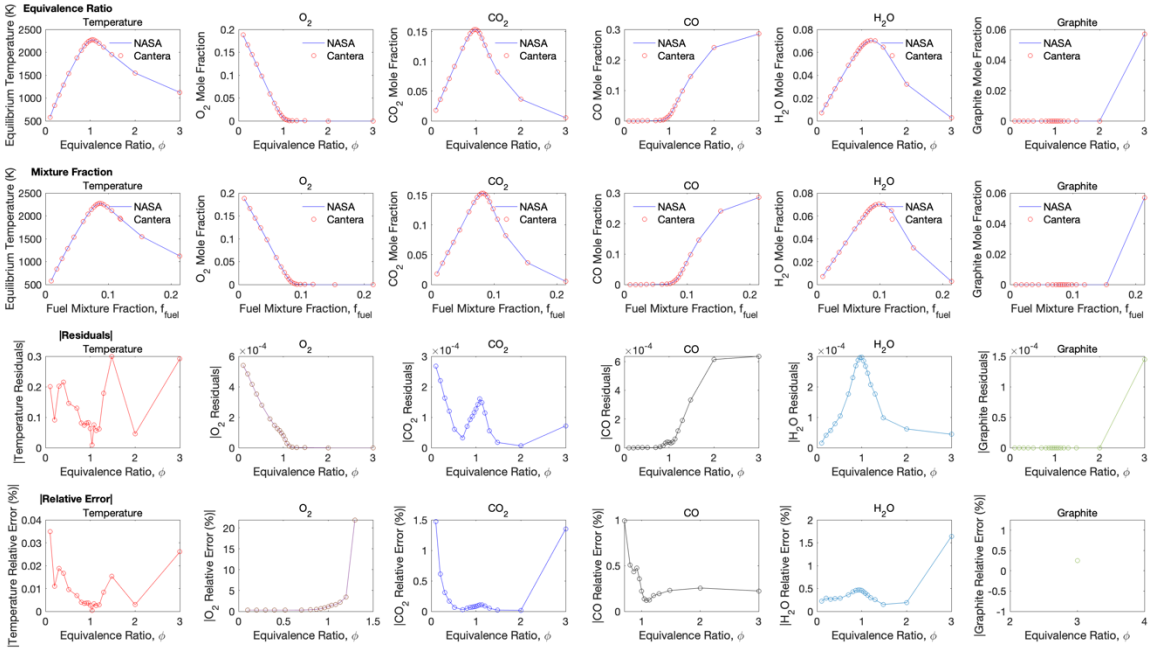

Figure E-14. Case E1-14 (Pitt 8 coal, corr.) NASA-CEA to Cantera comparison.

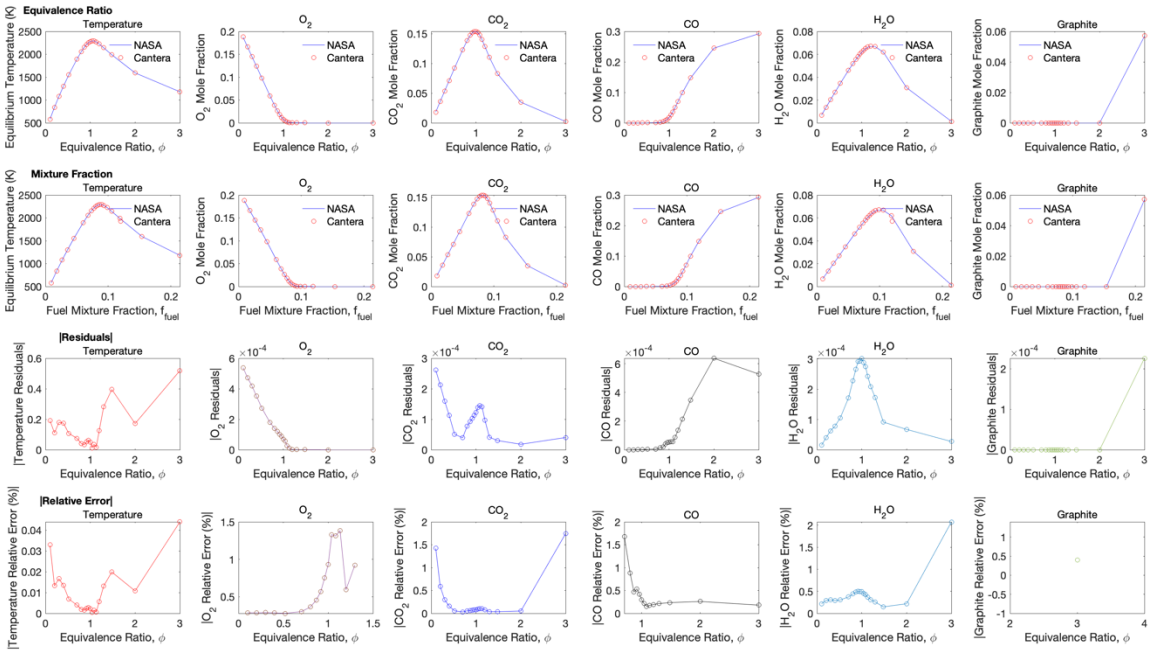

Figure E-15. Case E1-15 (Pitt 8 char, corr.) NASA-CEA to Cantera comparison.

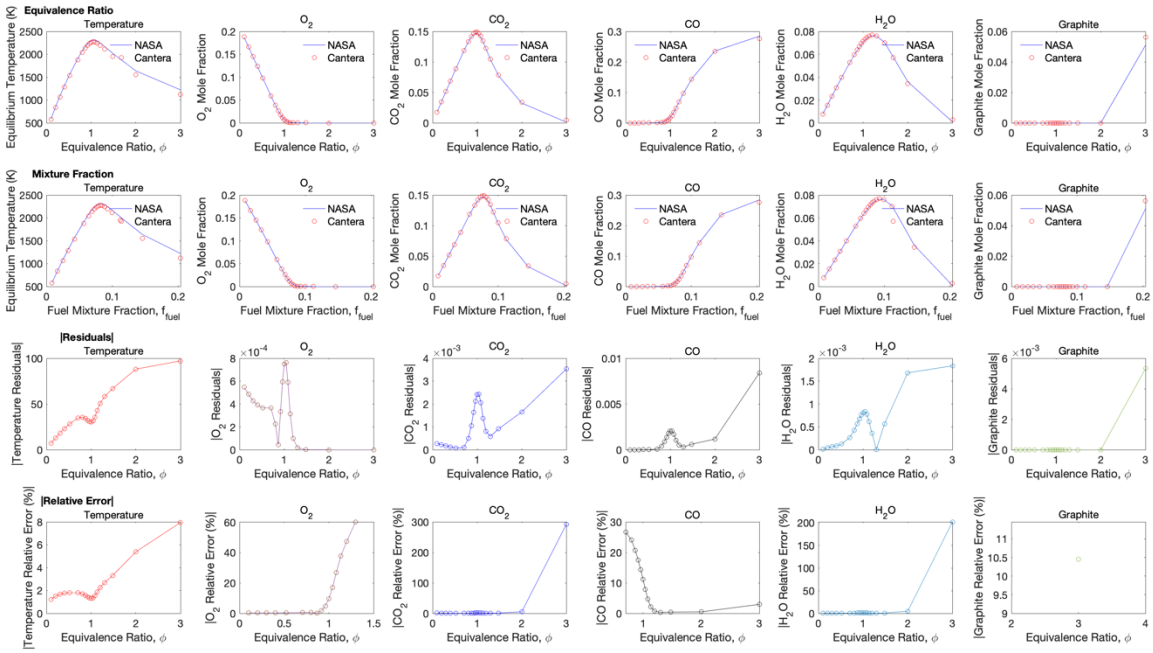

Figure E-16. Case E1-16 (Pitt 8 tar, corr.) NASA-CEA to Cantera comparison.

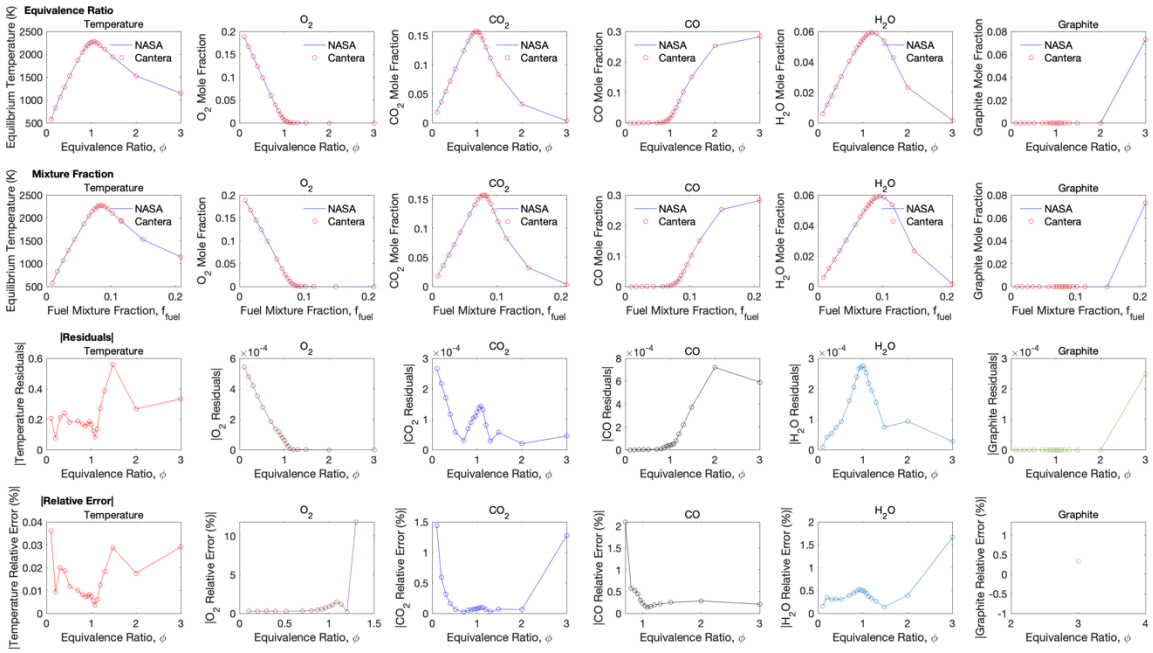

Figure E-17. Case E1-17 (Lower Kittanning coal, corr.) NASA-CEA to Cantera comparison.

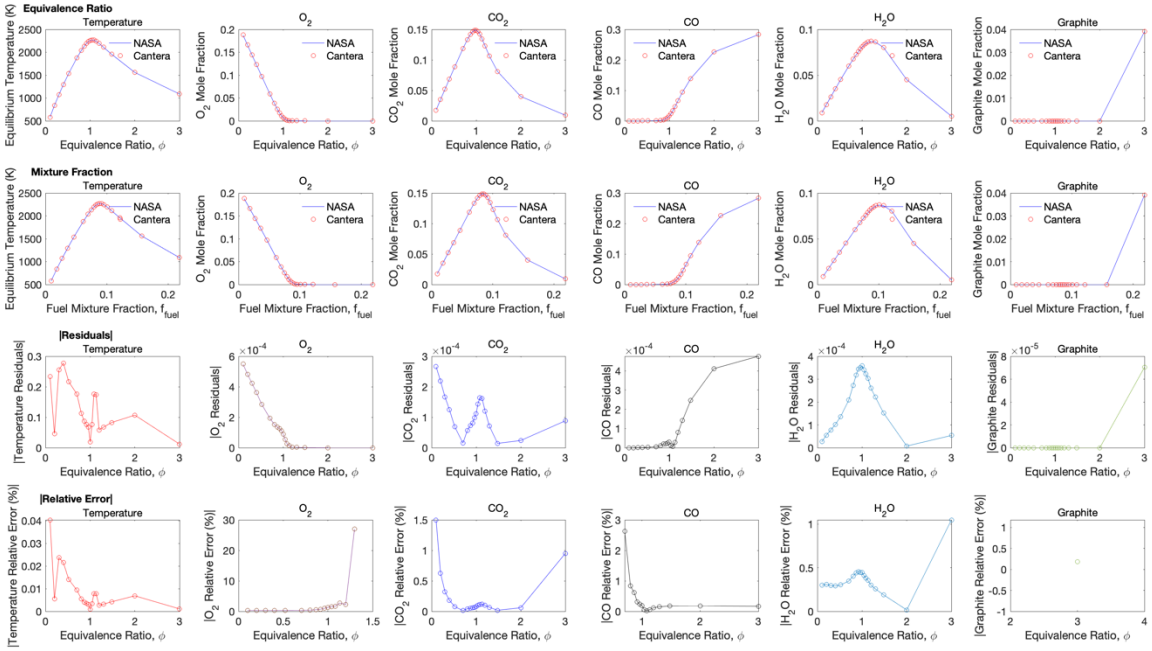

Figure E-18. Case E1-18 (Millmerran coal, corr.) NASA-CEA to Cantera comparison.

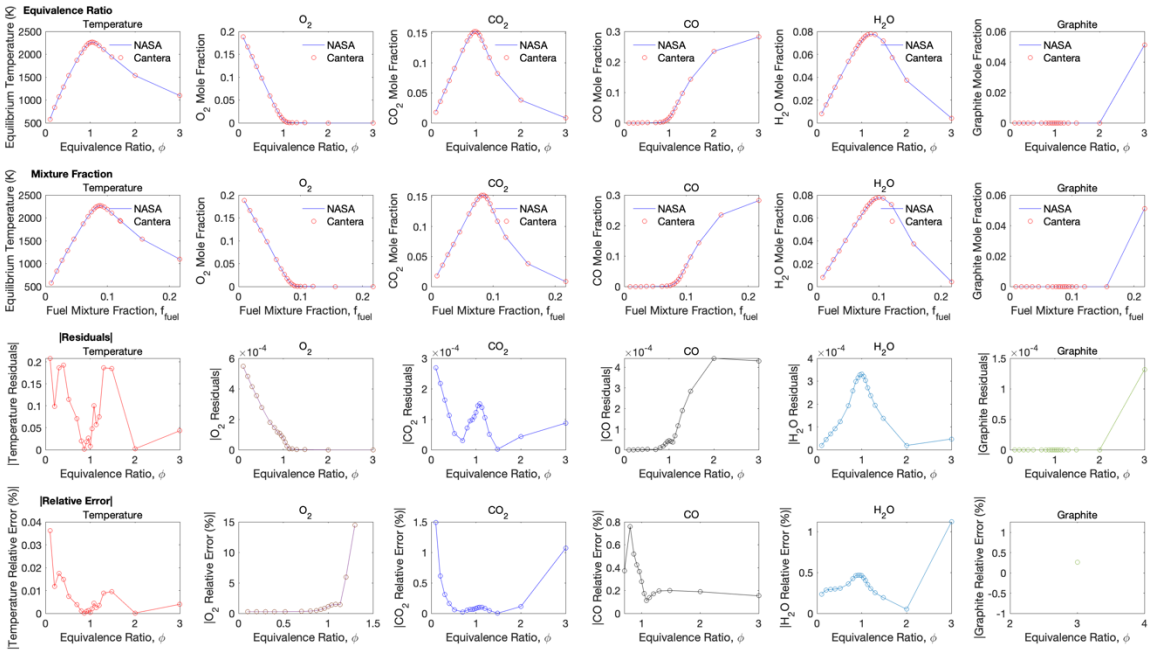

Figure E-19. Case E1-19 (Liddell coal, corr.) NASA-CEA to Cantera comparison.

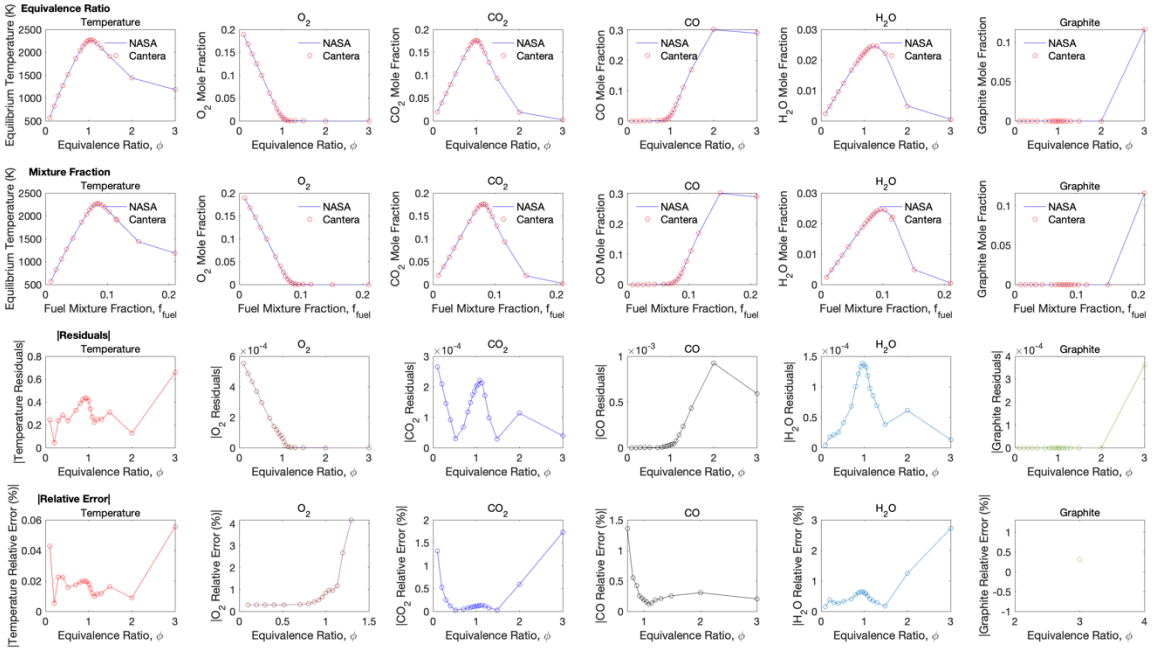

Figure E-20. Case E1-20 (Mammoth coal, corr.) NASA-CEA to Cantera comparison.

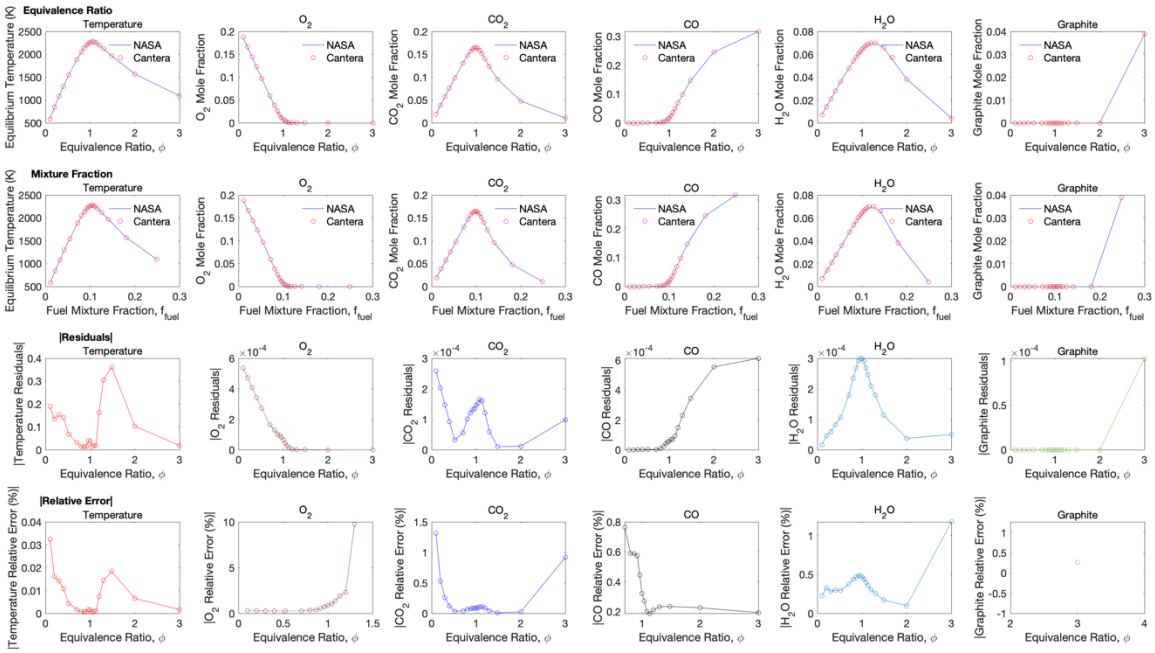

Figure E-21. Case E1-21 (Beulah coal, corr.) NASA-CEA to Cantera comparison.

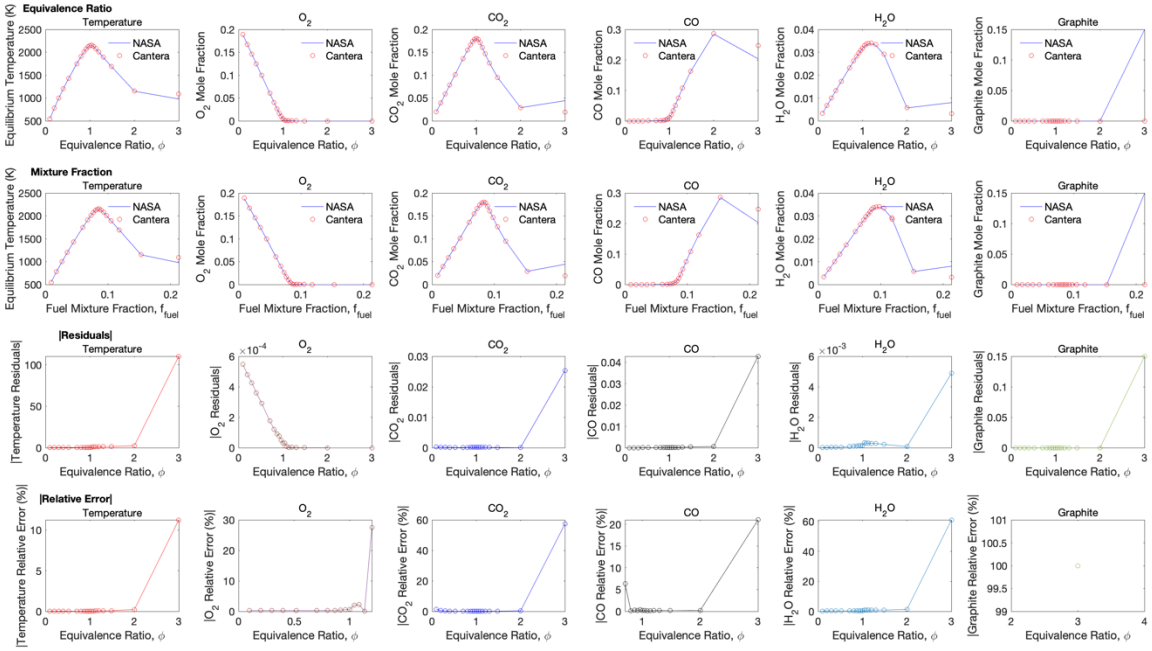

Figure E-22. Case E1-22 (Buck Mountain coal) NASA-CEA to Cantera comparison.

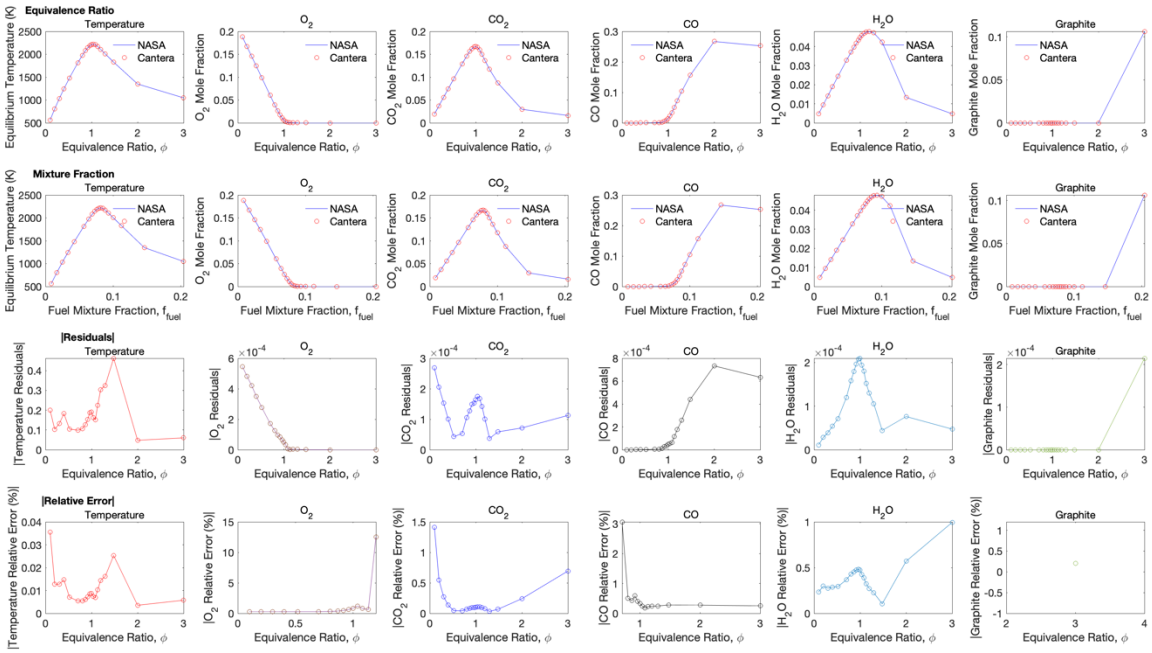

Figure E-23. Case E1-23 (#8 Leader coal) NASA-CEA to Cantera comparison.

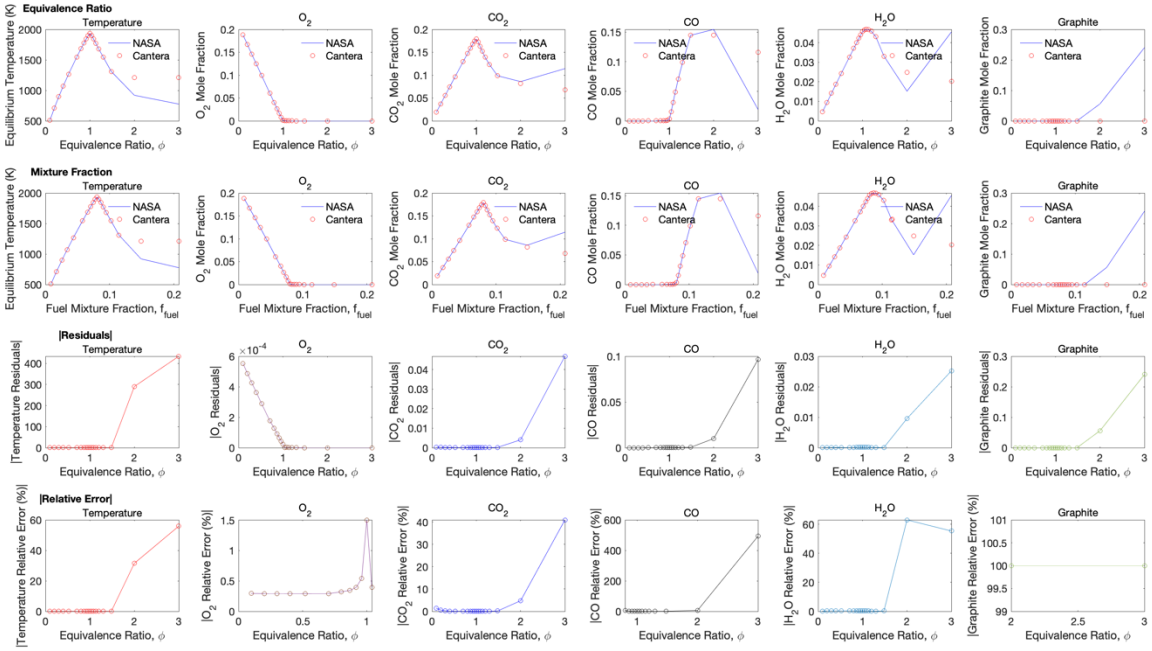

Figure E-24. Case E1-24 (#8 coal) NASA-CEA to Cantera comparison.

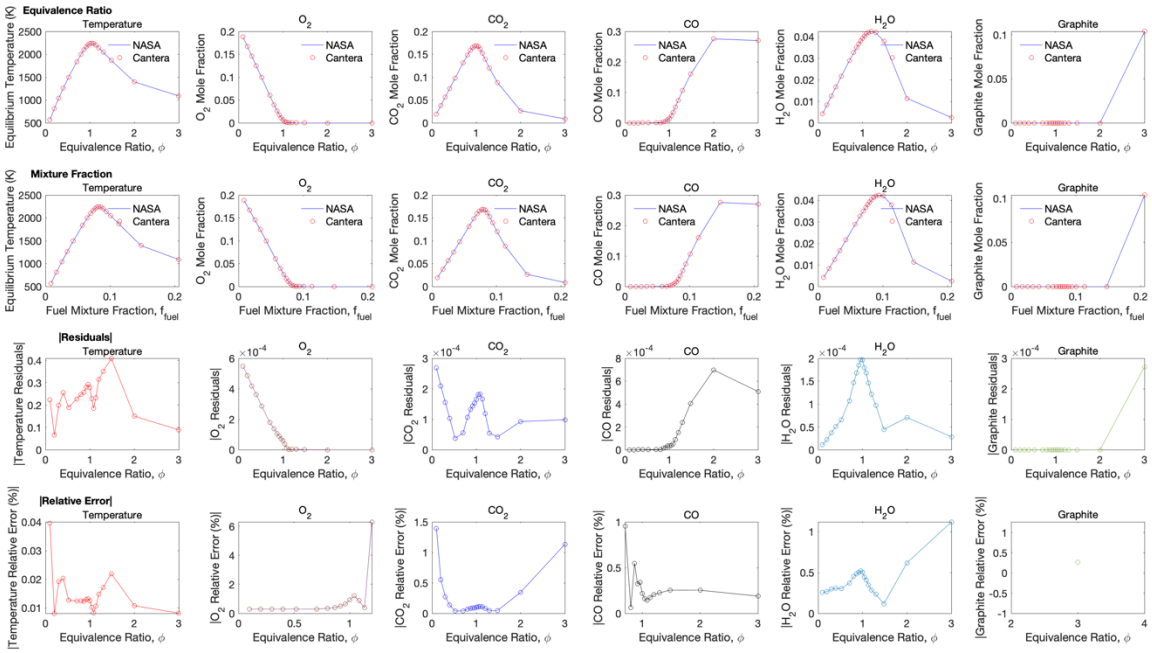

Figure E-25. Case E1-25 (Gunnison coal) NASA-CEA to Cantera comparison.

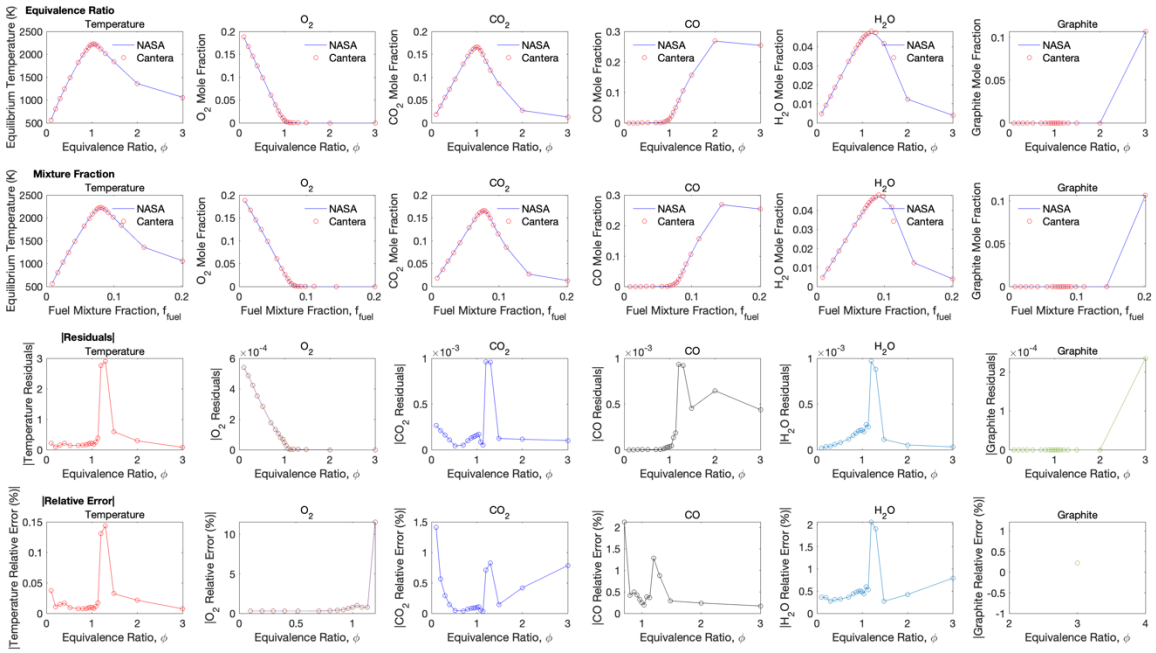

Figure E-26. Case E1-26 (L. Spadra coal) NASA-CEA to Cantera comparison.

This comparison generated a lot of data. Most of the fuel comparisons are very close between NASA-CEA and Cantera, however, there are a few that did not do well, mostly a few of the higher rank coals, including the Mammoth anthracite (experimental heating value, see Figure E-12), the Buck mountain anthracite (Figure E-22), and the #8 semi-anthracite (Figure E-24). Interestingly enough, the Mammoth anthracite with correlated heating value had a much better agreement between NASA-CEA and Cantera, despite the only difference being the heat of formation between the experimental and correlated equilibrium inputs. In addition, Chapter 8 discusses that the main disparities between NASA-CEA and Cantera only occur at the highest equivalence ratios, where the mixture is the most fuel rich. The dashboard comparison figures further enforce this conclusion. Chapter 8 summarizes the NASA-CEA to Cantera comparison using Figure 8-1, which shows the RMSE of most one-mixture fraction cases for all six variables

of interest. Figure E-27 shows similar results for all five statistical measures (L_1, L_2, and infinity norms, and average and maximum relative error values) for all fuel cases in Table E-1.

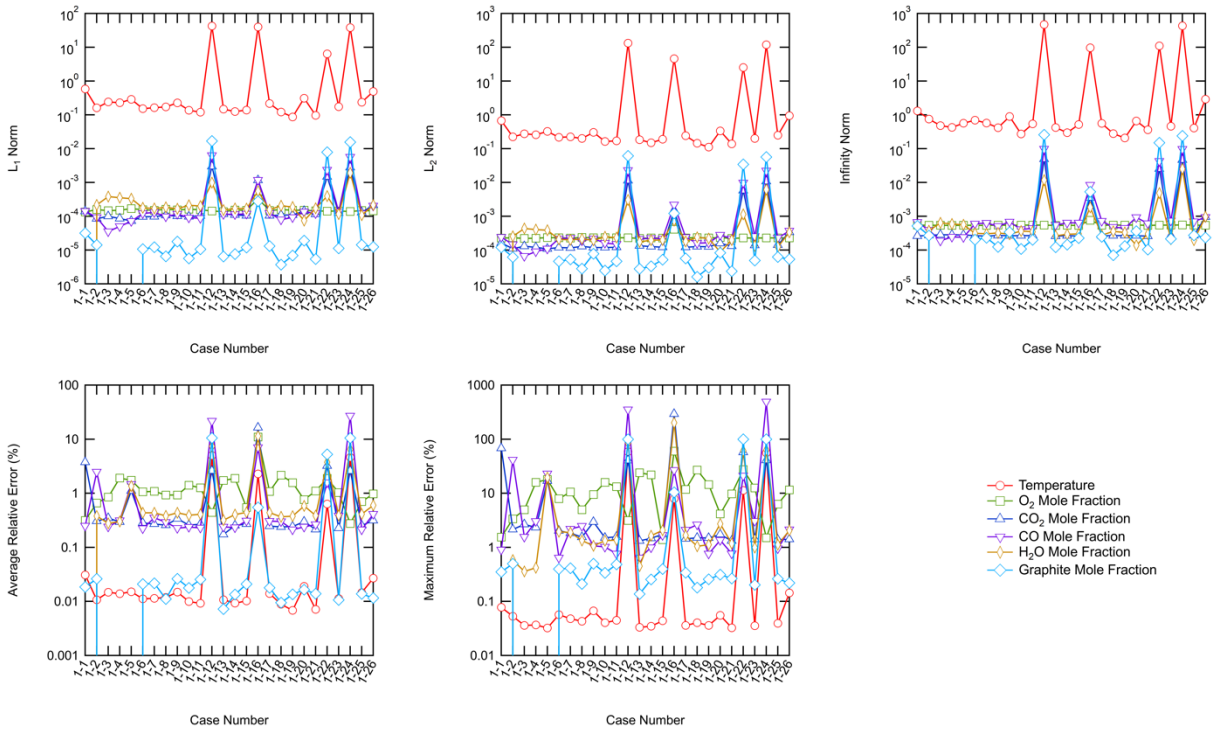

Figure E-27. Complete Statistical Results for NASA-CEA to Cantera Comparison.

While relative error can be a valuable tool in determining a good comparison from a poor comparison, it is not as effective in this case for most of the equilibrium mole fractions. This is because many of the values are very small and dividing by a very small number to get a relative error can often make the relative error appear artificially large. That is why there appears to be much more noise in the relative error plots (d and e), but especially in the maximum relative error. The L_1, L_2, and infinity norms are much less prone to numerical instabilities because they only rely on the difference between NASA-CEA and Cantera. The statistical plots show that the fuel cases already discussed earlier find poor agreement between NASA-CEA and Cantera, but the plots also identify one other fuel case that gives poor agreement between NASA-CEA and

Cantera—the Pitt 8 tar with a correlated heating value (case E1-16, see Figure E-16 for the dashboard comparison between NASA-CEA and Cantera). In looking at the comparison for case E1-16, there is some divergence between the NASA-CEA and Cantera values at high equivalence ratio, with greatest deviations in equilibrium temperature and graphite mole fraction, and almost imperceptible deviations in CO_2, CO, and H_2O mole fractions. As stated in Chapter 8, the deviations at high equivalence ratios are not concerning for most industrial coal combustion applications since most applications do not operate in such fuel-rich conditions. However, this may become an issue with specialized combustion applications such as gasification.

E.1.2 Complete Comparison of Different Fuels

Chapter 8 shows several plots of the NASA-CEA results for all fuels, not including the correlated heating value cases. Most of these plots were based on equivalence ratio, however, similar plots vs. fuel mixture fraction can be made. Like Chapter 8 shows with the temperature plots (Figure 8-3), the comparison with respect to equivalence ratio does not differ much when plotted against fuel mixture fraction. The following figures show these differences for each of the variables of interest as predicted by NASA-CEA.

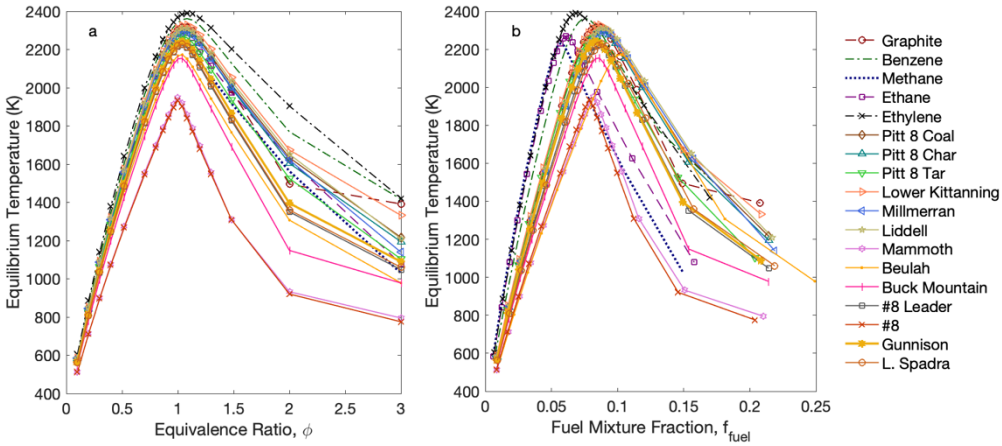

Figure E-28. Full fuel comparison of equilibrium temperature. a) vs. equivalence ratio and b) vs. fuel mixture fraction.

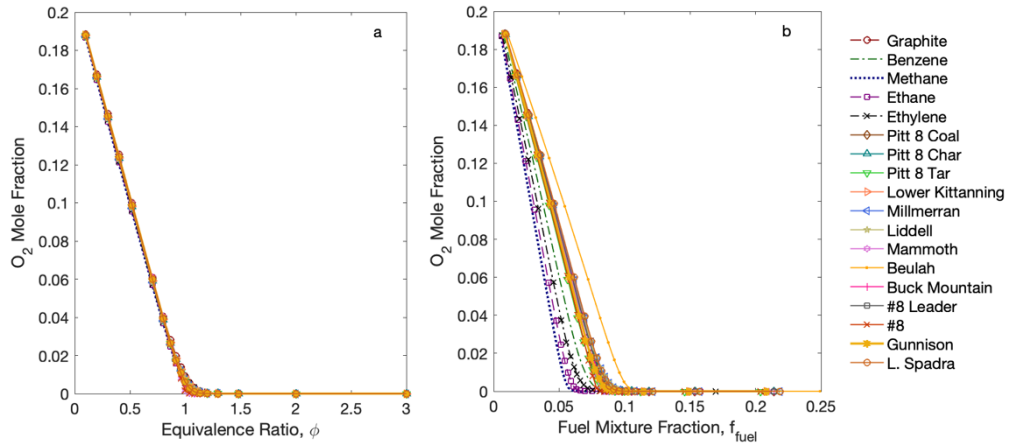

Figure E-29. Full fuel comparison of O_2 mole fraction. a) vs. equivalence ratio and b) vs. fuel mixture fraction.

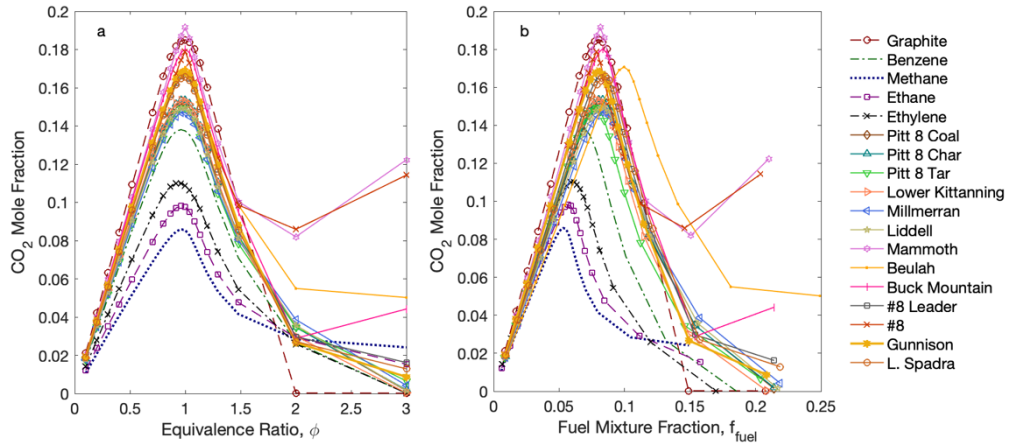

Figure E-30. Full fuel comparison of CO_2 mole fraction. a) vs. equivalence ratio and b) vs. fuel mixture fraction.

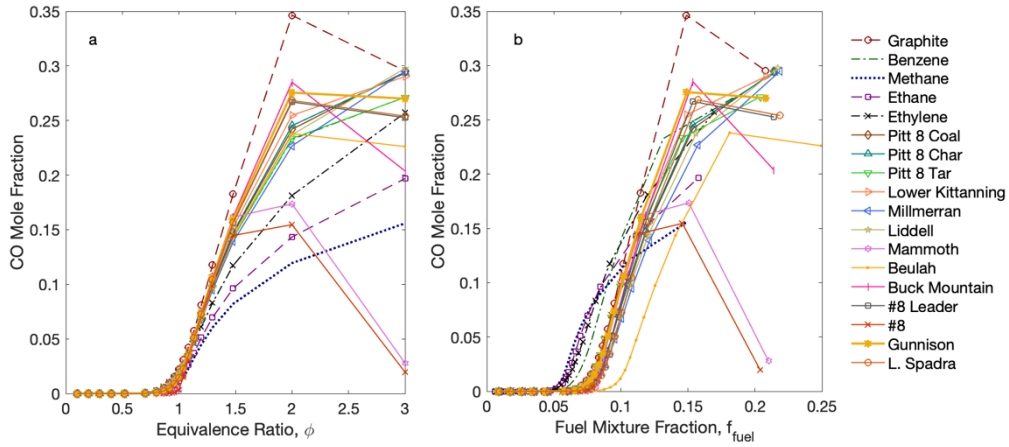

Figure E-31. Full fuel comparison of CO mole fraction. a) vs. equivalence ratio and b) vs. fuel mixture fraction.

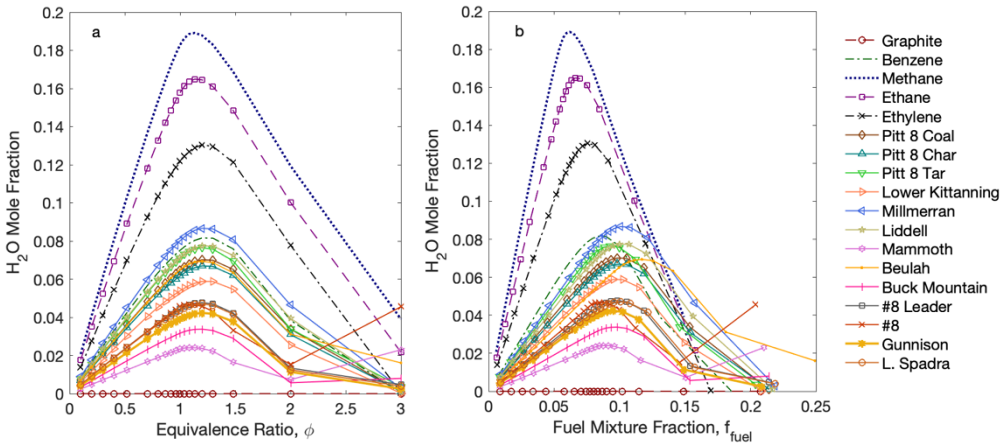

Figure E-32. Full fuel comparison of H_2O mole fraction. a) vs. equivalence ratio and b) vs. fuel mixture fraction.

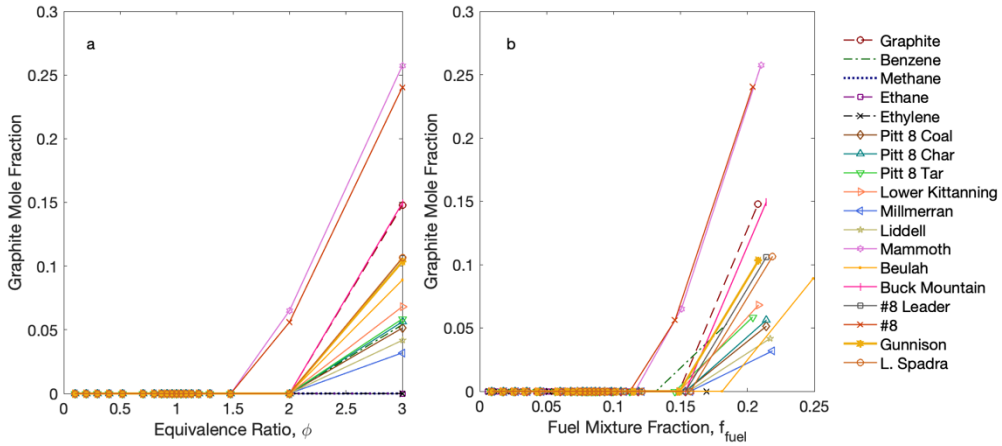

Figure E-33. Full fuel comparison of graphite mole fraction. a) vs. equivalence ratio and b) vs. fuel mixture fraction.

Most of the discussion of the results of the comparison of all fuels is included in Chapter 8, however, the equilibrium oxygen mole fraction was not included there because of the overwhelming similarity over all fuels. In addition, only the plot of equilibrium temperature with respect to fuel mixture fraction was shown in Chapter 8. This was because the only difference between the plots of equivalence ratio and fuel mixture fraction is the horizontal shift of the different fuels. The peak values remain the same with respect to equivalence ratio and fuel

mixture fraction, but the curves with respect to fuel mixture fraction are shifted to the left and right when compared to the equivalence ratio curves.

The peak (or maximum) value of many of the variables at equilibrium depend on different fuel-specific properties. The peak values for temperature and mole fractions of CO_2 and H_2O were plotted against several of the fuel- and equilibrium-specific properties. Figure E-34 shows the peak temperature with respect to the fuel heating value, both in terms of NASA-CEA to Cantera as well as separated by fuel type. Peak CO_2 mole fractions are compared to fuel heating value (Figure E-35), fuel oxygen content (Figure E-36), and peak equilibrium temperature (Figure E-37). Figure E-38 shows the peak H_2O mole fraction compared to the hydrogen content of the fuel.

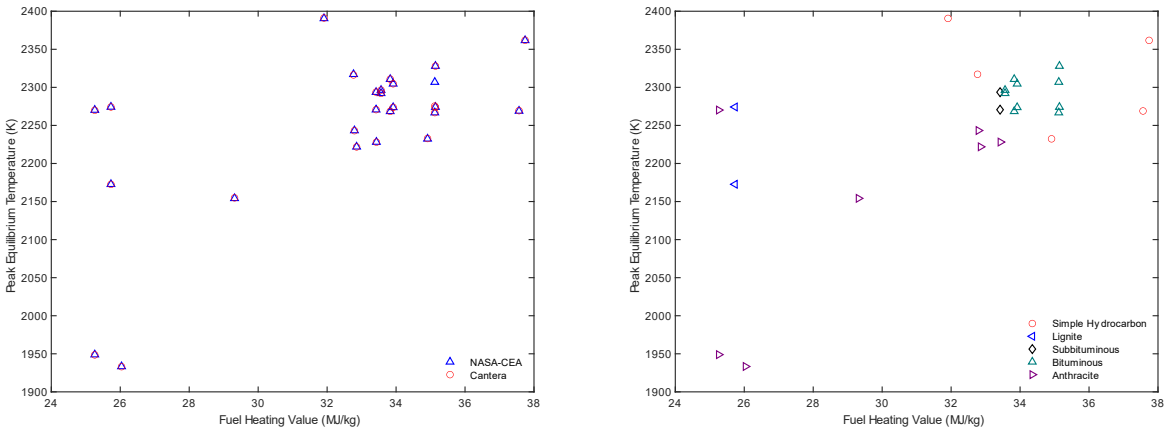

Figure E-34. Peak equilibrium temperature vs fuel heating value:
a) NASA-CEA to Cantera and b) by fuel type.

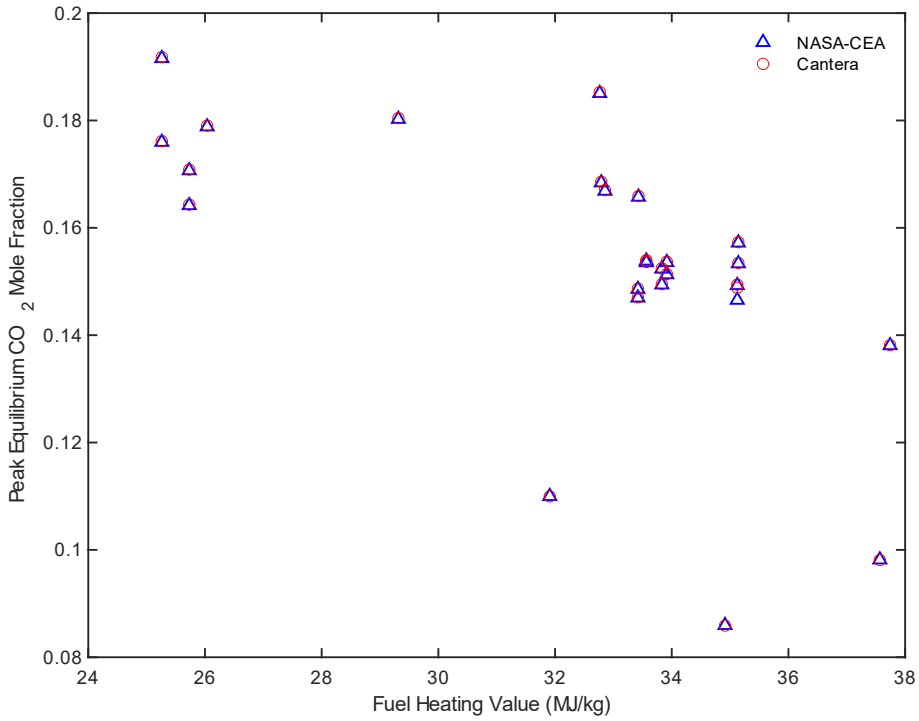

Figure E-35. Peak CO_2 mole fraction compared to fuel heating value.

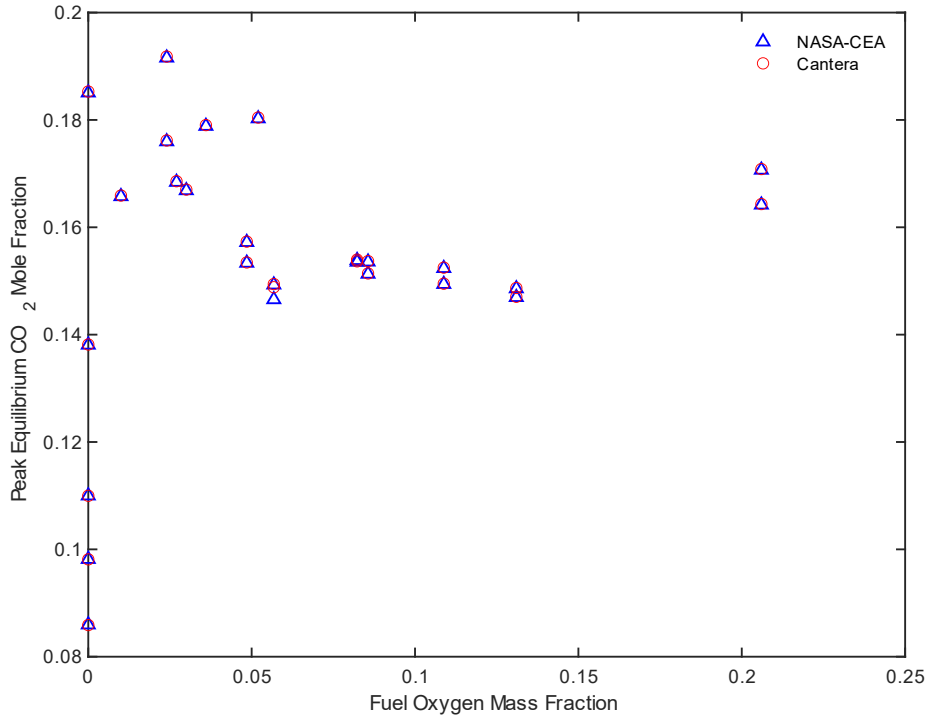

Figure E-36. Peak CO_2 mole fraction compared to fuel oxygen content.

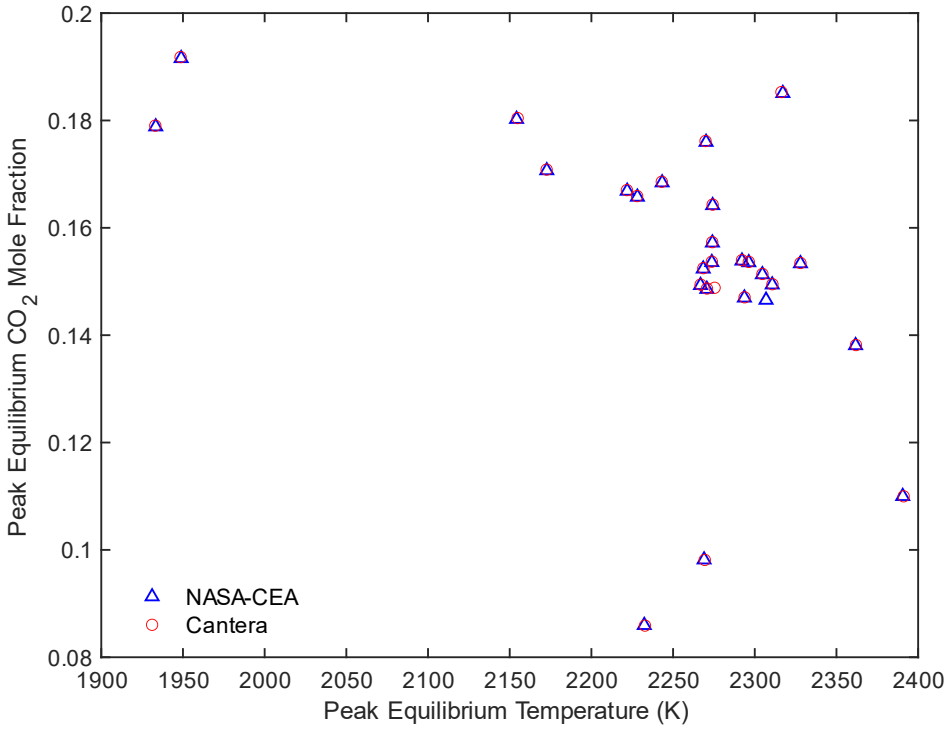

Figure E-37. Peak CO_2 mole fraction compared to peak equilibrium temperature.

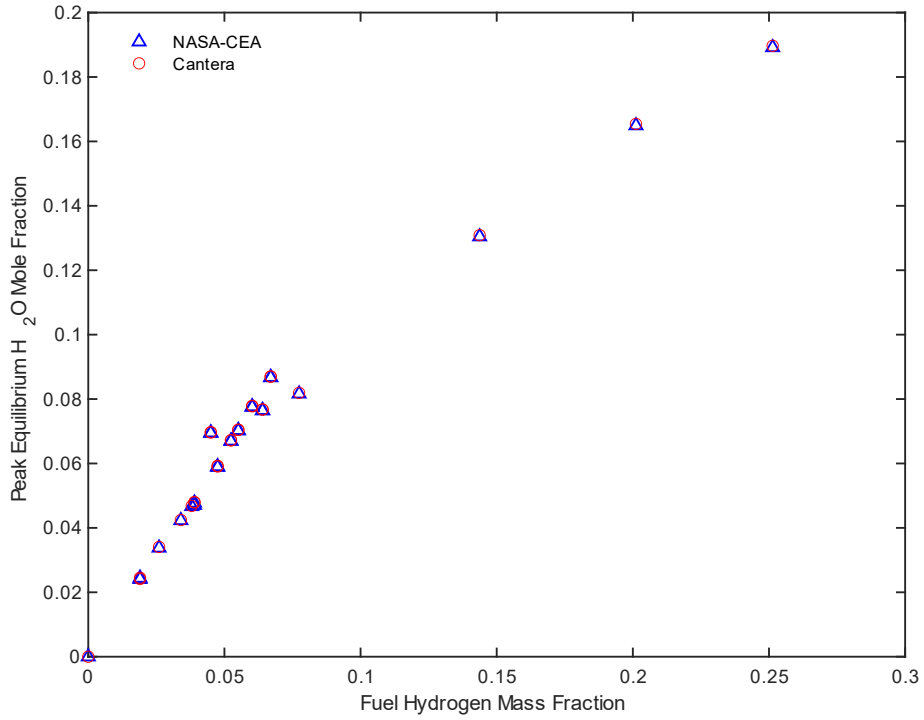

Figure E-38. Peak H_2O mole fraction compared to fuel hydrogen content.

Fuels with higher heating values tend to have a higher peak equilibrium temperature, which makes sense from a thermodynamic standpoint. If a fuel has a high energy of combustion, that also means the equilibrium temperature of an adiabatic system will also be higher than a similar system using a fuel with a lower heating value. This relationship is not linear, but it appears to increase sharply at the lowest heating rates, then it appears to taper off at higher heating rates. This divide is also observed when separated by fuel type, with the lowest and highest rank coals (lignites and anthracites) having the lowest heating values, followed by the mid-rank coals (subbituminous and bituminous coals), with most of the simple fuels having the highest heating values of the data set.

The CO_2 mole fraction is slightly less correlated, but the peak CO_2 mole fraction appears to decrease with increasing fuel heating value. This makes some sense with coals, since heating value correlates weakly with carbon content for some coals. The simpler hydrocarbon fuels tend to have higher heating values and lower carbon content than coals. There appears to be very slight correlation of peak CO_2 mole fraction with fuel oxygen for the coals, decreasing slightly with increasing oxygen content. This makes some sense with respect to elemental composition. If a fuel has more oxygen, its carbon content would tend to decrease. When compared to peak equilibrium temperature, the peak CO_2 mole fraction appears to decrease with increasing temperature, slowly at lower temperatures and more quickly at higher temperatures. This might be due to the equilibrium relationship between CO_2 and CO, which can be highly temperature dependent.

As expected, the peak H_2O mole fraction is highly dependent on the fuel hydrogen. When plotted against the hydrogen mass fraction in the fuel, the relationship is roughly linear and would be exactly linear if plotted against the hydrogen mole fraction in the fuel. There is only

one source of hydrogen in the equilibrium system, and that is the fuel used. The oxidizer stream (air) has no additional hydrogen to add to the H_2O mole fraction. The fuels used in this analysis were all on a dry basis, however, many industrial applications do not always have perfectly dry fuels. For wet systems (from not quite completely dry to some specialized slurry-type applications), the peak H_2O mole fraction would be much higher and much more dependent on the dryness (or wetness) of the system.

E.1.3 Complete Comparison of Experimental to Correlated Heating Values

In an effort to apply the correlations developed and presented in Chapter 7, several of the coal-based fuels with experimentally observed heating values were compared to fuels with the same elemental composition and heating values calculated using several of the correlations found in Chapter 7. The experimental heating values were used in cases E1-6 to E1-13 and the correlated heating values in E1-14 to E1-21. Some of the variability between the experimental and correlated heating values can be observed in the respective dashboard figures (see Figure E-6 to Figure E-21), however, the same statistical measures of fit discussed earlier (L_1, L_2, and infinity norms, and average and maximum relative error) can be used here to give a good overall picture of the disparities between the experimental and correlated heating values. Figure E-39 shows the five statistical values for equilibrium temperature and mole fractions of O_2, CO_2, CO, H_2O, and graphite. This plot compares the equilibrium states as calculated by NASA-CEA, although a similar comparison could be made using the Cantera-calculated equilibrium states.

The disparity between experimental and correlated heating values is higher than that between NASA-CEA and Cantera. While many of the cases led to a temperature difference of around 5 to 50 K between the experimental and correlated heating value equilibrium states, some differed by up to almost 1000 K (Mammoth anthracite). The greatest disparity is in the highest-

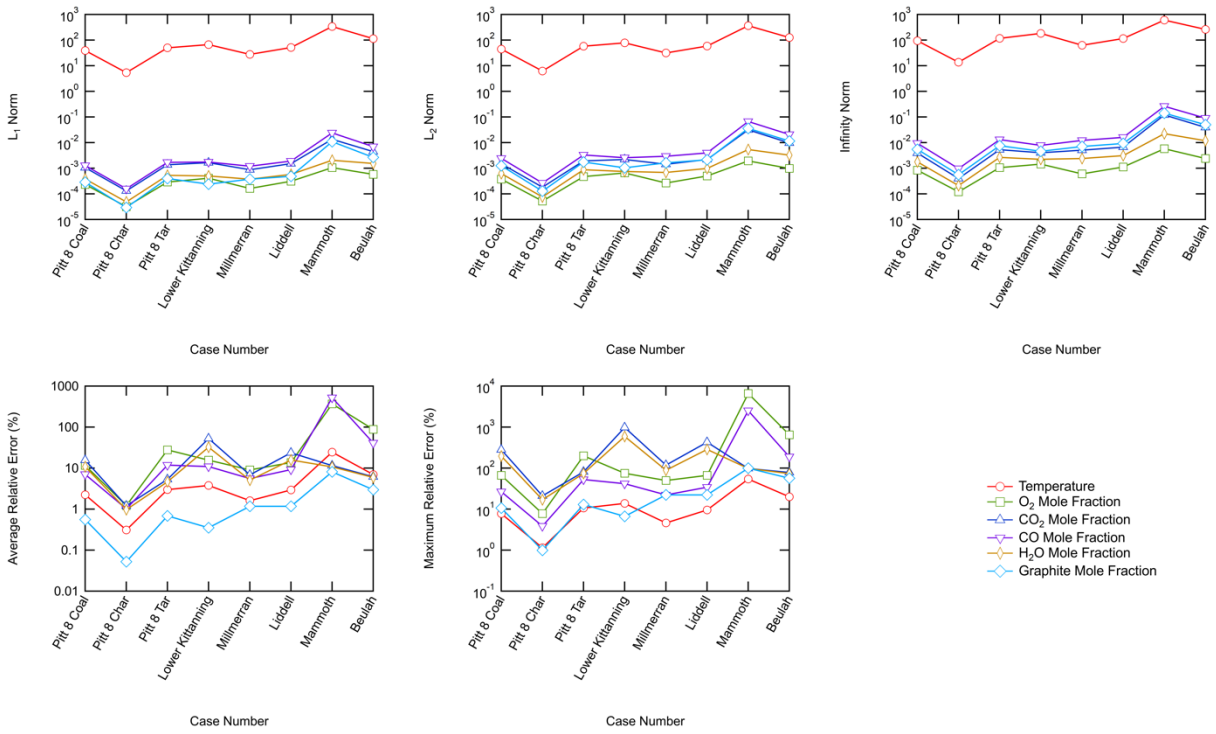

Figure E-39. Comparison of fuels using experimental vs. correlated heating values.

and lowest-rank coals, many of which would not be used regularly in common industrial applications; however, this comparison indicates that there is potentially a bit of improvement to be made in the heating value correlations, particularly in the highest- and lowest-rank coals.

E.2 Two-Mixture Fraction Results

Like the one-mixture fraction comparison, too much data was generated in the two-mixture fraction comparison to be included in Chapter 8. This appendix section is divided into two main categories: (1) the complete set of contour plots for all of the two-mixture fraction fuel cases listed in Table 8-4 and (2) a comparison of several coals using experimental and correlated heating values. Table E-2 details all two-mixture fraction fuel cases, with four additional cases not found in Table 8-4. Also included here are a few details about the pyrolysis conditions at

which the char and tar/volatiles were formed, including high or low temperature and measured total volatiles yield.

Table E-2. Complete Two-Mixture Fraction Fuel Cases

Case No.	Char	Volatiles	ΔH_f	Pyrolysis Yield
E2-1	Graphite	Benzene	Exp.	-
E2-2	Graphite	Methane	Exp.	-
E2-3	Graphite	Ethane	Exp.	-
E2-4	Graphite	Ethylene	Exp.	-
E2-5	Pitt 8 char (low temperature)	Pitt 8 TAR	Exp.	0.1491
E2-6	Pitt 8 char (high temperature)	Pitt 8 TAR	Exp.	0.4102
E2-7	Pitt 8 char (low temperature)	Pitt 8 VOLATILES	Exp.	0.1491
E2-8	Pitt 8 char (high temperature)	Pitt 8 VOLATILES	Exp.	0.4102
E2-9	Millmerran char (high temperature)	Millmerran TAR	Exp.	0.545
E2-10	Millmerran char (high temperature)	Millmerran VOLATILES	Exp.	0.545
E2-11	Millmerran char (low temperature)	Millmerran TAR	Exp.	0.313
E2-12	Millmerran char (low temperature)	Millmerran VOLATILES	Exp.	0.313
E2-13	Pitt 8 char (low temperature)	Pitt 8 VOLATILES	Corr.	0.1491
E2-14	Pitt 8 char (high temperature)	Pitt 8 VOLATILES	Corr.	0.4102
E2-15	Millmerran char (high temperature)	Millmerran VOLATILES	Corr.	0.545
E2-16	Millmerran char (low temperature)	Millmerran VOLATILES	Corr.	0.313

E.2.1 Contour Plots of Six Equilibrium Variables

Section 8.3.2 shows only a couple of cases in contour plots for each variable to show general trends that occur in all fuel cases. This section of Appendix E shows contour plots for

cases E2-1 through E2-12, which are the cases that use simplified hydrocarbon surrogates of char and volatiles as well as coal-based fuels with experimental heating values. The following contour plots are shown in the same order as all the variables of interest, starting with equilibrium temperature followed by the mole fractions of O_2, CO_2, CO, H_2O, and graphite. In each contour plot figure, rows correspond to the different fuel cases in Table E-2 and columns correspond to different "mixing" conditions of the fuels, from no volatiles to 100 percent volatiles in the fuel mixture. All contour plots are kept at the same range for each variable, shown with the colorbar at the top right of each contour plot. Discussion will follow each set of contour plots for each of the variables of interest. Figure E-40 shows the contour plots for equilibrium temperature.

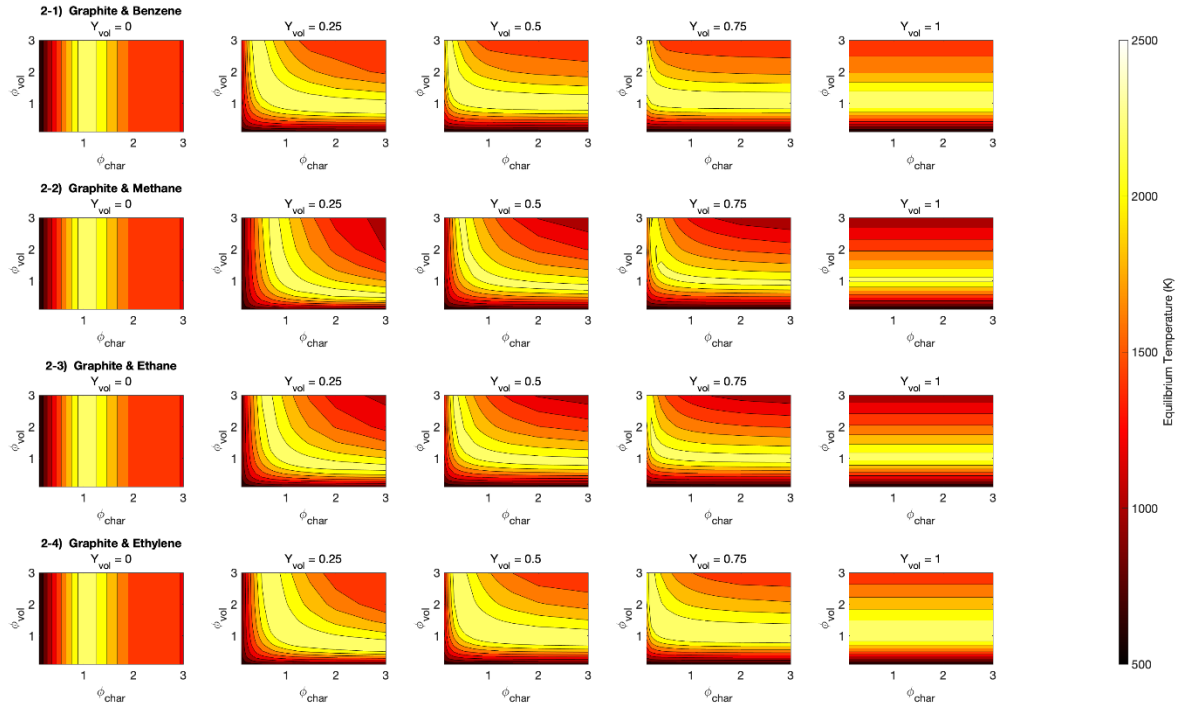

Figure E-40. Complete contour plots of equilibrium temperature.

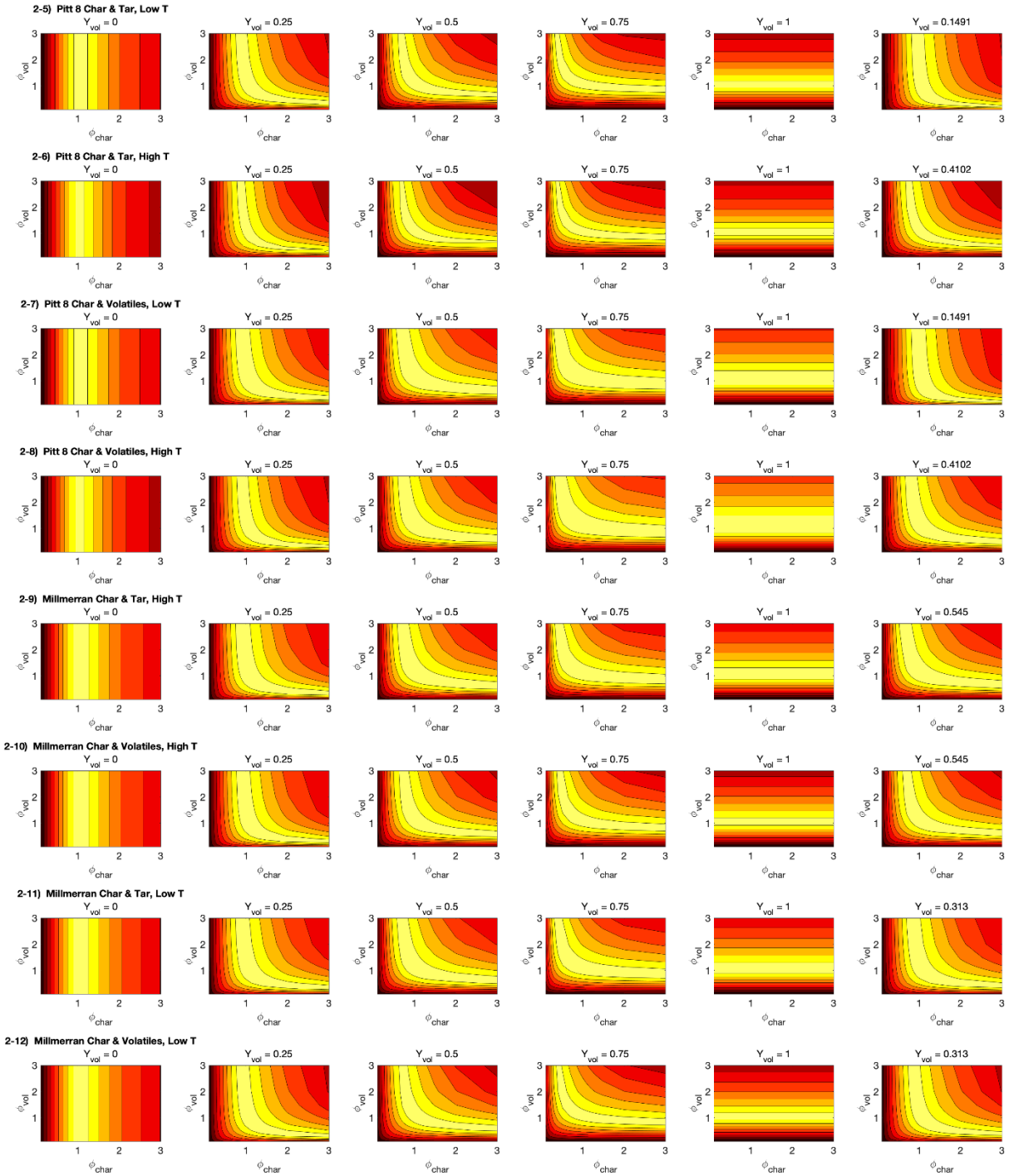

Figure E-40. Complete contour plots of equilibrium temperature, CONTINUED.

Looking up and down each column compares similar mixing conditions for each fuel case. The general shapes are similar for each fuel case, however, there are slight differences, especially with higher volatiles mixtures (a volatiles mix of 75 percent and higher). The difference is more pronounced between the coal-based fuels (bottom eight rows) and the simpler hydrocarbon surrogate gases (top four rows) but is less pronounced among just the coal-based fuels. The simpler fuels also tend to have higher temperatures than the coal-based fuels, particularly around stoichiometric conditions (equivalence ratios of around one). Figure E-47 shows the peak temperature ranges for all 12 cases.

Oxygen is only briefly described in Section 8.3.2 due to very few deviations among fuel cases, like the one-mixture fraction comparison. Figure E-41 shows the contour plots of the O_2 mole fractions at equilibrium.

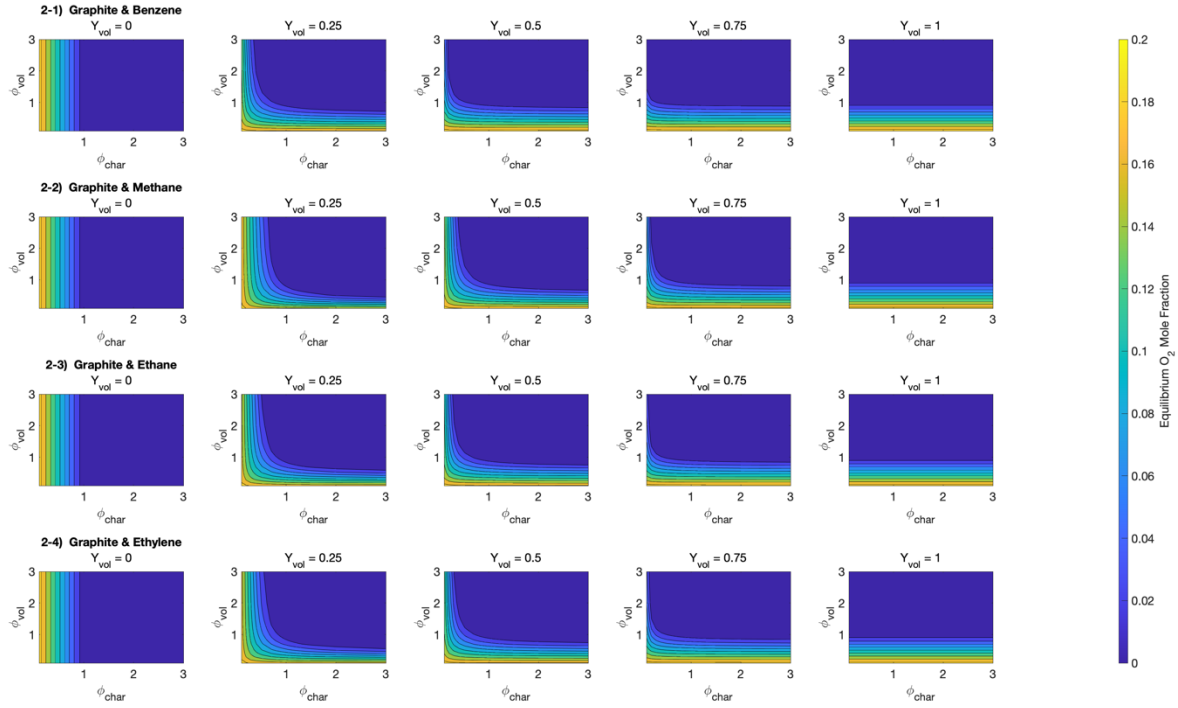

Figure E-41. Complete contour plots of equilibrium O_2 mole fraction.

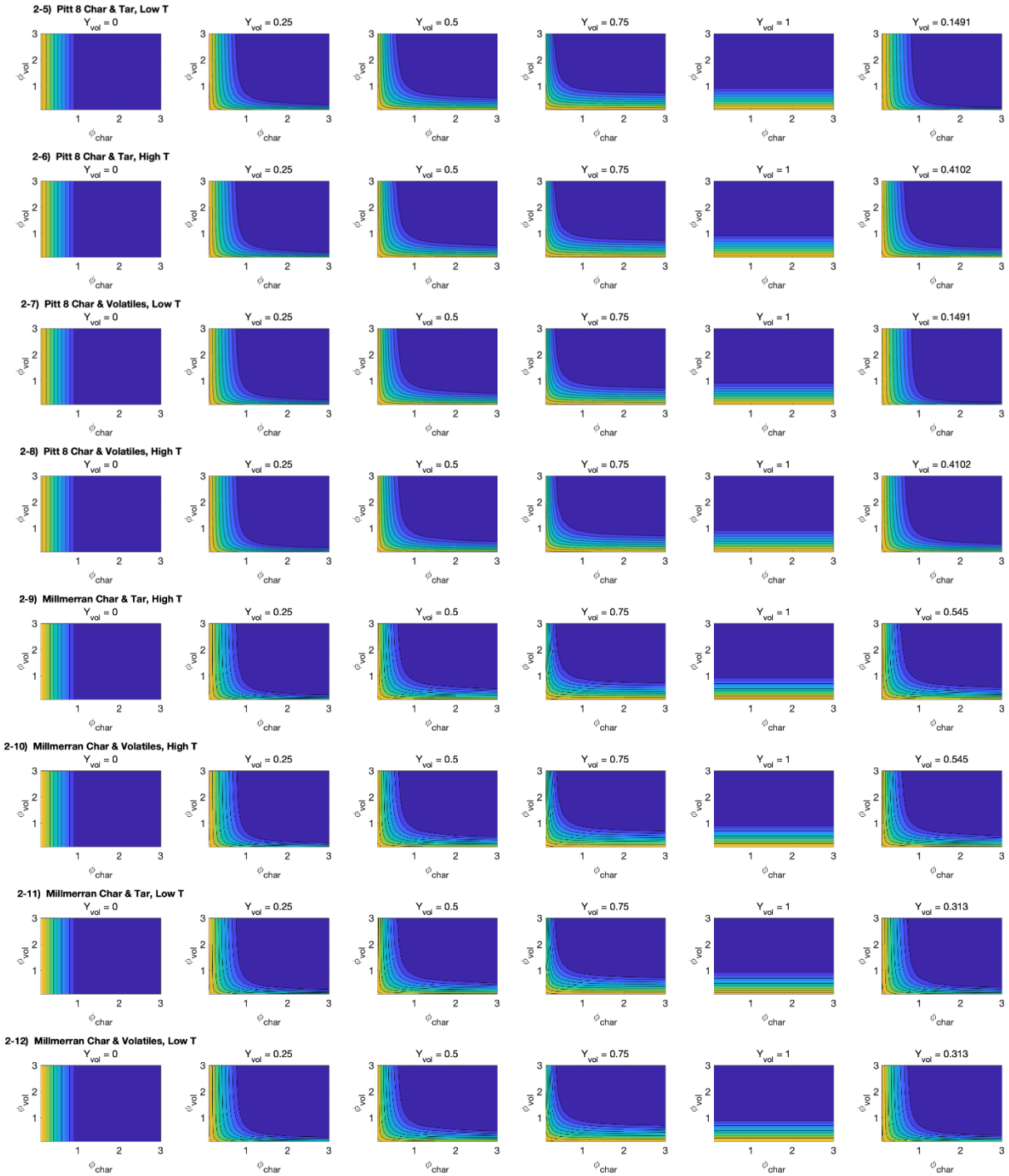

Figure E-41. Complete contour plots of equilibrium O_2 mole fraction, CONTINUED.

The equilibrium O_2 mole fraction does not change much with the fuel type used. This makes sense since most (or all for simple hydrocarbon surrogates) equilibrium oxygen comes from the air, and the amount of O_2 at equilibrium is highly dependent on equivalence ratio. Like the one-mixture fraction comparison, O_2 is only prevalent at lower equivalence ratios (from very fuel-lean to just fuel-rich of stoichiometric conditions). Most common industrial coal combustion applications will operate in the vicinity of stoichiometric conditions, either slightly fuel-lean or slightly fuel-rich.

The equilibrium CO_2 mole fraction is highly dependent on the carbon content of the parent fuel but is slightly attenuated at high equivalence ratios by the CO mole ratio. The CO_2 mole fraction contour plots are found in Figure E-42 and the CO mole fraction contour plots are in Figure E-43.

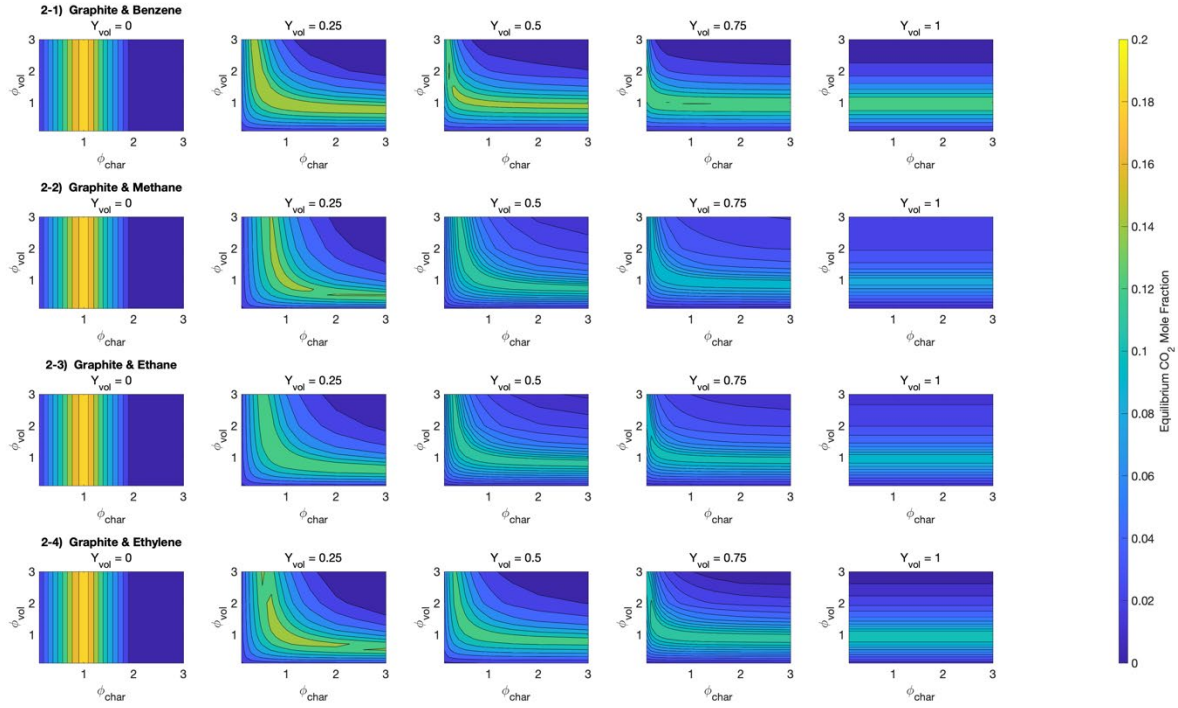

Figure E-42. Complete contour plots of equilibrium CO_2 mole fraction.

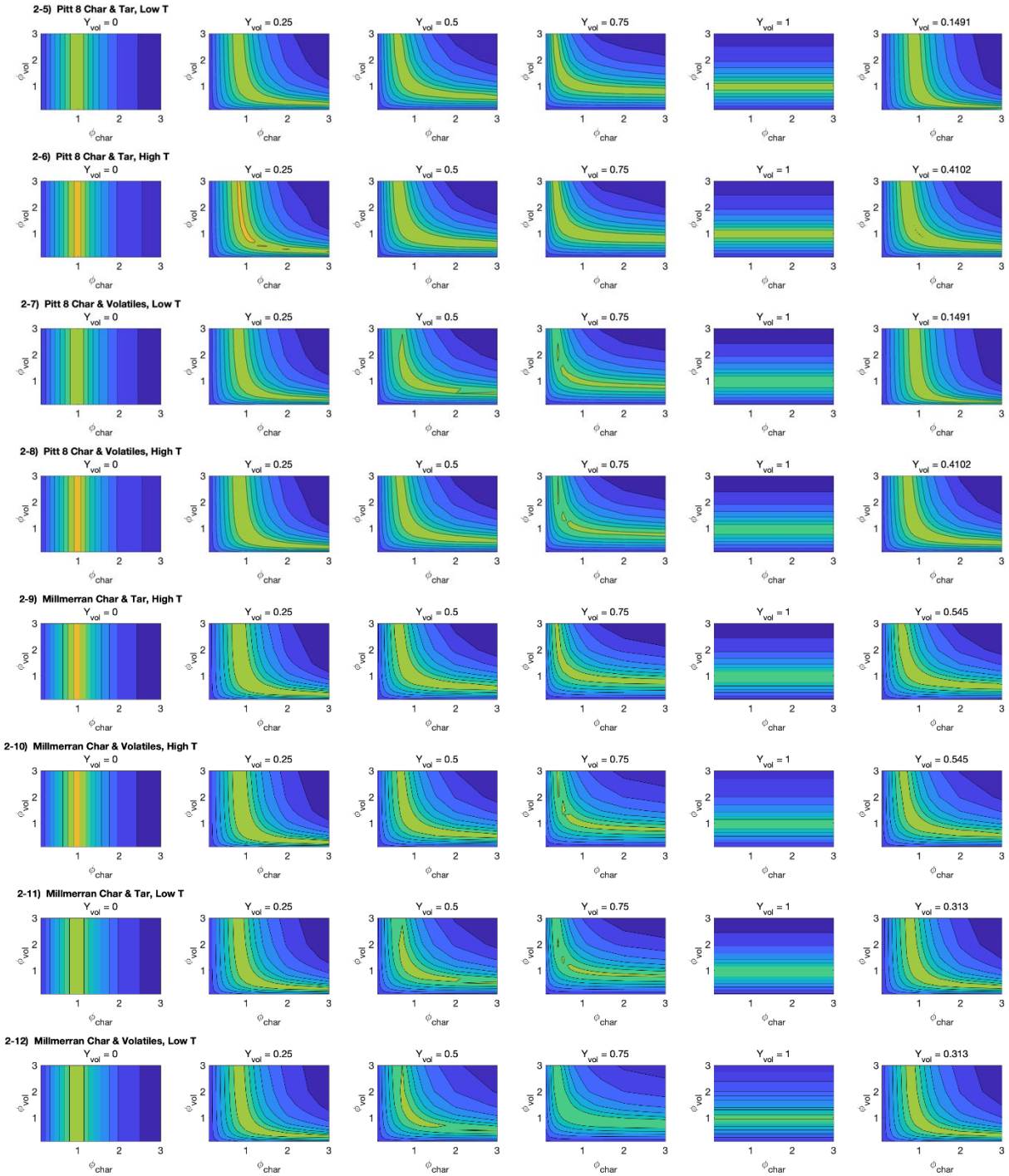

Figure E-42. Complete contour plots of equilibrium CO_2 mole fraction, CONTINUED.

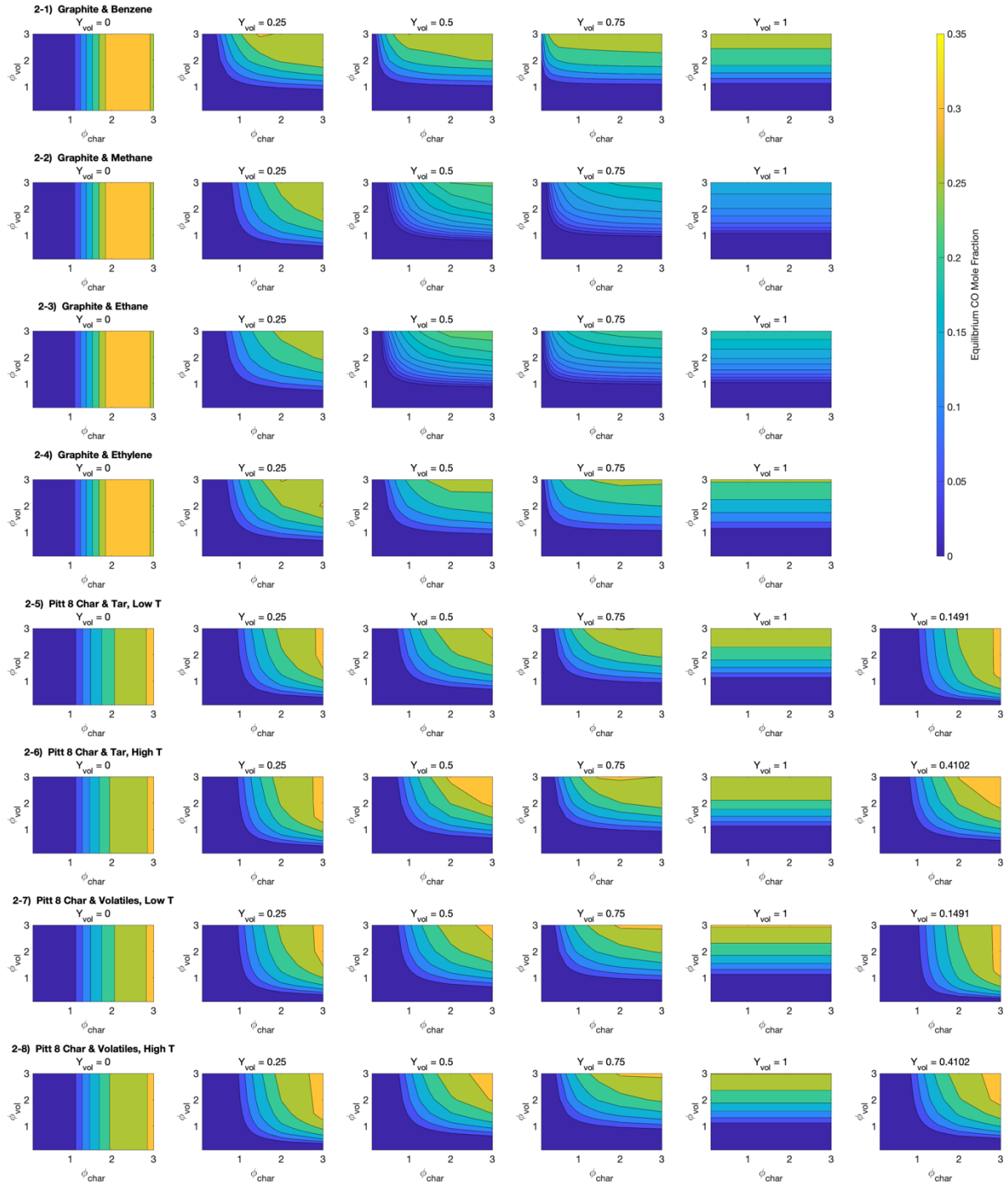

Figure E-43. Complete contour plots of equilibrium CO mole fraction.

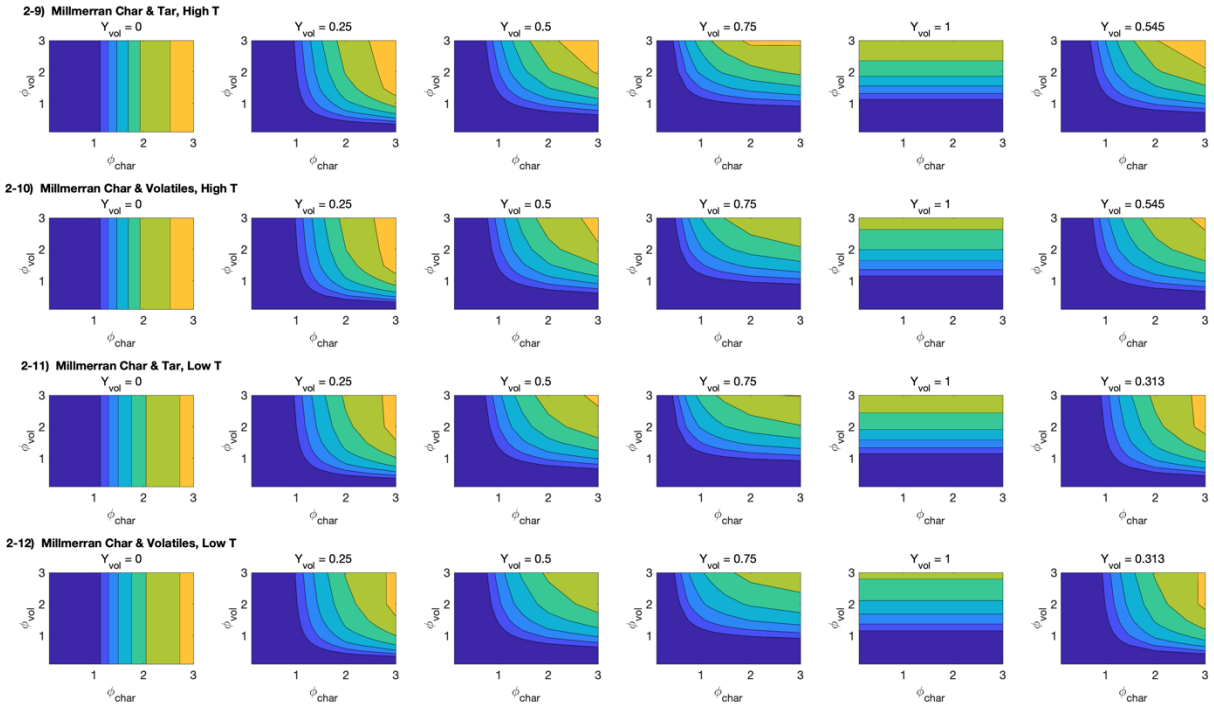

Figure E-43. Complete contour plots of equilibrium CO mole fraction, CONTINUED.

The contour plots of the CO_2 mole fractions exhibit a similar shape to the equilibrium temperature plots. This trend was also observed in the one-mixture fraction comparison. The peak CO_2 mole fractions are a bit more variable than the temperature plots, generally being highly dependent on the fraction of carbon in the original fuel. The simple hydrocarbon surrogates tend to exhibit the highest and lowest peaks depending on the fuel mixing condition. Graphite is entirely carbon, leading to the largest peak CO_2 mole fractions while the simple volatile surrogates are lower in carbon, leading to the smallest peak CO_2 mole fractions. The peak ranges are shown in Figure E-51. Equilibrium CO mole fractions follow an inverse trend to the equilibrium O_2 mole fractions—where O_2 is highest, CO is lowest and vice-versa. This means that CO only becomes prevalent in extreme fuel-rich conditions. Peak CO mole fraction ranges are shown in Figure E-53.

Equilibrium H_2O mole fractions are highly dependent on what fuel is used, since the only source of hydrogen in the equilibrium mixture comes from the fuel. Figure E-44 shows the contour plots of equilibrium H_2O mole fraction.

The char-only mixing conditions of the simple hydrocarbon fuel cases (first four rows) are graphite, which is only carbon. This is why the contour plots in the first column of the first four rows appear blank because no H_2O is formed at equilibrium. Because the equilibrium H_2O mole fraction is highly dependent on fuel hydrogen, the simple hydrocarbon volatiles surrogates produce much higher H_2O mole fractions since they have a higher amount of fuel hydrogen. The H_2O mole fraction contours exhibit a similar shape as both the temperature and CO_2 mole fraction contours, in a similar fashion to the one-mixture fraction comparison. There is a large variability in the peak H_2O mole fraction ranges, as shown in Figure E-55.

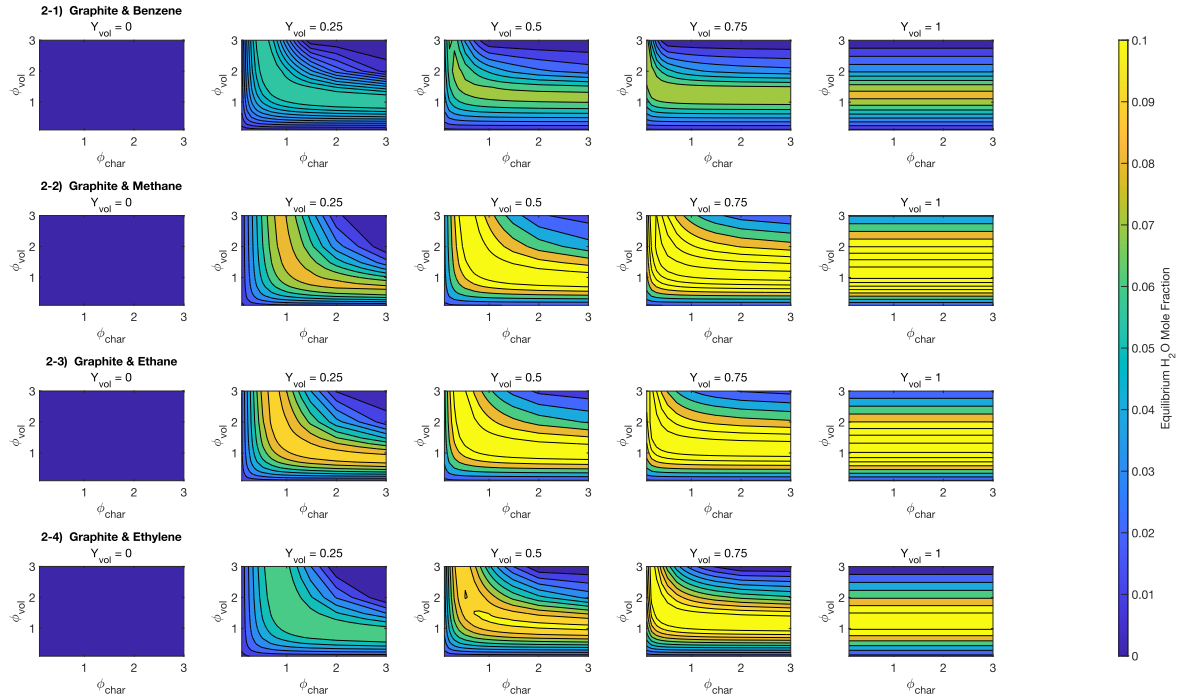

Figure E-44. Complete contour plots of equilibrium H_2O mole fraction.

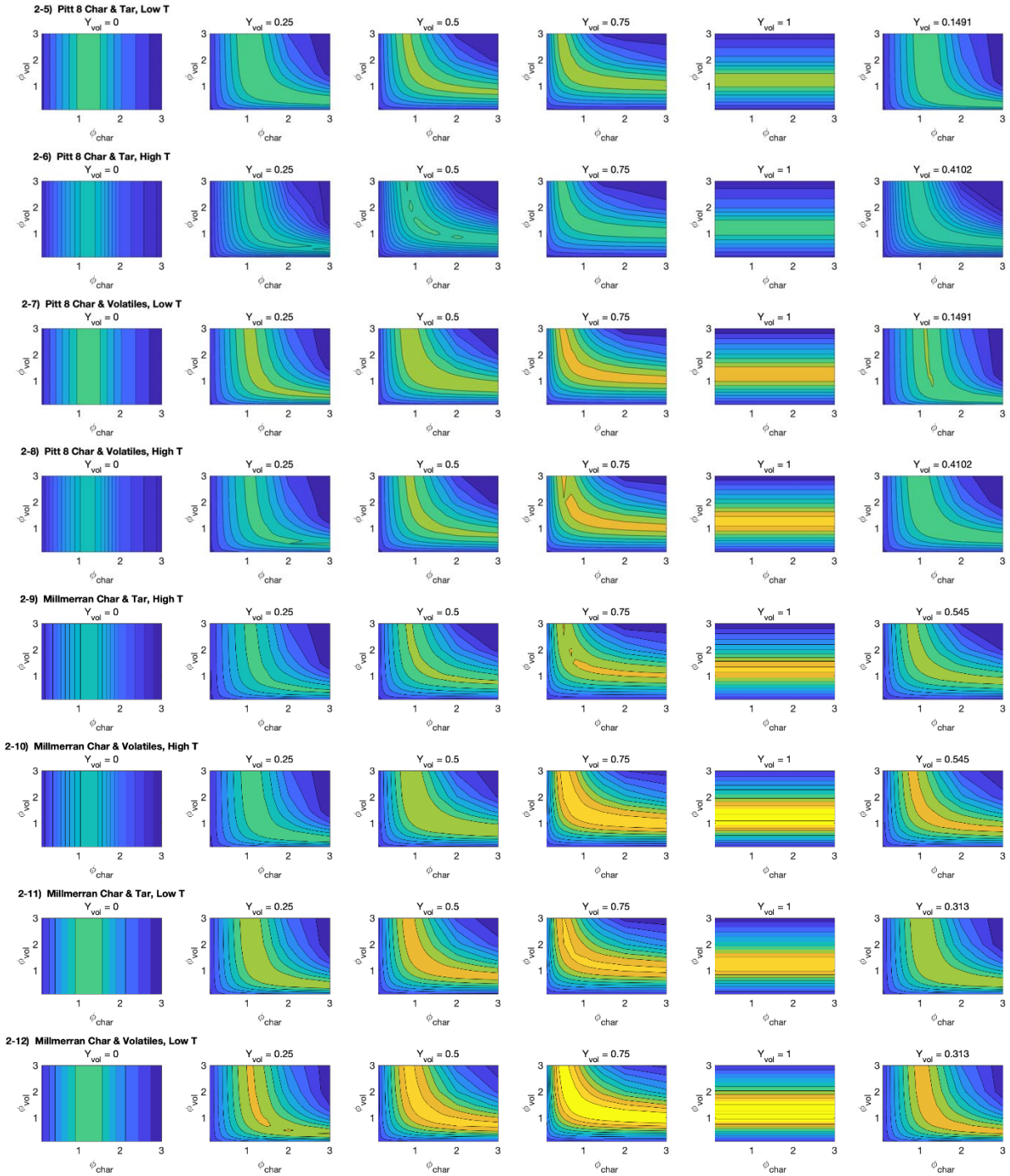

Figure E-44. Complete contour plots of equilibrium H_2O mole fraction, CONTINUED.

The final variable of interest is the equilibrium mole fraction of graphite. The contour plots for equilibrium graphite mole fraction are shown in Figure E-45.

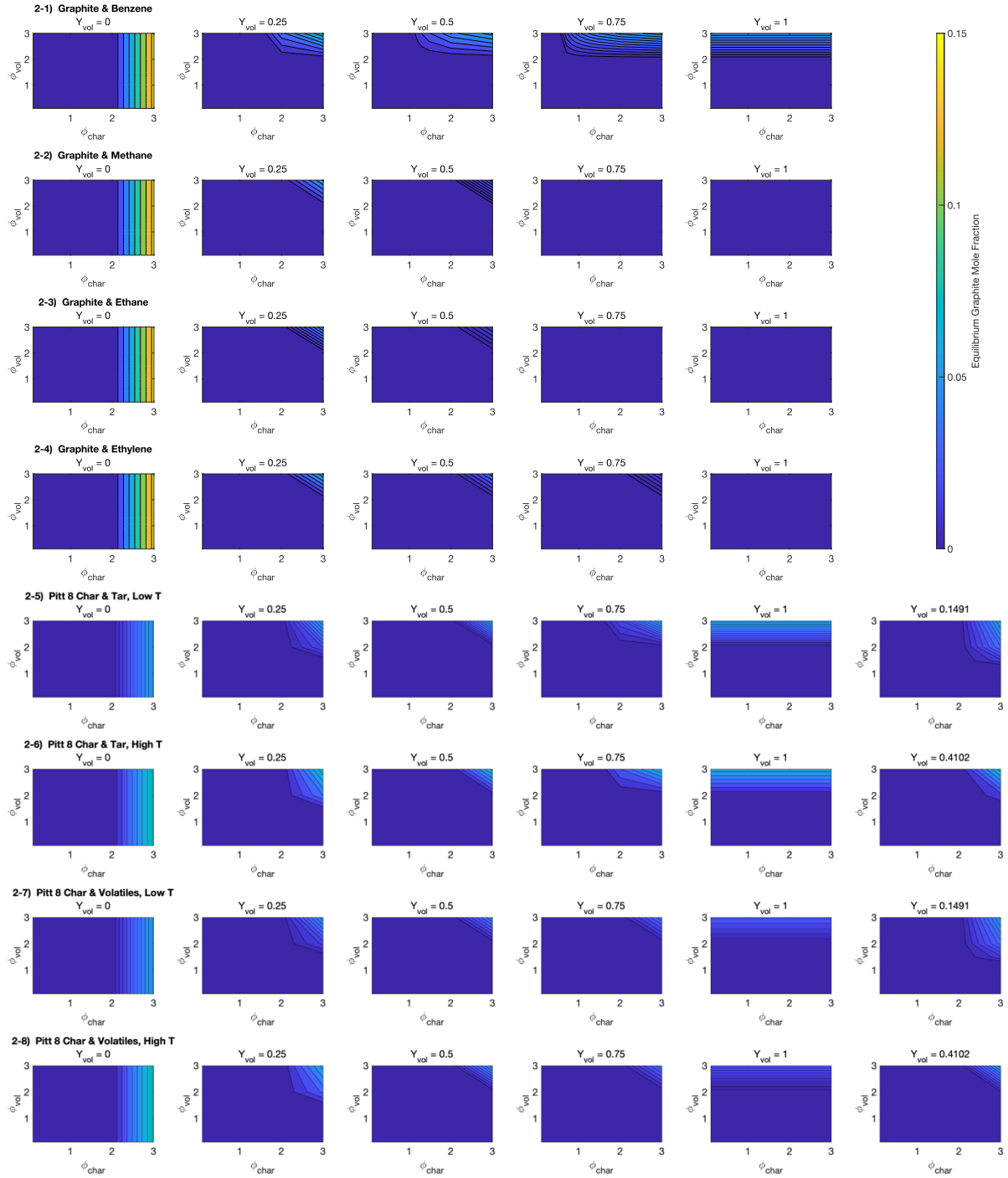

Figure E-45. Complete contour plots of equilibrium graphite mole fraction.

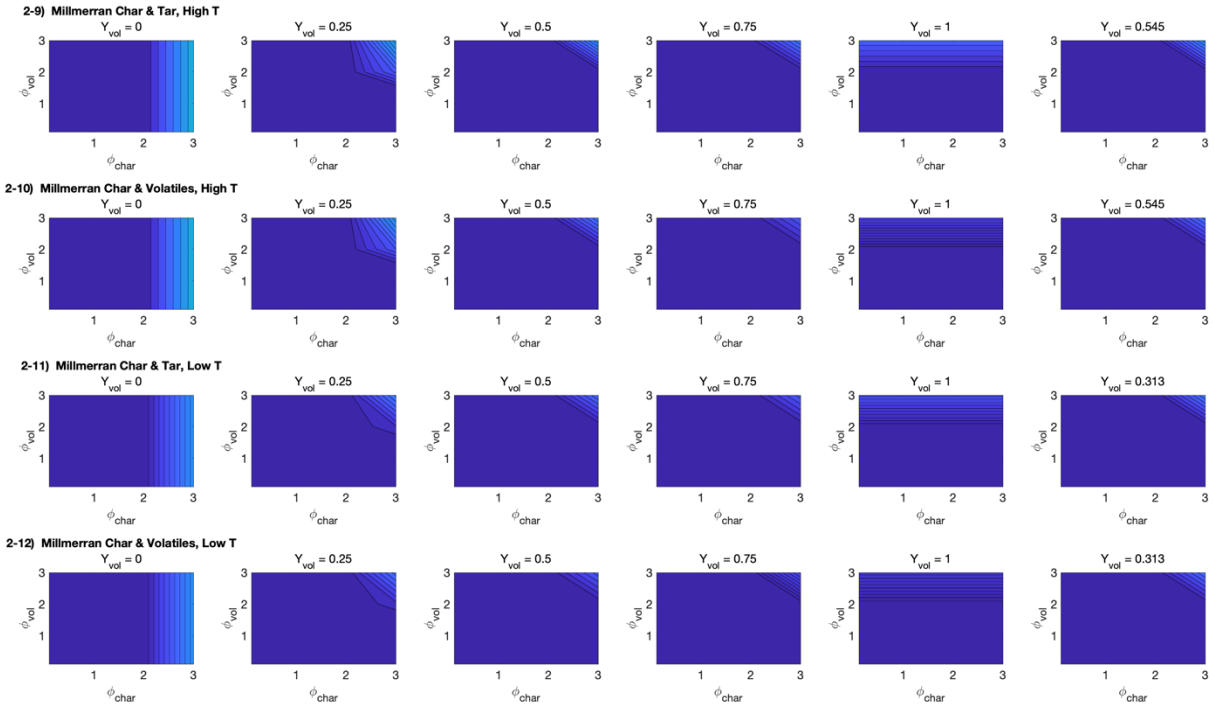

Figure E-45. Complete contour plots of equilibrium graphite mole fraction, CONTINUED.

Both NASA-CEA and Cantera programs generally convert unreacted fuel to graphite. Like the CO mole fraction, graphite only becomes significant in extreme fuel-rich conditions. In addition, many of the fuel cases form very small amounts of graphite, even at high equivalence ratios. Some of the plots in Figure E-45 appear blank because those fuel cases did not form any graphite at equilibrium.

E.2.2 Experimental vs. Correlated Heating Values

The final four fuel cases in Table E-2 are coal-based fuels with correlated heating values. The equilibrium states of these four cases were compared to the equivalent fuel cases with experimentally observed heating values. In order to discover where the correlated heating value cases diverge from the experimental heating value cases, contour plots of the absolute value of the residuals between the two equilibrium states were made. In addition, the peak variable ranges

were added to those of the first 12 fuel cases. The equilibrium temperature plots are shown first, with the contour plots of the residuals in Figure E-46 and the complete peak temperature ranges in Figure E-47. The new peak temperature ranges are shown in green to differentiate from the other fuel cases.

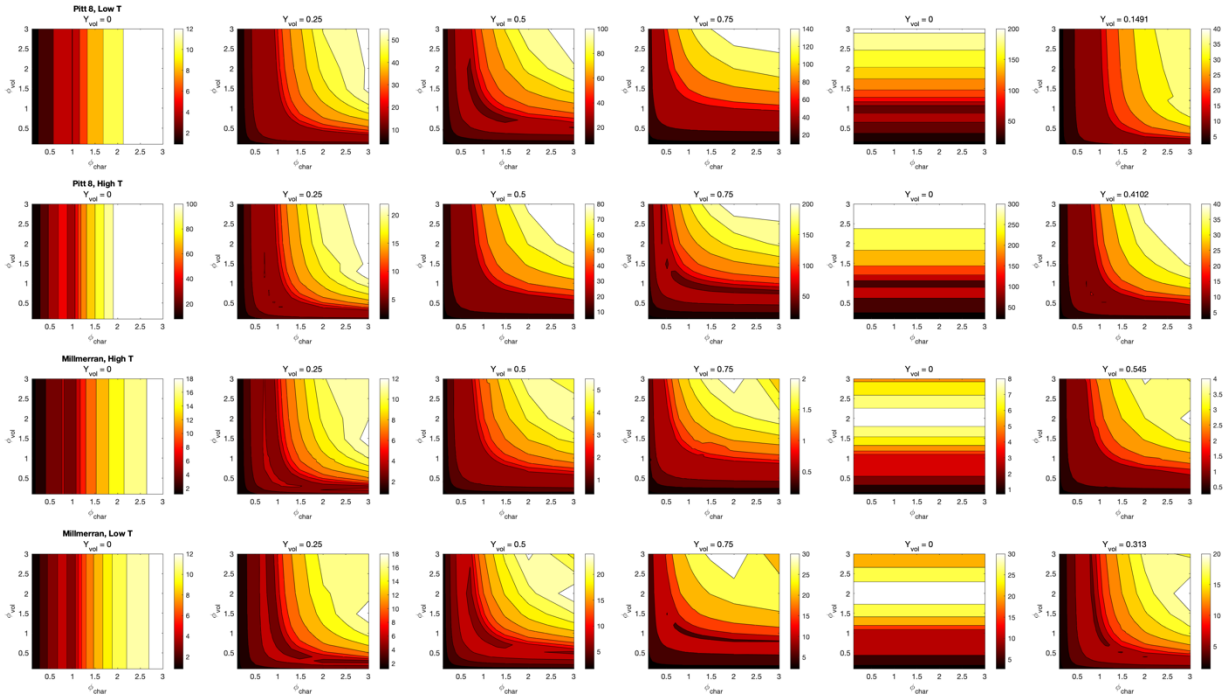

Figure E-46. Contour plots of experimental to correlated heating value—temperature.

The residuals show that most of the variability in the equilibrium temperature generally occurs in the highest equivalence ratios. This is not worrisome for most industrial coal combustion applications since they do not operate in such extreme fuel-rich conditions. The correlated heating value cases correspond to the following experimental heating value cases: E2-13 to E2-7, E2-14 to E2-8, E2-15 to E2-10 and E2-16 to E2-12. Looking at the peak temperature ranges, there is some overlap for the Pitt 8 coals (E2-13 and E2-14), but the ranges are vastly different, being much smaller for the correlated heating value cases. The ranges are much closer

for the Millmerran coals with the correlated heating value ranges mostly overlapping with the experimental.

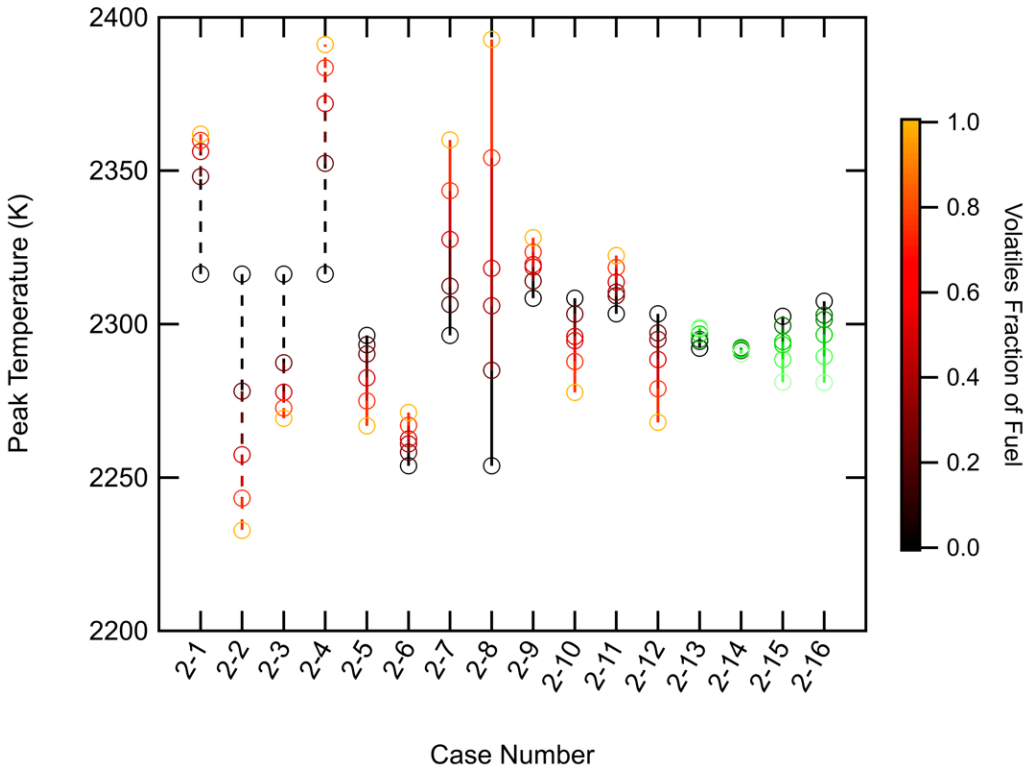

Figure E-47. Complete peak equilibrium temperature ranges.

The results for the O_2 mole fraction comparison are shown next. Figure E-48 shows the residual contour plots between experimental and correlated heating value cases and Figure E-49 shows the peak O_2 mole fraction ranges with the addition of the correlated heating value cases.

Overall, there is very little variability in the equilibrium O_2 mole fractions between experimental and correlated heating value cases, however, the most significant deviation is in mixtures of close to stoichiometric conditions. Unlike the peak temperature ranges, the peak O_2 mole fraction ranges are virtually identical between experimental and correlated heating value cases.

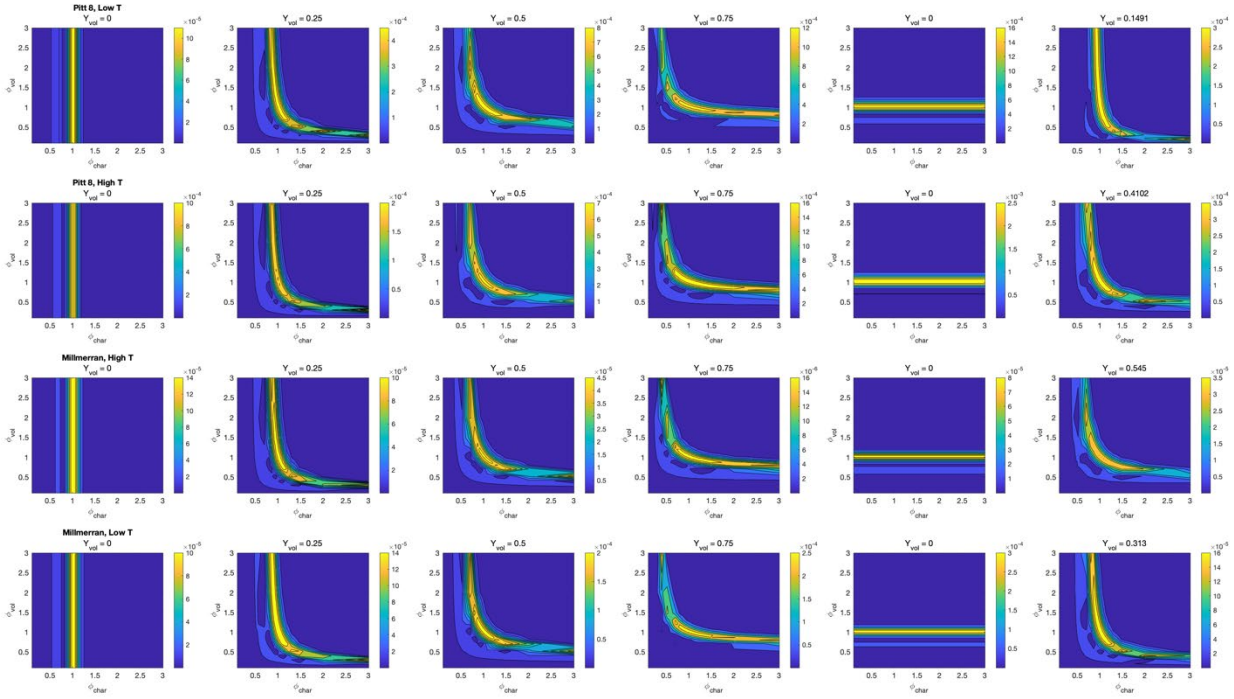

Figure E-48. Contour plots of experimental to correlated heating value—O_2 mole fractions.

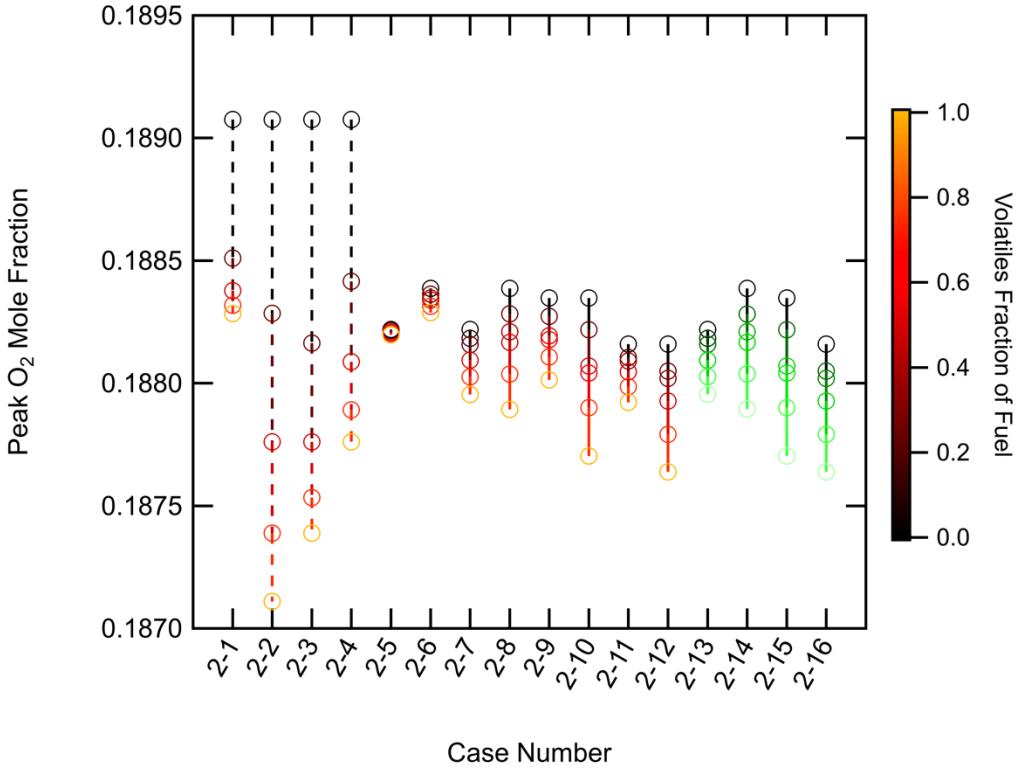

Figure E-49. Complete peak O_2 mole fraction ranges.

The next equilibrium variables are the mole fractions of CO_2 and CO. These two compounds are usually in equilibrium with each other, with CO being more prevalent in fuel-rich conditions. The contour plots of the residuals of CO_2 mole fractions between experimental and correlated heating value cases are found in Figure E-50 with the updated peak CO_2 mole fraction ranges in Figure E-51. Similarly, the contour plots of CO mole fractions are shown in Figure E-52 and the updated peak CO mole fraction ranges are in Figure E-53.

For equilibrium CO_2 mole fraction, the experimental heating value cases are a bit different than the correlated heating value cases in terms of where the most deviation occurs. According to Figure E-50, there are two main areas of significant deviation in most comparisons: at or near stoichiometric conditions and in extreme fuel-rich conditions. These two areas of deviation are also observed in the equilibrium CO mole fraction comparisons in Figure E-52, although to a lesser extend at or near stoichiometric conditions. This makes sense since CO_2 and

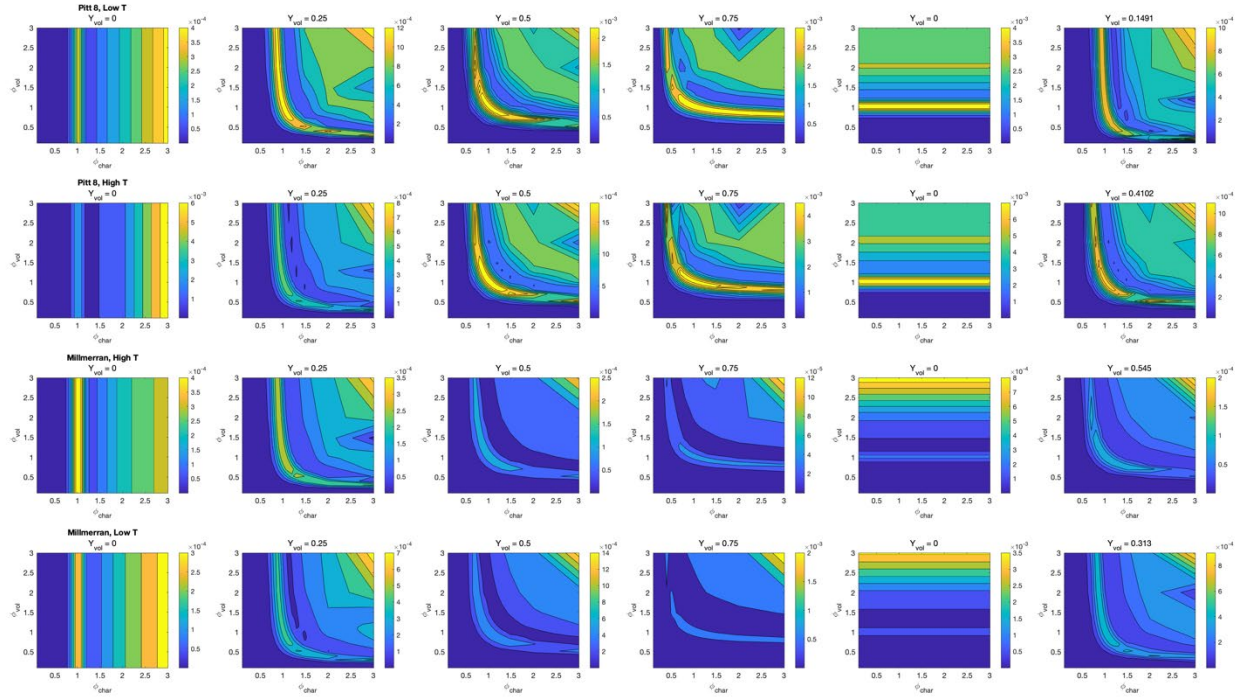

Figure E-50. Contour plots of experimental to correlated heating value—CO_2 mole fractions.

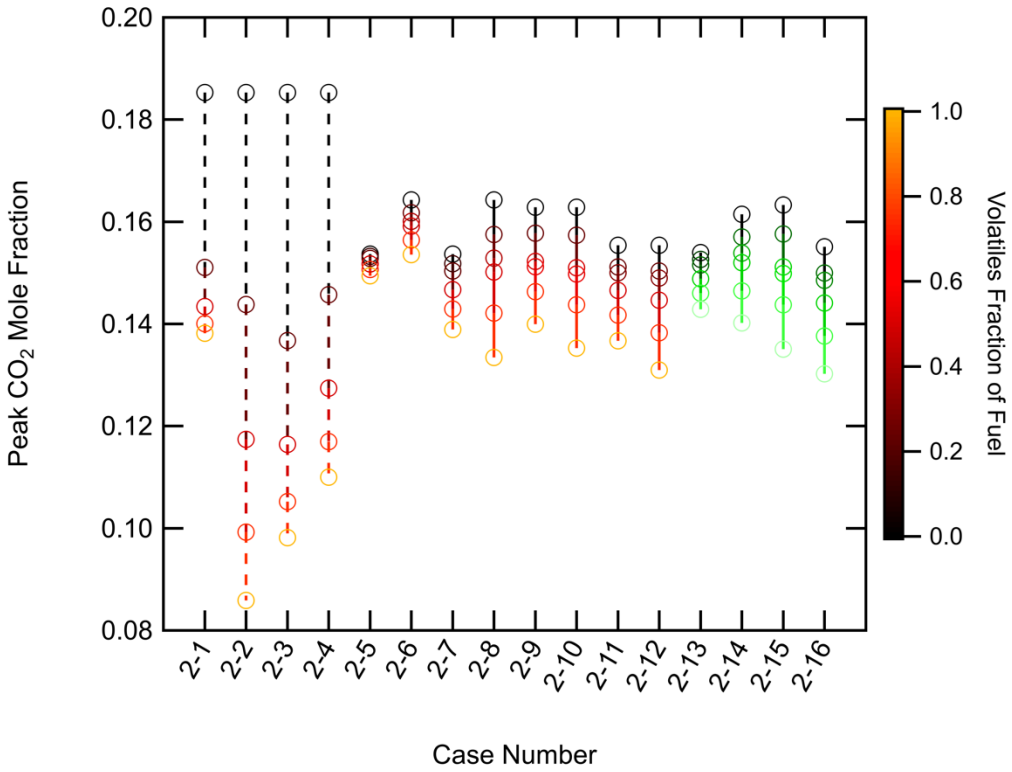

Figure E-51. Complete peak CO_2 mole fraction ranges.

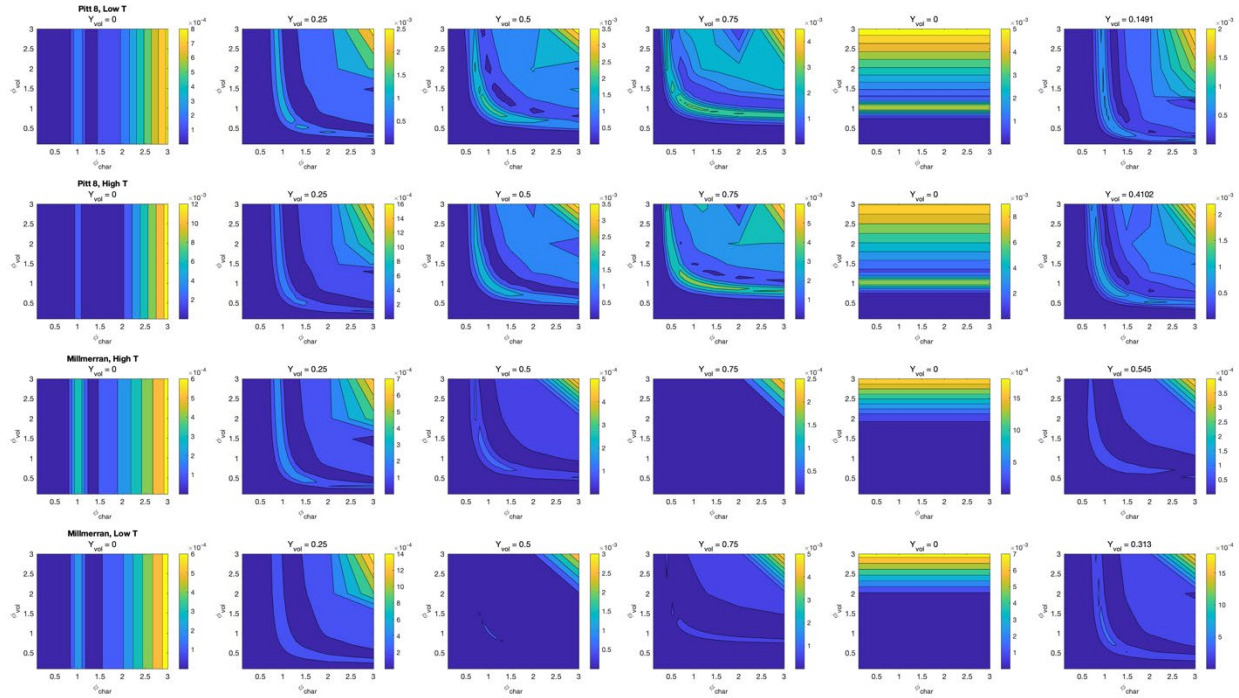

Figure E-52. Contour plots of experimental to correlated heating value—CO mole fractions

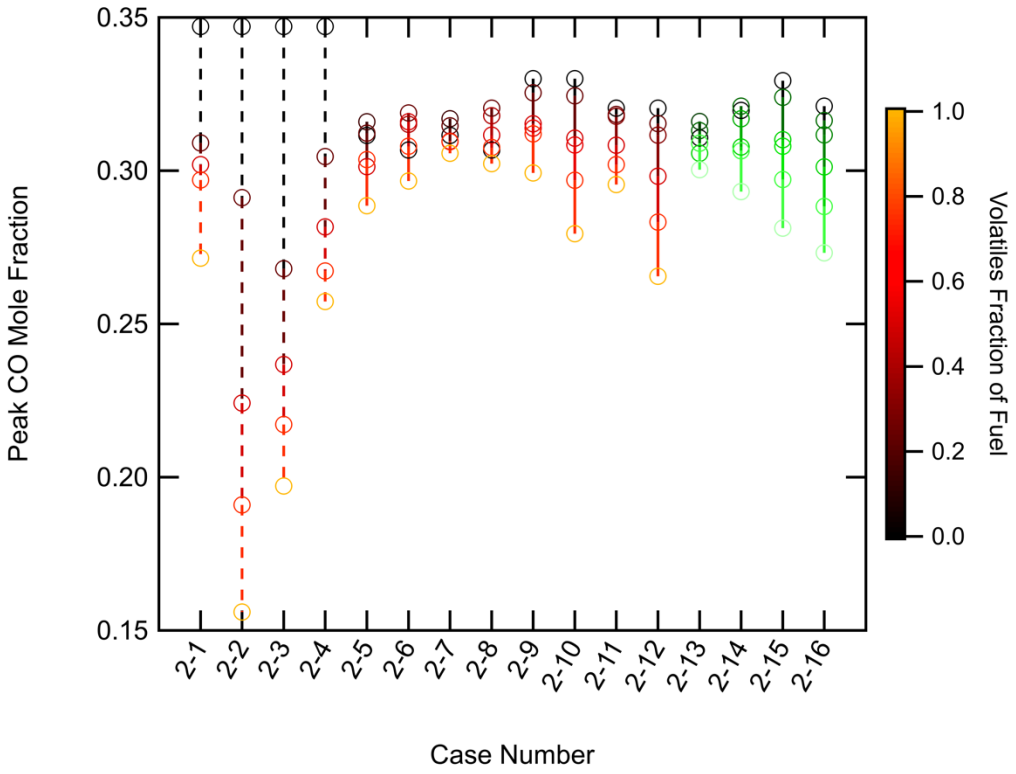

Figure E-53. Complete peak CO mole fraction ranges.

CO are generally in equilibrium with each other, depending highly on both temperature and oxygen availability in the system. Interestingly, there is very little difference in the peak CO_2 and CO mole fraction ranges between experimental and correlated heating value cases.

The equilibrium H_2O mole fraction generally follows similar trends to both temperature and CO_2 mole fractions. The contour plots of the residuals between experimental and correlated heating value cases are found in Figure E-54 and the peak H_2O mole fraction ranges are shown in Figure E-55.

Like the CO_2 and CO mole fraction comparisons, there is some slight deviation between experimental and correlated heating value cases in H_2O mole fraction at or near stoichiometric conditions, however, most of the deviation occurs in fuel-rich conditions. In the Pitt 8 cases (top two rows), the greatest deviation actually occurs not at the highest equivalence ratios, but at

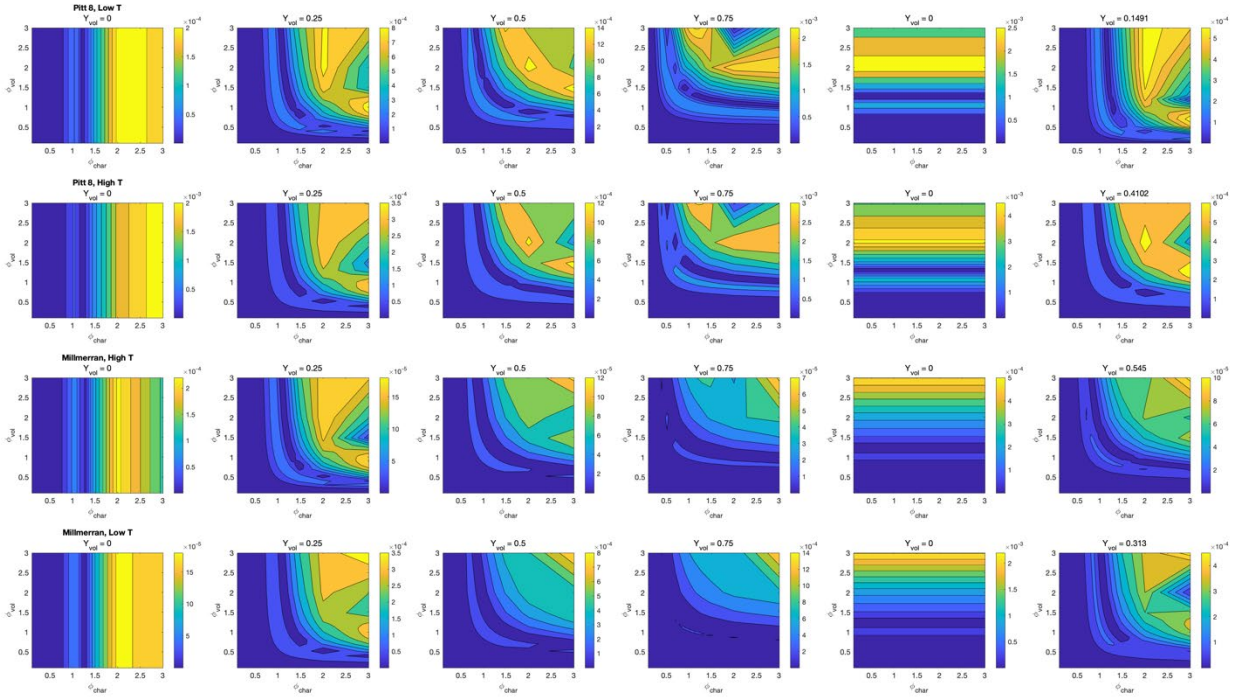

Figure E-54. Contour plots of experimental to correlated heating value—H_2O mole fraction.

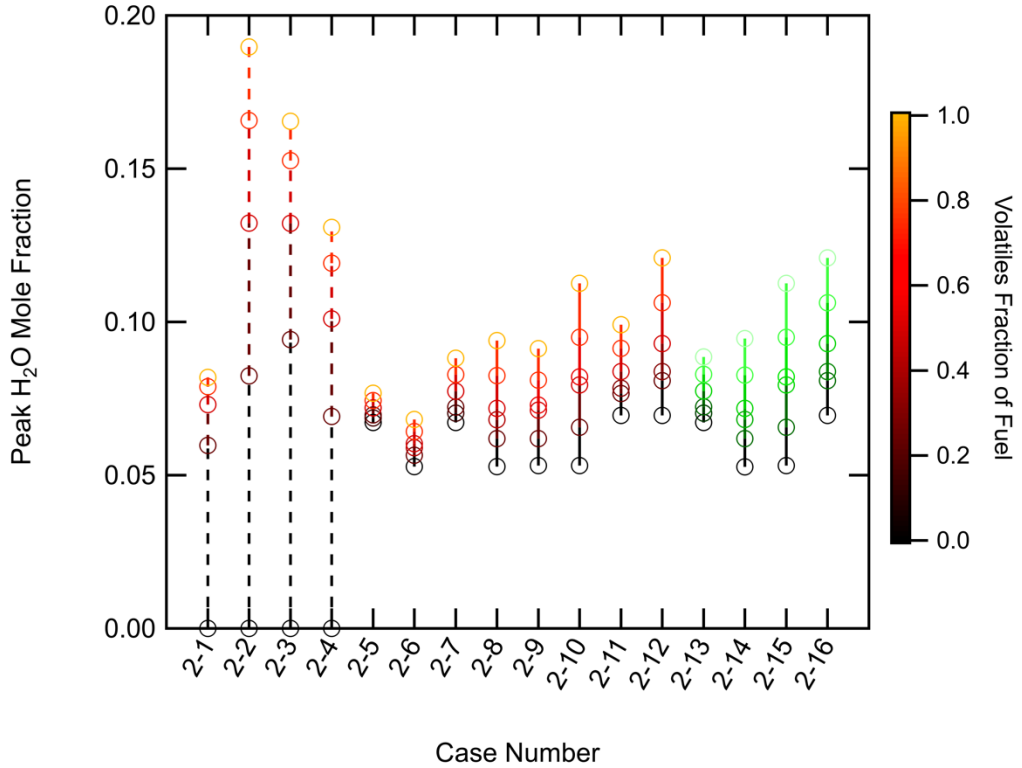

Figure E-55. Complete peak H_2O mole fraction ranges.

equivalence ratios of around 2 to 2.5 with less deviation at higher equivalence ratios. It is unclear why this occurs in the Pitt 8 cases but not in the Millmerran cases. Like the O_2 mole fraction ranges, the H_2O mole fraction ranges do not appear to vary between experimental and correlated heating value cases. This is understandable because the only source of hydrogen is the parent fuel, which the composition does not change between heating value cases.

Graphite is the final equilibrium variable observed in this analysis. Like the CO mole fraction, graphite usually only occurs in extreme fuel-rich conditions. The contour plots showing the residual graphite mole fractions between experimental and correlated heating value cases are found in Figure E-56 and the updated graphite mole fraction ranges are in Figure E-57.

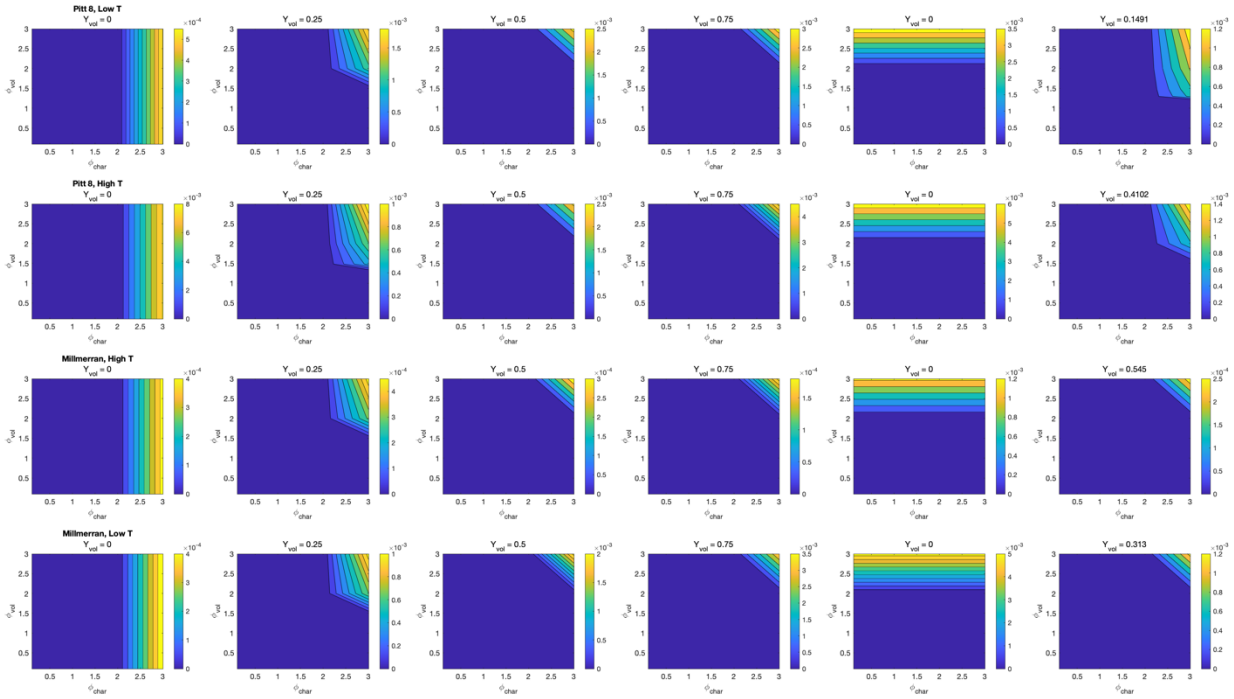

Figure E-56. Contour plots of experimental to correlated heating value—graphite.

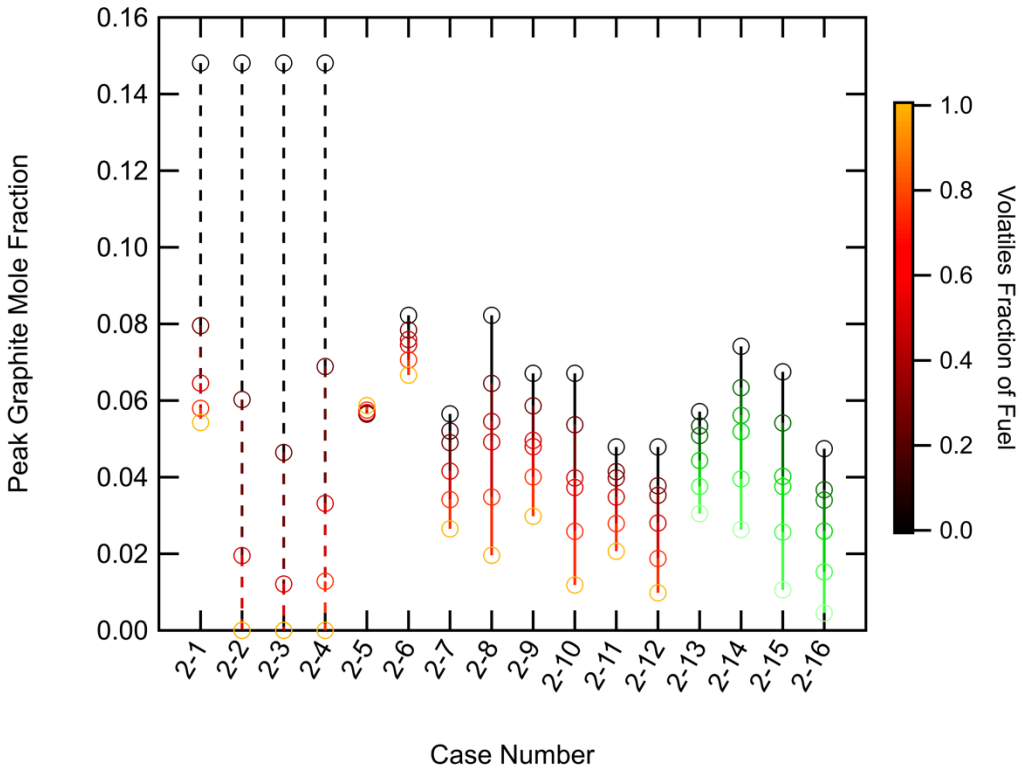

Figure E-57. Complete peak graphite mole fraction ranges.

Because graphite only occurs in extremely fuel-rich conditions, the maximum deviation between experimental and correlated heating value cases also occurs in extremely fuel-rich conditions. Also, like the O_2 and H_2O mole fraction comparisons, the peak graphite mole fraction ranges are very similar between the experimental and correlated heating value cases. The major difference is some slight increase of the peak ranges in most of the correlated heating value cases and a slight decrease in the low temperature Pitt 8 case.

In conclusion, using a correlated heating value with experimentally determined elemental compositions can be different in many respects to cases using experimentally determined heating values and elemental compositions. This is especially true for equilibrium temperature, which is much more dependent on the thermodynamic properties of the fuel (i.e., energies of formation) than on the elemental composition. The mole fractions of O_2, CO_2, CO, H_2O, and graphite are

much less dependent on the thermodynamic properties and more dependent on elemental composition of the fuel. It is preferable to use experimentally determined thermodynamic properties if available, however, correlated values can be used to varying degrees of accuracy when experimentally determined properties are not available.

E.3 Three-Mixture Fraction Results

The three-mixture fraction approach generated a lot of data for each fuel case. Only the case for the experimentally determined elemental composition and thermodynamic properties is presented in Section 8.3.3, however, a few more cases were considered for the three-mixture fraction approach. The complete list of three-mixture fraction fuel cases is shown in Table E-3. Only the low-temperature pyrolysis products (char, tar, and light gases) of the Pitt 8 coal were used in this comparison, along with the simplified hydrocarbon surrogate gases. This was because Proscia et al. (1994) were the only source to report enough information to calculate light gas properties. Benzene was also used as the only tar surrogate in the simple cases.

Table E-3. Complete Three-Mixture Fraction Fuel Cases

Case No.	Char	Tar	Light Gas	ΔH_f	Char Yield	Tar Yield
E3-1	Graphite	Benzene	Methane	-	-	-
E3-2	Graphite	Benzene	Ethane	-	-	-
E3-3	Graphite	Benzene	Ethylene	-	-	-
E3-4	Pitt 8 char	Pitt 8 tar	Pitt 8 light gas	Exp.	0.8509	0.1226
E3-5	Pitt 8 char	Pitt 8 tar	Pitt 8 light gas	Corr.	0.8509	0.1226

Too much data was generated to show in contour or other complete plots; even side-by-side, the different cases have too many data points to observe anything other than the general shapes of the curves (see Figure 8-17 to Figure 8-18). While not always ideal to get a complete picture, a statistical comparison was performed for all three-mixture fraction fuel cases that

considered the experimentally determined Pitt 8 case as the "true" value that all other cases were compared to. Using this kind of comparison shows how the other cases differ from "reality." Such a comparison was performed using both the full and the "viable" data, which are explained in more detail in Section 8.3.3. The full data include all mixing conditions from the extremes of all char, tar, or light gas in the fuel mixture to everything else in between, while the viable data eliminates any mixing conditions that would not be observed in real combustion applications (e.g., only char present in the fuel stream). Figure E-58 shows the five key statistical parameters for the full data comparisons and Figure E-59 shows the same parameters for the viable data comparisons.

While the deviation in temperature between the "true" case and the other fuel cases is consistently poor, the mole fractions of O_2, CO_2, CO, H_2O, and graphite are generally around an order of magnitude better when comparing equilibrium states using experimentally determined

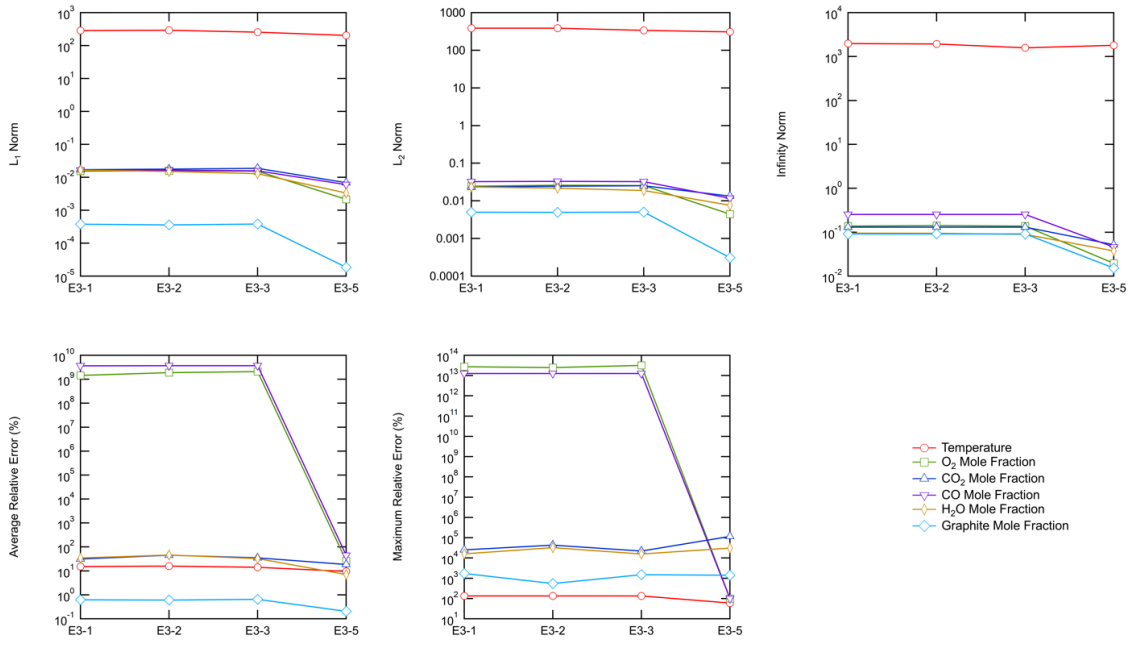

Figure E-58. Comparison of full data of three-mixture fraction fuel cases.

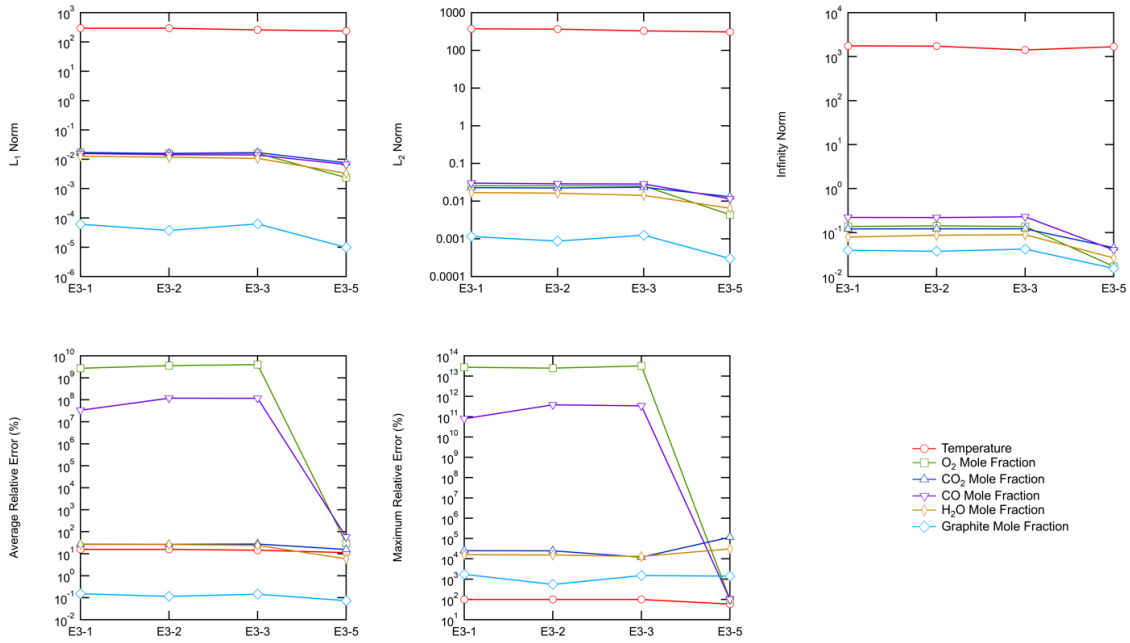

Figure E-59. Comparison of viable data of three-mixture fraction fuel cases.

elemental compositions and correlated heating values than when using simplified hydrocarbon surrogates. In addition, though it is a little more difficult to observe on a log-scale plot, there is some slight improvement made when using certain simplified hydrocarbon surrogates over others. This indicates that if smarter choices are made in choosing simplified surrogates for coal combustion applications, the results might be closer to physical reality. That being said, it is still preferable to use experimentally determined fuel properties if available since that results in large-scale simulations that are much closer to what would be observed in real-world applications.

There is some improvement when using the viable data rather than the full data, which means that some of the worst deviations between the “true” and surrogate cases occur in conditions that would not be observed in industrial coal combustion applications outside of very few specialized research applications. When using three fuel mixture fractions, it is advantageous

to choose mixing conditions wisely in order to minimize both computational complexity and time as well as to minimize the error between the simulation results and real-world observations.

Section 8.3.3 details most of the one-two-three-mixture fraction comparison, however, like the one- and two-mixture fraction comparisons, the results for equilibrium O_2 and graphite mole fractions are not discussed in detail because of the similarity in these products when using different fuels. The full results of the O_2 and graphite mole fractions from the one-two-three-mixture fraction comparison using the Pittsburgh #8 coal are discussed here and shown in Figure E-60.

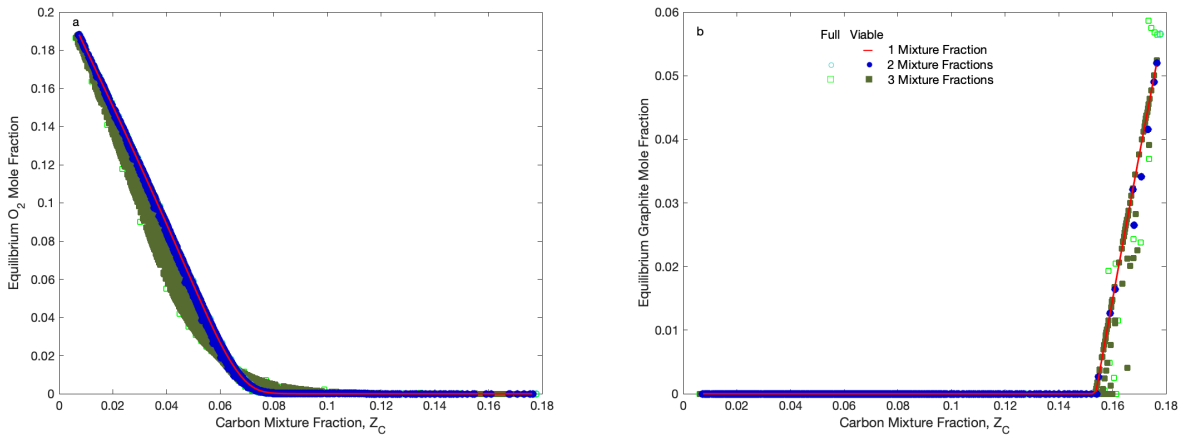

Figure E-60. (a) Equilibrium O_2 and (b) graphite mole fraction calculations by Cantera for the Pitt 8 coal using one, two, and three mixture fractions.

The plots for these two equilibrium products were not included in the main dissertation chapter because there is not enough information to be gained. All three mixture fraction analyses displayed here were performed using the same parent fuel—Pittsburgh #8 coal and its pyrolysis products—which means that the equilibrium calculations using each level of mixture fraction would be very similar. The conclusions reached using equilibrium O_2 and graphite mole fractions

would be very different if comparing between fuel types, like the conclusions reached in the one-mixture fraction comparison.

E.4 Summary and Conclusions

This appendix chapter is intended to supplement and not replace the results and conclusions detailed in Chapter 8, with many of the results and conclusions here supporting those in Chapter 8. However, there are some additional results and conclusions that were not discussed in Chapter 8, mainly being those related to linking the mixture fraction and heating value correlation analyses. This chapter also provides the complete analysis results that were only summarized in Chapter 8.

The main conclusions of this appendix (for the one-, two-, and three-mixture fraction comparisons) deal with comparing experimental to correlated thermodynamic properties (heating values and by extension enthalpies of formation) of coal-based fuels with experimentally determined elemental compositions. In all three mixture fraction comparisons, the correlated heating value cases have potential to act as replacements for most experimental heating value cases, however, the experimental heating values are still preferred if available. In addition, some of the highest- and lowest-rank coal-based fuels were not accurately represented using correlated heating values, particularly in calculating equilibrium temperatures. This indicates that the heating value correlations discussed in Chapter 7 likely need to be improved with additional low- and high-rank coals (lignites/brown coals and anthracites).